

AJNR

AMERICAN JOURNAL OF NEURORADIOLOGY

SEPTEMBER 2014
VOLUME 35
NUMBER 9
WWW.AJNR.ORG

THE JOURNAL OF DIAGNOSTIC AND
INTERVENTIONAL NEURORADIOLOGY

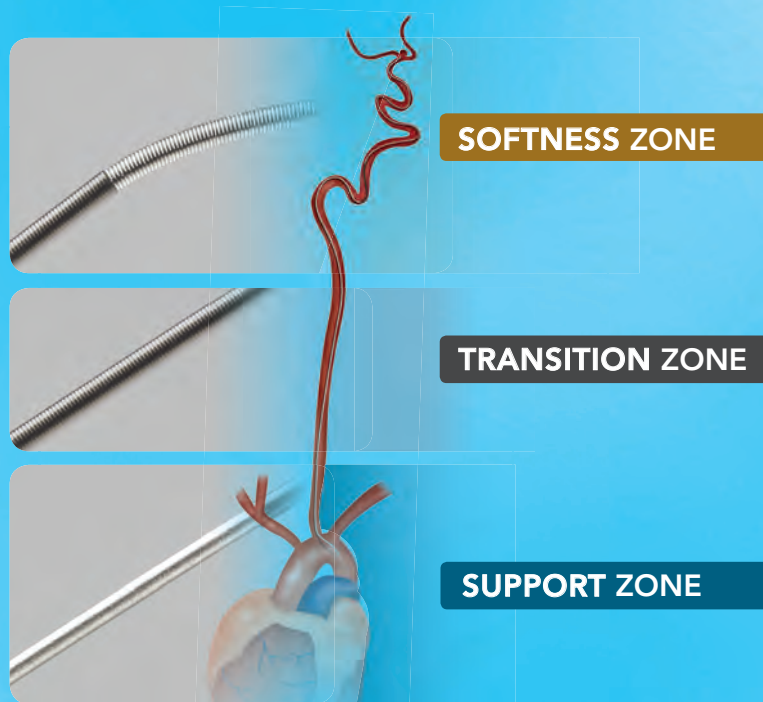
Imaging of facial reanimation procedures
MRA vs. DSA for coiled aneurysm follow-up
CTA in pediatric cervical "seatbelt" injuries

Official Journal ASNR • ASFNR • ASHNR • ASPNR • ASSR



Advanced

by MicroVention



ENHANCED CONTROL TO MAXIMIZE COIL PERFORMANCE

The V-Trak® Advanced Coil System, the next generation to power the performance of our most technically advanced line of coils. Offering the optimal combination of support and flexibility.

microvention.com

MICROVENTION, V-Trak, HyperSoft and Headway are registered trademarks of MicroVention, Inc. Scientific and clinical data related to this document are on file at MicroVention, Inc. Refer to Instructions for Use for additional information. Federal (USA) law restricts this device for sale by or on the order of a physician.
© 2014 MicroVention, Inc. 8/14

Expanded

by MicroVention



Advanced

HyperSoft 3D
complex coil
Advanced

A NEW DIMENSION IN COMPLEX SOFTNESS

MicroVention has expanded the scope of use for the popular HyperSoft® Coil by creating a complex form. This all-in-one hybrid design lets you Frame, Fill and Finish with the softness you need.

- A V-Trak® Advanced Coil for enhanced control
- Used with



For more information or a product demonstration,
contact your local MicroVention representative:



MicroVention, Inc.

Worldwide Headquarters

1311 Valencia Avenue

Tustin, CA 92780 USA

MicroVention UK Limited

MicroVention Europe, S.A.R.L.

MicroVention Deutschland GmbH

PH +1.714.247.8000

PH +44 (0) 191 258 6777

PH +33 (1) 39 21 77 46

PH +49 211 210 798-0



BARRICADETM COIL SYSTEM

PERFORMANCE AND VALUE DELIVERED



BLOCKADE
M E D I C A L

18 TECHNOLOGY DRIVE #169, IRVINE CA 92618 | P 949.788.1443
WWW.BLOCKADEMEDICAL.COM

 MADE IN AMERICA

CE
0297
MKTG-020 REV. B



AJNR

AMERICAN JOURNAL OF NEURORADIOLOGY

SEPTEMBER 2014
VOLUME 35
NUMBER 9
WWW.AJNR.ORG

Publication Preview at www.ajnr.org features articles released in advance of print. Visit www.ajnrblog.org to comment on AJNR content and chat with colleagues and AJNR's News Digest at <http://ajnrdigest.org> to read the stories behind the latest research in neuroimaging.

EDITORIAL




PERSPECTIVES

- 1653 **The Fraud and Retraction Epidemic** *M. Castillo*

REVIEW ARTICLES

-   1655 **MRA Versus DSA for Follow-Up of Coiled Intracranial Aneurysms: A Meta-Analysis** *M.J. van Amerongen, H.D. Boogaarts, J. de Vries, A.L.M. Verbeek, F.J.A. Meijer, M. Prokop, and R.H.M.A. Bartels*
-  1662 **Facial Reanimation Procedures Depicted on Radiologic Imaging** *D.T. Ginat, P. Bhamra, M.E. Cunnane, and T.A. Hadlock*

LEVEL 1 EBM EXPEDITED PUBLICATION

-    1667 **Patients Prone to Recurrence after Endovascular Treatment: Periprocedural Results of the PRET Randomized Trial on Large and Recurrent Aneurysms** *J. Raymond, R. Klink, M. Chagnon, S.L. Barnwell, A.J. Evans, J. Mocco, B.L. Hoh, A.S. Turk, R.D. Turner, H. Desal, D. Fiorella, S. Bracard, A. Weill, F. Guilbert, and D. Roy, on behalf of the PRET Collaborative Group*






RESEARCH PERSPECTIVES









- 1677 **Comparative Effectiveness Research** *J.A. Hirsch, P.W. Schaefer, J.M. Romero, J.D. Rabinov, P.C. Sanelli, and L. Manchikanti*

GENETICS VIGNETTE

- 1681 **Genetics of Ataxias: Hereditary Forms** *N. Tirada and L.M. Levy*

BRAIN

- 1683 **Relative Filling Time Delay Based on CT Perfusion Source Imaging: A Simple Method to Predict Outcome in Acute Ischemic Stroke** *W. Cao, B.C.V. Campbell, Q. Dong, S.M. Davis, and B. Yan*
-  1688 **Early Basal Ganglia Hyperperfusion on CT Perfusion in Acute Ischemic Stroke: A Marker of Irreversible Damage?** *V. Shahi, J.E. Fugate, D.F. Kallmes, and A.A. Rabinstein*
-  1693 **An In Vivo, MRI-Integrated Real-Time Model of Active Contrast Extravasation in Acute Intracerebral Hemorrhage** *R.I. Aviv, T. Huynh, Y. Huang, D. Ramsay, P. Van Slyke, D. Dumont, P. Asmah, R. Alkins, R. Liu, and K. Hynynen*
-  1700 **Brain Changes in Kallmann Syndrome** *R. Manara, A. Salvalaggio, A. Favaro, V. Palumbo, V. Citton, A. Elefante, A. Brunetti, F. Di Salle, G. Bonanni, and A.A. Sinisi, for the Kallmann Syndrome Neuroradiological Study Group*
-   1707 **Quantitative 7T Phase Imaging in Premanifest Huntington Disease** *A.C. Apple, K.L. Possin, G. Satris, E. Johnson, J.M. Lupo, A. Jakary, K. Wong, D.A.C. Kelley, G.A. Kang, S.J. Sha, J.H. Kramer, M.D. Geschwind, S.J. Nelson, and C.P. Hess*

-  Indicates Editor's Choices selection
-  Indicates Fellows' Journal Club selection
-  Indicates open access to non-subscribers at www.ajnr.org
-  Indicates article with supplemental on-line table
-  Indicates article with supplemental on-line photo
-  Indicates article with supplemental on-line video
-  Indicates Evidence-Based Medicine Level 1
-  Indicates Evidence-Based Medicine Level 2



Pipeline device before and after retraction uncovering the ophthalmic artery.



Trevo[®] XP


PROVUE RETRIEVER

Take Control. Capture More.





The newly designed Trevo[®] XP ProVue Retriever takes proven Trevo Retriever performance to new levels for **easy delivery, easy placement, and easy visualization.**

When you're in control, it's amazing what you can capture.

stryker[®]
Neurovascular

-     **1714 Cost-Effectiveness of CT Angiography and Perfusion Imaging for Delayed Cerebral Ischemia and Vasospasm in Aneurysmal Subarachnoid Hemorrhage** P.C. Sanelli, A. Pandya, A.Z. Segal, A. Gupta, S. Hurtado-Rua, J. Ivanidze, K. Kesavabhotla, D. Mir, A.I. Mushlin, and M.G.M. Hunink
-    **1721 Direct Visualization of Anatomic Subfields within the Superior Aspect of the Human Lateral Thalamus by MRI at 7T** M. Kanowski, J. Voges, L. Buentjen, J. Stadler, H.-J. Heinze, and C. Tempelmann
-  **1728 Neuroimaging Features and Predictors of Outcome in Eclamptic Encephalopathy: A Prospective Observational Study** V. Junewar, R. Verma, P.L. Sankhwar, R.K. Garg, M.K. Singh, H.S. Malhotra, P.K. Sharma, and A. Parihar
- 1735 Cranial Arachnoid Protrusions and Contiguous Diploic Veins in CSF Drainage** S. Tsutsumi, I. Ogino, M. Miyajima, M. Nakamura, Y. Yasumoto, H. Arai, and M. Ito
-  **1740 A Novel Technique for the Measurement of CBF and CBV with Robot-Arm-Mounted Flat Panel CT in a Large-Animal Model** O. Beuing, A. Boese, Y. Kyriakou, Y. Deuerling-Zengh, B. Jöllenbeck, C. Scherlach, A. Lenz, S. Serowy, S. Gugel, G. Rose, and M. Skalej

FUNCTIONAL

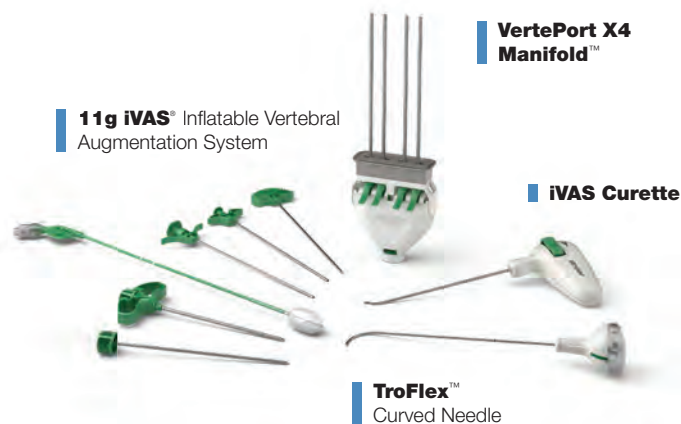
-   **1746 Time-Shift Homotopic Connectivity in Mesial Temporal Lobe Epilepsy** Q. Xu, Z. Zhang, W. Liao, L. Xiang, F. Yang, Z. Wang, G. Chen, Q. Tan, Q. Jiao, and G. Lu
-   **1753 Brain Structure and Function in Patients after Metal-on-Metal Hip Resurfacing** M.J. Clark, J.R. Prentice, N. Hoggard, M.N. Paley, M. Hadjivassiliou, and J.M. Wilkinson

INTERVENTIONAL *Published in collaboration with Interventional Neuroradiology*

-  **1759 Flat Detector Angio-CT following Intra-Arterial Therapy of Acute Ischemic Stroke: Identification of Hemorrhage and Distinction from Contrast Accumulation due to Blood-Brain Barrier Disruption** T. Kau, M. Hauser, S.M. Obmann, M. Niedermayer, J.R. Weber, and K.A. Hausegger
- 1765 Intracranial Aneurysmal Pulsatility as a New Individual Criterion for Rupture Risk Evaluation: Biomechanical and Numeric Approach (IRRAs Project)** M. Sanchez, O. Ecker, D. Ambard, F. Jourdan, F. Nicoud, S. Mendez, J.-P. Lejeune, L. Thines, H. Dufour, H. Brunel, P. Machi, K. Lobotesis, A. Bonafe, and V. Costalat
-   **1772 Effect of Structural Remodeling (Retraction and Recoil) of the Pipeline Embolization Device on Aneurysm Occlusion Rate** L.-D. Jou, B.D. Mitchell, H.M. Shaltoni, and M.E. Mawad
-  **1779 Enhanced Aneurysmal Flow Diversion Using a Dynamic Push-Pull Technique: An Experimental and Modeling Study** D. Ma, J. Xiang, H. Choi, T.M. Dumont, S.K. Natarajan, A.H. Siddiqui, and H. Meng
- 1786 Thromboembolic Complications in Patients with Clopidogrel Resistance after Coil Embolization for Unruptured Intracranial Aneurysms** B. Kim, K. Kim, P. Jeon, S. Kim, H. Kim, H. Byun, J. Cha, S. Hong, and K. Jo
- 1793 Transarterial Onyx Embolization of Cranial Dural Arteriovenous Fistulas: Long-Term Follow-Up** R.V. Chandra, T.M. Leslie-Mazwi, B.P. Mehta, A.J. Yoo, J.D. Rabinov, J.C. Pryor, J.A. Hirsch, and R.G. Nogueira
-  **1798 Preoperative Embolization of Intracranial Meningiomas: Efficacy, Technical Considerations, and Complications** D.M.S. Raper, R.M. Starke, F. Henderson Jr, D. Ding, S. Simon, A.J. Evans, J.A. Jane Sr, and K.C. Liu
-   **1805 Complex Hemodynamic Insult in Combination with Wall Degeneration at the Apex of an Arterial Bifurcation Contributes to Generation of Nascent Aneurysms in a Canine Model** J. Wang, H.-Q. Tan, Y.-Q. Zhu, M.-H. Li, Z.-Z. Li, L. Yan, and Y.-S. Cheng

Your **single source** for the latest in innovative **solutions.**


Introducing **the most complete and least invasive vertebral augmentation portfolios** on the market today.



We are also proud to announce **a new paradigm in radiofrequency ablation.**



HEAD & NECK

- 1813 **Lymphoepithelial Carcinoma of the Salivary Gland: Morphologic Patterns and Imaging Features on CT and MRI** *X. Ban, J. Wu, Y. Mo, Q. Yang, X. Liu, C. Xie, and R. Zhang*
-  1820 **Use of Non-Echo-Planar Diffusion-Weighted MR Imaging for the Detection of Cholesteatomas in High-Risk Tympanic Retraction Pockets** *A. Alvo, C. Garrido, Á. Salas, G. Miranda, C.E. Stott, and P.H. Delano*
- 1825 **Clinical Significance of an Increased Cochlear 3D Fluid-Attenuated Inversion Recovery Signal Intensity on an MR Imaging Examination in Patients with Acoustic Neuroma** *D.Y. Kim, J.H. Lee, M.J. Goh, Y.S. Sung, Y.J. Choi, R.G. Yoon, S.H. Cho, J.H. Ahn, H.J. Park, and J.H. Baek*
- 1830 **Imaging Appearance of the Lateral Rectus–Superior Rectus Band in 100 Consecutive Patients without Strabismus** *S.H. Patel, M.E. Cunnane, A.F. Juliano, M.G. Vangel, M.A. Kazlas, and G. Moonis*

PEDIATRICS

-   1836 **Screening CT Angiography for Pediatric Blunt Cerebrovascular Injury with Emphasis on the Cervical “Seatbelt Sign”** *N.K. Desai, J. Kang, and F.H. Chokshi*

SPINE

- 1841 **Large-Volume Blood Patch to Multiple Sites in the Epidural Space through a Single-Catheter Access Site for Treatment of Spontaneous Intracranial Hypotension** *J. Griauzde, J.J. Gemmete, N. Chaudhary, T.J. Wilson, and A.S. Pandey*

ONLINE FEATURES (www.ajnr.org)

BOOK REVIEWS *R.M. Quencer, Section Editor*

Please visit www.ajnrblog.org to read and comment on Book Reviews.

ASNR 53rd Annual Meeting & The Foundation of the ASNR Symposium 2015



ASNR

CHICAGO ★ 2015

April 25-30, 2015

Sheraton Chicago Hotel & Towers

ASFNR ASHNR ASPNR ASSR SNIS

THE FOUNDATION OF THE ASNR



Abstract Deadline:

Friday, December 12, 2014

Please visit www.asnr.org/2015
for more information

ASNR 2015 Program Chair/President Elect Laurie A. Loevner, MD

Programming developed in cooperation with the:

Society of NeuroInterventional Surgery (SNIS)
Donald F. Frei, Jr. MD

American Society of Functional Neuroradiology (ASFNR)
Pratik Mukherjee, MD, PhD

American Society of Head and Neck Radiology (ASHNR)
Richard H. Wiggins, III, MD

American Society of Pediatric Neuroradiology (ASPNR)
Thierry A.G.M. Huisman, MD

American Society of Spine Radiology (ASSR)
Adam E. Flanders, MD

Health Policy Committee
Robert M. Barr, MD, FACR

Request Programming and Registration Materials for the ASNR 53rd Annual Meeting, Contact:

ASNR 53rd Annual Meeting
c/o American Society of Neuroradiology
800 Enterprise Drive, Suite 205
Oak Brook, Illinois 60523-4216
Phone: 630-574-0220
Fax: 630-574-0661
Email: meetings@asnr.org
Website: www.asnr.org/2015



Scan now to visit our website

Official Journal:

American Society of Neuroradiology
American Society of Functional Neuroradiology
American Society of Head and Neck Radiology
American Society of Pediatric Neuroradiology
American Society of Spine Radiology

EDITOR-IN-CHIEF

Mauricio Castillo, MD

Professor of Radiology and Chief, Division of Neuroradiology, University of North Carolina, School of Medicine, Chapel Hill, North Carolina

SENIOR EDITORS

Harry J. Cloft, MD, PhD

Professor of Radiology and Neurosurgery, Department of Radiology, Mayo Clinic College of Medicine, Rochester, Minnesota

Nancy J. Fischbein, MD

Professor of Radiology, Otolaryngology-Head and Neck Surgery, Neurology, and Neurosurgery and Chief, Head and Neck Radiology, Department of Radiology, Stanford University Medical Center, Stanford, California

Jeffrey S. Ross, MD

Staff Neuroradiologist, Barrow Neurological Institute, St. Joseph's Hospital, Phoenix, Arizona

Pamela W. Schaefer, MD

Clinical Director of MRI and Associate Director of Neuroradiology, Massachusetts General Hospital, Boston, Massachusetts, and Associate Professor, Radiology, Harvard Medical School, Cambridge, Massachusetts

Charles M. Strother, MD

Professor of Radiology, Emeritus, University of Wisconsin, Madison, Wisconsin

Jody Tanabe, MD

Professor of Radiology and Psychiatry, Chief of Neuroradiology, University of Colorado, Denver, Colorado

EDITORIAL BOARD

Ashley H. Aiken, *Atlanta, Georgia*
A. James Barkovich, *San Francisco, California*
Walter S. Bartynski, *Charleston, South Carolina*
Barton F. Branstetter IV, *Pittsburgh, Pennsylvania*
Jonathan L. Brisman, *Lake Success, New York*
Julie Bykowski, *San Diego, California*
Donald W. Chakeres, *Columbus, Ohio*
Alessandro Cianfoni, *Lugano, Switzerland*
Colin Derdeyn, *St. Louis, Missouri*
Rahul S. Desikan, *San Diego, California*
Richard du Mesnil de Rochemont, *Frankfurt, Germany*
Clifford J. Eskey, *Hanover, New Hampshire*
Massimo Filippi, *Milan, Italy*
David Fiorella, *Cleveland, Ohio*
Allan J. Fox, *Toronto, Ontario, Canada*
Christine M. Glastonbury, *San Francisco, California*
John L. Go, *Los Angeles, California*
Wan-Yuo Guo, *Taipei, Taiwan*
Rakesh K. Gupta, *Lucknow, India*
Lotfi Hacein-Bey, *Sacramento, California*
David B. Hackney, *Boston, Massachusetts*
Christopher P. Hess, *San Francisco, California*
Andrei Holodny, *New York, New York*
Benjamin Huang, *Chapel Hill, North Carolina*
Thierry A.G.M. Huisman, *Baltimore, Maryland*
George J. Hunter, *Boston, Massachusetts*
Mahesh V. Jayaraman, *Providence, Rhode Island*
Valerie Jewells, *Chapel Hill, North Carolina*
Timothy J. Kaufmann, *Rochester, Minnesota*
Kenneth F. Layton, *Dallas, Texas*
Ting-Yim Lee, *London, Ontario, Canada*
Michael M. Lell, *Erlangen, Germany*
Michael Lev, *Boston, Massachusetts*
Karl-Olof Lovblad, *Geneva, Switzerland*
Lisa H. Lowe, *Kansas City, Missouri*
Franklin A. Marden, *Chicago, Illinois*
M. Gisele Matheus, *Charleston, South Carolina*
Joseph C. McGowan, *Merion Station, Pennsylvania*
Kevin R. Moore, *Salt Lake City, Utah*
Christopher J. Moran, *St. Louis, Missouri*
Takahisa Mori, *Kamakura City, Japan*

Suresh Mukherji, *Ann Arbor, Michigan*
Amanda Murphy, *Toronto, Ontario, Canada*
Alexander J. Nemeth, *Chicago, Illinois*
Laurent Pierot, *Reims, France*
Jay J. Pillai, *Baltimore, Maryland*
Whitney B. Pope, *Los Angeles, California*
M. Judith Donovan Post, *Miami, Florida*
Tina Young Poussaint, *Boston, Massachusetts*
Joana Ramalho, *Lisbon, Portugal*
Otto Rapalino, *Boston, Massachusetts*
Álex Rovira-Cañellas, *Barcelona, Spain*
Paul M. Ruggieri, *Cleveland, Ohio*
Zoran Rumboldt, *Rijeka, Croatia*
Amit M. Saindane, *Atlanta, Georgia*
Erin Simon Schwartz, *Philadelphia, Pennsylvania*
Aseem Sharma, *St. Louis, Missouri*
J. Keith Smith, *Chapel Hill, North Carolina*
Maria Vittoria Spampinato, *Charleston, South Carolina*
Gordon K. Sze, *New Haven, Connecticut*
Krishnamoorthy Thamburaj, *Hershey, Pennsylvania*
Kent R. Thielen, *Rochester, Minnesota*
Cheng Hong Toh, *Taipei, Taiwan*
Thomas A. Tomsick, *Cincinnati, Ohio*
Aquila S. Turk, *Charleston, South Carolina*
Willem Jan van Rooij, *Tilburg, Netherlands*
Arastoo Vossough, *Philadelphia, Pennsylvania*
Elysa Widjaja, *Toronto, Ontario, Canada*
Max Wintermark, *Charlottesville, Virginia*
Ronald L. Wolf, *Philadelphia, Pennsylvania*
Kei Yamada, *Kyoto, Japan*

EDITORIAL FELLOW

Asim F. Choudhri, *Memphis, Tennessee*

YOUNG PROFESSIONALS ADVISORY COMMITTEE

Asim K. Bag, *Birmingham, Alabama*
Anna E. Nidecker, *Sacramento, California*
Peter Yi Shen, *Sacramento, California*

HEALTH CARE AND SOCIOECONOMICS EDITOR

Pina C. Sanelli, *New York, New York*

Founding Editor

Juan M. Taveras

Editors Emeriti

Robert I. Grossman, Michael S. Huckman,
Robert M. Quencer

Special Consultants to the Editor

Sandy Cheng-Yu Chen, Girish Fatterpekar,
Ryan Fitzgerald, Katherine Freeman,
Yvonne Lui, Greg Zaharchuk

INR Liaisons

Timo Krings, Karel terBrugge

Managing Editor

Karen Halm

Electronic Publications Manager

Jason Gantenberg

Editorial Assistant

Mary Harder

Executive Director, ASNR

James B. Gantenberg

Director of Communications, ASNR

Angelo Artemakis

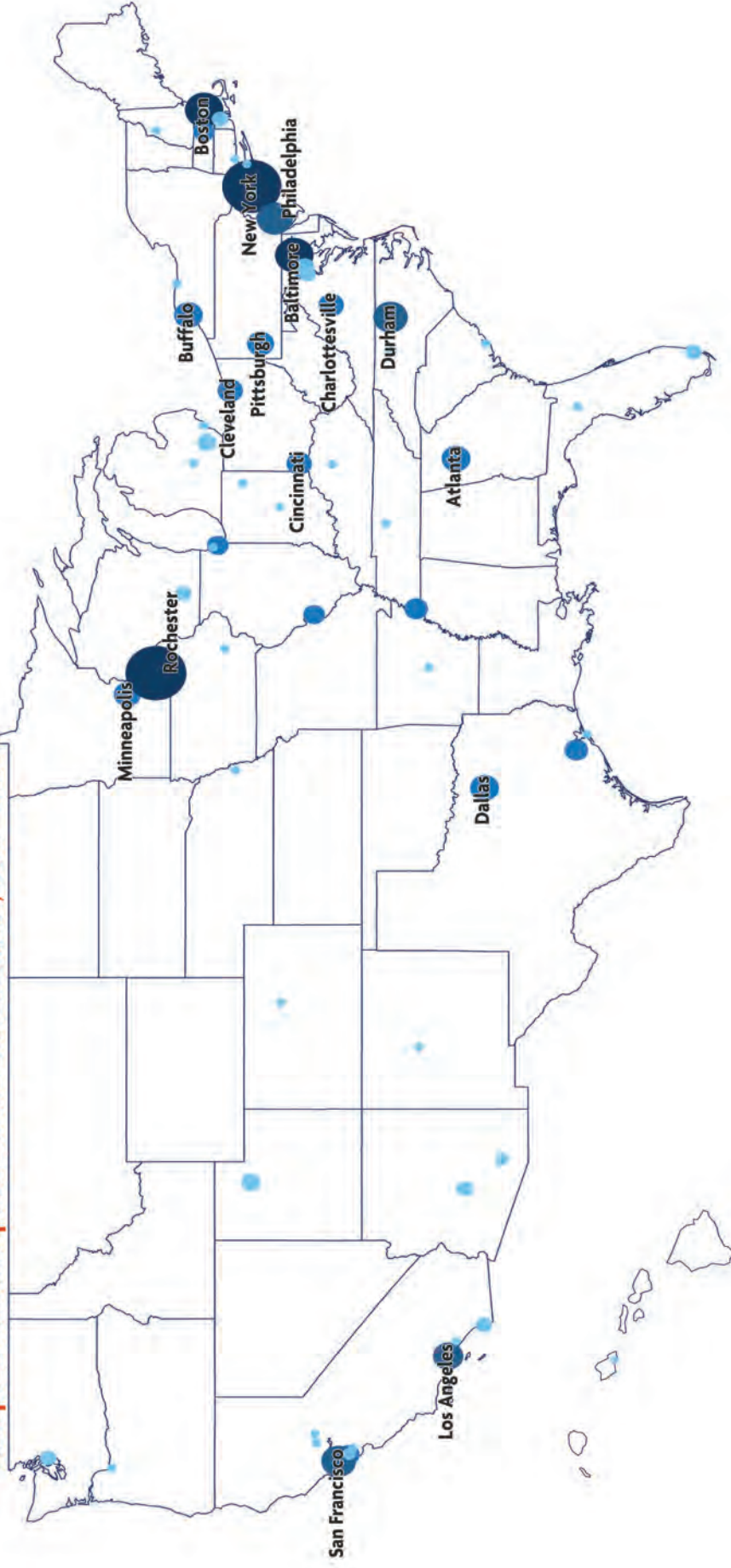
AJNR (Am J Neuroradiol ISSN 0195-6108) is a journal published monthly, owned and published by the American Society of Neuroradiology (ASNR), 800 Enterprise Drive, Suite 205, Oak Brook, IL 60523. Annual dues for the ASNR include \$170.00 for journal subscription. The journal is printed by Cadmus Journal Services, 5457 Twin Knolls Road, Suite 200, Columbia, MD 21045; Periodicals postage paid at Oak Brook, IL and additional mailing offices. Printed in the U.S.A. POSTMASTER: Please send address changes to American Journal of Neuroradiology, P.O. Box 3000, Denville, NJ 07834, U.S.A. Subscription rates: nonmember \$370 (\$440 foreign) print and online, \$300 online only; institutions \$430 (\$495 foreign) print and basic online, \$850 (\$915 foreign) print and extended online, \$355 online only (basic), extended online \$770; single copies are \$35 each (\$40 foreign). Indexed by PubMed/Medline, BIOSIS Previews, Current Contents (Clinical Medicine and Life Sciences), EMBASE, Google Scholar, HighWire Press, Q-Sensei, RefSeek, Science Citation Index, and SCI Expanded. Copyright © American Society of Neuroradiology.



PUBLICATION METRICS

AMERICAN JOURNAL OF NEURORADIOLOGY

Accepted Manuscripts from the United States, 2012 – 2014



The Fraud and Retraction Epidemic

M. Castillo, *Editor-in-Chief*

A recent article in the *Proceedings of the National Academy of Science (PNAS)* examines the cause of retractions involving more than 2000 articles published in biomedical and life-science-related journals.¹ Of these, nearly 70% were retracted due to author misconduct, with the most common problem being suspected fraud (43.4%), followed by duplications and plagiarism. When compared with data obtained in 1975, the incidence of misconduct-related retractions has increased 10-fold.

Overall, misconduct-related retractions involve only a tiny portion of the more than 25 million articles housed on PubMed. The issue is not that the number of retractions is small but that their number is increasing considerably and rapidly. Exactly how many articles are retracted due to misconduct is difficult to establish as published retraction notices are often vague and unclear as to the cause of the problem (estimates place the figure at 0.2% of 1.4 million articles annually published). Whereas from 2002 to 2006 fraud-related article retractions were 20% higher than error-related ones, from 2007 to 2011 error-related retractions were less than 40% of fraud-related ones.¹

It is hard not to point fingers; most fraud-related retractions come from our own backyard: the United States (probably reflecting the fact that about 26% of all scientific publications originate here). China and India account for the most retractions due to duplications and plagiarism (probably reflecting difficulties with the use of English). China's share of scientific publications went up from 4.4% to 10.2% from 2003 to 2008, while those from the United States and United Kingdom went down, positioning China to become the largest source of origin in science in the near future.

Another interesting observation made by Fang et al¹ refers to the quality of journals in which most retractions happen. There was a direct correlation between Impact Factor (IF) and retraction numbers. Prestigious journals such as *Science* (IF: 31.2), *PNAS* (IF: 9.68), and *Nature* (IF: 36.28) have the most retracted articles, while 16 journals with IFs less than 3 (as is the *American Journal of Neuroradiology [AJNR]*) had none (in my time as Editor-in-Chief, only 1 *AJNR*-related article had to be retracted, and this was actually done by another journal because the original appearance of the duplicated article was published by us). Because retractions are generally initiated by journal editors and some may not wish to accept the mistake of publishing a fraudulent article, many articles that should be retracted are not and remain viable and gain citations. Thus, the current number of retractions is probably underestimated.

Stephen Breuning was the assistant director of the largest institution for the mentally impaired in Pennsylvania. In 1983, it was discovered that he falsified data presented in a symposium abstract, which led the National Institute of Mental Health to

review his publications, reaching a conclusion that 24 of 25 were fraudulent.² Surprisingly, only 3 were retracted at that time, and 24 years later, a study showed that they continue to be cited even by prestigious journals such as the *British Journal of Psychiatry* (IF: 6.61).³ In another study, 235 retracted articles accumulated 2034 citations, and depending on how the data were analyzed, the retractions were acknowledged in only 6.4%–7.7% of the journals.⁴ Also, “infamous” articles may be quoted more often than “famous” ones. On the Scholarly Kitchen Web site* (<http://scholarlykitchen.sspnet.org>), Kent Anderson said about retractions: “In high impact journals, there is no reason to believe that these citations don't contribute their fair share to the impact factor. After all, an infamous paper may be more readily cited because it's top of mind for a busy author.”⁵ (This is a common joke among journal editors: if you want your IF to go up, publish a fraudulent article!)

If we have the IF, the *h*-index, and other metrics, why not have a retraction factor? Drs Ferric Fang and Arturo Casadevall, editors of *Infection and Immunology* (IF: 4.16) and *mBio* (IF: 5.3), respectively, set out to do this. Fang and Casadevall⁶ simply took the number of retractions per journal from 2001 to 2010 and divided it by the total number of articles appearing on PubMed during the same period. Because the number of retractions tends to be small, they multiplied their results by 1000 to obtain whole numbers. This recent article pointed out again that retractions occur more often in higher IF journals. In a different article, the policies on retractions found in major biomedical journals were studied.⁷ For this investigation, the author selected the 122 journals with the highest IFs and found that 62% did not have a formal policy regarding retractions (*AJNR* does and it can be found at <http://www.ajnr.org/site/misc/ifora.xhtml#dupl>). In August 2012, *The Scientist* published an opinion piece calling for a “transparency index” similar in spirit to the IF.⁸ The authors suggested that this index should include the following: the article review protocol of the journal (*AJNR* has one), whether underlying data are made available (*AJNR* does not unless something is called into question), whether the journal uses plagiarism-detection software (yes, *AJNR* does this), whether a mechanism for dealing with fraud issues exists (see the Web address above for the policy of *AJNR*), and whether corrections and retractions are as clear as possible (I believe ours are).

Older research told us that retractions took some time to take place; an observation that no longer holds true as seen in a recent investigation.⁹ In that study, the entire universe of biomedical literature between 1972 and 2006 was examined. While other investigations have used loose controls, in this one, the authors chose as controls only articles published immediately before and after a retraction and in the journal where the fraud had occurred. Let me spend a few lines here because their results were very interesting. They found that most fraudulent articles were authored by top researchers at US universities and that retracted articles were likely to be highly cited in their first year. However, they also found some good and honest things that happen after retractions: The system is fast with nearly 50% of retractions occurring 2 years postpublication (and it seems that this delay is getting shorter

<http://dx.doi.org/10.3174/ajnr.A3835>

with time), retractions are unbiased, and the effects of retractions are severe and long-lived (citations for retractions were down 72% by 10 years). Most retractions are American articles, and the number of retractions reported by journals published outside the United States is small. Does this imply that research done elsewhere is more honest? I believe that this is not the case and that foreign journals perhaps have less well-established policies and procedures on retractions and/or pay less attention to this problem.

If you want to be entertained (not to say amazed or even disgusted) by the retraction epidemic, I suggest visiting the Retraction Watch Web site (<http://retractionwatch.wordpress.com>). This is a moderated blog that reports instances of fraud and allows visitors to comment. Recently posted, there is a new twist: retraction of an article “in press,” meaning that its final version was not yet available and that it had not been assigned space (issue, pages) in the journal.¹⁰ The implication is that fraud is occurring and being detected even at the preliminary submission stage. As in many other cases, the reason for this retraction was opaque and listed as “article withdrawn at the request of the authors and editor.”

However, all of this should not come as a surprise. An article by John Ioannidis, a meta-researcher who specializes in this sort of thing, states that 80% of nonrandomized studies (the most common type published) are eventually proved wrong as are 25% of randomized trials and 10% of large multi-institutional randomized ones.¹¹ He has been able to identify the characteristics of articles that make them more likely to contain false information: small populations, small overall effect on science, financial interests, and a “hotter” field, among others. All of these features contribute to eventual retractions. Dr Ioannidis said, “At every step in the process, there is room to distort results, a way to make a stronger claim or to select what is going to be concluded.”¹²

As shown in 2 cases just last year, the retraction (and fraud) epidemic continues and is growing. The first case involved the dean of the School of Social and Behavioral Sciences at Tilburg University in the Netherlands.¹³ His studies involved the effects of trash-ridden environments and eating meat on behavior, and some were published in *Science*. Dr Stapel’s deception was driven (according to him) by his “quest for beauty—instead of truth.” People like him, obsessed by order and symmetry, have difficulty accepting the often messy results of research. A university committee concluded that 55 of his articles were fraudulent, and he is now being investigated for misuse of public funds given to him in the form of grants.

In the second case, Dr Yoshitaka Fujii, a researcher and anesthesiologist from the University of Tsukuba in Japan went on for years publishing fraudulent articles.¹⁴ The first allegations of fraud came in 2000, and by 2012, a panel of investigators had concluded that he had been publishing falsified data since 1993. In April 2012, twenty-three journals publicly requested that the Japanese Society of Anesthesiology investigate Dr Fujii. By June, a

commission had found that 172 of his articles contained some fabricated data, and of these, 126 were “totally fabricated.”

This last example is the largest case of scientific fraud to date, and I am sure that, unfortunately, it will not be the last. In 1 survey, 2% of academics admitted to falsifying or fabricating data and 28% claimed to know colleagues who had done it.¹⁵

*The Scholarly Kitchen is a moderated blog established by the Society for Scholarly Publishing to “advance communication through education and networking.” It is a must for anyone interested in scientific publication.

REFERENCES

1. Fang FC, Steen RG, Casadevall A. **Misconduct accounts for the majority of retracted scientific publications.** *Proc Natl Acad Sci U S A* 2012;109:17028–33
2. Boffey PM. **US study finds fraud in top researcher’s work on mentally retarded.** *The New York Times*. May 24, 1987. <http://www.nytimes.com/1987/05/24/us/us-study-finds-fraud-in-top-researcher-s-work-onmentally-retarded.html?src=pm>. Accessed November 5, 2013
3. Korpela KM. **How long does it take for the scientific literature to purge itself of fraudulent material?: The Breuning case revisited.** *Curr Med Res Opin* 2010;26:843–47
4. Budd JM, Sievert ME, Schultz TR, et al. **Effects of article retraction on citation and practice in medicine.** *Bull Med Libr Assoc* 1999; 87:437–43
5. Anderson K. Mountains out of molehills and the search for a retraction index. September 2011. <http://scholarlykitchen.sspnet.org/2011/09/01/mountains-out-of-molehills-and-the-search-for-a-retraction-index>. Accessed November 5, 2013
6. Fang FC, Casadevall A. **Retracted science and the retraction index.** *Infect Immun* 2011;79:3855–59
7. Atlas MC. **Retraction policies of high-impact biomedical journals.** *J Med Libr Assoc* 2004;92:242–50
8. Marcus A, Oransky I. **Bring on the transparency index.** *The Scientist*. August 1, 2012. <http://www.the-scientist.com/?articles.view/articleNo/32427/title/Bring-On-the-Transparency-Index>. Accessed November 5, 2013
9. Furman JL, Jensen K, Murray F. **Governing knowledge in the scientific community: exploring the role of retractions in biomedicine.** *Research Policy* 2012;41:276–90
10. Is an “article in press” “published?” A word about Elsevier’s withdrawal policy. Retraction Watch. <http://retractionwatch.com/2013/02/25/is-an-article-in-press-published-a-word-about-elseviers-withdrawal-policy>. Accessed November 5, 2013
11. Ioannidis JPA. **Why most published research findings are false.** *PLoS Med* 2005;2:e124
12. Freedman DH. **Lies, damned lies, and medical science.** *The Atlantic*. November 2010. <http://www.theatlantic.com/magazine/archive/2010/11/lies-damned-lies-and-medical-science/308269>. Accessed November 5, 2013
13. Bhattacharjee Y. **The mind of a con man.** *The New York Times*. April 26, 2013. http://www.nytimes.com/2013/04/28/magazine/diederik-stapels-audacious-academic-fraud.html?pagewanted=9&_r=1&src=dayp. Accessed November 5, 2013
14. Yoshitaka Fujii. http://en.wikipedia.org/wiki/Yoshitaka_Fujii. Accessed November 5, 2013
15. Fanelli D. **How many scientists fabricate and falsify research? A systematic review and meta-analysis of survey data.** *PLoS One* 2009;4:e5738

MRA Versus DSA for Follow-Up of Coiled Intracranial Aneurysms: A Meta-Analysis

M.J. van Amerongen, H.D. Boogaarts, J. de Vries, A.L.M. Verbeek, F.J.A. Meijer, M. Prokop, and R.H.M.A. Bartels



ABSTRACT

SUMMARY: MR angiography is proposed as a safer and less expensive alternative to the reference standard, DSA, in the follow-up of intracranial aneurysms treated with endovascular coil occlusion. We performed a systematic review and meta-analysis to evaluate the accuracy of TOF-MRA and contrast-enhanced MRA in detecting residual flow in the follow-up of coiled intracranial aneurysms. Literature was reviewed through the PubMed, Cochrane, and EMBASE data bases. In comparison with DSA, the sensitivity of TOF-MRA was 86% (95% CI: 82–89%), with a specificity of 84% (95% CI: 81–88%), for the detection of any recurrent flow. For contrast-enhanced MRA, the sensitivity and specificity were 86% (95% CI: 82–89%) and 89% (95% CI: 85–92%), respectively. Both TOF-MRA and contrast-enhanced MRA are shown to be highly accurate for detection of any recanalization in intracranial aneurysms treated with endovascular coil occlusion.

ABBREVIATIONS: CE = contrast-enhanced; GRADE = grades of recommendation, assessment, development, and evaluation; SROC = summary receiver operating characteristic

The prevalence of unruptured intracranial aneurysms in the world population is approximately 2–3%.^{1,2} The current standard treatment to eliminate the risk of (re)bleeding is exclusion of the aneurysm from the intracranial circulation by use of endovascular detachable coil occlusion.³ However, recurrences occur in approximately 20% of treated patients, leading to a need for retreatment in approximately 9% of all cases.⁴

DSA is the reference standard for evaluating aneurysms after coiling. However, this technique exposes patients to risks such as cerebral thromboembolism, contrast nephrotoxicity, and ionizing radiation. The transient neurologic complication rate after DSA has been reported to be in the range of 0.34–1.3%, with a risk for permanent neurologic complications of 0.5%. This risk accumulates because repeated follow-ups are necessary.^{5–7}

MRA can be used for follow-up of coiled intracranial aneurysms, with TOF and contrast-enhanced (CE) MRA being the most commonly used techniques currently available. MRA eliminates the risks of cerebral thromboembolism and ionizing radiation. There is, however, a continuing debate about which of these

2 MRA techniques is best suited for aneurysm follow-up. The systematic review and meta-analysis performed by Kwee and Kwee⁸ in 2007 compared TOF-MRA and CE-MRA with DSA for follow-up of coiled aneurysms. The analysis revealed a moderate to high diagnostic performance of both MRA techniques. Because of the moderate methodologic quality of the studies available at the time, Kwee and Kwee⁸ could not conclude whether MRA can replace DSA as the standard method of reference. Since then, the number of studies on this subject has more than doubled, and study setup and statistical methodology have substantially improved.

The goal of the current study is to systematically review the medical literature to establish whether TOF-MRA and CE-MRA can now be considered good enough for follow-up of patients with coiled intracranial aneurysms.

MATERIALS AND METHODS

Data Sources

The medical literature comparing MRA and DSA for evaluating intracranial aneurysms after coiling was reviewed through the use of a variety of data bases—PubMed, EMBASE, and the Cochrane Library—and was updated until March 2012 (On-line Table 1).

Study Selection

After an initial search of the literature by an experienced librarian, duplicate publications were removed. From the pooled list of publications, 2 researchers (M.J.v.A. and H.D.B.) independently reviewed the titles and abstracts of the articles. Studies were ex-

From the Departments of Neurosurgery (M.J.v.A., H.D.B., J.d.V., R.H.M.A.B.), Epidemiology and Biostatistics (A.L.M.V.), and Radiology/Neuroradiology (F.J.A.M., M.P.), Radboud University Nijmegen Medical Centre, Nijmegen, The Netherlands.

Please address correspondence to Hieronymus D. Boogaarts, MD, Department of Neurosurgery, Radboud University Nijmegen Medical Centre, Reinier Postlaan 4, PO Box 9101, 6500 HB, Nijmegen, The Netherlands; e-mail: h.boogaarts@nch.umcn.nl

Indicates open access to non-subscribers at www.ajnr.org

Indicates article with supplemental on-line tables

<http://dx.doi.org/10.3174/ajnr.A3700>

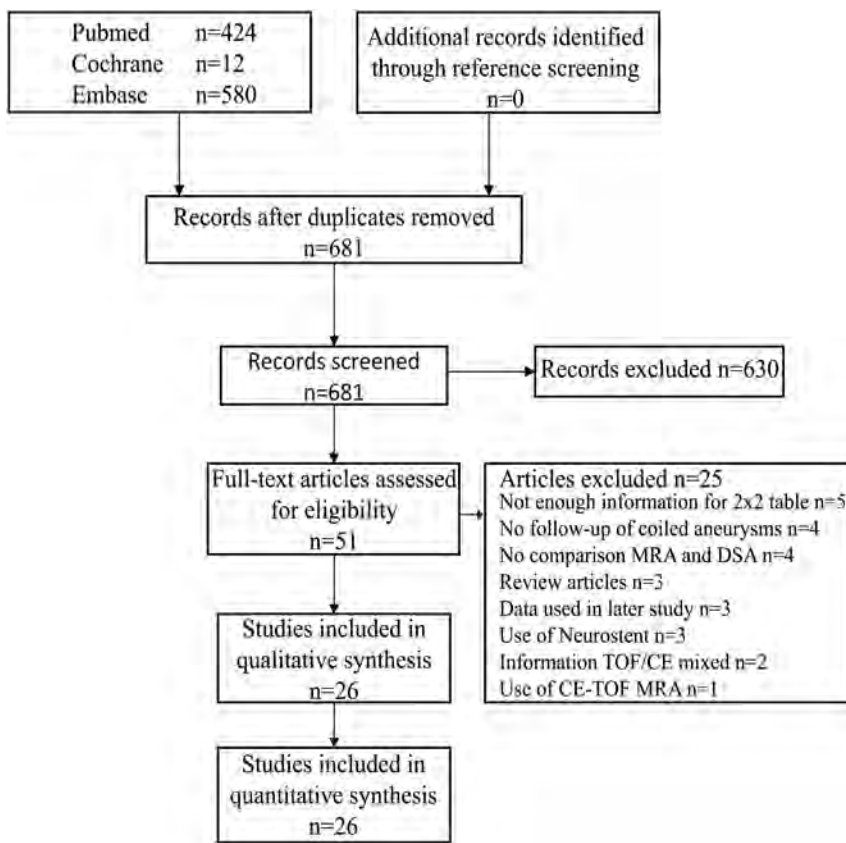


FIG 1. Search results.

cluded if they did not compare MRA with DSA for follow-up of patients with intracranial aneurysms treated with endovascular coil occlusion. Conference abstracts, reviews, editorials, meta-analyses, and animal studies were also excluded. Only articles in English were screened. From the remaining articles, full-text versions were obtained and were independently evaluated by the same researchers (M.J.v.A. and H.D.B.). Studies were eligible for inclusion if they 1) evaluated MRA and DSA for follow-up of patients with intracranial aneurysms treated with endovascular coil occlusion; 2) contained data for 2×2 contingency tables; 3) used the Raymond et al classification or other compatible scales to grade recurrent flow in intracranial aneurysms⁹⁻¹¹; 4) analyzed TOF and CE MRA separately; and 5) provided data that excluded stent-assisted coiling of intracranial aneurysms. If the same data were used in more than 1 article, the most recent version was included. If the 2 researchers disagreed about selection of articles, an independent third reviewer (R.H.M.A.B.) decided the outcome.

Study Quality

The Grades of Recommendation, Assessment, Development, and Evaluation (GRADE) method was used to assess the methodologic quality of the studies included in this review.¹²⁻²² The studies were independently assessed by the 2 researchers (M.J.v.A. and H.D.B.) for limitations, indirectness, inconsistency, imprecision, and publication bias. Agreement between the researchers was quantified by use of Cohen κ .²³ In the case of disagreement, a third reviewer (R.H.M.A.B.) made the final decision.

Data Analysis

The *Meta-DiSc* software (http://www.hrc.es/investigacion/metadisc_en.htm) and SPSS statistical package (version 19.0.0; IBM, Armonk, New York) were used for statistical analysis.²⁴ To evaluate effect size, 2×2 contingency tables were constructed from the articles comparing MRA and DSA. If the true-positive rate, false-positive rate, true-negative rate, or false-negative rate was zero, a standard correction of 0.5 was added to all of the cells of the contingency table. Pooled sensitivity and specificity with 95% confidence intervals were constructed. Data about the accuracy of MRA for grading recurrent flow, as defined by Raymond et al,⁹⁻¹¹ were extracted if available. Classification scales that were compatible with Raymond et al were also utilized, meaning that the findings could be assigned to 1 of the following categories: complete occlusion; residual neck (1–3 mm); and residual aneurysm (>3 mm). Results were depicted in a Forest plot and a summary receiver operating characteristic (SROC) curve. An SROC curve plots the positive rate against the false-positive rate of a diagnostic test at the different possible cut-

points. Heterogeneity between the studies was examined by use of the I^2 test. As an indicator of low heterogeneity, a percentage <40% was taken.²⁰

RESULTS

Included Studies

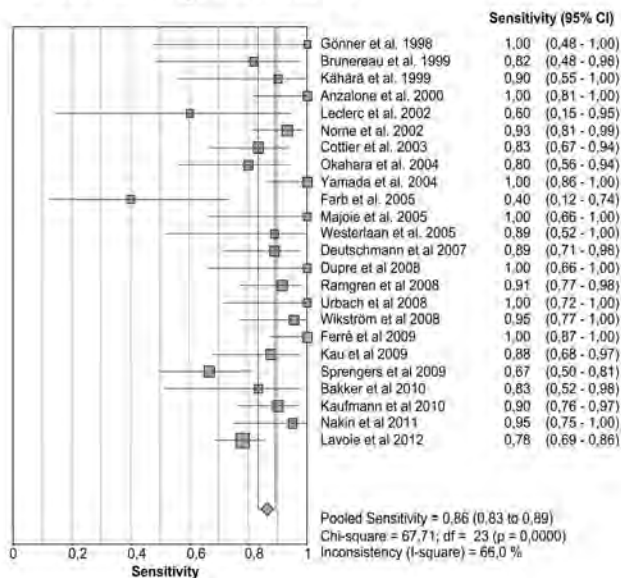
Our search string found 424 studies in PubMed, 12 in Cochrane, and 580 articles in EMBASE (On-line Table 1). A total of 681 studies remained after removal of duplicates. After screening titles and abstracts, 51 articles were deemed fit for full-text evaluation.²⁵⁻⁷⁵ No new articles were found by screening their references. After evaluation of the full-text versions, 3 articles were excluded because they were review papers.^{37,51,58} Another 5 studies were omitted because they did not provide enough data for the 2×2 contingency tables.^{31,45,46,50,53} Four further studies were left out because they did not compare MRA with DSA,^{34,65,72,73} and another 4 were not studying intracranial aneurysms treated with endovascular coil occlusion.^{47,49,57,67} Two articles were excluded because information about TOF-MRA and CE-MRA could not be separated.^{25,71} One article was excluded because it used CE-TOF-MRA.³⁰ Another 3 articles were excluded because their data were used in earlier studies.^{35,41,44} Three studies included patients who had been treated with a secondary Neuroform stent (Stryker Neurovascular, Fremont, California) and were thus omitted (Fig 1).^{52,54,63} This left 26 studies that were eligible for inclusion (Fig 1) (On-line Table 2).^{26-29,32,33,36,38-40,42,43,48,55,56,59-62,64,66,68-70,74,75} Of these articles, 24 researched TOF-MRA^{26-29,32,33,36,38-40,42,43,48,55,60-62,64,66,68-70,74,75} and 14 researched CE-MRA.^{29,32,36,40,42,56,59,60,62,66,68,70,74,75}

Table 1: Pooled sensitivity and specificity for MRA versus DSA

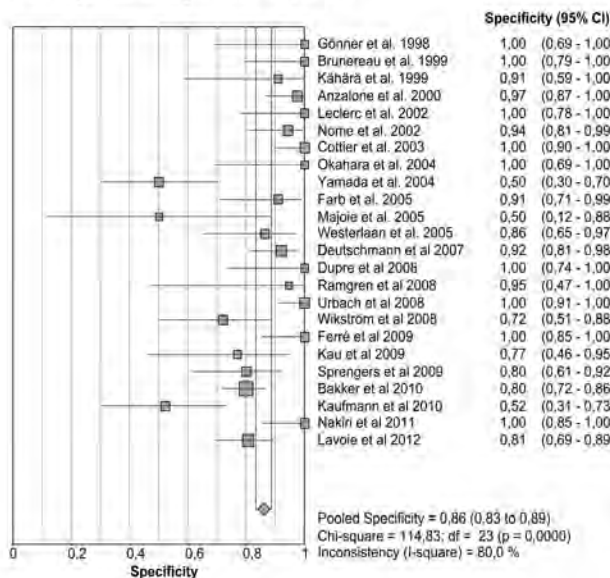
	TOF-MRA				CE-MRA			
	Sensitivity	Specificity	Positive LR	Negative LR	Sensitivity	Specificity	Positive LR	Negative LR
Any recanalization	86% (83–89%)	86% (83–89%)	6.3 (4.1–9.8)	0.17 (0.11–0.25)	85% (81–89%)	88% (84–91%)	6.2 (3.6–10.6)	0.16 (0.08–0.33)
Residual neck	78% (71–84%)	93% (90–95%)	9.6 (4.5–20.6)	0.29 (0.19–0.46)	56% (41–70%)	91% (84–95%)	6.3 (1.8–22.5)	0.40 (0.15–1.08)
Residual aneurysm	83% (77–88%)	96% (94–97%)	21.4 (10.5–43.7)	0.21 (0.13–0.35)	77% (68–85%)	90% (86–94%)	7.5 (3.8–14.7)	0.29 (0.18–0.48)

Note:—Percentages are shown with 95% confidence intervals in parentheses; LR indicates likelihood ratio.

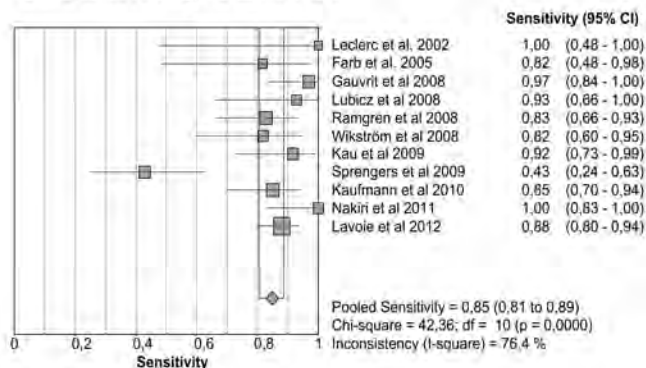
A: Sensitivity TOF-MRA



B: Specificity TOF-MRA



C: Sensitivity CE-MRA



D: Specificity CE-MRA

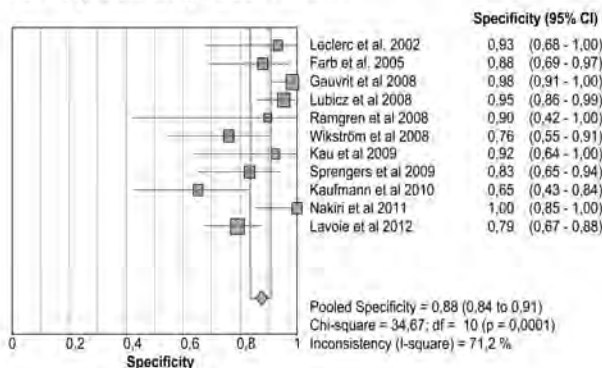


FIG 2. Pooled sensitivity/specificity in detecting any recurrent flow. A, Sensitivity for TOF-MRA. B, Specificity for TOF-MRA. C, Sensitivity for CE-MRA. D, Specificity for CE-MRA.

Twelve studies assessed both TOF-MRA and CE-MRA for the detection of recanalization in coiled intracranial aneurysms in the same subjects.^{29,32,36,40,42,60,62,66,68,70,74,75}

Study Quality Assessment

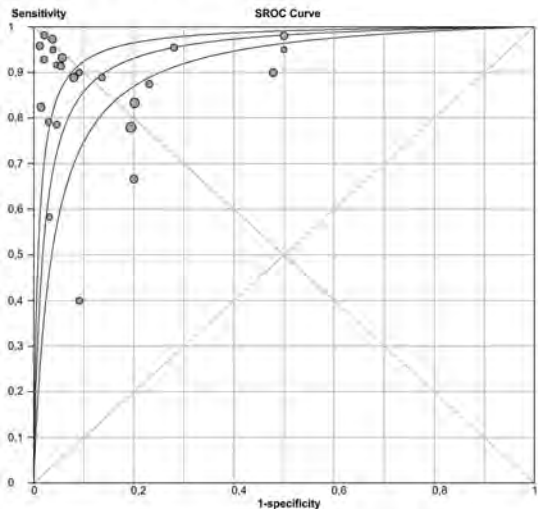
We analyzed the methodologic quality of the 26 articles included in our review according to the GRADE criteria (On-line Table 3).¹²⁻²² There was disagreement between the assessments by the 2 researchers with respect to 5 of 104 GRADE scores, resulting in a Cohen κ of 0.81. All of the articles comprised valid studies comparing MRA with the reference standard (DSA). Because of this validity, all of the studies started with a maximal quality score of 4.¹² None of the articles gave any indication that they contained

serious inconsistencies or were imprecise.¹²⁻²² Two studies were rated down because of indirectness; they did not provide enough information concerning their MRA techniques or only included anterior communicating artery aneurysms.^{28,32} Quality was rated down in 14 studies because of the following major limitations: the studies did not include consecutive patients, the studies were not prospective, or there was no blinding of the researchers.^{26,29,33,36,38-40,43,55,59,60,62,68,70}

Data Analysis

The pooled results for the sensitivity and specificity of TOF-MRA and CE-MRA are presented in Table 1. The sensitivity and specificity for the detection of any recanalization, meaning residual

A: SROC TOF-MRA



B: SROC CE-MRA

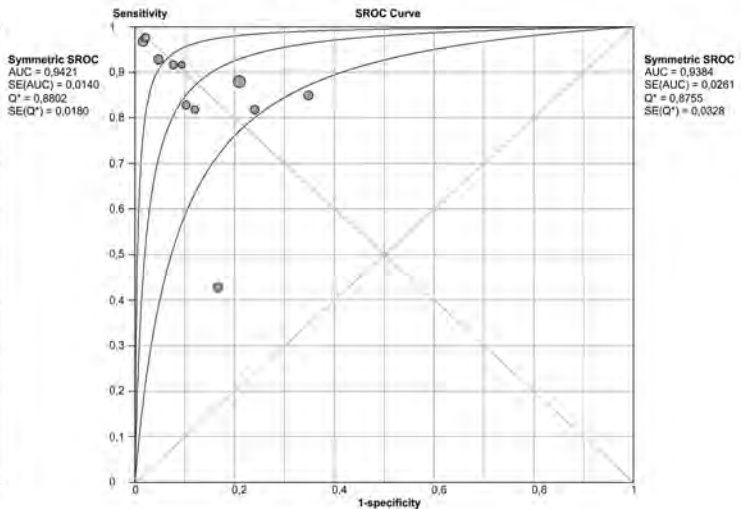


FIG 3. A, Summary receiver operating characteristic for TOF-MRA. B, Summary receiver operating characteristic for CE-MRA.

Table 2: Subclasses of sensitivity and specificity in TOF-MRA and CE-MRA

	TOF-MRA		CE-MRA	
	Sensitivity (95% CI)	Specificity (95% CI)	Sensitivity (95% CI)	Specificity (95% CI)
Retrospective	90% (85–94%)	87% (82–91%)	93% (85–97%)	95% (90–98%)
Prospective	85% (81–88%)	86% (82–89%)	82% (77–87%)	82% (75–87%)
2D DSA	85% (82–89%)	91% (88–93%)	80% (74–85%)	82% (76–88%)
3D DSA	90% (84–95%)	76% (70–82%)	92% (86–96%)	93% (88–96%)
1–1.5T	86% (83–89%)	85% (81–88%)	89% (84–92%)	87% (83–91%)
3T	88% (82–92%)	87% (80–92%)	79% (71–86%)	83% (74–91%)
GRADE 2–3	87% (82–90%)	86% (81–89%)	77% (70–84%)	85% (79–90%)
GRADE 4	86% (81–90%)	87% (83–90%)	92% (86–95%)	90% (85–94%)
Weighted results	86% (85–88%)	86% (85–88%)	87% (85–89%)	88% (86–90%)

Percentages are shown with 95% confidence intervals in parentheses.

neck or residual aneurysm, are shown in Fig 2A–D. TOF-MRA had both a pooled sensitivity and specificity of 86% (95% CI: 83–89%). Pooled sensitivity and specificity of CE-MRA were 85% (95% CI: 81–89%) and 88% (95% CI: 84–91%), respectively. SROC curves are displayed in Fig 3A,–B for TOF-MRA and CE-MRA. As shown in Fig 2A–D, the results were subject to heterogeneity, with I^2 values ranging between 66–80%. For subanalysis, different study variables were distinguished: retrospective versus prospective studies, 2D versus 3D DSA, different MR field strengths, GRADE criteria, and weighted results according to GRADE (Table 2).

DISCUSSION

The results of our meta-analysis reveal that MRA now has a high degree of sensitivity and specificity in detecting any recanalization during the follow-up of coiled intracranial aneurysms. However, a subanalysis for residual neck or residual aneurysm (Raymond scale 2 or 3, respectively) revealed lower sensitivity and specificity of both MRA techniques compared with DSA as the reference standard (Table 1). A possible explanation is the small number of studies and patients included therein, which is reflected in the large 95% confidence intervals. Another potential explanation is false-positive findings seen on DSA possibly caused by pulsation artifacts.⁴⁸ However, this comparison makes MRA the reference standard compared with DSA. Because our study compared MRA

with the reference standard, DSA, these cases also were judged in favor of DSA. This results in false-negative values for the MRA and a lower sensitivity.

This subanalysis also showed lower sensitivities of the CE-MRA compared with the TOF-MRA for the detection of residual neck or residual aneurysm. The contrast timing together with the narrow interval of scanning in CE-MRA might be the cause of this lower sensitivity. The short time window between the arterial and venous phase of contrast enhancement to avoid venous enhancement and vessel overlap lowers the spatial resolution.⁶⁰ Additionally, the acquisition time for TOF-MRA is much longer compared with CE images, leading to improved resolution. The disadvantage of TOF-MRA is its limited coverage; however, TOF is adequate for the evaluation of intracranial vessels. Suboptimal imaging in CE-MRA may therefore lead to more false-negative values, especially in small remnants, lowering the sensitivity.

Significant sources of heterogeneity in this meta-analysis are variations in study design and reporting of data. Evaluation of the studies revealed 5 possible explanations for this heterogeneity: 1) Publication bias remains a potential cause of heterogeneity, because articles with better results are more likely to be published than studies with insignificant or negative findings. 2) Not all of the studies had a prospective design and enrolled patients consec-

utively, which can be a cause of bias.⁷⁶ Sixteen of the 26 were prospective^{27,28,32,36,38,42,55,60-62,64,68-70,74,75}; only 12 studies included consecutive patients.^{28,32,42,48,56,60,61,64,66,69,74,75} Retrospective studies tended to be better, with low heterogeneity, compared with the results of the prospective studies, though these findings were not statistically significant (Table 2). 3) For the reference standard, 8 reference studies used 3D (rotational) DSA for comparison to MRA,^{38,39,56,59,66,69,70,74} whereas the other studies used 2D DSA. Because 3D DSA is better at evaluating recurrent flow in intracranial aneurysms,^{77,78} the use of the 2D DSA may reduce calculated specificity but also increase calculated sensitivity of MRA if a true recanalization is missed by DSA. The use of DSA as the reference standard will potentially cause DSA false-negative values to count as MRA false-positive values. In general, MRA tends to perform better when compared with 3D DSA than when compared with 2D DSA (Table 2). 4) Heterogeneity may also be caused by different field strengths used in the various studies.^{79,80} Five studies only researched 3T MRA,^{42,61,64,68,74} whereas 2 articles studied both 3T and 1.5T MRA techniques.^{60,70} Two studies were performed with a 1T scanner.^{27,33} The rest of the articles evaluated MRA by use of 1.5T units. There is a trend toward higher pooled sensitivity and specificity of TOF-MRA with 3T units compared with 1.5T scanners, though the 95% confidence intervals overlap (Table 2). This trend might be caused by the higher resolution of images created with a 3T MR imaging compared with 1.5T scanners.⁸¹ However, the sensitivity and specificity of 3T CE-MRA is lower than that at 1.5T, though this difference is not statistically significant. Again, the small number of studies researching CE-MRA at 3T limits the interpretation of results and might be the cause of this nonsignificant difference without reflecting any underlying inferiority.^{42,60,68,70,74} 5) A final cause of heterogeneity might be the difference in study quality as judged by the GRADE criteria.¹²⁻²² GRADE 4 quality studies tend to have higher sensitivity and specificity. This difference reaches significance in sensitivity for CE-MRA (Table 2). Weighted by GRADE, overall comparisons between TOF-MRA and CE-MRA revealed results that were similar to the overall pooled results.

Our results provide a more detailed and updated evaluation of the accuracy of MRA for follow-up of coiled intracranial aneurysms than earlier work by Kwee and Kwee.⁸ Our detailed subanalysis of results reveals consistently good performance of MRA techniques with pooled sensitivities and specificities well above 80%. For the important question of residual aneurysms (Raymond grade 4), CE-MRA even provides a pooled sensitivity and specificity >90%, with a lower 95% confidence interval of ≥85%.

CONCLUSIONS

This meta-analysis has revealed that MRA has a high diagnostic performance when it comes to the detection of residual flow in the follow-up of intracranial aneurysms treated with endovascular coil occlusion and therefore should be routinely used for follow-up. CE-MRA did not perform significantly better than TOF-MRA, indicating that follow-up with the latter should be adequate.

ACKNOWLEDGMENTS

We would like to thank A.H.J. Tillema for support with our literature search.

Disclosures: Joost de Vries—UNRELATED: Consultancy: Stryker Neurovascular (consultancy and proctoring); Stock/Stock Options: Stock options in relation to Surpass-Stryker Neurovascular; Other: Compensation for training courses for Stryker Neurovascular held at the campus of the Radboud UMC Nijmegen, Netherlands.* Ronald Bartels—UNRELATED: Board Membership: Secretary of CSRS-es, Comments: Only traveling costs and hotel costs for board meetings are reimbursed (*money paid to institution).

REFERENCES

- Rinkel GJ, Djibuti M, Algra A, et al. **Prevalence and risk of rupture of intracranial aneurysms: a systematic review.** *Stroke* 1998;29:251–56
- Vlak MH, Algra A, Brandenburg R, et al. **Prevalence of unruptured intracranial aneurysms, with emphasis on sex, age, comorbidity, country, and time period: a systematic review and meta-analysis.** *Lancet Neurol* 2011;10:626–36
- Molyneux A, Kerr R, Stratton I, et al. **International Subarachnoid Aneurysm Trial (ISAT) of neurosurgical clipping versus endovascular coiling in 2143 patients with ruptured intracranial aneurysms: a randomised trial.** *Lancet* 2002;360:1267–74
- Naggara ON, White PM, Guilbert F, et al. **Endovascular treatment of intracranial unruptured aneurysms: systematic review and meta-analysis of the literature on safety and efficacy.** *Radiology* 2010;256:887–97
- Dawkins AA, Evans AL, Wattam J, et al. **Complications of cerebral angiography: a prospective analysis of 2,924 consecutive procedures.** *Neuroradiology* 2007;49:753–59
- Thiex R, Norbash AM, Frerichs KU. **The safety of dedicated-team catheter-based diagnostic cerebral angiography in the era of advanced noninvasive imaging.** *AJNR Am J Neuroradiol* 2010;31:230–34
- Willinsky RA, Taylor SM, TerBrugge K, et al. **Neurologic complications of cerebral angiography: prospective analysis of 2,899 procedures and review of the literature.** *Radiology* 2003;227:522–28
- Kwee TC, Kwee RM. **MR angiography in the follow-up of intracranial aneurysms treated with Guglielmi detachable coils: systematic review and meta-analysis.** *Neuroradiology* 2007;49:703–13
- Raymond J, Guilbert F, Weill A, et al. **Long-term angiographic recurrences after selective endovascular treatment of aneurysms with detachable coils.** *Stroke* 2003;34:1398–403
- Roy D, Raymond J, Bouthillier A, et al. **Endovascular treatment of ophthalmic segment aneurysms with Guglielmi detachable coils.** *AJNR Am J Neuroradiol* 1997;18:1207–15
- Roy D, Milot G, Raymond J. **Endovascular treatment of unruptured aneurysms.** *Stroke* 2001;32:1998–2004
- Schunemann HJ, Oxman AD, Brozek J, et al. **Grading quality of evidence and strength of recommendations for diagnostic tests and strategies.** *BMJ* 2008;336:1106–10
- Guyatt GH, Oxman AD, Schunemann HJ, et al. **GRADE guidelines: a new series of articles in the Journal of Clinical Epidemiology.** *J Clin Epidemiol* 2011;64:380–82
- Guyatt G, Oxman AD, Akl EA, et al. **GRADE guidelines, 1: introduction: GRADE evidence profiles and summary of findings tables.** *J Clin Epidemiol* 2011;64:383–94
- Guyatt GH, Oxman AD, Kunz R, et al. **GRADE guidelines, 2: framing the question and deciding on important outcomes.** *J Clin Epidemiol* 2011;64:395–400
- Balshem H, Helfand M, Schunemann HJ, et al. **GRADE guidelines, 3: rating the quality of evidence.** *J Clin Epidemiol* 2011;64:401–06
- Guyatt GH, Oxman AD, Vist G, et al. **GRADE guidelines, 4: rating the quality of evidence: study limitations (risk of bias).** *J Clin Epidemiol* 2011;64:407–15
- Guyatt GH, Oxman AD, Montori V, et al. **GRADE guidelines, 5: rating the quality of evidence: publication bias.** *J Clin Epidemiol* 2011;64:1277–82

19. Guyatt GH, Oxman AD, Kunz R, et al. **GRADE guidelines, 6: rating the quality of evidence: imprecision.** *J Clin Epidemiol* 2011;64:1283–93
20. Guyatt GH, Oxman AD, Kunz R, et al. **GRADE guidelines, 7: rating the quality of evidence: inconsistency.** *J Clin Epidemiol* 2011;64:1294–302
21. Guyatt GH, Oxman AD, Kunz R, et al. **GRADE guidelines, 8: rating the quality of evidence: indirectness.** *J Clin Epidemiol* 2011;64:1303–10
22. Guyatt GH, Oxman AD, Sultan S, et al. **GRADE guidelines, 9: rating up the quality of evidence.** *J Clin Epidemiol* 2011;64:1311–16
23. Brennan P, Silman A. **Statistical methods for assessing observer variability in clinical measures.** *BMJ* 1992;304:1491–94
24. Zamora J, Abraira V, Muriel A, et al. **Meta-DiSc: a software for meta-analysis of test accuracy data.** *BMC Med Res Methodol* 2006;6:31
25. Derdeyn CP, Graves VB, Turski PA, et al. **MR angiography of saccular aneurysms after treatment with Guglielmi detachable coils: preliminary experience.** *AJNR Am J Neuroradiol* 1997;18:279–86
26. Gonner F, Heid O, Remonda L, et al. **MR angiography with ultra-short echo time in cerebral aneurysms treated with Guglielmi detachable coils.** *AJNR Am J Neuroradiol* 1998;19:1324–28
27. Brunereau L, Cottier JP, Sonier CB, et al. **Prospective evaluation of time-of-flight MR angiography in the follow-up of intracranial saccular aneurysms treated with Guglielmi detachable coils.** *J Comput Assist Tomogr* 1999;23:216–23
28. Kahara VJ, Seppanen SK, Ryymin PS, et al. **MR angiography with three-dimensional time-of-flight and targeted maximum-intensity-projection reconstructions in the follow-up of intracranial aneurysms embolized with Guglielmi detachable coils.** *AJNR Am J Neuroradiol* 1999;20:1470–75
29. Anzalone N, Righi C, Simionato F, et al. **Three-dimensional time-of-flight MR angiography in the evaluation of intracranial aneurysms treated with Guglielmi detachable coils.** *AJNR Am J Neuroradiol* 2000;21:746–52
30. Boulin A, Pierot L. **Follow-up of intracranial aneurysms treated with detachable coils: comparison of gadolinium-enhanced 3D time-of-flight MR angiography and digital subtraction angiography.** *Radiology* 2001;219:108–13
31. Weber W, Yousry TA, Felber SR, et al. **Noninvasive follow-up of GDC-treated saccular aneurysms by MR angiography.** *Eur Radiol* 2001;11:1792–97
32. Leclerc X, Navez JF, Gauvrit JY, et al. **Aneurysms of the anterior communicating artery treated with Guglielmi detachable coils: follow-up with contrast-enhanced MR angiography.** *AJNR Am J Neuroradiol* 2002;23:1121–27
33. Nome T, Bakke SJ, Nakstad PH. **MR angiography in the follow-up of coiled cerebral aneurysms after treatment with Guglielmi detachable coils.** *Acta Radiol* 2002;43:10–14
34. Park SW, Han MH, Cha SH, et al. **PC-based 3D reconstruction of MR angiography in evaluation of intracranial aneurysms. The value of pre-treatment planning for embolization and post-treatment follow-up.** *Interv Neuroradiol* 2002;8:169–81
35. Cottier JP, Bleuzen-Couthon A, Gallas S, et al. **Follow-up of intracranial aneurysms treated with detachable coils: comparison of plain radiographs, 3D time-of-flight MRA and digital subtraction angiography.** *Neuroradiology* 2003;45:818–24
36. Cottier JP, Bleuzen-Couthon A, Gallas S, et al. **Intracranial aneurysms treated with Guglielmi detachable coils: is contrast material necessary in the follow-up with 3D time-of-flight MR angiography?** *AJNR Am J Neuroradiol* 2003;24:1797–803
37. Zizka J, Krajina A, Lojik M. **The reliability of MR angiography as the sole imaging method for non-invasive follow-up of intracranial aneurysms treated with Guglielmi detachable coils.** *Rivista di Neurologia* 2003;16:1137–38
38. Okahara M, Kiyosue H, Hori Y, et al. **Three-dimensional time-of-flight MR angiography for evaluation of intracranial aneurysms after endosaccular packing with Guglielmi detachable coils: comparison with 3D digital subtraction angiography.** *Eur Radiol* 2004;14:1162–68
39. Yamada N, Hayashi K, Murao K, et al. **Time-of-flight MR angiography targeted to coiled intracranial aneurysms is more sensitive to residual flow than is digital subtraction angiography.** *AJNR Am J Neuroradiol* 2004;25:1154–57
40. Farb RI, Nag S, Scott JN, et al. **Surveillance of intracranial aneurysms treated with detachable coils: a comparison of MRA techniques.** *Neuroradiology* 2005;47:507–15
41. Gauvrit JY, Leclerc X, Pernodet M, et al. **Intracranial aneurysms treated with Guglielmi detachable coils: usefulness of 6-month imaging follow-up with contrast-enhanced MR angiography.** *AJNR Am J Neuroradiol* 2005;26:515–21
42. Majoie CBLM, Sprengers ME, Van Rooij WJJ, et al. **MR angiography at 3T versus digital subtraction angiography in the follow-up of intracranial aneurysms treated with detachable coils.** *AJNR Am J Neuroradiol* 2005;26:1349–56
43. Westerlaan HE, van der Vliet AM, Hew JM, et al. **Time-of-flight magnetic resonance angiography in the follow-up of intracranial aneurysms treated with Guglielmi detachable coils.** *Neuroradiology* 2005;47:622–29
44. Gauvrit JY, Leclerc X, Caron S, et al. **Intracranial aneurysms treated with Guglielmi detachable coils: imaging follow-up with contrast-enhanced MR angiography.** *Stroke* 2006;37:1033–37
45. Pierot L, Delcourt C, Bouquigny F, et al. **Follow-up of intracranial aneurysms selectively treated with coils: prospective evaluation of contrast-enhanced MR angiography.** *AJNR Am J Neuroradiol* 2006;27:744–49
46. Saguchi T, Murayama Y, Ishibashi T, et al. **Efficacy of 3-D reconstructed time of flight MRA follow-up of the embolized cerebral aneurysms.** *Intervent Neuroradiol* 2006;12(Suppl 1):45–48
47. de Gast AN, Sprengers ME, van Rooij WJ, et al. **Long-term 3T MR angiography follow-up after therapeutic occlusion of the internal carotid artery to detect possible de novo aneurysm formation.** *AJNR Am J Neuroradiol* 2007;28:508–10
48. Deutschmann HA, Augustin M, Simbrunner J, et al. **Diagnostic accuracy of 3D time-of-flight MR angiography compared with digital subtraction angiography for follow-up of coiled intracranial aneurysms: influence of aneurysm size.** *AJNR Am J Neuroradiol* 2007;28:628–34
49. Lubicz B, Levivier M, Sadeghi N, et al. **Immediate intracranial aneurysm occlusion after embolization with detachable coils: a comparison between MR angiography and intra-arterial digital subtraction angiography.** *J Neuroradiol* 2007;34:190–97
50. Poncyjusz W, Czechowski J, Corr P, et al. **MR-angiography as a method for evaluating endovascular coiled cerebral aneurysms.** *Med Sci Monit* 2007;13(Suppl 1):59–64
51. Wallace RC, Karis JP, Partovi S, et al. **Noninvasive imaging of treated cerebral aneurysms, part I: MR angiographic follow-up of coiled aneurysms.** *AJNR Am J Neuroradiol* 2007;28:1001–08
52. Wong JH, Mitha AP, Willson M, et al. **Assessment of brain aneurysms by using high-resolution magnetic resonance angiography after endovascular coil delivery.** *J Neurosurg* 2007;107:283–89
53. Agid R, Willinsky RA, Lee SK, et al. **Characterization of aneurysm remnants after endovascular treatment: contrast-enhanced MR angiography versus catheter digital subtraction angiography.** *AJNR Am J Neuroradiol* 2008;29:1570–74
54. Buhk JH, Kallenberg K, Mohr A, et al. **No advantage of time-of-flight magnetic resonance angiography at 3 Tesla compared to 1.5 Tesla in the follow-up after endovascular treatment of cerebral aneurysms.** *Neuroradiology* 2008;50:855–61
55. Dupre S, Coulthard A. **Follow up of coiled intracranial aneurysms with standard resolution and higher resolution magnetic resonance angiography.** *J Med Imaging Radiat Oncol* 2008;52:57–63
56. Gauvrit JY, Caron S, Taschner CA, et al. **Intracranial aneurysms treated with Guglielmi detachable coils: long-term imaging follow-up with contrast-enhanced magnetic resonance angiography.** *J Neurosurg* 2008;108:443–49

57. Hiratsuka Y, Miki H, Kiriyama I, et al. **Diagnosis of unruptured intracranial aneurysms: 3T MR angiography versus 64-channel multi-detector row CT angiography.** *Magn Reson Med Sci* 2008; 7:169–78
58. Khan R, Wallace RC, Fiorella DJ. **Magnetic resonance angiographic imaging follow-up of treated intracranial aneurysms.** *Top Magn Reson Imaging* 2008;19:231–39
59. Lubicz B, Neugroschl C, Collignon L, et al. **Is digital subtraction angiography still needed for the follow-up of intracranial aneurysms treated by embolisation with detachable coils?** *Neuroradiology* 2008;50:841–48
60. Ramgren B, Siemund R, Cronqvist M, et al. **Follow-up of intracranial aneurysms treated with detachable coils: comparison of 3D inflow MRA at 3T and 1.5T and contrast-enhanced MRA at 3T with DSA.** *Neuroradiology* 2008;50:947–54
61. Urbach H, Dorenbeck U, Von Falkenhausen M, et al. **Three-dimensional time-of-flight MR angiography at 3 T compared to digital subtraction angiography in the follow-up of ruptured and coiled intracranial aneurysms: a prospective study.** *Neuroradiology* 2008;50:383–89
62. Wikstrom J, Ronne-Engstrom E, Gal G, et al. **Three-dimensional time-of-flight (3D TOF) magnetic resonance angiography (MRA) and contrast-enhanced MRA of intracranial aneurysms treated with platinum coils.** *Acta Radiol* 2008;49:190–96
63. Buhk JH, Kallenberg K, Mohr A, et al. **Evaluation of angiographic computed tomography in the follow-up after endovascular treatment of cerebral aneurysms: a comparative study with DSA and TOF-MRA.** *Eur Radiol* 2009;19:430–36
64. Ferre JC, Carsin-Nicol B, Morandi X, et al. **Time-of-flight MR angiography at 3 T versus digital subtraction angiography in the imaging follow-up of 51 intracranial aneurysms treated with coils.** *Eur J Radiol* 2009;72:365–69
65. Gallas S, Januel AC, Pasco A, et al. **Long-term follow-up of 1036 cerebral aneurysms treated by bare coils: a multicentric cohort treated between 1998 and 2003.** *AJNR Am J Neuroradiol* 2009; 30:1986–92
66. Kau T, Gasser J, Celedin S, et al. **MR angiographic follow-up of intracranial aneurysms treated with detachable coils: evaluation of a blood-pool contrast medium.** *AJNR Am J Neuroradiol* 2009;30: 1524–30
67. Monninghoff C, Maderwald S, Theysohn JM, et al. **Evaluation of intracranial aneurysms with 7 T versus 1.5 T time-of-flight MR angiography: initial experience.** *Rofa* 2009;181:16–23
68. Sprengers ME, Schaafsma JD, van Rooij WJ, et al. **Evaluation of the occlusion status of coiled intracranial aneurysms with MR angiography at 3T: is contrast enhancement necessary?** *AJNR Am J Neuroradiol* 2009;30:1665–71
69. Bakker NA, Westerlaan HE, Metzemaekers JD, et al. **Feasibility of magnetic resonance angiography (MRA) follow-up as the primary imaging modality after coiling of intracranial aneurysms.** *Acta Radiol* 2010;51:226–32
70. Kaufmann TJ, Huston IJ, Cloft HJ, et al. **A prospective trial of 3T and 1.5T time-of-flight and contrast-enhanced MR angiography in the follow-up of coiled intracranial aneurysms.** *AJNR Am J Neuroradiol* 2010;31:912–18
71. Schaafsma JD, Velthuis BK, Majoie CB, et al. **Intracranial aneurysms treated with coil placement: test characteristics of follow-up MR angiography: multicenter study.** *Radiology* 2010;256:209–18
72. Shankar JJS, Lum C, Parikh N, et al. **Long-term prospective follow-up of intracranial aneurysms treated with endovascular coiling using contrast-enhanced MR angiography.** *AJNR Am J Neuroradiol* 2010;31:1211–15
73. Tailor J, Goetz P, Chandrashekar H, et al. **Stability of ruptured intracranial aneurysms treated with detachable coils: is delayed follow-up angiography warranted?** *Br J Neurosurg* 2010;24:405–09
74. Nakiri GS, Santos AC, Abud TG, et al. **A comparison between magnetic resonance angiography at 3 Teslas (time-of-flight and contrast enhanced) and flat-panel digital subtraction angiography in the assessment of embolized brain aneurysms.** *Clinics* 2011;66: 641–48
75. Lavoie P, Gariepy JL, Milot G, et al. **Residual flow after cerebral aneurysm coil occlusion: diagnostic accuracy of MR angiography.** *Stroke* 2012;43:740–46
76. Berbano EP, Baxi N. **Impact of patient selection in various study designs: identifying potential bias in clinical results.** *South Med J* 2012;105:149–55
77. Sugahara T, Korogi Y, Nakashima K, et al. **Comparison of 2D and 3D digital subtraction angiography in evaluation of intracranial aneurysms.** *AJNR Am J Neuroradiol* 2002;23:1545–52
78. Shi WY, Li YD, Li MH, et al. **3D rotational angiography with volume rendering: the utility in the detection of intracranial aneurysms.** *Neurol India* 2010;58:908–13
79. Bernstein MA, Huston J 3rd, Lin C, et al. **High-resolution intracranial and cervical MRA at 3.0T: technical considerations and initial experience.** *Magn Reson Med* 2001;46:955–62
80. Al-Kwif O, Emery DJ, Wilman AH. **Vessel contrast at three Tesla in time-of-flight magnetic resonance angiography of the intracranial and carotid arteries.** *Magn Reson Imaging* 2002;20:181–87
81. Willinek WA, Born M, Simon B, et al. **Time-of-flight MR angiography: comparison of 3.0-T imaging and 1.5-T imaging—initial experience.** *Radiology* 2003;229:913–20

Facial Reanimation Procedures Depicted on Radiologic Imaging

D.T. Ginat, P. Bhamra, M.E. Cunnane, and T.A. Hadlock



ABSTRACT

SUMMARY: Various facial reanimation procedures can be performed for treating patients with chronic facial nerve paralysis. The radiologic imaging features of static and dynamic techniques are reviewed in this article with clinical correlation, including brow lift, eyelid weights and springs, gracilis free flaps, fascia lata grafts, temporalis flaps, and Gore-Tex suspension slings. Although the anatomic alterations resulting from facial reanimation surgery may not necessarily be the focus of the imaging examination, it is important to recognize such changes and be familiar with MR imaging compatibility of the associated implanted materials. Furthermore, imaging is sometimes used to specifically evaluate the postoperative results, such as vessel patency following free gracilis transfer.

Chronic facial nerve paralysis can result in significant morbidity, including brow ptosis, lagophthalmos, ectropion, exposure keratopathy, nasal alar collapse, effacement of the nasolabial fold, ptosis of the oral commissure, and drooling. Static and dynamic facial reanimation surgical techniques are available to prevent and treat these complications. Static facial nerve rehabilitation procedures include brow lift, eyelid weight implantation, lower eyelid canthoplasty and tightening, fascia lata and alloplastic slings, and cheiloplasty. Dynamic facial reanimation procedures include nerve transfer and grafting, eyelid springs, free muscle transfer, regional muscle transfer, and lengthening myoplasty. The anatomic changes brought about by these procedures can be delineated by using conventional radiologic imaging modalities, including radiographs, CT, sonography, and MR imaging. Furthermore, in certain instances, imaging may be requested specifically to evaluate the results of facial reanimation surgery, such as interrogating the patency of the vascular pedicle following gracilis muscle transfer. The imaging findings after selected static and dynamic facial reanimation surgeries are described and depicted in the following sections.

From the Department of Radiology (D.T.G.), Division of Neuroradiology, Massachusetts General Hospital, Boston, Massachusetts; and Department of Otolaryngology (P.B., T.A.H.), Division of Facial Plastic and Reconstructive Surgery, and Department of Radiology (M.E.C.), Massachusetts Eye and Ear Infirmary, Boston, Massachusetts.

Please address correspondence to Daniel Thomas Ginat, MD, MS, University of Chicago, Department of Radiology, 5841 S. Maryland Ave, MC 2026, Rm. P220, Chicago, IL 60637; e-mail: ginatd01@gmail.com

Indicates open access to non-subscribers at www.ajnr.org

<http://dx.doi.org/10.3174/ajnr.A3684>

Brow Lift

Brow ptosis can be addressed by performing a brow lift. Several methods exist to elevate the brow, one of which consists of implanting a fixation device into the frontal calvaria to which a permanent suture is secured (Fig 1).¹ Brow lift can be performed in conjunction with ablation of the brow depressor muscles and blepharoplasty. Numerous fixation devices can be used, including pins, screws, tacks, K-wires, and tissue adhesives. Metallic fixation devices can be depicted on CT and should not be mistaken for unintended foreign bodies (Fig 2).

Eyelid Weights

Implantation of gold and platinum eyelid weights into the upper eyelid is a static reanimation procedure for treating lagophthalmos.² Although gold weights are more commonly used, platinum weights have a thinner profile and therefore offer an increased aesthetic benefit.³ Available eyelid implant designs include curved metal sheets with holes to permit anchoring with a suture (Fig 3) and flexible metal chains. In-growth of fibrous tissue through the holes also helps secure the weight in position. Eyelid weights are secured to the superficial aspect of the upper eyelid tarsal plate. The eyelid weights generally produce considerable streak artifacts on CT, which can obscure surrounding structures (Fig 4). Platinum and gold eyelid weights are considered MR imaging-compatible up to 7T^{4,5} but may cause local field inhomogeneity (Fig 5). Complications related to eyelid weight implantation include suboptimal eyelid contour, infection, allergic reaction, migration, and extrusion.⁶

Eyelid Springs

Eyelid springs are used to augment eyelid closure in patients with eyelid paralysis.^{7,8} The spring has the ability to achieve complete eye

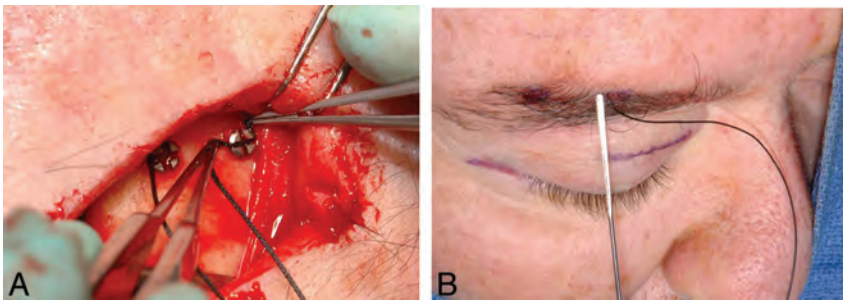


FIG 1. Brow lift. Intraoperative photographs show screws in the frontal bone used to secure sutures tunneled under the subcutaneous tissues toward the brow.

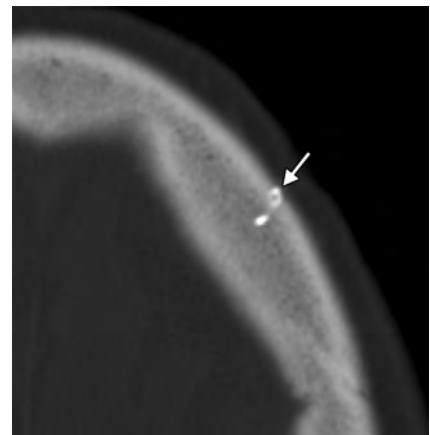


FIG 2. Brow lift. Axial CT image shows a metallic left frontal bone pin (arrow) used for suture fixation.



FIG 3. Eyelid weight. Frontal radiograph shows a gold implant containing 3 drill holes at the level of the left upper eyelid.

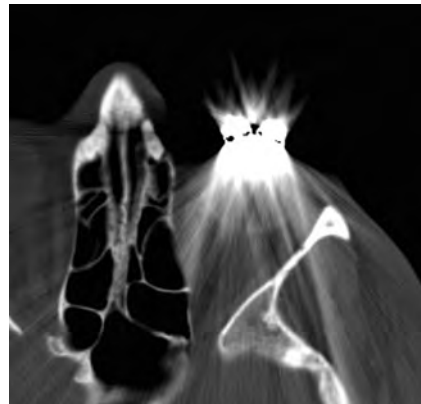


FIG 4. Eyelid weight. Axial CT image shows extensive streak artifacts related to the left eyelid weight, which obscures surrounding structures.



FIG 5. Eyelid weight. Axial post-contrast fat-suppressed T1-weighted image shows field inhomogeneity associated with the left eyelid weight (arrow).

closure in the supine position.⁹ The device is implanted via orbitotomy and consists of a palpebral branch and an orbital branch connected by a spring mechanism at the fulcrum. The springs are generally composed of stainless steel and are MR imaging-compatible up to at least 1.5T.¹⁰ The positioning and function of the device can be evaluated on radiographs obtained in the open and closed lid positions, whereby the palpebral branch is expected to descend with lid closure (Fig 6). Potential complications of eyelid springs include dislocation, metal fatigue resulting in failure, and exposure.

Gracilis Free Flap

Free gracilis transfer is an effective method of smile rehabilitation for facial paralysis in selected patients (Fig 7).¹¹⁻¹⁴ The gracilis muscle is harvested from the thigh with its neurovascular supply (Fig 8). The graft is then inset in the plane deep to the superficial musculoaponeurotic system and extends from the zygomatic arch to the modiolus of the oral commissure (Fig 9). The vascular pedicle of the graft is typically anastomosed to the facial artery and vein, and the obturator nerve can be anastomosed to a cross-face nerve graft and/or the masseteric branch of the trigeminal nerve.^{15,16} Vascular ring coupler devices are often used for the venous anastomosis.¹⁷ Depending on the particular type, the ring coupler may appear as a hyperattenuated circular structure overlying the angle of the mandible (Fig 10). Postoperative flap monitoring by physical examination alone is challenging and is often supplemented with use of a hand-held Doppler probe. Color Dopp-

ler sonography is an effective and noninvasive tool for evaluating arterial and venous flow through the pedicle of the buried free flap, whereby a sharp systolic upstroke should be evident in the artery and continuous flow should be observed in the vein (Fig 11). The examination can potentially avoid wound exploration to verify appropriate muscle perfusion and is typically performed on the first postoperative day.¹⁸ The arterial waveform of the graft should normally demonstrate a sharp systolic upstroke, while the vein may normally exhibit a continuous waveform and should be compressible, except at the site of the ring connector device. A good functional outcome correlates with normal muscle structure of the free flap depicted on MR imaging.¹⁹ Imaging may also be useful for measuring the graft thickness,²⁰ which potentially relates to function.

Fascia Lata Graft

Autogenous fascia lata grafts can be used as the primary therapeutic option in static facial rebalancing or in conjunction with dynamic muscle reanimation.²¹ In particular, fascia lata slings can be used to improve oral competence and external nasal valve patency (Fig 12). The fascia lata graft is similarly inset into the sub-superficial musculoaponeurotic system plane and appears as a



FIG 6. Eyelid spring. Frontal (A) and lateral (B) radiographs show that the inferior limb of the spring is positioned in the superior eyelid (arrows), while the superior limb is positioned along the orbital rim.

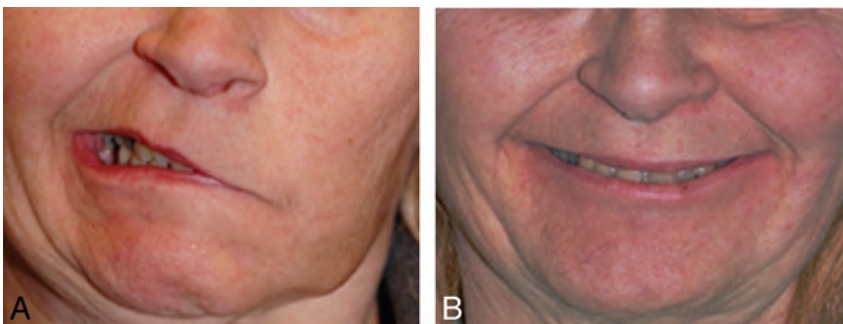


FIG 7. Gracilis free flap. Clinical photographs before (A) and after (B) gracilis free flap reanimation show marked restoration of the patient's smile.

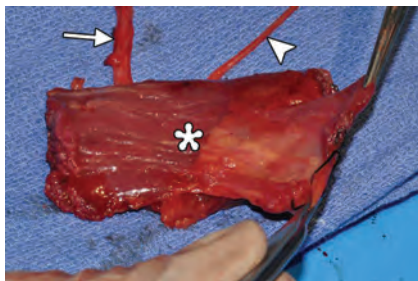


FIG 8. Gracilis free flap. Intraoperative photograph shows the harvested flap (asterisk) with an attached vascular pedicle (arrow) and nerve (arrowhead).

thin band of soft tissue that courses through the subcutaneous tissues of the face on cross-sectional imaging (Fig 13).

Temporalis Flap

The temporalis flap (temporalis muscle transposition) procedure is an effective option for reanimation of the smile.²² An approximately 1.5-cm-wide strip of the midportion of the temporalis muscle is dissected off the calvaria and reflected in the subdermal plane from the zygomatic arch to the modiolus of the oral commissure (Fig 14). The course of the transposed temporalis muscle can be delineated on cross-sectional imaging as a thin band of soft tissue (Fig 15).

Gore-Tex Sling Suspension

Gore-Tex (expanded polytetrafluoroethylene) (W.L. Gore and Associates, Reisterstown, Maryland) can be used for static suspen-

sion in facial paralysis.^{23,24} It is manufactured in thin 1- to 2-mm sheets, which can be cut into strips and implanted through small incisions. On CT, Gore-Tex slings appear as linear hyperattenuations (Fig 16).²⁵ Although the use of Gore-Tex in facial reanimation eliminates donor site morbidity associated with the harvest of autologous grafts, the allograft is prone to complications, such as delayed wound infection.²⁴

Disclosures: Mary E. Cunnane—UNRELATED: Other: WorldCare Clinical. Comments: I was a radiologist for a clinical trial of a chemotherapy drug for head and neck cancer.

REFERENCES

1. Foustanos A. Suture fixation technique for endoscopic brow lift. *Semin Plast Surg* 2008;22:43–49
2. Bladen JC, Norris JH, Malhotra R. Cosmetic comparison of gold weight and platinum chain insertion in primary upper eyelid loading for lagophthalmos. *Ophthalmol Plast Reconstr Surg* 2012;28:171–75
3. Silver AL, Lindsay RW, Cheney ML, et al. Thin-profile platinum eyelid weighting: a superior option in the paralyzed eye. *Plast Reconstr Surg* 2009;123:1697–703
4. Schrom T, Thelen A, Asbach P, et al. Effect of 7.0 Tesla MRI on upper eyelid implants. *Ophthalmol Plast Reconstr Surg* 2006;22:480–82
5. Marra S, Leonetti JP, Konior RJ, et al. Effect of magnetic resonance imaging on implantable eyelid weights. *Ann Otol Rhinol Laryngol* 1995;104:448–52
6. Dinces EA, Mauriello JA Jr, Kwartler JA, et al. Complications of gold weight eyelid implants for treatment of fifth and seventh nerve palsy. *Laryngoscope* 1997;107:1617–22
7. Fay A, Santiago YM. A modified Levine palpebral spring for the treatment of myogenic ptosis. *Ophthalmol Plast Reconstr Surg* 2012;28:372–75
8. Demirci H, Frueh BR. Palpebral spring in the management of lagophthalmos and exposure keratopathy secondary to facial nerve palsy. *Ophthalmol Plast Reconstr Surg* 2009;25:270–75
9. Levine RE, Shapiro JP. Reanimation of the paralyzed eyelid with the enhanced palpebral spring or the gold weight: modern replacements for tarsorrhaphy. *Facial Plast Surg* 2000;16:325–36
10. Gardner TA, Rak KM. Magnetic resonance imaging of eyelid springs and gold weights. *Arch Ophthalmol* 1991;109:1498
11. Chuang DC. Free tissue transfer for the treatment of facial paralysis. *Facial Plast Surg* 2008;24:194–203
12. Hadlock TA, Malo JS, Cheney ML, et al. Free gracilis transfer for smile in children: the Massachusetts Eye and Ear Infirmary Experience in excursion and quality-of-life changes. *Arch Facial Plast Surg* 2011;13:190–94
13. Boahene KD. Dynamic muscle transfer in facial reanimation. *Facial Plast Surg* 2008;24:204–10
14. Vakharia KT, Henstrom D, Plotkin SR, et al. Facial reanimation of patients with neurofibromatosis type 2. *Neurosurgery* 2012;70:237–43
15. Bianchi B, Copelli C, Ferrari S, et al. Facial animation with free-muscle transfer innervated by the masseter motor nerve in unilateral facial paralysis. *J Oral Maxillofac Surg* 2010;68:1524–29
16. Faria JC, Scopel GP, Busnardo FF, et al. Nerve sources for facial reanimation with muscle transplant in patients with unilateral fa-

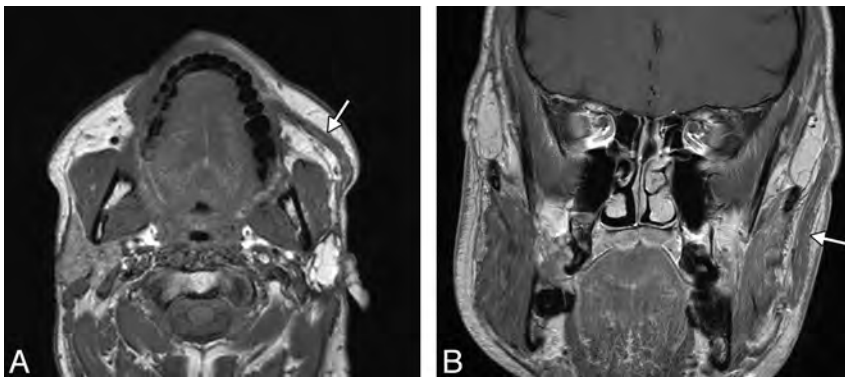


FIG 9. Gracilis free flap. Axial (A) and coronal (B) postcontrast T1-weighted MR images show a healthy gracilis flap (arrows), which extends from the zygomatic arch to the oral commissure following total left parotidectomy, with facial nerve sacrifice for resection of mucoepidermoid carcinoma.

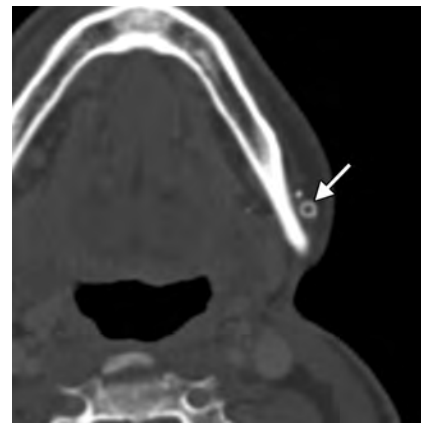


FIG 10. Gracilis free flap. Axial CT image shows a hyperattenuated circular ring connector (arrow) used to facilitate the vascular anastomosis.

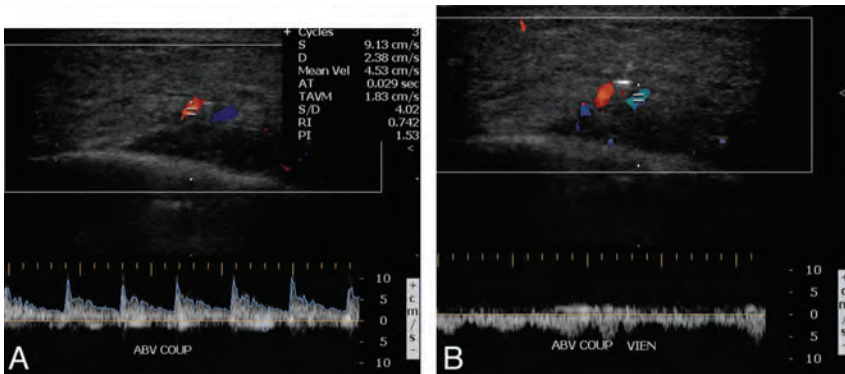


FIG 11. Gracilis free flap. Color Doppler sonographic images of the vascular pedicle show normal arterial (A) and venous (B) waveforms.



FIG 12. Fascia lata graft. Intraoperative photograph shows the prepared fascia lata graft (arrow) over its planned course toward the left nasal ala before implantation.



FIG 13. Fascia lata graft. The patient did not obtain optimal muscular function after the gracilis free flap procedure. Axial CT shows a tenuous right gracilis flap (arrowheads) and a linear band of soft tissue that extends from the gracilis flap to the right alar base, which corresponds to the fascia lata sling resuspension for external nasal valve correction (arrow).

cial palsy: clinical analysis of 3 techniques. *Ann Plast Surg* 2007;59:87–91

17. Barker EV, Enepekides DJ. The utility of microvascular anastomotic devices in head and neck reconstruction. *Curr Opin Otolaryngol Head Neck Surg* 2008;16:331–34
18. Vakharia KT, Henstrom D, Lindsay R, et al. Color Doppler ultrasound: effective monitoring of the buried free flap in facial reanimation. *Otolaryngol Head Neck Surg* 2012;146:372–76
19. Ylä-Kotola TM, Kauhanen MS, Koskinen SK, et al. Magnetic resonance imaging of microneurovascular free muscle flaps in facial reanimation. *Br J Plast Surg* 2005;58:222–27
20. Salmi A, Ahovuori J, Tuikiainen E, et al. Use of ultrasonography to evaluate muscle thickness and blood flow in free flaps. *Microsurgery* 1995;16:601–05
21. Rose EH. Autogenous fascia lata grafts: clinical applications in reanimation of the totally or partially paralyzed face. *Plast Reconstr Surg* 2005;116:20–32, discussion 33–35

22. White TP, Faulkner JA, Markley JM Jr, et al. Translocation of the temporalis muscle for treatment of facial paralysis. *Muscle Nerve* 1982;5:500–04
23. Liu YM, Sherris DA. Static procedures for the management of the midface and lower face. *Facial Plast Surg* 2008;24:211–15
24. Constantinides M, Galli SK, Miller PJ. Complications of static facial suspensions with expanded polytetrafluoroethylene (ePTFE). *Laryngoscope* 2001;111:2114–21
25. Schatz CJ, Ginat DT. Imaging of cosmetic facial implants and grafts. *AJNR Am J Neuroradiol* 2013;34:1674–81

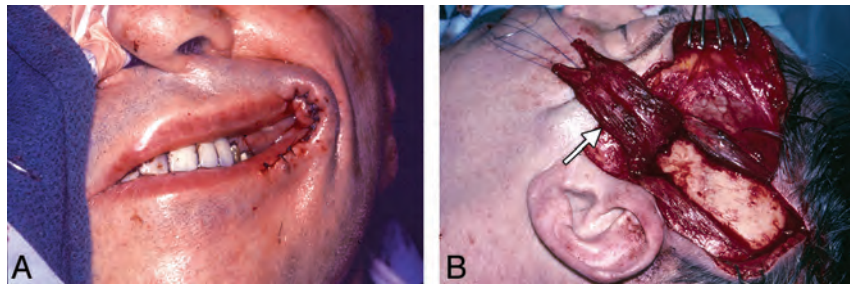


FIG 14. Temporalis flap. Intraoperative photographs show that the middle portion of the temporalis muscle (*arrow*) has been dissected free and transposed toward the oral commissure. The flap was subsequently tunneled beneath the subcutaneous tissues.

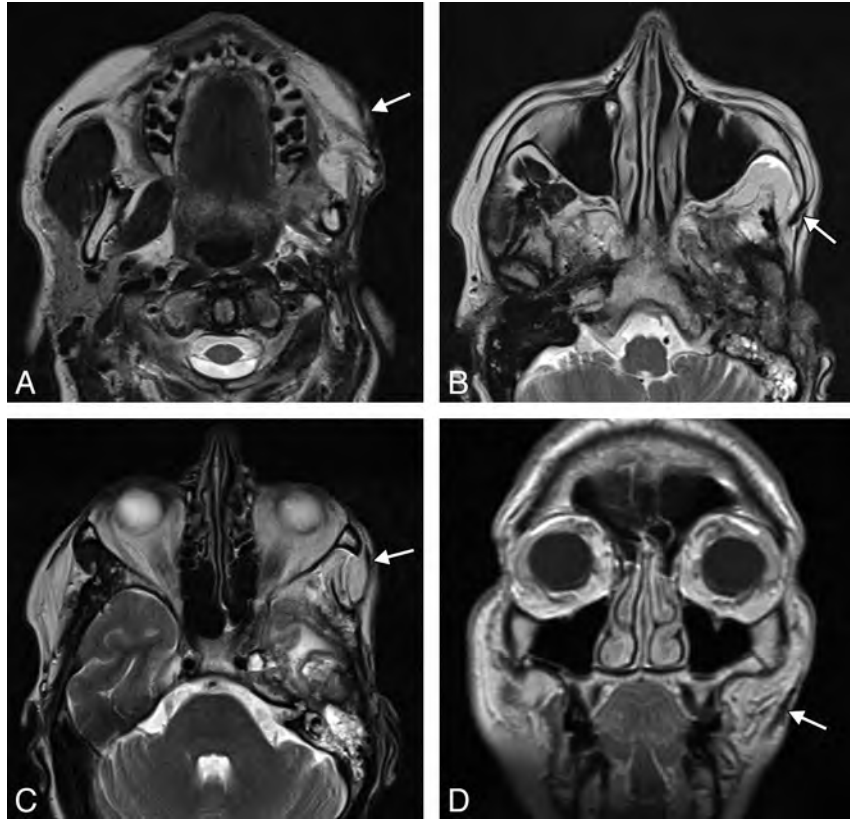


FIG 15. Temporalis flap. Axial T2 MR imaging (A–C) and coronal T1 MR imaging (D) show that the left temporalis muscle with the overlying fascia (*arrows*) is directed retrograde from the temporal fossa to the orbicularis oris.

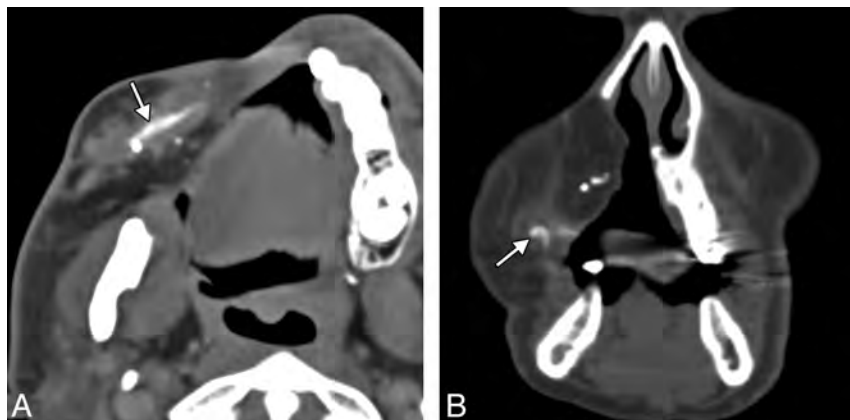


FIG 16. Gore-Tex sling. Axial (A) and coronal (B) CT images show the linear hyperattenuated strip of Gore-Tex that supports the right oral commissure (*arrows*). The patient is status post right complete maxillectomy with myocutaneous flap reconstruction.

Patients Prone to Recurrence after Endovascular Treatment: Periprocedural Results of the PRET Randomized Trial on Large and Recurrent Aneurysms

J. Raymond, R. Klink, M. Chagnon, S.L. Barnwell, A.J. Evans, J. Mocco, B.L. Hoh, A.S. Turk, R.D. Turner, H. Desal, D. Fiorella, S. Bracard, A. Weill, F. Guilbert, and D. Roy, on behalf of the PRET Collaborative Group



ABSTRACT

BACKGROUND AND PURPOSE: Some patients with large or recurrent aneurysms may be at increased risk of recurrence postcoiling. The Patients Prone to Recurrence after Endovascular Treatment (PRET) trial was designed to assess whether hydrogel coils were superior to platinum coils in these high-risk patients. This article reports periprocedural safety and operator-assessed angiographic results from the PRET trial.

MATERIALS AND METHODS: PRET was a pragmatic, multicenter, randomized controlled trial. Patients had ≥ 10 -mm aneurysms (PRET-1) or a major recurrence after coiling of an aneurysm of any size (PRET-2). Patients were randomly allocated to hydrogel or control arms (any platinum coil) by using concealed allocation with minimization. Assist devices could be used as clinically required. Aneurysms could be unruptured or recently ruptured. Analyses were on an intent-to-treat basis.

RESULTS: Four hundred forty-seven patients were recruited (250 PRET-1; 197 PRET-2). Aneurysms were recently ruptured in 29% of PRET-1 and 4% of PRET-2 patients. Aneurysms were ≥ 10 mm in all PRET-1 and in 50% of PRET-2 patients. They were wide-neck (≥ 4 mm) in 70% and in the posterior circulation in 24% of patients. Stents were used in 28% of patients (35% in PRET-2). Coiling was successful in 98%. Adverse events occurred in 28 patients with hydrogel and 23 with platinum coils. Mortality ($n = 2$, unrelated to treatment) and morbidity (defined as mRS > 2 at 1 month) occurred in 25 patients (5.6%; 12 hydrogel, 13 platinum), related to treatment in 10 (4 hydrogel; 6 platinum) (or 2.3% of 444 treated patients). No difference was seen between hydrogel and platinum for any of the indices used to assess safety up to at least 30 days after treatment. At 1 month, 95% of patients were home with a good outcome (mRS ≤ 2 or unchanged). Operator-assessed angiographic outcomes were satisfactory (complete occlusion or residual neck) in 339 of 447 or 76.4% of patients, with no significant difference between groups.

CONCLUSIONS: Endovascular treatment of large and recurrent aneurysms can be performed safely with platinum or hydrogel coils.

ABBREVIATIONS: CCT = Cerecyte Coil Trial; DSMC = Data Safety and Monitoring Committee; HELPS = HydroCoil Endovascular Aneurysm Occlusion and Packing Study; MAPS = Matrix and Platinum Science; PI = Principal Investigator; PRET = Patients Prone to Recurrence after Endovascular Treatment

Endovascular treatment with platinum coils is safe and effective in the treatment of ruptured intracranial aneurysms. Coiling has been shown to improve the 1-year clinical outcome compared

with surgical clipping.^{1,2} Unfortunately, angiographic recurrences may occur in 10%–20% of patients, necessitating further treatment or generating concern for future rupture or retreatment-related morbidity.³ The clinical significance of angiographic recurrence is difficult to determine. A multicenter registry has reported up to 15% retreatment rates 2 years after coiling of ruptured aneurysms but a yearly rerupture rate of only 0.20% after the first year.⁴ Similar findings were reported after the Inter-

Received May 12, 2014; accepted after revision June 2.

From the Department of Radiology (J.R., A.W., F.G., D.R.), Centre Hospitalier de l'Université de Montréal and Laboratory of Interventional Neuroradiology (J.R., R.K.), Centre de recherche du Centre Hospitalier de l'Université de Montréal, Notre-Dame Hospital, Montreal, Quebec, Canada; Département de mathématiques et de statistique (M.C.), Université de Montréal, Montreal, Quebec, Canada; Department of Neurological Surgery (S.L.B.), Oregon Health & Science University, Portland, Oregon; Department of Radiology and Medical Imaging (A.J.E.), University of Virginia Health System, Charlottesville, Virginia; Department of Neurosurgery (J.M., B.L.H.), University of Florida, Gainesville, Florida; Departments of Radiology and Neurosurgery (A.S.T., R.D.T.), Medical University of South Carolina, Charleston, South Carolina; Service de Neuroradiologie Diagnostique et Interventionnelle (H.D.), Centre Hospitalier Universitaire de Nantes, Nantes, France; Department of Neurological Surgery (D.F.), Stony Brook University Medical Center, Stony Brook, New York; and Département de Neuroradiologie Diagnostique et Interventionnelle (S.B.), Centre Hospitalier Universitaire de Nancy, Nancy, France.

Paper previously presented in part at: Annual Meeting of the American Society of Neuroradiology and the Foundation of the ASNR Symposium, May 17–22, 2014; Montreal, Quebec, Canada.

Please address correspondence to Jean Raymond, MD, CHUM, Notre-Dame Hospital, Department of Radiology, 1560 Sherbrooke East, Pavilion Simard, Suite Z12909, Montreal, Quebec, Canada H2L 4M1; e-mail: jean.raymond@umontreal.ca

Indicates open access to non-subscribers at www.ajnr.org

Indicates article with supplemental on-line table.

Evidence-Based Medicine Level 1.

<http://dx.doi.org/10.3174/ajnr.A4035>

national Subarachnoid Aneurysm Trial.⁵ If posttreatment ruptures have been rare, we must remember that such low rates were observed in patients who were followed and retreated when recurrences occurred.⁶ The management of unruptured aneurysms remains controversial, but coiling is increasingly used, even though it has never been proved superior to surgery⁷ or to observation.⁸ Because the efficacy of coiling in preventing aneurysmal ruptures in patients with unruptured aneurysms has never been shown, angiographic occlusion of aneurysms remains the most frequent surrogate marker of clinical efficacy.⁹ Recurrence after endovascular treatment may affect patients with ruptured or unruptured aneurysms.

If the endovascular approach is to be improved in terms of long-term efficacy, this improvement should preferably be accomplished without compromise regarding procedural safety. Second generations of coils have been introduced for this purpose.¹⁰ However, there is no rigorous evidence that coated coils improve the angiographic or clinical outcomes. Two randomized trials have failed to demonstrate a benefit from the use of coils coated with or containing resorbable suture material.^{11,12} Hydrogel coils were initially designed to improve volumetric filling of the aneurysm with an expansive material that should fill a higher percentage of the aneurysm lumen than standard platinum coils, aiming to improve aneurysm stability after treatment. One trial comparing hydrogel and platinum coiling in 500 patients with aneurysms showed a lower proportion of core laboratory–adjudicated angiographic recurrences in the hydrogel arm at follow-up (a secondary outcome measure) but no significant difference in the composite primary outcome measure.¹³ The Patients Prone to Recurrence after Endovascular Treatment (PRET) trial was designed before the aforementioned trials had completed recruitment and follow-up of patients and before results were published. PRET was designed with the premise that some patients were at such a high risk of aneurysm recurrence at follow-up (in the range of 50%) that this risk should be revealed to patients before treatment and perhaps a different approach should at least be offered. Furthermore, given the unknown risks of alternative coils and the lack of evidence that they are beneficial, treatment with these coils should be offered only within the context of a randomized trial, until convincingly shown to be superior.¹⁴ Patients identified to be at high risk for recurrences were those with a large aneurysm (≥ 10 mm or PRET-1 patients) and those already presenting with a recurrence after previous coiling (PRET-2).^{11,13,15} We aimed to establish whether the use of hydrogel coils for high-risk patients improved angiographic outcomes compared with bare platinum coils, without increasing procedural risks. The present report focuses on operator-assessed immediate treatment success and procedural morbidity and mortality up to 1 month after the procedure. The primary outcome of the trial will be reported once the 18-month follow-up is complete.

MATERIALS AND METHODS

PRET is an investigator-led, pragmatic, multicenter, international, randomized controlled trial comparing a policy of using hydrogel versus bare platinum coils in the endovascular treatment of intracranial aneurysms in patients prone to recurrence. There were 25 participating centers from 6 countries (United States,

Canada, United Kingdom, France, Chile, Japan). The ClinicalTrials.gov registration number from the US National Institutes of Health is NCT00626912. All trial sites had local institutional review board approval. All patients (or legal representatives) signed a standardized informed consent form.

Patients

Patients with an intracranial aneurysm requiring endovascular treatment by the neurovascular team, but prone to recurrence, were eligible for the trial; the aneurysm could be ruptured (World Federation of Neurological Societies ≤ 3) or unruptured. Such patients fell into 1 of 2 groups: PRET-1, with a large aneurysm (longest dimension, ≥ 10 mm, including any thrombosed portion), never treated; PRET-2, with an aneurysm of any size, presenting with a major recurrence after previous coiling.¹⁵ A recurrence qualified as “major” if it was “saccular and its size would theoretically permit re-treatment with coils.”¹⁵ There were few selection criteria: the patient was 18 years of age or older; life expectancy was >2 years; anatomy was such that endovascular treatment was considered possible with both types of coils; the endovascular operator was satisfied with using either type of coil, but no other type; and the patient or authorized representative had given fully informed consent and had signed the consent form. Patients were not eligible if they met any of the following criteria: the presence of other aneurysms requiring treatment during the same session; the presence of an associated cerebral arteriovenous malformation; the primary intent of the procedure being parent vessel occlusion without simultaneous endovascular coiling of the aneurysm; and any absolute contraindication to endovascular treatment, angiography, or anesthesia.

Randomization

Randomized allocation was through the Web-based PRET application package (designed by MediSciNet, Stockholm, Sweden), ensuring that allocation was concealed before the decision to include a patient. From the moment of randomization, the patient was in the trial and accounted for in the analysis (intention-to-treat). PRET-1 and PRET-2 patient groups were randomized separately; treatment groups were matched according to the following minimization criteria: rupture status (yes, no); if the aneurysm was unruptured, planned use of an adjunct device (yes, no).

Embolization Procedure

Endovascular operators were not blinded to treatment allocation. Patients were masked to allocation unless they specifically requested otherwise. Standard local procedures were followed. Any locally approved bare platinum coil with controlled detachment was permitted, as were any assist devices believed necessary by the operator, provided they had local regulatory approval, excluding flow diverters, irrespective of intended use indicated at randomization. Antiplatelet and anticoagulation regimens were left to individual operator judgment, according to the clinical practice at each site.

When treatment allocation was to “platinum,” types of coils other than bare platinum were forbidden. When treatment allocation was to “hydrogel,” any coil of the hydrogel family was al-

lowed but any bare platinum coil could also be used if the operator believed it was in the patient's best interest. Recommendations concerning hydrogel coil use pertaining to type, size, and sequence of introduction were issued but not enforced. No minimum percentage of hydrogel coils was prescribed; the protocol required "the substitution, as far as possible, of platinum by hydrogel coils, the operator always being allowed to use the coils he/she believes is appropriate at any time during the procedure."¹⁴ Other technical considerations such as steaming of hydrogel coils and the type of bare platinum coil were left entirely to the operator's discretion. The goal of the procedure was to occlude the aneurysm as completely as possible, keeping the risks of the procedure as low as possible.¹⁴

Trial Monitoring

Monitoring of trial data quality was Web-based and was performed by periodic review of data stored in the data base. Blinded data were prepared for periodic reviews at prespecified intervals by an independent Data Safety and Monitoring Committee (DSMC) to ensure patient safety. A DSMC Charter predefined all trial-monitoring procedures. Unblinding criteria were prespecified in the DSMC Charter, but the need for unblinding did not arise during the conduct of the trial.

Data Collection

Data capture and management were held independent of the Steering Committee, sponsor, and funder on the secure servers of MedSciNet, ensuring FDA 21 Code of Federal Regulations Part 11, Good Clinical Practice requirements compliance. The Registration form included the following: demographics (age, sex); other aneurysms; subarachnoid hemorrhage; date and World Federation of Neurological Societies grade at the time of randomization if SAH occurred; mRS grade (if no SAH); whether the target aneurysm was a symptomatic, additional or incidental aneurysm; aneurysm location and dimensions (maximum size, length, width, and neck size); and planned use of adjunct devices. The procedure form included the following: the use of adjunct devices (mainly stents; balloon-assistance, virtually in routine use for such difficult aneurysms in many PRET centers; these were not recorded); aneurysm occlusion grade based on the Montreal grading system¹⁶ as judged by the operator; medication used during the procedure; and clinical outcome and complications during treatment (categorized as hemorrhagic, thromboembolic, or other). The total length of each type of coil was also recorded. Because the HydroSoft, HydroFrame, and HydroFill (MicroVention, Tustin, California) were marketed at different times in July 2008, April 2011, and April 2012, respectively, after the launch of the PRET trial in June 2007, a single new entry mentioning "hydrogel-core" coils was added to the Case Report Forms in December 2007, to indicate the use of those newer coil types.

The discharge form included dates of admission and discharge, discharge destination (home, hospital, rehabilitation center), whether the patient was discharged with a prescription for antiplatelet therapy, any imaging performed after the procedure, any new neurologic or imaging changes, whether ventricular shunting was performed during hospitalization, any adverse

event, and mRS score at discharge. Follow-up forms (at 1, 6, 12, and 18 months) were all designed on the same pattern, including questions regarding new symptoms (including headaches, fever, or chills), neurologic events, new imaging findings, other treatments, any admission since the last assessment, and the modified Rankin Scale as the clinical outcome measure. Adverse events were reported at any time during the trial, and automatic notification was sent to the study monitor immediately. The present article is limited to procedural results, including events occurring within 30 days of treatment (or more if within the initial admission) as reported in the procedure and discharge forms ($n = 444$, including 14 patients with no further follow-up), 1-month follow-up (392 patients) form, or later (38 patients). Imaging studies (procedural and follow-ups) were anonymized and sent to the core laboratory (P.W. White, Newcastle University, Newcastle upon Tyne, United Kingdom) for central adjudication, and follow-up angiographic results will be the object of a future publication. The angiographic results given here were the ones reported by local investigators at the end of treatment.

Safety End Points

The protocol hypothesized that "the number of adverse events was similar for both hydrogel and platinum groups, and that morbidity and mortality related to treatment remained unchanged for both PRET-1 and PRET-2 patients."¹⁴ All adverse events were reviewed by an independent Adverse Event Committee and categorized as the following: 1) related to the illness (SAH for example), 2) related to coil embolization, or 3) unrelated. The protocol also prespecified that morbidity would be defined per patient, according to the mRS score. Adverse events reports and individual case report forms were cross-checked to determine the safety of coil embolization (periprocedure and ≥ 30 days after if events occurred during the same admission) for each patient, categorized as the following: 1) death or dependency (mRS > 2) at 30 days (unrelated to the coiling procedure when no adverse events were reported; related if any serious adverse event was reported), 2) any stroke or neurologic event periprocedure or within 30 days, without dependency (mRS 0–2), 3) any procedural or pre-discharge complication or adverse event, and 4) uneventful hospitalization and procedure (no complication). Other safety indices are also reported, including procedural complications (sorted as hemorrhagic, thromboembolic, or others), neurologic deteriorations after the procedure or at discharge, mRS at discharge and 1 month, discharge destination, location at 1 month, and length of hospitalization (mean-median number of days and number of patients hospitalized for > 5 days for unruptured aneurysms and > 15 days for SAH). The number and severity of adverse events are also reported per group. To detect inflammatory complications potentially related to coils, we reviewed all adverse events within 30 days: new imaging findings (when performed and reported); new headaches; fever or chills or cranial nerve deficits up to 30 days after the procedure; and the number of patients in whom ventricular drainage was performed.

Statistical Methods

All analyses were performed by the trial statistician (M.C.), according to the published trial protocol.¹⁴ Analyses were intent-to-

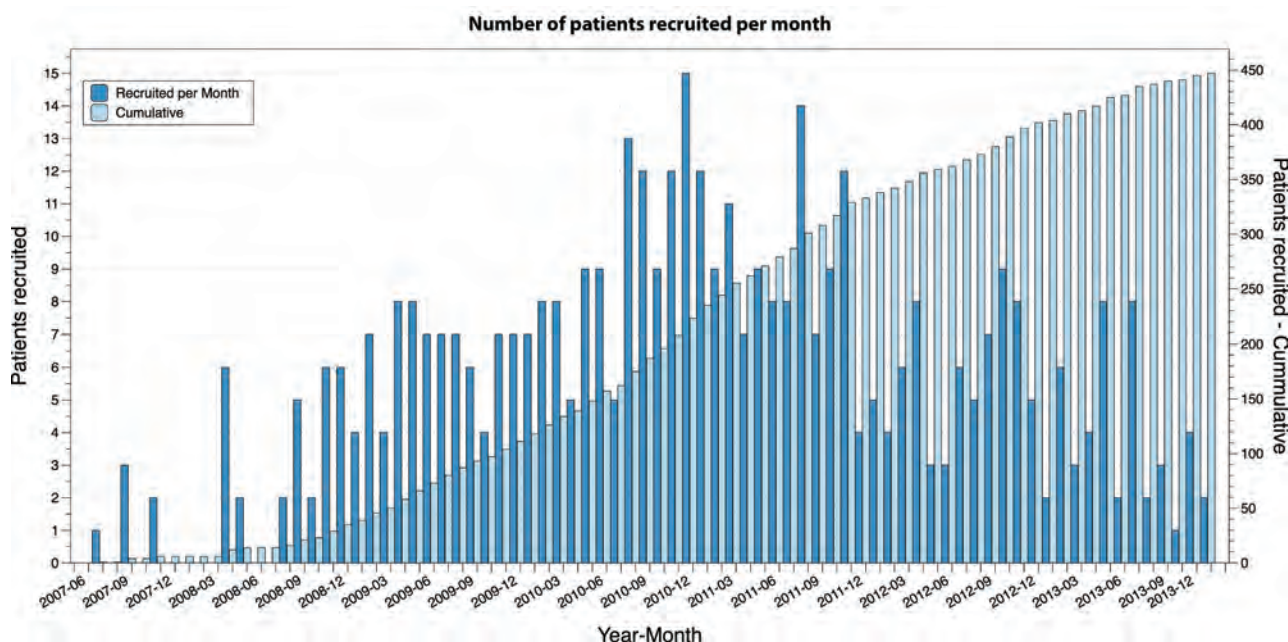


FIG 1. Recruitment. Notice how recruitment decreased progressively from December 2010 to December 2013, a possible sign of case selection.

treat. Categorical variables were compared by using the Fisher exact test, and continuous variables, by using the Student *t* test. To evaluate the possibility of different results for PRET-1 and PRET-2, we stratified descriptive and safety analyses by group. All analyses were done with SPSS, Version 21 (IBM, Armonk, New York) by using a significance level of 5%.

Roles of the Sponsor and Funding Source

The trial was sponsored by the Centre Hospitalier de l’Université de Montréal and funded by MicroVention Terumo Incorporated. The sponsor and funder had no part in study design, data collection, analysis, or reporting and had no direct or indirect access to the data or source documents. The Steering Committee bears the sole responsibility for all aspects of the trial.

RESULTS

Recruitment

Recruitment started in June 2007, but only 6 patients were included in a single center by the end of the year. Recruitment increased to reach a peak rate of 15 patients per month in December 2010, and slowly decreased thereafter (Fig 1). On December 13, 2013, when close to 250 patients had been recruited in PRET-1, the Steering Committee decided to stop recruitment before reaching the target number of patients for PRET-2 (*n* = 197 instead of 250) because of the following: 1) recruitment had decreased, particularly for patients in PRET-2 during the previous years; 2) the trial was already 2 years behind schedule; and 3) provisions had to be made to continue monitoring and cover compensations to participating sites for the 18-month follow-up data. This decision was made despite the recommendation of the DSMC meeting of February 2013 to continue recruitment. The registration Web site was closed to patient entry and randomization on January 15, 2014. By that date, target recruitment had been reached for PRET-1 (*n* = 250). The part of the data base containing baseline and early safety information was locked, but we are still collecting

6-, 12-, and 18-month follow-up data. A total of 447 patients were randomized by 25 centers in 6 countries (250 in PRET-1 and 197 in PRET-2).

Baseline Characteristics

Baseline characteristics of patients and aneurysms recruited in both PRET-1 and -2 are shown in On-line Table 1. There was no significant difference between the hydrogel and platinum groups.

Flow Chart

All patients are included in the present analyses. Results up to 30 days (or events during the initial admission if longer) were collected and reported in the procedural, discharge, and 1-month follow-up forms for all 444 treated patients, as depicted in Fig 2.

Withdrawal, Failures, and Protocol Deviations

Three patients (2 PRET-1 and 1 PRET-2) were withdrawn before any treatment was attempted (1 protocol violation [World Federation of Neurological Societies 4 after SAH]), 1 PRET-1 aneurysm judged untreatable, 1 patient in PRET-2 in whom no true recurrence was found; all 3 allocated to hydrogel). Treatment was attempted, but coils were not deployed in 4 patients in PRET-1 (1 hydrogel; 3 platinum) and 4 in PRET-2 (4 hydrogel) (or 1.8% of patients). Failure to catheterize branches for balloon-assisted or stent-assisted coiling or unstable first coils was the cause of these failures. All 8 patients were discharged home without complication within 2 days (6 with mRS 0) or 20 days (1 mRS 1 and 1 mRS 0, the last 2 patients after SAH).

Three patients in PRET-1 were not treated as allocated: One patient allocated to hydrogel was treated with only platinum coils (87 cm). One patient allocated to platinum coils was treated with some hydrogel coils (118 cm of platinum; 67 cm of hydrogel coils). Cerecyte coils (247 cm; Codman Neurovascular, Raynham,

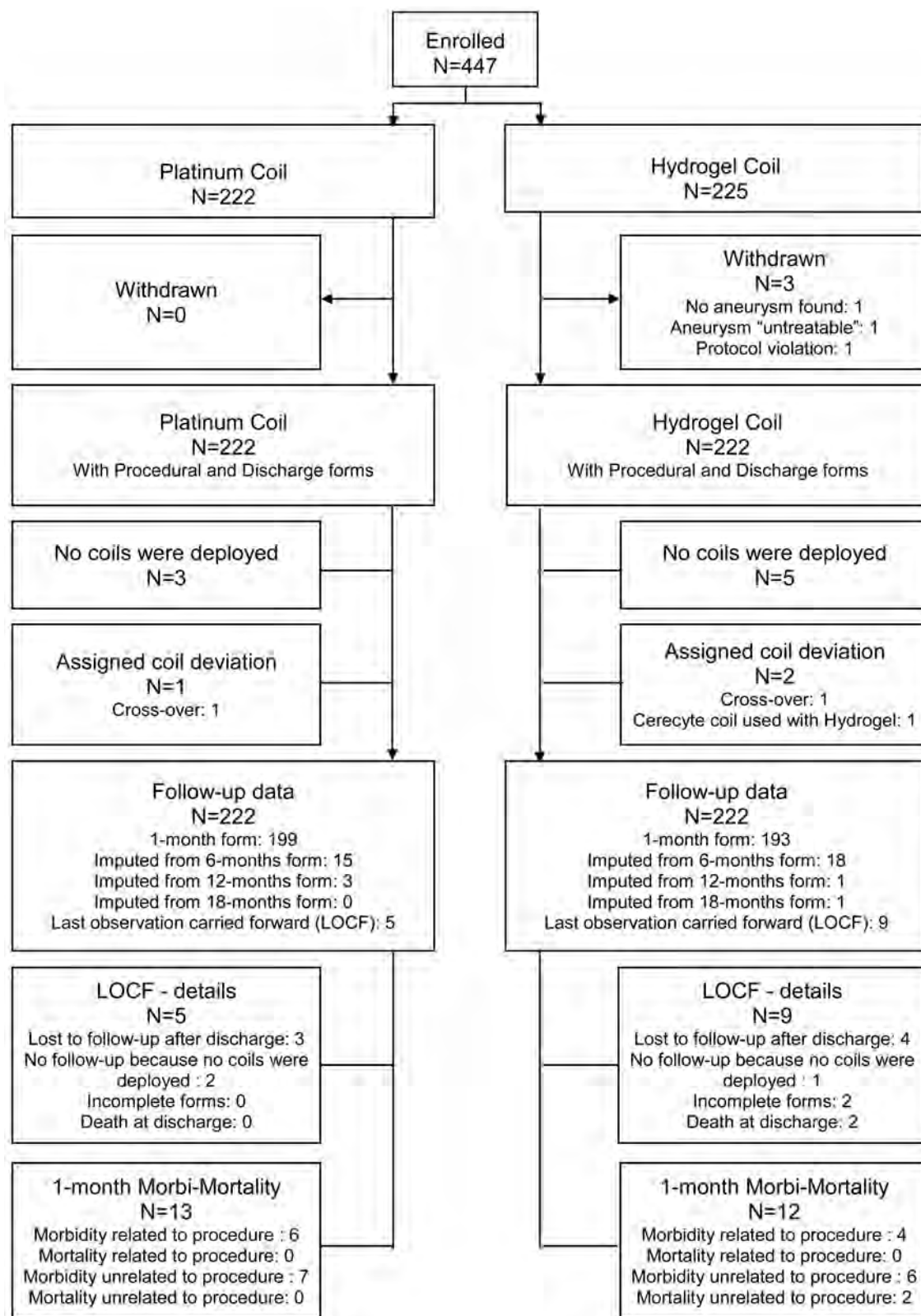


FIG 2. Flow chart. Diagram shows patient flow from randomization to periprocedural safety end points.

Massachusetts) were used in 1 other patient allocated to and treated with hydrogel coils (237-cm hydrogel; 50-cm platinum). None of these 3 patients had any complications.

The mean total length of coils was 129 cm for platinum cases

(178 cm for PRET-1; 68 cm for PRET-2) and 149 cm for hydrogel cases (125 cm for hydrogel; 24 cm for platinum) (158-cm hydrogel + 33-cm platinum for patients in PRET-1; 83-cm hydrogel + 12-cm platinum for those in PRET-2). In 202 of 222 patients

Table 1: Morbidity and mortality adjudicated per patient

	PRET-1		PRET-2		PRET	
	Platinum	Hydrogel	Platinum	Hydrogel	Platinum	Hydrogel
Death						
Total	0	2 (1.6%)	0	0	0	2 (0.9%)
Treatment-related	0	0	0	0	0	0
Morbidity (mRS > 2)						
Total	11 (8.8%)	5 (4.0%)	2 (2.1%)	5 (5.0%)	13 (5.9%)	10 (4.4%)
Treatment-related	5 (4.0%)	2 (1.6%)	1 (1.0%)	2 (2.0%)	6 (2.7%)	4 (1.8%)
Any stroke	11 (8.8%)	5 (4.0%)	8 (8.2%)	9 (9.0%)	19 (8.6%)	14 (6.2%)
Any complication	8 (6.4%)	4 (3.2%)	1 (1.0%)	2 (2.0%)	9 (4.1%)	6 (2.7%)
No complication	95 (76.0%)	107 (85.6%)	86 (88.7%)	83 (83.0%)	181 (81.5%)	190 (84.4%)
Withdrawn	0	2 (1.6%)	0	1 (1.0%)	0	3 (1.3%)
Fisher exact test <i>P</i> value	.052		.612		.174	

allocated to hydrogel (91%), more than two-thirds of the total coil length was hydrogel.

Periprocedural Outcomes

Procedural and discharge case report forms were available for all 444 treated patients, and follow-up at ≥ 1 month, in 430 (97% of treated patients).

There is no follow-up observation beyond discharge for 2 patients due to death and 12 other patients for whom no complication or adverse event was reported. These patients are included in the 1-month analyses (last observation carried forward). Three previously mentioned failures (1 hydrogel, 2 platinum) had no further follow-up. Nine other patients (6 hydrogel; 3 platinum) were discharged home after successful procedures, after 1 day ($n = 6$; mRS 0 for 5 patients and mRS 1 [hydrogel] for 1 patient) or 7 days ($n = 1$; mRS 0 [platinum]) for 7 patients with unruptured aneurysms and after 11 days (hydrogel; mRS 0) or 13 days (platinum; mRS 2) for 2 patients with SAH.

The 1-month case report forms were available in 392 patients. In 38 other patients, the follow-up information was taken from the 6-month ($n = 33$; hydrogel = 18; platinum = 15), 12-month ($n = 4$; hydrogel = 1; platinum = 3), or 18-month ($n = 1$; hydrogel) case report forms (Fig 2).

Periprocedural outcomes are summarized in Table 1. Two patients in PRET-1 (0.45%) died in the hospital 13 and 56 days after SAH, 11 and 55 days after uneventful, completed procedures (both hydrogel), one from vasospasm (related to the initial SAH), the other from cardiac arrest while on dialysis (unrelated).

Five patients were dependent before admission (1 hydrogel; 4 platinum). Twenty-three patients (5.2%) became and were still dependent 1 month after admission (16 PRET-1; 7 PRET-2; 10 hydrogel; 13 platinum). Of those, 13 patients (5 hydrogel; 8 platinum) were dependent at 1 month from SAH or aneurysm-related events (4 from vasospasm [1 hydrogel; 3 platinum]; 1 from hydrocephalus [platinum]; or without adverse events being reported [8 patients; 4 hydrogel; 4 platinum]). Ten patients were dependent from treatment-related complications, such as thromboembolic events ($n = 5$; 1 hydrogel; 4 platinum), coil perforation ($n = 2$; 2 hydrogel; 0 platinum), or postoperative strokes reported at discharge or 1 month ($n = 3$; 1 hydrogel; 2 platinum).

Strokes revealed by neurologic deficits without dependency or by asymptomatic imaging findings were found in 33 (7.4%) additional patients (14 hydrogel; 19 platinum).

Procedural complications were reported in 15 additional patients (6 hydrogel; 9 platinum), but without clinical or imaging consequences.

Technical complications related to coils were reported in 9 patients (6 hydrogel; 3 platinum) including coil stretching, fracturing, or premature detachment. Four of these events necessitated coil retrieval with a snare (3 hydrogel; 1 platinum). In 1 patient (hydrogel), the technical complication was associated with a clinical deterioration (mRS 3 at 1 month).

Other indices of safety, such as procedural complications, neurologic deteriorations, length of hospitalization, mRS, and location at discharge and 1 month, are summarized in Table 2. There was no significant difference between hydrogel and platinum for any of these comparisons.

Other Adverse Events

Adverse events within 30 days, reported in 51 patients (28 hydrogel; 23 platinum), were serious in 27 cases (14 hydrogel; 13 platinum). In addition to previously reported procedural events, 3 patients presented with transient ischemic symptoms in a delayed fashion (1 hydrogel; 2 platinum) and 2 patients (both hydrogel) had femoral artery complications, 1 serious, with retroperitoneal hematoma. Two hemorrhagic complications possibly related to antiplatelet therapy (epistaxis, gastrointestinal hemorrhage) occurred in a delayed fashion (1 hydrogel; 1 platinum).

Seven patients had new or increasing cranial nerve deficits immediately after the procedure (3 patients with cavernous [$n = 2$] or ophthalmic aneurysms) or 6–18 days later (2 patients with hydrogel with ophthalmic or carotid bifurcation aneurysms; 2 patients with platinum with ophthalmic or midbasilar aneurysms). None were serious events; they were variously labeled as “mass effect” or “inflammation” and treated with steroids.

Increased headaches were reported at 1 month in 63 patients (31 hydrogel; 32 platinum); and fever or chills, in 6 patients (4 hydrogel; 2 platinum) without neurologic events or imaging findings. Ventricular drainage was reported in 9 patients (5 hydrogel; 4 platinum) at discharge, all after the initial SAH ($n = 8$) or after coil perforation during the procedure ($n = 1$).

Angiographic Results and Exploratory Analyses

Immediate angiographic results assessed by local investigators are presented for 447 enrolled patients. They are summarized in Table 3. There was no significant difference between groups ($P = .28$).

Table 2: Safety indices reported at time of the procedure and during follow-up

	PRET-1		PRET-2		PRET	
	Platinum	Hydrogel	Platinum	Hydrogel	Platinum	Hydrogel
Procedural complications						
Thromboembolic	10 (8.0%)	6 (4.9%)	1 (1.0%)	3 (3.0%)	11 (5.0%)	9 (4.1%)
Hemorrhagic	2 (1.6%)	1 (0.8%)	1 (1.0%)	1 (1.0%)	3 (1.4%)	2 (0.9%)
Other	4 (3.2%)	6 (4.9%)	4 (4.1%)	3 (3.0%)	8 (3.6%)	9 (4.1%)
Anti-GP IIb/IIIa used during embolization	8 (6.4%)	11 (8.9%)	7 (7.2%)	4 (4.0%)	15 (6.8%)	15 (6.8%)
Clinical deterioration at end of procedure	5 (4.0%)	1 (0.8%)	2 (2.1%)	3 (3.0%)	7 (3.2%)	4 (1.9%)
Hospitalization						
Days (median) (min) (max)	2 (1) (94)	1 (0) (70)	1 (0) (51)	1 (0) (30)	1 (0) (94)	1 (0) (70)
Days >5 for unruptured aneurysms	9 (7.2%)	7 (5.7%)	5 (5.2%)	5 (5.1%)	14 (6.3%)	12 (5.4%)
Days >15 for ruptured aneurysms	10 (8.0%)	10 (8.1%)	1 (1.0%)	0	11 (5.0%)	10 (4.5%)
New imaging findings at discharge	17 (13.6)	11 (8.9%)	7 (7.2%)	9 (9.1%)	24 (10.8%)	20 (9.0%)
mRS >2 at discharge	17 (13.6%)	9 (7.3%)	1 (1.0%)	5 (5.1%)	18 (8.1%)	14 (6.3%)
Discharge destination						
Home	107 (85.6%)	108 (87.8%)	95 (97.9%)	92 (92.9%)	202 (91.0%)	200 (90.1%)
Other than home	18 (14.4%)	15 (12.2%)	2 (2.1%)	7 (7.1%)	20 (9.0%)	22 (9.2%)
mRS >2 at 1 month	11 (8.8%)	6 (4.9%)	3 (3.1%)	5 (5.1%)	14 (6.3%)	11 (5%)
Location at 1 month						
Home	117 (93.6%)	116 (94.3%)	95 (97.9%)	95 (96.0%)	212 (95.5%)	211 (95.0%)
Other than home	8 (6.4%)	7 (5.7%)	2 (2.1%)	4 (4.0%)	10 (4.5%)	11 (5%)
AE						
No. reported	16	18	7	10	23	28
No. (%) serious	10 (62%)	8 (44.4%)	3 (42.9%)	6 (60%)	13 (56.5%)	14 (50%)
AE attribution (No.) (% of total No. reported)						
Related to treatment	14 (87.5%)	14 (77.8%)	7 (100%)	10 (100%)	21 (91.3%)	24 (85.7%)
Related to aneurysm	2 (12.5%)	3 (16.7%)	0	0	2 (8.7%)	3 (10.7%)
Unrelated	0	1 (5.5%)	0	0	0	1 (3.6%)

Note:—Anti-GP IIb/IIIa indicates antiglycoprotein IIb/IIIa; AE, adverse events; min, minimum; max, maximum.

Table 3: Operator-assessed immediate angiographic results

	PRET-1		PRET-2		PRET	
	Platinum	Hydrogel	Platinum	Hydrogel	Platinum	Hydrogel
No coiling, for any reason	3 (2.4%)	3 (2.4%)	0	5 (5.0%)	3 (1.4%)	8 (3.6%)
Residual aneurysm	32 (25.6%)	39 (31.2%)	12 (12.4%)	14 (14.0%)	44 (19.8%)	53 (23.6%)
Residual neck	48 (38.4%)	48 (38.4%)	40 (41.2%)	40 (40.0%)	88 (39.6%)	88 (39.1%)
Complete obliteration	42 (33.6%)	35 (28.0%)	45 (46.4%)	41 (41.0%)	87 (39.2%)	76 (33.8%)
Fisher exact test <i>P</i> value	.723		.151		.280	

Exploratory analyses of procedural morbidity and immediate angiographic results, for all unruptured aneurysms, for carotid aneurysms, for patients treated by stent-assisted coiling, and for all patients according to aneurysm size categories, are provided in On-line Tables 2–5. There was no difference between patients receiving hydrogel and platinum.

DISCUSSION

The main findings of this report are the following: 1) coiling of large and recurrent aneurysms could be performed in 436 or 98% of 447 patients; treatment-related morbidity and mortality, defined as mRS >2 at 1 month and attributed to treatment, occurred in 2.3% (1.2%–4.1%) (10 of 444 treated patients; Table 1); 2) there was no significant difference between hydrogel and platinum coiling for any of the safety indices we reviewed (Table 2); 3) immediate angiographic results, judged by local investigators, were satisfactory (complete occlusion or residual neck) in 339 of 447 or 76.4% of patients, with no significant difference between groups (Table 3).

The selection of patients recruited in the PRET trial differs (by design and as a consequence of the design) from the patients recruited in the 4 other major randomized trials on aneurysm coil-

ing: None of the other trials included patients presenting with recurrences (an exclusion criterion for most trials); 44% of patients in PRET were PRET-2. PRET aneurysms were larger (78% of PRET, or all patients in PRET-1 and 50% of those in PRET-2 had ≥ 10 mm aneurysms); the proportion of aneurysms of ≥ 10 mm was 10% in the International Subarachnoid Aneurysm Trial,¹ 12% in the Cerecyte Coil Trial (CCT),¹⁷ 21% in the Matrix and Platinum Science (MAPS)¹¹ trial, and 24% in the HydroCoil Endovascular Aneurysm Occlusion and Packing Study (HELPS).¹⁸ Aneurysms were wide-neck (≥ 4 mm) in 70% of patients in PRET, compared with 37% in MAPS, 32% in HELPS, and 19% in CCT. Stents were used in 28% of patients in PRET (35% of those in PRET-2), 22% in MAPS, 20% in HELPS, and 0.6% of those in the CCT. Posterior circulation aneurysms were more frequent in PRET (108 or 24%, including 73 basilar bifurcation aneurysms, compared with 12% in CCT, 13% in MAPS, and only 2.7% in the International Subarachnoid Aneurysm Trial). The proportion of patients treated for ruptured aneurysms was approximately 36% in MAPS, 48% in CCT, 53% in HELPS, 100% in the International Subarachnoid Aneurysm Trial, but only 18% in PRET (29% in PRET-1; 4% in PRET-2).

These differences are expected to impact clinical results, in-

cluding periprocedural complications. For example, procedural aneurysmal ruptures or perforations may be less frequent during the treatment of larger, unruptured aneurysms.^{17,19,20} Conversely, thromboembolic complications may be more frequent, though size as a potential risk factor for complications did not reach a prespecified *P* value of .01 in a previous meta-analysis of coiling of unruptured aneurysms.⁹ Hemorrhagic complications have occurred in approximate proportion to the number of patients treated acutely (approximately 2% in MAPS, 4% in CCT and HELPS, but only 1.1% in PRET). Thromboembolic complications have varied from 4% to 28% of cases in the literature (between 5% and 10% in the CCT, MAPS, and HELPS studies), depending on the case selection, definitions, and methods of detection.²¹ Many thromboembolic complications detected at the time of coiling (3%–4% in MAPS; 5%–7% in CCT; 5%–10% in HELPS; 4.5% in PRET) may be successfully managed without clinical consequence, while others may occur, sometimes unnoticed, immediately after treatment or be confounded with vasospasm-related strokes. Fifty-six neurologic events or imaging findings (or 12.6% of patients) up to 1 month after treatment were consistent with any stroke (symptomatic or not, treatment-related or not) in PRET. There was no difference between the hydrogel and platinum groups.

The morbidity associated with coiling is perhaps best estimated when we focus on patients with unruptured aneurysms. The overall 1-month treatment-related mortality and morbidity (mRS >2) was 0% and 2.3% (1.2%–4.4%) for 361 patients in PRET-1 or -2 with unruptured aneurysms and 0% and 1.7% (0.5%–4.8%) for the 178 patients in PRET-1 treated for previously untreated large unruptured aneurysms, including 122 patients treated with stent-assisted coiling (associated with 4.1% [1.8%–9.2%] morbidity [On-line Tables 2 and 4]).

Technical problems during coil deployment (stretching or premature detachment) may have been more frequent with hydrogel (*n* = 6) than platinum (*n* = 3), but we did not find a statistical difference between coils. The 20% reduction of the total length of coils deployed when hydrogel was used in the HELPS trial¹³ was not confirmed in PRET. This difference may be due, in part, to the availability of smaller hydrogel-core finishing coils.

Inflammatory problems (cranial nerve deficits, meningitis-like syndromes, and hydrocephalus in patients with unruptured aneurysms) have previously been reported with the use of hydrogel coils.^{13,18,22-25} Even though reports such as “increased mass effect” or “inflammation” were slightly more frequent with hydrogel (5 versus 2 platinum), we did not find a significant difference with platinum or did not show an impact on treatment morbidity. Differences in immediate angiographic outcomes, with a higher (but not statistically significant) proportion of residual aneurysms after hydrogel coiling, have been reported in the HELPS trial.¹⁸ It is unclear whether this finding, if real, is an artifact from different coil densities or is caused by coil thrombogenicity or by premature interruption of coiling when operators encounter difficulties or expect hydrogel coil expansion. We did not find a significant difference. In HELPS, differences in occlusion grades were reversed (favoring hydrogel) at the time of follow-up imaging.¹³ Thus, if one keeps in mind that angiographic outcomes judged locally are typically more optimistic than core-

laboratory results,^{26,27} these preliminary findings cannot be used to anticipate follow-up imaging results, which remain to be collected, analyzed by the core lab, and reported. While we wait for long-term results from this trial and witness an increasing use of flow diversion for large, wide-neck, and recurrent aneurysms (a practice with as-yet-unknown short- and long-term benefits),²⁸ the PRET trial serves as a reminder that difficult aneurysms can be coiled with a safety that will be difficult to improve.

Limitations

The PRET trial had several limitations. First, operators could not be blinded to coil type. This unavoidable fact may have affected case selection and the use of adjunct devices, coil selection, and perhaps even premature interruption of coiling. Second, different types of hydrogel coils were being manufactured and approved during the course of the trial. This moving-target problem may create difficulties in the interpretation of results. Third, recruitment slowed down during the last 2 years (Fig 1), perhaps because treatment alternatives (such as flow diverters) were increasingly used for the same types of aneurysms. This change possibly introduces a selection bias that could weaken the generalizability of trial results. Fourth, the PRET-2 substudy was interrupted before the target number of patients was enrolled, possibly affecting the power of the study to reach meaningful conclusions for that subgroup at the end of the trial. Fifth, data monitoring was done on-line, with no local site visits to verify the data that were being reported. Finally, postprocedural studies were not imposed by protocol to verify the absence of complications detectable by imaging. These choices made the completion of an important trial at low cost possible. However, the lack of on-site monitoring and of postprocedural brain imaging is not expected to affect the validity of the present conclusions, due to the pragmatic design of the trial, which relies on relatively hard clinical outcomes and the consistency of outcome assessment across several time points. In addition, these perceived deficiencies are expected to affect treatment groups in a balanced manner.

CONCLUSIONS

There was no significant difference in the safety or immediate efficacy of the procedure between hydrogel and platinum coiling of large and recurrent aneurysms.

PRET Trial Collaborators

The PRET trial collaborators are listed in the order that participating sites joined the trial, with the number of patients recruited given in parentheses.

CHUM-Notre Dame Hospital, Montreal, Quebec, Canada: Principal Investigators (PIs), Jean Raymond, Alain Weill, and Daniel Roy; Coordinator, Ruby Klink (120). The Methodist Hospital, Houston, Texas: PIs, Richard Klucznik and Orlando Diaz; Coordinator, Marilyn Bautista (12). Kobe City Medical Center General Hospital, Kobe, Japan: PIs, Nobuyuki Sakai and Horotoshi Imamura (4). Medical University of South Carolina, Charleston, South Carolina: PIs, Aquilla Turk and Raymond Turner; Coordinator, Adrian Parker (26). State University of New York at Stony Brook University Medical Center, Stony Brook, New York: PI, Henry Woo; Coordinators, Susan Fiore and Dawn

Madigan (20). Oregon Health & Science University, Portland, Oregon: PI, Stanley Barnwell; Coordinator, Sarah Ross-Jamieson (63). Cleveland Clinic, Cleveland, Ohio: PI, Thomas Masaryk; Coordinator, Terese Wheeler (1). Centre Hospitalier Universitaire de Nancy-Hôpital Central, Nancy, France: PI, Serge Bracard; special thanks to Dr Anne Laure Derelle (8). Leeds General Infirmary, Leeds, United Kingdom: PI, Tony Goddard; Coordinator, Jonathan Pearce (also, central coordinator for the UK) (10). The Ottawa Hospital, Ottawa, Ontario, Canada: PI, Marlise Santos; Coordinator, Betty Anne Schwarz (14). Instituto de Neurocirugía Dr Asenjo, Santiago, Chile: PIs, Juan-Gabriel Sordo Jara and Eduardo Bravo (14). University of Florida (Shands Hospital), Gainesville, Florida: PIs, J. Mocco and Brian Hoh; Coordinators, Bree Burks and Nicole Wilson-Davis (29). University of Virginia Health System, Charlottesville, Virginia: PI, Avery Evans; Coordinators, Claire McKinley and Thomas Tandy (39). Centre Hospitalier Universitaire de Nantes-Hôpital Guillaume et René Laennec, Nantes, France: PI, Hubert Desal (23). West Virginia University Hospital, Morgantown, West Virginia: PI, Jeffrey Carpenter; Coordinator, Jennifer Domico (8). State University of New York Upstate Medical University, Syracuse, New York: PI, Eric Deshaies; Coordinators, Tina Craig, Kim Kasprovicz, Susan Hemingway, and Mark Villwock (10). University of Cincinnati Medical Center, Cincinnati, Ohio: PI, Andrew Ringer; Coordinator, Rebecca Reinert (4). Washington University in St. Louis, St. Louis, Missouri: PI, Christopher Moran; Coordinator, Angela Campbell (6). Queens Medical Centre, Nottingham, United Kingdom: PI, Robert Lenthall; Coordinator, Alison Southam (12). Saint Francis Medical Center, Cape Girardeau, Missouri: PI, Louis Caragine; Coordinators, Adrienne Jones and Kathy O'Howell (2). University of Oklahoma Health Sciences Center, Oklahoma City, Oklahoma: PI, Steven Hoover; Coordinators, Brian Bridges and Bradley Hightower (11). Centre Hospitalier Sainte Anne, Paris, France: PI, Olivier Naggara (2). University of Mississippi Health Care, Jackson, Mississippi: PI, Razvan Buciu; Coordinator, David Gordy (3). University of Alberta Hospital, Alberta, Canada: PI, Tim E. Darsaut (2). Vanderbilt University Medical Center, Nashville, Tennessee: PI, J. Mocco; Coordinators, Chesney Sarah Oravec and Jessica Sparks Marlin (4).

ACKNOWLEDGMENTS

First and foremost, we acknowledge the support of patients and their relatives who agreed to participate in the study and who continue to provide us with follow-up data. We also thank the medical, radiologic, and nursing staff of all participating centers. We are grateful to members of the DSMC (Sylvain Lanthier, Allan Fox). Implementing a study such as PRET requires considerable effort over a long time. Special thanks are due to Guylaine Gevry and her team at the PRET Coordination Head Office in Montreal for their outstanding work and indefatigable commitment.

Disclosures: Jean Raymond—*RELATED: Grant: MicroVention,* Comments: Grant for an investigator-led, unrestricted research funding for the PRET studies (2007–2012); UNRELATED: Grants/Grants Pending: funding for the Canadian Unruptured Endovascular versus Surgery (CURES) clinical trial from Canadian Institutes of Health research*; Other: participation in a clinical trial.* Comments: an amount per patient for participation in the new generation Hydrogel Endovas-*

cular Aneurysm Treatment (HEAT) Trial (Northwestern University Feinberg School of Medicine). Ruby Klink—RELATED: Grant: MicroVention funded the PRET trial (industry-funded, investigator-led study); Stanley L. Barnwell—RELATED: Other: MicroVention,* Comments: support to Stroke Center at OHSU for running trial, not the publication; UNRELATED: Consultancy: MicroVention, Comments: occasional consulting, work unrelated to the trial. Avery J. Evans—RELATED: Grant: MicroVention*; UNRELATED: Consultancy: Stryker, MicroVention, Covidien; Grants/Grants Pending: MicroVention, Stryker; Payment for Lectures (including service on Speakers Bureaus): Stryker, MicroVention, Covidien; Patents (planned, pending or issued): patent personally applied for; Payment for Development of Educational Presentations: Stryker; Travel/Accommodations/Meeting Expenses Unrelated to Activities Listed: Stryker, MicroVention, Covidien. J. Mocco—UNRELATED: Board Membership: Codman Neurovascular (advisory board)*; Consultancy: Lazarus Effect, Medina Medical, Pulsar Vascular, Reverse Medical, Edge Therapeutics; Grants/Grants Pending: National Institutes of Health Funding: NIH 1U01NS086492-01; NIH 1R01NS078828-01A1; Other: Blockade Medical, Medina Medical, Comments: personal investment. Brian L. Hoh—RELATED: Grant: Our institution receives funding for participating in the trial, with payment made by the Centre hospitalier de l'université de Montréal through an unrestricted grant from Microvention.* UNRELATED: Grants/Grants Pending: National Institutes of Health*; Other: Steering Committee for clinical trial for Edge Therapeutics. Aquilla S. Turk—RELATED: Grant: MicroVention,* Comments: study paid per patient for research personnel to collect data for trial purposes; UNRELATED: Consultancy: Penumbra, Stryker, MicroVention, Codman, Medina, Pulsar Vascular; Expert Testimony: defense litigation; Grants/Grants Pending: Penumbra,* Stryker,* MicroVention,* Codman,* Medina,* Pulsar Vascular,* Comments: LARGE trial and POSITIVE trial, enrolling site for multiple other trials; Payment for Lectures (including service on Speakers Bureaus): Penumbra, MicroVention; Stock/Stock Options: Pulsar Vascular, Medina, Lazarus Effect; Travel/Accommodations/Meeting Expenses Unrelated to Activities Listed: Penumbra,* Covidien,* Codman,* Stryker. Raymond D. Turner—RELATED: Grant: Codman,* Covidien,* MicroVention,* Stryker,* Blockade Medical,* Reverse Medical*; Consulting Fee or Honorarium: MicroVention, Codman, Covidien, Blockade Medical, Pulsar Vascular, Reverse Medical. David Fiorella—RELATED: Grant: MicroVention/Terumo*; UNRELATED: Consultancy: Covidien/ev3, Codman/JNJ; Grants/Grants Pending: Siemens Medical Imaging,* Sequent Medical,* Comments: LVIS IDE study PI, Sequent WEB IDE trial PI; Patents (planned, pending or issued): Codman/JNJ; Royalties: Codman/JNJ; Travel/Accommodations/Meeting Expenses Unrelated to Activities Listed: Penumbra. Serge Bracard—UNRELATED: Grants/Grants Pending: French Ministry of Health Program STIC,* Comments: randomized study THRACE on thrombectomy in stroke. Alain Weill—UNRELATED: Grants/Grants Pending: fellowship grants from Codman,* Stryker,* Covidien*; Payment for Lectures (including service on Speakers Bureaus): MicroVention,* for lecture given at AAFITN 2014 on bailout strategies in aneurysm coiling. Daniel Roy—RELATED: Grant: MicroVention,* Comments: grant support for the study. No role in design, data management, or manuscript. *Money paid to the institution.*

REFERENCES

1. Molyneux A, Kerr R, Stratton I, et al. **International Subarachnoid Aneurysm Trial (ISAT) of neurosurgical clipping versus endovascular coiling in 2143 patients with ruptured intracranial aneurysms: a randomised trial.** *Lancet* 2002;360:1267–74
2. Molyneux AJ, Kerr RS, Yu LM, et al. **International Subarachnoid Aneurysm Trial (ISAT) of neurosurgical clipping versus endovascular coiling in 2143 patients with ruptured intracranial aneurysms: a randomised comparison of effects on survival, dependency, seizures, rebleeding, subgroups, and aneurysm occlusion.** *Lancet* 2005;366:809–17
3. Ferns SP, Sprengers ME, van Rooij WJ, et al. **Coiling of intracranial aneurysms: a systematic review on initial occlusion and reopening and retreatment rates.** *Stroke* 2009;40:e523–29
4. Carat Investigators. **Rates of delayed rebleeding from intracranial aneurysms are low after surgical and endovascular treatment.** *Stroke* 2006;37:1437–42
5. Campi A, Ramzi N, Molyneux AJ, et al. **Retreatment of ruptured cerebral aneurysms in patients randomized by coiling or clipping in the International Subarachnoid Aneurysm Trial (ISAT).** *Stroke* 2007;38:1538–44
6. Raymond J. **Counterpoint: has the last word been said?** *AJNR Am J Neuroradiol* 2009;30:1649–52
7. Darsaut TE, Findlay JM, Raymond J. **The design of the Canadian**

- UnRuptured Endovascular versus Surgery (CURES) trial. *Can J Neurol Sci* 2011;38:236–41
8. Raymond J, Molyneux AJ, Fox AJ, et al. **The TEAM trial: safety and efficacy of endovascular treatment of unruptured intracranial aneurysms in the prevention of aneurysmal hemorrhages—a randomized comparison with indefinite deferral of treatment in 2002 patients followed for 10 years.** *Trials* 2008;9:43
 9. Naggara ON, Lecler A, Oppenheim C, et al. **Endovascular treatment of intracranial unruptured aneurysms: a systematic review of the literature on safety with emphasis on subgroup analyses.** *Radiology* 2012;263:828–35
 10. White PM, Raymond J. **Endovascular coiling of cerebral aneurysms using “bioactive” or coated-coil technologies: a systematic review of the literature.** *AJNR Am J Neuroradiol* 2009;30:219–26
 11. McDougall CG, Johnston SC, Gholkar A, et al. **Bioactive versus bare platinum coils in the treatment of intracranial aneurysms: the MAPS (Matrix and Platinum Science) Trial.** *AJNR Am J Neuroradiol* 2014;35:935–42
 12. Molyneux AJ, Clarke A, Sneade M, et al. **Cerecyte Coil Trial: angiographic outcomes of a prospective randomized trial comparing endovascular coiling of cerebral aneurysms with either Cerecyte or bare platinum coils.** *Stroke* 2012;43:2544–50
 13. White PM, Lewis SC, Gholkar A, et al. **Hydrogel-coated coils versus bare platinum coils for the endovascular treatment of intracranial aneurysms (HELPS): a randomised controlled trial.** *Lancet* 2011;377:1655–62
 14. Raymond J, Roy D, White PM, et al. **A randomized trial comparing platinum and hydrogel-coated coils in Patients Prone to Recurrence after Endovascular Treatment (the PRET Trial).** *Interv Neuroradiol* 2008;14:73–83
 15. Raymond J, Guilbert F, Weill A, et al. **Long-term angiographic recurrences after selective endovascular treatment of aneurysms with detachable coils.** *Stroke* 2003;34:1398–403
 16. Roy D, Milot G, Raymond J. **Endovascular treatment of unruptured aneurysms.** *Stroke* 2001;32:1998–2004
 17. Coley S, Sneade M, Clarke A, et al. **Cerecyte coil trial: procedural safety and clinical outcomes in patients with ruptured and unruptured intracranial aneurysms.** *AJNR Am J Neuroradiol* 2012;33:474–80
 18. White PM, Lewis SC, Nahser H, et al. **HydroCoil Endovascular Aneurysm Occlusion and Packing Study (HELPS trial): procedural safety and operator-assessed efficacy results.** *AJNR Am J Neuroradiol* 2008;29:217–23
 19. Cloft HJ, Kallmes DF. **Cerebral aneurysm perforations complicating therapy with Guglielmi detachable coils: a meta-analysis.** *AJNR Am J Neuroradiol* 2002;23:1706–09
 20. Nguyen TN, Raymond J, Guilbert F, et al. **Association of endovascular therapy of very small ruptured aneurysms with higher rates of procedure-related rupture.** *J Neurosurg* 2008;108:1088–92
 21. Pelz DM, Lownie SP, Fox AJ. **Thromboembolic events associated with the treatment of cerebral aneurysms with Guglielmi detachable coils.** *AJNR Am J Neuroradiol* 1998;19:1541–47
 22. Meyers PM, Lavine SD, Fitzsimmons BF, et al. **Chemical meningitis after cerebral aneurysm treatment using two second-generation aneurysm coils: report of two cases.** *Neurosurgery* 2004;55:1222
 23. Turner RD, Byrne JV, Kelly ME, et al. **Delayed visual deficits and monocular blindness after endovascular treatment of large and giant paraophthalmic aneurysms.** *Neurosurgery* 2008;63:469–74, discussion 474–75
 24. Xu DS, Hurley MC, Batjer HH, et al. **Delayed cranial nerve palsy after coiling of carotid cavernous sinus aneurysms: case report.** *Neurosurgery* 2010;66:E1215–16
 25. Im SH, Han MH, Kwon BJ, et al. **Aseptic meningitis after embolization of cerebral aneurysms using hydrogel-coated coils: report of three cases.** *AJNR Am J Neuroradiol* 2007;28:511–12
 26. Tollard E, Darsaut TE, Bing F, et al. **Outcomes of endovascular treatments of aneurysms: observer variability and implications for interpreting case series and planning randomized trials.** *AJNR Am J Neuroradiol* 2012;33:626–31
 27. Rezek I, Lingineni RK, Sneade M, et al. **Differences in the angiographic evaluation of coiled cerebral aneurysms between a core laboratory reader and operators: results of the Cerecyte Coil Trial.** *AJNR Am J Neuroradiol* 2014;35:124–27
 28. Becks T, Kallmes DF, Saatci I, et al. **Pipeline for uncoilable or failed aneurysms: results from a multicenter clinical trial.** *Radiology* 2013;267:858–68

Comparative Effectiveness Research

J.A. Hirsch, P.W. Schaefer, J.M. Romero, J.D. Rabinov, P.C. Sanelli, and L. Manchikanti

ABSTRACT

SUMMARY: The goal of comparative effectiveness research is to improve health care while dealing with the seemingly ever-rising cost. An understanding of comparative effectiveness research as a core topic is important for neuroradiologists. It can be used in a variety of ways. Its goal is to look at alternative methods of interacting with a clinical condition, ideally, while improving delivery of care. While the Patient-Centered Outcome Research initiative is the most mature US-based foray into comparative effectiveness research, it has been used more robustly in decision-making in other countries for quite some time. The National Institute for Health and Clinical Excellence of the United Kingdom is a noteworthy example of comparative effectiveness research in action.

ABBREVIATIONS: CER = comparative effectiveness research; PCORI = Patient-Centered Outcomes Research Institute; PCORTF = Patient-Centered Outcomes Research Trust Fund

“Neo-modern” effectiveness research began with James Lind in Scotland in the mid-18th century. Graduates of the Edinburgh Medical School developed a concept of “arithmetical medicine.”^{1,2} Dr Lind’s historic controlled study of 6 different treatments for scurvy was, in reality, the first true “evidence” of comparative effectiveness research (CER).³ In the early 20th century, Ernest Codman started looking at “outcomes management” in patient care.⁴

The Institute of Medicine provided the current definition of CER as “the generation and synthesis of evidence that compares the benefits and harms of alternative methods to prevent, diagnose, treat, and monitor a clinical condition or to improve the delivery of care.”⁵ The purpose of CER is to help all role groups associated with the health care enterprise make informed decisions useful in the management of an individual patient. In this article, we will explore the historical development of CER at the federal level in the United States up to and including the present day. We will reflect on some of the opportunities available through the American Society of Neuroradiology.

Meaningful geographic variation exists in health care. This, at least in part, relates to limited evidence and is one of the issues that augur well for CER differences in use corresponding to large discrepancies in Medicare spending per enrollee in various geographies.^{6,7}

Geographic variation occurs, in part, when definitive evidence for a treatment does not exist. For neurointerventional specialists, a ready example might be the application of the International Study of Unruptured Intracranial Aneurysms data or application of intra-arterial stroke therapy. This challenge is widely pervasive and not limited to neurointerventional or neuroradiology practice.⁸ It is rational to believe that patients in different locations have varying disease prevalence. It is also equally rational to believe that the variation known to exist and meticulously documented in treatment paradigms might reflect more than just different underlying diseases. Variability in practice can result in waste and inefficiency.⁹⁻¹¹

Selective History of CER with a Focus on Recent US Regulatory and Legislative Actions

“Arithmetical medicine” was first practiced in 18th century Edinburgh, Scotland.¹ As stated above, at the University of Edinburgh, James Lind performed a controlled trial for scurvy by using 6 separate treatments.³ Pierre Louis developed what could be loosely translated as the numeric method in 19th century France. This approach ended the use of phlebotomy in pneumonia.¹ In the US, in the early 1900s, Ernest Codman published *A Study in Hospital Efficiency: As Demonstrated by the Case Report of the First Five Years of a Private Hospital*.⁴ In that book, Codman described the field that would burgeon into outcomes management by re-

Received February 11, 2014; accepted after revision March 12.

From the Department of Radiology (J.A.H., P.W.S., J.M.R., J.D.R.), Massachusetts General Hospital, Harvard Medical School, Boston, Massachusetts; Department of Radiology (P.C.S.), Weill Cornell Medical College, New York-Presbyterian Hospital, New York, New York; Pain Management Center of Paducah (L.M.), Paducah, Kentucky; and Department of Anesthesiology and Perioperative Medicine (L.M.), University of Louisville, Louisville, Kentucky.

Please address correspondence to Joshua A. Hirsch, MD, Department of Radiology, Massachusetts General Hospital, Harvard Medical School, Boston, MA 02114; e-mail: Hirsch@snisonline.org

<http://dx.doi.org/10.3174/ajnr.A3985>

viewing 337 discharged patients between 1911 and 1916. Codman's work was also noteworthy for recording and publicizing 123 errors.

In 1972, the Office of Technology Assessment was created with a portion of its mandate focused on clinical effectiveness in health care.¹² The Office of Technology Assessment was eliminated in 1995.

In 1978, the National Center for Health Care Technology was created. As the name suggests, the Center was designed to conduct health care technology-related research that provided advice on research priorities. The Center closed 3 years later but, in that time, had made approximately 75 recommendations to the Centers for Medicare and Medicaid Services regarding coverage.⁶

The Agency for Health Care Policy and Research was established in 1989 and created the National Guideline Clearinghouse to guide treatment decisions.¹³ The Patient-Centered Outcomes Research Trust Fund (PCORTF) was reorganized as it is known today into the Agency for Healthcare Research and Quality.

In 2003, the Medicare Modernization Act authorized that as much as US \$50 million be spent on CER.¹⁴ This funding (at lower levels) has continued with time, and the Agency for Healthcare Research and Quality established an "effective healthcare" program, which is charged with reviewing and synthesizing existing evidence.¹⁵

Veterans Affairs has long focused on the clinical effectiveness of treatments given to its patients. This has been aided by a forward-looking approach aimed at using electronic medical records. Veterans Affairs sponsors reviews through the Technology Assessment Program, which could also be properly characterized as CER.

The Centers for Medicare and Medicaid Services is critical in paying for health care but has had only a finite role with CER. Bearing that in mind, the Centers for Medicare and Medicaid Services has indeed taken small steps into CER.^{6,16}

The 2009 American Recovery and Reimbursement Act brought CER into the forefront on the basis of the size of the federal financial commitment (see below).^{17,18} The CER was apportioned \$1.1 billion, and it gave birth to the Federal Coordinating Council, whose job was to help coordinate federally funded CER activities.¹⁷ There are 15 members of the council.

On June 30, 2009, the council made recommendations for CER funding priorities. They also categorized activity, seeing where there were holes, and identified how these holes would inform their recommendations going forward. The council indicated that the expansion of CER will improve health care decision-making going forward.^{18,19}

On March 23, 2010, the Patient Protection and the Affordable Care Act (also known as the Affordable Care Act) became law.²⁰⁻²² Building on the work that had already occurred during the Obama administration, the Affordable Care Act had critical elements related to CER. The Patient-Centered Outcomes Research Institute (PCORI) is an integral part of the legislation, and its explicit tasks are to evaluate and use CER.^{22,23}

The Patient-Centered Outcomes Research Institute

The PCORI set about identifying research priorities and developing an agenda that will inform the various participants (health

Table 1: Examples of patient-centered questions addressed in PCORI research^a

Examples
"Given my personal characteristics, conditions and preferences, what should I expect will happen to me?"
"What are my options and what are the potential benefits and harms of those options?"
"What can I do to improve the outcomes that are most important to me?"
"How can clinicians and the care delivery systems they work in help me make the best decisions about my health and health care?"

^a Source: Patient-Centered Outcomes Research Institute (PCORI).²³

care providers, patients, administrators, payers, and so forth) about different health care choices. Much of the basis of the PCORI had been established by the previously discussed Federal Coordinating Council. PCORI is headed by a 21-member Board of Governors, which, by design, includes a broad section of role groups reflecting the diverse constituents of the PCORI. A 17-member Methodology Committee defines the methodologic standards for research. The Government Accountability Office appoints the Board of Governors and the members of the Methodology Committee. At the time of the founding legislation, it was thought that the PCORI, as an independent body, required funding outside the normal appropriations process. As such, the Patient-Centered Outcomes Research Trust Fund was created.

The PCORTF receives funds from 2 separate sources. In the aggregate, the funding is significant. The initial funding from the US Treasury during 2010–2012 provided \$210 million. Beginning in 2013, the Trust Fund started receiving funds from its second source—fees assessed on health insurance plans, including Medicare. In 2013, the PCORTF received \$150 million from the US Treasury and an annual fee assessed on different health care plans of approximately \$170 million dollars for a total of \$320 million. From 2014 through 2019, the PCORTF will continue to receive the same appropriation from the US Treasury and a larger assessment from the various health plans for an estimated \$650 million per year. In total, the calculation is that \$3.5 billion will be provided by these different funding sources before September 30, 2019. This represents the largest federally funded commitment to comparative effectiveness research in the history of our nation.²³

On March 5, 2012, the Board of Governors approved the following definition of patient-centered outcomes research: "Patient-centered outcomes research helps people and their caregivers communicate and make informed health care decisions, allowing their voices to be heard in assessing the value of health care options."²³

PCORI also developed methodologic standards in the form of questions (Table 1). The answers to these questions are found in Table 2.

PCORI established the National Priorities for Research and Research Agenda as part of their basic charge. This framework will provide guidance to funding CER with federal funds.²³ The 5 research priorities are the following: 1) assessment of prevention, diagnosis, and treatment options; 2) improving health care systems; 3) communication and dissemination of research; 4) addressing disparities; and 5) accelerating patient-centered outcomes research and methodologic research.

Table 2: PCORI responses to patient-centered questions^a

Responses
Assess the benefits and harms of preventive, diagnostic, therapeutic, palliative, or health-delivery system interventions to inform decision-making, highlighting comparisons and outcomes that matter to people.
Be inclusive of an individual's preferences, autonomy, and needs, focusing on outcomes that people notice and care about such as survival, function, symptoms, and health-related quality of life.
Incorporate a wide variety of settings and diversity of participants to address individual differences and barriers to implementation and dissemination.
Investigate (or may investigate) optimizing outcomes, while addressing the burden to individuals, the availability of services, technology, and personnel and other stakeholder perspectives.

^a Source: Patient-Centered Outcomes Research Institute (PCORI).²³

As part of developing this National Priorities and Research Agenda, the PCORI held a 53-day public comment period on the draft plan in 2012.²⁴ The high level of public interest is reflected in the fact that the Institute received 474 comments for the Priorities and Agenda. The result was that 15 major, aggregated themes emerged from the public comments; these were in line with the 5 proposed priorities.

One can obtain funding from the PCORI using 2 fundamental approaches. The first is an investigator-initiated approach, which was launched in May 2012 and, in some ways, is typical of more traditional methodologies. The second approach relies on patients and other stakeholders to initiate. Five topics have been identified for accelerated consideration by using that second initiative.²³

While comparative effectiveness has been celebrated, issues continue to affect the research. A key issue underlying all major clinical research, whether randomized clinical trials or observational, is dissemination and implementation of findings. This issue may be the greatest challenge of CER, because even well-conducted and very prominent randomized controlled trials may not result in changes in physician behavior. Dissemination is included as one of the goals of the PCORI Methodology Committee.²⁵ Even then, given the strong tendency for inertia and much previous effort intended to promote dissemination of research findings and incorporation into practice that did not succeed, it is not clear whether or how this will ultimately translate into action.

Many national medical societies are addressing this growing interest in CER by developing educational materials, providing training courses, and creating funding support. The American Society of Neuroradiology has initiated a new funding mechanism specifically for CER in neuroimaging. Other efforts include developing CER workshops at its annual meeting and jointly sponsoring national CER training programs targeting junior investigators.

Summary

CER is designed to compare research of alternative approaches to prevent, diagnose, treat, and monitor clinical conditions and to support patient-centered care that will produce superior patient outcomes. Comparative effectiveness research has captured the attention of the biomedical community, including physicians, other health care professionals, and clinical researchers; the public, including patients and their advocates; and policy makers,

including funding agencies and health care insurers.²⁶ CER should allow us to improve the evidence base and better inform decisions going forward. Ultimately, the authors hope that it will improve the quality of care and help control health care costs.²⁷

ACKNOWLEDGMENTS

The authors thank Irina Badayan and Cynthia Hynes for their help with this article.

Disclosures: Joshua A. Hirsch—UNRELATED: served as a consultant and received royalties from CareFusion, and holds stocks/stock options from Intratech.

REFERENCES

- Evans H. **Comparative effectiveness in health care reform: lessons from abroad.** *Backgrounder No. 2239 on Health Care.* February 4, 2009. <http://www.heritage.org/research/reports/2009/02/comparative-effectiveness-in-health-care-reform-lessons-from-abroad>. Accessed January 4, 2014
- Manchikanti L, Falco FJ, Boswell MV, et al. **Facts, fallacies, and politics of comparative effectiveness research. Part I. Basic considerations.** *Pain Physician* 2010;13:E23–54
- Brown SR. *Scurvy: How a Surgeon, a Mariner, and a Gentleman Solved the Greatest Medical Mystery of the Age of Sail.* New York: St. Martin's Press; 2003
- Codman EA. *A Study in Hospital Efficiency: As Demonstrated by the Case Report of the First Five Years of a Private Hospital.* Boston: Thomas Todd Co; 1918
- Committee on Comparative Effectiveness Research Prioritization, Institute of Medicine. *Initial National Priorities for Comparative Effectiveness Research.* Washington, DC: National Academy of Sciences; 2009
- Sung NS, Crowley WF Jr, Genel M, et al. **Central challenges facing the national clinical research enterprise.** *JAMA* 2003;289:1278–87
- Murillo H, Reece EA, Snyderman R, et al. **Meeting the challenges facing clinical research: solutions proposed by leaders of medical specialty and clinical research societies.** *Acad Med* 2006;81:107–12
- Mackey J, Brown RD Jr, Moomaw CJ, et al. **Unruptured intracranial aneurysms in the Familial Intracranial Aneurysms and International Study of Unruptured Intracranial Aneurysms cohorts: differences in multiplicity and location.** *J Neurosurg* 2012;117:60–64
- Lauer MS. **Comparative effectiveness research: the view from the NHLBI.** *J Am Coll Cardiol* 2009;53:1084–86
- Emanuel EJ. **What cannot be said on television about health care.** *JAMA* 2007;297:2131–33
- Midwest Business Group on Health in collaboration with Juran Institute, Inc, The Severyn Group, Inc. *Reducing the Costs of Poor-Quality Health Care through Responsible Purchasing Leadership.* Chicago: Midwest Business Group on Health; 2003
- Office of Technology Assessment. Congress of the United States. *Identifying Health Technologies that Work: Searching for Evidence.* Daryby: Diane Publishing Co; 1994
- US Department of Health and Human Services. Agency for Healthcare Research and Quality. <http://www.ahrq.gov/>. Accessed December 5, 2013
- The Medicare Prescription Drug, Improvement and Modernization Act of 2003 (MMA). Vol P.L. §108–173/2003 (2003)
- Agency for Healthcare Research and Quality. Effective Health Care Program. <http://www.effectivehealthcare.ahrq.gov/>. Accessed January 10, 2014
- Manchikanti L, Helm Ii S, Singh V, et al. **Accountable interventional pain management: a collaboration among practitioners, patients, payers, and government.** *Pain Physician* 2013;16:E635–70
- American Recovery and Reinvestment Act of 2009 (Recovery Act). Vol P.L., USC §111–5200 (2009)
- Federal Coordinating Council for Comparative Effectiveness Research. *Report to the President and Congress.* Washington DC: U.S. Department of Health and Human Services; 2009. <http://www.ahrq.gov/>

- tuftsctsi.org/~media/Files/CTSI/Library%20Files/FCC%20for%20CER%20Rpt%20to%20Pres%20and%20Congress_063009.ashx. Accessed January 5, 2014
19. Dougherty D, Conway PH. **The “3T’s” road map to transform US health care: the “how” of high-quality care.** *JAMA* 2008;299:2319–21
 20. HealthCare.gov. Health Insurance Marketplace. <https://www.healthcare.gov/marketplace/b/welcome/>. Accessed January 5, 2014
 21. Manchikanti L, Hirsch JA. **Obamacare 2012: prognosis unclear for interventional pain management.** *Pain Physician* 2012;15:E629–40
 22. Manchikanti L, Hirsch JA. **Patient protection and affordable care act of 2010: a primer for neurointerventionalists.** *J Neurointerv Surg* 2012;4:141–46
 23. Patient-Centered Outcomes Research Institute (PCORI). www.pcori.org. Accessed November 10, 2013
 24. Selby JV, Beal AC, Frank L. **The Patient-Centered Outcomes Research Institute (PCORI) national priorities for research and initial research agenda.** *JAMA* 2012;307:1583–84
 25. Methodology Committee of the Patient-Centered Outcomes Research Institute (PCORI). **Methodological standards and patient-centeredness in comparative effectiveness research: the PCORI perspective.** *JAMA* 2012;307:1636–40
 26. Golub RM, Fontanarosa PB. **Comparative effectiveness research: relative successes.** *JAMA* 2012;307:1643–45
 27. Concato J. **Is it time for medicine-based evidence?** *JAMA* 2012;307:1641–43

Genetics of Ataxias: Hereditary Forms

N. Tirada and L.M. Levy

ABBREVIATION: SCA = spinocerebellar ataxia

WHAT ARE HEREDITARY ATAXIAS?

Ataxia is a neurologic disorder in which there is loss of coordination of movement. It can result from dysfunction of the cerebellum and brain stem and their afferent or efferent pathways. The etiology of ataxia can be divided into 3 main categories: acquired, sporadic, and hereditary.^{1,2} Hereditary ataxias are one of the largest groups of hereditary progressive neurodegenerative diseases with an estimated prevalence for all ataxias of 3–4 per 20,000.^{2,3} Although there is no present curative therapy for hereditary ataxias, novel treatments aim to impact the disease process at the molecular level. Neuroimaging, particularly MR imaging, should be performed in all patients with suspected hereditary ataxias. Neuroimaging can help to make the correct diagnosis, identify treatable causes, monitor disease progression, and exclude secondary causes. The objective of this vignette is to describe the heterogeneous group of hereditary ataxias and to discuss their diverse clinical presentations, imaging characteristics, and diagnostic challenges.

WHAT ARE THE MODES OF INHERITANCE OF HEREDITARY ATAXIA?

There are multiple modes of inheritance of hereditary ataxia: These include autosomal recessive, autosomal dominant, X-linked (paternal), mitochondrial forms (maternal), and incomplete penetrance.

AUTOSOMAL DOMINANT MODE OF INHERITANCE

Classification of autosomal dominant spinocerebellar ataxias (SCAs) is traditionally described by using the Harding classification, which is based on clinical presentation.⁴ However, given the

significant overlap of clinical symptoms, a genetic classification is now favored and subtypes of SCAs are now largely established via genetic testing. To date, there are more than 30 types of SCAs that have been identified (SCA1-SCA36). The pathophysiology of nearly half of the autosomal dominant ataxias is secondary to trinucleotide or codon repeat expansions.⁵ The most common trinucleotide repeat expansions are associated with polyglutamine repeats (SCA1, SCA2, SCA3, SCA6, and SCA7). However, polyglutamine repeats are not unique to SCAs and can also be seen with Huntington disease and dentatorubral-pallidolusian atrophy. It is hypothesized that the large number of polyglutamine repeats can lead to misfolding of mutant protein, cellular dysfunction, and eventually cell death.¹ Larger numbers of expanded alleles can also precipitate earlier disease onset and worsen the clinical course. In addition, germline expansion or instability can cause an anticipation effect with progressive worsening of disease in subsequent generations. Intermediate expansion of trinucleotides may not express phenotypes in tested individuals but may lead to disease in their offspring. Anticipation may be more pronounced in males (eg, fragile X) secondary to the high number of cell divisions during spermatogenesis.⁶ Other type of mutations occurring in autosomal dominant spinocerebellar ataxia include missense (SCA5, SCA13, SCA14, SCA23, SCA27, SCA28, and SCA35), frameshift (SCA11), and deletion (SCA15 and SCA16) mutations.⁷

AUTOSOMAL RECESSIVE MODE OF INHERITANCE

Autosomal recessive ataxias are another diverse group of diseases that can be broadly categorized into the following 4 groups: 1) degenerative such as Friedreich ataxia, CoQ10 deficiency, and Charlevoix-Saguenay spastic ataxia; 2) congenital such as Joubert syndrome subtypes 1–5 and Cayman ataxia; 3) metabolic such as ataxia associated with vitamin E deficiency, abetalipoproteinemia, Tay-Sachs disease, and Wilson disease; and 4) ataxias with DNA repair defects such as ataxia telangiectasia, ataxia with oculomotor apraxia subtypes 1 and 2, and spinocerebellar ataxia with neuropathy.¹ The most common autosomal recessive cerebellar

Received September 14, 2013; accepted after revision September 17.

From the George Washington University Medical Center, Department of Radiology, Washington, DC.

Please address correspondence to Lucien M. Levy, MD, PhD, George Washington University Medical Center, Department of Radiology, 900 23rd St NW, Washington, DC 20037; e-mail: llevy@mfa.gwu.edu

<http://dx.doi.org/10.3174/ajnr.A3783>

ataxia is Friedreich ataxia, which is secondary to GAA trinucleotide repeat expansions.^{1,5} In Friedreich ataxia, the mutant proteins cause loss of function of frataxin, an iron storage or chaperone protein in the mitochondria, resulting in iron overload and cellular oxidative damage.^{3,8} Patients with Friedreich ataxia can have non-neurologic manifestations such as cardiomyopathy and diabetes,⁵ in addition to ataxia.

DIAGNOSING HEREDITARY ATAXIA

Once hereditary ataxia is suspected, a detailed medical history should be obtained before genetic testing and imaging studies.⁹ This should include a physical examination, a neurologic examination, and at least a 3-generation family history to exclude secondary causes of ataxia.⁹ However, a lack of family history does not preclude a diagnosis of hereditary ataxia because patients with autosomal recessive ataxia, incomplete penetrance, or trinucleotide repeat expansion may have a negative family history. The age of onset can also be important because autosomal dominant ataxias are associated with later ages of onset compared with autosomal recessive ataxias, the former occurring between the third and fourth decades and the latter in the second decade, though findings can vary markedly.^{1,2}

LABORATORY AND GENETIC TESTING

Specific genetic tests are available for SCA1, SCA2, SCA3, SCA6, SCA8, SCA10, SCA12, SCA17, dentatorubral-pallidolusian atrophy ataxias, and fragile X-associated tremor ataxia syndrome, all of which are trinucleotide repeat disorders. However, with the exception of fragile X-associated tremor ataxia syndrome, there is no established consensus on the normal range for the number of repeats.⁸ Patients with negative findings on genetic testing who have idiopathic sporadic cerebellar ataxias, mutations associated with many SCAs, and Friedreich ataxias account for nearly 20% of cases; but whether this percentage is secondary to insufficient medical and family history, incomplete phenotypic penetrance, or de novo mutations is unclear.⁵ Despite the critical role of genetic testing in making an accurate diagnosis, only 60%–75% of SCAs have identifiable foci.^{1,2,5} Nongenetic laboratory tests are also available but are much less specific. For instance, elevated α -fetoprotein is associated with ataxia-telangiectasia and ataxia with oculomotor apraxia type 2.^{1,5,9}

ROLE OF NEUROIMAGING

Neuroimaging, particularly MR imaging, should be performed in all patients with suspected hereditary ataxias. Neuroimaging can help make the correct diagnosis, identify treatable causes, monitor disease progression, and exclude secondary causes of ataxia such as tumor or infarct.

In patients with advanced hereditary ataxias, there can be atrophy of the cerebellum and pons and involvement of the basal ganglia nuclei, pyramidal tracts, and cortex.^{9,10} Imaging techniques such as diffusion tensor imaging, quantitative 3D volumetric analysis, and spectroscopy can provide valuable additional information.^{3,11–13} Studies using voxel-based morphometry and quantitative 3D volumetric analysis suggest that SCA1 ataxias display prominent pontine atrophy, while SCA6 ataxias predominantly show cerebellar atrophy and gray matter involvement.^{11,13}

N-acetylaspartate is considered a marker for neuronal integrity and has been shown to correlate with the degree of atrophy and clinical dysfunction in the pons and cerebellum in SCA1 but not in SCA2.¹² Abnormal signal in the basal ganglia and putamen has also been associated with SCAs.^{11,13} The degeneration of pontocerebellar fibers (the hot cross bun sign), which is considered pathognomonic for multiple system atrophy of the cerebellum, can also be observed with some SCA subtypes and with idiopathic cerebellar ataxias.¹³ The relationship between the degree of atrophy and the number of trinucleotide repeats is difficult to assess from imaging because findings can be influenced by other factors such as the degree of disease progression and the age of onset.^{3,13}

TREATMENT

Presently, there is no curative therapy for hereditary ataxia. Most current therapies only provide symptomatic relief. In patients with Friedreich ataxias, high-dose β -blockers and idebenone can yield some benefit in those with cardiomyopathy, though idebenone has failed to show efficacy in phase 3 trials.^{1,3} Erythropoietin has also been shown to increase the level of frataxin proteins.^{1,3} In SCAs, patients are often treated with acetazolamide for episodic ataxia and baclofen/tizanidine for spasticity.¹⁴ Many novel treatments presently under investigation aim to impact the disease process at the molecular level or inhibit polyglutamine expansions. These include modulation of phosphorylation to reduce toxicity and silencing or down-regulating gene expression via RNA interference.^{5,14}

REFERENCES

1. Manto M, Marmolino D. Cerebellar ataxias. *Curr Opin Neurol* 2009;22:419–29
2. Manto MU. The wide spectrum of spinocerebellar ataxias (SCAs). *Cerebellum* 2005;4:2–6
3. Klockgether T. Update on degenerative ataxias. *Curr Opin Neurol* 2011;24:339–45
4. Harding AE. Classification of the hereditary ataxias and paraplegias. *Lancet* 1983;1:1151–55
5. Schöls L, Bauer P, Schmidt T, et al. Autosomal dominant cerebellar ataxias: clinical features, genetics, and pathogenesis. *Lancet Neurol* 2004;3:291–304
6. McMurray CT. Mechanisms of trinucleotide repeat instability during human development. *Nat Rev Genet* 2010;11:786–99
7. Sailer A, Houlden H. Recent advances in the genetics of cerebellar ataxias. *Curr Neurol Neurosci Rep* 2012;12:227–36
8. Schmitz-Hübsch T, Klockgether T. An update on inherited ataxias. *Curr Neurol Neurosci Rep* 2008;8:310–19
9. Brusse E, Maat-Kievit JA, van Swieten JC. Diagnosis and management of early- and late-onset cerebellar ataxia. *Clin Genet* 2007;71:12–24
10. Wüllner U, Klockgether T, Petersen D, et al. Magnetic resonance imaging in hereditary and idiopathic ataxia. *Neurology* 1993;43:318–25
11. Döhlinger S, Hauser TK, Borkert J, et al. Magnetic resonance imaging in spinocerebellar ataxias. *Cerebellum* 2008;7:204–14
12. Guerrini L, Lolli F, Ginestroni A, et al. Brainstem neurodegeneration correlates with clinical dysfunction in SCA1 but not in SCA2: a quantitative volumetric, diffusion and proton spectroscopy MR study. *Brain* 2004;127(pt 8):1785–95
13. Schulz JB, Borkert J, Wolf S, et al. Visualization, quantification and correlation of brain atrophy with clinical symptoms in spinocerebellar ataxia types 1, 3 and 6. *Neuroimage* 2010;49:158–68
14. Margulis BA, Vigont V, Lazarev VF, et al. Pharmacological protein targets in polyglutamine diseases: mutant polypeptides and their interactors. *FEBS Lett* 2013;587:1997–2007

Relative Filling Time Delay Based on CT Perfusion Source Imaging: A Simple Method to Predict Outcome in Acute Ischemic Stroke

W. Cao, B.C.V. Campbell, Q. Dong, S.M. Davis, and B. Yan

ABSTRACT

BACKGROUND AND PURPOSE: Collateral vessel status is strongly associated with clinical outcome in ischemic stroke but can be challenging to assess. The aim of this study was to develop a tomography perfusion source imaging–based assessment of collateral vessel status.

MATERIALS AND METHODS: Consecutive patients with ischemic stroke who received intravenous thrombolysis or intra-arterial reperfusion therapy after CTP were retrospectively analyzed. In those with middle cerebral artery or internal carotid artery occlusion, CT perfusion source imaging was used to identify the relative filling time delay between the normal MCA Sylvian branches and those in the affected hemisphere. Receiver operating characteristic analysis and logistic regression were used to assess the association of the relative filling time delay with the 24-hour Alberta Stroke Program Early CT Score based on noncontrast CT and the 90-day modified Rankin Scale score.

RESULTS: There were 217 patients treated in 2009–2011 who had CTP data, of whom 60 had MCA or ICA occlusion and 55 had 90-day mRS data. The intraclass correlation coefficient for relative filling time delay was 0.95. Relative filling time delay was correlated with 24-hour ASPECTS (Spearman $\rho = -0.674$; $P < .001$) and 90-day mRS score ($\rho = 0.516$, $P < .01$). Increased relative filling time delay was associated with poor radiologic outcome (ASPECTS, 0–7) (area under the curve = 0.79, $P < .001$) and poor functional outcome (mRS score, 3–6) (area under the curve = 0.77, $P = .001$). In multivariate logistic regression, the association of longer relative filling time delay with poor outcome remained significant, independent of age, sex, and baseline National Institutes of Health Stroke Scale score.

CONCLUSIONS: Relative filling time delay is a useful independent predictor of clinical outcome after ischemic stroke.

ABBREVIATIONS: CTP-SI = CT perfusion source imaging; rFTD = relative filling time delay

Leptomeningeal collateral flow has an important role in maintaining blood flow to brain regions distal to an arterial occlusion.^{1–5} Imaging assessment of leptomeningeal collaterals in humans does not depict the small interarteriolar connections directly but, instead, relies on an indirect assessment of the extent and rate of backfilling of pial arteries receiving blood flow through these collateral vessels.^{1,4,6,7} Many leptomeningeal collateral flow studies, most of which were CT angiography studies, used various grading methods to assess the vessel filling status in the Sylvian fissure by observers.^{3,8–11} Traditional assessment of leptomeningeal

collateral flow by using static CTA images lacks temporal resolution. Although newer scanners offer whole-brain perfusion acquisitions that can be reconstructed to provide dynamic CTA by using advanced software,¹² this technology is not yet widely available.

CT perfusion expands the role of CT in the evaluation of acute stroke by providing physiologic insights into cerebral hemodynamics and, in so doing, complements the strength of CTA by determining the consequences of vessel occlusions and stenosis.^{9,12,13} Although 1 study used CTP source data to confirm that contrast opacification was indeed retrograde collateral flow, no prior studies have graded collateral status by rating CTP source imaging (CTP-SI). We investigated a simple, time-resolved scale of collateral-derived contrast opacification in the Sylvian fissure as a predictor of radiologic and functional outcome. We hypothesized that delayed filling of the middle cerebral artery in the Sylvian fissure due to poor collateral flow would be associated with worse radiologic and functional outcome after ischemic stroke.

Received October 15, 2013; accepted after revision February 6, 2014.

From the Department of Medicine and Neurology, Melbourne Brain Centre at the Royal Melbourne Hospital (W.C., B.C.V.C., S.M.D., B.Y.), University of Melbourne, Parkville, Victoria, Australia; and Department of Neurology (W.C., Q.D.), Huashan Hospital, Shanghai, China.

Please address correspondence to Bernard Yan, MD, Royal Melbourne Hospital, Parkville, Victoria 3050, Australia; e-mail: Bernard.yan@mh.org.au

<http://dx.doi.org/10.3174/ajnr.A3931>

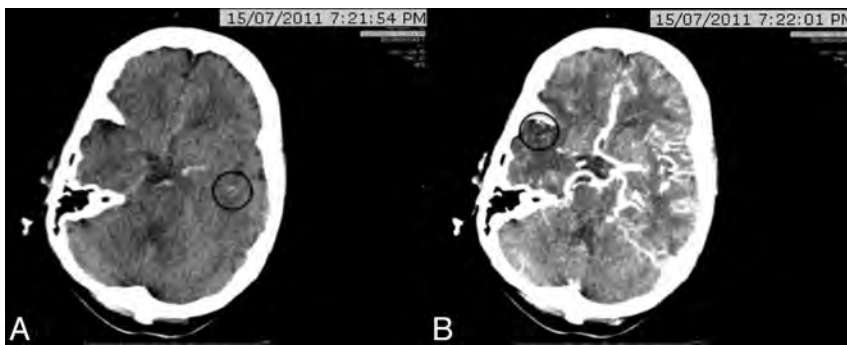


FIG 1. A 67-year-old woman with left hemiparesis and dysarthria who presented to the hospital 2 hours after onset. CTA identified a right intracranial ICA occlusion. CTP-SI showed that the contrast (black circles) was first detected at 20 seconds in the left Sylvian fissure (A) and at 27 seconds in the affected right hemisphere (B). The relative filling time delay was, therefore, 7 seconds.

MATERIALS AND METHODS

Patients

We identified patients with acute ischemic stroke presenting to our institution between January 2009 and December 2011 within 4.5 hours of stroke-symptom onset who underwent multimodal CT imaging before reperfusion therapy from our prospectively recorded stroke data base. The subgroup with MCA or internal carotid artery occlusion was selected for this analysis. Patients with MCA occlusion of the M1 or both M2 segments proximal to the Sylvian fissure were included. Baseline National Institutes of Health Stroke Scale scores and 90-day modified Rankin Scale scores were obtained from the data base. The study was approved by the Melbourne Health Human Research Ethics Committee.

Imaging

Noncontrast CT, CT perfusion, and CT angiography were performed before therapy. Two separate CTP slabs, each 24-mm thick, were acquired consecutively (16-section Somatom CT; Siemens, Erlangen, Germany; 80 kV (peak), 209 mAs) and positioned to maximize supratentorial coverage. Iodinated contrast (40-mL iohexol 350 mg I/mL, Omnipaque 350; GE Healthcare, Milwaukee, Wisconsin) was injected at 8 mL/s, and 40 images were acquired every second (total acquisition time, 44 seconds). Each slab was formatted as two 12-mm sections. Follow-up NCCT was performed at a minimum of 24 hours after onset.

Imaging Analysis

NCCT, CTP, and CTA were reviewed by using standard PACS software, allowing reviewers to freely window and view the images. CTA images were reviewed by 1 stroke neurologist, to identify patients with complete (Thrombolysis in Myocardial Infarction, 0) occlusion of the MCA or ICA. In patients with MCA or ICA occlusion, review of cervical CTA did not detect any cases with moderate-to-severe stenosis (>50%), which might have confounded relative filling time delay (rFTD) interpretation. Unprocessed CTP-SI DICOM images were used to identify the relative filling time delay between the normal MCA Sylvian branches and those in the affected hemisphere. It was calculated as the time difference between the first appearance of contrast in each Sylvian fissure (Fig 1). rFTD was then independently assessed by a neurointerventionalist (W.C.) and a stroke neurologist (B.C.V.C.), blinded to clinical outcomes. The agreement in rFTD assessment

between observers (with a tolerance of ± 1 -second difference) was calculated. Cases with 1-second difference between the 2 raters were averaged, and those with ≥ 2 -second difference were reviewed by an interventional neuroradiologist (B.Y.) to determine consensus. The Alberta Stroke Program Early CT Score of 24-hour NCCT was independently assessed by the neurointerventionalist and stroke neurologist blinded to all other information before consensus was reached.

Statistical Analysis

Statistical analyses were performed by using the Statistical Package for the Social Sciences, Version 19 (IBM, Armonk, New York), and STATA, Version 12 (StataCorp, College Station, Texas). $P < .05$ was considered to indicate statistical significance. Interobserver agreement (with tolerance of ± 1 -second difference) for the assessment of rFTD between the 2 observers was tested by using Cohen κ and intraclass correlation. Patients were dichotomized by using the 90-day mRS score into good (mRS score, 0–2) versus poor (mRS score, 3–6) outcome, and mortality (mRS score, 6) was analyzed separately.¹⁴ The 24-hour ASPECTS was dichotomized into good (ASPECTS, 8–10) versus poor (ASPECTS, 0–7) radiologic outcomes.^{15,16} Differences in patient characteristics between outcomes were tested by the Fisher exact test for categorical and the Mann-Whitney U test for continuous values. Comparisons of rFTD and baseline NIHSS scores between groups were performed by using the Mann-Whitney U test. The Spearman nonparametric rank correlation was performed to assess the correlation between rFTD and baseline NIHSS scores, 90-day mRS scores, and 24-hour ASPECTS. Multivariate binary logistic regression (including variables with P values $< .05$) was used to assess the association of rFTD with 24-hour ASPECTS and 90-day mRS scores. Receiver operating characteristic analysis was performed to determine the optimal threshold. Positive predictive value, sensitivity, and specificity at the optimal threshold were calculated.

RESULTS

Between January 2009 to December 2011, two hundred seventeen patients with acute ischemic stroke presented to our institution within 4.5 hours of stroke-symptom onset, were imaged with CTP, and then received intravenous tPA or intra-arterial therapy. Of those, 60 patients with acute occlusion identified in the ICA or MCA were included in this study. The mean patient age was 70 ± 10 years with 27/60 (45%) being women. Hypertension was found in 58.3% (35/60); diabetes mellitus, in 28.3% (17/60); hyperlipidemia, in 55% (33/60); atrial fibrillation, in 38.3% (23/60); and current or past smoking, in 18.3% (11/60) of the patients. The baseline median pretreatment NIHSS score was 16 (interquartile range, 3–27). Mean onset-to-therapy time was 141 ± 48 minutes. There were 41 patients (68.3%) treated with intravenous recombinant tissue plasminogen activator, and 19 patients (31.7%) received intra-arterial therapy, including 5 (8.3%) with rtPA/urokinase and 14 (23.3%) with mechanical thrombectomy. The site of

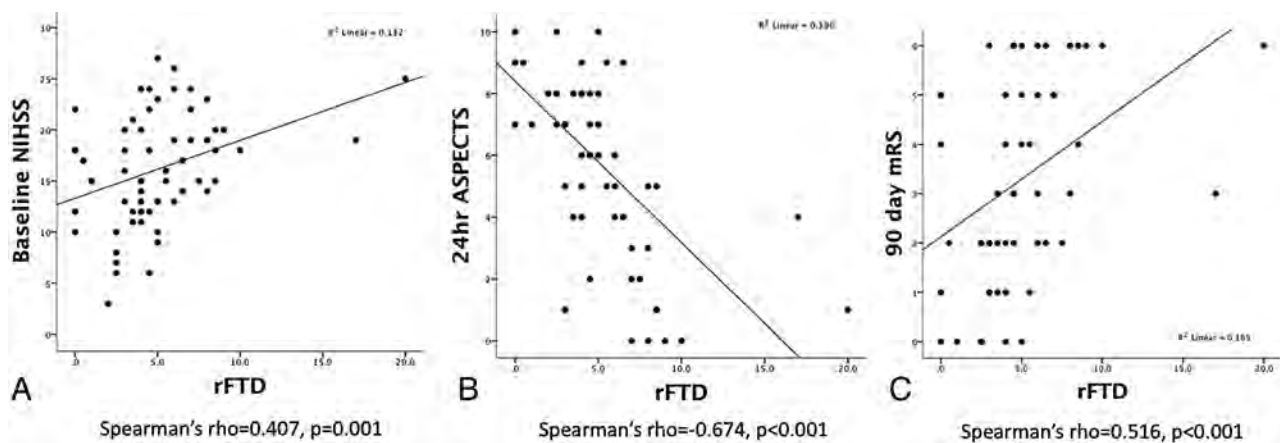


FIG 2. Correlation between rFTD and baseline NIHSS scores, 24-hour ASPECTS, and 90-day mRS scores.

Table 1: Comparison of patient characteristics in those with good-versus-poor outcomes

	mRS (0–2) (n = 23)	mRS (3–6) (n = 32)	P Value	Alive (n = 43)	Dead (n = 12)	P Value	ASPECTS (>7) (n = 21)	ASPECTS (≤7) (n = 39)	P Value
Age (median) (yr)	69 (41–85)	73.5 (54–88)	.014	69 (41–85)	79 (66–88)	.005	72 (52–83)	73 (41–88)	.877
Female (%)	26	56.2	.026	37.2	66.6	.101	33.3	51.2	.277
Hypertension (%)	52.1	62.5	.444	60.4	50	.516	56.4	61.9	.786
Diabetes mellitus (%)	26	28.1	.867	23.2	41.6	.205	33.3	25.6	.560
Hyperlipidemia (%)	60.8	46.8	.305	48.8	66.6	.274	61.9	51.2	.587
Current or past smoker (%)	26	9.3	.143	20.9	0	.181	14.2	20.5	.731
Atrial fibrillation (%)	34.3	34.7	.975	32.5	41.7	.733	42.8	35.8	.781
Baseline NIHSS (median)	13 (6–20)	19 (6–27)	.001	15 (6–27)	21 (15–26)	.001	12 (3–24)	18 (6–27)	.003
OTT (median) (min)	120 (61–255)	140 (75–265)	.366	140 (61–265)	124 (77–200)	.683	137 (61–250)	140 (76–265)	.364
IV-tPA (%)	60.9	71.9	.561	67.4	66.7	1.000	69.2	66.7	1.000
IA-tPA/UK (%)	13	6.2	.639	7.3	16.7	.298	11.7	8.3	1.000
Clot retrieval (%)	26.1	21.9	.717	25.5	16.7	.709	23.1	23.8	1.000
rFTD (median) (sec)	3.5 (0–7.5)	5.75 (0–10)	.001	4 (0–17)	6.5 (3–20)	.002	3.5 (0–6.5)	5.5 (2–20)	.002

Note:—IA indicates intra-arterial; rFTD, relative filling delay time; UK, urokinase; OTT, onset to treatment time.

arterial occlusion on CTA was in the proximal (M1) MCA in 44 (73.3%) patients, the distal MCA (M2) in 8 (13.3%) patients, and the ICA in 8 (13.3%) patients. The 90-day mRS score was available in 55 patients. There was no significant difference in baseline characteristics in these patients compared with the entire population. Good functional outcome (mRS score, 0–2) was seen in 23 patients (41.8%), and death occurred in 21.8% (12/55).

Exact agreement of rFTD between the 2 observers was found in 32 of 60 patients ($\kappa = 0.47, P < .001$). Tolerance of a ± 1 -second difference increased agreement to 52 of 60 patients ($\kappa = 0.82, P < .001$). The intraclass correlation coefficient was 0.95, which represents excellent agreement between raters.

The variables in 60 patients with 24-hour ASPECTS and 55 patients with 90-day mRS scores and mortality were analyzed. Longer rFTD was correlated with increased baseline NIHSS scores (Spearman $\rho = 0.407, P = .001$), lower 24-hour ASPECTS ($\rho = -0.674, P < .001$), and higher 90-day mRS scores ($\rho = 0.516, P < .001$, Fig 2). In the 2 outliers with rFTD values > 15 seconds, one had contrast filling detected at 17 seconds and the other had no contrast filling and was conservatively scored at 20 seconds based on the time between perfusion of the opposite Sylvian fissure and the end of the perfusion acquisition. Excluding these 2 outliers, rFTD remained significantly correlated with baseline NIHSS score ($\rho = 0.37, P = .004$), 24-hour ASPECTS ($\rho = -0.654, P < .001$), and 90-day mRS score ($\rho = 0.511, P < .001$).

Patient characteristics stratified by outcome are listed in

Table 1. As expected, increased age and higher baseline NIHSS scores were significantly associated with worse functional and mortality outcomes. Female sex was associated with worse functional outcome. Higher baseline NIHSS scores were strongly associated with worse radiologic outcome ($P = .003$). Longer median rFTD was significantly found in worse functional, mortality, and radiologic outcomes (Fig 3). In multivariate logistic regression, rFTD was associated with functional and radiologic outcomes after adjustment for age, sex, and baseline NIHSS scores (Table 2).

In receiver operating characteristic analysis, increased rFTD was associated with 24-hour ASPECTS of ≤ 7 (area under curve = 0.79; 95% CI, 0.68–0.9; $P < .001$), 90-day mRS scores (3–6) (area under the curve = 0.77; 95% CI, 0.65–0.9; $P = .001$), and 90-day mortality (area under the curve = 0.79; 95% CI, 0.65–0.93; $P = .002$). The optimal threshold determined by the Youden index was 4.25 seconds for both functional and radiologic outcomes.

The threshold of rFTD of > 4 seconds predicted poor functional outcome (mRS score, 3–6) with a sensitivity of 75% (95% CI, 56%–88%), a specificity of 73% (95% CI, 51%–89%), and a positive predictive value of 80% (95% CI, 61%–92%); predicted mortality with a sensitivity of 91% (95% CI, 61%–99%), a specificity of 55% (95% CI, 39%–70%), and a positive predictive value of 36% (95% CI, 19%–56%); and predicted poor radiologic outcome (ASPECTS, 0–7) with a sensitivity of 71% (95% CI, 55%–

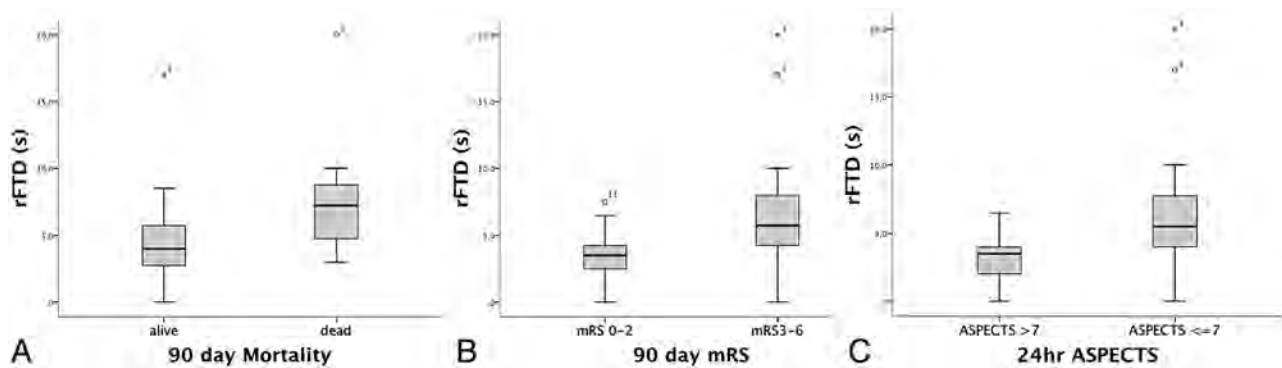


FIG 3. Longer median rFTD was significantly associated with poor functional and radiologic outcomes.

Table 2: Multivariate logistic regression for clinical and radiologic outcome

Poor Outcomes	Predictors	β	SE	P Value
90-Day mRS 3–6	Age	0.097	0.043	.024
	Sex	0.548	0.816	.501
	Baseline NIHSS	0.207	0.091	.023
	rFTD	0.354	0.178	.047
90-Day death	Age	0.185	0.074	.01
	Baseline NIHSS	0.239	0.116	.028
	rFTD	0.302	0.158	.039
24-Hour ASPECTS \leq 7	Baseline NIHSS	0.114	0.065	.082
	rFTD	0.456	0.162	.005

85%), a specificity of 76% (95% CI, 52%–91%), and a positive predictive value of 84% (95% CI, 68%–94%).

DISCUSSION

We found that a simple visual rating of collateral flow by using CTP source images is significantly associated with clinical and radiologic outcome in ischemic stroke. The relative filling time delay assessed in the Sylvian fissure represents the abundance of leptomeningeal collateral supply. Longer rFTD was associated with adverse outcomes, independent of standard prognostic variables, including age and baseline NIHSS scores. These results suggest that rFTD, especially >4 seconds, may be clinically useful as a marker of poor prognosis after ischemic stroke with proximal vessel occlusion.

Several studies have established the importance of collateral supply in the prediction of clinical and radiologic outcome after ischemic stroke.^{17–19} Collateral blood flow plays a pivotal role in the pathophysiology of cerebral ischemia but is difficult to quantify due to its complexity. In this study, we developed a method to evaluate the collateral status in patients with acute ischemic stroke with MCA or ICA occlusions by using CTP-SI. In contrast to standard CTA, which is a single “snapshot” of cerebral blood flow, CTP-SI provides a dynamic view of filling in the intracranial collateral arteries. Additionally, previous CTA studies used a variety of methods for grading leptomeningeal collateral flow, and limited data on interobserver agreement are available.²⁰ We developed rFTD as a marker to assess the collateral circulation. The simplicity of rating the first appearance of contrast minimized observer subjectivity and translated to excellent inter-rater agreement for rFTD. The variability in the assessment of contrast-appearance time between raters was generally <2 seconds. A more quantitative rFTD could be obtained by using time-attenuation

curve analysis with a manually positioned region of interest, though this would require dedicated software. Because rFTD is normalized to contralateral delay, factors such as the contrast injection and cardiac output, which affect the absolute delay to filling, are negated.

Studies of CTP in acute stroke commonly focus on 4 perfusion map–based parameters: cerebral blood volume, cerebral blood flow, mean transit time, and time-to-peak enhancement, with the aim of distinguishing salvageable tissue (penumbra) from the irreversibly injured ischemic core. The use of CTP-SI in evaluating collateral blood flow has been largely untested but has the advantage of combining anatomic information with temporal resolution to assess both the structure and function of collateral pathways. Assessing rFTD based on CTP-SI is also robust to motion in uncooperative patients. No special software is needed to perform CTP-SI assessment, so the method is feasible in most hospitals.

Recently, timing-invariant CTA was used to obtain CTA images from the CT perfusion source data that are insensitive to the timing of contrast arrival²¹ and, therefore, display collateral vessels that are undetectable on standard CTA. With a visual 4-point grading scale, poor retrograde collateral flow on timing-invariant CTA was associated with poor clinical outcome.²¹ However, the temporal information provided by CTP is a key strength, and timing-invariant CTA does not consider the potential impact of delay, which, in our data, seems highly predictive of outcome. There are more sophisticated methods to assess collateral flow by using whole-brain CTP.²² However, these require 320-slice CT, which would limit their applicability. In contrast, rFTD assessment can be performed by using any CT scanner technology and is simple and robust in clinical practice.

There are several limitations of this study. First, this is a retrospective study in a selected population of patients with ischemic stroke with ICA or MCA occlusion. Second, the rFTD method is limited to large-vessel-occlusion stroke, and the utility and value of rFTD requires validation in an independent cohort. rFTD focuses on the Sylvian fissure and does not account for more peripherally located collateral flow. Finally, recanalization following treatment was not analyzed in this study because repeat vascular imaging was not routinely performed in clinical practice. Variable recanalization and the mix of IV-tPA and endovascular therapy may have potentially affected the outcome independent of collateral status. The recent neutral endovascular trials such as the Interventional Management of Stroke III trial²³ and the Mechanical

Retrieval and Recanalization of Stroke Clots Using Embolectomy (MR-RESCUE) trial²⁴ suggest that rates of recanalization between IV and intra-arterial-treated patients during the period of our study were not likely to be very different. However, any effect of recanalization heterogeneity would have reduced the strength of association observed between rFTD and the clinical and radiologic outcomes, and our results would, therefore, be a conservative estimate of the prognostic value of rFTD.

CONCLUSIONS

rFTD obtained by CTP-SI is a simple method to quantify cerebral collateral circulation and help overcome the lack of temporal resolution of CTA for collateral assessment. Patients with longer rFTD are at increased risk of developing adverse radiologic and functional outcomes in the future. However, further studies are needed to validate our findings in an independent cohort of patients.

Disclosures: Stephen M. Davis—UNRELATED: Consultancy: Boehringer Ingelheim, EVER Pharma, Covidien, Payment for Lectures (including service on Speakers Bureau): Boehringer Ingelheim, EVER Pharma, Covidien.

REFERENCES

- Christoforidis GA, Mohammad Y, Kehagias D, et al. **Angiographic assessment of pial collaterals as a prognostic indicator following intra-arterial thrombolysis for acute ischemic stroke.** *AJNR Am J Neuroradiol* 2005;26:1789–97
- Maas MB, Lev MH, Ay H, et al. **Collateral vessels on CT angiography predict outcome in acute ischemic stroke.** *Stroke* 2009;40:3001–05
- Miteff F, Levi CR, Bateman GA, et al. **The independent predictive utility of computed tomography angiographic collateral status in acute ischaemic stroke.** *Brain* 2009;132:2231–38
- Menon BK, Smith EE, Modi J, et al. **Regional leptomeningeal score on CT angiography predicts clinical and imaging outcomes in patients with acute anterior circulation occlusions.** *AJNR Am J Neuroradiol* 2011;32:1640–45
- Bang OY, Saver JL, Kim SJ, et al. **Collateral flow predicts response to endovascular therapy for acute ischemic stroke.** *Stroke* 2011;42:693–99
- Kim JJ, Fischbein NJ, Lu Y, et al. **Regional angiographic grading system for collateral flow: correlation with cerebral infarction in patients with middle cerebral artery occlusion.** *Stroke* 2004;35:1340–44
- Tan JC, Dillon WP, Liu S, et al. **Systematic comparison of perfusion-CT and CT-angiography in acute stroke patients.** *Ann Neurol* 2007;61:533–43
- Knauth M, von Kummer R, Jansen O, et al. **Potential of CT angiography in acute ischemic stroke.** *AJNR Am J Neuroradiol* 1997;18:1001–10
- Wildermuth S, Knauth M, Brandt T, et al. **Role of CT angiography in patient selection for thrombolytic therapy in acute hemispheric stroke.** *Stroke* 1998;29:935–38
- Rosenthal ES, Schwamm LH, Roccatagliata L, et al. **Role of recanalization in acute stroke outcome: rationale for a CT angiogram-based “benefit of recanalization” model.** *AJNR Am J Neuroradiol* 2008;29:1471–75
- Lima FO, Furie KL, Silva GS, et al. **The pattern of leptomeningeal collaterals on CT angiography is a strong predictor of long-term functional outcome in stroke patients with large vessel intracranial occlusion.** *Stroke* 2010;41:2316–22
- Frölich AM, Schrader D, Klotz E, et al. **4D CT angiography more closely defines intracranial thrombus burden than single-phase CT angiography.** *AJNR Am J Neuroradiol* 2013;34:1908–13
- Lev MH, Farkas J, Rodriguez VR, et al. **CT angiography in the rapid triage of patients with hyperacute stroke to intraarterial thrombolysis: accuracy in the detection of large vessel thrombus.** *J Comput Assist Tomogr* 2001;25:520–28
- Anderson CS, Heeley E, Huang Y, et al. **Rapid blood-pressure lowering in patients with acute intracerebral hemorrhage.** *N Engl J Med* 2013;368:2355–65
- Demchuk AM, Hill MD, Barber PA, et al. **Importance of early ischemic computed tomography changes using ASPECTS in NINDS rtPA stroke study.** *Stroke* 2005;36:2110–15
- Hill MD, Rowley HA, Adler F, et al. **Selection of acute ischemic stroke patients for intra-arterial thrombolysis with pro-urokinase by using ASPECTS.** *Stroke* 2003;34:1925–31
- Harrison MJ, Marshall J. **The variable clinical and CT findings after carotid occlusion: the role of collateral blood supply.** *J Neurol Neurosurg Psychiatry* 1988;51:269–72
- Bozzao L, Fantozzi LM, Bastianello S, et al. **Early collateral blood supply and late parenchymal brain damage in patients with middle cerebral artery occlusion.** *Stroke* 1989;20:735–40
- Henderson RD, Eliasziw M, Fox AJ, et al. **Angiographically defined collateral circulation and risk of stroke in patients with severe carotid artery stenosis: North American Symptomatic Carotid Endarterectomy Trial (NASCET) group.** *Stroke* 2000;31:128–32
- McVerry F, Liebeskind DS, Muir KW. **Systematic review of methods for assessing leptomeningeal collateral flow.** *AJNR Am J Neuroradiol* 2012;33:576–82
- Smit EJ, Voncken EJ, van Seeters T, et al. **Timing-invariant imaging of collateral vessels in acute ischemic stroke.** *Stroke* 2013;44:2194–99
- Menon BK, O’Brien B, Bivard A, et al. **Assessment of leptomeningeal collaterals using dynamic CT angiography in patients with acute ischemic stroke.** *J Cereb Blood Flow Metab* 2013;33:365–71
- Broderick JP, Palesch YY, Demchuk AM, et al. **Endovascular therapy after intravenous t-PA versus t-PA alone for stroke.** *N Engl J Med* 2013;368:893–903
- Kidwell CS, Jahan R, Alger JR, et al. **Design and rationale of the mechanical retrieval and recanalization of stroke clots using embolectomy (MR RESCUE) trial.** *Int J Stroke* 2014;9:110–16

Early Basal Ganglia Hyperperfusion on CT Perfusion in Acute Ischemic Stroke: A Marker of Irreversible Damage?

V. Shahi, J.E. Fugate, D.F. Kallmes, and A.A. Rabinstein



ABSTRACT

BACKGROUND AND PURPOSE: CT perfusion scans are often used in acute stroke evaluations. We aimed to assess the outcome of areas of basal ganglia hyperperfusion on CTP in patients with acute ischemic stroke.

MATERIALS AND METHODS: We retrospectively reviewed the medical records and brain imaging of 139 patients presenting with acute stroke who underwent CTP for consideration of endovascular recanalization. Hyperperfusion was assessed qualitatively and defined as a matched region of increased cerebral blood flow and cerebral blood volume. CTA was used to locate arterial occlusion. Follow-up imaging was used to determine whether regions of hyperperfusion at baseline became infarcted or developed hemorrhage. Angiographic imaging was assessed to determine the presence or absence of early venous opacification.

RESULTS: Six patients (4.3%) demonstrated hyperperfusion in the basal ganglia of the affected side (4 in the lenticular nucleus and 2 in the caudate). In all cases, the area of hyperperfusion ultimately proved to be infarcted. All patients had received intravenous thrombolysis before the CTP. CTA at the time of CTP showed middle or distal M1 occlusion but patency of the proximal M1 and A1 segments. Intracranial hemorrhage was noted in 2 of these 6 patients at follow-up.

CONCLUSIONS: Acute basal ganglia hyperperfusion in patients with stroke may indicate nonviable parenchyma and risk of hemorrhagic conversion.

ABBREVIATION: PH = parenchymal hemorrhage

CT perfusion scans are widely applied to assess ischemia (low flow) and allow the identification of potentially salvageable brain tissue (ischemic penumbra) with delineation of irreversibly damaged brain (core infarct).^{1,2} While definitions vary considerably, most studies using CTP define nonviable regions of brain tissue by the reduction in cerebral blood flow³ or reduced cerebral blood volume.^{4,5} Regions of hyperperfusion (increased CBF and increased CBV) before recanalization are generally not considered areas that are infarcted or at risk of infarction.^{6,7}

Nonviable brain typically has disturbed autoregulation. Following recanalization, a phenomenon called “luxury” perfusion—elevated CBF in areas of infarcted tissue beyond what is needed for metabolic needs—can occur.^{8,9} These areas may be at risk for hemorrhage,^{8,9} but this has not been a consistent finding.¹⁰ In our practice, we observed cases in which areas of basal

ganglia hyperperfusion on CTP obtained during acute stroke evaluation evolved to completed infarction on subsequent imaging. We hypothesized that baseline CTP can demonstrate areas of hyperperfused but nonviable parenchyma, if local recanalization, either spontaneous or in response to lytic therapy, occurs before CTP imaging. The purpose of this study was to determine the prevalence of regions of hyperperfusion on baseline CTP and their rate of progression to infarction and reperfusion hemorrhage at follow-up.

MATERIALS AND METHODS

This study was approved by the Mayo Clinic Institutional Review Board. We performed a retrospective review of consecutive patients presenting with acute ischemic stroke who underwent CTP for consideration of endovascular treatment from September 2008 to October 2012. In general, we apply CTP to select patients for endovascular therapy either after intravenous thrombolysis without improvement (CTP is performed toward the conclusion of the infusion) or when patients are ineligible for intravenous thrombolysis. A neuroradiologist (D.F.K., with 24 years of experience) reviewed all CTP images to identify patients with areas of hyperperfusion. Identified cases were evaluated and confirmed by

Received December 6, 2013; accepted after revision February 13, 2014.

From the Mayo Medical School (V.S.) and Departments of Neurology (J.E.F., A.A.R.) and Radiology (D.F.K.), Mayo Clinic, Rochester, Minnesota.

Please address correspondence to Jennifer E. Fugate, DO, Department of Neurology, Mayo Clinic, 200 First St SW, Rochester, MN 55905; e-mail: fugate.jennifer@mayo.edu

<http://dx.doi.org/10.3174/ajnr.A3935>

Baseline patient characteristics

	Age/Sex	HTN	CAD	DM	A. fib	Initial BP, (mm Hg)	NIHSS	MCA Territory	Time to CTP (mins) ^a	TICI Grade	ICH
1	79/F	Y	N	N	N	125/63	16	R	343	2a	Y
2	61/M	N	Y	N	Y	116/70	21	L	187	2b	Y
3	61/M	N	N	N	N	114/72	17	R	125	2b	N
4	66/M	Y	N	N	Y	155/99	21	L	190	2b	N
5	61/F	Y	N	N	N	140/80	20	R	230	0	N
6	65/F	Y	N	N	N	146/92	16	L	210	NA ^b	N

Note:—HTN indicates hypertension; CAD, coronary artery disease; DM, diabetes mellitus; A. fib, atrial fibrillation; BP, blood pressure; ICH, intracranial hemorrhage; R, right; L, left; Y, yes; N, no; NA, not applicable.

^aTICI 0 indicates no perfusion; 2a, perfusion of $\leq 50\%$ of MCA distribution; 2b, perfusion of $>50\%$ of MCA distribution; 3, full perfusion.

^bEndovascular therapy was not attempted because of large core on CTP.

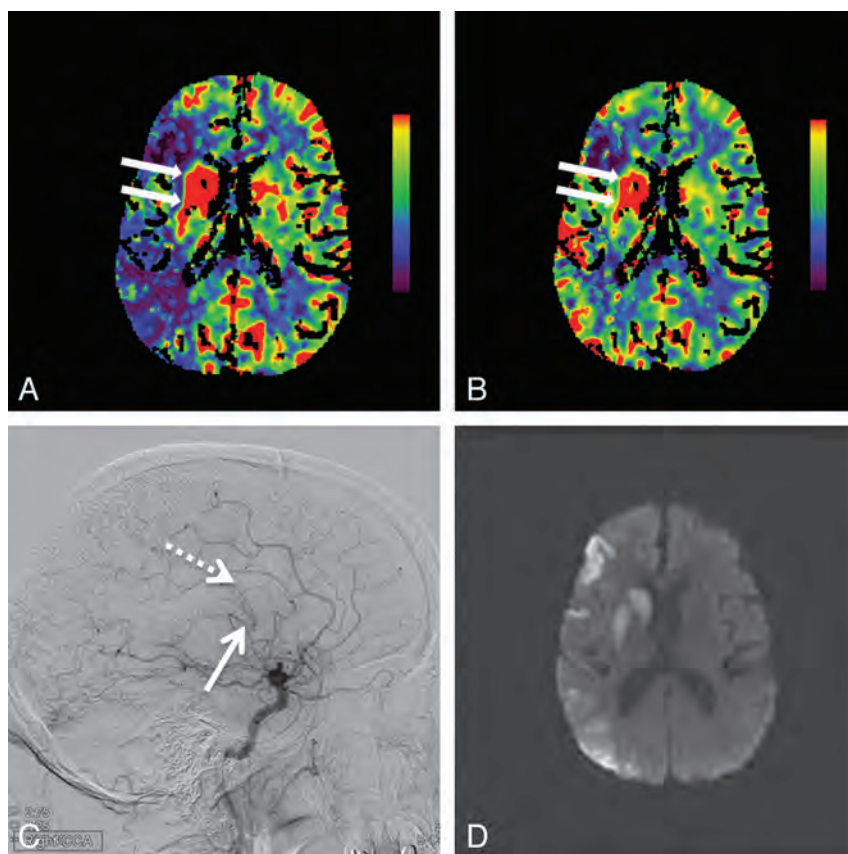


FIG 1. Hyperperfusion in the right basal ganglia is demonstrated by increased cerebral blood flow (arrows, A) and increased cerebral blood volume (arrows, B). Also seen is a large region of right middle cerebral artery territory ischemia as evidenced by reduced CBF (A) with relative preservation of CBV (B). Lateral digital subtraction angiogram from a right carotid artery injection demonstrates early opacification of the basal vein of Rosenthal (solid arrow, C) and the internal cerebral vein (dashed arrow, C). Follow-up MR imaging 12 hours later shows restricted diffusion indicating infarction of the right basal ganglia, along with patchy cortical infarctions in the right MCA territory (D).

a vascular neurologist (A.A.R., with 12 years of experience). Perfusion parametric maps were created by using a deconvolution technique. Fifty milliliters of contrast dye was injected at 7 mL/s, followed by 50 mL normal saline through an 18-ga right antecubital IV catheter. Scanning took place over 71 seconds total with 20 scans every 1.5 seconds followed by 6 scans every 7.5 seconds. Our postprocessing was done using a single value deconvolution algorithm from GE software licensed to Siemens (Erlangen, Germany). This allowed the creation of time-to-peak, mean transit time, cerebral blood flow, and cerebral blood volume maps. For the purpose of this study, hyperperfusion was defined as an increase in both CBF and CBV in the same brain region compared

with the contralateral region. The site of vascular occlusion was determined by using CTA images obtained at the time of CTP imaging. Conventional angiography was assessed to determine early venous opacification.

Final area of infarction was determined by using follow-up brain imaging and was compared with the initial CTP to evaluate the outcome of the region of hyperperfusion. At our institution, every patient who undergoes attempted IV or intra-arterial stroke revascularization therapy has follow-up brain imaging at or within 24 hours, usually with noncontrast head CT. Further MR imaging is performed at the discretion of the treating clinicians. No patients were excluded on the basis of lack of follow-up brain imaging. Hemorrhagic events were classified according to European Cooperative Acute Stroke Study II definitions.¹¹ Hemorrhagic infarction consists of petechial hemorrhage without mass effect, parenchymal hemorrhage (PH) 1 indicates blood clot occupying $\leq 30\%$ of the infarcted area with slight mass effect, and PH 2 is blood clot in $>30\%$ of the infarcted area with substantial space-occupying effect.¹¹ Thrombolysis in Cerebral Infarction grades were used to evaluate the degree of reperfusion.¹²

RESULTS

One hundred thirty-nine patients were reviewed. Endovascular stroke therapy was attempted in approximately half of patients ($n = 67$, 48%). Six patients (4.3%) had CTP evidence of hyperperfusion of the basal ganglia on the side of arterial occlusion (Table). Among these 6 patients, median age at diagnosis was 63 years (range, 61–79). The median NIHSS score was 18.5 (range, 16–21). All patients received intravenous rtPA before CTP. Three of the patients had effacement of the gray-white differentiation of the basal ganglia on noncontrast head CT. Median time to intravenous thrombolysis was 87.5 minutes (range, 56–135 minutes). Median time from stroke-symptom onset to CTP was 200 minutes (range, 125–343 minutes).

The median diameter of the region of hyperperfusion was 2.73 cm (range, 1.67–3.89 cm). On CT angiography, all patients had

arterial occlusions of the minor distal aspect of the M1 segment of the middle cerebral artery, distal to at least a portion of the medial lenticulostriate arteries. Four occlusions involved the midportion of the M1, and 2 patients had occlusions at the junction of the middle and distal one-third of the M1 segment. The A1 segment was patent in all cases. Five patients also underwent digital subtraction angiography showing early venous opacification in 2 cases, one in the deep venous system and one

involving superficial veins. In the latter case, areas of extravasation were also noted in addition to attenuated capillary blush. Endovascular recanalization was attempted in 5 cases and achieved partial ($n = 1$) or near-complete reperfusion ($n = 3$) in 4 of them.

Follow-up brain imaging was noncontrast head CT in 4 patients and MR imaging in 2. In all patients, the region of basal ganglia hyperperfusion proved to be infarcted on follow-up imaging (Figs 1–3). Two patients also had intracranial hemorrhage following recanalization (PH 2 in one case and PH 1 in another). In both cases, the hemorrhage occurred in the basal ganglia, which had signs of hyperperfusion on the preintervention CTP. In the former case, early venous opacification into superficial veins, attenuated capillary blush, and areas of extravasation were noted, while the latter case had no angiographic abnormality suggestive of hyperperfusion or hemorrhage.

DISCUSSION

We present a series of patients with acute stroke who had evidence of basal ganglia hyperperfusion on CTP, which ultimately proved to be part of the infarction and/or a nidus for hemorrhagic transformation on follow-up imaging. All patients had received intravenous thrombolysis before CTP; CTA imaging at the time of CTP acquisition showed patency of the proximal M1 segment and A1 segment, perhaps suggesting that partial recanalization, either spontaneous or in response to intravenous rtPA, may have resulted in luxury perfusion. Angiographic evidence of hyperperfusion, with early venous opacification, was present in a minority of cases.

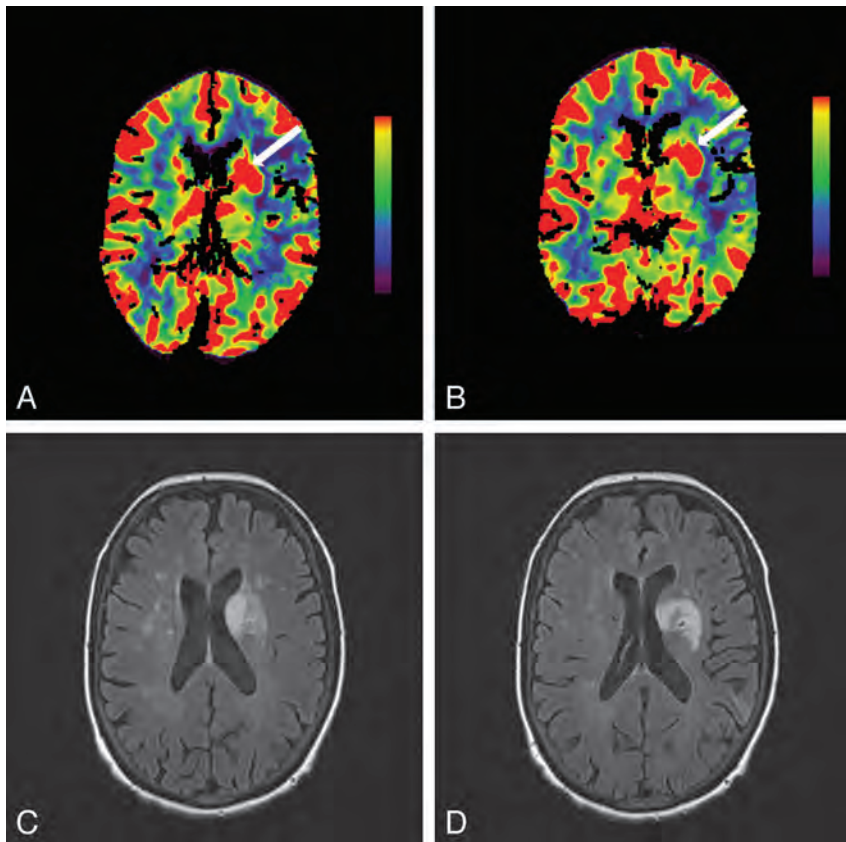


FIG 2. Hyperperfusion of the left basal ganglia is shown by increased cerebral blood flow (arrow, A) and increased cerebral blood volume (arrow, B) on CT perfusion. Follow-up FLAIR MR imaging 3.5 days later shows regions of T2 hyperintensity indicating infarction of this same region (C and D).



FIG 3. Increased cerebral blood flow in the right basal ganglia (arrow, A) in addition to a large region of reduced CBF in the right middle cerebral artery territory is shown on the CT perfusion scan at presentation. Noncontrast head CT 1 day later demonstrates right MCA infarction but apparent sparing of the right basal ganglia (B). Follow-up CT at day 6 shows hypoattenuation involving right basal ganglia (arrow, C) in addition to evolution of a large right MCA infarction with mass effect.

Hemorrhagic transformation occurred in 2 patients, only one of whom had early venous opacification on angiography.

Our observation regarding hyperperfusion on CTP has potential clinical implications. First, practitioners should inspect CTP imaging for areas of hyperperfusion within the territory of the target artery, recognizing that these areas may be nonviable and may be at risk for hemorrhage. Failure to do this may cause underestimation of the ultimate size of the infarction and the risk of complications from mass effect when swelling develops. Furthermore, hyperperfusion in the basal ganglia may need to be considered part of the unsalvageable core when selecting appropriate candidates for endovascular therapy by using CTP, though our findings need to be confirmed in larger populations before this can be concluded with certainty. Advanced imaging with CTP is not necessary before the administration of IV thrombolysis for acute stroke, and we do not think that these findings should impact the decision to administer IV thrombolysis.

It is not exactly clear what the regions of hyperperfusion in the basal ganglia represent. This could be a result of partial recanalization of the M1 segment of the middle cerebral artery with a return of blood flow to blood vessels that had been maximally dilated because of ischemia. The basal ganglia receive blood from the lenticulostriate arteries, which usually arise from the M1 segment. On occasion, there is a truncated M1 segment due to normal anatomic variability, and the lateral lenticulostriate arteries may arise from the superior division of the M2 segment. The deep-seated basal ganglia may receive less collateral blood flow, have longer duration of ischemia compared with cortical regions, and thus may be more susceptible to reperfusion injury. Reperfusion after stroke has been associated with disruption of the blood-brain barrier as evidenced by postgadolinium enhancement of CSF on MR imaging.¹³ This may be an indirect marker of reperfusion injury, which involves inflammation, increased cytokine release, excessive production of oxygen-free radicals, and formation of edema. Reperfusion injury is one reason why angiographic recanalization is not always associated with good clinical outcomes.

A “luxury perfusion syndrome” characterized by overabundant CBF relative to neuronal and glial metabolic demand is well-known.^{8,9} Much of our knowledge of postischemic reperfusion is derived from experimental models,¹⁴ but the finding that postischemic hyperperfusion may include brain regions that become infarcted has also been demonstrated in small studies of human patients with stroke.⁶ In 1 study of patients with stroke who underwent large-vessel recanalization with intra-arterial fibrinolysis, hyperperfusion was demonstrated in 5/12 by perfusion MR imaging several hours after recanalization.⁶ Hyperperfusion developed mainly in regions that subsequently were shown to be infarcted, and patients with hyperperfusion had larger final infarct volumes.

Others have produced discrepant results. A study by using PET within 5–18 hours of ischemic stroke showed that regions of hyperperfusion did not ultimately become infarcted on delayed follow-up imaging and suggested that hyperperfusion may not only be a harmless phenomenon but could even potentially be beneficial.¹⁵ Hyperperfusion in these cases predominantly affected patchy cortical regions remote from the deeper areas of

ultimate infarction, with the limitation that all follow-up imaging was done with CT rather than MR imaging. These discrepant results across studies may be at least partially explained by differences in the time from arterial occlusion to reperfusion, the technique used to evaluate perfusion, and the type of follow-up brain imaging.

This study has several limitations. The small sample size and retrospective nature preclude definitive conclusions. This is a single-center study from a tertiary referral center, which may limit the generalizability of our findings. Our time to CTP was sometimes prolonged because most of our patients were treated at local emergency departments and then transferred to our center. The chances of finding basal ganglia hyperperfusion may be different if CTP is performed after a short interval from symptom onset. Finally, nearly all of our patients underwent endovascular recanalization, which may have affected the outcomes.

CONCLUSIONS

In acute stroke evaluations, basal ganglia hyperperfusion on CTP is an infrequent finding but important to recognize because it does not always predict a benign course.

These areas of hyperperfusion may represent irreversible ischemic damage and become the nidus for reperfusion hemorrhage, despite timely and successful recanalization therapy. These observations should be considered hypothesis-generating and require validation in larger prospective studies.

Disclosures: David F. Kallmes—UNRELATED: Consultancy: GE Healthcare,* ev3,* Comments: consulting on clinical trial planning and implementation, cost effectiveness research, Grants/Grants Pending: ev3,* MicroVention,* Micrus,* Codman,* Sequent,* Medina Medical,* NeuroSigma,* Surmodics,* Comments: funds for clinical trials and preclinical research, Royalties: University of Virginia Patent Foundation, Comments: Spine fusion. Alejandro A. Rabinstein—UNRELATED: Grants/Grants Pending: DJO Global,* Comments: for investigator-initiated project on upper limb digital volume tomography, Royalties: Elsevier, Oxford, UpToDate, Comments: for authored books and chapters. *Money paid to the institution.

REFERENCES

1. Biesbroek JM, Niesten JM, Dankbaar JW, et al. **Diagnostic accuracy of CT perfusion imaging for detecting acute ischemic stroke: systematic review and meta-analysis.** *Cerebrovasc Dis* 2013;35:493–501
2. Lin K, Do KG, Ong P, et al. **Perfusion CT improves diagnostic accuracy for hyperacute ischemic stroke in the 3-hour window: study of 100 patients with diffusion MRI confirmation.** *Cerebrovasc Dis* 2009;28:72–79
3. Campbell BC, Christensen S, Levi CR, et al. **Cerebral blood flow is the optimal CT perfusion parameter for assessing infarct core.** *Stroke* 2011;42:3435–40
4. Eastwood JD, Lev MH, Wintermark M, et al. **Correlation of early dynamic CT perfusion imaging with whole-brain MR diffusion and perfusion imaging in acute hemispheric stroke.** *AJNR Am J Neuroradiol* 2003;24:1869–75
5. Schramm P, Schellinger PD, Klotz E, et al. **Comparison of perfusion computed tomography and computed tomography angiography source images with perfusion-weighted imaging and diffusion-weighted imaging in patients with acute stroke of less than 6 hours' duration.** *Stroke* 2004;35:1652–58
6. Kidwell CS, Saver JL, Mattiello J, et al. **Diffusion-perfusion MRI characterization of post-recanalization hyperperfusion in humans.** *Neurology* 2001;57:2015–21
7. Marchal G, Young AR, Baron JC. **Early postischemic hyperperfusion: pathophysiologic insights from positron emission tomography.** *J Cereb Blood Flow Metab* 1999;19:467–82

8. Lassen NA. **The luxury-perfusion syndrome and its possible relation to acute metabolic acidosis localised within the brain.** *Lancet* 1966;2:1113–15
9. Ohta H. **Postoperative luxury perfusion syndrome in patients with severe subarachnoid hemorrhage treated by early aneurysmal clipping.** *Neurol Med Chir (Tokyo)* 1990;30:16–23
10. Nguyen TB, Lum C, Eastwood JD, et al. **Hyperperfusion on perfusion computed tomography following revascularization for acute stroke.** *Acta Radiol* 2005;46:610–15
11. Hacke W, Kaste M, Fieschi C, et al. **Randomised double-blind placebo-controlled trial of thrombolytic therapy with intravenous alteplase in acute ischaemic stroke (ECASS II): Second European-Australasian Acute Stroke Study Investigators.** *Lancet* 1998;352:1245–51
12. Higashida RT, Furlan AJ, Roberts H, et al. **Trial design and reporting standards for intra-arterial cerebral thrombolysis for acute ischemic stroke.** *Stroke* 2003;34:e109–37
13. Warach S, Latour LL. **Evidence of reperfusion injury, exacerbated by thrombolytic therapy, in human focal brain ischemia using a novel imaging marker of early blood-brain barrier disruption.** *Stroke* 2004;35:2659–61
14. Heiss WD, Graf R, Lottgen J, et al. **Repeat positron emission tomographic studies in transient middle cerebral artery occlusion in cats: residual perfusion and efficacy of postischemic reperfusion.** *J Cereb Blood Flow Metab* 1997;17:388–400
15. Marchal G, Furlan M, Beaudouin V, et al. **Early spontaneous hyperperfusion after stroke: a marker of favourable tissue outcome?** *Brain* 1996;119:409–19

An In Vivo, MRI-Integrated Real-Time Model of Active Contrast Extravasation in Acute Intracerebral Hemorrhage

R.I. Aviv, T. Huynh, Y. Huang, D. Ramsay, P. Van Slyke, D. Dumont, P. Asmah, R. Alkins, R. Liu, and K. Hynnen



ABSTRACT

BACKGROUND AND PURPOSE: The “spot sign” or contrast extravasation is strongly associated with hematoma formation and growth. An animal model of contrast extravasation is important to test existing and novel therapeutic interventions to inform present and future clinical studies. The purpose of this study was to create an animal model of contrast extravasation in acute intracerebral hemorrhage.

MATERIALS AND METHODS: Twenty-eight hemispheres of Yorkshire male swine were insonated with an MR imaging–guided focused sonography system following lipid microsphere infusion and mean arterial pressure elevation. The rate of contrast leakage was quantified by using dynamic contrast-enhanced MR imaging and was classified as contrast extravasation or postcontrast leakage by using postcontrast T1. Hematoma volume was measured on gradient recalled-echo MR imaging performed 2 hours postprocedure. Following this procedure, sacrificed brain was subjected to histopathologic examination. Power level, burst length, and blood pressure elevation were correlated with leakage rate, hematoma size, and vessel abnormality extent.

RESULTS: Median (intracerebral hemorrhage) contrast extravasation leakage was higher than postcontrast leakage (11.3; 6.3–23.2 versus 2.4; 1.1–3.1 mL/min/100 g; $P < .001$). Increasing burst length, gradient recalled-echo hematoma ($\rho = 0.54$; 95% CI, 0.2–0.8; $P = .007$), and permeability were correlated ($\rho = 0.55$; 95% CI, 0.1–0.8; $P = .02$). Median permeability ($P = .02$), gradient recalled-echo hematoma ($P = .02$), and dynamic contrast-enhanced volumes ($P = .02$) were greater at 1000 ms than at 10 ms. Within each burst-length subgroup, incremental contrast leakage was seen with mean arterial pressure elevation ($\rho = 0.2–0.8$).

CONCLUSIONS: We describe a novel MR imaging–integrated real-time swine intracerebral hemorrhage model of acute hematoma growth and contrast extravasation.

ABBREVIATIONS: CE = contrast extravasation; DCE = dynamic contrast-enhanced; GRE = gradient recalled-echo; ICH = intracerebral hemorrhage; IQR = interquartile range; KPS = rate of leakage; MAP = mean arterial pressure elevation; PCL = postcontrast leakage

Intracerebral hemorrhage (ICH) accounts for 10%–30% of strokes and is the most deadly and disabling stroke type with little improvement in mortality seen during the past 20 years.¹ These characteristics underscore the importance of developing a

better understanding of the pathophysiology of ICH formation and growth to facilitate the development of improved therapeutic agents or interventions.² The causative lesion in primary ICH is yet to be elucidated, though pathologic studies demonstrate focal vessel integrity loss in association with blood extravasation into the brain parenchyma.³ Following initial ICH formation, continuous^{4,5} or delayed⁶ extravasation results in hematoma expansion,⁷ which is associated with early neurologic deterioration and significant mortality.⁸

Several recent studies have shown an association between contrast extravasation (CE) detected on CTA, coined the CTA “spot sign,” and hematoma growth.^{9–14} Prospective studies have demonstrated that contrast extravasation independently predicts a larger hematoma size and a poorer clinical outcome.^{13,14} These are the first clinical studies to suggest a robust “real-time” imaging marker of hematoma expansion. Three clinical studies are presently enrolling patients dichotomized by the CTA spot sign to validate the prior study findings and to determine the therapeutic

Received October 3, 2013; accepted after revision February 2, 2014.

From the Department of Medical Imaging (T.H., R.I.A., R.L.), Sunnybrook Health Sciences Centre, Toronto, Ontario, Canada; Departments of Medical Biophysics (K.H., D.D., R.A., P.A.) and Medical Imaging (T.H., K.H., R.I.A.), University of Toronto, Toronto, Ontario, Canada; Department of Pathology (D.R.), London Health Sciences Centre, London, Ontario, Canada; and The Centre for Proteomic Studies (D.D., P.V.S.) and Imaging Research (Y.H., K.H.), Sunnybrook Research Institute, Toronto, Ontario, Canada.

Dr Aviv was supported by a grant from the Heart and Stroke Foundation of Canada (grant No. 7299). Dr Huynh was supported by grants from Canadian Institute for Health Research and the Physician Services Incorporated Foundation.

Please address correspondence to Richard I Aviv, MD, Sunnybrook Health Sciences Centre, 2075 Bayview Ave, Room AG-31E, Toronto, ON, M4N 3M5 Canada; e-mail: Richard.aviv@sunnybrook.ca

Indicates open access to non-subscribers at www.ajnr.org

<http://dx.doi.org/10.3174/ajnr.A3939>

efficacy of recombinant factor VIIa or tranexamic acid.¹⁵⁻¹⁷ A more recent study using dynamic spot sign imaging with a biphasic CT perfusion protocol¹⁸ has confirmed 2 patterns of contrast extravasation associated with significantly different rates of leakage. These patterns, comprising a brisker active extravasation (spot sign) and slower postcontrast leakage (PCL),¹⁹ are also demonstrated with early and late structural imaging,^{10,19} dynamic CTA/CTP,¹⁸ and biphasic or repeat delayed CTA acquisitions.¹²

Morphologic patterns and more recent studies illustrate that the spot sign is not an all-or-none phenomenon but constitutes a spectrum of extravasation.^{18,19} The extravasation rate likely significantly impacts timely and clinically meaningful hemostasis.²⁰ A bleeding threshold likely exists beyond which prothrombotic treatment is futile, exposing patients to harmful adverse effects without hope of therapeutic benefit.²¹ Increasingly, new innovative surgical techniques are being developed to address contrast extravasation.²² Knowledge of the impact of the extravasation rate on therapeutic response is critical to stratify patients to the most appropriate therapies. An animal model of acute contrast extravasation in ICH could potentially inform the patient-selection process. We describe a novel MR imaging-integrated real-time swine model of acute hematoma growth and contrast extravasation.

MATERIALS AND METHODS

This study was conducted with the approval of the local Research Institute Animal Care Committee (Animal Use Protocol No. 12-435) in compliance with the guidelines established by the Canadian Council on Animal Care and the Animals for Research Act. Fourteen 6- to 8-week-old (approximately 16-18 kg) Yorkshire male swine were chemically immobilized by using xylazine HCl (2.2 mg/kg), ketamine (15 mg/kg), and atropine (0.05 mg/kg) mixed together in a syringe by intramuscular injection into the dorsal neck or gluteal muscles. Anesthesia was initially maintained with 2%-3% isoflurane in oxygen (>2 L/min). Percutaneous insertion of two 10-cm 5F catheters (Pinnacle; Terumo, Tokyo, Japan) via a Seldinger technique into the femoral artery and vein was performed for continuous arterial blood pressure monitoring and central line access, respectively. Physiologic monitoring at 5-minute intervals included clinical observation, tail pulse oximetry, rectal temperature, and blood pressure measurement through the femoral artery line. Fluid balance was maintained with intravenous normal saline (10 mL/kg/h) and equivalent normal saline volume replacement of any other losses.

The animal was transferred to the MR imaging suite and placed in a supine position with the head immersed in degassed water and its limbs secured (Fig 1). Degassed water served as a conduction medium for sonography emitted from an upwardly positioned modified clinical MR imaging-guided focused sonography brain system (ExAblate 4000; Insightec, Tirat Carmel, Israel). The focused sonography system consists of a 1024-element hemispheric phased array with a diameter of 30 cm. Accurate anatomic localization of vessels within the basal ganglia was achieved by using MR imaging localization sequences. The basal ganglia represent a frequent site for ICH and are a commonly targeted location for experimental ICH models due to lower subarachnoid risk and intraventricular extension.

Following this procedure, 0.08-mL/kg (1.5 mL) perflutren

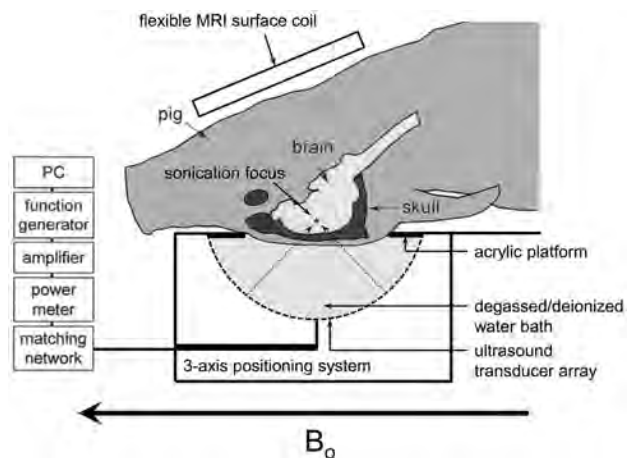


FIG 1. Schematic of swine model. Adapted with permission from McDannold N, King RL, Hynynen K. MRI monitoring of heating produced by ultrasound absorption in the skull: in vivo study in pigs. *Magn Reson Med* 2004;51:1061-65.

lipid microsphere infusion (Definity; Lantheus Medical Imaging, North Billerica, Massachusetts) and focused low-frequency sonography (230 kHz) were delivered. MR imaging was performed before and after focused sonography vessel disruption by using 3T MR imaging (Discovery MR750; GE Healthcare, Milwaukee, Wisconsin) and a 6-channel phased array flexible coil (GE Healthcare). The following sequences were obtained at baseline: FSE T2 (TR/TE, 3000/71 ms; echo-train length, 4; FOV, 16 × 16 cm; slice thickness, 2 mm; 256 × 192); 3D spoiled gradient recalled-echo (GRE) T1 (TR/TE, 6/2 ms; FOV, 12 × 12 cm; slice thickness, 2 mm); axial T2 FLAIR (TR/TE, 8000/127 ms; 12 × 12 cm; slice thickness, 2 mm; 128 × 128); and fast GRE (TR/TE, 100/13 ms; 12 × 12 cm; slice thickness, 2 mm). Thirty seconds after perflutren injection and sonographic insonation, a dynamic contrast-enhanced sequence (DCE) (3D T1 spoiled GRE; TR/TE, 6/2 ms; 12 × 12 cm; slice thickness, 3 mm; 128 × 128; temporal sampling, 10 seconds; scan duration, 20 minutes) was performed. Gadobutrol, 1 mmol/mL (Gadovist; Bayer Schering Pharma, Toronto, Canada), was injected via a pump injector (Spectris MR injector; MedRad, Indianola, Pennsylvania; and Solaris; Bayer HealthCare, Pittsburgh, Pennsylvania) at 0.5 mL/kg and 5 mL/s followed by a 10-mL normal saline bolus. A postgadolinium T1 study was performed at the termination of the DCE sequence (20 minutes after gadolinium injection). Fast GRE, FLAIR, and FSE T2 sequences were repeated following DCE and before procedure termination.

Experimental Design

Number of Experiments. Twenty-eight hemispheres were insonated; 16 hemispheres were used to determine optimal power delivery; and 12, to test the effect of burst length.

Power Delivery. On the basis of prior studies of blood-brain barrier disruption²³⁻²⁵ aiming at a temporary BBB opening but reporting complications of red blood cell extravasation, 2 power ranges were selected for evaluation. Sixteen hemispheres were subjected to basal ganglia insonation, with either 70-kW ($n = 8$ hemispheres) or 80-kW ($n = 8$ hemispheres) power delivery at a

constant burst length (10 ms, 1-Hz pulse-repetition frequency) and sonication duration (120 seconds). Animals were compared for DCE leakage rate, final hematoma size (see below), and vascular abnormality on histopathology. The 8 hemispheres at 80 kW were then used to compare with the 3 higher burst lengths also performed at 80 kW.

Burst Length

The burst length determines the interaction time between sonography and bubbles and is central to the production of the desired cavitation effects, which result in blood vessel wall disruption. Altering burst length, therefore, determines the magnitude and threshold of disruption thereby modulating the rate of extravasation.²⁶ Following 80-kW power-level selection, 3 additional burst lengths (1000 ms [continuous wave], 800 ms, and 600 ms) in 4 hemispheres each were acquired. The 8 hemispheres at 10 ms by using the 80-kW power delivery described above were included in a comparison of the 4 different burst lengths tested. Rate of extravasation and hematoma volumes were compared for each group. Within each burst-length subgroup, mean arterial pressure was increased at the time of insonation to achieve a 0%–60% elevation over baseline by using a 15- μ g/kg/min phenylephrine infusion.²⁷

MR Image Processing. Hematoma and DCE contrast volume measurements were performed on GRE and DCE images, respectively, by using the auto-trace feature with Medical Image Processing, Analysis, and Visualization, Version 4.4.1, Center for Information Technology (National Institutes of Health, Bethesda, Maryland; <http://mipav.cit.nih.gov>). The largest region-of-interest volume within the temporal DCE dataset was selected as the final DCE volume. Rate of leakage (KPS) was measured within each region of contrast leakage from the permeability maps calculated using custom IDL software (Exelis Visual Information Solutions, Boulder, Colorado) by using a previously described unidirectional 2-compartment kinetic model.²⁸ The DCE-derived region of interest, representing the volume of contrast leakage, was used for the permeability measurement from the KPS maps. Because the contrast leakage volumes were drawn on the same sequence from which the KPS maps were derived, the ROIs were intrinsically coregistered with the KPS maps.

Morphologic Characterization of Contrast Extravasation. On the basis of clinical studies, 2 distinct patterns of contrast leakage were identified.¹⁹ Active contrast extravasation demonstrated a brisk contrast leak with well-delineated margins, visible from early within the DCE sequence. Postcontrast leakage demonstrated slower leakage on DCE with ill-defined contrast enhancement becoming more confluent on a postcontrast T1 study performed following DCE (Figs 2 and 3).

Histopathologic Examination. Animals were observed for 2 hours following the last insonation and were euthanized by exsanguination followed by transcarotid perfusion of heparinized saline (2 L) and 4% paraformaldehyde (2 L). The anterior and posterior cranium was removed to better facilitate immersion-fixation in 4% paraformaldehyde. Following fixation, the brain was removed, blocked in 5-mm sections, and subjected to gross pathologic examination and photography. Regions of hematoma were sectioned at 5 μ m and stained with hematoxylin-eosin and

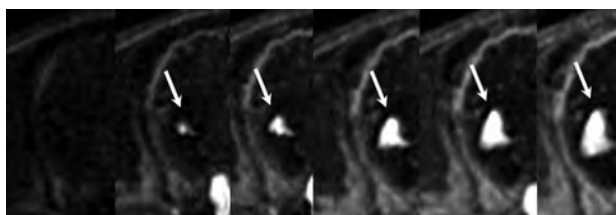


FIG 2. Individual frames from a DCE sequence demonstrating progressive accumulation of contrast with time within a right basal ganglia hematoma. Rapid accumulation of confluent and well-defined contrast consistent with active extravasation. KPS measured 6.39 mL/min/100 g.

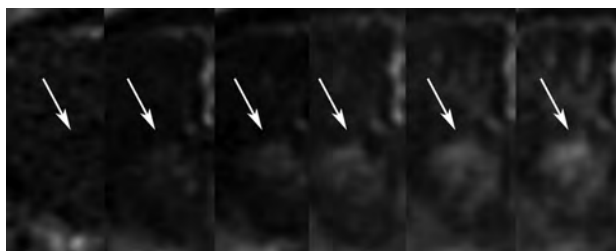


FIG 3. Individual frames from a DCE sequence demonstrating slow accumulation of contrast with time within a right basal ganglia hematoma consistent with postcontrast leakage. KPS measured 1.1 mL/min/100 g.

Masson elastin trichrome stain; and immunohistochemistry for smooth-muscle actin was used on selected sections.

Statistical Analysis

Statistical analysis was performed by using MedCalc (Version 12.7.0.0; MedCalc Software, Mariakerke, Belgium). Median (interquartile range [IQR]) contrast leakage, DCE contrast, and GRE hematoma volumes were calculated and compared between 70- and 80-kW power groups and between each burst-length category by using the Mann-Whitney *U* test. Spearman correlation coefficients were calculated for increasing burst length and GRE hematoma and DCE volumes. Correlation among the rate of contrast leak, GRE hematoma volume, and mean arterial pressure ratio was assessed for each burst-length group. The association between burst length and morphologic pattern of contrast leakage (CE versus PCL) was tested with the Fisher exact test. We compared the rate of leakage, hematoma, and DCE volumes between CE and PCL using the Mann-Whitney *U* test. $P < .05$ was considered significant.

RESULTS

Power Determination

Median rates of contrast leakage were similar at 70 kW and 80 kW (4.5 mL/min/100 g [IQR, 2.4–25.1] versus 3.2 mL/min/100 g [IQR, 1.2–7.6]; $P = .75$, respectively), though the range of values was more heterogeneous in the 70-kW group. Similar median (IQR) GRE hematoma (0.6 cm³ [0.4–1.5] versus 0.5 cm³ [0.4–0.8]; $P = .98$) and DCE volumes (0.1 cm³ [0.1–0.7] versus 0.2 cm³ [0.1–0.4]; $P = .39$) were present. Due to the more homogeneous values achieved at 80 kW, this power level was selected for further study. Histopathologic analysis of cases performed at 10 ms demonstrated predominantly focal injury of small intracerebral blood vessel walls (40–70 μ m) characterized by segmental bland, gran-

Comparison of contrast leakage rate, GRE hematoma, and DCE volume by burst-length subgroup for 20 hemispheres at 80 kW power

Burst Length (ms) (n = Hemispheres)	Contrast Leak Median (IQR) (mL/min/100 g)	GRE Hematoma Volume (cm ³)	DCE Contrast Volume (cm ³)	ρ KPS-to-Hematoma Volume	ρ KPS-to-MAP Ratio
1000 (n = 4)	17.4 (9.5–29.0)	1.6 (1.2–2.1)	1.3 (1.1–1.4)	0.8 (–0.7–0.9, P = .3)	0.8 (–0.6–0.9, P = .2)
800 (n = 4)	6.0 (4.2–7.4)	0.9 (0.7–1.7)	0.4 (0.2–0.7)	0.7 (–0.5–0.9, P = .2)	0.5 (–0.7–0.9, P = .7)
600 (n = 4)	2.9 (1.5–3.7)	1.0 (0.4–1.6)	0.4 (0.2–1.0)	0.6 (–0.8–1.0, P = .4)	0.2 (–0.9–0.9, P = .8)
10 (n = 8)	3.21 (1.7–7.3)	0.5 (0.4–0.9)	0.2 (0.1–0.4)	0.3 (–0.4–0.7, P = .5)	0.6 (–0.1–0.9, P = .01)

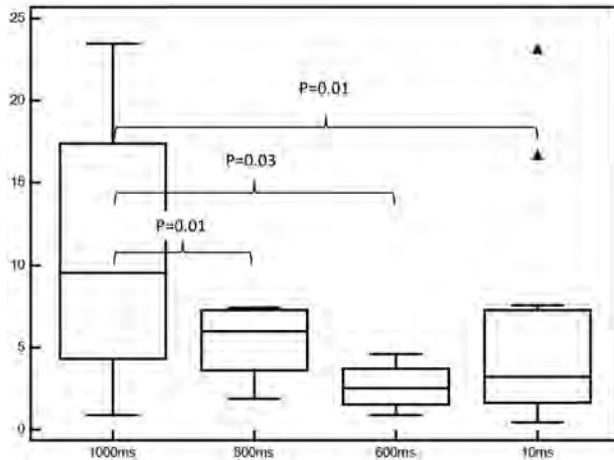


FIG 4. Rate of contrast leakage stratified by burst length. Median, IQR, and 95% CI values are displayed as bar, box, and whiskers respectively.

ular smooth-muscle eosinophilia, shrinkage, and hyperchromatism of their nuclei occasionally associated with margination of neutrophils. Larger vessels (70–120 μ m) were rarely affected and showed relatively minor abnormality. The order of magnitude of small-vessel involvement was not unexpected, given that the initially selected parameters mirrored those used to disrupt the blood-brain barrier.^{23–25} Increasing the burst length reduces the amount of time for bubbles to enter the microcirculation before cavitating, theoretically shifting this process to larger sized vessels.

Optimal Burst-Length Determination

Median (IQR) rates of contrast leak, DCE contrast and hematoma volume by burst length and correlation for contrast leak mean arterial pressure elevation (MAP) ratio, and DCE contrast and GRE hematoma volume are listed in the Table. Median rates of contrast leakage were significantly higher at 1000 ms compared with 800-ms ($P = .01$), 600-ms ($P = .02$), and 10-ms ($P = .01$) burst lengths (Table and Fig 4). Increasing burst length was associated with increasing DCE contrast ($\rho = 0.55$; 95% CI, 0.11–0.81; $P = .02$) and hematoma volumes ($\rho = 0.54$; 95% CI, 0.17–0.78; $P = .007$). Within each burst-length subgroup, incremental contrast leakage was seen with an increasing MAP ratio ($\rho = 0.2–0.8$; Table). The strongest correlation between KPS and hematoma volume and KPS and MAP ratio was present in the 1000-ms group. The 800- and 10-ms subgroups demonstrated moderate KPS-to-MAP correlation. KPS-to-GRE hematoma-volume correlation was moderate in the 600- and 800-ms subgroups.

Morphologic Patterns of Leakage in 20 Hemispheres at 80 kW

The median (IQR) rate of contrast leakage (CE or PCL) for all experiments was 5.2 (2.9–10.7) mL/min/100 g. CE was more common at

higher (1000 and 800) than lower (600 and 10) burst lengths ($P = .03$). Median (IQR) CE KPS was significantly elevated compared with PCL (11.3 mL/min/100 g; 6.3–23.2 versus 2.4 mL/min/100 g; 1.1–3.1; $P < .001$). The median (IQR) final GRE hematoma volume was significantly higher for CE compared with PCL (0.7 cm³; 0.4–1.6 versus 0.4 cm³; 0.06–0.7; $P = .02$). Similarly, CE demonstrated a median (IQR) DCE contrast volume of 0.4 cm³ (0.1–1.3) compared with PCL (0.04 cm³; 0.02–0.1; $P = .01$).

Histologic Examination of the Brain

Multiple whole-mount hematoxylin-eosin coronal step sections through the intracerebral hemorrhage were screened microscopically. Although the extent of bleeding and the vascular changes varied with the sonication parameters, a distinctive pattern of vascular injury emerged within arteries and arterioles typically 50–100 μ m in diameter. Pathologic vessels were distributed throughout the sonicated tissue and in the subarachnoid space, associated with varying degrees of subarachnoid bleeding, particularly in the interhemispheric fissure. Sonication changes, which we have termed “sonication vasculopathy,” were characterized by fairly extensive vascular injury, demonstrating varying degrees of segmental blood vessel wall bland eosinophilia and loss of nuclear detail. In some instances, early neutrophil margination was present. Abnormality extended for some distance along the blood vessels and, in some instances, alternated with more normal vascular structure, producing segmental lesions. Associated with these changes were red cells in the blood vessel wall suggesting “mini dissection.” Almost without exception, the injured vessels were associated with perivascular collections of red blood cells of various sizes ranging from petechiae to substantial intracerebral hematomas. Many of the involved small vessels showed focal defects blending with perivascular fibrin-platelet debris, both in the small petechial hemorrhages and around the larger hematomas. Increasing burst length was characterized by involvement of larger perforating vessels in which bland mural eosinophilia, reminiscent of necrosis, and rupture sites were identified (Fig 5A). Smaller vessels were less involved in cases with large hematomas, and greater difficulty was experienced identifying a ruptured vessel in larger hematomas. Although this could be a problem of sampling, the presence of actin-immunopositive fragments supports extensive segmental vessel injury and fragmentation.

DISCUSSION

We report the first MR imaging–integrated real-time swine model of contrast extravasation and hematoma growth. The median rate of contrast leakage reported is consistent with that reported by d’Esterre et al¹⁸ for humans, showing a leakage rate of 6.5 \pm 1.6 mL/min/100 g. The 1000-ms subgroup emerged as the optimal model for further study of prothrombotic agents by virtue of a strong correlation between the contrast leakage rate and final he-

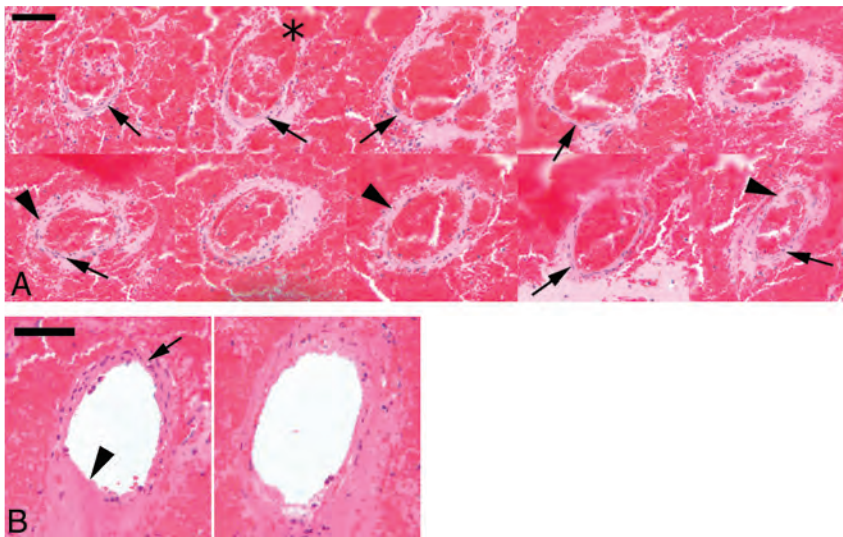


FIG 5. A, Hematoxylin-eosin stain showing multiple levels along the course of a small intracerebral artery, encased in a recent hematoma. The rupture site is illustrated in most of the top row profiles (*asterisk*). Although fragments of normal vessel wall remain (*arrows*), there are many areas, particularly in the lower row, where the apparently intact vessel wall is formed by bland eosinophilic material whose appearance is reminiscent of necrosis (*arrowheads*). B, Penetrating branch of the circle of Willis. The profile on the left is close to the inferior/basilar surface, whereas the one on the right is deeper in the brain. A rupture site in the superficial profile is indicated by an arrowhead. Note the intact segment of the artery (*arrow*). A small rupture site in the deeper vessel portion is similarly present, but most of the vessel wall exhibits loss of the normal microscopic anatomy and replacement by bland eosinophilia. Scale bar = 50 μ m.

matoma size. The strong correlation between the MAP ratio and leakage rate within the 1000-ms subgroup indicates an ability to further regulate the leakage rate through blood pressure manipulation.

Although contrast extravasation is best characterized in the CT literature, Murai et al²⁹ described MR imaging contrast extravasation as a marker of ongoing hemorrhage in acute ICH. Of 108 patients with acute hypertensive ICH, contrast extravasation was seen in 39 MR imaging and 17 cerebral angiography studies. Significant correlation with follow-up hematoma growth was confirmed. A recent case report describes a patient experiencing an acute ICH while undergoing MR imaging for unrelated reasons, illustrating progressive contrast extravasation and hematoma formation.⁴ The volume of contrast extravasation in the present model was smaller than the final GRE hematoma size in all burst-length groups. Notably, this difference was most pronounced at lower burst lengths. If the difference was attributable to gradient blooming, similar disparity should be present in each group. It is more likely that the greater difference at lower burst length reflects the notion that not all contrast opacification represents irreversible blood-brain barrier disruption and extravasation.³⁰ The greater correlation at higher burst lengths between the rate of contrast leak and hematoma size underscores the association between the increased sonography intensity exposure and the increased severity of vessel injury, also confirmed by histopathologic analysis and prior studies.²⁶

The present technique represents a significant evolution over existing ICH models by mimicking mural disruption suspected in human ICH pathophysiology. In humans, the vascular abnormalities underlying ICH formation and expansion are poorly understood. Pathologic examination of ICH specimens is hindered by

the friable nature of formalin-fixed blood and the time-consuming and technically demanding processes that are needed to conduct a “complete” histopathologic survey of large hematomas. Observations derived from pathologic studies by Fisher³ report focal rupture of a 0.6-mm arteriole with aneurysmal dilation in hypertensive ICH, fibrin globes,⁷ and microdissections.³¹ Common to the many proposed etiologies in the diseased state is the segmental involvement of vessels with “skip lesions.”³ Vessel wall rupture in the present model is induced by intraluminal cavitation mediated through the interaction of sonography waves and injected bubbles. Our histopathologic analysis revealed a mini-dissection appearance and also frank arterial disruption with concomitant red blood cell extravasation mirroring a recent histopathologic description of dissection in a 920- μ m artery found at the periphery of a spot-positive hematoma.³²

The proposed swine model serves as a paradigm for contrast extravasation in human ICH, offering a unique opportunity to study the efficacy of drug and non-

invasive imaging-guided therapies. The use of contrast extravasation to select patients most likely to benefit from therapy has been recently incorporated into the American Heart Association guidelines.³³ Swine are the National Institute of Neurological Disorders and Stroke model of choice for ICH study because they offer several advantages over traditional animal models, including proportional gray and white matter representation similar to that in humans and the ability to create hematoma volumes 20–30 times larger than those in rodent species.^{34,35} The MR imaging integration environment allows real-time monitoring and objective measurement of hematoma formation and contrast extravasation with susceptibility and dynamic contrast-enhanced T1 sequences, respectively. Unlike rodents, swine do not have potentially toxic hemostatic doses of recombinant factor VIIa,³⁶ a critical limitation given the use of the drug in current hemostatic ICH studies (Spot Sign for Predicting and Treating ICH Growth, “Spot Sign” Selection of Intracerebral Hemorrhage to Guide Hemostatic Therapy).^{15,16}

Study limitations include the small sample size because of the need to test multiple burst lengths. MR imaging was selected due to the integration of sonography, facilitating rapid scan acquisition following insonation. A CT model is feasible and faster than MR imaging but would require removal of the sonication device before scanning, thereby increasing the delay between vessel disruption and imaging, complicating coregistration, and requiring repeat calibration if further insonation is considered. Other disadvantages of the present model include the significantly higher experimental cost compared with rodent models. The first iteration of the model was complicated by subarachnoid hemorrhage formation due to sonography wave refraction caused by the flat swine skull. Future model iterations are underway that will miti-

gate or minimize these effects. The model application is, therefore, presently limited to the study of acute ICH formation and contrast extravasation.

CONCLUSIONS

We describe a swine model of ICH formation and contrast extravasation. We anticipate that the model will facilitate the study of therapeutic interventions against active contrast extravasation and its effect on hematoma formation and clinical outcome.

ACKNOWLEDGMENTS

We thank the animal technologists and Comparative Research and Sunnybrook Research Institute Animal Care Committee without whom this work would not be possible.

Disclosures: Richard I. Aviv—RELATED: Grant: Heart and Stroke Foundation (grant No.7299).* Thien Huynh—RELATED: Grant: Physician Services Incorporated,* Canadian Institute for Health Research.* Dan Dumont—UNRELATED: Grants/Grants Pending: Heart and Stroke Foundation, Comments: The Heart and Stroke Foundation paid for research on Vasculotide, but the topic was completely unrelated to this current manuscript, Patents (planned, pending or issued): Vasomune, Comments: Vasculotide is licensed to Vasomune and forms the basis for this startup. There are currently 3 active patents being pursued, Other: I am a codiscoverer of Vasculotide, and I act as a chair of the Scientific advisory board for Vasomune Therapeutics. *Money paid to the institution.

REFERENCES

1. Broderick JP, Adams HP Jr, Barsan W, et al. Guidelines for the management of spontaneous intracerebral hemorrhage: a statement for healthcare professionals from a special writing group of the Stroke Council, American Heart Association. *Stroke* 1999;30:905–15
2. Broderick J, Connolly S, Feldmann E, et al. Guidelines for the management of spontaneous intracerebral hemorrhage in adults: 2007 update: a guideline from the American Heart Association/American Stroke Association Stroke Council, High Blood Pressure Research Council, and the Quality of Care and Outcomes in Research Interdisciplinary Working Group. *Stroke* 2007;38:2001–23
3. Fisher CM. Hypertensive cerebral hemorrhage: demonstration of the source of bleeding. *J Neuropathol Exp Neurol* 2003;62:104–07
4. Jeong D, Jhaveri MD, Prabhakaran S. Magnetic resonance imaging characteristics at onset of spontaneous intracerebral hemorrhage. *Arch Neurol* 2011;68:826–27
5. Bermejo PG, Garcia JA, Perez-Fernandez S, et al. Spot sign and live-imaged dramatic intracerebral hematoma expansion. *Neurology* 2010;75:834
6. Rizos T, Rohde S, Dorner N, et al. Ongoing intracerebral bleeding despite hemostatic treatment associated with a spot sign in a patient on oral anticoagulation therapy. *Cerebrovasc Dis* 2009;28:623–24
7. Fisher CM. Pathological observations in hypertensive cerebral hemorrhage. *J Neuropathol Exp Neurol* 1971;30:536–50
8. Brott T, Broderick J, Kothari R, et al. Early hemorrhage growth in patients with intracerebral hemorrhage. *Stroke* 1997;28:1–5
9. Goldstein JN, Fazen LE, Snider R, et al. Contrast extravasation on CT angiography predicts hematoma expansion in intracerebral hemorrhage. *Neurology* 2007;68:889–94
10. Wada R, Aviv RI, Fox AJ, et al. CT angiography “spot sign” predicts hematoma expansion in acute intracerebral hemorrhage. *Stroke* 2007;38:1257–62
11. Kim J, Smith A, Hemphill JC 3rd, et al. Contrast extravasation on CT predicts mortality in primary intracerebral hemorrhage. *AJNR Am J Neuroradiol* 2008;29:520–25
12. Delgado Almandoz JE, Yoo AJ, Stone MJ, et al. Systematic characterization of the computed tomography angiography spot sign in primary intracerebral hemorrhage identifies patients at highest risk for hematoma expansion: the spot sign score. *Stroke* 2009;40:2994–3000
13. Demchuk AM, Dowlatshahi D, Rodriguez-Luna D, et al. Prediction of haematoma growth and outcome in patients with intracerebral haemorrhage using the CT-angiography spot sign (PREDICT): a prospective observational study. *Lancet Neurol* 2012;11:307–14
14. Li N, Wang Y, Wang W, et al. Contrast extravasation on computed tomography angiography predicts clinical outcome in primary intracerebral hemorrhage: a prospective study of 139 cases. *Stroke* 2011;42:3441–46
15. Clinicaltrials.gov. The Spot Sign for Predicting and Treating ICH Growth Study (STOP-IT). Published 15 December 2008. Updated 12 June 2012. <http://www.clinicaltrials.gov/ct2/show/NCT00810888?term=stop-it&rank=1>. Accessed February 20, 2013
16. Clinicaltrials.gov. “Spot Sign” Selection of Intracerebral Hemorrhage to Guide Hemostatic Therapy (SPOTLIGHT). Published 20 May 2011. Updated 12 October 2012. <http://www.clinicaltrials.gov/ct2/show/NCT01359202?term=spotlight&rank=1>. Accessed February 20, 2013
17. Clinicaltrials.gov. STOP-AUST: The Spot Sign and Tranexamic Acid On Preventing ICH Growth-AUstralia Trial. Published 3 October 2012. Updated 14 December 2012. <http://www.clinicaltrials.gov/ct2/show/NCT01702636?term=stop-aust&rank=1>. Accessed January 20, 2013
18. d’Este CD, Chia TL, Jairath A, et al. Early rate of contrast extravasation in patients with intracerebral hemorrhage. *AJNR Am J Neuroradiol* 2011;32:1879–84
19. Ederies A, Demchuk A, Chia T, et al. Postcontrast CT extravasation is associated with hematoma expansion in CTA spot negative patients. *Stroke* 2009;40:1672–76
20. Sapsford W, Watts S, Cooper G, et al. Recombinant activated factor VII increases survival time in a model of incompressible arterial hemorrhage in the anesthetized pig. *J Trauma* 2007;62:868–79
21. Diringner MN, Skolnick BE, Mayer SA, et al. Thromboembolic events with recombinant activated factor VII in spontaneous intracerebral hemorrhage: results from the Factor Seven for Acute Hemorrhagic Stroke (FAST) trial. *Stroke* 2010;41:48–53
22. Nagasaka T, Inao S, Wakabayashi T. What does the CT angiography “spot sign” of intracerebral hemorrhage mean in modern neurosurgical settings with minimally invasive endoscopic techniques? *Neurosurg Rev* 2013;36:341–48
23. Hynynen K, McDannold N, Vykhodtseva N, et al. Noninvasive MR imaging-guided focal opening of the blood-brain barrier in rabbits. *Radiology* 2001;220:640–46
24. Hynynen K, McDannold N, Sheikov NA, et al. Local and reversible blood-brain barrier disruption by noninvasive focused ultrasound at frequencies suitable for trans-skull sonications. *Neuroimage* 2005;24:12–20
25. Hynynen K, McDannold N, Vykhodtseva N, et al. Focal disruption of the blood-brain barrier due to 260-kHz ultrasound bursts: a method for molecular imaging and targeted drug delivery. *J Neurosurg* 2006;105:445–54
26. McDannold N, Vykhodtseva N, Hynynen K. Effects of acoustic parameters and ultrasound contrast agent dose on focused-ultrasound induced blood-brain barrier disruption. *Ultrasound Med Biol* 2008;34:930–37
27. Troncy E, Francoeur M, Salazkin I, et al. Extra-pulmonary effects of inhaled nitric oxide in swine with and without phenylephrine. *Br J Anaesth* 1997;79:631–40
28. Roberts HC, Roberts TP, Bollen AW, et al. Correlation of microvascular permeability derived from dynamic contrast-enhanced MR imaging with histologic grade and tumor labeling index: a study in human brain tumors. *Acad Radiol* 2001;8:384–91
29. Murai Y, Ikeda Y, Teramoto A, et al. Magnetic resonance imaging-documented extravasation as an indicator of acute hypertensive intracerebral hemorrhage. *J Neurosurg* 1998;88:650–55
30. Molina CA, Alvarez-Sabin J, Montaner J, et al. Thrombolysis-related hemorrhagic infarction: a marker of early reperfusion, reduced infarct size, and improved outcome in patients with proximal middle cerebral artery occlusion. *Stroke* 2002;33:1551–56

31. Challa VR, Moody DM, Bell MA. **The Charcot-Bouchard aneurysm controversy: impact of a new histologic technique.** *J Neuropathol Exp Neurol* 1992;51:264–71
32. Huynh TJ, Keith J, Aviv RI. **Histopathological characteristics of the “spot sign” in spontaneous intracerebral hemorrhage.** *Arch Neurol* 2012;69:1654–55
33. Morgenstern LB, Hemphill JC 3rd, et al. **Guidelines for the management of spontaneous intracerebral hemorrhage: a guideline for healthcare professionals from the American Heart Association/American Stroke Association.** *Stroke* 2010;41:2108–29
34. NINDS ICH Workshop Participants. **Priorities for clinical research in intracerebral hemorrhage: report from a National Institute of Neurological Disorders and Stroke workshop.** *Stroke* 2005;36:e23–41
35. Wagner KR. **Lobar intracerebral hemorrhage model in pigs: rapid edema development in perihematomal white matter.** *Stroke* 1996;27:490–97
36. Zhang J, Groff RF 4th, Chen XH, et al. **Hemostatic and neuroprotective effects of human recombinant activated factor VII therapy after traumatic brain injury in pigs.** *Exp Neurol* 2008;210:645–55

Brain Changes in Kallmann Syndrome

R. Manara, A. Salvalaggio, A. Favaro, V. Palumbo, V. Citton, A. Elefante, A. Brunetti, F. Di Salle, G. Bonanni, and A.A. Sinisi, for the Kallmann Syndrome Neuroradiological Study Group



ABSTRACT

BACKGROUND AND PURPOSE: Kallmann syndrome is a rare inherited disorder due to defective intrauterine migration of olfactory axons and gonadotropin-releasing hormone neurons, leading to rhinencephalon hypoplasia and hypogonadotropic hypogonadism. Concomitant brain developmental abnormalities have been described. Our aim was to investigate Kallmann syndrome–related brain changes with conventional and novel quantitative MR imaging analyses.

MATERIALS AND METHODS: Forty-five male patients with Kallmann syndrome (mean age, 30.7 years; range, 9–55 years) and 23 age-matched male controls underwent brain MR imaging. The MR imaging study protocol included 3D-T1, FLAIR, and diffusion tensor imaging (32 noncollinear gradient-encoding directions; b-value = 800 s/mm²). Voxel-based morphometry, sulcation, curvature, and cortical thickness analyses and tract-based spatial statistics were performed by using Statistical Parametric Mapping 8, FreeSurfer, and the fMRI of the Brain Software Library.

RESULTS: Corpus callosum partial agenesis, multiple sclerosis–like white matter abnormalities, and acoustic schwannoma were found in 1 patient each. The total amount of gray and white matter volume and tract-based spatial statistics measures (fractional anisotropy and mean, radial, and axial diffusivity) did not differ between patients with Kallmann syndrome and controls. By specific analyses, patients with Kallmann syndrome presented with symmetric clusters of gray matter volume increase and decrease and white matter volume decrease close to the olfactory sulci; reduced sulcal depth of the olfactory sulci and deeper medial orbital-frontal sulci; lesser curvature of the olfactory sulcus and sharper curvature close to the medial orbital-frontal sulcus; and increased cortical thickness within the olfactory sulcus.

CONCLUSIONS: This large MR imaging study on male patients with Kallmann syndrome featured significant morphologic and structural brain changes, likely driven by olfactory bulb hypo-/aplasia, selectively involving the basal forebrain cortex.

ABBREVIATIONS: KS = Kallmann syndrome; FA = fractional anisotropy; MNI = Montreal Neurological Institute; TBSS = tract-based spatial statistics; VBM = voxel-based morphometry

Kallmann syndrome (KS) is a rare inherited disorder (affecting about 1 in 10,000 males),¹ clinically characterized by the association of hypogonadotropic hypogonadism and hypo-/anosmia.² Both KS clinical hallmarks derive from a disturbed intrauterine migration process involving olfactory axons and gonadotropin-releasing hormone neurons from the olfactory pla-

code to the hypothalamus.^{3,4} The failure of the migration process results in hypo-/aplasia of the rhinencephalon (olfactory bulbs and tracts)³⁻⁶ and in altered gonadotropic axis function with low levels of sex hormones. Besides rhinencephalon abnormalities, distinctive KS neuroradiologic changes have been detected in the brain and bone structures of the anterior cranial fossa by conventional MR imaging⁷⁻¹⁴ and CT studies.¹⁵ The most known morphologic brain feature is the reduction in depth and length of the

Received December 20, 2013; accepted after revision February 3, 2014.

From the Department of Neuroradiology (R.M., F.D.S.), University of Salerno, Salerno, Italy; Istituto di Ricovero e Cura a Carattere Scientifico S. Camillo (R.M., V.C.), Venezia, Italy; Departments of Neurology (A.S.), and Psychiatry (A.F.), Department of Neurosciences; Unità di Endocrinologia (G.B.), Department of Medicine, University of Padova, Padova, Italy; Department of Clinical and Experimental Medicine and Surgery (V.P., A.A.S.), Endocrinology and Medical Andrology Section, Second University of Napoli, Napoli, Italy; and Department of Neuroradiology (A.E., A.B.), Department of Scienze Biomediche Avanzate, and ENT section (R.M., A.S.), Department of Neurosciences, "Federico II" University, Napoli, Italy.

Renzo Manara and Alessandro Salvalaggio equally contributed to the study and should be considered first authors.

Guglielmo Bonanni and Antoio Agostino Sinisi should be considered senior coauthors.

Paper previously presented in part at: Annual Meeting of the European Society of Neuroradiology, September 28 to October 1, 2013; Frankfurt, Germany.

Please address correspondence to Renzo Manara, MD, Neuroradiology, University of Salerno, Via S Allende 1, Baronissi 89081 (SA), Italy; e-mail: rmanara@unisa.it

Indicates article with supplemental on-line appendix and table.

<http://dx.doi.org/10.3174/ajnr.A3946>

olfactory sulcus, which typically turns medially, opening anteriorly into the interhemispheric fissure.⁷⁻¹³ This sulcal abnormality is thought to be driven by the absence/hypoplasia of the olfactory bulbs and represents an intriguing model of genetically driven developmental brain abnormalities. Furthermore, a few case reports postulated the strict relationship between KS and midline brain abnormalities, such as corpus callosum agenesis and holoprosencephaly,^{6,16} though pathologic and neuroimaging data are relatively scarce and often contradictory.⁷

In 2008, a pioneering study by voxel-based morphometry (VBM) MR imaging analysis revealed distinct regional gray and white matter volume changes in male patients with KS outside the frontal orbital regions.¹⁷ No study so far has replicated a larger sample of these findings, which would imply a much more profound effect of KS-related genes (*KALI*, *FGFR1*, *PROK2*, *PROKR2*, *FGF8*, *NELF*, etc.)¹⁸ and/or sex hormone deficiency on brain morphogenesis and development. Moreover, no study has investigated regional white matter changes revealed by VBM by diffusion tensor imaging, a powerful quantitative technique able to investigate the structural nature of white matter involvement. Finally, novel MR imaging-based analyses have been developed that allow assessing precise curvature, sulcation, and cortical thickness quantitative evaluations,¹⁹⁻²¹ thus providing further insights into cortex developmental abnormalities. Such analyses have not been applied to KS, though they might represent useful tools for investigating the structural underpinnings of neurologic and psychiatric disorders anecdotally reported in patients with KS.^{22,23}

By conventional MR imaging and novel quantitative sulcation, curvature, cortical thickness, and tract-based spatial statistics (TBSS) analyses, we aimed to feature, more precisely and in a large sample of male patients, the morphologic and structural brain involvement in KS.

MATERIALS AND METHODS

Subjects

Forty-five male patients (mean age, 30.7 years; range, 9–55 years) affected with KS underwent brain MR imaging. All patients met the diagnostic criteria for KS based on clinical observations and smell analysis (main clinical and demographic features are shown in On-line Table 1). One patient had a history of severe head trauma. Twenty-three healthy male subjects (mean age, 32.6 years; range: 12–55 years) or patients referred to neuroimaging for headache with no history of prematurity, head trauma, neurologic or psychiatric disease, or neurosurgery represented our control group.

Seven patients with KS and 2 controls were left-handed, according to the Edinburgh Handedness Inventory.²⁴ No patients or subjects required sedation during MR imaging acquisition. The study was approved by the local ethics committee, and written informed consent was obtained from patients or their parents.

Patients with KS younger than 12 years of age or presenting with midline brain abnormalities or significant parenchymal lesions were excluded from VBM, sulcation, curvature, and TBSS analyses to avoid the interference of maturation, malformative, or incidental factors on the quantitative parenchymal and morphologic evaluation.

MR Imaging Acquisition

All MR imaging scans were obtained in 2 centers (University Hospital of Padova and Medicanova Diagnostic Center, Battipaglia, Italy) equipped with the same 1.5T MR imaging scanner (Achieva; Philips Healthcare, Best, the Netherlands) with a standard quadrature head coil. The MR imaging study protocol included the following: 3D T1-weighted imaging (TR/TE, 20/3.8 ms; flip angle, 20°; section thickness, 1 mm; acquired pixel size, 1 × 1 mm; reconstructed pixel size, 0.66 × 0.66 mm; acquisition matrix, 212 × 210; reconstructed matrix, 320 × 320; acquisition time, approximately 7 minutes); and FLAIR (TR/TE/TI, 10,000/140/2800 ms; echo-train length, 53; flip angle, 90°; section thickness, 5 mm; intersection gap, 0.5 mm; acquisition pixel, 0.90 × 1.15 mm; reconstructed pixel, 0.9 × 0.9 mm; acquisition time, 3 minutes 20 seconds).

Diffusion tensor images were acquired with single-shot echo-planar diffusion-weighted imaging (TR/TE, 11,114/80 ms; acquisition matrix, 112 × 110; echo-train length, 59; reconstructed matrix, 128 × 128; acquisition pixel, 2 × 2 mm; reconstructed pixel, 1.75 × 1.75 × 2 mm; sensitivity encoding p reduction, 2; section thickness, 2 mm without gap; NEX, 2; acquisition time, 12 minutes 24 seconds). The axial sections covered the whole brain including the cerebellum. The diffusion-sensitizing gradients were applied along 32 noncollinear gradient-encoding directions with maximum $b=800$ s/mm². One additional image without diffusion gradients ($b=0$ s/mm²) was also acquired.

Image Processing

Data Processing of Volumetric Images and DTI (TBSS). The imaging processing methods are presented in detail in the On-line Appendix.

Specifically, we used the optimized VBM protocol (Diffeomorphic Anatomical Registration Through Exponentiated Lie Algebra) available in the statistical parametric mapping software (SPM8; Wellcome Department of Imaging Neuroscience, London, UK, www.fil.ion.ucl.ac.uk/spm).²⁵ For statistical analyses, we used parametric *t* tests as implemented by SPM8, by using age as a covariate of no interest. Results for gray matter were considered significant for $P < .05$, family-wise error-corrected.

All 3D T1-weighted data were also processed by FreeSurfer (<http://surfer.nmr.mgh.harvard.edu/>) to derive quantitative estimates of cortical thickness, sulcation, and curvature. The sulcation conveys information on how far a particular surface vertex point is from a hypothetical “midsurface,” which exists between the gyri and sulci. The curvature conveys information on the curvature (not distance) at a specific vertex point. The sharper the curve, the higher the value (positive or negative) is. The color conveys the sign and is just an arbitrary choice. Cortical thickness, sulcation, and curvature were estimated for the whole brain. Group analysis was performed by using generalized linear models, including age as a nuisance variable. Results were considered significant for $P < .05$, false discovery rate-corrected.

All DTI data were preprocessed by the FMRIB Diffusion Toolbox within FSL (<http://www.fmrib.ox.ac.uk/fsl/fdt/index.html>).²⁶ For group comparisons concerning fractional anisotropy (FA) and diffusivity values, data were fed into the voxelwise statistics analysis, which was based on nonparametric permutation testing (5000 permutations) by using the threshold-free cluster enhance-

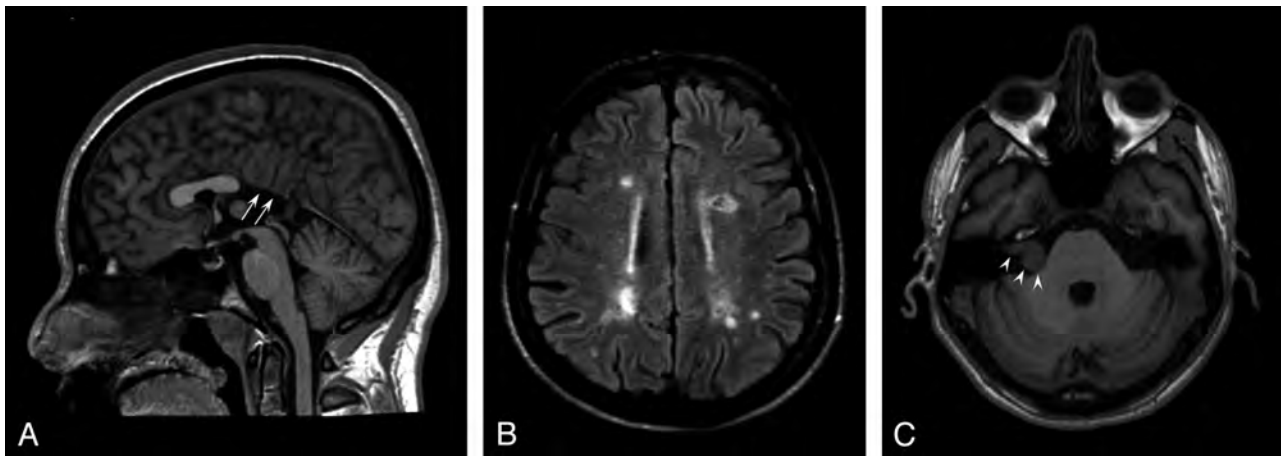


FIG 1. Conventional brain MR imaging findings in 45 patients with Kallmann syndrome. *A*, Midsagittal T1-weighted image of a patient with agenesis of the posterior portion of the corpus callosum (*white arrows*). *B*, Axial FLAIR image of the patient disclosing several multiple sclerosis–like white matter signal abnormalities in the centrum semiovale bilaterally. *C*, Non-enhanced axial T1-weighted image at the level of the internal acoustic meatus showing a right intra/extrameatal dumbbell-shaped mass consistent with an acoustic schwannoma.

ment²⁷ method to account for multiple comparison correction across space. Age and sites of MR imaging acquisition were entered into the analysis as covariates.

RESULTS

Conventional MR Imaging Findings Evaluation

One patient with KS had midline brain abnormalities (partial corpus callosum agenesis) (Fig 1*A*), and 1 had diffuse multiple sclerosis–like white matter abnormalities (Fig 1*B*).

On FLAIR images, nonspecific white matter signal abnormalities (1–20 punctuate hyperintensities) were observed in 15/45 patients (33%; mean age, 35.3 years; age range, 15–55 years); age did not differ between patients with and without white matter hyperintensities ($P = .07$). Similarly, the presence of obesity (7/45), hypertension (0/45), and cardiopathy (0/45) did not differ between these 2 subgroups.

One patient had small cortical abnormalities in the right superior frontal and inferior temporal gyri, consistent with sequelae of a known previous head trauma. One patient had a right intra/extrameatal acoustic nerve schwannoma (20 × 14 mm), with no significant mass effect on the pons (Fig 1*C*).

Quantitative MR Imaging Analysis

The 3 patients with partial agenesis of the corpus callosum, diffuse multiple sclerosis–like white matter lesions, and age younger than 12 years were excluded from quantitative analyses. Forty-two patients with KS were, therefore, considered for subsequent analyses (mean age, 30.6 years; range, 15–55 years).

Voxel-Based Morphometry

The total amount of gray and white matter did not differ between patients with KS and controls (gray matter, 919 ± 132 mL versus 949 ± 108 mL; white matter, 677 ± 091 mL versus 710 ± 081 mL, respectively) by using as covariates age, total intracranial volume, and site of MR imaging.

Patients with KS showed, compared with controls, 2 almost symmetric clusters of significant white matter volume decrease in the frontal basal regions (Montreal Neurological Institute

[MNI] coordinates: –16, 26, –26 and 14, 32, –28; P value family-wise error–corrected, respectively, <.001 and .002), 2 almost symmetric clusters of significant gray matter volume increase in the frontal basal regions (MNI coordinates: 16, 38, –12 and –16, 34, –12; P value family-wise error–corrected, .001), and 2 almost symmetric clusters of significant gray matter volume decrease in the frontal basal regions (MNI coordinates: –10, 32, –24 and 12, 26, –18; P value family-wise error–corrected <.001) by using as covariates age, total intracranial volume, and site of MR imaging. As shown in Fig 2, these regions were very close to the olfactory sulci. Patients with KS did not show clusters of significant white matter volume increase compared with controls.

Sulcation, Curvature, and Cortical Thickness Whole-Brain Analyses

Significant differences between male patients with KS and controls are shown in the Table and Fig 2, in particular in the following manner:

By sulcation analysis, the sulcal depth was reduced at the level of the olfactory sulci and increased at the level of the medial orbital-frontal sulci in patients with KS.

By curvature analysis, patients with KS presented with a decreased curvature in the olfactory sulcus and a sharper curvature close to the medial orbital-frontal sulcus, bilaterally.

By cortical thickness analysis, patients with KS had thicker cortices than controls in a region corresponding to the olfactory sulcus, bilaterally. In the left hemisphere, 2 small areas of decreased cortical thickness were found at the level of the medial and lateral orbital-frontal sulci, the larger close to the olfactory sulcus.

Tract-Based Spatial Statistics Analysis

TBSS whole-brain analysis showed no differences between patients with KS and controls regarding fractional anisotropy, mean diffusivity, radial diffusivity, and axial diffusivity.

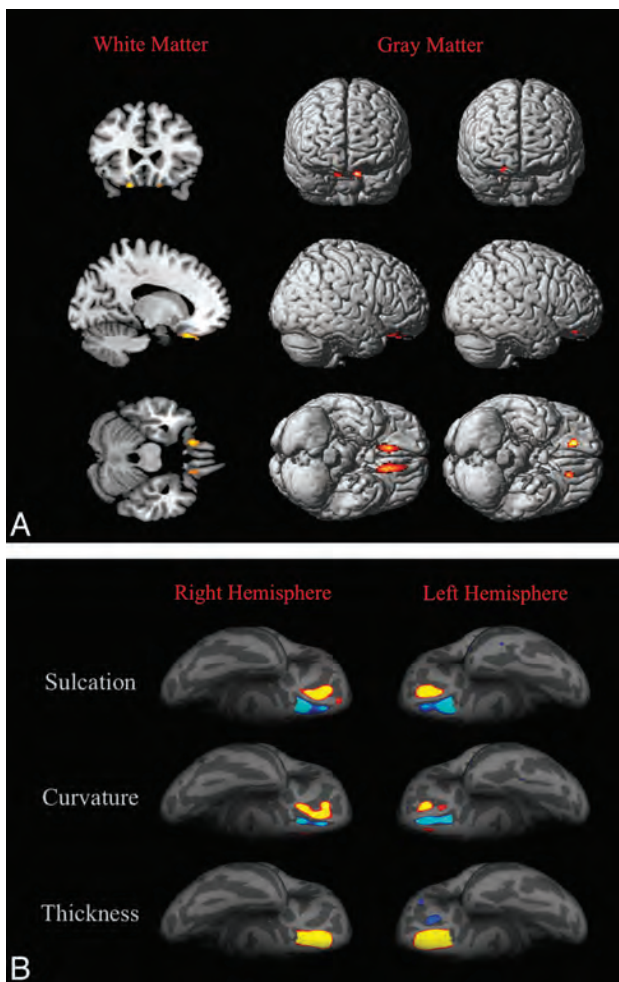


FIG 2. 3D-T1-based whole-brain analyses on 42 patients with Kallmann syndrome versus 23 controls. *A*, Voxel-based morphometry findings. Clusters of significantly decreased white matter volume (colored areas in the multiplanar reconstructions in the first column) were detected exclusively and symmetrically in the posterior portion of the medial orbital-frontal gyrus close to the olfactory sulcus; no regions of increased white matter volume were detected in our sample. Clusters of significantly decreased (second column) and increased (third column) gray matter volume are shown as colored cortical areas in the volume-rendering technique images within or close to the olfactory sulci. *B*, Sulcation, curvature, and thickness findings. Colored areas represent increased (yellow-red) and decreased (blue) values in patients with KS. Almost all differences are clustered within the olfactory sulci and the neighboring cortex of the rectus and medial orbital-frontal gyri.

DISCUSSION

The present study showed that patients with KS display surface cortical variations and gray and white matter volume changes, which clustered symmetrically in the frontal basal regions, close to the olfactory bulbs (gyrus rectus, medial orbital-frontal gyrus).

Changes in the frontal basal regions have been consistently described in the rhinencephalon and contiguous cerebral cortical and bone structures by pathology,^{5,6} conventional MR imaging,⁷⁻¹⁴ and CT studies in patients with KS.¹⁵ Increased volume of the corticospinal tracts and corpus callosum has been also depicted by conventional MR imaging,²⁸ suggesting the involvement of brain structures beyond the basal forebrain, though these findings have not been confirmed in larger series.^{7,17} A single MR

imaging study formerly applied VBM to investigate gray and white matter volume in male patients with KS, detecting changes in several areas outside the basal forebrain, namely regions of increased gray matter volume (precentral gyrus bilaterally, left middle occipital and middle frontal gyri), decreased gray matter volume (right parahippocampal gyrus), increased white matter volume (left cuneus and right subcallosal gyrus), and decreased white matter volume (left superior frontal gyrus, right medial frontal gyrus, left frontal lobe subgyral and left insula).¹⁷ In our VBM whole-brain analysis, gray and white matter changes appeared fairly symmetric and limited to the frontal basal regions. White matter volume changes (ie, decrease of white matter volume) were found exclusively in small subcortical areas of the medial orbital-frontal gyri close to the olfactory sulci. Similarly, VBM analysis disclosed small symmetric and contiguous areas of increased and decreased gray matter volume in the frontal basal regions close to the olfactory sulcus. The striking relationship between white and gray matter changes seems to suggest that these changes embody a fairly localized cortical-subcortical abnormal architectural development. Moreover, because all parenchymal changes are very close to the olfactory sulcus, they are most likely induced by the rhinencephalon hypo-/aplasia.

Except for these areas, by VBM analysis, cerebral gray and white matter did not differ between patients with KS and healthy controls. Similarly, TBSS analysis did not reveal any significant difference between patients with KS and controls, revealing that the ultrastructure of the white matter is preserved despite significant forebrain cortical changes. Nonetheless, KS genetic heterogeneity does not allow the exclusion of white matter hypertrophic or degenerative phenomena in specific subgroups of patients with KS because a strict genotypic/MR imaging phenotypic correlation requires a larger sample. Actually, no pathologic study reported brain parenchyma abnormalities in patients with KS, even though histologic data are very scarce. Peripheral axonal degeneration due to the absence of the olfactory bulbs has been shown in the olfactory mucosa,²⁹ but concomitant significant processes of axonal degeneration within the brain are not supported by VBM and TBSS findings.

Differences from previous MR imaging studies may be due to several issues, among them, the heterogeneity of the phenotypic spectrum of brain anomalies in KS or a different methodologic approach. The size of our study sample and the spatial coherence between gray/white matter volume changes and the well-known disease-related abnormalities of the olfactory sulcus seem to support the findings of the present study.

Consistently, the whole-brain curvature and sulcation analyses showed symmetric cortical abnormalities strictly confined to the frontal basal cortical regions (gyri recti and medial orbital-frontal gyri). Olfactory sulcus abnormalities were expected because the reduction in depth and length of the olfactory sulcus at gross pathology and conventional MR imaging evaluation is a known morphologic feature of the brain in patients with KS.⁷⁻¹² Olfactory sulcus abnormalities have been associated with embryogenic olfactory bulb-induced processes.^{10,11,30,31} In patients with KS, the aplasia/hypoplasia of the olfactory bulbs is associated with an ipsilaterally decreased depth of the olfactory sulcus, which might turn medially, opening anteriorly into the interhemis-

Cortical areas >40 mm² with significant differences between patients with Kallmann syndrome and controls by sulcation, curvature, and cortical thickness analyses

Hemisphere	Size (mm ²)		Local Maximum, Talairach			FDR Threshold	Cerebral Region
			X	Y	Z		
Sulcation							
Right	394.05	↓	11.2	13.8	-14.9	3.3429	Olfactory sulcus and contiguous cortex of the rectus gyri
Right	325.72	↑	16.4	28.7	-23.7	3.3429	Medial orbital-frontal gyrus
Left	518.07	↓	-9.8	16.0	-15.4	3.3159	Olfactory sulcus and contiguous cortex of the rectus gyri
Left	252.41	↑	-19.6	33.2	-17.3	3.3159	Medial orbital-frontal gyrus
Curvature							
Right	372.85	↑	14.4	32.3	-25.3	3.4704	Medial orbital-frontal gyrus
Right	77.61	↓	11.7	16.6	-14.2	3.4704	Olfactory sulcus
Right	44.71	↓	11.5	37.9	-19.1	3.4704	Olfactory sulcus
Left	196.94	↓	-11.6	38.7	-20.0	3.4704	Olfactory sulcus
Left	114.79	↑	-19.6	32.7	-14.9	3.4704	Medial orbital-frontal gyrus
Thickness							
Right	568.97	↑	-14.1	30.7	-19.2	3.3834	Olfactory sulcus and contiguous cortex of the rectus and medial orbital-frontal gyri
Left	686.38	↑	13.7	33.4	-23.3	3.2803	Olfactory sulcus and contiguous cortex of the rectus and medial orbital-frontal gyri
Left	78.39	↓	12.7	48.6	33.5	3.2803	Medial orbital-frontal sulcus
Left	40.54	↓	45.2	-62.3	36.9	3.2803	Lateral orbital-frontal gyrus

Note:— ↑ indicates that patients with KS showed increased sulcation, curvature, and cortical thickness; ↓, patients with KS showed decreased sulcation, curvature, and cortical thickness; FDR, false discovery rate.

spheric fissure.⁷ Indeed, as shown in Fig 2, the olfactory sulcus presented with decreased sulcation and curvature, while the medial orbital-frontal sulcus showed a “compensatory-like” increased sulcation and curvature. The concomitant changes of the contiguous orbital-frontal regions seem to highlight a more extensive effect of the olfactory bulbs on forebrain morphogenesis. Most interesting, patients with KS display increased cortical thickness very close to VBM, sulcation, and curvature forebrain anomalies, suggesting that olfactory bulb–induction failure might act not only on the sulcal but also on the structural organization of the cortex.

Regional gray matter increase has been associated with the absence of a sulcus,³² though so far no study investigated the correlation between cortical thickness and sulcation abnormalities, to our knowledge. We might speculate that a less deep sulcus results in an abnormal regional gray matter volume and cortical thickness as a consequence of overcrowding neurons migrated to this region. Alternatively, gray matter volume and cortical thickness changes might result from cortical functional differences between patients with KS and controls. The orbital-frontal cortex is deeply involved not only in olfaction (odor identification and olfactory memorization) but also in integrating emotion into cognition within decision-making processes.³³ KS is clinically characterized by the absence or reduction of olfaction, whereas few data are available on cognitive functioning and psychiatric risk, though schizophrenic disorders have been anecdotally reported among patients with KS.^{22,23} Nonetheless, the primary and secondary olfactory cortices correspond to piriform and periamygdalar cortices and the posterior orbital-frontal gyrus and insula, all areas that in our study did not present with gray matter and cortical thickness changes. Moreover, none of our patients presented with a history of overt psychiatric disease, even though a specific neuropsychological and psychiatric assessment was not

performed. Focused neurocognitive studies are warranted to investigate the presence of basal forebrain function impairment due to the above-mentioned morphologic and structural brain changes.

Finally, the changes observed in our study might be at least partly ascribed to hormonal differences between patients with KS and controls. Most of KS phenotypic features (hypogonadism, small penis, sexual secondary characteristics) are due to low testosterone levels during infancy and adolescence, which could also induce a feminine brain development. Sex brain dimorphism includes brain size, white and gray matter volume and regional cortical thickness changes.³⁴⁻³⁶ This study did not reveal significant differences in brain size between patients with KS and controls. Moreover, sex- and testosterone-related brain differences do not seem to involve the medial orbital-frontal basal regions, thus restraining the direct role of hormonal dysfunction in determining the morphologic pattern observed in patients with KS. Longitudinal studies on patients with KS enrolled before hormone replacement therapy will help clarify the effects of testosterone in postnatal brain development, even though the effect of hormone milieu on prenatal and early brain development phases will remain difficult to unravel.

Because KS is a disease due to mutation of genes that are involved in neuronal migration,³⁷ patients with KS have been previously reported to present with midline head and brain abnormalities, such as cleft palate, corpus callosum dysgenesis, and holoprosencephaly.^{6,38,39} These abnormalities have been thoroughly mentioned in studies on patients with KS.^{7,10,40} Nonetheless, brain MR imaging evaluation of our large sample revealed corpus callosum partial agenesis in only 1/45 patients with KS (2.2%), thus supporting the observation by Quinton et al⁷ that patients with KS mostly do not present significant intracranial midline abnormalities. A biased inclusion of syndromic patients

in the initial case series⁶ might explain the difference with more recent larger samples. On the other hand, holoprosencephalic patients might be underdiagnosed as also being affected by hypogonadotropic hypogonadism and hyposmia due to their shorter life expectancy and overwhelming clinical issues.

Among our patients with KS, 15 (33%) showed small nonspecific punctuate FLAIR hyperintensities; 1 showed diffuse multiple sclerosis-like white matter lesions; and 1, an acoustic nerve schwannoma. These findings should be considered incidental unless otherwise demonstrated.

Even though these multimodality MR imaging analyses were applied to a large homogeneous sample of patients with KS with a strictly uniform MR imaging protocol (same scanner, same sequence parameters, and so forth), this study presents some limits. We evaluated KS-related brain MR imaging changes only in males, and further studies are warranted to confirm our findings in female patients with KS. Moreover, the genetic heterogeneity of our sample and its still ongoing molecular characterization did not allow investigating a precise genotypic/MR imaging correlation. Finally, because this was a cross-sectional study with almost no pediatric patients with KS, we could not investigate the brain changes related to aging or the effects of sex hormone deprivation and subsequent replacement on brain development.

The enrollment of specific subgroups, subdivided according to genetics, sex, age, ancillary clinical features (eg, the presence of mirror movement and psychiatric disorders), and treatment will help define more precisely the specific brain changes in KS.

CONCLUSIONS

This MR imaging study on a large group of male patients with KS showed significant brain changes specifically involving the gyri recti and the contiguous medial orbital-frontal regions. Even though further validation is warranted, curvature, sulcation, cortical thickness, gray/white matter volume, and bone changes in patients with KS point toward a profound structural and morphologic involvement of the basal forebrain that is far more consistent than a simple hypoplasia of the olfactory sulcus, driven by the olfactory bulbs. Future studies on the cognitive and psychiatric domains will define the clinical impact of these morphologic and structural brain changes.

APPENDIX

Members of the Kallmann Syndrome Neurological Study Group were the following: Arianna D'Errico, "Federico II" University, Napoli, Italy; Giancarlo Ottaviano, University of Padova, Padova, Italy; Elena Cantone, "Federico II" University, Napoli, Italy; Chiara Briani, University of Padova, Padova, Italy; Nella A. Greggio, Azienda Ospedaliera, University of Padova, Padova, Italy; Silvia Rizzati, University of Padova, Padova, Italy; Marco Rossato, University of Padova, Padova, Italy; Eugenio De Carlo, University of Padova, Padova, Italy; Elvira Napoli, Medicanova Diagnostic Center, Battipaglia, Italy; Gianfranco D'Agosto, Medicanova Diagnostic Center, Battipaglia, Italy; Giannennaro Coppola, University of Salerno, Salerno, Italy.

Disclosures: Renzo Manara—UNRELATED: Payment for Lectures (including service on Speakers Bureau); BioMarin, Comments: lecture on mucopolysaccharidosis type 6 (600 Euro).

REFERENCES

1. Seminara SB, Hayes FJ, Crowley WF Jr. **Gonadotropin-releasing hormone deficiency in the human (idiopathic hypogonadotropic hypogonadism and Kallmann's syndrome): pathophysiological and genetic considerations.** *Endocr Rev* 1998;19:521–39
2. Kallmann FJ, Schonfeld WA, Barvera SE. **The genetic aspects of primary eunuchoidism.** *Am J Ment Defic* 1944;48:203–36
3. Schwanzel-Fukuda M, Bick D, Pfaff DW. **Luteinizing hormone-releasing hormone (LHRH)-expressing cells do not migrate normally in an inherited hypogonadal (Kallmann) syndrome.** *Brain Res Mol Brain Res* 1989;6:311–26
4. Okubo K, Sakai F, Lau EL, et al. **Forebrain gonadotropin-releasing hormone neuronal development: insights from transgenic medaka and the relevance to X-linked Kallmann syndrome.** *Endocrinology* 2006;147:1076–84
5. Maestre de San Juan A. **Falta total de los nervios olfatorios con anosmia en un individuo en quien existia una atrofia congénita de los testículos y miembro viril.** *Siglo Medico* 1856;131–211
6. De Morsier G. **Studies in cranio-encephalic dysraphia. I. Agenesis of the olfactory lobe (lateral telencephaloschisis) and of the callous and anterior commissures (median telencephaloschisis); olfactory-genital dysplasia** [in French]. *Schweiz Arch Neurol Psychiatr* 1954;74:309–61
7. Quinton R, Duke VM, de Zoysa PA, et al. **The neuroradiology of Kallmann's syndrome: a genotypic and phenotypic analysis.** *J Clin Endocrinol Metab* 1996;81:3010–17
8. Birnbacher R, Wandl-Vergesslich K, Frisch H. **Diagnosis of X-recessive Kallmann syndrome in early infancy: evidence of hypoplastic rhinencephalon.** *Eur J Pediatr* 1994;153:245–47
9. Truwit CL, Barkovich AJ, Grumbach MM, et al. **MR imaging of Kallmann syndrome, a genetic disorder of neuronal migration affecting the olfactory and genital systems.** *AJNR Am J Neuroradiol* 1993;14:827–38
10. Vogl TJ, Stemmler J, Heye B, et al. **Kallman syndrome versus idiopathic hypogonadotropic hypogonadism at MR imaging.** *Radiology* 1994;191:53–57
11. Yousem DM, Turner WJ, Li C, et al. **Kallmann syndrome: MR evaluation of olfactory system.** *AJNR Am J Neuroradiol* 1993;14:839–43
12. Knorr JR, Ragland RL, Brown RS, et al. **Kallmann syndrome: MR findings.** *AJNR Am J Neuroradiol* 1993;14:845–51
13. Koenigkam-Santos M, Santos AC, Versiani BR, et al. **Quantitative magnetic resonance imaging evaluation of the olfactory system in Kallmann syndrome: correlation with a clinical smell test.** *Neuroendocrinology* 2011;94:209–17
14. de m Freitas P, Carvalho S, Ribeiro F, et al. **Neuroradiology of Kallmann's syndrome** [in Portuguese]. *Acta Med Port* 2001;14:123–26
15. Maione L, Benadjaoud S, Eloit C, et al. **Computed tomography of the anterior skull base in Kallmann syndrome reveals specific ethmoid bone abnormalities associated with olfactory bulb defects.** *J Clin Endocrinol Metab* 2013;98:E537–46
16. Ueno H, Yamaguchi H, Katakami H, et al. **A case of Kallmann syndrome associated with Dandy-Walker malformation.** *Exp Clin Endocrinol Diabetes* 2004;112:62–67
17. Koenigkam-Santos M, Santos AC, Borduqui T, et al. **Whole-brain voxel-based morphometry in Kallmann syndrome associated with mirror movements.** *AJNR Am J Neuroradiol* 2008;29:1799–804
18. Costa-Barbosa FA, Balasubramanian R, Keefe KW, et al. **Prioritizing genetic testing in patients with Kallmann syndrome using clinical phenotypes.** *J Clin Endocrinol Metab* 2013;98:E943–53
19. Dale AM, Fischl B, Sereno MI. **Cortical surface-based analysis. I. Segmentation and surface reconstruction.** *Neuroimage* 1999;9:179–94
20. Fischl B, Sereno MI, Dale AM. **Cortical surface-based analysis. II: inflation, flattening, and a surface-based coordinate system.** *Neuroimage* 1999;9:195–207
21. Fischl B, Dale AM. **Measuring the thickness of the human cerebral cortex from magnetic resonance images.** *Proc Natl Acad Sci U S A* 2000;97:11050–55

22. Vagenakis GA, Hyphantis TN, Papageorgiou C, et al. **Kallmann's syndrome and schizophrenia.** *Int J Psychiatry Med* 2004;34:379–90
23. Verhoeven WM, Egger JI, Hovens JE, et al. **Kallmann syndrome and paranoid schizophrenia: a rare combination.** *BMJ Case Rep* 2013; 2013: pii: bcr2012007387
24. Oldfield RC. **The assessment and analysis of handedness: the Edinburgh inventory.** *Neuropsychologia* 1971;9:97–113
25. Ashburner J, Friston KJ. **Voxel-based morphometry: the methods.** *Neuroimage* 2000;11(6 pt 1):805–21
26. Maldjian JA, Laurienti PJ, Kraft RA, et al. **An automated method for neuroanatomic and cytoarchitectonic atlas-based interrogation of fMRI data sets.** *Neuroimage* 2003;19:1233–39
27. Smith SM, Nichols TE. **Threshold-free cluster enhancement: addressing problems of smoothing, threshold dependence and localisation in cluster inference.** *Neuroimage* 2009;44:83–98
28. Krams M, Quinton R, Ashburner J, et al. **Kallmann's syndrome: mirror movements associated with bilateral corticospinal tract hypertrophy.** *Neurology* 1999;52:816–22
29. Schwob JE, Szumowski KE, Leopold DA, et al. **Histopathology of olfactory mucosa in Kallmann's syndrome.** *Ann Otol Rhinol Laryngol* 1993;102:117–22
30. Abolmaali ND, Hietschold V, Vogl TJ, et al. **MR evaluation in patients with isolated anosmia since birth or early childhood.** *AJNR Am J Neuroradiol* 2002;23:157–64
31. Nguyen AD, Pelavin PE, Shenton ME, et al. **Olfactory sulcal depth and olfactory bulb volume in patients with schizophrenia: an MRI study.** *Brain Imaging Behav* 2011;5:252–61
32. Buda M, Fornito A, Bergström ZM, et al. **A specific brain structural basis for individual differences in reality monitoring.** *J Neurosci* 2011;31:14308–13
33. Bechara A, Damasio H, Damasio AR. **Emotion, decision making and the orbitofrontal cortex.** *Cereb Cortex* 2000;10:295–307
34. Sacher J, Neumann J, Okon-Singer H, et al. **Sexual dimorphism in the human brain: evidence from neuroimaging.** *Magn Reson Imaging* 2013;31:366–75
35. Witte AV, Savli M, Holik A, et al. **Regional sex differences in grey matter volume are associated with sex hormones in the young adult human brain.** *Neuroimage* 2010;49:1205–12
36. Im K, Lee JM, Lee J, et al. **Gender difference analysis of cortical thickness in healthy young adults with surface-based methods.** *Neuroimage* 2006;31:31–38
37. Bonomi M, Libri DV, Guizzardi F, et al, for the Idiopathic Central Hypogonadism Study Group of the Italian Societies of Endocrinology and Pediatric Endocrinology and Diabetes. **New understandings of the genetic basis of isolated idiopathic central hypogonadism.** *Asian J Androl* 2012;14:49–56
38. Parr JH. **Midline cerebral defects and Kallmann's syndrome.** *JR Soc Med* 1988;81:355–56
39. Gibby OM, Rayner PHW, West RJ, et al. **Short stature due to median craniocephalic dysraphia with nasal encephalocele.** In: *Proceedings of the 1st Meeting of the British Endocrine Society*, 1982; Abstract 98:48
40. Dodé C, Hardelin JP. **Kallmann syndrome.** *Eur J Hum Genet* 2009; 17:139–46

Quantitative 7T Phase Imaging in Premanifest Huntington Disease

A.C. Apple, K.L. Possin, G. Satris, E. Johnson, J.M. Lupo, A. Jakary, K. Wong, D.A.C. Kelley, G.A. Kang, S.J. Sha, J.H. Kramer, M.D. Geschwind, S.J. Nelson, and C.P. Hess



ABSTRACT

BACKGROUND AND PURPOSE: In vivo MR imaging and postmortem neuropathologic studies have demonstrated elevated iron concentration and atrophy within the striatum of patients with Huntington disease, implicating neuronal loss and iron accumulation in the pathogenesis of this neurodegenerative disorder. We used 7T MR imaging to determine whether quantitative phase, a measurement that reflects both iron content and tissue microstructure, is altered in subjects with premanifest Huntington disease.

MATERIALS AND METHODS: Local field shift, calculated from 7T MR phase images, was quantified in 13 subjects with premanifest Huntington disease and 13 age- and sex-matched controls. All participants underwent 3T and 7T MR imaging, including volumetric T1 and 7T gradient recalled-echo sequences. Local field shift maps were created from 7T phase data and registered to caudate ROIs automatically parcellated from the 3T T1 images. Huntington disease–specific disease burden and neurocognitive and motor evaluations were also performed and compared with local field shift.

RESULTS: Subjects with premanifest Huntington disease had smaller caudate volume and higher local field shift than controls. A significant correlation between these measurements was not detected, and prediction accuracy for disease state improved with inclusion of both variables. A positive correlation between local field shift and genetic disease burden was also found, and there was a trend toward significant correlations between local field shift and neurocognitive tests of working memory and executive function.

CONCLUSIONS: Subjects with premanifest Huntington disease exhibit differences in 7T MR imaging phase within the caudate nuclei that correlate with genetic disease burden and trend with neurocognitive assessments. Ultra-high-field MR imaging of quantitative phase may be a useful approach for monitoring neurodegeneration in premanifest Huntington disease.

ABBREVIATIONS: AUC = area under the curve; CAG = cytosine-adenine-guanine; CAP_s = CAG-age-product scaled; eTIV = estimated total intracranial volume; HD = Huntington disease; LFS = local field shift; PLIC = posterior limb of the internal capsule; pmHD = premanifest Huntington disease; UHDRS = Unified Huntington's Disease Rating Scale

Huntington disease (HD) is an autosomal dominant disorder caused by abnormal expansion of a CAG (cytosine-adenine-guanine) nucleotide triplet within the *Huntingtin* gene, on the

short arm of chromosome 4.^{1,2} The disease is characterized clinically by motor, cognitive, and behavioral symptoms and neuropathologically by degeneration across the brain, most prominently in the striatum.^{1,3} Genetic testing makes it possible to identify carriers before symptom onset, thereby opening a therapeutic window for interventions designed to delay or prevent the onset of disease. Currently, quantitative imaging of striatal volume is considered the most reliable method for monitoring progression in premanifest HD (pmHD).³⁻⁷ However, striatal volume is relatively insensitive,^{6,8,9} and additional markers are necessary to follow subclinical changes in clinical trials and to help define prognosis for the individual patient.⁸

Postmortem neuropathology and in vivo 1.5T and 3T MR imaging in HD have demonstrated increased iron in the caudate and putamen.¹⁰⁻¹⁴ As a recent example, Dumas et al¹⁵ used 3T magnetic field correlation, a composite measure of iron levels, to compare subjects with early HD, premanifest gene carriers, and


Received September 16, 2013; accepted after revision January 9, 2014.


From the Departments of Radiology and Biomedical Imaging (A.C.A., J.M.L., A.J., S.J.N., C.P.H.) and Neurology (K.L.P., G.S., E.J., K.W., G.A.K., S.J.S., J.H.K., M.D.G.), University of California, San Francisco; and GE Healthcare (D.A.C.K.), Global Applied Sciences Laboratory, Menlo Park, California.

This work was funded in part by the University of California Discovery ITL-BIO04-10148, an academic-industry partnership grant with GE Healthcare, and by the National Institutes of Health grant 1S10RR026845-01.

Paper previously presented in part at: Annual Meeting of the International Society for Magnetic Resonance in Medicine, May 5-11, 2012; Melbourne, Australia.

Please address correspondence to Christopher P. Hess, MD, PhD, University of California, San Francisco, 505 Parnassus Ave, Room L-358, Box 0628, San Francisco, CA 94143-0628; e-mail: Christopher.Hess@ucsf.edu

 Indicates open access to non-subscribers at www.ajnr.org

 Indicates article with supplemental on-line figure.

<http://dx.doi.org/10.3174/ajnr.A3922>

healthy controls. Higher field correlation was found in patients with early HD compared with controls, but no difference was observed between the premanifest gene carrier group and controls. Among techniques sensitive to the presence of iron, MR phase imaging offers high contrast and permits numeric quantitation.¹⁶⁻¹⁹ Compared with 3T and lower field MR imaging, 7T phase imaging has higher signal-to-noise, heightened contrast and sensitivity, and improved visualization of anatomy.¹⁹⁻²¹ Together, these factors result in textural heterogeneity within the caudate that differs between matched controls and subjects with premanifest HD.²² In this study, we aimed to determine whether quantitative 7T phase differs within the caudate nuclei between subjects with pmHD and healthy controls. Secondly, we tested the association between caudate phase and volume and assessed relationships among phase and disease burden, severity of motor symptoms, and neurocognitive evaluation.

MATERIALS AND METHODS

Research Participants

The University of California, San Francisco Committee on Human Research provided institutional review board approval for this Health Insurance Portability and Accountability Act–compliant prospective study, and written consent was obtained from all subjects. Seventeen volunteers with genetically confirmed pmHD and 16 age- and sex-matched controls were recruited from a registry maintained by the UCSF Memory and Aging Center clinic or via their participation in other research projects at our institution between August 2011 and August 2013. Participants in the pmHD group tested positive for the HD mutation and had at least 40 CAG repeats. Three neurologists with expertise in HD (G.A.K., M.D.G., and S.J.S.) used the Unified Huntington's Disease Rating Scale (UHDRS) to determine the total motor score, between 0 and 124, and the diagnostic confidence level, between 0 (healthy, no abnormalities) and 4 (motor abnormalities consistent with HD, $\geq 99\%$ confidence), for each subject. Similar to prior studies of premanifest HD,^{23,24} 1 subject who scored above 3 was excluded. Three other participants and 3 controls were excluded because they were unable to complete 7T MR imaging. Thirteen patients with pmHD and 13 controls were included for analysis.

Disease Burden

CAG-Age-Product Scaled (CAP_s), an index developed in the PREDICT-HD study to approximate the time to HD diagnosis by using the age at motor onset and the number of CAG repeats, was calculated for each subject with pmHD as $CAP_s = \text{Age} \times (CAG - 33.66)/432.3326$.^{23,25,26} CAP_s is classified as low ($0 < CAP_s \leq 0.67$), medium ($0.67 < CAP_s \leq 0.85$), or high ($CAP_s > 0.85$), reflecting higher cumulative disease burden and closer proximity to diagnosis. According to previously established norms, CAP_s of less than, equal to, or greater than 1 indicates a 5-year diagnosis probability of less than, equal to, or greater than 50%, respectively.

Cognitive Assessments

Executive function and working memory are especially vulnerable to early brain changes in pmHD.²⁷⁻²⁹ We assessed cognitive function in these domains by using the National Institutes of

Health EXAMINER, a neuropsychological tool used to evaluate patients with pmHD in our clinical cohorts.³⁰ The EXAMINER yields 4 scores: the overall Executive Composite score, the Working Memory score, the Cognitive Control score, and the Fluency score.

MR Imaging Data Acquisition

Subjects were scanned on 3T and 7T MR imaging scanners (GE Healthcare, Milwaukee, Wisconsin) in a single session by using a standardized protocol at both field strengths. Eight- and 32-channel head coils were used for 3T (GE Signa HDx 3T scanner) and 7T (GE MR950 7T scanner; a non-significant-risk investigational device), respectively. For 7T phase imaging, a gradient recalled-echo scan was acquired with TR/TE = 250/12.5 ms, flip angle = 15°, FOV = 22 cm, matrix = 1024 × 768, and 4-mm section thickness with a 2-mm intersection gap for a scanning time of 6 minutes, 28 seconds. Volumetric T1-weighted images were also acquired at 7T by using an inversion recovery T1-weighted sequence with the following parameters, optimized empirically for gray-white contrast: TR/TE = 11/5 ms, flip = angle 20°, FOV = 22 cm, matrix = 256 × 256, and 1-mm section thickness for a duration of 3 minutes, 33 seconds. For accurate segmentation of caudate nuclei, volumetric T1-weighted imaging was also performed at 3T (TR/TE = 7/2 ms, flip angle = 15°, FOV = 23 cm, matrix = 256 × 192, 1-mm section thickness, 6 minutes, 18 second scanning time). A subspecialty certified neuroradiologist (C.P.H.) reviewed all images to assess whether subjective striatal atrophy was present in subjects with pmHD compared with controls.

Image Processing and Analysis

Magnitude and phase images were constructed from the multichannel 7T gradient recalled-echo data following the method of Hammond et al.³¹ Caudate ROIs were automatically delineated from the 3T T1 data by using the subcortical segmentation algorithm³² from Version 5.0.1 of the fMRI of the Brain Software Library image-processing package (FSL; <http://www.fmrib.ox.ac.uk/fsl>) (Fig 1A) and were normalized by estimated total intracranial volume ($eTIV$) in each subject. Using the T1 data from both field strengths as an intermediate for 6-parameter rigid-body registration, we aligned the caudate volumes with the 7T images by using the FMRIB Linear Registration Tool in FSL (Fig 1B).³³ $eTIV$ was calculated from the 3T T1 images by using in-house software written to implement the atlas-based method described by Buckner et al.³⁴

White matter ROIs in the left and right posterior limb of the internal capsule (PLIC) were manually drawn for each subject on the 7T phase images by using in-house software (Fig 1C). With the approach of Hammond et al.,²⁰ we used PLIC phase (recorded in hertz) to normalize phase measurements across the brain. Specifically, phase images were converted into quantitative maps of local field shift (LFS) by first subtracting the mean PLIC phase and then dividing by $\gamma \times B_0$, measured in parts per billion at each pixel. Mean LFS was calculated within each caudate nucleus from the coregistered ROIs.

Statistical Analysis

Statistical analysis was performed using STATA, Version 13 (StataCorp, College Station, Texas). Groups were assessed for differences in sex by using χ^2 tests for equality of proportions, and

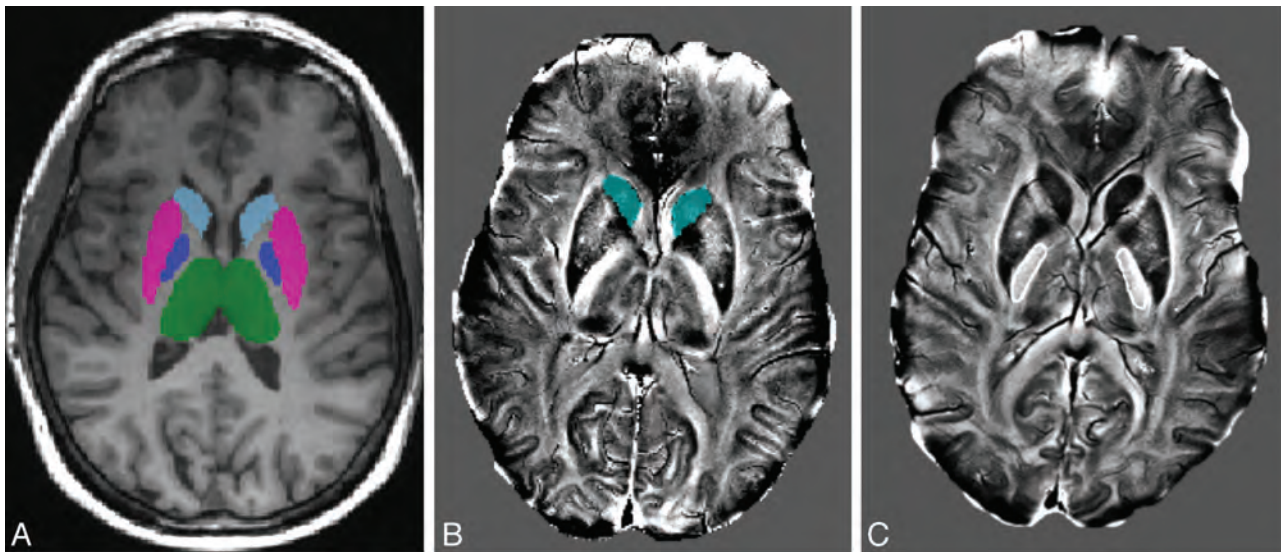


FIG 1. A, ROIs are extracted automatically from 3T T1-weighted images by using FSL; the segmented caudate nuclei from 1 subject are shown in light blue. B, Caudate ROIs are automatically coregistered with the 7T data and overlaid onto the phase images. C, PLIC ROIs drawn manually (thin region drawn on each side of the brain in white) on 7T phase images. Mean PLIC phase was used for normalization in the construction of LFS maps in each patient.

1-way ANOVA was used to evaluate differences in age at the time of the MR imaging, years of education, and eTIV. Caudate volumes and mean LFS were compared across hemispheres by using *t* tests for paired samples separately within each group. Because neither volume nor LFS departed significantly from Gaussian distributions based on tests of skewness and kurtosis, standard parametric analysis was used for all comparisons.

One-way ANCOVA was used to compare LFS and normalized volume between controls and subjects with pmHD, with age and sex included as covariates. Next, to investigate the relationship between LFS and normalized volume, we performed 2 separate analyses. First, Pearson partial correlation was applied, controlling for age, sex, and diagnosis. Second, logistic regression models were constructed to compare the accuracy of using LFS alone, normalized volume alone, and both values together as predictors to distinguish controls and subjects with pmHD. Finally, multivariate linear regressions were applied to evaluate relationships between LFS and CAP_s (disease burden), total motor UHDRS score, and EXAMINER score, by using sex as a covariate in the first case, age as a covariate in the second case, and both age and sex as covariates in the third case. For all tests, *P* values ≤ .05 were considered significant, adjusted for multiple comparisons with the Bonferroni correction in the regressions of LFS with EXAMINER scores.

RESULTS

Subjects

The Table summarizes baseline characteristics of subjects with pmHD and controls. There was no difference in age, sex, or eTIV between groups. A trend toward a greater number of years of education was seen in controls (*P* = .077). Two subjects with pmHD fell into the low disease burden group; 4, into the medium group, and 7, into the high group based on computed CAP_s indices. The medium and low groups were combined for further statistical analyses. Total motor UHDRS scores for participants

Baseline characteristics for participants

	pmHD	Control	<i>P</i> Value
No.	13	13	—
Sex (female/male)	7/6	7/6	1.00
Age (yr)	46.1 ± 12.4	45.7 ± 15.3	0.88
Years of education	15.7 ± 2.5	17.2 ± 1.4	0.077
CAG repeats	42.2 ± 2.0	—	—
CAP _s	0.867 ± 0.153	—	—
UHDRS	8.7 ± 6.5	—	—
eTIV (cm ³)	1465.1 ± 137.5	1431.0 ± 71.4	0.44

Note: — indicates not applicable.

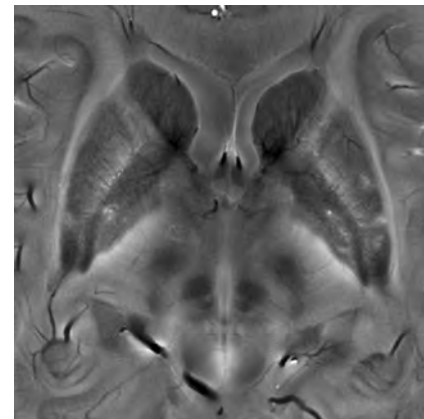


FIG 2. Magnified phase image centered on the basal ganglia in a representative subject with pmHD. The numeric values of phase reflect the composite effects of iron concentration, deoxyhemoglobin within veins, myelin, and tissue microstructure.

ranged from 0 to 21. Visual inspection of 7T LFS maps confirmed that the caudate and PLIC boundaries were accurately delineated in each subject (Fig 2).

Normalized Caudate Volume

There was no difference between left and right normalized caudate volume in the pmHD or control groups; therefore, the mean

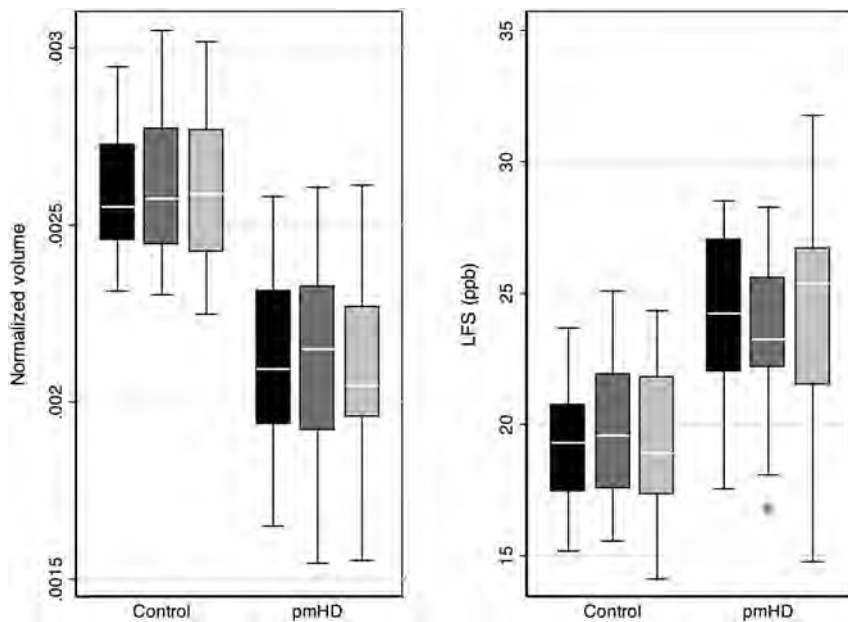


FIG 3. Boxplots comparing caudate volume (left), normalized by the total intracranial volume (cubic millimeter/cubic millimeter); and LFS (right), normalized by mean PLIC phase (in parts per billion), in subjects with pmHD and controls. Caudate LFS and normalized volume are depicted for the interhemispheric average value (dark gray), the right caudate nucleus (intermediate gray), and the left caudate nucleus (light gray).

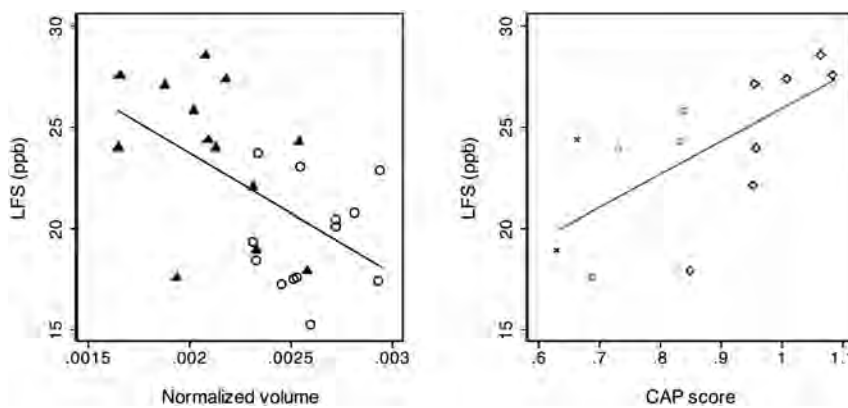


FIG 4. Scatterplots comparing caudate LFS with normalized caudate volume (left) and with CAP_s (right) for subjects with pmHD and controls. In the left plot, triangles and circles refer to subjects with pmHD and controls, respectively. There was no correlation between caudate LFS and caudate volume. In the right plot, subjects in the low (x), medium (□), and high (◇) CAP_s groups. There is a strong positive correlation between CAP_s and caudate LFS ($R^2 = 0.61, P = .003$).

normalized volume for both nuclei was used for comparisons. Although visual inspection did not reveal disproportionate striatal atrophy, caudate volume was smaller ($P = .0001$) in the pmHD group (Fig 3A). The difference in volume between the high and the medium-low CAP_s groups was also significant ($P = .04$). Age and sex did not influence this difference.

Caudate Local Field Shift

No difference between left and right caudate LFS was observed within either subjects with pmHD or controls; therefore, the mean LFS for both nuclei was used for comparisons. Subjects with pmHD had higher caudate LFS ($P = .0013$) than controls (Fig 3B). Although sex did not impact this difference, age was a significant covariate ($P = .024$). A difference in LFS between the high and the medium-low CAP_s groups was also found ($P = .03$).

Relationship between Caudate LFS and Disease Burden

Figure 4 shows scatterplots illustrating the relationship between LFS and normalized caudate volume and CAP_s. In evaluating the relationship between LFS and these imaging and genetic markers of disease burden, partial correlations, controlled for age and sex, did not reveal an association between LFS and volume ($P = .42$). In contrast, there was a strong correlation between LFS and CAP_s ($R^2 = 0.61, P = .003$).

Logistic regression analyses showed that both LFS ($P = .008$) and normalized volume ($P = .01$) separately predicted disease state, as did bivariate modeling with both measurements ($P = .0004$). There was no difference in the accuracy of the univariate models (area under the curve [AUC] = 0.89 [95% CI, 0.77–1.0] for LFS, and AUC = 0.92 [95% CI, 0.81–1.0] for normalized volume). Accuracy was higher for the bivariate logistic regression by using LFS and volume together (AUC = 0.95 [95% CI, 0.88–1.0]), implying that both variables contribute to the prediction of disease state. However, differences in AUC among the 3 models did not meet the criteria for significance, due to the small group sizes.

Relationship between Caudate Measures and Total Motor UHDRS Score

Controlled for age, partial correlations did not reveal an association between total motor UHDRS score and either normalized volume ($P = .97$) or LFS ($P = .63$) (On-line Figure).

Relationship between Caudate LFS and Cognitive Assessments

The results of multivariate regressions comparing LFS with EXAMINER scores for the pmHD and control groups are depicted in Fig 5. After Bonferroni correction, there was no correlation between LFS and EXAMINER scores when controlling for age and sex. There was, however, a trend toward correlation between LFS and Executive Composite score ($R^2 = 0.32, P = .031$) and between LFS and Working Memory Factor ($R^2 = 0.35, P = .018$).

DISCUSSION

The main result of this work is that measurements of LFS calculated from 7T gradient-echo phase MR imaging differ between subjects with pmHD and matched controls within the caudate nuclei. This result stands in contrast to prior work with iron-sensitive techniques in HD, which have shown elevated iron in the

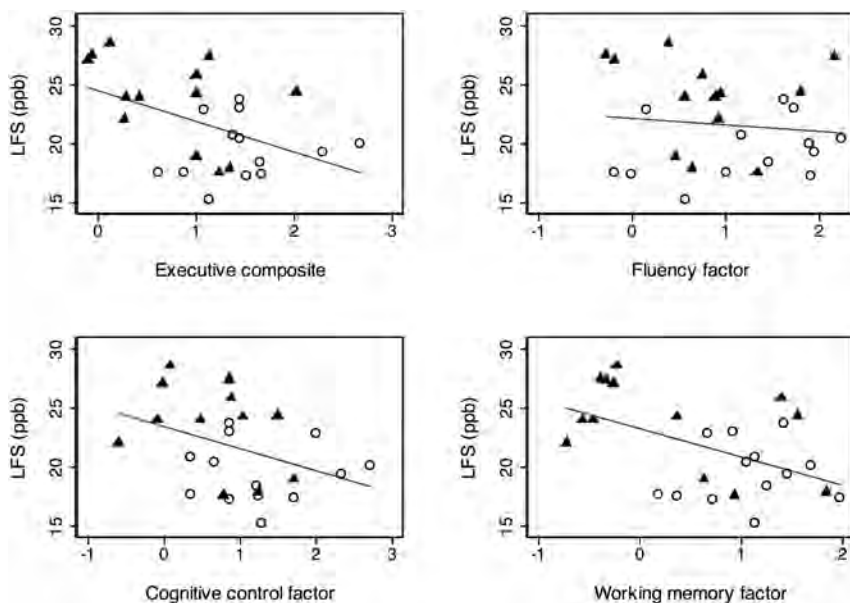


FIG 5. Scatterplots illustrating relationships between LFS and EXAMINER indices, including Executive Composite (top left), Fluency Factor (top right), Cognitive Control Factor (bottom left), and Working Memory Factor (bottom right). After correction for multiple comparisons, correlations were not significant but confirmed trends for Executive Composite ($R^2 = 0.32$, $P = .031$) and Working Memory Factor ($R^2 = 0.35$, $P = .018$). Circles (○) and triangles (▲) refer to controls and subjects with pmHD, respectively.

striatum of subjects with early- and late-stage HD but have not found increased iron in premanifest disease.¹⁵ We also found that a positive caudate phase shift correlates with the genetic burden of disease and permits accurate prediction of disease state that improves when used together with normalized caudate volume. Finally, we determined that caudate LFS trends negatively with neuropsychological assessments of executive function and working memory, 2 cognitive domains previously reported to be affected when the National Institutes of Health EXAMINER is used in subjects with pmHD.³⁵

In agreement with prior quantitative structural MR imaging studies, we found smaller caudate volume in subjects with premanifest HD.^{3-5,7} Similar to measurements of striatal volume, LFS can be quantitated semiautomatically to reduce interobserver variability and render analysis more feasible for large-scale clinical trials and research cohorts. PLIC measurements for normalizing phase were obtained manually in this study because fully automated analysis was not the focus of this work. However, template-based techniques to define other ROIs, including the PLIC, could be similarly automated for fully automated quantitation.

Measurements of phase by using 7T MR imaging are modulated by a number of factors. Based on autopsy data derived from patients with late-stage HD¹⁰ and other MR imaging studies in HD,^{11,13,15} we hypothesize that the phase differences seen in this work primarily reflect abnormal deposition of iron. It is also possible that other magnetic susceptibility-shifting metabolites, including calcium, play a contributing role. The tissue magnetic architecture on ultra-high-field MR imaging is defined by the arrangement of normal proteins, lipids, and nonheme iron and other compounds at the cellular and subcellular level; disruptions in the normal arrangement of these molecular structures could also impact phase measurements.³⁶ Compared with magnetic

field correlation and phase imaging at lower field strengths, 7T has higher sensitivity to small alterations in tissue susceptibility and thus may enhance the ability to detect neuropathologic alterations related to HD before the onset of disease.

Age also impacts phase in many deep gray nuclei, including the caudate nuclei.^{37,38} This effect was confirmed in the present work because age was found to be a significant covariate independent of disease status in multivariate analyses. Although we did not find that normalized caudate volume was impacted by age, it is recognized that the volumes of subcortical structures, including the caudate, decrease with advancing age,³⁹ and the absence of this effect in the present study more likely reflects its limited power to detect small differences in caudate volume.

The absence of a correlation between caudate volume and LFS, together with the improved accuracy of delineating control and pmHD groups by using logistic regression with both variables simulta-

neously, suggests that these 2 measures reflect different pathologic end points of disease. This result is similar to that reported by Dumas et al,¹⁵ who did not observe a correlation between magnetic field correlation values and volume in their comparison of subjects with HD (both premanifest and manifest) and controls from the TRACK-HD study. Further work is necessary, however, to define the degree to which these 2 variables define different and overlapping dimensions of disease burden.

The strength of the correlation between LFS and CAP_s implies that progressively higher phase shifts portend a shorter onset to clinically manifest disease. It is possible that alterations in phase indicate a greater magnitude of iron-dependent oxidative damage and neurotoxicity⁴⁰ and thus provide a more direct predictor of disease onset than volume, which correlates largely to neuronal loss. The small number of subjects in this study precluded analysis of multiple brain regions; because of its known involvement in the earliest stages of HD, we focused on the caudate. The fact that phase differences were detected between groups illustrates the high sensitivity of ultra-high-field MR imaging. In the future, studying phase in other parts of the brain may provide a broader picture of neurodegeneration in these patients.

Our study has several limitations. First, the number of subjects was small, and larger studies are necessary to delineate the strengths and limitations of using phase as a disease marker in HD. Second, because of the radio frequency-related intensity variation in the 7T images, caudate volumes could not be reliably extracted from the 7T T1 data and a second 3T MR imaging was necessary for this purpose. With further technical refinement, we expect that both volumetric and phase measures can be reliably extracted from a single 7T examination. Furthermore, air-tissue interfaces and other sources of macroscopic susceptibility significantly distort 7T gradient-echo images and thereby make accu-

rate phase measurement difficult. Although not prohibitive for studying the striatum, which is situated at some distance from most of these interfaces, the technique would currently be limited in parenchymal regions closer to the skull base or paranasal sinuses. Finally, the present work did not account for phase anisotropy in 7T MR imaging. We anticipate that quantitative susceptibility mapping will mitigate the orientation dependence of phase contrast and further enhance the sensitivity of phase measurements to neurodegenerative pathology in patients with HD.

CONCLUSIONS

Quantitative measurements of 7T phase within the caudate nucleus in patients with pmHD differ from those in matched controls, most likely on the basis of differences in underlying tissue iron concentration. Because phase did not correlate with caudate volume and improved prediction of disease state when used together with caudate volume, we hypothesize that these measurements represent different pathologic endpoints of neurodegeneration in HD.

ACKNOWLEDGMENTS

The authors are grateful to the subjects who volunteered for this study.

Disclosures: Katherine L. Possin—RELATED: Grant: National Institute on Aging.* UNRELATED: Grants/Grants Pending: Michael J. Fox Foundation,* Hellman Family Foundation,* Payment for Lectures (including service on Speakers Bureaus): SAFRA nursing course, Janine M. Lupo—RELATED: Grant: GE Healthcare.* Comments: We received grant support for scan time and the development of the acquisition and postprocessing techniques used in this study. However, this grant support has no impact on the results presented in this study. Angela Jakary—RELATED: Grant: University of California Discovery Grant.* Comments: My staff research associate's salary was paid by Dr Sarah Nelson's University of California Discovery Grant (UCSF RAS System Award Number A115600) during the time that I contributed to the above article. Joel H. Kramer—UNRELATED: Consultancy: AbbVie, Royalties: Pearson Inc. Michael D. Geschwind—RELATED: Grant: BIO University of California Discovery Grant.* Comments: Funds obtained from the Department of Radiology and Biomedical Imaging supported the imaging for this study, UNRELATED: Consultancy: MEDA-Corp, The Council of Advisors, Guidepoint Global, Neurophage, Grants/Grants Pending: National Institutes of Health/High Q A104204 PREDICT-HD Study,* National Institutes of Health/National Institute on Aging (R01 AG-031189, R01 AG-031189-6, K23 AG021989, AG031220),* Michael J Home Family Fund,* Tau Consortium,* National Institutes of Health/NCRN-CTSI (UL1RR024131),* National Institutes of Health/National Institute on Aging (AG021601),* National Institutes of Health/National Institute of Neurological Disorders and Stroke contract (N01-NS-0-2328),* contract number 12621 CHDI Inc,* Travel/Accommodations/Meeting Expenses Unrelated to Activities Listed: HD Action Meeting, Comments: second meeting of Huntington Disease Clinics of California, Utah, and Nevada (HD Action) March 2–3, 2013. Airfare, lodging, meals, and ground transportation were provided by Lundbeck, Inc. Sarah J. Nelson—RELATED: Grant: National Institutes of Health (1S10RR026845-01). This was an academic-industry partnership grant from the University of California, San Francisco.* Christopher P. Hess—RELATED: Grant: GE Healthcare.* Comments: funds for 7T imaging and technical support. *Money paid to the institution.

REFERENCES

- Vonsattel JP, DiFiglia M. Huntington disease. *J Neuropathol Exp Neurol* 1998;57:369–84
- Li SH, Li XJ. Huntingtin and its role in neuronal degeneration. *Neuroscientist* 2004;10:467–75
- Bohanna I, Georgiou-Karistianis N, Hannan AJ, et al. Magnetic resonance imaging as an approach towards identifying neuropathological biomarkers for Huntington's disease. *Brain Res Rev* 2008;58:209–25
- Aylward EH, Codori AM, Rosenblatt A, et al. Rate of caudate atrophy in presymptomatic and symptomatic stages of Huntington's disease. *Mov Disord* 2000;15:552–60
- Rosas HD, Goodman J, Chen YI, et al. Striatal volume loss in HD as measured by MRI and the influence of CAG repeat. *Neurology* 2001;57:1025–28
- Kipps CM, Duggins AJ, Mahant N, et al. Progression of structural neuropathology in preclinical Huntington's disease: a tensor based morphometry study. *J Neurol Neurosurg Psychiatry* 2005;76:650–55
- Tabrizi SJ, Langbehn DR, Leavitt BR, et al. Biological and clinical manifestations of Huntington's disease in the longitudinal TRACK-HD study: cross-sectional analysis of baseline data. *Lancet Neurol* 2009;8:791–801
- Weir DW, Sturrock A, Leavitt BR. Development of biomarkers for Huntington's disease. *Lancet Neurol* 2011;10:573–90
- Rosas HD, Salat DH, Lee SY, et al. Cerebral cortex and the clinical expression of Huntington's disease: complexity and heterogeneity. *Brain* 2008;131:1057–68
- Dexter DT, Carayon A, Javoy-Agid F, et al. Alterations in the levels of iron, ferritin and other trace metals in Parkinson's disease and other neurodegenerative diseases affecting the basal ganglia. *Brain* 1991;114:1953–75
- Bartzokis G, Lu PH, Tishler TA, et al. Myelin breakdown and iron changes in Huntington's disease: pathogenesis and treatment implications. *Neurochem Res* 2007;32:1655–64
- Bartzokis G, Tishler TA. MRI evaluation of basal ganglia ferritin iron and neurotoxicity in Alzheimer's and Huntington's disease. *Cell Mol Biol (Noisy-le-Grand)* 2000;46:821–33
- Bartzokis G, Cummings J, Perlman S, et al. Increased basal ganglia iron levels in Huntington disease. *Arch Neurol* 1999;56:569–74
- Chen JC, Hardy PA, Kucharczyk W, et al. MR of human postmortem brain tissue: correlative study between T2 and assays of iron and ferritin in Parkinson and Huntington disease. *AJNR Am J Neuroradiol* 1993;14:275–81
- Dumas EM, Versluis MJ, van den Bogaard SJ, et al. Elevated brain iron is independent from atrophy in Huntington's disease. *Neuroimage* 2012;61:558–64
- Haacke EM, Mittal S, Wu Z, et al. Susceptibility-weighted imaging: technical aspects and clinical applications, part 1. *AJNR Am J Neuroradiol* 2009;30:19–30
- Haacke EM, Cheng NY, House MJ, et al. Imaging iron stores in the brain using magnetic resonance imaging. *Magn Reson Imaging* 2005;23:1–25
- Haacke EM, Gollapalli L, Rosas DH, et al. Using SWI as a means to better visualize the caudate nucleus in Huntington's disease. In: *Proceedings of 14th Annual Meeting of the International Society for Magnetic Resonance in Medicine*; Seattle, Washington. May 6–12, 2006:2657
- Haacke EM, Ayaz M, Khan A, et al. Establishing a baseline phase behavior in magnetic resonance imaging to determine normal vs. abnormal iron content in the brain. *J Magn Reson Imaging* 2007;26:256–64
- Hammond KE, Metcalf M, Carvajal L, et al. Quantitative in vivo magnetic resonance imaging of multiple sclerosis at 7 Tesla with sensitivity to iron. *Ann Neurol* 2008;64:707–13
- Abduljalil AM, Schmalbrock P, Novak V, et al. Enhanced gray and white matter contrast of phase susceptibility-weighted images in ultra-high-field magnetic resonance imaging. *J Magn Reson Imaging* 2003;18:284–90
- Doan NT, van den Bogaard SJA, Dumas EM, et al. Texture analysis of ultrahigh field T₂*-weighted MR images of the brain: application to Huntington's disease. *J Magn Reson Imaging* 2014;39:633–40
- Paulsen JS, Hayden M, Stout JC, et al. Preparing for preventive clinical trials: the Predict-HD study. *Arch Neurol* 2006;63:883–90
- Harrington DL, Smith MM, Zhang Y, et al. Cognitive domains that predict time to diagnosis in prodromal Huntington disease. *J Neurol Neurosurg Psychiatry* 2012;83:612–19
- Zhang Y, Long JD, Mills JA, et al. Indexing disease progression at study entry with individuals at-risk for Huntington disease. *Am J Med Genet B Neuropsychiatr Genet* 2011;156B:751–63
- Paulsen JS, Langbehn DR, Stout JC, et al. Detection of Huntington's

- disease decades before diagnosis: the PREDICT-HD study. *J Neurol Neurosurg Psychiatry* 2008;79:874–80
27. Duff K, Paulsen JS, Beglinger LJ, et al. “Frontal” behaviors before the diagnosis of Huntington’s disease and their relationship to markers of disease progression: evidence of early lack of awareness. *J Neuropsychiatry Clin Neurosci* 2010;22:196–207
 28. Hart E, Middelkoop H, Jurgens CK, et al. Seven-year clinical follow-up of premanifest carriers of Huntington’s disease. *PLoS Curr* 2011;3:RRN1288
 29. Stout JC, Paulsen JS, Queller S, et al. Neurocognitive signs in prodromal Huntington disease. *Neuropsychology* 2011;25:1–14
 30. You SC, Geschwind MD, Sha SJ, et al. Executive functions in premanifest Huntington’s disease. *Mov Disord* 2014;29(suppl 3):405–09
 31. Hammond KE, Lupo JM, Xu D, et al. Development of a robust method for generating 7.0 T multichannel phase images of the brain with application to normal volunteers and patients with neurological diseases. *Neuroimage* 2008;39:1682–92
 32. Patenaude B, Smith SM, Kennedy DN, et al. A Bayesian model of shape and appearance for subcortical brain segmentation. *Neuroimage* 2011;56:907–22
 33. Jenkinson M, Bannister P, Brady M, et al. Improved optimization for the robust and accurate linear registration and motion correction of brain images. *Neuroimage* 2002;17:825–41
 34. Buckner RL, Head D, Parker J, et al. A unified approach for morphometric and functional data analysis in young, old, and demented adults using automated atlas-based head size normalization: reliability and validation against manual measurement of total intracranial volume. *Neuroimage* 2004;23:724–38
 35. You C, Satris G, Apple A, et al. New sensitive measures of executive functioning in premotor Huntington’s disease. *Neurology* 2013;80:S20.002
 36. He X, Yablonskiy DA. Biophysical mechanisms of phase contrast in gradient echo MRI. *Proc Natl Acad Sci U S A* 2009;106:13558–63
 37. Bilgic B, Pfefferbaum A, Rohlfing T, et al. MRI estimates of brain iron concentration in normal aging using quantitative susceptibility mapping. *Neuroimage* 2012;59:2625–35
 38. Hagemeyer J, Dwyer MG, Bergsland N, et al. Effect of age on MRI phase behavior in the subcortical deep gray matter of healthy individuals. *AJNR Am J Neuroradiol* 2013;34:2144–51
 39. Murphy DG, DeCarli C, Schapiro MB, et al. Age-related differences in volumes of subcortical nuclei, brain matter and cerebrospinal fluid in healthy men as measured with magnetic resonance imaging. *Arch Neurol* 1992;49:839–45
 40. Berg D, Youdim MB. Role of iron in neurodegenerative disorders. *Top Magn Reson Imaging* 2006;17:5–17

Cost-Effectiveness of CT Angiography and Perfusion Imaging for Delayed Cerebral Ischemia and Vasospasm in Aneurysmal Subarachnoid Hemorrhage

P.C. Sanelli, A. Pandya, A.Z. Segal, A. Gupta, S. Hurtado-Rua, J. Ivanidze, K. Kesavabhotla, D. Mir, A.I. Mushlin, and M.G.M. Hunink



ABSTRACT

BACKGROUND AND PURPOSE: Delayed cerebral ischemia and vasospasm are significant complications following SAH leading to cerebral infarction, functional disability, and death. In recent years, CTA and CTP have been used to increase the detection of delayed cerebral ischemia and vasospasm. Our aim was to perform comparative-effectiveness and cost-effectiveness analyses evaluating CTA and CTP for delayed cerebral ischemia and vasospasm in aneurysmal SAH from a health care payer perspective.

MATERIALS AND METHODS: We developed a decision model comparing CTA and CTP with transcranial Doppler sonography for detection of vasospasm and delayed cerebral ischemia in SAH. The clinical pathways were based on the "Guidelines for the Management of Aneurysmal Subarachnoid Hemorrhage: A Guideline for Healthcare Professionals from the American Heart Association/American Stroke Association" (2012). Outcome health states represented mortality and morbidity according to functional outcomes. Input probabilities of symptoms and serial test results from CTA and CTP, transcranial Doppler ultrasound, and digital subtraction angiography were directly derived from an SAH cohort by using a multinomial logistic regression model. Expected benefits, measured as quality-adjusted life years, and costs, measured in 2012 US dollars, were calculated for each imaging strategy. Univariable, multivariable, and probabilistic sensitivity analyses were performed to determine the independent and combined effect of input parameter uncertainty.

RESULTS: The transcranial Doppler ultrasound strategy yielded 13.62 quality-adjusted life years at a cost of \$154,719. The CTA and CTP strategy generated 13.89 quality-adjusted life years at a cost of \$147,097, resulting in a gain of 0.27 quality-adjusted life years and cost savings of \$7622 over the transcranial Doppler ultrasound strategy. Univariable and multivariable sensitivity analyses indicated that results were robust to plausible input parameter uncertainty. Probabilistic sensitivity analysis results yielded 96.8% of iterations in the right lower quadrant, representing higher benefits and lower costs.

CONCLUSIONS: Our model results suggest that CTA and CTP are the preferred imaging strategy in SAH, compared with transcranial Doppler ultrasound, leading to improved clinical outcomes and lower health care costs.

ABBREVIATIONS: CTAP = CTA and CTP; DCI = delayed cerebral ischemia; ISAT = International Subarachnoid Aneurysm Trial; QALY = quality-adjusted life year; TCD = transcranial Doppler ultrasound; WTP = willingness to pay

Aneurysmal SAH is a devastating condition resulting in poor clinical outcomes of patients who survive long enough to be admitted, with approximately 15% mortality and 58% functional

disability.¹ Additionally, as many as 20% of survivors have global cognitive impairment, also contributing to poor functional status.² Thus, SAH is associated with a substantial burden on health care resources, most of which are related to long-term care.³ Despite advances in techniques for aneurysm repair, poor outcomes remain in SAH partly due to delayed diagnosis and treatment of its secondary complications, mainly vasospasm and delayed cerebral ischemia (DCI).

Currently, there are several methods available to assist with the diagnosis of vasospasm and DCI, including clinical examination,

Received November 7, 2013; accepted after revision January 25, 2014.

From the Departments of Radiology (P.C.S., A.G., J.I., K.K., D.M.), Public Health (P.C.S., A.P., S.H.-R., A.I.M.), and Neurology (A.Z.S.), Weill Cornell Medical College, New York-Presbyterian Hospital, New York, New York; and Departments of Radiology and Epidemiology (M.G.M.H.), Erasmus University Medical Center, Rotterdam, the Netherlands.

This work was funded by grant 5K23NS058387 from the National Institute of Neurological Disorders and Stroke, a component of the National Institutes of Health.

The content of this work is solely the responsibility of the authors and does not necessarily represent the official view of National Institute of Neurological Disorders and Stroke or the National Institutes of Health.

Please address correspondence to Pina C. Sanelli, MD, MPH, FACR, Department of Radiology, Weill Cornell Medical College, New York-Presbyterian Hospital, 525 East 68th St, Starr Pavilion, New York, NY 10065; e-mail: pcs9001@med.cornell.edu

Indicates open access to non-subscribers at www.ajnr.org

Indicates article with supplemental on-line appendix and table.

Indicates article with supplemental on-line figures.

<http://dx.doi.org/10.3174/ajnr.A3947>

neurologic monitoring devices, transcranial Doppler sonography (TCD), CTA and CTP (CTAP), MR diffusion and perfusion imaging, and digital subtraction angiography. In clinical practice, patients with SAH are primarily assessed by clinical examination and TCD, with clinical examination limited because symptoms are variable and difficult to detect⁴ and TCD limited by poor sensitivity and specificity.⁵⁻⁷ At the same time, there are studies reported in the literature that support the use of CTAP for detection of both vasospasm and perfusion deficits thought to occur in DCI because of the high sensitivity and specificity of CTAP.⁸⁻¹¹ Additionally, emerging data indicate that perfusion imaging may be more accurate for identification of DCI than anatomic imaging of arterial narrowing or changes in blood flow velocity by TCD.^{8,12} Yet, according to the most recent “Guidelines for the Management of Aneurysmal Subarachnoid Hemorrhage: A Guideline for Healthcare Professionals from the American Heart Association/American Stroke Association” (2012),¹³ both TCD and perfusion imaging with CT or MR imaging have been assigned the same class IIa recommendation and level B evidence for detection of vasospasm and DCI. Although CTAP has potential to add important diagnostic information for guiding management and treatment decisions, there are no studies to date, to our knowledge, that have assessed the added value of CTAP on clinical outcomes to fully understand its impact in this patient population. Furthermore, there have been no randomized trials comparing the impact of different diagnostic methods on patient outcomes in SAH.

In the past several years, demonstrating the value of imaging has become a major focus in our changing health care environment. Both quality and safety advocates and third-party payers have raised concerns regarding medical practice patterns with inappropriate use of CT, particularly as it relates to radiation exposure. It has become particularly important to substantiate imaging for specific clinical conditions with scientific evidence to guide management and treatment decisions. The purpose of this study was to perform comparative effectiveness and cost-effectiveness analyses evaluating imaging strategies in SAH for detection of vasospasm and DCI by using evidence-based guidelines from a health care payer perspective. Our hypothesis was that CTAP is a cost-effective approach, despite higher imaging costs, compared with the standard imaging strategy using TCD, resulting in improved patient outcomes and averted downstream health care costs.

MATERIALS AND METHODS

Model Design

We developed a decision model to perform comparative effectiveness and cost-effectiveness analyses by using a decision analytic framework in the TreeAge software program (TreeAge Pro Software, Williamstown, Massachusetts) to compare imaging strategies in SAH from a health care payer perspective. The detailed model structure is provided in On-line Fig 1. CTAP was considered the “new imaging strategy” and was compared with TCD as the “standard imaging strategy.” Clinical examination was included in the model before CTAP or TCD imaging to assess symptoms of vasospasm and/or DCI, as would typically occur in the clinical setting. The model was designed to assess patients during

the typical time point at which vasospasm and DCI occur, between 4 and 14 days after SAH.

In the standard strategy, positive concordance between the clinical examination and TCD results led to induced hypertensive therapy, and negative concordance of the clinical examination and TCD led to observation, whereas discordance between the clinical examination and TCD results (such as symptoms but negative TCD findings or no symptoms but positive TCD findings) led to further testing with DSA. In the new strategy, CTA and CTP were evaluated as a single examination termed CTAP because these examinations are typically performed concurrently in clinical practice. If a patient was symptomatic, a positive CTAP finding was defined as a positive result on either CTA or CTP, whereas a negative CTAP finding was defined as a negative result on both CTA and CTP. The rationale is that given the presence of symptoms, a positive result on either examination provides sufficient supportive evidence to prompt treatment decisions. If a patient was asymptomatic, a positive CTAP finding was defined as a positive result on both CTA and CTP, whereas a negative CTAP finding was defined as a negative result on either CTA or CTP. The rationale is that in the absence of symptoms, a single positive result on either examination does not provide sufficient evidence to prompt treatment decisions. All management and treatment decisions are based on the clinical examination and TCD or CTAP combination tests.

The subsequent management and treatment decisions in the clinical pathway incorporated in the model were based on the most recent recommendations in the “Guidelines for the Management of Aneurysmal Subarachnoid Hemorrhage: A Guideline for Healthcare Professionals from the American Heart Association/American Stroke Association” (2012).¹³ Oral nimodipine was administered to all patients with aneurysmal subarachnoid hemorrhage (class I recommendation, level A evidence) because it has been shown to improve neurologic outcomes after SAH. Treatment of DCI is recommended with induction of hypertension (class I recommendation, level B evidence) and cerebral angioplasty and/or selective intra-arterial vasodilator therapy in symptomatic patients, particularly those who are not rapidly responding to hypertensive therapy (class IIa recommendation, level B evidence).

Each clinical pathway terminated in an outcome health state reflecting the downstream morbidity and mortality. A patient was assigned to only 1 of the 3 following health states: recovered, disability with dependence, or death. The long-term complications of testing or treatment affecting mortality and morbidity (as defined by the health states) were included in the model. Short-term complications such as mild allergic reactions were not included because patients recovered from these temporary ailments; this outcome would not imply significant reductions in quality of life contributing to these health states.

Input Parameter Probabilities

An outcomes-based approach was used in developing the decision model to directly assess the effectiveness of CTAP compared with TCD on clinical outcomes instead of primarily modeling the operating characteristics of these imaging examinations. We modeled probabilities of test results combined with distributions

across clinical outcomes, both determined conditional on the clinical examination and imaging results. The probabilities assigned for the occurrence of symptoms and test results of CTAP, TCD, and DSA were directly derived from an SAH cohort enrolled in a diagnostic accuracy study.¹⁰ In this cohort, patients had both CTAP and TCD performed, which allowed direct comparison of these imaging strategies in the same patients. According to the study protocol, CTAP was performed at days 6–8 in asymptomatic patients and the same day that symptoms occurred in symptomatic patients with clinical deterioration. Day 7 was the median day CTAP was performed, at which time 45% (44/97) of patients had developed evidence of clinical deterioration.¹⁰ Clinical deterioration may manifest by alterations in consciousness, worsening on the Glasgow Coma Scale, or new neurologic deficits. For patients with limited clinical examinations, particularly patients who are comatose or mechanically ventilated, continuous monitoring of laboratory data and neurologic and systemic parameters was used. The details of the CTP scanning protocol and postprocessing methods are provided in the On-line Appendix. TCD was performed daily at the patient's bedside with comparisons between TCD examinations to evaluate changes in blood flow velocity measurements.

Clinical outcomes of functional disability were also assessed in the same SAH cohort¹⁰ and obtained from medical record review by a neurologist blinded to the hospitalization course and imaging data. Outcomes were based on the modified Rankin Scale and were categorized into 3 main health states as recovered (mRS 0–2), disability with dependence (mRS 3–5), and death (mRS 6). A multinomial prediction model, incorporating conditional dependence of serial imaging with CTAP and DSA or TCD and DSA, was developed and fitted to determine the predictive probabilities for each outcome based on the test results and on being symptomatic or asymptomatic. The 95% simultaneous confidence intervals for predictive probabilities were computed by using an asymptotic multivariate normal theory and were based on χ^2 tests.¹⁴ Statistical analysis was performed with “R: A Language and Environment for Statistical Computing” (Version 2.13.0; <http://www.r-project.org/>).¹⁵

Literature sources were used to determine the probabilities of long-term complications from testing (CTAP and DSA) and/or treatment with induced hypertension and intra-arterial (IA) therapy. On-line Table 1 demonstrates these input probabilities and their literature sources.

Assessment of Health Benefits and Costs

Health benefits were measured in quality-adjusted life years (QALYs). For each health state, we assigned a QALY score ranging between 0 and 1.0. Lifetime QALYs were calculated by multiplying the sum of the number of years spent in each health state by the utility associated with that state. The life expectancies were estimated from the literature as 28 years for “recovered”^{16,17} and 10.8 years for “disability.”^{18,19} The utilities were calculated as a weighted average from a systematic review of utilities assigned according to mRS scores.²⁰ The utility of “recovered” (mRS 0–2) was 0.80, and it was 0.22 for “disability” (mRS 3–5). By convention, “death” (mRS 6) was assigned a value of zero for both life years and utility.

The economic costs included in the model were those associated with imaging from CTAP, TCD, and DSA; treatment with induced hypertension and IA-therapy; complications from imaging and treatment; and disability after SAH, including both short- and long-term care. The costs for the imaging and treatment were based on the 2012 Medicare reimbursement rates, including both technical and professional fees. The costs for long-term care for patients with stroke have been reported in the literature.²¹ The estimated cost for recovered patients was calculated as the cumulative annual cost for the expected life years in this health state. The estimated cost for the disability patients was calculated as the first-year rehabilitation costs added to the cumulative annual cost for the remaining expected life years in this health state. By convention, death was assigned no additional cost.

Benefits and costs were discounted at a rate of 3% per year as recommended for cost-effectiveness analyses in the United States.^{22,23}

Model Validation

Internal validity (sometimes referred to as model verification) examines the extent to which the model calculations produced expected outcomes based on the data that were used to derive the model inputs.²⁴ We assessed the internal validity of the model by comparing the predicted probabilities of the health states (recovered, disability, and death) for each imaging strategy in the decision model with the observed outcome data from the SAH cohort. The percentage difference for the model results compared with the observed outcomes was calculated as a measure of deviation for the probabilities of each health state for the standard and new imaging strategies separately.

External validity is performed in a similar fashion but uses outcome data that were not used to develop the model as benchmarks for the predictive performance of the model.²⁴ To evaluate external validity of the decision model, we compared the overall predicted probabilities of the health states for both imaging strategies from the decision model with the published outcome probabilities from the International Subarachnoid Aneurysm Trial (ISAT).¹ The percentage difference was also calculated as a measure of deviation for model results relative to published outcomes.

Cost-Effectiveness and Sensitivity Analyses

We calculated the expected benefits and costs associated with each imaging strategy from the perspective of the health care payer. In the primary analysis for policy decision-making, the symptomatic and asymptomatic subgroups were combined in each imaging strategy, weighted by the frequency of symptoms. Additional subgroup analyses were performed to compare the symptomatic and asymptomatic groups separately. An imaging strategy that yielded the greatest quality-adjusted life years and lowest costs would be considered the imaging strategy of choice (dominant strategy).

Sensitivity analyses were performed to test the robustness of the results of the model, given the uncertainty in the input values for the parameters. One-way sensitivity analyses were performed for each parameter by altering the input values across the entire range of possible values (0–1) to identify the key drivers of the model results. In addition, 2-way sensitivity analyses were performed by simultaneously altering the input values for 2 param-

eters together to assess their combined effects on the results of the model. A willingness-to-pay (WTP) threshold of \$100,000 per QALY was used in the 1-way and 2-way sensitivity analyses.

Probabilistic sensitivity analysis was performed to assess the uncertainty in the model results, incorporating the uncertainty of all parameter values together. Distributions for the key model parameters were derived by nonparametric bootstrapping of the SAH cohort,²⁵ focusing attention on the probability of symptoms and the probabilities of imaging (CTAP, TCD, and DSA) conditional on symptoms. Nonparametric bootstrapping was performed by resampling analytic datasets with replacement to evaluate the precision around point estimates without making assumptions regarding the distribution of these variables.²⁶ Parameters that were not directly derived from the cohort ($n = 97$), such as all other probability inputs, costs, and utilities, were assigned distributions (such as β , uniform, and γ) and varied on the basis of the SD estimates around the mean values. β distribution is a flexible one, which is bounded by 0 and 1, which makes it useful

Health benefits (QALYs) and costs for the base case scenario and subgroup analyses in symptomatic and asymptomatic patients

Imaging Strategy	QALYs	Cost
Base case scenario:		
CTAP	13.89	\$147,097
TCD	13.62	\$154,719
Difference (CTAP-TCD)	+0.27	-\$7,622
Symptomatic subgroup:		
CTAP	13.75	\$149,382
TCD	13.74	\$152,820
Difference (CTAP-TCD)	+0.01	-\$3,438
Asymptomatic subgroup:		
CTAP	13.99	\$145,228
TCD	13.51	\$156,272
Difference (CTAP-TCD)	+0.48	-\$11,044

for varying probability inputs in probabilistic sensitivity analysis.²⁶ Uniform distributions assume equal probability of possible random values between 0 and 1.²⁶ γ distributions are rightward skewed with a lower bound at zero, which makes them useful for varying cost inputs in probabilistic sensitivity analysis.²⁶ On-line Table 1 demonstrates the input values and distributions used for all parameters in the model. Results of the probabilistic analysis (10,000 iterations) were used to generate a cost-effective scatterplot and cost-effectiveness acceptability curves to demonstrate the probability that the new strategy is cost-effective for varying cost per QALY thresholds.

RESULTS

Input Parameter Probabilities

On-line Table 1 demonstrates the probabilities of positive and negative test results for CTAP, TCD, and DSA in symptomatic and asymptomatic patients calculated directly from the SAH cohort¹⁰ and the predictive probabilities of the outcome health states derived from the multinomial prediction model, incorporating serial imaging and clinical data with conditional dependence.

Model Validation Results

The internal validation revealed that the deviations in the overall probabilities of patients with good (recovered) and poor (disability and death) outcomes estimated from the decision model for the new strategy were 1.2% and 3.4%, respectively, relative to the observed data from the SAH cohort. Within the poor-outcomes group, deviations in the probabilities for disability and death were 0.9% and 13.7%, respectively. For the standard strategy, the deviations in the overall probabilities of patients with good and poor outcomes estimated from the decision model were 5.4% and 16.7%, respectively. Within the poor-outcomes group, deviations in the probabilities for disability and death were 20% and 3.8%, respectively.

The external validation revealed that the deviations in the overall probabilities of patients with good and poor outcomes derived from the decision model were 1.4% and 3.0%, respectively, compared with the published outcomes data from the ISAT.¹ Within the poor-outcomes group, deviations in the probabilities for disability and death were 55.3% and 62.2%, respectively.

Base Case Analysis

The Table demonstrates the health benefits (QALYs) and costs for the base case scenario and the subgroup analyses in the symptomatic and asymptomatic patients separately. CTAP resulted in a gain of health benefits with a cost savings in all analyses, thereby dominating the standard imaging strategy.

Sensitivity Analysis

Univariable (1-way) sensitivity analyses indicated that the study results were ro-

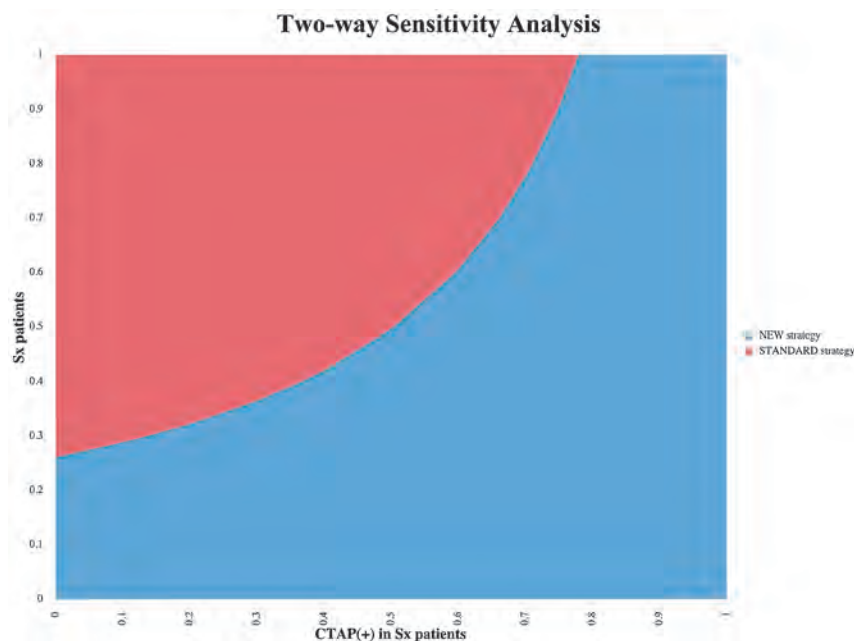


FIG 1. Multivariable (2-way) sensitivity analysis graph demonstrating how the decision depends on the values of the probability of positive findings on a CTA and CTP examination in symptomatic patients (Sx) and the probability of symptoms in the SAH population across all ranges. The new strategy represents CTAP imaging, and the standard strategy represents TCD imaging.

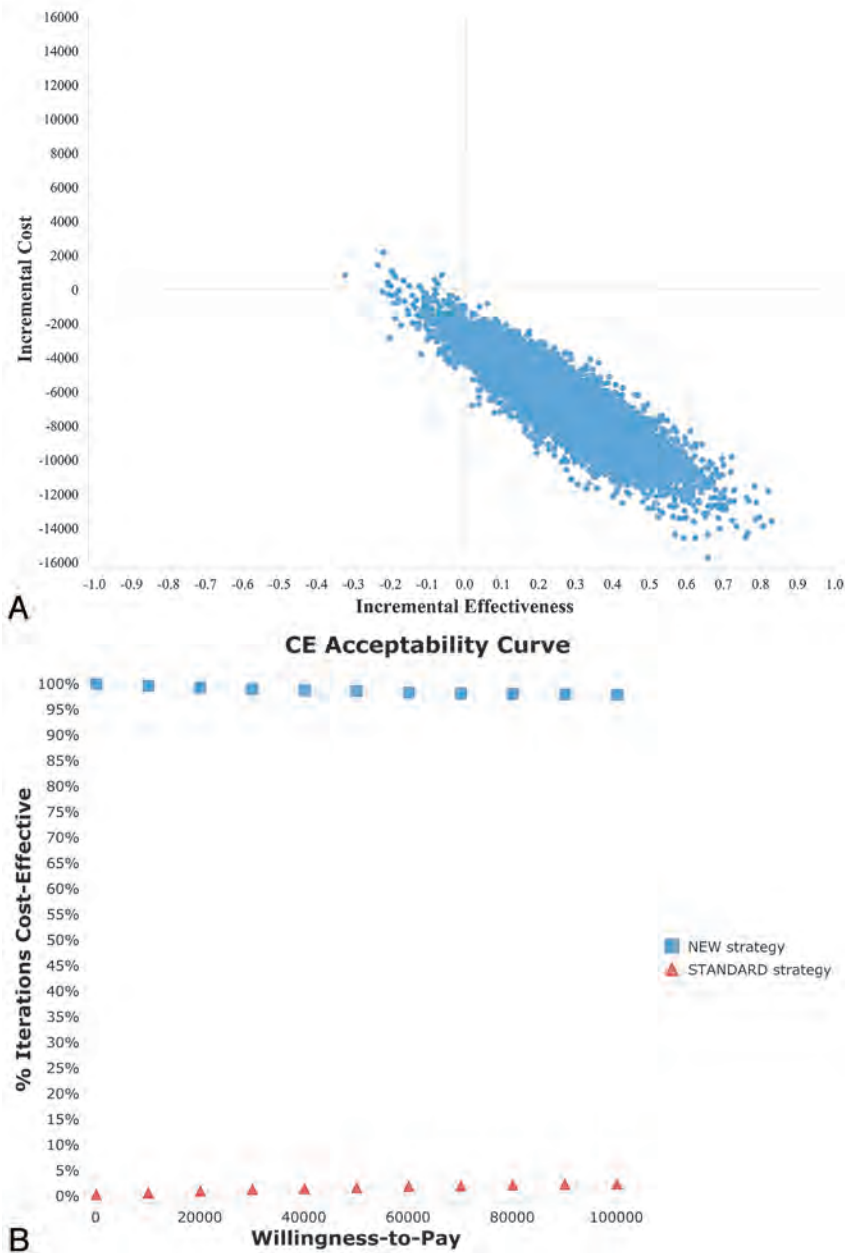


FIG 2. Probabilistic sensitivity analysis scatterplot (A) and cost-effectiveness acceptability curves (B) comparing the new strategy versus the standard strategy. The new strategy represents CTAP imaging and the standard strategy represents TCD imaging.

bust to plausible uncertainty in the parameter values. The CTAP strategy remained preferred (assuming a WTP of \$100,000 per QALY) for all parameters varied over the full range of possible input values, except for the following: 1) the probability of positive CTAP fell below 44.2% in symptomatic patients; 2) the probability of complications from induced hypertension rose above 20.5%; and 3) the probability of recovery with negative CTAP findings fell below 51.1% in symptomatic and 85.9% in asymptomatic patients. Multivariable (2-way) sensitivity analyses using the probability of positive CTAP findings in symptomatic patients and the probability of symptoms revealed that the CTAP strategy is dominant when the probability of positive CTAP findings in symptomatic patients is >75% (Fig 1).

The results of the probabilistic sensitivity analysis (10,000 iterations) were used to generate a cost-effectiveness scatterplot (Fig 2A) and cost-effectiveness acceptability curves (Fig 2B). The cost-effectiveness scatterplot shows that 96.8% of the iterations in the probabilistic sensitivity analysis lie in the right lower quadrant, representing higher effectiveness and lower costs. The cost-effectiveness acceptability curves show that the probability that the new strategy is cost-effective is consistently high for varying cost per QALY thresholds. At the WTP of \$50,000 and \$100,000 per QALY, the probabilities that the CTAP strategy is preferred are 98.5% and 98.0%, respectively.

DISCUSSION

Our study reveals that performing CTAP in patients with SAH improves clinical outcomes compared with TCD, with increased quality of life from less functional disability. Although CTAP is associated with higher upfront imaging and treatment costs, there are substantial cost savings associated with this imaging strategy due to overall decreased costs spent on long-term care for patients with functional disability. Our 1-way and probabilistic sensitivity analyses assessed a range of costs for CTAP, from \$0 to \$2000, and revealed that across these different thresholds, CTAP is still the preferred strategy compared with TCD. CTAP represents a dominant strategy because it provides both better health outcomes and lower costs in the overall patient population and in the symptomatic and asymptomatic subgroups separately. These results support the implementation of CTAP in all SAH, including both symptomatic and asymptomatic patients. Furthermore, our study demonstrates that changing the WTP threshold from

\$50,000 to \$100,000 does not significantly change the model results. The cost-effective acceptability curves generated from the probabilistic sensitivity analysis are helpful in visualizing the effect that a change in WTP can have on these results (Fig 2). CTAP remains the preferred imaging strategy across the entire range of commonly used WTP thresholds in the United States.²⁷

In this cost-effectiveness analysis, an outcomes-based approach was used to directly assess the effectiveness of CTAP compared with TCD on clinical outcomes. Most decision analyses for diagnostic tests model the underlying diagnostic truth in combination with the sensitivity and specificity of the test.²⁷ Here we modeled probabilities of test results combined with distributions across clinical outcomes, both determined conditional on the

clinical examination and previous test results. We chose this alternative approach because of controversy about the appropriate reference standard test for DCI and lack of diagnostic performance data of these tests. Because all conditional probabilities of test results and distributions across clinical outcomes were derived from one and the same well-documented cohort of patients with SAH,¹⁰ this alternative modeling approach ensures internal consistency of the model. We are confident that the model structure accurately reflects SAH disease pathways because the model results matched the health states (good and poor outcomes) compared with the SAH cohort and ISAT populations in our internal and external model validation analyses. Additionally, the sensitivity analyses demonstrated that the model results were robust to variations in the input values for all parameters.

There are several limitations of our study. First, we modeled health outcomes conditional on diagnostic tests performed in a single cohort, calling into question the generalizability of the model. This approach had the advantage of direct comparison of CTAP and TCD in the same patients, and ensured internal consistency of the data. Even though the external validation of the model revealed that the proportion of patients with good (recovered) and poor (disability and death) outcomes were similar to those in the ISAT,¹ greater variation was seen within the poor-outcomes group. The ISAT reported higher mortality compared with the decision model; this would be expected because the older data presented in the ISAT (1994–2002) do not adequately reflect the currently improved mortality rates due to more aggressive management of complications related to SAH such as hydrocephalus, vasospasm, and DCI.¹³ Additionally, the ISAT reported a 5-year mortality rate rather than the mortality rate within the hospitalization period that we report, which likely also contributed to its higher mortality compared with the decision model because some of our patients may experience delayed mortality due to stroke complications. Furthermore, deviation in the internal validation results was also seen in the poor-outcomes group with the model predicting higher disability and death compared with the SAH cohort. This deviation in the results may be partly attributed to the real-world variation in clinical decision making observed in the SAH cohort compared with the decision model, in which standardized management and treatment decisions were based strictly on the clinical examination and imaging results. Second, the potential long-term effects from low-level radiation exposure used in medical imaging, such as cancer induction, were not included in the model because cancer risks at low doses are very uncertain in the adult population and depend on limited data extrapolating risks from atomic bomb survivors who were exposed to high doses.²⁸ Currently, there are no data available on the lifetime cancer risk from CTAP imaging according to patient age at exposure, sex, and reduced life expectancy from underlying disease, particularly aneurysmal subarachnoid hemorrhage, delayed cerebral ischemia, and/or vasospasm. Because our model was designed to specifically assess patients during the typical time point of DCI and vasospasm between days 4 and 14 after SAH, we only included the morbidity and mortality during the hospitalization period and at discharge. Last, the possible added benefits of performing serial TCD examinations at the bedside to improve detection of vasospasm by monitoring temporal changes in

blood-velocity measurements and avoiding intrahospital transportation were not included in the decision analysis because of the lack of estimates in the literature to accurately incorporate them in the model.

CONCLUSIONS

In summary, our results have important implications in clinical practice in managing patients with SAH. Our model suggests that CTAP is the preferred initial imaging strategy compared with TCD because it results in both improved clinical outcomes and lower health care costs. Furthermore, the results of this study provide supportive evidence for the widespread implementation of CTAP in both symptomatic and asymptomatic patients. In the current economic environment aimed at improving health care quality and reducing costs, imaging patients with SAH with CTAP should achieve both aims.

Disclosures: Pina C. Sanelli—RELATED: Grant: National Institute of Neurological Disorders and Stroke.* Ajay Gupta—UNRELATED: Grants/Grants Pending: Association of University Radiologists/General Electric Radiology Research Academic Fellowship Award.* Alvin I. Mushlin—UNRELATED: Travel/Accommodations/Meeting Expenses Unrelated to Activities Listed: Association of University Radiologists/General Electric Radiology Research Academic Fellowship board meeting. *Money paid to the institution.

REFERENCES

1. Molyneux AJ, Kerr RS, Birks J, et al. Risk of recurrent subarachnoid haemorrhage, death, or dependence and standardised mortality ratios after clipping or coiling of an intracranial aneurysm in the International Subarachnoid Aneurysm Trial (ISAT): long-term follow-up. *Lancet Neurol* 2009;8:427–33
2. Springer MV, Schmidt JM, Wartenberg KE, et al. Predictors of global cognitive impairment 1 year after subarachnoid hemorrhage. *Neurosurgery* 2009;65:1043–50
3. Roos YB, Dijkgraaf MG, Albrecht KW, et al. Direct costs of modern treatment of aneurysmal subarachnoid hemorrhage in the first year after diagnosis. *Stroke* 2002;33:1595–99
4. Schmidt JM, Wartenberg KE, Fernandez A, et al. Frequency and clinical impact of asymptomatic cerebral infarction due to vasospasm after subarachnoid hemorrhage. *J Neurosurg* 2008;109:1052–59
5. Carrera E, Schmidt JM, Oddo M, et al. Transcranial Doppler for predicting delayed cerebral ischemia after subarachnoid hemorrhage. *Neurosurgery* 2009;65:316–23
6. Lysakowski C, Walder B, Costanza MC, et al. Transcranial Doppler versus angiography in patients with vasospasm due to a ruptured cerebral aneurysm: a systematic review. *Stroke* 2001;32:2292–98
7. Naval NS, Thomas CE, Urrutia VC. Relative changes in flow velocities in vasospasm after subarachnoid hemorrhage: a transcranial Doppler study. *Neurocrit Care* 2005;2:133–40
8. Dankbaar JW, de Rooij NK, Velthuis BK, et al. Diagnosing delayed cerebral ischemia with different CT modalities in patients with subarachnoid hemorrhage with clinical deterioration. *Stroke* 2009;40:3493–98
9. Aralasmak A, Akyuz M, Ozkaynak C, et al. CT angiography and perfusion imaging in patients with subarachnoid hemorrhage: correlation of vasospasm to perfusion abnormality. *Neuroradiology* 2009;51:85–93
10. Sanelli PC, Ugorec I, Johnson CE, et al. Using quantitative CT perfusion for evaluation of delayed cerebral ischemia following aneurysmal subarachnoid hemorrhage. *AJNR Am J Neuroradiol* 2011;32:2047–53
11. Wintermark M, Ko NU, Smith WS, et al. Vasospasm after subarachnoid hemorrhage: utility of perfusion CT and CT angiography on diagnosis and management. *AJNR Am J Neuroradiol* 2006;27:26–34
12. van der Schaaf I, Wermer MJ, van der Graaf Y, et al. CT after sub-

- arachnoid hemorrhage: relation of cerebral perfusion to delayed cerebral ischemia.** *Neurology* 2006;66:1533–38
13. Connolly ES, Rabinstein AA, Carhuapoma JR, et al. **Guidelines for the management of aneurysmal subarachnoid hemorrhage: a guideline for healthcare professionals from the American Heart Association/American Stroke Association.** *Stroke* 2012;43:1711–37
 14. Gold RZ. **Tests auxiliary to chi-square tests in a Markov chain.** *The Annals of Mathematical Statistics* 1963;34:56–74
 15. R Development Core Team (2011). R: A language and environment for statistical computing. R Foundation for Statistical Computing, Vienna, Austria. <http://www.R-project.org>. Accessed August 1, 2012
 16. de Rooij NK, Linn FH, van der Plas JA, et al. **Incidence of subarachnoid haemorrhage: a systematic review with emphasis on region, age, gender and time trends.** *J Neurol Neurosurg Psychiatry* 2007; 78:1365–72
 17. Eden SV, Meurer WJ, Sanchez BN, et al. **Gender and ethnic differences in subarachnoid hemorrhage.** *Neurology* 2008;71:731–35
 18. Yoshimoto Y, Wakai S. **Cost-effectiveness analysis of screening for asymptomatic, unruptured intracranial aneurysms: a mathematical model.** *Stroke* 1999;30:1621–27
 19. Kallmes DF, Kallmes MH. **Cost-effectiveness of angiography performed during surgery for ruptured intracranial aneurysms.** *AJNR Am J Neuroradiol* 1997;18:1453–62
 20. Post PN, Stiggelbout AM, Wakker PP. **The utility of health states after stroke: a systematic review of the literature.** *Stroke* 2001;32: 1425–29
 21. Young KC, Benesch CG, Jahromi BS. **Cost-effectiveness of multimodal CT for evaluating acute stroke.** *Neurology* 2010;75:1678–85
 22. Hunink MGM, Glasziou PP, Siegel JE, et al. **Constrained resources.** In: Hunink GM, Glasziou PP, Siegel JE. *Decision Making in Health and Medicine: Integrating Evidence and Values.* Cambridge, UK; Cambridge University Press; 2001:245–304
 23. Weinstein MC, Siegel JE, Gold MR, et al. **Recommendations of the Panel on Cost-Effectiveness in Health and Medicine.** *JAMA* 1996;276:1253–58
 24. Eddy DM, Hollingworth W, Caro JJ, et al, for the Modeling Good Research Practices Task Force. **Model transparency and validation: a report of the ISPOR-SMDM Modeling Good Research Practices Task Force-7.** *Med Decis Making* 2012;32:733–43
 25. Efron B, Tibshirani RJ. *An Introduction to the Bootstrap.* New York: Chapman & Hall; 1994
 26. Briggs AH, Weinstein MC, Fenwick EAL, et al, for the ISPOR-SMDM Good Research Practices Task Force. **Model parameter estimation and uncertainty analysis: a report of the ISPOR-SMDM Modeling Good Research Practices Task Force Working Group-6.** *Med Decis Making* 2012;32:722–32
 27. Genders TS, Meijboom WB, Meijjs MF, et al. **CT coronary angiography in patients suspected of having coronary artery disease: decision making from various perspectives in the face of uncertainty.** *Radiology* 2009;253:734–44
 28. Brenner DJ, Hall EJ. **Computed tomography—an increasing source of radiation exposure.** *N Engl J Med* 357:2277–84
 29. Wintermark M, Maeder P, Thiran JP, et al. **Quantitative assessment of regional blood flows by perfusion CT studies at low injection rates: a critical review of the underlying theoretical models.** *Eur Radiol* 2001;11:1220–30
 30. Sanelli PC, Lev MH, Eastwood JD, et al. **The effect of varying user-selected input parameters on quantitative values in CT perfusion maps.** *Acad Radiol* 2004;11:1085–92
 31. Wintermark M, Lau BC, Chen J, et al. **The anterior cerebral artery is an appropriate arterial input function for perfusion-CT processing in patients with acute stroke.** *Neuroradiology* 2008;50:227–36
 32. Sanelli PC, Ugorec I, Johnson CE, et al. **Using quantitative CT perfusion for evaluation of delayed cerebral ischemia following aneurysmal subarachnoid hemorrhage.** *AJNR Am J Neuroradiol* 2011;32:2047–53
 33. Miller JA, Dacey RG Jr, Diringer MN. **Safety of hypertensive hypervolemic therapy with phenylephrine in the treatment of delayed ischemic deficits after subarachnoid hemorrhage.** *Stroke* 1995; 26:2260–66
 34. Willinsky RA, Taylor SM, TerBrugge K, et al. **Neurologic complications of cerebral angiography: prospective analysis of 2,899 procedures and review of the literature.** *Radiology* 2003;227:522–28
 35. Hoh BL, Ogilvy CS. **Endovascular treatment of cerebral vasospasm: transluminal balloon angioplasty, intra-arterial papaverine, and intra-arterial nicardipine.** *Neurosurg Clin N Am* 2005;16:501–16
 36. Schmidt U, Bittner E, Pivi S, et al. **Hemodynamic management and outcome of patients treated for cerebral vasospasm with intra-arterial nicardipine and/or milrinone.** *Anesth Analg* 2010;110:895–902
 37. Kanamaru K, Waga S, Kuga Y, et al. **Transcranial Doppler pattern after intracarotid papaverine and prostaglandin E1 incorporated in lipid microsphere in patients with vasospasm.** *Neurol Med Chir (Tokyo)* 1998;38(suppl):152–55

Direct Visualization of Anatomic Subfields within the Superior Aspect of the Human Lateral Thalamus by MRI at 7T

M. Kanowski, J. Voges, L. Buentjen, J. Stadler, H.-J. Heinze, and C. Tempelmann



ABSTRACT

BACKGROUND AND PURPOSE: The morphology of the human thalamus shows high interindividual variability. Therefore, direct visualization of landmarks within the thalamus is essential for an improved definition of electrode positions for deep brain stimulation. The aim of this study was to provide anatomic detail in the thalamus by using inversion recovery TSE imaging at 7T.

MATERIALS AND METHODS: The MR imaging protocol was optimized on 1 healthy subject to segment thalamic nuclei from one another. Final images, acquired with 0.5²-mm² in-plane resolution and 3-mm section thickness, were compared with stereotactic brain atlases to assign visualized details to known anatomy. The robustness of the visualization of thalamic nuclei was assessed with 4 healthy subjects at lower image resolution.

RESULTS: Thalamic subfields were successfully delineated in the dorsal aspect of the lateral thalamus. T1-weighting was essential. MR images had an appearance very similar to that of myelin-stained sections seen in brain atlases. Visualized intrathalamic structures were, among others, the lamella medialis, the external medullary lamina, the reticulatum thalami, the nucleus centre médian, the boundary between the nuclei dorso-oralis internus and externus, and the boundary between the nuclei dorso-oralis internus and zentrolateralis intermedius internus.

CONCLUSIONS: Inversion recovery–prepared TSE imaging at 7T has a high potential to reveal fine anatomic detail in the thalamus, which may be helpful in enhancing the planning of stereotactic neurosurgery in the future.

ABBREVIATIONS: ACPC = anterior/posterior commissure; DBS = deep brain stimulation; D.o.e = nucleus dorso-oralis externus; D.o.i = nucleus dorso-oralis internus; IR-TSE = inversion recovery turbo-spin-echo; La.m = lamella medialis; Z.im.i = nucleus zentrolateralis intermedius internus

MR imaging, due to its excellent soft-tissue-contrast capabilities, has become the most important imaging technique for the living brain. Nevertheless, the thalamus, characterized by its rich structural variety,^{1–3} appears virtually isointense in routine high-resolution MR images. The lack of visible anatomic detail within the thalamus affects presurgical planning of deep brain stimulation (DBS) procedures. Considering that thalamic mor-

phology can show significant interindividual variability,³ direct visualization of intrathalamic anatomy is necessary for a more precise patient-specific planning of brain electrode positions.

Besides the small size of some thalamic nuclei, the main reason for the lack of contrast is the similarity of MR imaging–relevant tissue parameters such as relaxation times and/or proton densities of adjacent thalamic structures. However, as long as differences in contrast-relevant tissue properties exist, their delineation by an appropriate MR imaging technique is mainly a question of SNR. Several years ago, the wide availability of 3T MR imaging scanners triggered a series of studies aiming to visualize internal substructures of the thalamus,^{4–11} extending the research done at 1.5T.^{12–16} Although noticeable progress was made, the visualization of thalamic nuclei with 3T MR imaging for DBS surgery is not a clinical routine to date. It seemed reasonable to assume that the SNR boost offered by MR imaging at 7T could further improve the visualization of thalamic nuclei. Indeed, the first encouraging results have been reported by using SWI, quantitative susceptibility mapping, and MPRAGE imaging.^{17–19} This feasibility study aims to investigate the usefulness of inversion recovery turbo-spin-echo (IR-TSE) MR imaging at 7T

Received December 9, 2013; accepted after revision March 1, 2014.

From the Departments of Neurology (M.K., H.-J.H., C.T.) and Stereotactic Neurosurgery (J.V., L.B.), Otto-von-Guericke-University Magdeburg, Magdeburg, Germany; Leibniz Institute for Neurobiology Magdeburg (J.V., J.S., H.-J.H.), Magdeburg, Germany; and German Center for Neurodegenerative Diseases (H.-J.H.), Magdeburg, Germany.

This work was supported by the German Research Foundation (SFB 779, TP A2 and A11).

Please address correspondence to Martin Kanowski, PhD, Otto-von-Guericke-University Magdeburg, Department of Neurology, Leipziger Str 44, 39120 Magdeburg, Germany; e-mail: martin.kanowski@medizin.uni-magdeburg.de

Indicates open access to non-subscribers at www.ajnr.org

Indicates article with supplemental on-line table.

Indicates article with supplemental on-line figure.

<http://dx.doi.org/10.3174/ajnr.A3951>

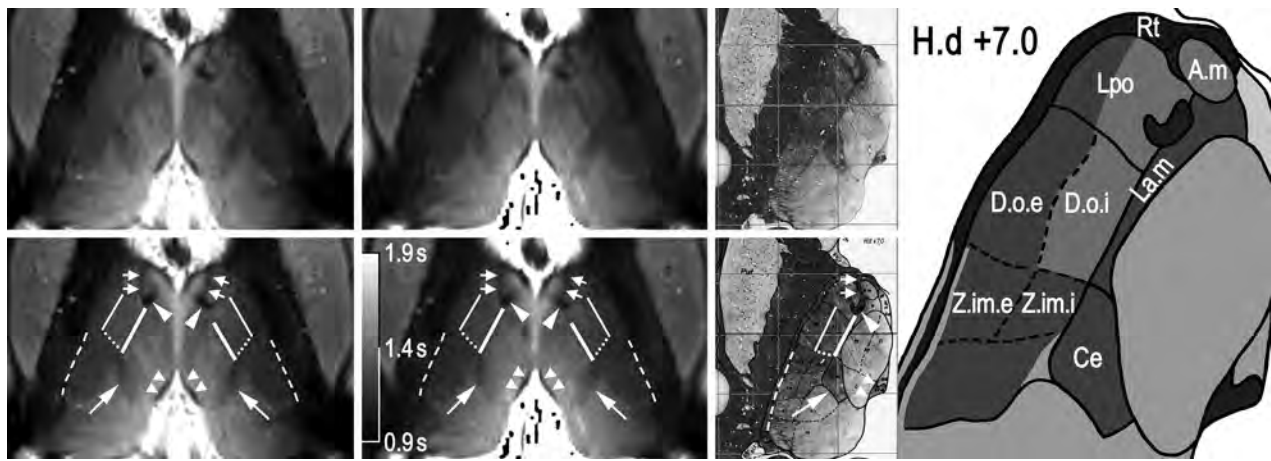


FIG 1. Display of MR and brain atlas images. An IR-TSE MR image (left column) and a T1 map (middle column) of the thalamus of a healthy subject and the corresponding axial section from the Schaltenbrand and Wahren atlas for *Stereotaxy of the Human Brain*,²¹ including an illustrative sketch (right columns, plate LXXVIII H.d +7.0). Reproduced with permission from Thieme Medical Publishers. To facilitate comparison, the images are scaled so that thalami exhibit comparable sizes in the anteroposterior direction. The MR images were acquired with a resolution of $0.5^2 \times 3 \text{ mm}^3$ (left column) and $0.6^2 \times 3 \text{ mm}^3$ (middle column). In the bottom row, which is identical to the top row, note the following structures: Bold lines mark the lamella medialis (La.m), thin lines mark the border between the internal and external part of the nucleus dorso-oralis (D.o.i and D.o.e), dotted lines show the border between the internal parts of the nuclei dorso-oralis (D.o.i) and zentrolateralis intermedius (Z.im.i), dashed lines indicate the posterior part of external medullary lamina, arrows point to the centre médian (Ce), arrowheads indicate the mamillothalamic tract, paired arrowheads indicate the stria medullaris, and pairs of arrows indicate a myelinic sheet separating the nuclei lateropolaris (Lpo) and anteromedialis (A.m). Note the very similar contrast in the IR-TSE image (TI = 500 ms) and the T1 map.

in revealing anatomic detail within the thalamus. This task comprises both the optimization of the MR imaging acquisition and the assignment of visualized structures to thalamic anatomy.

MATERIALS AND METHODS

We examined 5 healthy subjects (2 men; 21–28 years of age) in accordance with stipulations put forth by the local ethics committee. All subjects gave written informed consent before the experiment.

MR imaging was performed at 7T (Siemens, Erlangen, Germany) with a 32-channel head coil (Nova Medical, Wilmington, Massachusetts). Each subject's head was immobilized by using cushions. Optimization of the IR-TSE protocol was done with a subject who had been specifically trained to keep his head still during prolonged scanning times. Scanning parameters of the final IR-TSE acquisitions with high in-plane resolution were the following: transversal-section orientation parallel to the anterior/posterior commissure (ACPC) plane; section thickness, 3-mm; in-plane resolution, 0.5^2 mm^2 ; turbo factor, 5–7; TR, 3–3.2 seconds; TE, 10–14 ms; TI, 480–500 ms; bandwidth, 140–203 Hz/pixel; 1 section or 10 sections with 2 interleaved concatenations; averages, 2–5; scanning time, 13 minutes 45 seconds through 19 minutes 10 seconds. To estimate longitudinal relaxation time, T1, we acquired a series of the IR-TSE protocol, measuring a single section at a section position of 10 mm cranial to the ACPC plane with a TR of 3.2 seconds and a varied TI of 25, 250, 500, 750, 1000, 1250, 1500, and 2000 ms with an in-plane resolution of 0.6^2 mm^2 . The T2 map was measured at the same section position with a series of spin-echo measurements with a constant difference between the TR and TE.²⁰

For the sake of comparison, TSE images were acquired as well with the following parameters: 2.5-mm section thickness and 0.5-mm intersection gap; 0.5^2 mm^2 in-plane resolution; turbo

factor, 5; TR, 3 seconds; TE, 15 ms; bandwidth, 131 Hz/pixel; 1 concatenation with an inferior saturation band; averages, 3; scanning time, 13 minutes 30 seconds. The other 4 subjects were imaged for the first time in a 7T scanner. To reduce the risk of motion-induced image degradation, we selected an IR-TSE protocol with a shorter scan duration and a larger voxel volume (2-mm section thickness; 0.7^2 mm^2 in-plane resolution; turbo factor, 7; TR, 3.3 seconds; TE, 10 ms; TI, 500–700 ms; bandwidth, 186 Hz/pixel; 8 sections with 2 interleaved concatenations; averages, 2; scanning time, 10 minutes 2 seconds. To optimize the SNR of the applied sequences, we adjusted the global amplifier reference to ensure that the nominal flip angles of 90° and 180° applied in the thalamus.

The T1 map was fitted voxelwise to the signal-intensity equation: $I = c \{1 - 2 \exp(-TI/T1) + \exp[-(TR - TE_{\text{last}})/T1]\}$, where TE_{last} denotes the echo time of the last echo in the echo train and c is a scaling factor. The T2 map was fitted to a single exponential decay. MR images were compared with labeled photographs and drawings in stereotactic brain atlases^{3,21,22} to assign visible differentiation to known thalamic anatomy. Apart from a few exceptions, we used the terminology introduced by Hassler.¹

RESULTS

Figure 1 shows axial MR images through the thalamus at a position of about 10 mm dorsal to the ACPC plane, with the corresponding section of the atlas of Schaltenbrand and Wahren²¹ at position H.d +7.0. At first glance, a high degree of similarity between the IR-TSE image (TI = 500 ms) and the T1 map (calculated from a series of MR images with different TIs) is noticeable. However, more striking is the richness of visible anatomic detail in the lateral thalamus. For illustrative purposes, some salient landmarks are marked in white (Fig 1, bottom row). Arrowheads point to the mamillothalamic tract, paired arrowheads indicate the stria medullaris, and arrows point to the nucleus centre mé-

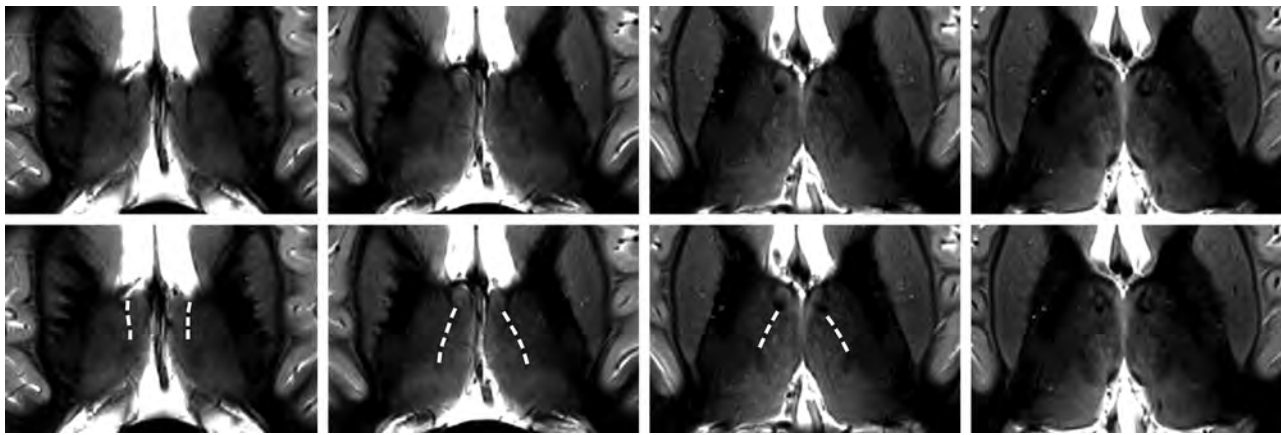


FIG 2. Axial MR images of the thalamus at different positions. Sections are located 16, 13, 10, and 7 mm dorsal to the ACPC plane (from left to right) and acquired with an IR-TSE sequence ($T_1 = 480$ ms and $0.5^2 \times 3$ mm³ resolution). In the bottom row, which is identical to the top row, the La.m is indicated by dashed lines.

dian (Ce). The bold white line connecting the mamillothalamic tract and the most anterior part of the centre médian depicts the lamella medialis (La.m). Pairs of arrows point to a hypointense band between the mamillothalamic tract and the rostral border of the thalamus, separating the nuclei lateropolaris (Lpo) and anteromedialis (A.m) thalami. This structure, not explicitly assigned in the Schaltenbrand and Wahren atlas, is identified in the atlas of Mai et al²² as the internal medullary lamina, (ie, the myelin-rich sheet that largely corresponds to the La.m in the atlas of Schaltenbrand and Wahren²¹). The dotted and the thin white lines in Fig 1 mark well-defined signal-intensity transitions in the lateral thalamus. According to the corresponding section in the Schaltenbrand and Wahren atlas,²¹ we assigned the thin line to the border between the nuclei dorso-oralis internus (D.o.i) and externus (D.o.e) and the dotted line to the boundary between the D.o.i and the nucleus zentrolateralis intermedius internus (Z.im.i). Finally, the dashed lines designate a narrow hypointense band in the posterior thalamus separated by narrow hyperintense bands from the internal capsule and the lateral thalamic nuclei. We identify this dark band as the external medullary lamina and the hyperintense band between the external medullary lamina and the internal capsule as the reticulatum thalami (Rt). Although the latter 2 bands are clearly distinguishable, at least in the posterior half of the thalamus, in the Schaltenbrand and Wahren atlas²¹ they are subsumed under the Rt. In contrast, Mai et al²² differentiate the external medullary lamina and Rt in the posterior thalamus (frontal sections, plates 42–49, position 26.5–36.0 mm).

The images in Fig 2 show axial sections through the thalamus 16, 13, 10, and 7 mm dorsal to the ACPC plane of the same subject as depicted in Fig 1 (recorded during a different session). The La.m can be clearly identified in the dorsal 3 sections, but it looks faded and weakly contoured in the most ventral section in the right image of Fig 2. The most probable reasons are intralaminar cell clusters and the larger lateromedial width of this lamina at more ventral levels.²³ Only in the section 10 mm dorsal to the ACPC plane does the boundary between the D.o.i and Z.im.i appear as a well-defined edge. In the neighboring sections, gradual signal-intensity transitions, in an anteroposterior direction, of the lateral thalamus are discernible. These diffuse changes in signal intensity hamper the demarcation of distinct thalamic structures.

At the present stage, we cannot definitively state whether partial voluming is the main reason or whether a smooth transition of the MR relevant tissue properties of neighboring thalamic compartments impedes the formation of a distinct boundary. Images of the same anatomic location for the 4 other measured subjects are shown in Fig 3. At the reduced in-plane resolution of 0.7^2 mm² and a section thickness of 2 mm, the boundary between the D.o.i and Z.im.i, the boundary between the D.o.i and D.o.e, and the La.m can be assigned in a reliable manner in almost all cases. The subject in Fig 3A seems to have a relatively slim D.o.e. Also of note is the rather diffuse appearance of the D.o.i/Z.im.i boundary in the left hemisphere in Fig 3A, -C.

Figure 4 shows the IR-TSE images of 2 of the subjects, acquired with TIs of 650 and 700 ms to substantiate that visualization of the D.o.e is definitely not the result of artifacts. The pronounced reversal in image intensity between the D.o.e and the internal capsule caused by different TIs proves that MR relaxation properties can be harnessed to delineate subfields of the nucleus dorso-oralis (D.o). Figure 5 shows side-by-side transversal IR-TSE and TSE images of the investigated section position. Despite the prominent vessels (arrows in Fig 5), there is hardly any contrast inside the lateral thalamus in the TSE image. In addition, the La.m and the centre médian are not visible in the TSE image. Due to a slightly different windowing of the IR-TSE image in Fig 5 compared with Fig 1, the corticospinal tract is unambiguously identified as the pale area in the posterior third quarter of the posterior limb of the internal capsule.²⁴ This brightening, also conspicuous in the examples in Fig 3, is caused by longer T1 and T2 relaxation times of the large axons with thick myelin sheaths in the corticospinal tract. The On-line Table shows T1 and T2 times measured in 1 subject, along with On-line Fig 1 showing marked regions of interest. The applied phase-encoding in the anteroposterior direction is necessary for the removal of flow artifacts caused by CSF pulsation in the third ventricle. However, at the same time, it is the reason for occasionally observed bright spots in medial thalamic fields. These artifacts arise from branches of thalamic veins and are indicated by the arrowheads on the IR-TSE image of Fig 5.

To understand why IR-TSE is beneficial compared with proton-density-weighted TSE imaging as a method of differentiating the D.o.i from the Z.im.i, we modeled the contrast behavior

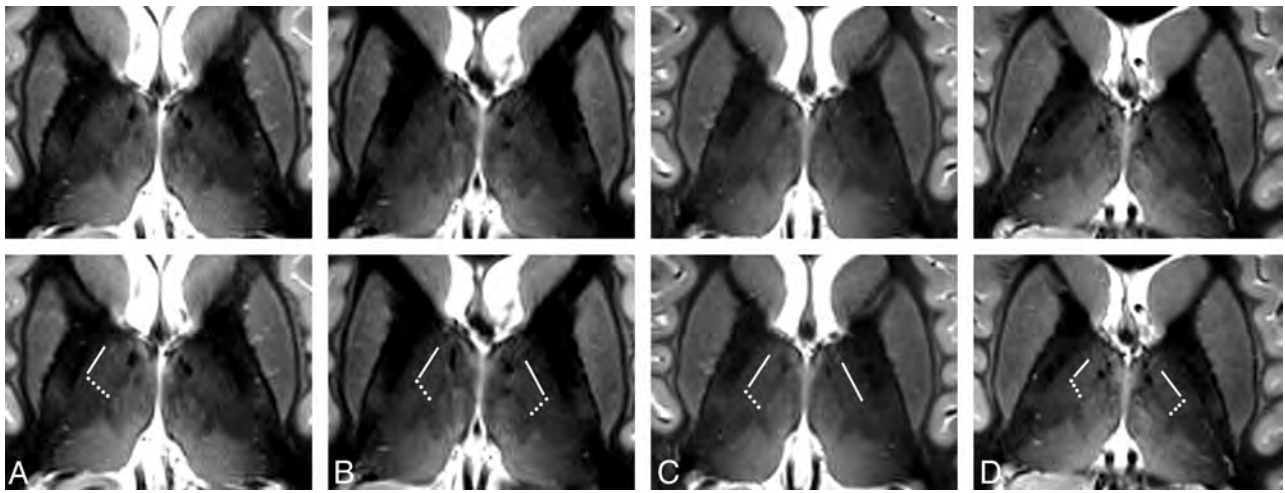


FIG 3. Axial MR images of different subjects. Axial sections through the thalamus in a plane approximately 10 mm dorsal to the ACPC plane of 4 different subjects (A–D) acquired with an IR-TSE sequence (TI = 500 ms and $0.7^2 \times 2 \text{ mm}^3$ resolution). In the bottom row, which is identical to the top row, lines mark the border between the anatomic subfields D.o.i and D.o.e and dotted lines show the border between the subfields D.o.i and Z.im.i. In the left hemispheres in A and C, diffuse-appearing boundaries are not marked. At this coarser in-plane resolution, the Lam appears more blurred than in Figs 1 and 2. Some images show blood flow artifacts in the medial thalamus (see also Fig 5).

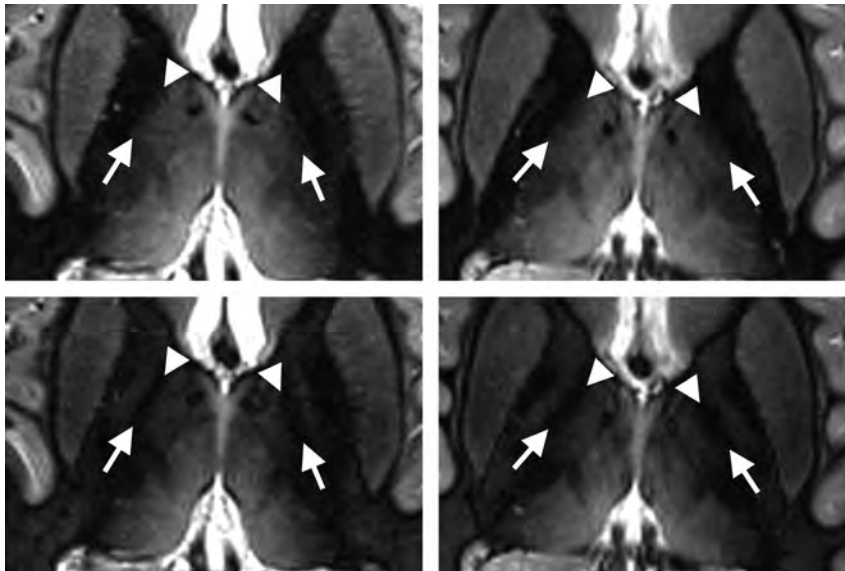


FIG 4. Accentuation of the external part of the D.o.e. Axial sections through the thalamus in a plane approximately 10 mm dorsal to the ACPC plane of 2 different subjects acquired with an IR-TSE sequence ($0.7^2 \times 2 \text{ mm}^3$ resolution) at different inversion times highlight the visualization of the external part of the dorso-oralis nucleus. The D.o.e is the elongated band between the arrow and the arrowhead. In the images with a TI of 650 ms (top row), the D.o.e exhibits intermediate intensity between the medially located more hyperintense D.o.i and the laterally located hypointense internal capsule. The appearance changes at a TI of 700 ms (bottom row). At this inversion time, the D.o.e appears as a hypointense band between the hyperintense D.o.i and internal capsule.

of the 2 applied MR sequences. The determined T1 times in the Z.im.i and D.o.i are 1.13 and 1.20 seconds, respectively. This difference is clearly visible in the T1 map of Fig 1. No signal difference is discernible in the T2 map (not shown). The graphs in Fig 6 show the calculated contrast (difference in signal intensity expressed in multiples of $\rho_{Z.im.i}$) between the Z.im.i and D.o.i versus the proton-density ratios $\rho_{D.o.i}/\rho_{Z.im.i}$ for the IR-TSE sequence with a TI of 500 ms (solid lines) and for the TSE sequence (dashed lines). The contrast of the IR-TSE protocol is only moderately influenced by

small changes of relative water content. On the other hand, the contrast of the TSE protocol is sensitive to slight changes of the proton-density ratio and even vanishes for $\rho_{D.o.i}/\rho_{Z.im.i}$ close to 1.01. Thus, the lack of contrast between the nuclei D.o.i and Z.im.i in the TSE example of Fig 5 may suggest an approximately 1% higher proton density in the D.o.i compared with the Z.im.i.

DISCUSSION

The comparison of MR images with photographs and drawings of stereotactic atlases revealed that the Schaltenbrand and Wahren atlas²¹ seems to be the most suitable one. Its myelin-stained plates appear similar to the presented MR images with hypointense myelin-rich and more hyperintense myelin-poor tissues. Furthermore, the overlayable transparencies with drawn borders of the different thalamic compartments based on their cytoarchitecture notably facilitate anatomic assignment. The remarkable Morel atlas³ shows photographs of the variety of applied stainings only exemplarily. For image comparison and assignment, however, we rate camera lucida drawings less

suitable than labeled photographs of stained sections. Unfortunately, the atlas of Mai et al²² presents only coronal views in high magnification with elaborate anatomic labeling but no sagittal and axial ones.

Despite the high degree of differentiation, the proposed assignment of areas with specific MR imaging contrast to anatomically described tissues remains somewhat ambiguous. One possible reason for discrepancies is the markedly different nature of the images under consideration. MR images integrate

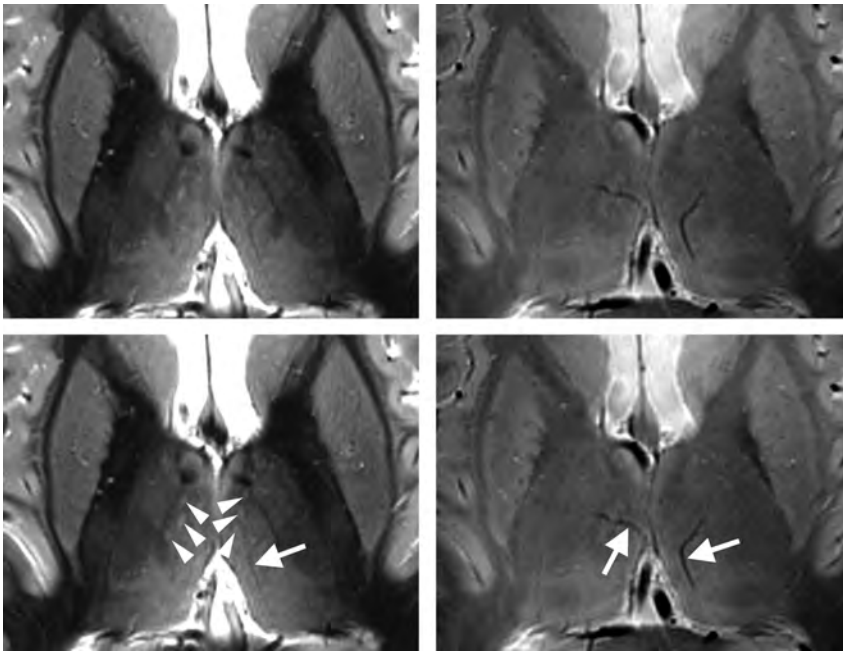


FIG 5. Comparison between IR-TSE (left column) and TSE (right column) images. The sections are located approximately 10 mm dorsal to the ACPC plane. The MR images were acquired with a resolution of $0.5^2 \times 3 \text{ mm}^3$ (IR-TSE, $T_1 = 500 \text{ ms}$) and $0.5^2 \times 2.5 \text{ mm}^3$ (TSE). In the bottom row, which is identical to the top row, arrows point to vessels, and arrowheads, to bright spots. The latter are flow artifacts in the medial thalamus originating from branches of thalamic veins. Note the nearly complete lack of contrast inside the lateral group of thalamic nuclei, the very faint appearance of the external medullary lamina, and the pronounced appearance of vessels in the TSE image.

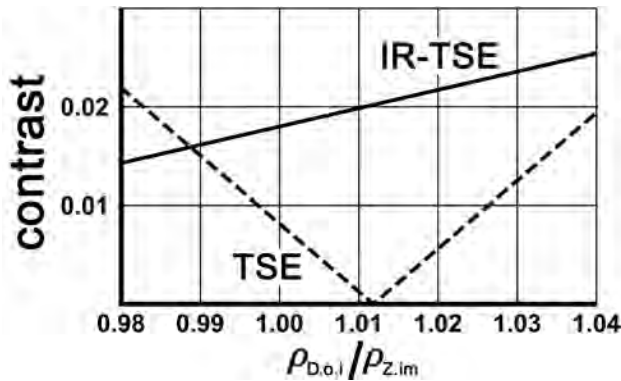


FIG 6. MR contrast for IR-TSE and TSE imaging in thalamic subfields. The solid and the dashed lines show the calculated contrast between the nuclei Z.im.i and D.o.i versus the proton-density ratios $\rho_{D.o.i} / \rho_{Z.im.i}$ for the IR-TSE and the TSE sequences, respectively. Note the relative low dependence of the IR-TSE contrast on variations of the proton-density ratio.

tissue properties over the applied section thickness and in-plane voxel resolution. In contrast to the presented MR images with 2- to 3-mm section thickness and 0.5^2 - 0.7^2 mm^2 in-plane resolutions, photographs in brain atlases based on much thinner histologic sections show the distribution of different tissue compartments for the specified position with extremely high resolution. Consequently, the MR images are more similar to an average of neighboring sections in anatomic atlases than to the MR imaging equivalent of 1 specific section. This observation complicates anatomic assignment, especially if anatomy changes considerably over short distances in a direction orthogonal to the sections. One exam-

ple is the nucleus zentrolateralis intermedius. Because it is a thin layer between the larger ventral and dorsal intermediate nuclei,¹ we cannot exclude the observation that the field here assigned to Z.im.i belongs to one of the latter subfields. Nevertheless, we decided to adopt the labeling of the atlas photograph with the best correspondence to the MR image.

Besides the Schaltenbrand and Wahren atlas,²¹ the partition of the lateral thalamus parallel to the La.m and internal capsule appears even more conspicuous in the myelin staining in Fig 46 in the work of Hirai and Jones.²⁵ Here the nuclei are named ventral lateral anterior (VLa) and ventral lateral posterior (VLp). For an elaborate analysis of which nuclei as defined by Hassler¹ correspond to the nomenclature of Hirai and Jones and a critical view on Hassler's very large number of subdivisions, we refer to the tables and discussions given elsewhere.^{23,25-28}

To successfully delineate the anatomic subfields in the lateral dorsal thalamus, T1-weighting is essential. Ultimately, an inversion recovery approach proved to be most suitable. The popularity of gradient echo imaging at $7T$ ¹⁷⁻¹⁹ is driven, to a

high degree, by the possibility of covering the whole brain in a couple of minutes in compliance with specific absorption rate regulations. The applied IR-TSE sequence, with adiabatic inversion and full 180° refocussing pulses, allows us to measure only a small brain slab within legal specific absorption rate limits. The resulting 8–10 possible sections are sufficient to cover the region of interest. To measure the planned number of sections, occasionally, we were forced by the specific absorption rate limit to increase the TR from the nominal 3 seconds up to 3.3 seconds. Whereas the concomitant slight increase in contrast is welcomed, the prolonging of scanning time is disadvantageous. For IR-TSE imaging, the application of specific absorption rate-reducing techniques is possible yet untested for the presently proposed application.

Unlike the specific absorption rate, CSF pulsation is a serious obstacle. Sharp and contrast-rich images can be reliably acquired in dorsal thalamic regions where the rather small flow distortions are controllable by an appropriately chosen phase-encoding direction. However, in a manner strongly dependent on the subject, IR-TSE images around the ACPC plane can be heavily distorted by flow artifacts arising from the strong pulsatile CSF flow in the third ventricle. Often these cannot be suppressed sufficiently by the flow compensation options of the product TSE sequence. Moreover, flow-synchronous triggering is far from simple—if not impossible—for inversion recovery-prepared MR images. Currently, CSF pulsation artifacts are the reason why only images of the dorsal aspect of the thalamus are described here.

In this regard, 3 recent studies explicitly described the delineation of thalamic nuclei at $7T$.¹⁷⁻¹⁹ Abosch et al¹⁷ and Deistung et al¹⁸ presented promising images directly dorsal to the ACPC

plane. Whereas Abosch et al did not show sections located more dorsally, images presented by Deistung et al showed no indication of parcellation in the dorsal aspect of the lateral thalamus. Also the La.m appears as a rather broad and diffuse band in the quantitative susceptibility map, notwithstanding the extremely high 0.4^3-mm^3 spatial resolution of the underlying MR images. The white matter–nullled MPRAGE images of Tourdias et al¹⁹ explicitly indicated the nuclei ventral lateral anterior and posterior in the dorsal thalamus; however, they did not depict a structure similar to the D.o.i/Z.im.i boundary shown here. The coarser appearance of the La.m and of boundaries between the nuclei in their axial images is probably a consequence of the isotropic 1-mm^3 resolution. All these points are not criticism. We just intended to underline the importance of determining the most suitable MR imaging approach to distinguish a particular thalamic nucleus from adjacent tissues.

Target definition is a core element in the complex process necessary for precise stereotactic implantation of brain electrodes. More precise localization of the supposed optimal target for therapeutic interventions cannot balance the impact of other sources of error such as image resolution or the mechanical accuracy of stereotactic systems. However, it reduces the total error of the procedure and thus promotes a more comprehensive understanding of therapeutic outcomes. In that regard, 2 recent studies^{29,30} investigated possible issues for neurosurgical targeting due to higher geometric distortions at 7T. Without dissent, they reported relatively small distortions in the central brain regions and concluded that targeting is feasible with 7T imaging. Without question, the assumed advantage of the clear visualization of intrathalamic anatomy for DBS planning has yet to be validated. We expect that among others, the La.m, the boundary between the nuclei D.o.i and Z.im.i, the boundary between the nuclei D.o.i and D.o.e, and the dorsal aspect of the centre médian are valuable landmarks. Because the boundary between the D.o.i and Z.im.i is located only a few millimeters dorsal to the anterior margin of the nucleus ventrointermedius internus, it has the potential to promote a more accurate DBS planning in patients with tremor. The successful transfer of the imaging protocol to patient scanning is strongly bound to an effective suppression of any head movement. A thorough comparison of the recorded images of the subject trained to keep his head very still, on the one hand, with the images of the other 4 subjects, on the other hand, suggests that residual head motion may explain the sometimes less compelling visualization of subfields in the lateral thalamus. Methods of mitigating these artifacts used in routine MR imaging investigations of patients with motor disorders, such as the use of sedative medications or MR imaging–compatible stereotactic head frames, are not, in our view, feasible options in a 7T context. Instead, prospective motion-correction technologies³¹ that do not require a tight fixation of the head present a promising alternative. Moreover, prospective correction of microscopic head motion has already been demonstrated to be fully compatible with 7T MR imaging.³²

CONCLUSIONS

This feasibility study demonstrates that IR-TSE-based MR imaging at 7T can reveal a high degree of anatomic detail in the dorsal thalamus. Even if none of the here-visualized subfields are cur-

rently a relevant DBS target, the more general hope for the future is that precise visualization of well-defined internal thalamic landmarks will improve the definition of target point coordinates for stereotactically guided implantation of DBS electrodes.

Disclosures: Jürgen Voges—UNRELATED: Consultancy: Medtronic, Sapiens, Grants/Grants Pending: German Research Foundation,* Payment for Lectures (including service on Speakers Bureaus): Medtronic, St. Jude Medical. Lars Buentjen—UNRELATED: Payment for Lectures (including service on Speakers Bureaus): lectures on spinal cord stimulation (St. Jude Medical) and occipital nerve stimulation (St. Jude Medical), Payment for Development of Educational Presentations: See above, Travel/Accommodations/Meeting Expenses Unrelated to Activities Listed: Neuropathic Pain Congress (St. Jude Medical), workshops on spinal cord stimulation (St. Jude Medical, Boston Scientific, Medtronic). *Money paid to the institution.

REFERENCES

- Hassler R. **Anatomy of the thalamus.** In: Schaltenbrand G, Bailey P, eds. *Introduction to Stereotaxis with an Atlas of the Human Brain.* Vol 1. Stuttgart, Germany: Thieme; 1959:230–90
- Jones EG. *The Thalamus.* New York: Plenum Press; 1985
- Morel A. *Stereotactic Atlas of the Human Thalamus and Basal Ganglia.* New York: Informa Healthcare; 2007
- Spiegelmann R, Nissim O, Daniels D, et al. **Stereotactic targeting of the ventrointermediate nucleus of the thalamus by direct visualization with high-field MRI.** *Stereotact Funct Neurosurg* 2006;84:19–23
- Yovel Y, Assaf Y. **Virtual definition of neuronal tissue by cluster analysis of multi-parametric imaging (virtual-dot-com imaging).** *Neuroimage* 2007;35:58–69
- Gringel T, Schulz-Schaeffer W, Eloff E, et al. **Optimized high-resolution mapping of magnetization transfer (MT) at 3 Tesla for direct visualization of substructures of the human thalamus in clinically feasible measurement time.** *J Magn Reson Imaging* 2009;29:1285–92
- Young GS, Feng F, Shen H, et al. **Susceptibility-enhanced 3-Tesla T1-weighted spoiled gradient echo of the midbrain nuclei for guidance of deep brain stimulation implantation.** *Neurosurgery* 2009;65:809–15
- Kanowski M, Voges J, Tempelmann C. **Delineation of the nucleus centre median by proton density weighted magnetic resonance imaging at 3 T.** *Neurosurgery* 2010;66(3 suppl operative):E121–23
- Bender B, Mänz C, Korn A, et al. **Optimized 3D magnetization-prepared rapid acquisition of gradient echo: identification of thalamic substructures at 3T.** *AJNR Am J Neuroradiol* 2011;32:2110–15
- Traynor CR, Barker GJ, Crum WR, et al. **Segmentation of the thalamus in MRI based on T1 and T2.** *Neuroimage* 2011;56:939–50
- Buentjen L, Kopitzki K, Schmitt FC, et al. **Direct targeting of the thalamic anteroventral nucleus for deep brain stimulation by T1-weighted magnetic resonance imaging at 3 T.** *Stereotact Funct Neurosurg* 2014;92:25–30
- Holmes CJ, Hoge R, Collins L, et al. **Enhancement of MR images using registration for signal averaging.** *J Comput Assist Tomogr* 1998;22:324–33
- Magnotta VA, Gold S, Andreasen NC, et al. **Visualization of subthalamic nuclei with cortex attenuated inversion recovery MR imaging.** *Neuroimage* 2000;11:341–46
- Behrens TE, Johansen-Berg H, Woolrich MW, et al. **Non-invasive mapping of connections between human thalamus and cortex using diffusion imaging.** *Nat Neurosci* 2003;6:750–57
- Wiegell MR, Tuch DS, Larsson HB, et al. **Automatic segmentation of thalamic nuclei from diffusion tensor magnetic resonance imaging.** *Neuroimage* 2003;19:391–401
- Deoni SC, Josseau MJ, Rutt BK, et al. **Visualization of thalamic nuclei on high resolution, multi-averaged T1 and T2 maps acquired at 1.5 T.** *Hum Brain Mapp* 2005;25:353–59
- Abosch A, Yacoub E, Ugurbil K, et al. **An assessment of current brain targets for deep brain stimulation surgery with susceptibility-weighted imaging at 7 Tesla.** *Neurosurgery* 2010;67:1745–56
- Deistung A, Schäfer A, Schweser F, et al. **Toward in vivo histology: a comparison of quantitative susceptibility mapping (QSM) with**

- magnitude-, phase-, and R_2^* -imaging at ultra-high magnetic field strength. *Neuroimage* 2013;65:299–314
19. Tourdias T, Saranathan M, Levesque IR, et al. **Visualization of intrathalamic nuclei with optimized white-matter-nulled MPRAGE at 7T.** *Neuroimage* 2014;84:534–45
 20. Sussman MS, Vidarsson L, Pauly JM, et al. **A technique for rapid single-echo spin-echo T2 mapping.** *Magn Reson Med* 2010;64:536–45
 21. Schaltenbrand G, Wahren W. *Atlas for Stereotaxy of The Human Brain.* 2nd ed. Stuttgart, Germany: Thieme; 1977
 22. Mai KM, Assheuer J, Paxinos G. *Atlas of the Human Brain.* 2nd ed. Amsterdam, the Netherlands: Elsevier; 2004
 23. Mai KM, Forutan F, Thalamus. In: Mai KM, Paxinos G, eds. *The Human Nervous System.* 3rd ed. Amsterdam, the Netherlands: Academic Press; 2012:618–77
 24. Yagishita A, Nakano I, Oda M, et al. **Location of the corticospinal tract in the internal capsule at MR imaging.** *Radiology* 1994; 191:455–60
 25. Hirai T, Jones EG. **A new parcellation of the human thalamus on the basis of histochemical staining.** *Brain Res Brain Res Rev* 1989; 14:1–34
 26. Macchi G, Jones EG. **Toward an agreement on terminology of nuclear and subnuclear divisions of the motor thalamus.** *J Neurosurg* 1997;86:670–85
 27. Percheron G, François C, Talbi B, et al. **The primate motor thalamus.** *Brain Res Brain Res Rev* 1996;22:93–181
 28. Lemaire JJ, Sakka L, Ouchchane L, et al. **Anatomy of the human thalamus based on spontaneous contrast and microscopic voxels in high-field magnetic resonance imaging.** *Neurosurgery* 2010;66(3 suppl operative):E161–72
 29. Dammann P, Kraff O, Wrede KH, et al. **Evaluation of hardware-related geometrical distortion in structural MRI at 7 Tesla for image-guided applications in neurosurgery.** *Acad Radiol* 2011;18: 910–16
 30. Duchin Y, Abosch A, Yacoub E, et al. **Feasibility of using ultra-high field (7 T) MRI for clinical surgical targeting.** *PLoS One* 2012; 7:e37328
 31. Maclaren J, Herbst M, Speck O, et al. **Prospective motion correction in brain imaging: a review.** *Magn Reson Med* 2013;69:621–36
 32. Maclaren J, Armstrong BS, Barrows RT, et al. **Measurement and correction of microscopic head motion during magnetic resonance imaging of the brain.** *PLoS One* 2012;7:e48088

Neuroimaging Features and Predictors of Outcome in Eclamptic Encephalopathy: A Prospective Observational Study

V. Junewar, R. Verma, P.L. Sankhwar, R.K. Garg, M.K. Singh, H.S. Malhotra, P.K. Sharma, and A. Parihar



ABSTRACT

BACKGROUND AND PURPOSE: Posterior reversible encephalopathy syndrome is associated with eclampsia. We assessed the distribution and nature of typical and atypical cranial MR imaging findings in these patients and their correlation with clinical and laboratory data and predictors of outcome.

MATERIALS AND METHODS: Forty-five clinically confirmed cases of eclampsia were included in this prospective observational study. Subjects with hemolysis, elevated liver enzymes, and low platelets syndrome ($n = 9$) and pre-existing neurologic conditions (1 with cerebral solitary cysticercus granuloma) were excluded. Patients underwent blood investigations and cranial MR imaging.

RESULTS: Twenty-seven patients had abnormal while 8 had normal MR imaging findings. Involvement of brain regions was as follows: frontal, 88.89%; temporal, 44.44%; parietal, 100%; occipital, 100%; deep gray matter, 29.63%; cerebellum, 22.22%; brain stem, 14.81%. Cytotoxic edema was present in 33.33% of cases; 66.67% of patients had mild posterior reversible encephalopathy syndrome; 25.92% had moderate posterior reversible encephalopathy syndrome; and 7.41% had severe posterior reversible encephalopathy syndrome. Abnormal neuroimaging findings were significantly associated with altered sensorium; visual disturbances; status epilepticus; and elevated serum creatinine, uric acid, and lactate dehydrogenase ($P = .006, P = .018, P = .015, P = .019, P = .003$, and $P = .001$, respectively). Serum creatinine, uric acid, and lactate dehydrogenase values and the presence of moderate or severe posterior reversible encephalopathy syndrome were significantly associated with mortality ($P < .001, P < .001, P = .009$, and $P = .027$, respectively).

CONCLUSIONS: Neuroimaging in eclampsia demonstrates a higher incidence of atypical distributions and cytotoxic edema than previously thought. Altered sensorium; visual disturbances; status epilepticus; and elevated serum uric acid, lactate dehydrogenase, and creatinine are associated with abnormal neuroimaging findings. Higher serum creatinine, uric acid, and lactate dehydrogenase levels and moderate and severe forms of posterior reversible encephalopathy syndrome are possible predictors of poor outcome.

ABBREVIATIONS: HELLP = hemolysis, elevated liver enzymes, and low platelets; LDH = lactate dehydrogenase; PRES = posterior reversible encephalopathy syndrome; UA = uric acid

Hypertensive disorders are the most common medical complications of pregnancy, with a reported incidence between 6% and 8%,¹ and they are an important cause of severe morbidity and mortality among mothers and babies. In Africa and Asia, hypertensive disorders of pregnancy, especially pre-eclampsia and eclampsia, are associated with nearly one-tenth of all maternal deaths.²

Eclampsia is defined as the occurrence of seizures that cannot be attributed to other causes in a woman with pre-eclampsia.¹ The

neurologic manifestations of eclampsia are similar to those of hypertensive encephalopathy.^{3,4} Neuroimaging in these patients shows edema of the cortex and subcortical white matter predominantly involving the occipital lobes. There is complete resolution of clinical features and most or all radiologic findings at the normalization of the patient's blood pressure, which can be achieved with administration of antihypertensive drugs and/or delivery of the child and placenta.⁴ This clinoradiologic entity that regresses in a few weeks with elimination of etiologic factors has been previously termed "hypertensive encephalopathy," "reversible posterior leukoencephalopathy syndrome,"⁵ "reversible posterior cerebral edema syndrome,"⁶ and "posterior reversible encephalopathy syndrome" (PRES).⁷ PRES has now become the preferred term,⁸ though to some extent, it is a misnomer because PRES is not always limited to the posterior region of the brain and is not always reversible. Beyond eclampsia, PRES can be associ-

Received December 13, 2013; accepted after revision January 23, 2014.

From the Departments of Neurology (V.J., R.V., R.K.G., M.K.S., H.S.M., P.K.S.), Obstetrics and Gynecology (P.L.S.), and Radiodiagnosis (A.P.), King George's Medical University, Lucknow, India.

Please address correspondence to Rajesh Verma, DM, DNB, Department of Neurology, King George's Medical University, Lucknow, India; e-mail: drrajeshverma32@yahoo.com

<http://dx.doi.org/10.3174/ajnr.A3923>

ated with hypertension due to other causes, immunosuppressant therapy (eg, cyclosporine A), antineoplastic chemotherapy, autoimmune diseases (eg, lupus), infections, sepsis, and shock.^{5,9}

Most studies conducted on the neuroradiologic aspects of eclampsia have had small sample sizes. Additionally, although there are studies that correlate various clinical and laboratory parameters with abnormalities on neuroimaging,^{4,8,10} only a few studies¹¹ provide information about predictors of outcome in eclamptic encephalopathy. The purpose of this study was to determine the spectrum of MR imaging findings in patients with eclampsia and to evaluate their correlation with clinical and laboratory data. We also sought to determine different predictors of outcome of eclamptic encephalopathy.

MATERIALS AND METHODS

This was a hospital-based prospective observational study conducted from October 2011 to September 2013 and approved by our institutional ethics committee. Clinically confirmed cases of eclampsia from the obstetrics and gynecology department of the hospital that were referred to the neurology department for opinions were included in the study. The following criteria of the American College of Obstetricians and Gynecologists were used for the diagnosis of eclampsia: 1) systolic blood pressure of ≥ 140 mm Hg or diastolic blood pressure of ≥ 90 mm Hg that occurs after 20 weeks of gestation in a previously normotensive female, 2) proteinuria of ≥ 0.3 g in a 24-hour urine sample, and 3) ≥ 1 episode of seizures.^{1,12} Subjects diagnosed as having hemolysis, elevated liver enzymes, and low platelets syndrome (HELLP, according to Tennessee criteria)¹³ were excluded from the study because hematologic abnormalities associated with it might confound with the interpretation of laboratory data. Those patients with pre-existing neurologic conditions were also excluded from the study. All patients were interviewed, examined, and investigated after written informed consent was obtained.

The blood pressure noted just before the onset of neurologic symptoms was recorded. For those patients who were not admitted to the hospital when the neurologic symptoms started, the blood pressure recordings obtained at admission were used. All patients underwent routine blood investigations, including hemoglobin, hematocrit, mean corpuscular volume, total leukocyte count, platelet count, lactate dehydrogenase (LDH), aspartate transaminase, alanine transaminase, serum creatinine, blood urea, and serum uric acid (UA) levels. Cranial MR imaging of all patients was performed between the first and seventh day of the onset of clinical symptoms in a 1.5T system. The standard protocol consisted of T1-weighted spin-echo and T2-weighted spin-echo and FLAIR sequences along with DWI and ADC maps. T2*-weighted imaging was included to detect hemorrhage. Cerebral venous thrombosis was ruled out by using MR venography. None of the patients received intravenous contrast.

Localization of Lesions and Description

MR imaging of all the cases was screened by 2 experienced neuroradiologists blinded to clinical data, and a consensus review was obtained. Cases were classified as "MR imaging positive" or "MR imaging negative," depending on presence or absence of abnormalities. MR imaging–positive cases were categorized according

to the involvement of the following locations: frontal, temporal, parietal, occipital, brain stem, basal ganglia, thalamus, cerebellum, corpus callosum, and periventricular region. In addition, the presence of restricted diffusion was noted. On FLAIR and T2*-weighted images, intracranial hemorrhages were noted and further categorized as microhemorrhage (< 5 mm), intraparenchymal hemorrhage (> 5 mm), or subarachnoid hemorrhage.

Severity of PRES

Cases were classified for severity of PRES on the basis of the extent of hyperintensity, mass effect, and signs of herniation and involvement of atypical locations by using FLAIR imaging¹⁴:

Mild: Cortical/subcortical white matter signal-intensity alterations without involvement of periventricular white matter and without mass effect, or involvement of none or only one of the following: cerebellum, brain stem, or basal ganglia.

Moderate: Edema involving the cortex and subcortical white matter without involvement of the periventricular white matter, with mild mass effect but without midline shift/herniation, or involvement of 2 of the following: cerebellum, brain stem, or basal ganglia.

Severe: Edema extending from the cortex to the periventricular white matter or the presence of midline shift/herniation, or involvement of all 3 of the following: cerebellum, brain stem, and basal ganglia.

Treatment

All patients received magnesium sulfate by the Pritchard regimen immediately at the time of admission. The regimen was aborted with the appearance of signs of toxicity (absent knee jerks, respiratory rate < 16 /min, or urine output < 25 mL/hr).¹⁵ Phenytoin (loading dose of 20 mg/kg intravenously for 30 minutes followed by 100 mg every 8 hours) was given in such patients if they continued to have seizures. Phenytoin was continued for 3 months after discharge and was then tapered off.¹⁶

Blood pressure control was achieved with labetalol (20-mg intravenous bolus dose followed by 40 mg if not effective within 10 minutes; then 80 mg every 10 minutes to a maximum total dose of 220 mg).^{1,12}

All patients underwent emergency termination of pregnancy by the obstetrician.¹⁷ Cesarean delivery was performed only for obstetric indications; the rest of the patients underwent vaginal delivery, either spontaneously or with induction of labor by using intracervical dinoprostone.

Clinical follow-up was at 1- and 3-month intervals after discharge. Outcome was assessed in the form of disability and death by using the modified Rankin scale. Multiple parameters (including demographic data, symptoms at presentation, examination findings, laboratory data, and neuroimaging features) were studied to determine possible predictors of outcome.

Data analysis was performed by using the Statistical Package for the Social Sciences, Version 16 (IBM, Armonk, New York). Discrete data were reported as frequency and percentages, and continuous data were reported as mean \pm SD. In univariate analysis, the Student *t* test was applied for continuous variables and the Fisher exact test was applied for discrete variables. In multivariate analysis, ordinal logistic regression and binary logistic re-

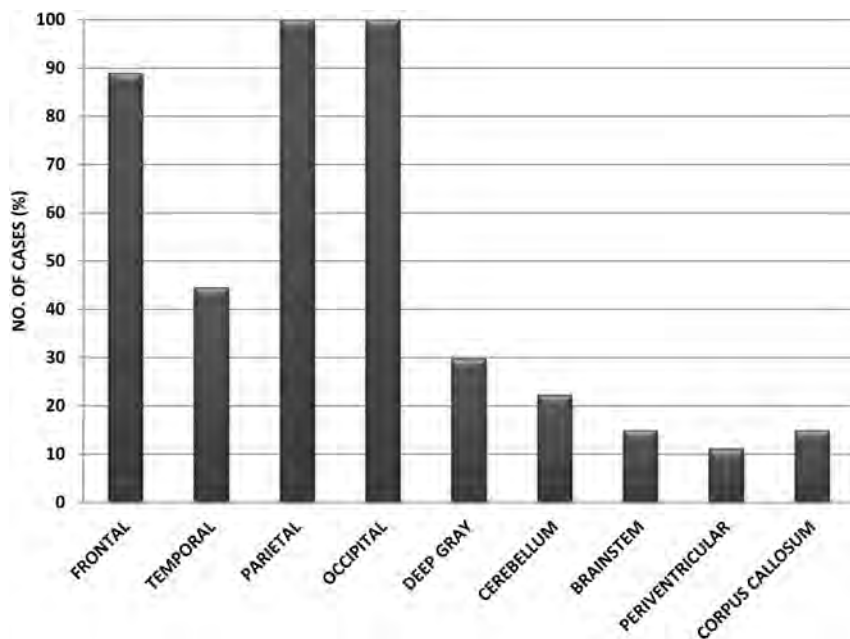


FIG 1. Distribution of lesions in MR imaging-positive cases.

Table 1: Correlation of various parameters with severity of PRES

Parameters	95% Confidence Interval		P Value
	Lower	Upper	
Systolic blood pressure	-0.09	0.07	.87
Diastolic blood pressure	-0.08	0.14	.56
Serum UA	-0.19	0.83	.22
Serum LDH	0.00	0.02	.26
Serum creatinine	-3.12	2.33	.78

gression were used to correlate the severity of PRES and outcome with different parameters, respectively. A *P* value < .05 was considered statistically significant.

RESULTS

Forty-five patients were enrolled. Ten patients were excluded from the study, 9 for HELLP syndrome and 1 for a solitary cysticercus granuloma on her brain MR imaging. Analysis of the remaining 35 cases follows.

Most of the patients (91.43%) belonged to the 20- to 29-year age group. Thirty cases (85.71%) were primigravida, whereas 5 (14.29%) were multigravida. Apart from seizures, symptoms included altered sensorium (94.29%), headache (68.57%), visual disturbances (28.57%), and focal neurologic deficit (8.57%). Thirteen (37.14%) patients had status epilepticus. Twenty-eight (80%) had antepartum eclampsia, 5 (14.29%) had early postpartum eclampsia (first 48 hours postpartum), and 2 (5.71%) had late postpartum eclampsia (48 hours' to 4 weeks' postpartum).

Most patients (32 of 35) underwent MR imaging within 3 days of the onset of neurologic symptoms. Twenty-seven (77.14%) cases were MR imaging-positive, while 8 (22.86%) cases were MR imaging-negative. In the MR imaging-positive cases, the frontal region was involved in 24 (88.89%) cases; the temporal, in 12 (44.44%) cases; and parietal and occipital regions, in all 27 (100%) cases. The deep gray matter was involved in 8 (29.63%) cases; the cerebellum, in 6 (22.22%) cases; the brain stem, in 4

(14.81%) cases; the periventricular region, in 3 (11.11%) cases; and the corpus callosum, in 4 (14.81%) cases (Fig 1). Hemorrhages were present in 6 (22.22%) cases. Five had intraparenchymal hemorrhages (3 lobar, 1 pontine, and 1 caudate), 1 had microhemorrhages, and none had subarachnoid hemorrhage; 33.33% showed the presence of cytotoxic edema. MR venography did not reveal any abnormality in any patient.

When analyzed for severity, of 27 MR imaging-positive cases, 18 (66.67%) had mild PRES, 7 (25.92%) had moderate PRES, and 2 (7.41%) had severe PRES. However, neither blood pressure nor any of the laboratory parameters (serum UA, serum LDH, and serum creatinine levels) had any significant correlation with the severity of PRES (Table 1).

When MR imaging-positive patients were compared with MR imaging-negative patients, there was no statistically significant difference between them in terms of mean age and frequency of the presence of headache, focal neurologic deficit, and edema. However, the difference was found to be statistically significant for altered sensorium (*P* = .006), visual disturbances (*P* = .018), and the presence of status epilepticus (*P* = .015). The difference among systolic, diastolic, and mean blood pressure was also statistically insignificant. Values of serum creatinine, serum UA, and serum LDH, however, were significantly higher in MR imaging-positive cases (*P* = .019, *P* = .003, and *P* = .001, respectively) (Table 2).

Twenty-nine patients survived and were discharged from the hospital within 1–2 weeks. Three patients had hemiparesis on presentation; 2 of them had intracerebral hemorrhage and died during the hospital stay. The remaining patient had infarct in the middle cerebral artery territory due to vasospasm, which was demonstrated on MR angiography. She was discharged with mild disability. At 1-month follow-up, there was complete recovery in her disability. Thus, all 29 surviving patients had full recovery (ie, mRS grade 0) at the end of 1 month. Six patients died during the hospital stay. Of these, 2 patients died of intraparenchymal hemorrhages (pontine and caudate), 2 had severe cerebral edema and developed signs of herniation during the course of their illness, one had acute renal failure, and one had acute pulmonary edema.

When baseline parameters of patients who survived and patients who died were compared, there was no statistically significant difference between them in terms of mean age and frequency of the presence of headache; altered sensorium; visual disturbances; focal neurologic deficit; status epilepticus; edema of the feet; and systolic, diastolic, and mean blood pressure. However, it was observed that the mean serum creatinine, serum UA, and serum LDH values were significantly higher in patients who died (*P* < .001, *P* < .001, and *P* = .009, respectively). In addition, the presence of the moderate or severe form of PRES was significantly more common in these patients (*P* = .027) (Table 3). On multi-

Table 2: Comparison of demographic data, clinical features, and laboratory data between MRI-positive and MRI-negative patients

	MRI-Positive (n = 27)	MRI-Negative (n = 8)	OR	95% CI		P Value
				Lower	Upper	
Age (yr)	24.44 ± 3.53	23.87 ± 2.47	—	−2.16	3.30	.67
Headache	19	5	1.42	0.27	7.44	1.00
Altered sensorium	26	4	26.0	2.29	295.65	.006 ^a
Visual disturbances	17	1	11.9	1.27	111.36	.018 ^a
Focal deficit	3	0	—	—	—	1.00
Status epilepticus	13	0	—	—	—	.015 ^a
Edema in feet	15	5	0.75	0.15	3.79	1.00
SBP (mm Hg)	164.52 ± 17.03	153.75 ± 14.07	—	−2.70	24.24	.11
DBP (mm Hg)	102.81 ± 12.71	98.75 ± 9.91	—	−5.90	14.03	.41
MBP (mm Hg)	123.85 ± 13.39	117.25 ± 9.80	—	−3.81	17.01	.21
Hematocrit (%)	32.33 ± 6.76	32.58 ± 6.49	—	−5.73	5.25	.93
MCV (fL)	88.97 ± 6.02	91.1 ± 6.17	—	−7.08	2.83	.39
TLC (10 ⁹ /L)	7.83 ± 2.23	8.41 ± 2.00	—	−2.37	1.20	.51
Plt (10 ⁵ /mm ³)	1.85 ± 0.49	2.00 ± 0.29	—	−0.52	0.22	.42
AST (IU/L)	47.15 ± 17.83	53.13 ± 15.22	—	−20.15	8.20	.40
ALT (IU/L)	46.48 ± 16.12	53.13 ± 16.14	—	−19.85	6.56	.32
Sr. Creatinine (mg/dL)	1.11 ± 0.41	0.74 ± 0.14	—	0.07	0.67	.019 ^a
Sr. UA (mg/dL)	9.47 ± 2.75	6.31 ± 0.76	—	1.14	5.17	.003 ^a
Sr. LDH (IU/L)	458.03 ± 107.94	319.50 ± 20.50	—	59.69	217.39	.001 ^a

Note:—SBP indicates systolic blood pressure; DBP, diastolic blood pressure; MBP, mean blood pressure; MCV, mean corpuscular volume; TLC, total leukocyte count; Plt, platelet count; AST, aspartate transaminase; ALT, alanine transaminase; Sr., serum.

^a Significant.

Table 3: Comparison of demographic data, clinical features, and laboratory data of cases with respect to outcome

	Survived (n = 29)	Deceased (n = 6)	OR	95% CI		P Value
				Lower	Upper	
Age (yr)	23.86 ± 2.76	26.50 ± 4.93	—	−5.55	0.27	.07
Headache	19	5	0.38	0.04	3.713	.64
Altered sensorium	24	6	—	—	—	.56
Visual disturbances	14	4	0.47	0.07	2.96	.66
Focal deficit	1	2	0.07	0.01	0.98	.07
Status epilepticus	12	1	3.53	0.36	34.19	.38
Edema in feet	16	4	0.62	0.10	3.91	.68
SBP (mm Hg)	159.72 ± 17.52	173.33 ± 5.16	—	−28.45	1.23	.07
DBP (mm Hg)	100.55 ± 11.35	108.33 ± 14.72	—	−18.66	3.10	.16
MBP (mm Hg)	120.76 ± 12.79	130 ± 10.95	—	−20.76	2.19	.11
Hematocrit (%)	32.76 ± 6.42	30.53 ± 7.79	—	−3.82	8.31	.46
MCV (fL)	89.94 ± 5.86	87.12 ± 6.84	—	−2.67	8.32	.30
TLC (10 ⁹ /L)	8.02 ± 2.31	7.65 ± 1.33	—	−1.62	2.38	.70
Plt (10 ⁵ /mm ³)	1.88 ± 0.49	1.88 ± 0.20	—	−0.41	0.43	.96
AST (IU/L)	50.17 ± 18.09	40.50 ± 9.75	—	−5.93	25.27	.22
ALT (IU/L)	47.66 ± 17.44	49.67 ± 7.99	—	−16.94	12.92	.79
Sr. Creatinine (mg/dL)	0.88 ± 0.26	1.72 ± 0.07	—	−1.06	.62	<.001 ^a
Sr. UA (mg/dL)	7.89 ± 1.54	12.87 ± 3.78	—	−6.84	−3.10	<.001 ^a
Sr. LDH (IU/L)	404.44 ± 109.06	532.33 ± 44.68	—	−220.90	−34.85	.009 ^a
Positive MRI findings	21	6	—	—	—	.30
Moderate and severe PRES	5	4	0.10	0.02	0.73	.027 ^a
Cytotoxic edema	7	2	0.64	0.10	4.25	.64

Note:—SBP indicates systolic blood pressure; DBP, diastolic blood pressure; MBP, mean blood pressure; MCV, mean corpuscular volume; TLC, total leukocyte count; Plt, platelet count; AST, aspartate transaminase; ALT, alanine transaminase; Sr., serum.

^a Significant.

variate analysis, however, we could not find any statistically significant correlation between outcome and any of these factors.

DISCUSSION

Eclampsia is one of the many causes of PRES. MR imaging of the brain in PRES is characterized by areas of altered signal intensity predominantly involving the occipital and parietal regions. The lesions are usually isointense to hypointense on T1WI and hyperintense on T2WI and FLAIR sequences. There is more involvement of white matter than gray matter, which is consistent with

vasogenic edema. Lesions are mostly hemispheric and bilaterally symmetric.¹⁸ Lesions with similar characteristics were detected in all of our MR imaging–positive cases. With more severe disease, extensive involvement of the brain occurs along with involvement of atypical areas like the frontal lobes, temporal lobes, corpus callosum, cerebellum, brain stem, basal ganglia, and thalami (Figs 2–4).¹⁸ Recently, it has been shown that the anterior regions are more commonly involved than previously observed. Various studies have shown that the range of frontal lobe involvement varies widely from 30% to 78.9%.^{4,14,19} In our study, the frontal

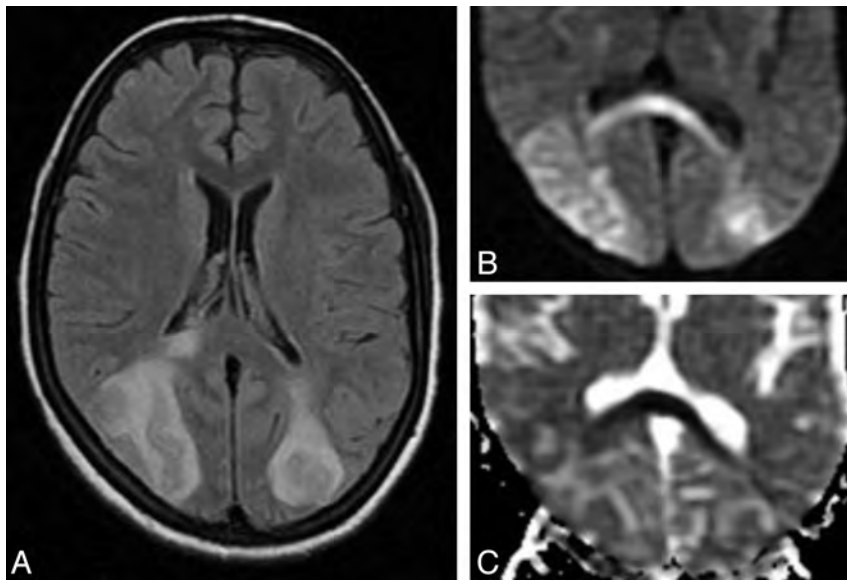


FIG 2. MR images of the brain of a 25-year-old woman with antepartum eclampsia. A, FLAIR MR image shows edema involving the cortex and subcortical white matter of the bilateral occipital and parietal regions and the splenium of the corpus callosum. B, DWI shows hyperintensity in corresponding areas. C, ADC image shows hyperintensity in the bilateral occipital and parietal regions but hypointensity in the splenium of the corpus callosum.

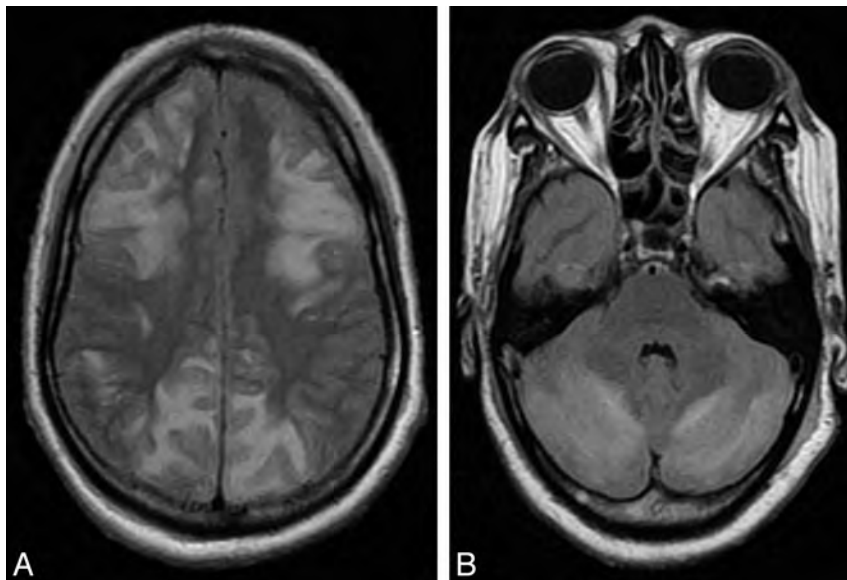


FIG 3. FLAIR MR images of the brain of a 19-year-old woman with antepartum eclampsia showing involvement of bilateral frontal, parietal (A), and cerebellar (B) regions.

lobe was involved in 88.89% of cases, thus reinforcing the thought that anterior regions are also frequently involved in PRES.

Hemorrhages in PRES may be seen in as many as 15% of cases.²⁰ Hefzy et al²¹ found 3 types of hemorrhages, namely, microhemorrhages, intraparenchymal hemorrhages, and subarachnoid hemorrhages, with equal frequency. Susceptibility-weighted imaging has increased the ability to detect microhemorrhages. They can be seen in more than half of patients.²² In our study, 6 (22.22%) patients had hemorrhagic lesions. Two of these patients died; one had pontine hemorrhage and the other had caudate hemorrhage. In terms of the presence of hemorrhage, the difference between the surviving (4/29) and deceased (2/6) patients was

statistically insignificant ($P = .58$). Therefore, it seems that the site of hemorrhage rather than just its presence is more important.

In our study, 8 (22.86%) patients had normal brain imaging findings. A recent study by Brewer et al²³ found PRES in 97.9% of patients with eclampsia by using ≥ 1 technique of imaging. They could find PRES only in 87.2% of patients by using MR imaging without contrast, however, which is close to the case positivity in our study (77.14%). MR imaging findings in eclampsia may be normal, especially if the syndrome had a short duration.¹⁹ The clinical course of MR imaging–negative patients was more benign because they had less frequent headaches and visual disturbances; none of them had status epilepticus and none died.

DWI helps to differentiate vasogenic edema of PRES from cytotoxic edema.²⁴ Focal areas of restricted diffusion (ADC dark, DWI bright) may be seen in PRES, however (Figs 2 and 4).^{19,24} This finding is believed to be due to compromised tissue microcirculation, either secondary to the mass effect of vasogenic edema or due to reactionary vasoconstriction.^{14,25} Although cases with restricted diffusion have been well-reported, we found that cytotoxic edema is more commonly seen than was previously thought. In our study, cytotoxic cerebral edema was seen in 33.33% of patients compared with 17.3% of patients in the study by McKinney et al in 2007.¹⁴ This higher frequency of cytotoxic edema in eclampsia is probably due to reactionary vasoconstriction. Reversible segmental narrowing of large and medium-sized cerebral arteries had been well documented previously in patients with eclampsia on conventional angiography and MR angiography. A high level of endothelin, a potent vasoconstrictor peptide seen in patients with eclampsia, might be responsible for the vasospasm.²⁶

The exact pathogenesis of PRES is not yet completely understood. Extravasation of fluid in the parenchyma is thought to be a major causative factor.⁸ This might be related to the disturbance of the cerebral autoregulation mechanism or endothelial dysfunction.^{4,8,25} In PRES with hypertension, dysfunction of cerebral autoregulation could be responsible for serum extravasation. However, PRES does occur without hypertension. It is proposed that direct endothelial dysfunction leading to an increase in the permeability of the blood-brain barrier may be the additional mech-

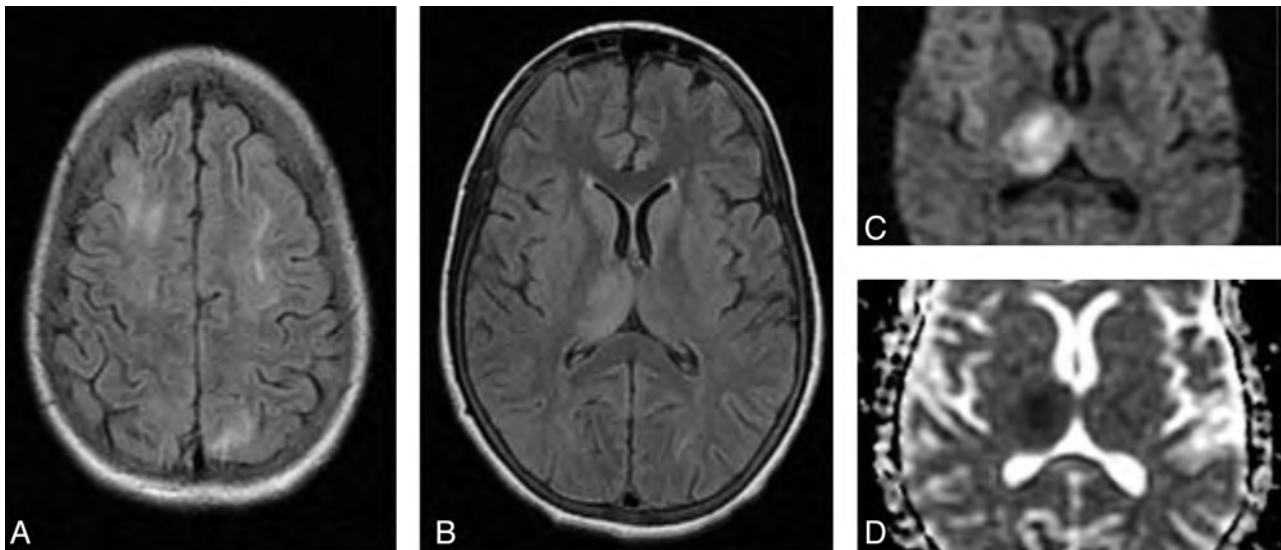


FIG 4. Brain MR images of a 20-year-old woman with early postpartum eclampsia. A, FLAIR MR image shows edema involving the bilateral frontal and parietal regions. FLAIR (B), DWI (C), and ADC (D) show involvement of the right thalamus with cytotoxic edema.

anism responsible for parenchymal fluid extravasation.^{4,8} Although the exact cause of the endothelial injury in patients with eclampsia is not known, circulating endothelial toxins or antibodies are thought to be responsible.⁴

In our study, abnormal neuroimaging was associated with high serum levels of LDH, which are an indicator of hemolysis. Endothelial injury causes microvascular hemolysis leading to a rise in serum LDH levels. In addition, the brain lesions were found to be associated with high serum UA and serum creatinine levels. Renal dysfunction secondary to renal endothelial injury results in a rise in serum levels of UA and creatinine. In our study, the difference between blood pressure values of patients with or without brain lesions on MR imaging was statistically insignificant. Therefore, it seems that brain lesions were secondary to endothelial injury, rather than a rise in blood pressure. These findings correlate with the findings of Schwartz et al⁴ and Demirtaş et al.⁸

Recently Gao et al¹⁰ showed the relation of serum levels of LDH with the degree of cerebral edema. However, we did not find any significant correlation of the severity of PRES with any biomarker of endothelial dysfunction. We postulate that eclampsia, being a multisystem disorder, is associated with widespread endothelial dysfunction. These markers are not specific for the cerebral vascular endothelium. Hence, their elevation suggests just diffuse endothelial dysfunction, and absolute values may not correlate with the degree of cerebral endothelial dysfunction and thus with the severity of cerebral edema. Therefore, more studies are required aiming at correlation between certain specific biomarkers of cerebral vascular endothelium and the severity of PRES.

To date, only a few studies¹¹ have commented on predictors of outcome in eclampsia. In our study, we found that the mean serum creatinine, UA, and LDH values were significantly higher in patients who died. In addition, the presence of the moderate or severe form of PRES was significantly higher in these patients as opposed to the mild form of PRES, which was more common in surviving patients.

CONCLUSIONS

Neuroimaging in eclampsia demonstrates a higher incidence of atypical distribution and the presence of cytotoxic edema than previously thought. Altered sensorium, visual disturbances, presentation with status epilepticus, and elevated serum UA, LDH, and creatinine levels are more likely to be associated with abnormal neuroimaging findings. Additionally, higher serum creatinine, UA, and LDH levels and moderate and severe forms of PRES on neuroimaging are possible predictors of poor outcome.

REFERENCES

1. Report of the National High Blood Pressure Education Program Working Group on high blood pressure in pregnancy. *Am J Obstet Gynecol* 2000;183:S1–22
2. World Health Organization. *WHO Recommendations for Prevention and Treatment of Pre-Eclampsia and Eclampsia*. Geneva, Switzerland: World Health Organization; 2011
3. Schwartz RB, Jones KM, Kalina P, et al. Hypertensive encephalopathy: findings on CT, MR imaging, and SPECT imaging in 14 cases. *AJR Am J Roentgenol* 1992;159:379–83
4. Schwartz RB, Feske SK, Polak JF, et al. Preeclampsia-eclampsia: clinical and neuroradiographic correlates and insights into the pathogenesis of hypertensive encephalopathy. *Radiology* 2000;217:371–76
5. Hinchey J, Chaves C, Appignani B, et al. A reversible posterior leukoencephalopathy syndrome. *N Engl J Med* 1996;334:494–500
6. Dillon WP, Rowley H. The reversible posterior cerebral edema syndrome. *AJNR Am J Neuroradiol* 1998;19:591
7. Casey SO, Sampaio RC, Michel E, et al. Posterior reversible encephalopathy syndrome: utility of FLAIR imaging in the detection of cortical and subcortical lesions. *AJNR Am J Neuroradiol* 2000;21:1199–206
8. Demirtaş O, Gelal F, Vidinli BD, et al. Cranial MR imaging with clinical correlation in preeclampsia and eclampsia. *Diagn Interv Radiol* 2005;11:189–94
9. Petrovic BD, Nemeth AJ, McComb EN, et al. Posterior reversible encephalopathy syndrome and venous thrombosis. *Radiol Clin N Am* 2011;49:63–80
10. Gao B, Liu FL, Zhao B. Association of degree and type of edema in posterior reversible encephalopathy syndrome with serum lactate

- dehydrogenase level: initial experience. *Eur J Radiol* 2012;81:2844–47
11. Jaiswar SP, Gupta A, Sachan R, et al. **Lactic dehydrogenase: a biochemical marker for preeclampsia-eclampsia.** *J Obstet Gynaecol India* 2011;61:645–48
 12. ACOG Committee on Practice Bulletins-Obstetrics. **ACOG practice bulletin: diagnosis and management of preeclampsia and eclampsia. number 33, January 2002.** *Obstet Gynecol* 2002;99:159–67
 13. Haram K, Svendsen E, Abildgaard U. **The HELLP syndrome: clinical issues and management: a review.** *BMC Pregnancy Childbirth* 2009;9:8
 14. McKinney AM, Short J, Truwit CL, et al. **Posterior reversible encephalopathy syndrome: incidence of atypical regions of involvement and imaging findings.** *AJR Am J Roentgenol* 2007;189:904–12
 15. Duley L. **Magnesium sulphate regimens for women with eclampsia: messages from the Collaborative Eclampsia Trial.** *Br J Obstet Gynaecol* 1996;103:103–05
 16. Chakravarty A, Chakrabarti SD. **The neurology of eclampsia: some observations.** *Neurol India* 2002;50:128–35
 17. Sibai BM. **Diagnosis and management of gestational hypertension and preeclampsia.** *Obstet Gynecol* 2003;102:181–92
 18. Feske SK. **Posterior reversible encephalopathy syndrome: a review.** *Semin Neurol* 2011;31:202–15
 19. Bartynski WS, Boardman JF. **Distinct imaging patterns and lesion distribution in posterior reversible encephalopathy syndrome.** *AJNR Am J Neuroradiol* 2007;28:1320–27
 20. Bartynski WS. **Posterior reversible encephalopathy syndrome. Part 1. Fundamental imaging and clinical features.** *AJNR Am J Neuroradiol* 2008;29:1036–42
 21. Hefzy HM, Bartynski WS, Boardman JF, et al. **Hemorrhage in posterior reversible encephalopathy syndrome: imaging and clinical features.** *AJNR Am J Neuroradiol* 2009;30:1371–79
 22. McKinney AM, Sarikaya B, Gustafson C, et al. **Detection of microhemorrhage in posterior reversible encephalopathy syndrome using susceptibility-weighted imaging.** *AJNR Am J Neuroradiol* 2012;33:896–903
 23. Brewer J, Owens MY, Wallace K, et al. **Posterior reversible encephalopathy syndrome in 46 of 47 patients with eclampsia.** *Am J Obstet Gynecol* 2013;208:468.e1–6
 24. Schaefer PW, Buonanno FS, Gonzalez RG, et al. **Diffusion-weighted imaging discriminates between cytotoxic and vasogenic edema in a patient with eclampsia.** *Stroke* 1997;28:1082–85
 25. Ay H, Buonanno FS, Schaefer PW, et al. **Posterior leukoencephalopathy without severe hypertension: utility of diffusion-weighted MRI.** *Neurology* 1998;51:1369–76
 26. Sengar AR, Gupta RK, Dhanuka AK, et al. **MR imaging, MR angiography, and MR spectroscopy of the brain in eclampsia.** *AJNR Am J Neuroradiol* 1997;18:1485–90

Cranial Arachnoid Protrusions and Contiguous Diploic Veins in CSF Drainage

S. Tsutsumi, I. Ogino, M. Miyajima, M. Nakamura, Y. Yasumoto, H. Arai, and M. Ito

ABSTRACT

BACKGROUND AND PURPOSE: Studies have suggested that arachnoid villi or granulations found in the walls of the cranial dural sinuses, olfactory mucosa, and cranial nerve sheaths function as outlets for intracranial CSF. However, their role as CSF outlets has not yet been verified. Here we show that arachnoid protrusions and contiguous diploic veins provide an alternative drainage route for intracranial CSF.

MATERIALS AND METHODS: Four hundred patients with intact skull, dura mater, and dural sinuses underwent MR imaging to explore arachnoids protruding into the skull and diploic veins. Patients with symptoms of increased intracranial pressure or intracranial hypotension were excluded. For 15 patients undergoing craniotomy, both peripheral and diploic venous blood was collected. Albumin and the CSF-specific biomarkers were measured by enzyme-linked immunosorbent assay.

RESULTS: With MR imaging, arachnoid protrusions into the skull and contiguous diploic veins were consistently identified throughout the cranium with their characteristic appearance depending on the cranial region. In addition, elevated amounts of prostaglandin D synthase and cystatin C were confirmed in diploic veins compared with peripheral venous blood.

CONCLUSIONS: Diploic veins are distributed ubiquitously throughout the cranium. A portion of the intracranial CSF may be drained through arachnoid protrusions and contiguous diploic veins.

ABBREVIATIONS: AP = arachnoid protrusion; CysC = cystatin C; DV = diploic vein; PGDS = prostaglandin D synthase

It has been suggested that arachnoid villi or granulations found in the walls of the cranial dural sinuses, olfactory mucosa, and cranial nerve sheaths function as outlets for intracranial CSF.¹⁻⁴ Arachnoid granulations located adjacent to or in the cranial dural sinuses have been explored by using a variety of methods, including neuroimaging,⁵⁻¹⁵ postmortem dissection,^{5,16,17} investigations by using casting material,¹⁸ and ex vivo studies.¹ However, no report has actually shown the process of CSF absorption in vivo. Diploic veins (DVs) are present throughout the cranium; however, their distribution and functional implications have rarely been documented.^{1,19} One previous MR imaging study proposed the hypothesis that major pathways of the DVs function as CSF drainage routes.¹⁹

Lipocalin-type prostaglandin D synthase (PGDS) is a major

endogenous β chaperone that is present in the brain and secreted into the CSF.^{20,21} It is thought to be a CSF-specific biomarker and sensitive to inflammatory demyelinating disease,²² Alzheimer disease,²³ and normal pressure hydrocephalus.¹⁹ Cystatin C (CysC), a low-molecular-weight cysteine proteinase inhibitor, is known to be expressed in greater amounts in CSF compared with plasma.²⁴ The purpose of the present study was to demonstrate that arachnoid pouches protruding into the skull (APs) and contiguous diploic veins provide an alternative CSF drainage route by high-resolution MR imaging; and we also aimed to measure CSF-specific biomarkers, PGDS, and CysC.

MATERIALS AND METHODS

These studies were performed in accordance with the guidelines for human research of our institution. Written informed consent was obtained for all imaging and laboratory studies.

Examinations with MR Imaging and Postmortem Dissection

All neuroimaging examinations were performed with a 3T MR imaging scanner equipped with a 32-channel head coil. Four hundred patients (mean age, 52 years) with intact skull, dura mater, and dural sinuses were selected as subjects. Patients with symp-

Received December 17, 2013; accepted after revision January 11, 2014.

From the Department of Neurological Surgery (S.T., Y.Y., M.I.), Juntendo University Urayasu Hospital, Chiba, Japan; Department of Neurological Surgery (I.O., M.M., H.A.), Juntendo University School of Medicine, Tokyo, Japan; and Division of Radiological Technology (M.N.), Medical Satellite Yaesu Clinic, Tokyo, Japan.

Please address correspondence to Satoshi Tsutsumi, MD, Department of Neurological Surgery, Juntendo University Urayasu Hospital, 2-1-1 Tomioka, Urayasu, Chiba 279-0021, Japan; e-mail address: shotaro@juntendo-urayasu.jp

<http://dx.doi.org/10.3174/ajnr.A4007>

toms of increased intracranial pressure or intracranial hypotension were excluded. A coronal T2-weighted sequence involving the whole cranial vault was performed in 150 patients to record all the APs in the cranial cavity, with parameters as follows: TR, 5598.69 ms; TE, 100.00 ms; section thickness, 1.00 mm; intersection gap, 0.2 mm; matrix, 230 × 230; FOV, 250 mm; flip angle, 90°; and scan duration, 6 minutes 40 seconds. The remaining 250 patients were analyzed with a coronal T2-weighted sequence focusing on the pterional region, with parameters as follows: TR, 4038.35 ms; TE, 90.00 ms; section thickness, 2 mm; intersection gap, 0.2 mm; matrix, 300 × 189; FOV, 150 mm; flip angle, 90°; and scan duration, 4 minutes 25 seconds. A contrast study with intravenous gadolinium infusion (0.1 mmol/kg), involving the whole cranial vault, was performed in 100 of 400 patients with parameters as follows: TR, 4.1 ms; TE, 1.92 ms; section thickness, 1 mm; intersection gap, 0 mm; matrix, 320 × 320; FOV, 250 mm; flip angle, 13°; and scan duration, 4 minutes 25 seconds. Imaging data were analyzed independently by 2 authors (Y.Y. and M.I.).

APs piercing the dura mater were also microscopically observed in an injected postmortem head.

Biochemical Analysis

For 15 patients (6 men and 9 women; mean age, 50 years) undergoing craniotomy, both peripheral and diploic venous blood was simultaneously collected. In each patient, 5 mL of diploic venous blood draining from the bony edges was manually aspirated by using syringes following removal of the bone flap. In 5 patients, CSF was also obtained intraoperatively. All samples of blood and CSF were poured into test tubes without any mounting reagent and were immediately centrifuged to remove cells and debris, aliquoted, and finally stored in polypropylene tubes at -80°C until ready for biochemical analysis. Albumin, PGDS, and CysC were measured in these 15 patients by enzyme-linked immunosorbent assay. Albumin was measured as a reference marker with a larger molecular weight than PGDS and CysC. Results were analyzed by using the Wilcoxon signed rank test (SPSS 18.0 software package; IBM, Armonk, New York). A *P* value <.05 was considered statistically significant.

RESULTS

On MR imaging, APs were roughly classifiable into vesicular, tubular, and extensive types (Fig 1B, -C). In the cerebral convexity, APs were commonly identified in the parasagittal region, connecting to either a linear or branching architecture with variable thickness, but showing a consistent course in the diploe. These APs were consistently distributed throughout the pterional region (Fig 1D), middle cranial fossa (Fig 1E), and posterior cranial fossa (Fig 1F), with contiguous DVs showing a characteristic course in each cranial region. DVs appeared with intensity similar to that of the CSF on noncontrast sequence imaging, whereas they showed configurations identical to those delineated on contrast-enhanced images. Therefore, we have concluded that both methods visualize the same DVs (Fig 1G, -H). This conclusion also indicates that DVs can appear both as fluid-filled channels and venous structures on MR imaging.

In 150 patients, the total number of AP-DV pairings located in

the cerebral convexity was 987—489 on the right and 498 on the left (Table 1). When the cerebral convexity was divided into 3 parts (anterior, middle, and posterior third; Fig 1A), 55% of the 987 pairings were found in middle, while 27% were identified in the posterior and 18% were in the anterior part (Table 1). The mean number of AP-DV pairings in 1 subject was 1.2 (range, 0–5) in the anterior part, 3.6 (range, 0–10) in the middle part, and 1.7 (range, 0–8) in the posterior part. In total, an average of 6.6 (range, 0–17) pairings was found in each subject, with an average of 6.9 in the population of subjects older than 18 years of age and 2.3 in the population younger than 18 years. In the cerebral convexity, vesicular APs were most predominant and comprised 68% of 987 pairings, followed by tubular (22%) and extensive (10%) AP types (Fig 1B).

The total number of AP-DV pairings distributed in the skull base was 375 in our 150 patients, 159 on the right and 216 on the left (Table 2). Fifty-three percent of the 375 pairings were located in the middle cranial fossa, and 47% were located in the posterior fossa. Neither APs nor DVs were identified in the anterior fossa. In the middle cranial fossa, AP-DV pairings were twice as often identified on the left side as on the right. The mean number of pairings in 1 subject was 1.3 (range, 0–8) in the middle cranial fossa and 1.2 (range, 0–7) in the posterior fossa. In total, an average of 2.5 (range, 0–11) pairings were found in each subject, with an average of 2.6 in the population of subjects older than 18 years of age and 0.6 in the population younger than 18 years of age. In the skull base, tubular APs were most predominant and comprised 61% of pairings in the middle cranial fossa and 94% in the posterior fossa, followed by vesicular AP pairings. Extensive APs were not found in the skull base (Table 2). In 100% of the subjects studied, at least 1 arachnoid granulation was found in the superior sagittal sinus, whereas in the transverse sinus, at least 1 was identified in 23% of subjects on the right and in 37% of subjects on the left.

In the pterional region, AP-DV pairings were identified in 20% of 250 patients on the right and in 29% of patients on the left. The identification of these pairings did not depend on patient age. All of the identified APs were of the tubular type and were located at the lower surface of the lateral lesser sphenoid wing.

In 15 patients who underwent craniotomy in various regions, albumin (66 kDa), PGDS (19 kDa), and CysC (13 kDa) levels were measured in the diploic and peripheral venous blood. In all patients, diploic venous blood was collected with ease. In 5 patients, CSF was also obtained intraoperatively. PGDS and CysC levels in the CSF were 8278.2 ± 1853.4 ng/mL and 2044.6 ± 390.5 μg/L, respectively. The PGDS and CysC levels in peripheral venous blood were 107.9 ± 59.3 ng/mL and 237.9 ± 77.8 μg/L and 212.4 ± 199.8 ng/mL and 294.9 ± 94.7 μg/L, respectively. In these 15 patients, the diploic vein/peripheral vein ratios were significantly elevated for PGDS and CysC, with values of 2.43 ± 1.99 (*P* = .011) and 1.31 ± 0.43 (*P* = .023), respectively (Fig 3).

On microscopic inspection of the cranial cavity, APs penetrated the dura mater through either a single, oval, or slit-like defect (Fig 2A) or through mesh-like lacunae (Fig 2B). These types of openings were observed throughout the cranial dura mater,

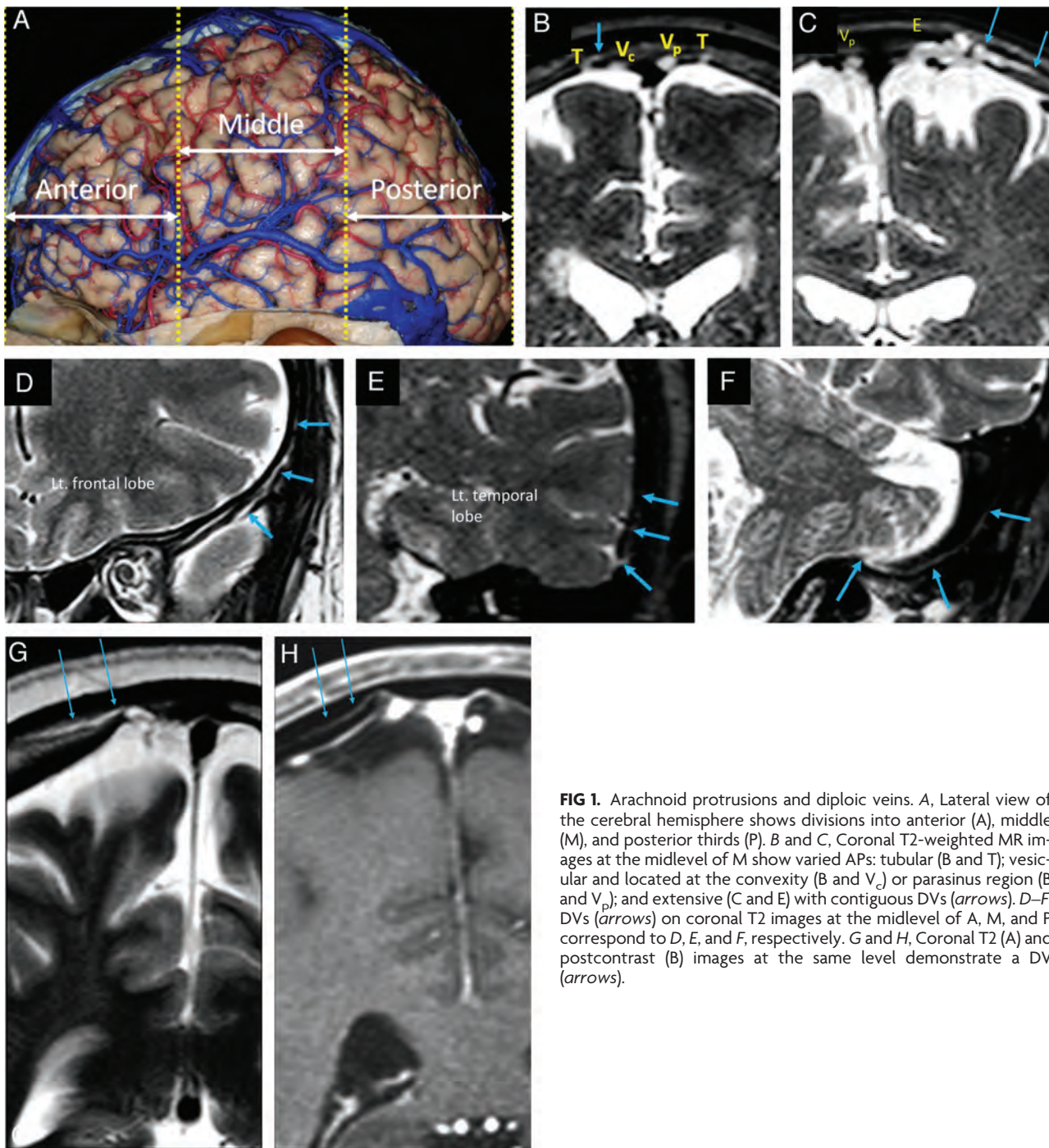


FIG 1. Arachnoid protrusions and diploic veins. A, Lateral view of the cerebral hemisphere shows divisions into anterior (A), middle (M), and posterior thirds (P). B and C, Coronal T2-weighted MR images at the midlevel of M show varied APs: tubular (B and T); vesicular and located at the convexity (B and V_c) or parasinus region (B and V_p); and extensive (C and E) with contiguous DVs (arrows). D–F, DVs (arrows) on coronal T2 images at the midlevel of A, M, and P correspond to D, E, and F, respectively. G and H, Coronal T2 (A) and postcontrast (B) images at the same level demonstrate a DV (arrows).

Table 1: Location of AP-DV pairings in the cerebral convexity

	Right	Left	Total
A	98	77	175 (18%)
M	257	288	545 (55%)
P	134	133	267 (27%)
	489	498	987

Note:—A indicates anterior third; M, middle third; P, posterior third.

especially in the parasagittal region, and, compared with observations during actual surgeries, a clearer view was obtained in post-mortem specimens in which bleeds resulting from disruption of vasculature connecting the dura mater and inner surface of the skull were less likely to disturb anatomic observations.

Table 2: Number of AP-DV pairings in the skull base

	AF	MF	PF
Right	0	69	90
Left	0	130	86
Tubular	0	121 (61%)	165 (94%)
Vesicular	0	78 (39%)	11 (6%)
Extensive	0	0	0

Note:—AF indicates anterior fossa; MF, middle fossa; PF, posterior fossa.

DISCUSSION

Despite their normal venous structure, DVs are inconsistently visualized by conventional neuroimaging techniques, including digital subtraction angiography.²⁵ They have been infrequently associated with dural arteriovenous fistulas,^{26–28} tumorous pa-

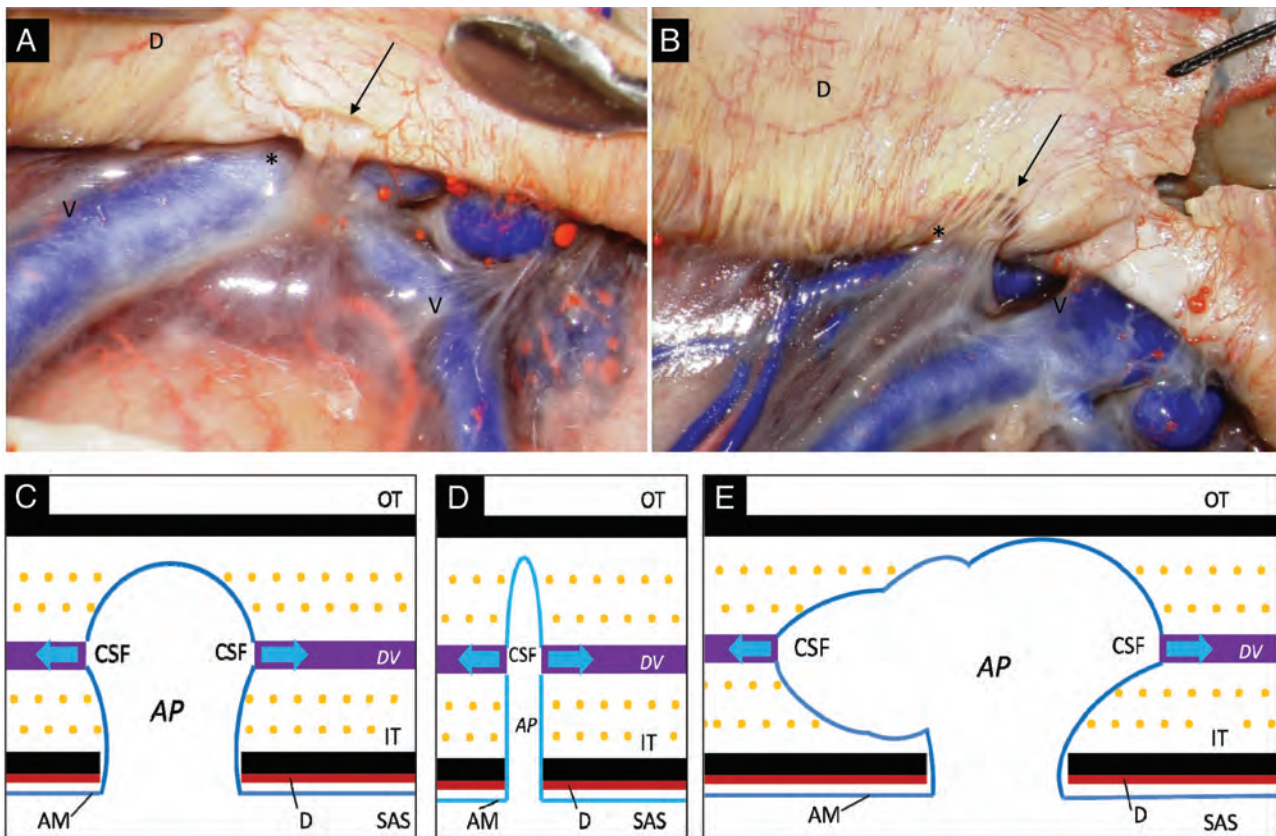


FIG 2. Gross appearance and schema of arachnoid protrusions and contiguous DVs. *A* and *B*, Postmortem specimen shows an arachnoid protrusion (asterisk) at the cerebral convexity that penetrates the dura mater (*D*) through a smooth-contoured single defect (*A*, arrow) or mesh-like lacunae (*B*, arrow). *C–E*, Schematic drawings of vesicular (*C*), tubular (*D*), and extensive types (*E*) of AP. AM indicates arachnoid membrane; IT, inner table; OT, outer table; SAS, subarachnoid space; V, cortical vein.

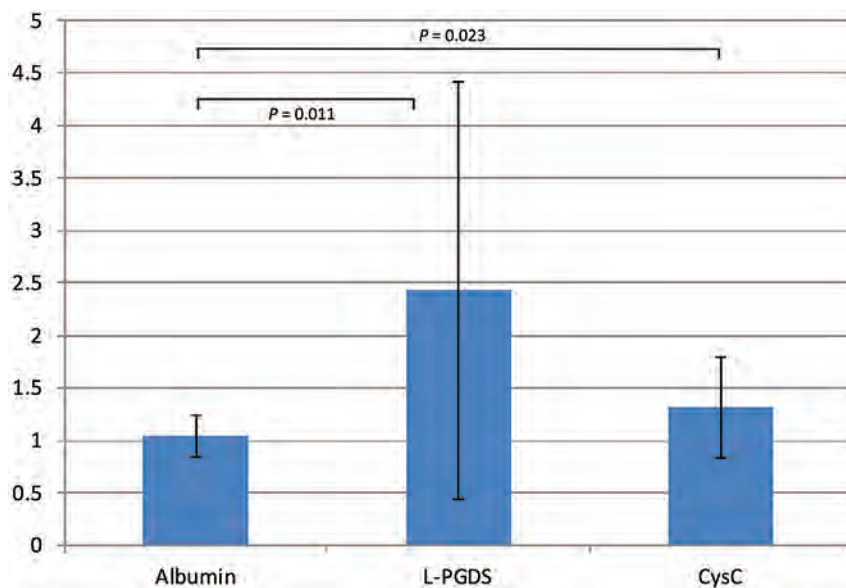


FIG 3. Diploic vein/peripheral vein ratios for PGDS and CysC.

thologies,^{29,30} and sinus pericranii.³¹ The distribution of DVs in the whole cranium is difficult to assess by intraoperative local observation or postmortem dissection because DVs lie intraosseously, surrounded by hard cortical bone. However, high-resolution MR imaging has now made the delineation of these fine structures possible *in vivo*.

A previous investigation revealed the major pathways of the cranial DVs.¹⁹ These pathways are distributed extensively throughout the cranium; in fact, at least 1 major route could be interrupted during any standard craniotomy procedure. In our 15 patients, diploic venous blood was collected without difficulty, regardless of the type of craniotomy.

The present study focused on delineating the APs and contiguous DVs throughout the cranium. By a combination of T2-weighted sequences and contrast images, APs and contiguous DVs were consistently visualized throughout the cranium with their characteristic appearance dependent on their regional location. Of note, while various types of APs were delineated in the cranial cavity, all the identified APs in the pterional region were the tubular type. In addition, our laboratory investigation of

PGDS and CysC levels confirmed that CSF and dissolved, low-molecular-weight proteins can pass through APs into DVs—that is, DVs function not only as venous channels formed in the diploë with abundant mutual connections with the extracranial venous systems¹⁹ but also as CSF drainage pathways to the extracranial spaces. In the physiologic condition, gadolinium did not permeate the

blood-brain barrier to dissolve into CSF,^{32,33} while DVs were well-enhanced on contrast examination. This enhancement indicated that gadolinium moved in the arterial blood stream to reach the arterioles and capillaries of the dura mater, next passing through the venules, and finally pouring into DVs. Furthermore, our laboratory results showed that PGDS and CysC could permeate APs and dissolve into DVs in the context of a normal range of intracranial pressure. Therefore, we considered that some quantity of intracranial CSF may drain through APs and DVs (Fig 2C–E).

The next step for these investigations would be the quantification of differences in CSF permeability in each cranial region and differences in CSF permeability in the context of increased intracranial pressure. Because various factors relevant to the proteomics experiments could have influenced the outcome of this study,²⁴ it will be important to provide confirmation of the validity and reproducibility of the PGDS and CysC results and verification by other appropriate biomarkers. Despite the shortcomings in our methodology, we believe that the present preliminary results convincingly support the notion that at least a fraction of intracranial CSF is drained through APs and DVs.

In the present study, the number of APs identified in the population older than 18 years of age was, except for in the pterional region, more than 3-fold higher compared with number of APs observed in patients younger than 18 years of age. As previously suggested,³⁴ the maturation of the dura mater may be related to the development of APs.

CONCLUSIONS

APs and contiguous DVs are distributed throughout the entire cranium and can be delineated by high-resolution MR imaging. Some portion of the intracranial CSF may be physiologically drained through AP-DV pairs.

REFERENCES

- Glimcher SA, Holman DW, Lubow M, et al. **Ex vivo model of cerebrospinal fluid outflow across human arachnoid granulations.** *Invest Ophthalmol Vis Sci* 2008;49:4721–28
- Kapoor KG, Katz SE, Grzybowski DM, et al. **Cerebrospinal fluid outflow: an evolving perspective.** *Brain Res Bull* 2008;77:327–34
- Pollay M. **The function and structure of the cerebrospinal fluid outflow system.** *Cerebrospinal Fluid Res* 2010;7:9
- Sakka L, Coll G, Chazal J. **Anatomy and physiology of cerebrospinal fluid.** *Eur Ann Otorhinolaryngol Head Neck Dis* 2011;128:309–16
- Chen F, Deng XF, Liu B, et al. **Arachnoid granulations of middle cranial fossa: a population study between cadaveric dissection and in vivo computed tomography examination.** *Surg Radiol Anat* 2011;33:215–21
- Farb RI. **The dural venous sinuses: normal intraluminal architecture defined on contrast-enhanced MR venography.** *Neuroradiology* 2007;49:727–32
- Haroun AA, Mahafza WS, Al Najjar MS. **Arachnoid granulations in the cerebral dural sinuses as demonstrated by contrast-enhanced 3D magnetic resonance venography.** *Surg Radiol Anat* 2007;29:323–28
- Ikushima I, Korogi Y, Makita O, et al. **MRI of arachnoid granulations within the dural sinuses using a FLAIR pulse sequence.** *Br J Radiol* 1999;72:1046–51
- Koshikawa T, Naganawa S, Fukatsu H, et al. **Arachnoid granulations on high-resolution MR images and diffusion-weighted MR images: normal appearance and frequency.** *Radiat Med* 2000;18:187–91
- Leach JL, Meyer K, Jones BV, et al. **Large arachnoid granulations involving the dorsal superior sagittal sinus: findings on MR imaging and MR venography.** *AJNR Am J Neuroradiol* 2008;29:1335–39
- Liang L, Korogi Y, Sugahara T, et al. **Normal structures in the intracranial dural sinuses: delineation with 3D contrast-enhanced**

- magnetization prepared rapid acquisition gradient-echo imaging sequence.** *AJNR Am J Neuroradiol* 2002;23:1739–46
- Miabi Z, Midia R, Rohrer SE, et al. **Delineation of lateral tentorial sinus with contrast-enhanced MR imaging and its surgical implications.** *AJNR Am J Neuroradiol* 2004;25:1811–18
- Roche J, Warner D. **Arachnoid granulations in the transverse and sigmoid sinuses: CT, MR, and MR angiographic appearance of a normal anatomic variation.** *AJNR Am J Neuroradiol* 1996;17:677–83
- Trimble CR, Harnsberger HR, Castillo M, et al. **“Giant” arachnoid granulations just like CSF?: NOT!!** *AJNR Am J Neuroradiol* 2010;31:1724–28
- Mase M, Yamada K, Shimazu N, et al. **Lipocalin-type prostaglandin D synthase (beta-trace) in cerebrospinal fluid: a useful marker for the diagnosis of normal pressure hydrocephalus.** *Neurosci Res* 2003;47:455–59
- Haybaeck J, Silye R, Soffer D. **Dural arachnoid granulations and “giant” arachnoid granulations.** *Surg Radiol Anat* 2008;30:417–21
- Yew M, Dubbs B, Tong O, et al. **Arachnoid granulations of the temporal bone: a histologic study of dural and osseous penetration.** *Otol Neurotol* 2011;32:602–09
- Johnston K, Walji AH, Fox RJ, et al. **Access to cerebrospinal fluid absorption sites by infusion into vascular channels of the skull diploë.** *J Neurosurg* 2007;107:841–43
- Tsutsumi S, Nakamura M, Tabuchi T, et al. **Calvarial diploic venous channels: an anatomic study using high-resolution magnetic resonance imaging.** *Surg Radiol Anat* 2013;35:935–41
- Urade Y, Hayashi O. **Prostaglandin D synthase: structure and function.** *Vitam Horm* 2000;58:89–120
- Yamashima T, Sakuda K, Tohma Y, et al. **Prostaglandin D synthase (beta-trace) in human arachnoid and meningioma cells: role as a cell marker or in cerebrospinal fluid absorption, tumorigenesis, and calcification process.** *J Neurosci* 1997;17:2376–82
- Huang YC, Lyu RK, Tseng MY, et al. **Decreased intrathecal synthesis of prostaglandin D2 synthase in the cerebrospinal fluid of patients with acute inflammatory demyelinating polyneuropathy.** *J Neuroimmunol* 2009;206:100–05
- Kanekiyo T, Ban T, Aritake K, et al. **Lipocalin-type prostaglandin D synthase/beta-trace is a major amyloid beta-chaperone in human cerebrospinal fluid.** *Proc Natl Acad Sci U S A* 2007;104:6412–17
- Carrette O, Burkhard PR, Hughes S, et al. **Truncated cystatin C in cerebrospinal fluid: technical [corrected] artefact or biological process?** *Proteomics* 2005;5:3060–65
- García-González U, Cavalcanti DD, Agrawal A, et al. **The diploic venous system: surgical anatomy and neurosurgical implications.** *Neurosurg Focus* 2009;27:E2
- Benndorf G, Lehmann. **Bilateral diploic arteriovenous fistula causing scalp hematoma.** *J Neurosurg* 2004;100:950–55
- Burger IM, Tamargo RJ, Broussard J, et al. **Combined surgical and endovascular treatment of a spontaneous diploic arteriovenous fistula: case report.** *J Neurosurg* 2005;103:179–81
- Shim JH, Yoon SM, Shim JJ, et al. **A case of intraosseous dural arteriovenous fistulas involving diploic vein treated with transarterial Onyx embolization.** *J Korean Neurosurg Soc* 2011;50:260–63
- Ohigashi Y, Tanabe A. **A huge frontal meningioma associated with intraoperative massive bleeding and severe brain swelling: case report.** *J Clin Neurosci* 2001;8(suppl 1):54–58
- Tsutsumi S, Yasumoto Y, Ito M. **Case of calvarial fibrous dysplasia presenting with cyst degeneration [in Japanese].** *No Shinkei Geka* 2011;39:163–68
- Rizvi M, Behari S, Singh RK, et al. **Sinus pericranii with unusual features: multiplicity, associated dural venous lakes and venous anomaly, and a lateral location.** *Acta Neurochir (Wien)* 2010;152:2197–204
- Bozzao A, Floris R, Fasoli F, et al. **Cerebrospinal fluid changes after intravenous injection of gadolinium chelate: assessment by FLAIRMR imaging.** *Eur Radiol* 2003;13:592–97
- Sorensen AG. **Science to practice: blood-brain barrier leakage— one size does not fit all.** *Radiology* 2010;257:303–04
- Squier W, Lindberg E, Mack J, et al. **Demonstration of fluid channels in human dura and their relationship to age and intradural bleeding.** *Childs Nerv Syst* 2009;25:925–31

A Novel Technique for the Measurement of CBF and CBV with Robot-Arm-Mounted Flat Panel CT in a Large-Animal Model

O. Beuing, A. Boese, Y. Kyriakou, Y. Deuerling-Zengh, B. Jöllenbeck, C. Scherlach, A. Lenz, S. Serowy, S. Gugel, G. Rose, and M. Skalej



ABSTRACT

BACKGROUND AND PURPOSE: Endovascular therapy is an emerging treatment option in patients with acute ischemic stroke and especially in cases presenting late after symptom onset. Information about remaining viable tissue as measured with perfusion imaging is crucial for proper patient selection. The aim of this study was to investigate whether perfusion imaging with C-arm CT in the angiography suite is feasible and provides measurements comparable with ones made by CTP.

MATERIALS AND METHODS: The MCA was occluded surgically in 6 sheep. Perfusion studies were performed before surgery, immediately after, and at 3 hours after MCA occlusion by using a robotic flat panel detector C-arm angiographic system. For comparison, conventional CTP was performed at the same time points. Two different protocols with the C-arm CT were tested. Images were analyzed by 2 readers with regard to the presence and size of perfusion abnormalities.

RESULTS: With C-arm CT, perfusion abnormalities were detected with a high sensitivity and specificity when vessel occlusion was confirmed by criterion standard DSA. No difference was found between lesions sizes measured with the 2 C-arm CT protocols and CTP. Growth of the CBV lesions with time was captured with C-arm CT and CTP.

CONCLUSIONS: In this small study, it was feasible to qualitatively measure CBV and CBF by using a flat panel detector angiographic system.

Stroke is a major cause of death and disability throughout the world. IV thrombolysis within 4.5 hours of symptom onset remains the only therapy with benefit for patients so far, as proved by randomized trials.¹⁻³ However, the results of studies investigating endovascular approaches indicate that the outcome of patients with large-artery occlusions may be improved in comparison with IV thrombolysis.⁴⁻⁸

Perfusion measurements are useful in selecting patients most likely to benefit from revascularization because they provide information about the ratio of infarct core to penumbra. This is especially true for those patients presenting outside the therapeutic time window for IV thrombolysis.

Despite the potential value of MR imaging or CTP measurements, these studies are often not performed because there is no solid evidence that they improve outcome, there is a significant time cost in obtaining the measurements, and they only provide a snapshot of a dynamic process.⁹ The ability to obtain these measurements in the angiography suite would eliminate the last 2 objections. Several experimental and clinical studies have demonstrated that measurement of CBV is feasible by using C-arm CT.¹⁰⁻¹² More recently, CBF was measured in healthy swine and canines with such a system.^{13,14} We report our experience using a modified C-arm system to measure steady-state CBV and also to make dynamic measurements of CBF in an experimental sheep stroke model.

MATERIALS AND METHODS

Creation of Stroke

The experiments were performed in accordance with the guidelines and with written consent of the local ethics authorities. Stroke was successfully created surgically in 6 of 7 German Black-headed sheep (1 animal died during surgery from ventricular fibrillation). For surgery, the animals were placed in a supine position on the angiography table. General anesthesia was inducted with propofol; isoflurane was used for maintenance. Vital parameters were monitored continuously. Surgery was necessary because in sheep, the ICA develops from a rete mirabile, which is

Received February 20, 2013; accepted after revision December 19.

From the Institute of Neuroradiology (O.B., C.S., A.L., S.S., M.S.), Department of Neurosurgery (B.J.), and Healthcare Telematics and Medical Engineering (A.B., S.G., G.R.), Otto von Guericke University, Magdeburg, Germany; and Siemens AG (Y.K., Y.D.-Z.), Healthcare Sector, Erlangen, Germany.

This work was supported by the Federal Ministry of Education and Research under grant FKZ 03IP710, and by Siemens AG, Healthcare Sector.

Please address correspondence to Oliver Beuing, MD, Institute of Neuroradiology, Otto von Guericke University Magdeburg, Leipziger Str 44, Magdeburg, 39120, Germany; e-mail: oliver.beuing@med.ovgu.de

Indicates open access to non-subscribers at www.ajnr.org

<http://dx.doi.org/10.3174/ajnr.A3973>

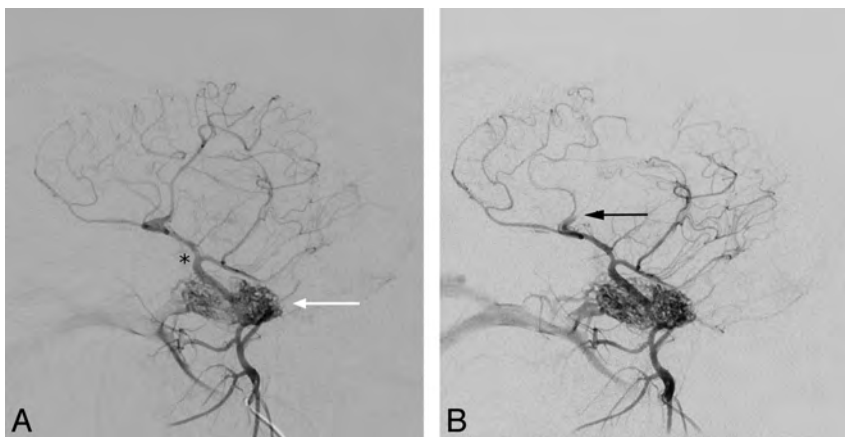


FIG 1. Intracranial vessels before (A) and after (B) vessel occlusion (black arrow). Contrast material was injected near the rete mirabile (white arrow in A). The MCA surfaces shortly after branching off the ICA (black asterisk in A), which also gives rise to the posterior cerebral artery. Due to early branching, the complete MCA territory was not affected.

formed by extracranial arteries at the skull base (Fig 1A). The vertebral arteries also join the rete. The intracranial vessels of both sides are connected via communicating arteries. Despite the anatomy, which does not allow direct access to the middle cerebral artery by catheterization, we chose sheep because of their gyrencephalic brain, which is larger than that in other animals used for experimental stroke studies.

The technique for surgical MCA occlusion has been described elsewhere in detail.¹⁵ In short, trepanation of the skull was followed by incision of the dura mater near where the MCA surfaces. The artery was then occluded by electrocoagulation. Due to anatomic variations in branching of the MCA, the M1 segment could not always be occluded. In 2 cases, only a large M2 branch was occluded. Intra-arterial DSA was performed before surgery to document the vascular anatomy and patency of the intracranial arteries and afterward to confirm artery occlusion (Fig 1B).

Data Acquisition

CBV and CBF perfusion measurements were performed with C-arm CT and with a conventional CT scanner. The C-arm of the flat panel angiography system is mounted on a robot arm (Artis zeego; Siemens, Erlangen, Germany), which, due to modifications of the software configuration, allows very fast serial forward and backward rotations, with data acquisition in both directions. With C-arm CT, 2 different protocols were tested. Each comprised 7 rotations (sweeps) of the C-arm before and after contrast administration (baseline and fill runs). The main differences between the 2 protocols lie in the duration of sweeps and the number of projections per rotation. The parameters for the first protocol (slow scan) were as follows: 7 sweeps with a duration of 4.43 seconds each; a 1.57-second pause between 2 sweeps; rotation angle, 200°; rotation speed, 60° per second; 248 projections per rotation; angulation step, 0.8°/frame. The second protocol (fast scan) also comprised 7 sweeps, but with a duration of 2.83 seconds each; a 1.57-second pause between rotations; rotation angle, 200°; rotation speed, 100° per second; 133 projections per rotation; angulation step, 1.5°/frame. The x-ray tube voltage was 90 kV in both protocols.

For CTP, a Somatom Emotion 6 (Siemens) was used. The animals were placed on the CT table in a supine position. The

head was tilted so that axial images oriented at the frontal skull base by using the topogram could be acquired. To minimize lateral tilting, we adjusted the head by using the laser guide. After contrast injection, the scan was started and the contrast bolus was followed for 60 seconds with 1 acquisition every second.

Identical injection parameters were used for C-arm CT and CTP: IV administration of 42-mL iomeprol (Iomeron 400; Bracco Imaging, Konstanz, Germany) with a power injector (Tennessee; Ulrich Medical, Ulm, Germany) with a flow rate of 6 mL/s and an x-ray delay of 12 seconds. The injection parameters were determined by testing different injection protocols with varying amounts of contrast media, flow rates, and delays in 2 animals not included in this study.

Total scan duration from the start of baseline runs to the end of the measurement amounted to approximately 100 seconds for the slow scan and 75 seconds for the fast scan and CTP, respectively. The radiation dose for the C-arm system was 1.2 μ Gy per projection based on the availability of the hardware and software at that time. Dose-length product was 1047 mGy-cm for CTP.

Because surgery was performed on the angiography table, imaging with C-arm CT was started immediately after postsurgical DSA. CTP was performed in the adjacent room within 15 minutes after perfusion measurement with C-arm CT. The animal was left in the CT scanner for 3 hours for the second postsurgical measurement and then transported back to the angiography suite. In addition, perfusion imaging with both modalities was performed before vessel occlusion. After completion of the protocols, the animals were euthanized.

Number of Datasets

Of 84 possible datasets in 7 sheep, only 60 (22 before and 38 after surgery) were evaluated (Table 1). Reasons for exclusion of data were death from cardiac failure during surgery ($n = 12$), failed vessel occlusion ($n = 8$), failed contrast injection ($n = 2$), and inability to open the datasets ($n = 2$). Because reconstruction of the data with the prototype software was time-consuming and performed after completion of the protocol, the failed contrast injection and the corruption of datasets were not observed during the course of the procedure. In the case of failed vessel occlusion, DSA could not confirm the success of the surgery. The reason was formation of a blood clot around a catheter that was left in the arteries feeding the rete mirabile for postsurgical DSA. As a result, ipsilateral DSA did not show intracranial vessels and contralateral DSA was not sufficient to depict the vessels on the operated side. Perfusion studies were performed nevertheless because the neurosurgeon was confident that the MCA was occluded.

Postprocessing and Data Analysis

The CTP data were calculated by using commercially available software (VPCT; Siemens) and also with prototype software

Table 1: Overview over the acquisition of datasets

	C-Arm 3 Seconds	C-Arm 5 Seconds	CTP Prototype ^a	CTP VPCT ^b
Sheep 1				
Pre	v	v	v	v
0 Hours	v	v	v	v
3 Hours	v	v	v	v
Sheep 2				
Pre	v	v	v	v
0 Hours	v	v	v	v
3 Hours	v	v	v	v
Sheep 3				
Pre	v	v	v	x
0 Hours	x	x	v	v
3 Hours	v	v	v	v
Sheep 4				
Pre	x	v	v	v
0 Hours	x	x	x	x
3 Hours	x	x	x	x
Sheep 5				
Pre	x	x	x	x
0 Hours	x	x	x	x
3 Hours	x	x	x	x
Sheep 6				
Pre	v	v	v	v
0 Hours	v	v	v	v
3 Hours	v	v	v	v
Sheep 7				
Pre	v	v	v	v
0 Hours	v	v	v	v
3 Hours	v	v	v	v
Total	14	15	16	15

Note:—Pre indicates data acquired before surgery; v, sets that were acquired as the protocol demanded and that were included in the evaluation; x, excluded datasets (The reasons are explained in the text).

^a Datasets acquired with CTP and calculated with the prototype software.

^b Datasets acquired with CTP and calculated with the commercial software VPCT (Siemens).

developed and provided by Siemens.¹⁶ This calculation was performed to find out whether the different software implementations would yield similar results with the same data and also to avoid a bias of one algorithm over the other. The data acquired with the C-arm CT were only compatible with the prototype software. So, at every time point (before surgery, immediately and 3 hours after surgery) 4 datasets, each consisting of 1 CBV and 1 CBF color map, were acquired per animal (Fig 2). MTT and TTP were not calculated because the prototype software was not optimized for these parameters.

The arterial input function was chosen manually at the ICA close to the site where it originates from the rete mirabile or the MCA on the side opposite the MCA occlusion (Fig 3). Both the time-attenuation curves and the arterial input functions are undersampled because of the limited temporal resolution (slow rotation) of the C-arm. Specifically, there is only 1 measurement time point per sweep. The intermediate values for all 1-second steps were determined by a bicubic spline interpolation.

Positioning of the head of the animals in the angiographic system was different from that in the CT scanner to allow uninhibited rotation of the C-arm. This required reformatting to generate comparable images concerning section orientation and thickness. Anatomic detail in the perfusion maps acquired was not sufficient to allow automatic registration, so matching of the CT and C-arm images had to be performed on a syngo worksta-

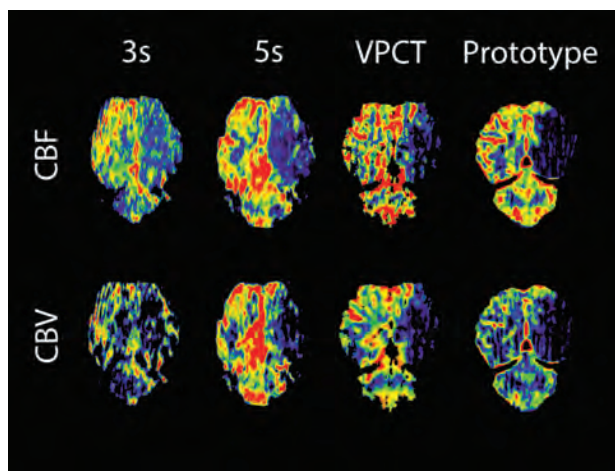


FIG 2. Color maps of CBF and CBV for all protocols 3 hours after vessel occlusion on the left side. Perfusion deficits are clearly visible, but image quality is impaired by streak artifacts, especially in the fast scan. The prototype is CTP data processed with the prototype software. VPCT is CTP data processed with commercial software.

tion (Siemens) on a visual basis by an experienced neuroradiologist who did not take part in the evaluation. The volume datasets acquired with the C-arm system were displayed on the workstation and adjusted by using reference lines, so that the final axial images paralleled the frontal lobe as it did in the CT images. The result of this procedure was directly compared with the timely matching CTP images of the same animal and was further corrected, if necessary, to achieve the best possible agreement.

After anonymization, the color maps were transferred to a certified OsiriX PRO workstation (aycan Digitalsysteme, Würzburg, Germany). They were randomly presented with regard to the time of acquisition and animal subject and were evaluated by 2 experienced neuroradiologists who were blinded to the surgical status. Each neuroradiologist was asked to decide whether perfusion abnormalities were present, and if present, to measure the size in the section exhibiting the largest lesion on a visual basis.

Statistical Analysis

Interobserver reliability was calculated by using the Cohen κ value and was classified according to the Landis and Koch¹⁷ scale. Sensitivity and specificity for the detection of perfusion deficits, with DSA-proved vessel occlusion serving as the criterion standard, were determined for each protocol and for both readers. For comparison of the measured sizes of the perfusion lesion, a 2-tailed Student *t* test was applied to search for differences between the 2 readers. A pair-wise testing was performed to compare the different protocols.

RESULTS

Interobserver agreement was “substantial” for the fast scan ($\kappa = 0.72$), “almost perfect” for the slow scan ($\kappa = 0.86$), and “perfect” for CTP ($\kappa = 1.00$). Sensitivity and specificity for the detection of perfusion lesions with the different protocols for both readers are outlined in Table 2. With regard to the C-arm protocols, specificity was higher and sensitivity was lower for the fast rather than the slow scans for both readers. For the data obtained with CTP and

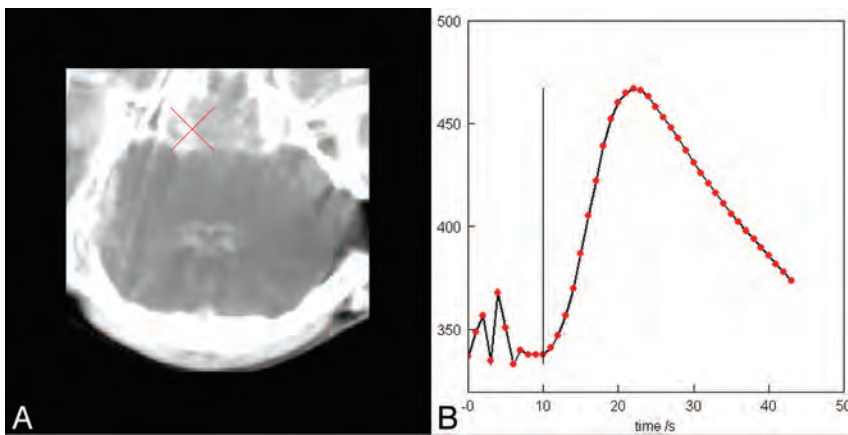


FIG 3. Manually chosen arterial input function in the ICA near the skull base and corresponding time-attenuation curve.

Table 2: Sensitivity and specificity for lesion detection shown separately for each reader and protocol

	Reader 1		Reader 2	
	Occl.	No Occl.	Occl.	No Occl.
Fast				
Positive	8	0	6	0
Negative	1	5	3	5
Sensitivity	88.9%		66.7%	
Specificity	100%		100%	
Slow				
Positive	9	1	8	1
Negative	0	5	1	5
Sensitivity	100%		88.9%	
Specificity	83.3%		83.3%	
Prototype				
Positive	10	0	10	0
Negative	0	6	0	6
Sensitivity	100%		100%	
Specificity	100%		100%	
VPCT				
Positive	10	0	10	0
Negative	0	5	0	5
Sensitivity	100%		100%	
Specificity	100%		100%	

Note:—Occl. indicates occlusion.

calculated with the commercial and the prototype software, sensitivity and specificity were 100%.

The average size of the CBF lesions as measured with CTP was $8.3 \pm 3.0 \text{ cm}^2$; and for CBV, $7.1 \pm 2.7 \text{ cm}^2$. Compared with CTP, the sizes of those lesions that were correctly identified by both readers in the C-arm protocols did not differ significantly in pairwise testing. Reader 2 tended to measure smaller sizes than reader 1, but this difference was significant only for CBV immediately after surgery ($P = .039$). CBF lesions were significantly larger than CBV lesions in all protocols ($P = .006$ for the slow scan, for the other protocols $P < .001$). No significant changes of CBF lesion sizes were noted with time ($P = .33$). In contrast, CBV lesions were significantly larger 3 hours after vessel occlusion than immediately after surgery ($P = .034$). Reader 1 correctly identified perfusion deficits in 3 datasets that were not detected by reader 2. Reader 2 did not detect a lesion that was overlooked by reader 1.

DISCUSSION

In ischemic stroke, several factors influence patient outcome. These comprise, among others, time from symptom onset to recanalization, collateral flow, thrombus size, and location of the vessel occlusion. IV thrombolysis is the standard therapy for patients without contraindications and presenting within 4.5 hours after symptom onset, but endovascular therapy may be more effective in patients with occlusion of major cerebral arteries. Additionally, several works indicate that interventional recanalization might be beneficial in patients presenting outside the therapeutic window accepted for IV thrombolysis.^{18,19} However, this rela-

tively new treatment option has drawbacks as well. One is the invasive nature of the procedure with the risk of severe or fatal complications. Consequently, interventional treatment should only be performed in cases with a reasonable chance for improvement of outcome. This alone requires more detailed information regarding the ratio of ischemic core to penumbra than is necessary for initiation of IV thrombolysis. There is evidence that perfusion imaging, though not generally recommended for treatment decisions, serves the purpose of proper patient selection.²⁰⁻²² It might help not only in deciding whether to treat patients but also in refraining from therapy even if the patient presents early after symptom onset. Another drawback of endovascular recanalization is that the time from imaging to treatment start is substantially longer than that for IV thrombolysis. Perfusion imaging is only a snapshot of a dynamic process that cannot predict the speed at which ischemia becomes final infarction. Therefore, saving time is also an essential requirement in optimizing both the efficacy and safety of interventional therapy.

Because performing imaging in the angiographic suite by using the novel C-arm CT addresses both issues, this small study was performed to evaluate whether it is possible, with the described technique, to gain relevant information about brain perfusion with the same device used for therapy, and, consequently, to save time.

The results are encouraging because perfusion lesions were detected in a high or very high percentage with the tested C-arm CT protocols in animals with DSA-proved vessel occlusion. Compared with CTP, the sensitivity was lower for most C-arm CT protocols, but on the other hand, all lesions were small, with the largest matching the size of the human basal ganglia.

The sizes of the perfusion deficits varied considerably among the animals. These differences were due to anatomic variations of the MCA. In some animals, early branching of the MCA was observed and not all branches could be visualized after surfacing. This finding resulted in partial MCA infarction. In other cases, electrocoagulation apparently led to occlusion of the ICA with infarction of the whole anterior circulation territory. Nevertheless, pairwise testing revealed comparable results with regard to size for the C-arm protocols and CTP. The smallest correctly identified lesion had an area of only approximately 2.5 cm^2 . That

reader 2 tended to measure a smaller size for all lesions might be the effect of evaluating datasets of the whole brain. Different sections might have been chosen. However, a more conservative approach to measurement might be taken into account as well.

Size differences between CBF and CBV lesions were measured at both time points, and CBV lesions were larger after 3 hours than immediately after surgery. These size differences of the CBV lesions were significant with all protocols. This finding probably reflects growth of the infarct core with time. That enlargement of CBV lesions found in all protocols and not only in CTP suggests that C-arm CT might be capable of depicting changes of brain perfusion, even if small. This possibility might have an impact on treatment decisions. Perfusion measurement with C-arm CT can be performed not only before therapy but at any time during endovascular stroke intervention. There are thus scenarios in which this information might influence treatment decisions. One such situation could be a difficult intervention with partial recanalization. If no improvement of functional outcome can be expected, the intervention might as well be terminated so that the patient is not exposed to unnecessary risk of complications due to the intervention. In addition, stent placement in the acute phase with all its negative consequences such as dual-antiplatelet therapy might be avoided if perfusion maps indicate a large infarct with little viable parenchyma. Of course, the presented data cannot serve as a basis for validating the use of this technique for such decisions. However, the encouraging results support further effort to reach the goal of making stroke imaging in the angiography suite feasible. C-arm CT already allows the exclusion of intracranial hemorrhage in many cases, and intracranial vessels can be well-depicted.²³⁻²⁶ Also, measurement of CBV was feasible by using a C-arm CT.¹⁰⁻¹² The described technique may additionally provide information about dynamic perfusion parameters.

There are several limitations in this study. First, only a small number of animals were examined. Therefore, the results should be interpreted with caution concerning statistical significance. Nevertheless, a positive trend with regard to lesion detection seems to exist. The complete and irreversible occlusion of a major intracranial artery led to large CBV lesions already in the early phase. Therefore, their enlargement was only slight, and significance might have occurred by chance. Therefore, whether progression of the core infarct can be depicted with C-arm CT remains unclear with this small sample number.

Second, we did not quantify perfusion changes. One reason was that the slow temporal sampling rate leads to an underestimation of the arterial input function; consequently, because CBF values are inversely proportional to the area under the arterial input function, CBF would have been overestimated.²⁷ Moreover, our focus was to find out whether assessment of dynamic perfusion parameters was feasible in a new large-animal model. However, quantification is possible as was demonstrated by Ganguly et al.¹³ They stated that CBF measured with C-arm cone beam CT correlated well with that from CTP, but in this work, multiple injections and multiple acquisitions were performed to overcome the temporal resolution limits of the C-arm system, whereas we chose a protocol with a single injection and only 1 fill run.

Third, we chose sheep for our experiments because the technique of surgical occlusion was described and sheep have a larger,

gyrencephalic brain, as opposed to that in most other animal stroke models. However, we were not aware that the attenuated bony anatomy of the sheep skull would cause such marked streak artifacts compared with humans. We did not appreciate this drawback during the experiments because postprocessing was performed after having completed the protocol for the animal. When we realized the occurrence of these artifacts, we initially tried to eliminate other possible causes like movement induced by the ventilation tube, exact centering of the brain, or minimizing overlying material needed for anesthesia. The artifacts were more pronounced in the fast scans. Although image quality was not assessed systematically, these artifacts might explain the lower sensitivity compared with the other protocols.

Finally, to ensure the best possible image quality, we chose a high-system x-ray dose. It is likely that new system hardware and advanced software will provide further dose reduction in the future. A dose measurement with an Alderson phantom is being planned.

CONCLUSIONS

With the described technique, we demonstrated that measurement of CBV and, additionally, CBF as a dynamic perfusion parameter is feasible by using the novel C-arm system. Information about brain perfusion considered helpful in modern concepts of diagnosis and treatment of acute ischemic stroke may be derived with the same device. This small study supports the effort of further development of a technique that may have the potential to improve management of patients with acute severe stroke by saving time from diagnosis to treatment and by adding information for proper patient selection.

Disclosures: Oliver Beuing—*RELATED: Grant:* Siemens AG Healthcare Sector,* Federal Ministry of Education and Research,* *Comments:* The money was used for purchase of the sheep; the facility in which the perfusion studies were performed was supported by the Federal Ministry for Education and Research. Axel Boese—*RELATED: Grant:* BMBF FKZ 03IP710 INKA,* *Provision of Writing Assistance, Medicines, Equipment, or Administrative Support:* Siemens AG, Healthcare Sector, Erlangen, Germany,* *Comments:* The manufacturer provided sponsored research funding through channels approved by Otto-von-Guericke University; the manufacturer provided equipment for this study and donated all costs associated with the animal study. Cordula Scherlach, Anja Lenz, Steffen Serowy, Georg Rose—*RELATED: Grant:* Siemens AG, Healthcare Sector,* Federal Ministry of Education and Research,* Sebastian Gugel—*RELATED: Support for Travel to Meetings for the Study or Other Purposes:* Siemens,* *Provision of Writing Assistance, Medicines, Equipment, or Administrative Support:* Siemens.* Martin Skalej—*RELATED: Grant:* Siemens Erlangen, Germany,* *Comments:* The grant was to pay service costs of a professional animal lab. *Money paid to the institution.

REFERENCES

1. **Tissue plasminogen activator for acute ischemic stroke: the National Institute of Neurological Disorders and Stroke rt-PA Stroke Study Group.** *N Engl J Med* 1995;333:1581-87
2. Lees KR, Bluhmki E, von Kummer R, et al. **Time to treatment with intravenous alteplase and outcome in stroke: an updated pooled analysis of ECASS, ATLANTIS, NINDS, and EPITHET trials.** *Lancet* 2010;375:1695-703
3. Sandercock P, Wardlaw JM, Lindley RI, et al. **The benefits and harms of intravenous thrombolysis with recombinant tissue plasminogen activator within 6 h of acute ischaemic stroke (the third International Stroke Trial [IST-3]): a randomised controlled trial.** *Lancet* 2012;379:2352-63
4. Mattle HP, Arnold M, Georgiadis D, et al. **Comparison of intraarte-**

- rial and intravenous thrombolysis for ischemic stroke with hyperdense middle cerebral artery sign. *Stroke* 2008;39:379–83
5. Penumbra Pivotal Stroke Trial Investigators. **The Penumbra Pivotal Stroke Trial: safety and effectiveness of a new generation of mechanical devices for clot removal in intracranial large vessel occlusive disease.** *Stroke* 2009;40:2761–68
 6. Dávalos A, Pereira VM, Chapot R, et al. **Retrospective multicenter study of Solitaire FR for revascularization in the treatment of acute ischemic stroke.** *Stroke* 2012;43:2699–705
 7. Nogueira RG, Lutsep HL, Gupta R, et al. **Trevo versus Merci retrievers for thrombectomy revascularisation of large vessel occlusions in acute ischaemic stroke (TREVO 2): a randomised trial.** *Lancet* 2012;380:1231–40
 8. Saver JL, Jahan R, Levy EI, et al. **Solitaire flow restoration device versus the Merci retriever in patients with acute ischaemic stroke (SWIFT): a randomised, parallel-group, non-inferiority trial.** *Lancet* 2012;380:1241–49
 9. Lev MH. **Perfusion imaging of acute stroke: its role in current and future clinical practice.** *Radiology* 2013;266:22–27
 10. Struffert T, Deuerling-Zheng Y, Engelhorn T, et al. **Feasibility of cerebral blood volume mapping by flat panel detector CT in the angiography suite: first experience in patients with acute middle cerebral artery occlusions.** *AJNR Am J Neuroradiol* 2012;33:618–25
 11. Struffert T, Deuerling-Zheng Y, Kloska S, et al. **Cerebral blood volume imaging by flat detector computed tomography in comparison to conventional multislice perfusion CT.** *Eur Radiol* 2011;21:882–89
 12. Bley T, Strother CM, Pulfer K, et al. **C-arm CT measurement of cerebral blood volume in ischemic stroke: an experimental study in canines.** *AJNR Am J Neuroradiol* 2010;31:536–40
 13. Ganguly A, Fieselmann A, Marks M, et al. **Cerebral CT perfusion using an interventional C-arm imaging system: cerebral blood flow measurements.** *AJNR Am J Neuroradiol* 2011;32:1525–31
 14. Royalty K, Manhart M, Pulfer K, et al. **C-arm CT measurement of cerebral blood volume and cerebral blood flow using a novel high-speed acquisition and a single intravenous contrast injection.** *AJNR Am J Neuroradiol* 2013;34:2131–38
 15. Boltze J, Forschler A, Nitzsche B, et al. **Permanent middle cerebral artery occlusion in sheep: a novel large animal model of focal cerebral ischemia.** *J Cereb Blood Flow Metab* 2008;28:1951–64
 16. Fieselmann A, Dennerlein F, Deuerling-Zheng Y, et al. **A model for filtered backprojection reconstruction artifacts due to time-varying attenuation values in perfusion C-arm CT.** *Phys Med Biol* 2011;56:3701–17
 17. Landis JR, Koch GG. **The measurement of observer agreement for categorical data.** *Biometrics* 1977;33:159–74
 18. Abou-Chebl A. **Endovascular treatment of acute ischemic stroke may be safely performed with no time window limit in appropriately selected patients.** *Stroke* 2010;41:1996–2000
 19. Turk A, Magarik JA, Chaudry I, et al. **CT perfusion-guided patient selection for endovascular treatment of acute ischemic stroke is safe and effective.** *J Neurointerv Surg* 2012;4:261–65
 20. Bivard A, McElduff P, Spratt N, et al. **Defining the extent of irreversible brain ischemia using perfusion computed tomography.** *Cerebrovasc Dis* 2011;31:238–45
 21. Davis S, Campbell B, Christensen S, et al. **Perfusion/diffusion mismatch is valid and should be used for selecting delayed interventions.** *Transl Stroke Res* 2012;3:188–97
 22. Kamalian S, Maas MB, Goldmacher GV, et al. **CT cerebral blood flow maps optimally correlate with admission diffusion-weighted imaging in acute stroke but thresholds vary by postprocessing platform.** *Stroke* 2011;42:1923–28
 23. Struffert T, Eyupoglu IY, Huttner HB, et al. **Clinical evaluation of flat-panel detector compared with multislice computed tomography in 65 patients with acute intracranial hemorrhage: initial results: clinical article.** *J Neurosurg* 2010;113:901–07
 24. Blanc R, Pistocchi S, Babic D, et al. **Intravenous flat-detector CT angiography in acute ischemic stroke management.** *Neuroradiology* 2012;54:383–91
 25. Jeon JS, Sheen SH, Hwang GJ, et al. **Feasibility of intravenous flat panel detector CT angiography for intracranial arterial stenosis.** *AJNR Am J Neuroradiol* 2013;34:129–34
 26. Doelken M, Struffert T, Richter G, et al. **Flat-panel detector volumetric CT for visualization of subarachnoid hemorrhage and ventricles: preliminary results compared to conventional CT.** *Neuroradiology* 2008;50:517–23
 27. Konstas AA, Goldmakher GV, Lee TY, et al. **Theoretic basis and technical implementations of CT perfusion in acute ischemic stroke. Part 1. Theoretic basis.** *AJNR Am J Neuroradiol* 2009;30:662–68

Time-Shift Homotopic Connectivity in Mesial Temporal Lobe Epilepsy

Q. Xu, Z. Zhang, W. Liao, L. Xiang, F. Yang, Z. Wang, G. Chen, Q. Tan, Q. Jiao, and G. Lu



ABSTRACT

BACKGROUND AND PURPOSE: Voxel-mirrored intrinsic functional connectivity allows the depiction of interhemispheric homotopic connections in the human brain, whereas time-shift intrinsic functional connectivity allows the detection of the extent of brain injury by measuring hemodynamic properties. We combined time-shift voxel-mirrored homotopic connectivity analyses to investigate the alterations in homotopic connectivity in mesial temporal lobe epilepsy and assessed the value of applying this approach to epilepsy lateralization and the prediction of surgical outcomes in mesial temporal lobe epilepsy.

MATERIALS AND METHODS: Resting-state functional MR imaging data were acquired from patients with unilateral mesial temporal lobe epilepsy ($n = 62$) (31 left- and 31 right-side) and healthy controls ($n = 33$). Dynamic interhemispheric homotopic architecture seeding from each hemisphere was individually calculated by 0, 1, 2, and 3 repetition time time-shift voxel-mirrored homotopic connectivity. Voxel-mirrored homotopic connectivity maps were compared between the patient and control groups by using 1-way ANOVA for each time-shift condition, separately. Group comparisons were further performed on the laterality of voxel-mirrored homotopic connectivity in each time-shift condition. Finally, we correlated the interhemispheric homotopic connection to the surgical outcomes in a portion of the patients ($n = 20$).

RESULTS: The patients with mesial temporal lobe epilepsy showed decreased homotopic connectivity in the mesial temporal structures, temporal pole, and striatum. Alterations of the bihemispheric homotopic connectivity were lateralized along with delays in the time-shift in mesial temporal lobe epilepsy. The patients with unsuccessful surgical outcomes presented larger interhemispheric voxel-mirrored homotopic connectivity differences.

CONCLUSIONS: This study showed whole patterns of dynamic alterations of interhemispheric homotopic connectivity in mesial temporal lobe epilepsy, extending the knowledge of abnormalities in interhemispheric connectivity in this condition. Time-shift voxel-mirrored homotopic connectivity has the potential for lateralization of unilateral mesial temporal lobe epilepsy and may have the capability of predicting surgical outcomes in this condition.

ABBREVIATIONS: HC = healthy controls; mTLE = mesial temporal lobe epilepsy; ts = time-shift; VMHC = voxel-mirrored homotopic connectivity

Interhemispheric communication and coordination facilitate information processing in the human brain.^{1,2} Thus homotopic connections represent a fundamental characteristic of brain anat-

omy and function^{3,4} and have been considered an important indicator for depicting the physiologic and pathologic features of the brain. On the basis of resting-state functional MR imaging measurements, an approach based on voxel-mirrored homotopic connectivity (VMHC) quantifies the interhemispheric homotopic connections by measuring the functional connectivity between each voxel in 1 hemisphere and its mirrored counterpart.⁵ Zuo et al⁵ found age-related increases in interhemispheric functional connectivity in the primary sensorimotor areas and de-

Received November 21, 2013; accepted after revision January 31, 2014.

From the Departments of Medical Imaging (Q.X., Z.Z., W.L., L.X., Q.J., G.L.), Neurology (F.Y., G.C.), and Neurosurgery (Q.T.), Jinling Hospital, Nanjing University School of Medicine, Nanjing, China; Center for Cognition and Brain Disorders and the Affiliated Hospital (W.L.), Hangzhou Normal University, Hangzhou, China; Zhejiang Key Laboratory for Research in Assessment of Cognitive Impairments (W.L.), Hangzhou, China; Department of Medical Imaging (Z.W.), Nanjing Drum Tower Hospital, The Affiliated Hospital of Nanjing University Medical School, Nanjing, China; and Department of Medical Imaging (Q.J.), Taishan Medical College, TaiAn, China.

This work was supported by the Natural Science Foundation of China (grant nos. 81271553, 81201155, 81201078, 81171328, 61131003, and 81020108022), Grants for Young Scholar of Jinling Hospital (grant nos. 2011060, 2011045, and 2011061), Chinese Key Grant (BWS11J063 and 10z026), and the China Postdoctoral Science Foundation (grant no. 2013M532229).

Please address correspondence to Zhiqiang Zhang, MD, and Guangming Lu, MD, Department of Medical Imaging, Nanjing Jinling Hospital, 305#, Eastern Zhongshan Rd, Nanjing 210002, China; e-mail: zhangzq2001@126.com (Z.Z.) or cjr.luguangming@vip.163.com (G.L.)

Indicates open access to non-subscribers at www.ajnr.org

Indicates article with supplemental on-line table.

<http://dx.doi.org/10.3174/ajnr.A3934>

Demographic and clinical information of patients and healthy controls

Characteristic	L-mTLE (n = 31)	R-mTLE (n = 31)	HC (n = 33)	ANOVA (P Value)	L-mTLE vs R-mTLE (P Value)	L-mTLE vs HC (P Value)	R-mTLE vs HC (P Value)
Age (yr)	26.5 ± 8.4	29.7 ± 8.5	26.7 ± 7.3	.231 ^a	.146 ^c	.903 ^c	.144 ^c
Sex	19 M/12 F	16 M/15 F	21 M/12 F	.592 ^b	.442 ^d	.846 ^d	.330 ^d
Successful outcome	8	6	N/A	N/A	N/A	N/A	N/A
Unsuccessful outcome	4	2	N/A	N/A	N/A	N/A	N/A

Note:—N/A indicates not applicable; L, left; R, right.

^a One-way analysis of variance.

^b Kruskal-Wallis ANOVA.

^c Two-sample *t* test.

^d χ^2 test.

creases in the higher order processing areas, which provided insight into the evolution of brain development. Studies have also revealed specific alterations of homotopic connection in a cohort of brain diseases.^{6–8} Decreased VMHC in schizophrenia has been suggested to reflect the substantial impairment of interhemispheric coordination in these patients.⁶ Anderson et al⁷ found homotopic connectivity alterations related to behavioral and developmental abnormalities in autism.⁷ More recently, studies have further correlated functional homotopic connectivity with microstructural impairment in multiple sclerosis⁸ and idiopathic generalized epilepsy.⁹

In contrast to the brain disorders featuring abnormal connection pathways as mentioned above,^{6,8} mesial temporal lobe epilepsy (mTLE) is a location-related disease characterized by hippocampal sclerosis.¹⁰ Unilateral mTLE can cause bilateral and distributed brain impairments due to seizure propagation via the mesial temporal epileptic network.^{11–13} Resting-state fMRI studies have shown asymmetric connections between bihemispheres^{14–16} and decreased connectivity between bilateral hippocampi in mTLE.^{17,18} These findings suggest that there are intra- and interhemispheric connection abnormalities in unilateral mTLE. However, neither the homotopic alterations of whole-brain functional connectivity nor the relationship between asymmetric lesions and interhemispheric communication in this disease has been investigated.

fMRI-based VMHC provides a feasible way to observe the whole-brain homotopic connectivity alterations in mTLE. However, the conventional nondirectional functional connectivity measure, as used in VMHC, cannot detect the connection abnormalities resulting from deficits of the seed or target region. Recently, Lv et al¹⁹ proposed a time-shift (ts) analysis for resting-state functional connectivity. They quantified the temporal shift correlation between time courses of each voxel and global mean signal¹⁹ and correlated the time shifts with the extent and degree of perfusion delay in patients with stroke.^{19,20} In addition, our previous study used time-shift correlation analysis to demonstrate the sequential effects of epileptic discharges on intrinsic network connectivity in children with absence epilepsy.²¹ Thus, time-shift delays in resting-state spontaneous connectivity were assumed to reflect brain hemodynamics and could measure the degree of brain injury; time-shift analysis also provides directional information as a measure of functional connectivity.²¹ In the current work, we combined the time-shift connectivity with the VMHC technique and applied them to resting-state fMRI data from patients with unilateral mTLE. We hypothesized that this strategy would allow us to assess the whole-brain homotopic con-

nection impairments resulting from different hemispheres and may potentially be a tool for epileptic focus lateralization and surgical outcome prediction in mTLE.

MATERIALS AND METHODS

Subjects

Sixty-two patients with unilateral mTLE (31 left-sided and 31 right-sided) were recruited (demographic and clinical information are detailed in the Table). Part of the patient population (23 patients with left-sided mTLE) was reported in our previous work in which the Granger causal information of the hippocampus in left-sided mTLE was estimated.¹³ Diagnosis of mTLE was performed according to the International League Against Epilepsy 2001 classification based on a comprehensive evaluation, including seizure history and semiology, neurologic examination, diagnostic MR imaging, and electroencephalography records in all patients. Patients were selected on the basis of several criteria: 1) Patients who were young and middle-aged were included (patients younger than 18 years or older than 50 years were excluded); 2) patients who exhibited identifiable structural MR imaging abnormalities other than hippocampal sclerosis, such as cortical dysplasia, vascular malformation, or tumor were excluded. Twenty patients of the 62 underwent standard anterior temporal lobectomy: Fourteen cases (8 left- and 6 right-sided mTLE) had successful surgical outcomes, and 6 cases (4 left- and 2 right-sided mTLE) had unsuccessful outcomes. A successful outcome was defined as seizure-free with or without auras at the latest follow-up that occurred at least 1 year after the surgery, which satisfies the International League Against Epilepsy Outcome Criteria 1 or 2²² and Engel category 1A or 1B.²³ No postoperative MR imaging data were used in this article.

Moreover, healthy controls (HC) (*n* = 33) were recruited from the hospital staff. These controls did not have neurologic or psychiatric disorders at the time of the study. There were no differences in ages and sexes between the controls and patients (Table).

This study was approved by the local Medical Ethics Committee, and written informed consent was obtained from all the participants.

Data Acquisition

We acquired functional and structural images in patients and HC by using a Trio 3T scanner (Siemens, Erlangen, Germany). We used foam padding to minimize head motion. We acquired resting-state functional images by using a single-shot, gradient-recalled echo-planar imaging sequence (250 volumes, TR = 2000 ms, TE = 30 ms, flip angle = 90°, FOV = 240 × 240 mm²,

intersection gap = 0.4 mm, voxel size = $3.75 \times 3.75 \times 4 \text{ mm}^3$, 30 transverse sections aligned along the anterior/posterior commissure). Subjects were instructed simply to rest with their eyes

closed, not to think about anything in particular, and not to fall asleep. Subsequently, we acquired high-resolution 3D T1-weighted anatomic images in a sagittal orientation by using a magnetization-prepared rapid acquisition of gradient echo sequence (TR = 2300 ms, TE = 2.98 ms, flip angle = 9° , FOV = $256 \times 256 \text{ mm}^2$, voxel size = $1 \times 1 \times 1 \text{ mm}^3$, 176 sections without intersection gap).

Data Preprocessing

Functional image preprocessing was performed by using the DPARSF 2.2 (<http://www.restfmri.net>) and SPM8 (Wellcome Department of Imaging Neuroscience, London, UK; <http://www.fil.ion.ucl.ac.uk/spm>) toolkits. We excluded the first 10 images to ensure steady-state longitudinal magnetization, and then we corrected the remaining images for temporal differences and head motion. No translation or rotation parameters in any given dataset exceeded $\pm 1 \text{ mm}$ or $\pm 1^\circ$. We then coregistered individual 3D T1 images to functional images. The 3D T1-weighted anatomic images were segmented into gray matter, white matter, and CSF by using unified segmentation.²⁴ Then, a nonlinear spatial deformation was calculated from the gray matter images to a gray

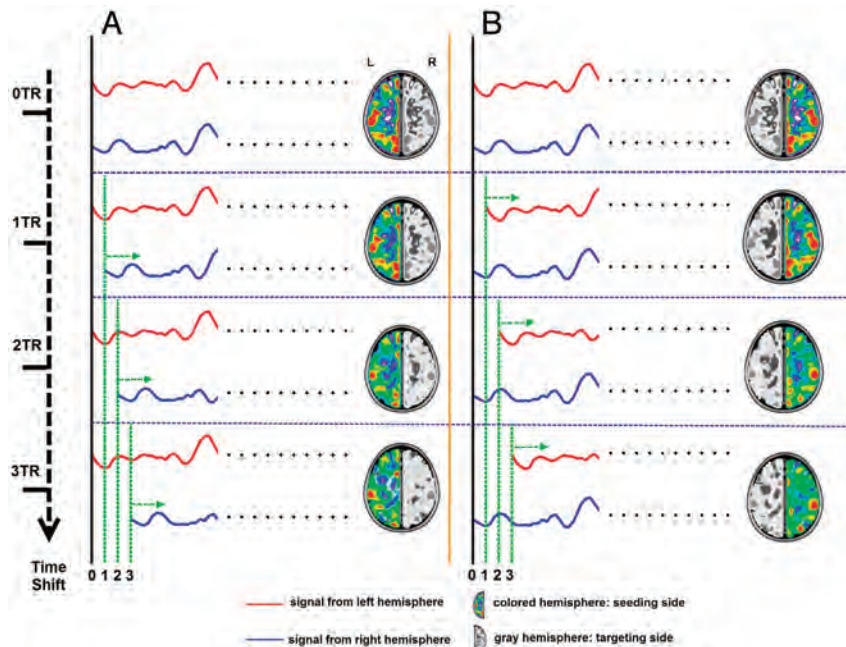


FIG 1. Workflow for time-shift voxel-mirrored homotopic connectivity calculation. *A*, Ts-VMHC of seeding from the left hemisphere. The left side was set as the seeding side; the right side, as the targeting side. The 0 TR, 1 TR, 2 TR, and 3 TR shifted time-courses of each voxel on the targeting side (blue line) were separately correlated with the time course of the mirrored voxel on the seeding side (red line), which generated 0 TR, 1 TR, 2 TR, and 3 TR ts-VMHC hemispheric maps of the seeding (left) side. *B*, Similarly, 4 hemispheric ts-VMHC maps of the right side were also generated when taking the right hemisphere as the seeding side and the left hemisphere as the targeting side.

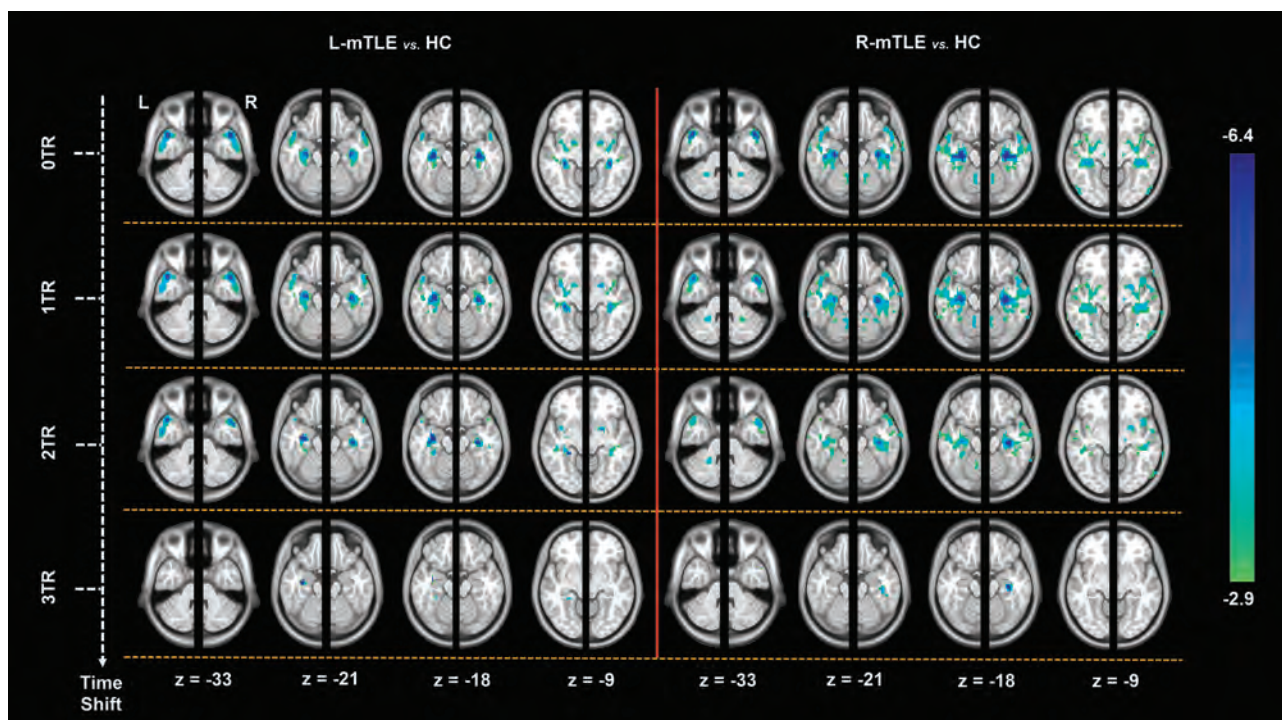


FIG 2. Group comparisons of ts-VMHC maps between the patients and healthy controls. The left and right hemispheric ts-VMHC maps (0 TR, 1 TR, 2 TR, and 3 TR) of each patient group were compared with those of the HC by using 2-sample *t* tests ($P < .05$, AlphaSim corrected) under ANOVA. For a better visualization, we combined the comparison results of the left and right hemispheric ts-VMHC maps with a whole-brain map. The mesial temporal structures, limbic/paralimbic areas, and striatum areas show time-shift-dependent VMHC decreases.

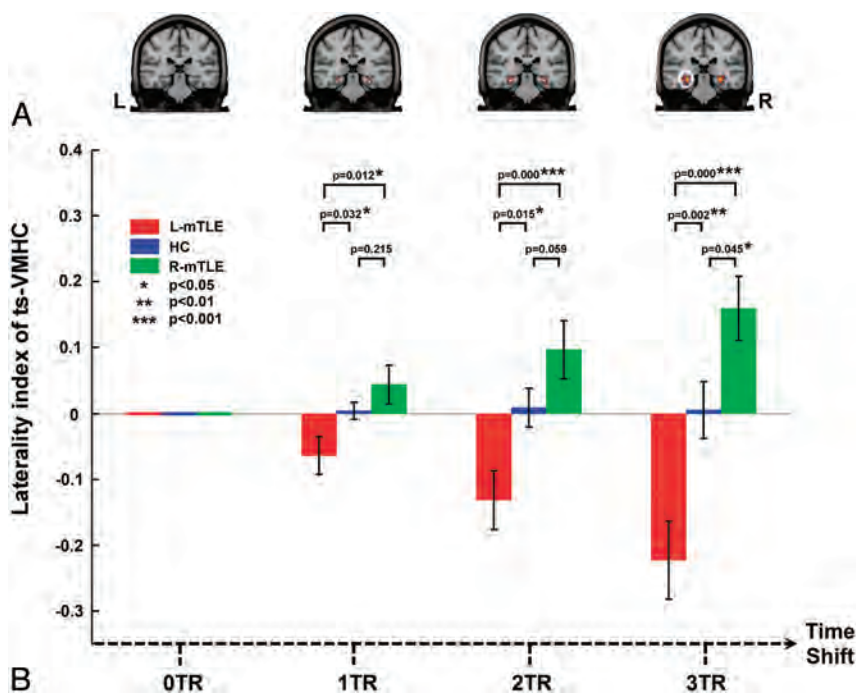


FIG 3. Lateral index analysis of ts-VMHC in mTLE. *A*, Group comparisons of voxelwise laterality maps of ts-VMHC. Along with the delay of time shifts, a more significant difference of VMHC laterality was found among the patient groups and healthy controls. *B*, Region of interest–based laterality analysis confirmed the above results. The region of interest was selected from the group comparing the result of voxelwise laterality map of ts-VMHC (white circle).

matter template in Montreal Neurological Institute space. This transformation was then applied to the functional images, which were resectioned at a resolution of $3 \times 3 \times 3$ mm³. The data were bandpass-filtered (0.01–0.08 Hz). Linear regression was performed to remove the effect of 6 head-motion-averaged signals from the CSF, white matter, and the global brain signal.²⁵ The residual images were further coregistered to a symmetric template according to previous studies.^{5,8} The symmetric template was created as follows: First, all participants' normalized gray matter images were averaged to create a mean normalized gray matter template. This template was then averaged with its left-right mirrored version to generate a group-specific symmetric template.⁵ Finally, we spatially smoothed the images with an 8-mm full width at half maximum isotropic Gaussian kernel.

Time-Shift Voxel-Mirrored Homotopic Connectivity

We combined the time-shift analysis¹⁹ with voxel-mirrored homotopic connectivity analysis.⁵ We first took the left hemisphere as the seeding side and the right hemisphere as the targeting side. The 0 TR, 1 TR, 2 TR, and 3 TR shifted time-courses of each voxel on the targeting side were separately correlated with the time course of the mirrored voxel on the seeding side, which generated 0 TR, 1 TR, 2 TR, and 3 TR ts-VMHC hemispheric maps of the seeding (left) side. Similarly, 4 hemispheric ts-VMHC maps of the right side were also generated when taking the right hemisphere as the seeding side and the left hemisphere as the targeting side (Fig 1). The correlation maps were then converted to z scores by using the Fisher r-to-z transformation.

Group Comparisons of ts-VMHC

In the second-level analyses, the left and right hemispheric ts-VMHC maps (0 TR, 1 TR, 2 TR, and 3 TR) of each patient group were compared with those of the HC by using a 2-sample *t* test (AlphaSim corrected $P < .05$, combined height threshold $P < .01$, and extent threshold $k > 20$ voxels). For a better visualization, we combined the comparison results of the left and right hemispheric ts-VMHC maps with a whole-brain map (Fig 2 and On-line Table).

Laterality Analyses of ts-VMHC

To quantitatively identify the difference between the left and right hemispheric ts-VMHC and to further determine whether the ts-VMHC could be used for mTLE lateralization, we performed a voxelwise laterality analysis. In each individual of all 3 participant groups, the right hemispheric ts-VMHC map was subtracted from the left hemispheric ts-VMHC map and the results were divided by the summation of both maps. Then the laterality (hemispheric) maps of all 3 groups of participants were compared by using 1-way ANOVA implemented in SPM8 in each time-shift condition ($P < .05$, AlphaSim correction). Then, a post hoc region of interest–based analysis was subsequently performed. The ROIs were selected from the above ANOVA result in 3 TR time-shift conditions. The laterality values in the ROIs were extracted for ANOVA among the 3 participant groups (Fig 3).

Predicting Surgical Outcomes of ts-VMHC

We performed a preliminary analysis to retrospectively investigate the relationship between ts-VMHC and surgical outcomes of mTLE. Twenty patients who underwent anterior temporal lobectomy were included. The patients with right-sided mTLE (R-mTLE) were left-right flipped to produce a homogeneous left-sided mTLE dataset. We calculated the difference of VMHC between bihemispheres by subtracting the connectivity values of the contralateral side from those of the lesional side (ie, the epileptogenic side). Subsequently, the interhemispheric differences were compared by using 2-sample *t* tests between the patients with successful surgical outcomes and those with unsuccessful outcomes.

RESULTS

Group Comparison Results of ts-VMHC

On the basis of the comparison of the results of VMHC without time-shift (ie, 0 TR shift), both patient groups showed decreased homotopic connectivity in the regions of limbic/paralimbic areas (mainly in the mesial temporal structures including the hippocampus/parahippocampus, temporal pole, amygdala, and insula) and striatum areas (mainly in the putamen and pallidum) relative to the HC ($P < .05$ AlphaSim correction). Along with the

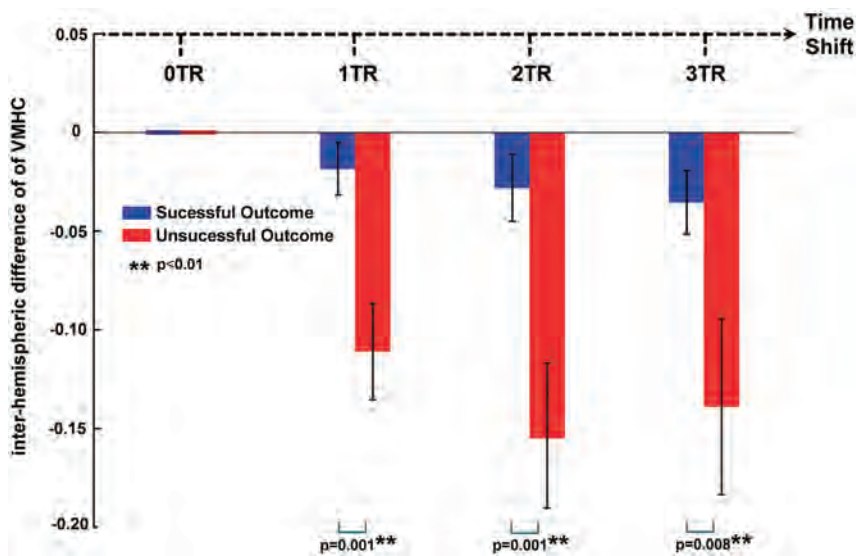


FIG 4. Ts-VMHC and prediction of surgical outcomes of mTLE. The interhemispheric VMHC differences were compared by using 2-sample *t* tests between the patients with successful surgical outcomes and those with unsuccessful outcomes. The patients with unsuccessful surgical outcomes had larger differences than those with successful outcomes at each time-shift condition. Moreover, along with the time shifts, the interhemispheric VMHC differences increased in both the groups.

time-shift delays, the decreases in homotopic connectivity in both hemispheres tended to be weaker, whereas the decreases on the lesioned side (ie, the left side in the left-sided mTLE and the right side in the right-sided mTLE patients) were more persistent. Until the 3 TR shift, only the difference in the mesial temporal structures of the lesioned side survived. No increase in homotopic connectivity was detected in the patient groups (On-line Table and Fig 2).

Laterality Analyses of ts-VMHC

Along with the time-shift delays at 1 TR, 2 TR, and 3 TR, the results of the 1-way ANOVA among subject groups showed more significant laterality of homotopic connectivity in the mesial temporal structures. Post hoc region-of-interest analyses repeated the above 3 TR time-shifted ANOVA results (Fig 3). Along with time shifts of 1 TR, 2 TR, and 3 TR, the difference between the patients with left-sided mTLE and those with right-sided mTLE became more significant ($P = .001$ in 1 TR, $P < .001$ in 2 TR, and $P < .001$ in 3TR).

Predicting Surgical Outcomes

The preliminary analysis correlating ts-VMHC with surgical outcomes showed that the patients with unsuccessful surgical outcomes had larger VMHC differences between the hemispheres than those with successful outcomes at each time-shift condition (1 TR-shifted, $P = .001$; 2 TR-shifted, $P = .001$; 3 TR-shifted, $P = .008$). Moreover, along with time shifts of 1 TR, 2 TR, and 3 TR, the interhemispheric VMHC differences increased in both the groups with successful and unsuccessful outcomes (Fig 4).

DISCUSSION

In this study, we innovatively combined time-shift functional connectivity analysis with VMHC analysis and applied them to data from patients with unilateral mTLE. First, our results showed

decreased homotopic connectivity in the mesial temporal structures, temporal pole, and striatum in mTLE, which provided the first complete picture of inter-hemispheric connectivity abnormalities in mTLE. Second, we found that the alterations in the bihemispheric homotopic connectivity led to lateralization along with time-shift delays in patients with mTLE. This finding suggests that ts-VMHC may have the potential for lateralization of unilateral mTLE. Third, the hemispheric differences in homotopic connectivity were related to surgical outcomes in patients with mTLE, which indicates that the time-shift homotopic connectivity may be predictive of surgical outcomes in mTLE.

We first revealed the whole-brain patterns of altered homotopic connectivity in mTLE. We found that the mesial temporal structures, including the hippocampus and parahippocampal gyrus, showed decreased homotopic connectivity, consistent with previous studies.^{14,15,17} Fur-

thermore, we found decreased homotopic connectivity in the temporal pole, amygdala, insula, putamen, and pallidum. These regions have been regarded as key nodes in the mesial temporal epileptic networks and play important roles in the generation, propagation, and modulation of epileptic activity.^{14,26} Imaging studies have demonstrated structural^{27,28} and functional abnormalities in these regions.²⁹⁻³³ Thus, we considered that reduced homotopic connectivity might result from nodal impairments of these regions in mTLE. Moreover, studies have proposed a variety of propagation patterns of epileptic activity from the originating focus to the contralateral side; the limbic structures and basal ganglia are the important nodes within the propagation pathway.^{34,35} Here we cautiously proposed another explanation, that time-shift-dependent alterations of VMHC of these regions might represent propagations of epileptic activity.

Along with the time-shift delays, the decreases of the bihemispheric homotopic connectivity were more lateralized in patients with unilateral mTLE. The lesioned side showed more persistent decrease in homotopic connectivity.⁵ We introduced a time-shift functional connectivity analysis, different from the conventional VMHC approach, which provided directional information to identify connectivity abnormalities resulting from different nodal impairments. Time-shift functional connectivity was first proposed by Lv et al¹⁹ in their fMRI study on stroke. They proposed that the time-shift delays in resting-state fMRI connectivity represent the hemodynamics/perfusion property of stroke and could be used to measure the extent of the brain lesions.^{19,20} Here, we assume that different decreases in the time-shift homotopic connectivity between the hemispheres may result from different hemodynamic properties between the hemispheres in mTLE. Previous studies showed that the epileptic focus presented interictal hypoperfusion in mTLE.^{36,37} This finding confirmed our hypothesis that the strategy of combining time-shift functional connectivity with VMHC had the potential to lateralize unilateral mTLE.

Our preliminary analysis showed that the results of ts-VMHC could be related to the surgical outcomes in patients with mTLE. The patients with unsuccessful outcomes had more interhemispheric VMHC differences. The finding suggested that the patients with unsuccessful outcomes might have more severe lesions and presented more disruption of interhemispheric communication. Previous studies have shown that resting-state fMRI has the capability of predicting surgical outcomes in mTLE.^{16,38} Different from those studies that used predefined region-of-interest analysis,^{16,38} our study used an unbiased voxelwise analysis approach and simultaneously observed the dynamic property of intrinsic connectivity in mTLE. Our study provided more comprehensive information for resting-state fMRI in the prediction of surgical outcome in mTLE.

Limitations

A few of the limitations in this study are noteworthy. First, we did not address the possible effects of antiepileptic drugs on fMRI in the study patients. Second, another presumption of time-shift connectivity might reflect propagation of epileptic activation; simultaneous electroencephalography and fMRI to record interictal epileptic discharges are needed in future studies. Third, the included patients had detectable hippocampal sclerosis, which might weaken the significance of epilepsy lateralization. Future study on patients with negative MR imaging findings is needed to validate this study. Finally, this work only observed the interhemispheric homotopic connectivity; measures of intrahemispheric and whole-brain connectivity might benefit from the understanding of the underlying mechanisms of connectivity alterations in epilepsy.

CONCLUSIONS

This study combined time-shift functional connectivity analysis with VMHC analysis and observed ts-VMHC alteration in patients with mTLE. The results showed the whole-brain pattern of aberrant interhemispheric connectivity in mTLE and further implicated the associated nodal impairment. Moreover, our study provided a novel fMRI approach that has potential value for epileptic focus lateralization and predicting the surgical outcome of mTLE.

REFERENCES

- Hervé PY, Zago L, Petit L, et al. **Revisiting human hemispheric specialization with neuroimaging.** *Trends Cogn Sci* 2013;17:69–80
- Doron KW, Bassett DS, Gazzaniga MS. **Dynamic network structure of interhemispheric coordination.** *Proc Natl Acad Sci U S A* 2012;109:18661–68
- Stark DE, Margulies DS, Shehzad ZE, et al. **Regional variation in interhemispheric coordination of intrinsic hemodynamic fluctuations.** *J Neurosci* 2008;28:13754–64
- Jo HJ, Saad ZS, Gotts SJ, et al. **Quantifying agreement between anatomical and functional interhemispheric correspondences in the resting brain.** *PLoS One* 2012;7:e48847
- Zuo XN, Kelly C, Di Martino A, et al. **Growing together and growing apart: regional and sex differences in the lifespan developmental trajectories of functional homotopy.** *J Neurosci* 2010;30:15034–43
- Hoptman MJ, Zuo X-N, D'Angelo D, et al. **Decreased interhemispheric coordination in schizophrenia: a resting state fMRI study.** *Schizophr Res* 2012;141:1–7
- Anderson JS, Druzgal TJ, Froehlich A, et al. **Decreased interhemispheric functional connectivity in autism.** *Cereb Cortex* 2011;21:1134–46
- Zhou Y, Milham M, Zuo XN, et al. **Functional homotopic changes in multiple sclerosis with resting-state functional MR imaging.** *AJNR Am J Neuroradiol* 2013;34:1180–87
- Ji GJ, Zhang Z, Xu Q, et al. **Generalized tonic-clonic seizures: aberrant interhemispheric functional and anatomical connectivity.** *Radiology* 2014;271:839–47
- Wieser HG. **ILAE commission report: mesial temporal lobe epilepsy with hippocampal sclerosis.** *Epilepsia* 2004;45:695–714
- Spencer SS. **Neural networks in human epilepsy: evidence and implications for treatment.** *Epilepsia* 2002;43:219–27
- Engel J. **Mesial temporal lobe epilepsy: what have we learned?** *Neuroscientist* 2001;7:340–52
- Ji GJ, Zhang Z, Zhang H, et al. **Disrupted causal connectivity in mesial temporal lobe epilepsy.** *PLoS One* 2013;8:e63183
- Bettus G, Guedj E, Joyeux F, et al. **Decreased basal fMRI functional connectivity in epileptogenic networks and contralateral compensatory mechanisms.** *Hum Brain Mapp* 2009;30:1580–91
- Morgan VL, Rogers BP, Sonmezurk HH, et al. **Cross hippocampal influence in mesial temporal lobe epilepsy measured with high temporal resolution functional magnetic resonance imaging.** *Epilepsia* 2011;52:1741–49
- Bettus G, Bartolomei F, Confort-Gouny S, et al. **Role of resting state functional connectivity MRI in presurgical investigation of mesial temporal lobe epilepsy.** *J Neurol Neurosurg Psychiatry* 2010;81:1147–54
- Pereira FR, Alessio A, Sercheli MS, et al. **Asymmetrical hippocampal connectivity in mesial temporal lobe epilepsy: evidence from resting state fMRI.** *BMC Neurosci* 2010;11:66
- Pittau F, Grova C, Moeller F, et al. **Patterns of altered functional connectivity in mesial temporal lobe epilepsy.** *Epilepsia* 2012;53:1013–23
- Lv Y, Margulies DS, Cameron Craddock R, et al. **Identifying the perfusion deficit in acute stroke with resting-state functional magnetic resonance imaging.** *Ann Neurol* 2013;73:136–40
- Amemiya S, Kunitatsu A, Saito N, et al. **Cerebral hemodynamic impairment: assessment with resting-state functional MR imaging.** *Radiology* 2014;270:548–55
- Zhang Z, Liao W, Wang Z, et al. **Epileptic discharges specifically affect intrinsic connectivity networks during absence seizures.** *J Neurol Sci* 2014;336:138–45
- Wieser H, Blume W, Fish D, et al, for the Commission on Neurosurgery of the International League Against Epilepsy (ILAE). **ILAE Commission Report: proposal for a new classification of outcome with respect to epileptic seizures following epilepsy surgery.** *Epilepsia* 2001;42:282–86
- Engel J Jr. **Update on surgical treatment of the epilepsies: summary of The Second International Palm Desert Conference on the Surgical Treatment of the Epilepsies (1992).** *Neurology* 1993;43:1612–17
- Ashburner J, Friston KJ. **Unified segmentation.** *Neuroimage* 2005;26:839–51
- Fox MD, Snyder AZ, Vincent JL, et al. **The human brain is intrinsically organized into dynamic, anticorrelated functional networks.** *Proc Natl Acad Sci U S A* 2005;102:9673–78
- Bertram EH, Zhang DX, Mangan P, et al. **Functional anatomy of limbic epilepsy: a proposal for central synchronization of a diffusely hyperexcitable network.** *Epilepsy Res* 1998;32:194–205
- Mueller SG, Laxer KD, Cashdollar N, et al. **Voxel-based optimized morphometry (VBM) of gray and white matter in temporal lobe epilepsy (TLE) with and without mesial temporal sclerosis.** *Epilepsia* 2006;47:900–07
- Li J, Zhang Z, Shang H. **A meta-analysis of voxel-based morphometry studies on unilateral refractory temporal lobe epilepsy.** *Epilepsy Res* 2012;98:97–103
- Jafari-Khouzani K, Elisevich K, Karvelis KC, et al. **Quantitative multi-compartmental SPECT image analysis for lateralization of temporal lobe epilepsy.** *Epilepsy Res* 2011;95:35–50

30. Kim BJ, Hong SB, Seo DW. **Differences in ictal hyperperfusion of limbic-related structures between mesial temporal and neocortical epilepsy.** *Epilepsy Res* 2008;81:167–75
31. Semah F, Baulac M, Hasboun D, et al. **Is interictal temporal hypometabolism related to mesial temporal sclerosis? A positron emission tomography/magnetic resonance imaging confrontation.** *Epilepsia* 1995;36:447–56
32. Zhang Z, Lu G, Zhong Y, et al. **fMRI study of mesial temporal lobe epilepsy using amplitude of low-frequency fluctuation analysis.** *Hum Brain Mapp* 2010;31:1851–61
33. Liao W, Zhang Z, Pan Z, et al. **Altered functional connectivity and small-world in mesial temporal lobe epilepsy.** *PLoS One* 2010;5:e8525
34. Kücken S, Töllner K, Piechotta M, et al. **Kindling as a model of temporal lobe epilepsy induces bilateral changes in spontaneous striatal activity.** *Neurobiol Dis* 2010;37:661–72
35. Pan J, Spencer D, Kuzniecky R, et al. **Metabolic networks in epilepsy by MR spectroscopic imaging.** *Acta Neurol Scand* 2012;126:411–20
36. Tae WS, Joo EY, Kim JH, et al. **Cerebral perfusion changes in mesial temporal lobe epilepsy: SPM analysis of ictal and interictal SPECT.** *Neuroimage* 2005;24:101–10
37. Marques LH, Ferraz-Filho JR, Lins-Filho ML, et al. **Interictal SPECT in the presurgical evaluation in epileptic patients with normal MRI or bilateral mesial temporal sclerosis.** *Arq Neuropsiquiatr* 2009;67:639–42
38. Negishi M, Martuzzi R, Novotny EJ, et al. **Functional MRI connectivity as a predictor of the surgical outcome of epilepsy.** *Epilepsia* 2011;52:1733–40

Brain Structure and Function in Patients after Metal-on-Metal Hip Resurfacing

M.J. Clark, J.R. Prentice, N. Hoggard, M.N. Paley, M. Hadjivassiliou, and J.M. Wilkinson



ABSTRACT

BACKGROUND AND PURPOSE: Hip prostheses that use a metal-on-metal articulation expose the brain to elevated metal concentrations that, in acute excess due to prosthesis malfunction, is associated with neurologic damage, including visual and hearing loss and motor deficits. Here, we examined whether chronic exposure to lower elevated metal levels, typical of well-functioning prostheses, also affects brain structure and function.

MATERIALS AND METHODS: We compared brain volumes, metal deposition, and gray matter attenuation by MR imaging and clinical neurologic function in patients 8 years after receiving a metal-on-metal hip resurfacing versus a matched group of patients with the same duration exposure to a conventional hip prosthesis.

RESULTS: Twenty-nine patients (25 men; mean, age 59 ± 7 years) after metal-on-metal hip resurfacing and 29 patients (25 men; 59 ± 8 years) after total hip arthroplasty were compared. Whole blood cobalt and chromium concentrations were 5–10 times higher in the metal-on-metal hip resurfacing group ($P < .0001$). Occipital cortex gray matter attenuation tended to be lower ($P < .005$ uncorrected, $P > .05$ corrected), and the optic chiasm area tended to be lower (mean difference, -2.7 mm^2 ; $P = .076$) in the metal-on-metal hip resurfacing group. Subgroup analyses in 34 patients (17 per group), after exclusion of primary ocular pathology, showed the same trend in gray matter attenuation in the occipital cortex and basal ganglia and a smaller optic chiasm in the metal-on-metal hip resurfacing group (mean difference, -3.9 mm^2 ; $P = .048$). No other structural or functional differences were found between the groups.

CONCLUSIONS: Chronic exposure to metal-on-metal hip resurfacing is associated with subtle structural change in the visual pathways and the basal ganglia in asymptomatic patients.

ABBREVIATIONS: Co = cobalt; Cr = chromium; MoMHR = metal-on-metal hip resurfacing; PRIME = partially refocused interleaved multiple-echo sequences; THA = total hip arthroplasty; UPDRS = Unified Parkinson's Disease Rating Scale

Cobalt (Co) and Chromium (Cr) are common component materials of joint prostheses, and these metals are released by many designs of joint replacement but particularly from those with a metal-on-metal articulating bearing.^{1,2} Co and Cr cross the blood-brain barrier and may be deposited in the brain.^{3,4} Co and Cr are toxic to neuronal cells in rats, causing brain cell apoptosis

mediated by the α subunit of hypoxia inducible factor-1 pathway.⁵⁻⁷ Metal toxicity presenting with neurologic deficit is reported in association with malfunctioning hip prostheses and excessive circulating Co and Cr.⁸ These neurologic deficits include visual and hearing loss, peripheral sensory and motor defects, tremor, and cognitive decline.^{9,10}

In the United States, >500,000 patients have received hip replacements by using a metal-on-metal bearing, and most have well-functioning devices.¹¹ Well-functioning prostheses also release metal species into the systemic circulation, albeit at much lower concentrations than those associated with malfunctioning prostheses. Steady-state median blood Co and Cr concentrations during 10 years in patients with well-functioning devices are typ-

Received November 14, 2013; accepted after revision February 13, 2014.

From the Departments of Human Metabolism (M.J.C., J.R.P., J.M.W.) and Cardiovascular Science (N.H., M.N.P.), University of Sheffield, The Medical School, Sheffield, United Kingdom; Department of Neurology (M.H.), Sheffield Teaching Hospitals National Health Service Foundation Trust, Royal Hallamshire Hospital, Sheffield, United Kingdom; and Department of Orthopaedics (J.M.W.), Sheffield Teaching Hospitals National Health Service Foundation Trust, Northern General Hospital, Sheffield, United Kingdom.

This study was funded by Sheffield Musculoskeletal Biomedical Research Unit through its core grant from the National Institute of Health Research in the United Kingdom.

The National Institute of Health Research in the United Kingdom had no role in the design and conduct of the study; collection, management, analysis, and interpretation of the data; or preparation, review, or approval of the manuscript.

Please address correspondence to J. Mark Wilkinson, MD, Department of Human Metabolism, University of Sheffield, DU24, The Medical School, Beech Hill Rd, Sheffield, S10 2RX, United Kingdom; e-mail: j.m.wilkinson@sheffield.ac.uk

Indicates open access to non-subscribers at www.ajnr.org

<http://dx.doi.org/10.3174/ajnr.A3922>

ically between 1.5 and 2.5 $\mu\text{g/L}$, and are 5 to 10-fold higher than normal physiologic concentrations.^{12,13} The effect on the brain of prolonged exposure to these moderately elevated concentrations of circulating metal for many years is unclear.

We examined whether prolonged exposure to circulating metal after metal-on-metal hip resurfacing (MoMHR) is associated with differences in brain structure and function assessed by MR imaging and clinical neurologic assessment in a group of clinically healthy patients after MoMHR versus an age-, sex-, diagnosis-, and time since surgery–matched group of patients who received a conventional total hip arthroplasty (THA) that did not use a metal-on-metal bearing to determine whether this choice of prosthesis has implications for brain health. We, therefore, chose demographically similar patients with conventional THA for the control group, rather than use background population controls, to minimize potential confounding due to brain structural change associated with underlying diagnosis or surgical treatment per se.¹⁴

MATERIALS AND METHODS

Subjects

We undertook this single-center cross-sectional study at a teaching hospital in the United Kingdom. Patients were recruited as part of a study examining the systemic effects of metal exposure after MoMHR ($n = 35$ patients in each group).¹⁵ The study was approved by a National Research Ethics Service Research Ethics Committee, and all patients provided written informed consent before participation. All patients underwent clinical neurologic examination, including an assessment of extrapyramidal tract function by using the Unified Parkinson's Disease Rating Scale (UPDRS), Part 2 (activities of daily living) and Part 3 (motor). The UPDRS is a standardized scale used to assess the severity of Parkinson disease symptoms and has previously been applied to the quantitation of movement disorders associated with metal neurotoxicity.^{16,17} Blood and plasma Co and Cr levels were measured by inductively coupled plasma–mass spectroscopy, as described previously.¹⁵

MR Imaging Acquisition

MR images were obtained by using a 3T system (Intera; Phillips Healthcare, Best, Netherlands) with an 8-channel sensitivity encoding head coil. The imaging protocol comprised structural, functional, and partially refocused interleaved multiple-echo (PRIME) sequences. 3D T1 magnetization-prepared rapid acquisition of gradient echo images were acquired for volumetric analysis (TR = 10.5 ms, TE = 4.8 ms, flip angle = 8°, 187 sagittal sections with 0.8-mm thickness, 256 × 205 mm FOV, acquired voxel size = 0.8 × 0.8 × 0.8 mm, scan time = 5 minutes 30 seconds). MR images were aligned parallel to the internal auditory meatus in the coronal plane and parallel with the midline of the brain in the sagittal plane. Sagittal images were reconstructed to continuous coronal images with a 0.9-mm section thickness.

The PRIME acquisition sequence was used to simultaneously measure quantitative relaxation rates, R2 and R2*, and hence R2', which is related to magnetic inhomogeneity caused by metal deposition. The sequence comprised 5 spin-echoes with 9 gradient recalled-echoes per spin-echo, leading to a total of 45 images per section (relaxation time = 3000 ms; spin-echo times = 30, 60, 90, 120,

and 150 ms; gradient-echo times at 3-ms increments for 9 echoes spaced symmetrically around the spin-echo; recon matrix = 512 × 512; flip angle = 90°; acquired voxel size = 1.44 × 1.8 × 2.5 mm; 14 coronal sections with a section thickness of 2.5 mm; scanning time, 5 minutes 0 seconds). All analyses were made by using the fMRI of the Brain (FMRIB) Software Library (FSL, Version 4.1.1; <http://www.fmrib.ox.ac.uk/fsl>), apart from metal deposition relaxation time measurements made using the PRIME sequence and optic chiasm area made using in-house software.

Data Analysis

Brain volume and subcortical nuclear volumes were measured by using the FSL FMRIB Integrated Registration and Segmentation Tool (FIRST) and automated segmentation and bias field correction tool (FAST) after deletion of nonbrain tissue from images by using the Brain Extraction Tool.¹⁸ FAST was applied to estimate total brain gray and white matter, and FIRST was used to measure brain stem volumes and the volumes of 7 subcortical regions, including the amygdala, caudate nucleus, putamen, thalamus, pallidum, hippocampus, and nucleus accumbens. FSLstats (<http://www2.warwick.ac.uk/fac/sci/statistics/staff/academic-research/nichols/scripts/fsl/fslstats.sh>) was used to output numeric data. All measured volumes were corrected for intracranial volume.

Metal deposition in the brain was assessed by using a relative-quantitative method with in-house Matlab software (Version 7.9; MathWorks, Natick, Massachusetts). We have previously used this method to measure brain iron concentration.^{19–21} Here we applied it to Co and Cr quantitation because both Co and Cr in their stable states (Co II and Cr III) are paramagnetic.²² Briefly, the method involves processing the images by using a nonlinear least-squares fitting routine to calculate values for R2'. The PRIME sequence provides a complete set of simultaneously acquired and registered T2 and T2* contrast-weighted images for each section, allowing calculation of the T2 and T2* relaxation times. T2 was calculated from the peak signal of the 5 acquired spin-echoes, and T2* was calculated from the peak signal from the 5 echoes, including the first spin-echo and subsequent 4 gradient echoes. R2' was calculated from the formula $R2' = (1/T2^* - 1/T2)$ by using the difference in the fits to the spin-echo and gradient-echo exponential decay curves from selected regions of interest. This measure indicates the additional inhomogeneity generated by the metal susceptibility difference from normal tissue and minimizes effects due to changes in the T2 relaxation time from other potential sources.

Quantitative measures of gray matter attenuation were made by using voxel-based morphometry (FSL-VBM, Version 1.1; <http://fsl.fmrib.ox.ac.uk/fsl/fsl-4.1.9/fslvbm/index.html>).^{23,24} Structural images had the brain extracted by using the Brain Extraction Tool.²⁵ The gray matter was then segmented and registered to the Montreal Neurological Institute 152 standard space by using nonlinear registration.²⁶ The resulting images were averaged to create a study-specific template to which the native gray matter images were nonlinearly registered and corrected for local expansion or contraction. The modulated gray matter images were then smoothed with an isotropic Gaussian kernel with a σ of 3 mm. Differences in gray matter attenuation were calculated by threshold free-cluster enhancement by using permutation-based nonparametric testing (5000 permutations) by using the Ran-

Table 1: Patient characteristics^a

Characteristic	MoMHR (n = 29)	THA (n = 29)	P Value
Age at surgery (yr)	58.9 ± 6.8	59.2 ± 7.5	.87
Sex (M/F)	25:4	25:4	1.00
Time since surgery (yr)	8.0 ± 1.7	7.7 ± 2.5	.51
UPDRS: Part 2 (ADLs) deficit	0 (0–1)	1 (0–2)	.34
UPDRS: Part 3 (motor) deficit	0 (0–1)	0 (0–1)	.76
Whole-blood cobalt (μg/L)	1.72 (1.10–6.01)	0.38 (0.33–0.50)	<.0001
Whole-blood chromium (μg/L)	1.42 (1.01–3.86)	<0.30 (<0.30 to <0.30)	<.0001
Plasma cobalt (μg/L)	1.66 (0.89–4.47)	<0.30 (<0.30 to <0.30)	<.0001
Plasma chromium (μg/L)	2.52 (1.60–13)	<0.30 (<0.30 to <0.30)	<.0001

Note:—ADL indicates activities of daily living.

^a Data are mean ± SD or median (interquartile range). Analyses of continuous data are MoMHR versus THA by unpaired *t* test or the Mann-Whitney *U* test; analysis of sex distribution is by the Fisher exact test.

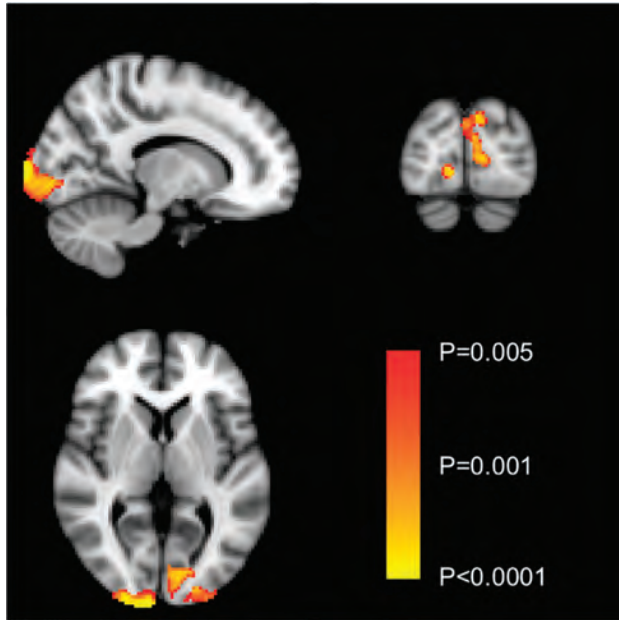


FIG 1. Voxel-based morphometric analysis of differences in brain gray matter attenuation between the MoMHR and THA groups before exclusion of patients with primary ocular pathology. Comparative areas of gray matter loss in the MoMHR group are highlighted by using the color bar across the significance value range $P < .05$ to $P < .001$ (uncorrected).

domize tool within FSL (<http://fsl.fmrib.ox.ac.uk/fsl/fslwiki/FSLVBM/UserGuide>). Image outputs were viewed by using fslview (<http://fsl.fmrib.ox.ac.uk/fsl/fslview/>).

The optic chiasm area was measured by using the ViewForum (Philips Healthcare) region-of-interest software. Manual regions outlining the optic chiasm were added to coronal sections and were quantitated by using methods described previously.²⁷ Interobserver repeatability of this method in our center by using a random sample of 20 subjects showed excellent agreement between 2 observers (linear regression $r^2 = 0.97$, $P < .0001$).

Statistical Analysis

All between-group analyses were completed by using the unpaired *t* test or Mann-Whitney *U* test when appropriate (Statistical Package for the Social Sciences, Version 20; IBM UK, Woking, United Kingdom). The results were considered significant at $P < .05$. Voxel-based morphometry analyses were completed by using the unpaired *t* test by using the Randomize software of FSL within

the framework of the General Linear Model. Because this was an exploratory study, results were considered significant at $P < .05$ corrected for the number of comparisons, as described previously.^{28–30}

RESULTS

Twenty-nine of the 35 recruited patients with MoMHR and 29 of the 35 recruited patients with conventional THA underwent brain MR imaging and neurologic assessment and are included in these

analyses. A key industry in our local population is metal grinding, and 5 subjects with a history of metal intraocular foreign bodies that precluded brain MR imaging were excluded from the study, 3 subjects were unable to complete the scanning protocol due to claustrophobia, and MR imaging data were lost in 4 subjects due to an archiving failure.

The patient groups were well-matched for age at surgery, sex, and time since surgery (Table 1, $P > .05$, all comparisons). Clinical neurologic examination demonstrated no abnormal clinical findings, with the exception of a benign essential tremor in 1 male subject with MoMHR and reduced facial expression, bradykinesia, and mild spasticity consistent with a mild extrapyramidal disorder in 1 man in the conventional THA group. UPDRS scores for dysfunction in Part 2 (activities of daily living) and Part 3 (motor symptoms) were similar between the 2 groups ($P > .05$, both comparisons). Median visual acuity at 6 meters in the MoMHR group was 12 (interquartile range, 6.8–51) in the left eye and 12 (interquartile range, 6.8–51) in the right eye; and in the THA group, it was 9 (interquartile range, 9–33) in the left eye and 12 (interquartile range, 9–33) in the right eye ($P > .05$, both comparisons). Median blood and plasma Co and Cr levels were 5- to 50-fold higher in patients with MoMHR versus those with THA ($P < .0001$, all comparisons, Table 1).

Brain gray matter attenuation measured by voxel-based morphometry was lower in the occipital cortex of the patients with MoMHR versus those with THA, corresponding to the primary visual cortex (Fig 1; $P < .005$, uncorrected; $P > .05$, corrected). In view of the location of this difference in gray matter attenuation, patients were invited to return for clinical ophthalmologic examination to exclude primary eye pathology as a confounding variable for this analysis. Forty-eight male patients returned for this examination. Fourteen of these subjects were identified as having a primary ocular pathology that might contribute to visual cortical dysfunction or optic atrophy, leaving 34 subjects (17 in each group) for the subgroup analysis. Gray matter attenuation remained reduced in the occipital region (Fig 2, top panel; $P < .005$, uncorrected; $P > .05$, corrected) but was also reduced in the right and left putamen and the left head of the caudate nucleus (Fig 2, bottom panel; $P < .005$, uncorrected; all regions, $P > .05$, corrected). The optic chiasm area, measured by using Viewforum, was $36.7 \pm 4.7 \text{ mm}^2$ and $39.5 \pm 6.7 \text{ mm}^2$ in the patients with MoMHR and THA, respectively (mean difference = -2.7 mm^2 ; 95% CI, -5.7 – 0.2 mm^2 ; $P = .076$). After we removed patients with primary ocular pathologies and those who did not return for ophthalmic assessment,

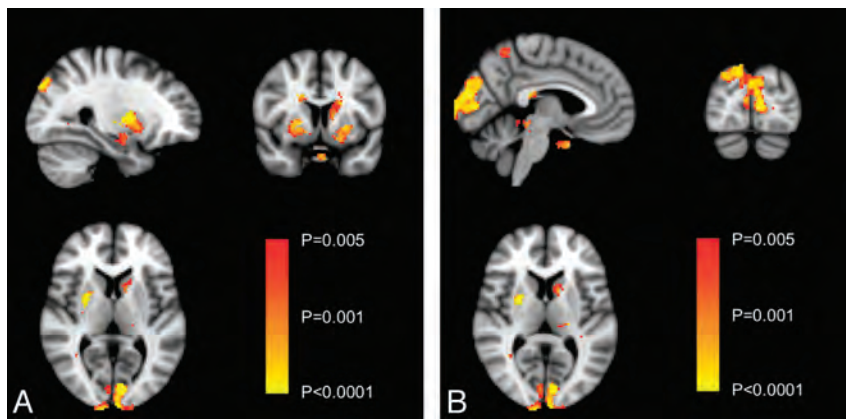


FIG 2. Voxel-based morphometric analysis of differences in brain gray matter attenuation between the MoMHR and THA groups, after exclusion of patients with primary ocular pathology. The top panel highlights occipital cortex differences between groups; the bottom panel highlights differences in basal ganglia between groups. Comparative areas of gray matter loss in the MoMHR group are highlighted by using the color bar across the significance value range $P < .05$ to $P < .001$ (uncorrected).

Table 2: Brain volumes^a

Structure (mm ³)	MoMHR	THA	P Value
Total brain volume	$1.20 \times 10^6 \pm 75219$	$1.18 \times 10^6 \pm 96956$.08
Gray matter	$5.89 \times 10^5 \pm 57984$	$5.74 \times 10^5 \pm 67886$.11
White matter	$6.14 \times 10^5 \pm 25380$	$6.01 \times 10^5 \pm 34845$.09
Brain stem	22798 ± 2407	22187 ± 2380	.34
Thalamus	14960 ± 989	14710 ± 1086	.36
Caudate nucleus	6544 ± 505	6615 ± 601	.63
Putamen	8512 ± 486	8384 ± 624	.39
Pallidum	3498 ± 339	3518 ± 424	.84
Hippocampus	7026 ± 670	6952 ± 793	.70
Amygdala	2505 ± 289	2342 ± 402	.08
Nucleus accumbens	729 ± 166	715 ± 163	.76

^a Data are mean \pm SD and are adjusted for intracranial volume. Analyses are MoMHR versus THA by unpaired *t* test or the Mann-Whitney *U* test.

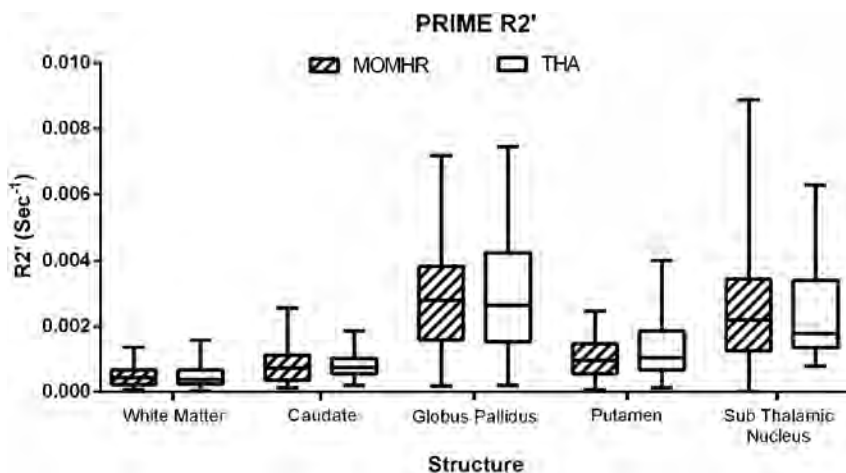


FIG 3. Quantitation of brain metal deposition by PRIME R2' values (second⁻¹). Analyses are MoMHR versus THA by the Wilcoxon test, $P > .05$ for all comparisons.

the optic chiasm area was $36.3 \pm 4.7 \text{ mm}^2$ in the MoMHR group and $40.3 \pm 6.3 \text{ mm}^2$ in the THA group ($n = 17$ per group; unpaired mean difference, -3.9 mm^2 ; 95% CI, -7.84 to -0.04 ; $P = .048$).

Total brain volume and white and gray matter volumes were similar in both patient groups (as measured by FAST, FSL), as were subcortical nuclei, basal ganglia, and brain stem volumes

computed by using FIRST, FSL (Table 2, values corrected for intracranial volume; $P > .05$, all comparisons). R2' relaxation times in the caudate nucleus, subthalamic nucleus, pallidum, putamen, and white matter were also similar between groups; this finding indicates that any possible difference in the level of metal deposition between the subjects with MoMHR and those with THA was below the level of detection available by using the PRIME sequence (Fig 3; $P > .05$, all comparisons).

DISCUSSION

In this study, we found that healthy asymptomatic patients with confirmed chronic exposure to elevated circulating concentrations of Co and Cr after MoMHR had differences in brain structure compared with a group of age-, sex-, and time since surgery–matched patients with the same underlying disease, but who had received a conventional hip prosthesis and who had circulating metal concentrations that are similar to normal physiologic levels. Patients who had received MoMHR tended toward lower gray matter attenuation in the occipital cortex and basal ganglia and had a smaller optic chiasm area than those patients who had received a conventional prosthesis, after exclusion of patients with primary ocular pathologies from the analysis. We found no evidence of association between MoMHR exposure and changes in brain structural volumes or with metal accumulation within the subcortical nuclei or basal ganglia. We also found no differences in neurologic function, measured by clinical examination and UPDRS, and no differences in visual function, measured by ophthalmologic assessment, between the groups.

These structural trends, though small, are consistent with known toxicologic effects of Co and Cr on the visual system observed in patients with acute exposure to high metal concentrations associated with prosthesis malfunction.⁸⁻¹⁰ Our data suggest that moderately elevated circulating metal concentrations for 8 years after MoMHR are associated with imaging features in keeping with possible cell loss in the visual system. A chronic insult to the anterior visual pathways has been previously reported in humans to cause voxel-based changes in the primary visual cortex in the context of glaucoma.³¹ The rational underpinning of these findings is

ately elevated circulating metal concentrations for 8 years after MoMHR are associated with imaging features in keeping with possible cell loss in the visual system. A chronic insult to the anterior visual pathways has been previously reported in humans to cause voxel-based changes in the primary visual cortex in the context of glaucoma.³¹ The rational underpinning of these findings is

that such visual cortex changes are produced by transneuronal degeneration in patients with optic nerve damage. Visual cortex abnormalities on voxel-based morphometry consistent with cortical atrophy have also been found in patients with macular degeneration.³² A recent animal study by Apostoli et al,³³ has shown rabbits with prolonged systemic exposure to Co or Cr in isolation or combined have optic and auditory neuropathy. Cobalt produces toxicity in rats, leading to glioma,³⁴ neuroblastoma,³⁵ and neuronal cell damage.³⁶ In addition, cobalt has a dose-dependent effect on apoptosis and secondary necrosis in astrocytes, through the generation of reactive oxygen species and subsequent α subunit of hypoxia inducible factor-1 pathway activation.⁶

Our FIRST data suggest that this concentration of metal exposure is not associated with a detectable loss in volume of the major brain structures. Both of our patient groups had brain and subcortical volumes similar to those found in the general population for individuals of similar age and sex.³⁷ Similarly, although both Co and Cr may be deposited in the basal ganglia, especially in the pallidum, putamen, and caudate nucleus,^{3,4,38} our PRIME analysis of R2' data suggest that this exposure does not result in an increase in detectable deposition of paramagnetic ions within these structures. Our methods have been used previously to assess iron concentration within the basal ganglia of patients with HIV and Parkinson disease. Concentrations of iron up to 200 $\mu\text{g/g}$ tissue wet weight are found in the globus pallidus, red nucleus, substantia nigra, and putamen regions.³⁹ A previous study showed a sensitivity of the PRIME sequence R2' relaxation time to iron deposition of approximately 0.02s/ $\mu\text{gFe/g}$ wet weight of tissue.¹⁹ In a study to measure R2* in intact postmortem brains followed by quantitative postmortem brain measurement with inductively coupled plasma mass spectrometry, Langkammer et al⁴⁰ found a formula for R2* (second⁻¹) = 14.3 + 0.27 \times [iron concentration] (mg Kg⁻¹ wet mass). The use of this approach to detect other metals such as Co and Cr is not so well-developed. Co, like iron, displays ferromagnetism, while Cr has a lower paramagnetic susceptibility of +167 $\chi\text{m}/10^{-6}\text{cm}^3\text{mol}^{-1}$. As a sulfate, this increases to +11,800 $\chi\text{m}/10^{-6}\text{cm}^3\text{mol}^{-1}$. No differences were observed for R2' between the patient groups we studied, but this may reflect the expected lower sensitivity of the PRIME sequence to effects from Co and Cr compared with iron and the relatively low concentrations of Co and Cr in the brain. Typical normal levels in the cortex are 2 $\mu\text{g/Kg}$ for Co and 10 $\mu\text{g/Kg}$ for Cr,⁴ which are several orders of magnitude lower than those of iron (50–250 mg/Kg). If the serum concentration of these elements was raised by a factor of 50 and they crossed the blood-brain barrier, the maximum levels of Co and Cr in the brain would be ~ 500 $\mu\text{g/Kg}$, and thus our failure to detect these metals may be due to insensitivity of the PRIME sequence method to these relatively low metal concentrations compared with iron in brain tissue.

This is the first study to explore whether chronic exposure to moderate circulating metal is associated with brain structural and functional change. It was, by its nature, exploratory and not powered for analysis of specific brain areas or with a priori knowledge of potential effect sizes. While we observed some differences in brain morphometry between the groups, these did not remain after multiple-comparison correction, possibly related to sample

size. Further study focusing analysis on the visual cortex and basal ganglia is warranted to confirm these preliminary findings in patients prescreened for potential confounders such as coexistence of primary ocular pathology.

CONCLUSIONS

This exploratory study was conducted in a clinically asymptomatic population and was cross-sectional in design. The patients with MoMHR who we studied had circulating metal concentrations that, though elevated, were not indicative of a failing prosthesis. We thus aimed to detect subclinical signals to indicate whether metal exposure due to prosthesis choice is associated with structural or functional changes in the brain and, if so, which systems show the greatest signal change. Our detection of subtle structural changes associated with metal exposure suggests that further examination of the relationship between metal exposure, brain structure, and clinical symptoms in a larger group of patients across a higher concentration range of metal exposure and for longer periods is warranted to definitively address the relationship between exposure and structural change and to determine their clinical relevance.

Disclosures: Jeremy Mark Wilkinson—RELATED: Grant: National Institutes of Health Research, United Kingdom.* Comments: This work was funded through a Biomedical Research Unit core grant from the National Institute for Health Research. *Money paid to the institution.

REFERENCES

1. Heisel C, Streich N, Krachler M, et al. **Characterization of the running-in period in total hip resurfacing arthroplasty: an in vivo and in vitro metal ion analysis.** *J Bone Joint Surg Am* 2008;90 (suppl 3):125–33
2. Daniel J, Ziaee H, Pradhan C, et al. **Blood and urine metal ion levels in young and active patients after Birmingham hip resurfacing arthroplasty: four-year results of a prospective longitudinal study.** *J Bone Joint Surg Br* 2007;89:169–73
3. Duckett S. **Abnormal deposits of chromium in the pathological human brain.** *J Neurol Neurosurg Psychiatry* 1986;49:296–301
4. Höck A, Demmel U, Schicha H, et al. **Trace element concentration in human brain: activation analysis of cobalt, iron, rubidium, selenium, zinc, chromium, silver, cesium, antimony and scandium.** *Brain* 1975;98:49–64
5. Quinteros FA, Poliandri AH, Machiavelli LI, et al. **In vivo and in vitro effects of chromium VI on anterior pituitary hormone release and cell viability.** *Toxicol Appl Pharmacol* 2007;218:79–87
6. Karovic O, Tonazzini I, Rebola N, et al. **Toxic effects of cobalt in primary cultures of mouse astrocytes: similarities with hypoxia and role of HIF-1 α .** *Biochem Pharmacol* 2007;73:694–708
7. Huk OL, Catelas I, Mwale F, et al. **Induction of apoptosis and necrosis by metal ions in vitro.** *J Arthroplasty* 2004;19:84–87
8. Oldenburg M, Wegner R, Baur X. **Severe cobalt intoxication due to prosthesis wear in repeated total hip arthroplasty.** *J Arthroplasty* 2009;24:825 e815–20
9. Rizzetti MC, Liberini P, Zarattini G, et al. **Loss of sight and sound: could it be the hip?** *Lancet* 2009;373:1052
10. Steens W, von Foerster G, Katzer A. **Severe cobalt poisoning with loss of sight after ceramic-metal pairing in a hip: a case report.** *Acta Orthop* 2006;77:830–32
11. Rising JP, Reynolds IS, Sedrakyan A. **Delays and difficulties in assessing metal-on-metal hip implants.** *N Engl J Med* 2012;367:e1
12. Hartmann A, Lutzner J, Kirschner S, et al. **Do survival rate and serum ion concentrations 10 years after metal-on-metal hip resurfacing provide evidence for continued use?** *Clin Orthop* 2012;470:3118–26
13. Holland JP, Langton DJ, Hashmi M. **Ten-year clinical, radiological**

- and metal ion analysis of the Birmingham hip resurfacing: from a single, non-designer surgeon. *J Bone Joint Surg Br* 2012;94:471–76
14. Gwilym SE, Filippini N, Douaud G, et al. **Thalamic atrophy associated with painful osteoarthritis of the hip is reversible after arthroplasty: a longitudinal voxel-based morphometric study.** *Arthritis Rheum* 2010;62:2930–40
 15. Prentice JR, Clark MJ, Hoggard N, et al. **Metal-on-metal hip prostheses and systemic health: a cross-sectional association study 8 years after implantation.** *PLoS One* 2013;8:e66186
 16. Bowler RM, Roels HA, Nakagawa S, et al. **Dose-effect relationships between manganese exposure and neurological, neuropsychological and pulmonary function in confined space bridge welders.** *Occup Environ Med* 2007;64:167–77
 17. Lucchini RG, Albini E, Benedetti L, et al. **High prevalence of Parkinsonian disorders associated to manganese exposure in the vicinities of ferroalloy industries.** *Am J Ind Med* 2007;50:788–800
 18. Patenaude B, Smith SM, Kennedy DN, et al. **A Bayesian model of shape and appearance for subcortical brain segmentation.** *Neuroimage* 2011;56:907–22
 19. Graham JM, Paley MN, Grunewald RA, et al. **Brain iron deposition in Parkinson's disease imaged using the PRIME magnetic resonance sequence.** *Brain* 2000;123(pt 12):2423–31
 20. Miszkiel KA, Paley MN, Wilkinson ID, et al. **The measurement of R2, R2* and R2' in HIV-infected patients using the prime sequence as a measure of brain iron deposition.** *Magn Reson Imaging* 1997;15:1113–19
 21. Wallis LI, Paley MN, Graham JM, et al. **MRI assessment of basal ganglia iron deposition in Parkinson's disease.** *Magn Reson Imaging* 2008;28:1061–67
 22. Ueno S, Susa N, Furukawa Y, et al. **Formation of paramagnetic chromium in liver of mice treated with dichromate (VI).** *Toxicol Appl Pharmacol* 1995;135:165–71
 23. Good CD, Johnsrude IS, Ashburner J, et al. **A voxel-based morphometric study of ageing in 465 normal adult human brains.** *Neuroimage* 2001;14:21–36
 24. Smith SM, Jenkinson M, Woolrich MW, et al. **Advances in functional and structural MR image analysis and implementation as FSL.** *Neuroimage* 2004;23(suppl 1):S208–19
 25. Smith SM. **Fast robust automated brain extraction.** *Hum Brain Mapp* 2002;17:143–55
 26. Zhang Y, Brady M, Smith S. **Segmentation of brain MR images through a hidden Markov random field model and the expectation-maximization algorithm.** *IEEE Trans Med Imaging* 2001;20:45–57
 27. Wagner AL, Murtagh FR, Hazlett KS, et al. **Measurement of the normal optic chiasm on coronal MR images.** *AJNR Am J Neuroradiol* 1997;18:723–26
 28. Henley SM, Ridgway GR, Scahill RI, et al. **Pitfalls in the use of voxel-based morphometry as a biomarker: examples from Huntington disease.** *AJNR Am J Neuroradiol* 2010;31:711–19
 29. Radua J, Mataix-Cols D, Phillips ML, et al. **A new meta-analytic method for neuroimaging studies that combines reported peak coordinates and statistical parametric maps.** *Eur Psychiatry* 2012;27:605–11
 30. Genovese CR, Lazar NA, Nichols T. **Thresholding of statistical maps in functional neuroimaging using the false discovery rate.** *Neuroimage* 2002;15:870–78
 31. Zikou AK, Kitsos G, Tzarouchi LC, et al. **Voxel-based morphometry and diffusion tensor imaging of the optic pathway in primary open-angle glaucoma: a preliminary study.** *AJNR Am J Neuroradiol* 2012;33:128–34
 32. Boucard CC, Hernowo AT, Maguire RP, et al. **Changes in cortical grey matter density associated with long-standing retinal visual field defects.** *Brain* 2009;132:1898–906
 33. Apostoli P, Catalani S, Zaghini A, et al. **High doses of cobalt induce optic and auditory neuropathy.** *Exp Toxicol Pathol* 2013;65:719–27
 34. Yang SJ, Pyen J, Lee I, et al. **Cobalt chloride-induced apoptosis and extracellular signal-regulated protein kinase 1/2 activation in rat C6 glioma cells.** *J Biochem Mol Biol* 2004;37:480–86
 35. Olivieri G, Hess C, Savaskan E, et al. **Melatonin protects SHSY5Y neuroblastoma cells from cobalt-induced oxidative stress, neurotoxicity and increased beta-amyloid secretion.** *J Pineal Res* 2001;31:320–25
 36. Wang G, Hazra TK, Mitra S, et al. **Mitochondrial DNA damage and a hypoxic response are induced by CoCl(2) in rat neuronal PC12 cells.** *Nucleic Acids Res* 2000;28:2135–40
 37. de Jong LW, van der Hiele K, Veer IM, et al. **Strongly reduced volumes of putamen and thalamus in Alzheimer's disease: an MRI study.** *Brain* 2008;131:3277–85
 38. Goody W, Hamilton EI, Williams TR. **Spark-source mass spectrometry in the investigation of neurological disease. II. Element levels in brain, cerebrospinal fluid and blood: some observations on their abundance and significance.** *Brain* 1975;98:65–70
 39. Haacke EM, Cheng NY, House MJ, et al. **Imaging iron stores in the brain using magnetic resonance imaging.** *Magn Reson Imaging* 2005;23:1–25
 40. Langkammer C, Krebs N, Goessler W, et al. **Quantitative MR imaging of brain iron: a postmortem validation study.** *Radiology* 2010;257:455–62

Flat Detector Angio-CT following Intra-Arterial Therapy of Acute Ischemic Stroke: Identification of Hemorrhage and Distinction from Contrast Accumulation due to Blood-Brain Barrier Disruption

T. Kau, M. Hauser, S.M. Obmann, M. Niedermayer, J.R. Weber, and K.A. Hausegger



ABSTRACT

BACKGROUND AND PURPOSE: Flat panel detector CT in the angiography suite may be valuable for the detection of intracranial hematomas; however, abnormal contrast enhancement frequently mimics hemorrhage. We aimed to assess the accuracy of flat panel detector CT in detecting/excluding intracranial bleeding after endovascular stroke therapy and whether it was able to reliably differentiate hemorrhage from early blood-brain barrier disruption.

MATERIALS AND METHODS: Seventy-three patients were included for retrospective evaluation following endovascular stroke therapy: 32 after stent-assisted thrombectomy, 14 after intra-arterial thrombolysis, and 27 after a combination of both. Flat panel CT images were assessed for image quality and the presence and type of intracranial hemorrhage and BBB disruption by 2 readers separately and in consensus. Follow-up by multisection head CT, serving as the reference standard, was evaluated by a single reader.

RESULTS: Conventional head CT revealed intracranial hematomas in 12 patients (8 subarachnoid hemorrhages, 7 cases of intracerebral bleeding, 3 SAHs plus intracerebral bleeding). Image quality of flat panel detector CT was considered sufficient in all cases supratentorially and in 92% in the posterior fossa. Regarding detection or exclusion of intracranial hemorrhage, flat panel detector CT reached a sensitivity, specificity, positive and negative predictive values, and accuracy of 58%, 85%, 44%, 91%, and 81%, respectively. Maximum attenuation measurements were not valuable for the differentiation of hemorrhage and BBB disruption.

CONCLUSIONS: Flat panel CT after endovascular stroke treatment was able to exclude the rare event of an intracranial hemorrhage with a high negative predictive value. Future studies should evaluate the predictive value of BBB disruptions in flat panel detector CT for the development of relevant hematomas.

ABBREVIATIONS: CCT = conventional CT; FPCT = flat panel detector CT; ICB = intracerebral bleeding; PH = parenchymal hematoma

Flat panel detectors in modern angiographic C-arm systems allow almost instant access to CT-like cranial imaging in the angiography suite.¹⁻⁴ While flat panel detector CT (FPCT) is currently not reliable in depicting ischemic brain lesions, it proved to be a sensitive tool for the detection of intracranial hematomas in both experimental and clinical settings.^{5,6} However, there have been numerous reports of abnormal contrast enhancement following neurovascular interventions that frequently mimic subarachnoid, intraventricular, or intracerebral hemorrhage.⁷⁻⁹ It is important to recognize such patterns of temporary blood-brain

barrier disruption in postprocedural imaging because misinterpretation may unnecessarily delay anticoagulant/antiaggregant treatment.

In the present study, we aimed to assess the diagnostic accuracy of FPCT for the detection of intracranial bleeding immediately after endovascular stroke therapy and whether it was able to reliably differentiate hemorrhage from early blood-brain barrier disruption.

MATERIALS AND METHODS

The study was approved by our local ethics commission.

Subjects

Between May 2008 and December 2011, 100 endovascular stroke interventions had been performed in our institution. Postinterventional FPCT was not available in 16 patients. Another 11 patients were excluded from further assessment due to a lack of early conventional CT (CCT) follow-up as defined below. Finally, 73 patients were included in this retrospective study.

Received December 13, 2013; accepted after revision February 18, 2014.

From the Institute of Diagnostic and Interventional Radiology (T.K., M.H., M.N., K.A.H.) and Department of Neurology (S.M.O., J.R.W.), Klinikum Klagenfurt, Klagenfurt, Austria.

Please address correspondence to Thomas Kau, MD, Klinikum Klagenfurt, Institute of Diagnostic and Interventional Radiology, Feschnigstr 11, 9020 Klagenfurt, Austria; e-mail: t.kau@gmx.at

Indicates article with supplemental on-line table.

<http://dx.doi.org/10.3174/ajnr.A4021>

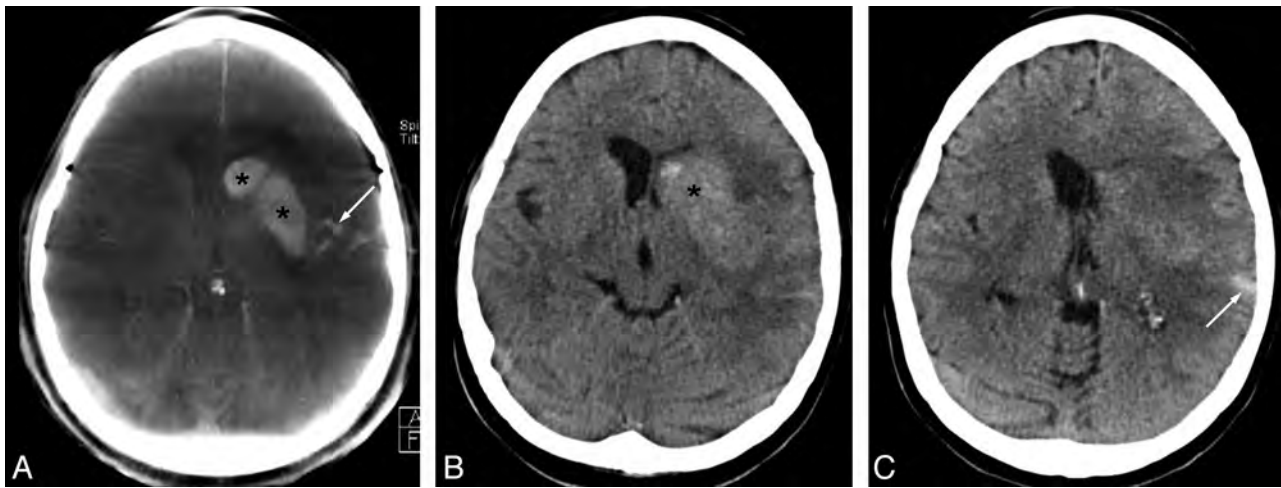


FIG 1. Blood-brain barrier disruption (*asterisks*) and subarachnoid hemorrhage (*arrows*) following combined intra-arterial thrombolysis (1,000,000 U of urokinase) and thrombectomy in a 62-year-old female patient with occlusion of the left middle cerebral artery (admission modified Rankin Scale score, 5; stroke time to admission uncertain; recanalization-to-follow-up CCT, 19.1 hours). Hyperattenuations in the left hemispheric sulci (SAH) sharply confined to the ipsilateral striatum (BBB disruption) are clearly visible on postinterventional FPCT (A) and confirmed by CCT (B and C).

Acute Stroke Therapy

Acute stroke therapy consisted of endovascular intervention in all cases with 7 patients (10%) having received a “bridging” dose of recombinant tissue plasminogen activator intravenously in advance. Thirty-two patients (44%) were treated by stent-assisted thrombectomy; 14 patients (19%), by intra-arterial thrombolysis with urokinase; and 27 patients (37%), by a combination of both. The mean dose of urokinase administered intra-arterially in 41 patients was 600,000 (range, 150,000–1,100,000) units. The technique of endovascular stroke treatment has been described elsewhere in the literature.^{10–12}

Flat Panel CT Image Acquisition and Interpretation

Flat panel CT images were acquired on a biplane angiography system (DynaCT, Axiom Artis dBA; Siemens, Erlangen, Germany) in 64 patients with the following parameters: voltage, 95.5 kV; tube current, 206.5 mA; acquisition time, 12.5 ms per frame; projection on 30 × 40 cm flat panel size; angulation, 0.4° per frame; total angle, 220°; exposure time, 20 seconds. In 9 patients, FPCT imaging was performed on a single-plane angiography system (XperCT, Allura Xper FD20 with Xtra Vision; Philips Healthcare, Best, the Netherlands) with the following parameters: voltage, 120 kV; tube current, 250 mA; frame speed, 30 frames per second; acquisition time, 5 ms per frame; total angle, 240°; exposure time, 20.8 seconds; FOV, 48 cm.

Flat panel CT images were assessed for the presence of subarachnoid hemorrhage, intracerebral bleeding (ICB), and BBB disruption by 2 readers (T.K., with 9 years of experience in radiology, Austrian board-certified radiologist, European board-certified neuroradiologist; M.H., with 7 years of experience in radiology, Austrian board-certified radiologist) separately, followed by consensus reading. Both readers were aware of which vessel had been occluded initially; however, they were blinded to further clinical data and conventional CT results. Pathologic intracerebral hyperattenuations were considered the result of BBB disruption if the borders of anatomic structures or vascular territories



FIG 2. Flat panel CT immediately after stent-assisted recanalization of a carotid bifurcation occlusion with intravenous thrombolytic bridging therapy in a 72-year-old male patient (admission modified Rankin Scale score, 4; stroke time to admission, >3 hours; recanalization-to-follow-up CCT, 14.7 hours). Focal hyperattenuation (*arrow*) of the right hippocampus is believed to be due to contrast enhancement attributable to disruption of the blood-brain barrier.

were clearly respected (Fig 1). If this criterion was not applicable because of small size, the differentiation between BBB disruption and ICB was made at the discretion of the observer (Fig 2). According to Fiorelli et al,¹³ we divided hemorrhagic transformations of cerebral infarcts into 4 subtypes: hemorrhagic infarction type I, hemorrhagic infarction type II, parenchymal hematoma type I, and parenchymal hematoma type II. Subarachnoid hemorrhage was classified as suggested by Fisher et al.¹⁴ The diagnostic quality of FPCT images was assessed by both readers in consensus (sufficient versus insufficient). Supratentorial image quality was considered good if a hemorrhage or BBB disruption could be detected or excluded with high confidence. With respect to typical FPCT artifacts in the posterior fossa, infratentorial image quality was considered sufficient if a parenchymal hematoma¹³ and a subarachnoid hemorrhage Fisher type 3 or 4 could be detected or

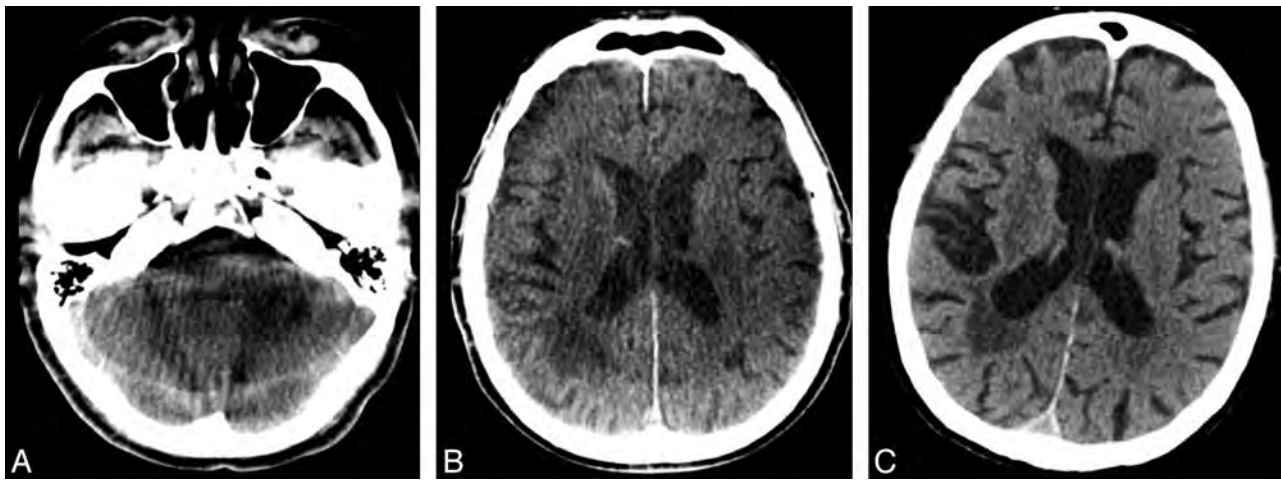


FIG 3. Correlation of image quality in an 84-year-old male patient (admission modified Rankin Scale score, 5; wake-up stroke, time to admission uncertain; recanalization-to-follow-up CCT, 22.2 hours). *A*, After mechanical recanalization of the right middle cerebral artery, FPCT shows moderate ring artifacts, however, no complication in the form of intracranial bleeding. *B*, Follow-up CCT depicts ischemic infarction of the ipsilateral putamen and no hemorrhage. *C*, Limited image quality of FPCT in the posterior fossa due to beam-hardening artifacts is evident.

excluded with high confidence (Fig 3). It was considered good if the readers were highly confident in detecting or excluding any hyperattenuation attributable to hemorrhage or BBB disruption.

Both readers performed maximum attenuation measurements in pathologically hyperattenuated regions with a predefined size of the region of interest (10 mm²).

Conventional CT Image Acquisition and Interpretation

Conventional head CT imaging was performed on a 2 × 32 detector row dual-source CT scanner (Somatom Definition; Siemens) on average 17.2 hours (mean, 17.5 hours; range, 0.6–45.9 hours) after FPCT. Typically, a single noncontrast CT acquisition was obtained ranging from the vertex to the craniocervical junction at an angle parallel to the skull base. Data were acquired in a caudocranial direction with the following CT parameters: pitch factor, 0.55; collimation, 64 × 0.6 mm; reconstructed section thickness, 4 mm; FOV, 220 mm; tube voltage and current, 120 kV and 300 mA; 64 sections per rotation at a rotation time of 1 second. Conventional CT, serving as the criterion standard for the detection and exclusion of intracranial hemorrhage, was evaluated by a single reader (K.A.H., with 26 years of experience, Austrian board-certified radiologist, European board-certified interventional radiologist). This radiologist was aware of which vessel had been occluded initially; however, he was blinded for further clinical data and FPCT results. Pathologic intracerebral hyperattenuation was thought due to BBB disruption if the borders of anatomic structures or vascular territories were clearly respected.

Statistics

In a first step, descriptive statistics were calculated. We used the McNemar test and κ statistics (GraphPad Prism software; GraphPad Software, San Diego, California) to compare FPCT with CCT for its ability to detect or exclude hemorrhage in general, SAH, ICB, and BBB disruption. The degree of agreement was assessed by sensitivity, specificity, positive and negative predictive values, and accuracy, including 95% confidence intervals (VassarStats; Vassar College, Poughkeepsie, New York). Interrater reliability was assessed by using κ statistics. After dividing

FPCT hyperattenuation into SAH, ICB, and BBB disruptions, we used the median test to compare median values of maximum attenuation measurements in true-positive and false-positive regions. A value of $P < .05$ was considered significant. The data were analyzed by using GraphPad and VassarStats, which are freely available on-line software tools.

RESULTS

Patient Characteristics

Of 73 patients, 39 were women and 34 were men with a median age of 70 years (range, 31–85 years). The thromboembolic clot was located in the M1 segment of the middle cerebral artery in 35 patients, in the carotid bifurcation in 16 patients, in both the proximal internal carotid artery and middle cerebral artery in 4 patients, and in the basilar artery in 18 patients. Twenty-six patients were admitted to the emergency department with a modified Rankin Scale score of 4, and 47 patients, with a score of 5. In 38 patients (52%), the time interval from stroke onset to initial CT was below a threshold of 3 hours. It was above 3 hours in 9 cases (12%) and entirely uncertain in 26 patients (36%).

Image Quality

In the supratentorial compartment, FPCT image quality was considered sufficient in all cases (100%). Infratentorially, it was rated sufficient in 67 cases (92%) and insufficient in the remaining 6 (8%).

Intracranial Hemorrhage

Conventional CT revealed an intracranial hematoma in 12 of 73 patients (16%). Of these, 8 subjects had SAH, and ICB was found in 7 patients. In 3 cases, both SAH and ICB were reported in the diagnostic test of reference. The On-line Table gives an overview of the findings of both readers. When comparing FPCT with CCT, the difference in their ability to detect or exclude intracranial bleeding in the follow-up of endovascular stroke treatment was found to be not statistically significant (reader 1, $P = .30$; reader 2, $P = .58$). However, the degree of agreement proved to be only fair ($\kappa = 0.36$; 95% CI, 0.07–0.65) and moderate ($\kappa = 0.41$; 95% CI,

Descriptive statistical data

	Hemorrhage		ICB		SAH		BBBD	
	Reader 1	Reader 2	Reader 1	Reader 2	Reader 1	Reader 2	Reader 1	Reader 2
True-positive	7	7	2	2	6	6	8	10
True-negative	51	53	58	64	61	57	53	50
False-positive	10	8	8	2	4	8	8	11
False-negative	5	5	5	5	2	2	4	2

Note:—BBBD indicates blood-brain barrier disruption.

0.12–0.70), respectively. Consensus reading led to 7 true-positive, 52 true-negative, 9 false-positive, and 5 false-negative results. Consequently, FPCT reached sensitivity, specificity, positive and negative predictive values, and accuracy of 58% (range, 29%–84%), 85% (range, 73%–93%), 44% (range, 21%–69%), 91% (range, 80%–97%), and 81% (7 range, 0%–88%). For descriptive statistical data, see the Table .

Type of Hemorrhage

While CT could exclude SAH in 65 cases (Fisher score 1) following stroke intervention, 3 patients were assigned a score of 2, two were assigned a score of 3, and 3 were assigned the highest Fisher score of 4 (Fig 1). Regarding hemorrhagic transformation of ischemic brain lesions, CT revealed hemorrhagic infarction type II in 4 patients. Parenchymal hematoma was found in 3 patients (1 type I and 2 type II), all of which showed a combination of ICB and SAH.

Blood-Brain Barrier Disruption

In 12 patients (16%), disruption of the BBB was found on CCT (Fig 1). With moderate agreement between FPCT and CCT, the difference in their diagnostic ability to detect or exclude BBB disruption was shown to be significant ($P = .03$) by 1 reader. The sensitivity, specificity, positive and negative predictive values, and accuracy for this feature were 75% (range, 43%–93%), 85% (range, 73%–93%), 50% (range, 27%–73%), 95% (range, 84%–99%), and 84% (range, 73%–90%). The inter-rater agreement was good for evaluating FPCT with respect to intracranial bleeding ($\kappa = 0.76$; 95% CI, 0.58–0.94) and BBB disruption ($\kappa = 0.68$; 95% CI, 0.48–0.87).

Attenuation Measurement

If one divided FPCT hyperattenuation into SAH, ICB, and BBB disruptions, the median values of maximum attenuation measurements in true-positive and false-positive regions were 159 versus 223 ($n = 6$ versus 4; $P = .524$), 375 versus 678 ($n = 2$ versus 2; $P = .833$), and 163 versus 114 ($n = 8$ versus 6; $P = .103$), respectively. A significant difference could not be found in any of the 3 subgroups.

DISCUSSION

Flat panel detector–based CT is known to be a very useful tool for the detection or exclusion of peri-interventional complications.⁶ It provides cross-sectional images of the brain without the necessity of transferring patients from the angiography suite to a conventional CT facility.^{4,15}

In a swine brain model, Arakawa et al⁵ were able to detect intracranial hematomas with a hematocrit level of 20%. Symptomatic intracerebral hemorrhage still represents the most feared

complication of treatment with intravenous tPA. While hemorrhagic infarction may be a clinically irrelevant epiphenomenon of ischemic damage and reperfusion,^{16,17} parenchymal hematoma was hypothesized to be related to the biologic effects of tPA and other pre-existing pathologic conditions associated with a worse outcome and higher mortality.^{18,19} Accordingly, the severity and duration of ischemia were found to be predictors of the type of hemorrhagic transformation, but not parenchymal hematoma type after IV thrombolysis.²⁰ In the present study, acute stroke therapy consisted of endovascular intervention in all patients. Instead of exclusive IV thrombolytic drug treatment, intra-arterial urokinase or the Solitaire FR thrombectomy system (Covidien, Irvine, California) were applied with or without IV rtPA bridging therapy. The Solitaire endovascular device has proved to be a valid tool in the treatment of acute ischemic stroke, providing effective and relatively safe arterial recanalization.^{11,12,21,22}

In our study of FPCT after endovascular stroke treatment—with IV bridging thrombolysis in 10%, intra-arterial thrombolysis in 56%, and mechanical thrombectomy in 81% of patients—an intracranial hematoma was present in 16% of all cases. While most ICB (5% of patients) was found to be a clinically less relevant hemorrhagic transformation, parenchymal hematoma was a rare incident (4%); however, it was combined with SAH in all 3 cases.¹³ Subarachnoid hemorrhage was still found in 11% of patients.

For the detection of intracranial bleeding by FPCT, the positive predictive value in our series of 73 patients was remarkably low (44%). In contrast to that, we were able to exclude hemorrhage in the interventional unit with a negative predictive value of 91%.

Inferior or, rarely, insufficient image quality in the posterior fossa was shown to be a drawback of FPCT, which may become relevant in macroembolic stroke of the posterior circulation. However, infratentorial blood was detected in only 2 patients in our series with peri-interventional extravasation during recanalization of 1 of their middle cerebral arteries, and it was combined with supratentorial hemorrhage in both cases.

Albeit in a small number of relevant cases, attenuation measurements did not seem to be useful for the differentiation of postinterventional hyperattenuation in FPCT.

Following diagnostic cerebral angiography and interventional procedures, immediate brain CT findings may reveal various patterns of abnormal contrast enhancement, with or without neurologic deficits.^{8,9,23–25} Such findings, which are believed to result from some degree of BBB disruption or a change in vascular permeability, can mimic SAH, intraventricular hemorrhage, or so-called hyperintense acute reperfusion marker on fluid-attenuated inversion recovery MR imaging^{25–27} and may cause unnecessary delay in anticoagulant/antiaggregant treatment. After apparently uneventful endovascular coiling of intracranial aneurysms, a sig-

nificant relationship was reported between the occurrence of transient cortical hyperattenuation and the amount of contrast material used per kilogram of body weight, the microcatheter time, the number of balloon inflations, the total time of balloon inflation, BBB changes following temporary and permanent ischemia, SAH, more advanced patient age, spontaneous hypertension as a result of transient ischemia, and IV heparin.

These previous findings may be transferred to transarterial stroke interventions with reservation. An inverse relation was reported between transient cortical hyperattenuation and the time elapsed until the CT was performed.⁸ In this context, a time interval of, on average, 17.2 hours (range, 0.6–45.9 hours) between FPCT and CCT must be considered for the interpretation of our results, with FPCT performed immediately postintervention. This latency period should be appropriate for intracranial hemorrhage to be confirmed by the criterion standard. On the other hand, it may be hypothesized that transient hyperattenuation due to BBB disruptions—as observed in 16% of CCT follow-up scans—may resolve earlier than bleeding-related hyperattenuation. With only moderate agreement between FPCT and CCT, a positive predictive value of not more than 50% contradicted a negative predictive value of 95%. Although BBB disruption was suspected in FPCT much more often than in CCT, it did not turn out to be hemorrhage in any case of our series.

In the study published by Baik et al,⁹ MR imaging did not reveal any corresponding abnormalities and the abnormal CT findings had partially or totally resolved on 24-hour follow-up CT scans. The breakdown of the BBB in the presence of iodine is known to be related to the osmolality and chemical structure of the contrast medium, the route of administration, and the speed of injection.^{28,29} Besides SAH, different types of abnormal hyperattenuation have been reported immediately after embolization of cerebral aneurysms, such as subarachnoid hyperattenuation, cortical hyperattenuation, and intraventricular and striatal contrast enhancement.^{9,15} This finding may be attributable to the fact that intravascular contrast media potentially passes the blood-brain interface, the blood-CSF interface, and/or the brain-CSF interface.³⁰ Following recanalization of the middle cerebral artery, incomplete striatal hyperattenuation was the most common imaging pattern attributable to BBB disruption in our study.

Potentially, a major limitation of this study is the latency between FPCT and CCT because early BBB disruption may be a precursor of symptomatic intracerebral hemorrhage.^{23,24} However, this progression has not been the case in any of our patients. While FPCT—the method under investigation—served as an instant postinterventional examination, there is a widely accepted recommendation for follow-up CCT, serving as the criterion standard, to be performed approximately 24 hours after acute stroke treatment. The dual-energy mode, which had been reported to be of great value in this context, was not applied during CCT acquisition.³¹ Second, a few patients with stroke had to be excluded from this retrospective study due to missing FPCT scans or unacceptably long follow-up periods—both caused by individual situations in clinical routine. Third, our study is based on a relatively inhomogeneous population as far as the mode of acute stroke treatment is concerned with intra-arterial thrombolysis or mechanical thrombectomy being the mainstay of therapy. Finally,

FPCT has considerable limited image quality below the tentorium. Even though playing a minor role in macroembolic stroke of the anterior circulation, limited image quality below the tentorium may potentially be relevant to patients after recanalization of the basilar artery. In our opinion, the qualitative image characteristics of both FPCT units were comparable for the objective of this study.

CONCLUSIONS

Severe bleeding complications seem to be rare after endovascular treatment of macroembolic stroke and may be associated with iatrogenic perforation of an intracranial artery. Flat panel CT in the immediate follow-up of endovascular stroke treatment was able to exclude intracranial hemorrhage with a high negative predictive value. Future studies should evaluate the predictive value of BBB disruptions in FPCT for the development of relevant hematomas.

Disclosures: Thomas Kau—UNRELATED: Travel/Accommodations/Meeting Expenses Unrelated to Activities Listed: Philips, Siemens, Guerbet, Bayer-Schering, Bracco, ev3, Boston Scientific. Michael Hauser—UNRELATED: Travel/Accommodations/Meeting Expenses Unrelated to Activities Listed: Medtronic (Congress), Covidien (Congress). Sonja M. Obmann—UNRELATED: Payment for Lectures (including service on Speakers Bureaus): Boehringer-Ingelheim, Pfizer, Lilly. Jörge R. Weber—UNRELATED: Consultancy: Biogen Idec, Novartis, Boehringer-Ingelheim, Bayer, Sanofi, Merck, Comments: consultancy and expert opinions. Payment for Development of Educational Presentations: Biogen, Idec Austria, Novartis Austria, Comments: The presentation for Biogen Idec was only for internal use within the company. Klaus A. Hausegger—UNRELATED: Board Membership: Cardiovascular and Interventional Radiological Society of Europe, Payment for Lectures (including service on Speakers Bureaus): Fachhochschule Kärnten.

REFERENCES

1. Jaffray DA, Siewerdsen JH. Cone-beam computed tomography with a flat-panel imager: initial performance characterization. *Med Phys* 2000;27:1311–23
2. Gupta R, Cheung AC, Bartling SH, et al. Flat-panel volume CT: fundamental principles, technology, and applications. *Radiographics* 2008;28:2009–22
3. Struffert T, Doerfler A. Flat-detector computed tomography in diagnostic and interventional neuroradiology [German]. *Radiolog* 2009;49:820–29
4. Hausegger KA, Fürstner M, Hauser M, et al. Clinical application of flat-panel CT in the angio suite [German]. *Rofo* 2011;183:1116–22
5. Arakawa H, Marks MP, Do HM, et al. Experimental study of intracranial hematoma detection with flat panel detector C-arm CT. *AJNR Am J Neuroradiol* 2008;29:766–72
6. Psychogios MN, Buhk JH, Schramm P, et al. Feasibility of angiographic CT in peri-interventional diagnostic imaging: a comparative study with multidetector CT. *AJNR Am J Neuroradiol* 2010;31:1226–31
7. Uchiyama Y, Abe T, Tanaka N, et al. Factors contributing to blood-brain barrier disruption following intracarotid injection of non-ionic iodinated contrast medium for cerebral angiography: experimental study in rabbits. *Radiat Med* 2006;24:3212–16
8. Ozturk A, Saatci I, Pamuk AG, et al. Focal increased cortical density in immediate postembolization CT scans of patients with intracranial aneurysms. *AJNR Am J Neuroradiol* 2006;27:1866–75
9. Baik SK, Kim YS, Lee HJ, et al. Immediate CT findings following embolization of cerebral aneurysms: suggestion of blood-brain barrier or vascular permeability change. *Neuroradiology* 2008;50:259–66
10. Mullen MT, Pisapia JM, Tilwa S, et al. Systematic review of outcome after ischemic stroke due to anterior circulation occlusion treated

- with intravenous, intra-arterial, or combined intravenous+intra-arterial thrombolysis. *Stroke* 2012;43:2350–55
11. Mordasini P, Brekenfeld C, Byrne JV, et al. Technical feasibility and application of mechanical thrombectomy with the Solitaire FR revascularization device in acute basilar artery occlusion. *AJNR Am J Neuroradiol* 2013;34:159–63
 12. Pereira VM, Gralla J, Davalos A, et al. Prospective, multicenter, single-arm study of mechanical thrombectomy using Solitaire flow restoration in acute ischemic stroke. *Stroke* 2013;44:2802–07
 13. Fiorelli M, Bastianello S, von Kummer R, et al. Hemorrhagic transformation within 36 hours of a cerebral infarct: relationships with early clinical deterioration and 3-month outcome in the European Cooperative Acute Stroke Study I (ECASS I) cohort. *Stroke* 1999;30:2280–84
 14. Fisher CM, Kistlet JP, Davis JM. Relation of cerebral vasospasm to subarachnoid hemorrhage visualized by computerized tomographic scanning. *Neurosurgery* 1980;6:1–9
 15. Shinohara Y, Sakamoto M, Takeuchi H, et al. Subarachnoid hyperattenuation on flat panel detector-based conebeam CT immediately after uneventful coil embolization of unruptured intracranial aneurysms. *AJNR Am J Neuroradiol* 2013;34:577–82
 16. Molina CA, Alvarez-Sabin J, Montaner J, et al. Thrombolysis-related hemorrhagic infarction: a marker of early reperfusion, reduced infarct size, and improved outcome in patients with proximal middle cerebral artery occlusion. *Stroke* 2002;33:1551–56
 17. von Kummer R. Brain hemorrhage after thrombolysis: good or bad? *Stroke* 2002;33:1446–47
 18. Larrue V, von Kummer RR, Muller A, et al. Risk factors for severe hemorrhagic transformation in ischemic stroke patients treated with recombinant tissue plasminogen activator: a secondary analysis of the European-Australasian Acute Stroke Study (ECASS II). *Stroke* 2001;32:438–41
 19. Berger C, Fiorelli M, Steiner T, et al. Hemorrhagic transformation of ischemic brain tissue: asymptomatic or symptomatic? *Stroke* 2001;32:1330–35
 20. Thomalla G, Sobesky J, Köhrmann M, et al. Two tales: hemorrhagic transformation but not parenchymal hemorrhage after thrombolysis is related to severity and duration of ischemia: MRI study of acute stroke patients treated with intravenous tissue plasminogen activator within 6 hours. *Stroke* 2007;38:313–18
 21. Mokin M, Dumont TM, Veznedaroglu E, et al. Solitaire flow restoration thrombectomy for acute ischemic stroke: retrospective multicenter analysis of early postmarket experience after FDA approval. *Neurosurgery* 2013;73:19–25
 22. Yoon YH, Yoon W, Jung MY, et al. Outcome of mechanical thrombectomy with Solitaire stent as first-line intra-arterial treatment in intracranial internal carotid artery occlusion. *Neuroradiology* 2013;55:999–1005
 23. Hjort N, Wu O, Ashkanian M, et al. MRI detection of early blood-brain barrier disruption: parenchymal enhancement predicts focal hemorrhagic transformation after thrombolysis. *Stroke* 2008;39:1025–28
 24. Kastrup A, Gröschel K, Ringer TM, et al. Early disruption of the blood-brain barrier after thrombolytic therapy predicts hemorrhage in patients with acute stroke. *Stroke* 2008;39:2385–87
 25. Köhrmann M, Struffert T, Frenzel T, et al. The hyperintense acute reperfusion marker on fluid-attenuated inversion recovery magnetic resonance imaging is caused by gadolinium in the cerebrospinal fluid. *Stroke* 2012;43:259–61
 26. Morris JM, Miller GM. Increased signal in the subarachnoid space on fluid-attenuated inversion recovery imaging associated with the clearance dynamics of gadolinium chelate: a potential diagnostic pitfall. *AJNR Am J Neuroradiol* 2007;28:1964–67
 27. Rozanski M, Ebinger M, Schmidt WU, et al. Hyperintense acute reperfusion marker on FLAIR is not associated with early haemorrhagic transformation in the elderly. *Eur Radiol* 2010;20:2990–96
 28. Wilson AJ, Evill CA, Sage MR. Effects of nonionic contrast media on the blood brain barrier: osmolality versus chemotoxicity. *Invest Radiol* 1991;26:1091–94
 29. Kuhn MJ, Burk TJ, Powell FC. Unilateral cerebral cortical and basal ganglia enhancement following overdosage of nonionic contrast media. *Comput Med Imaging Graph* 1995;19:307–11
 30. Sage MR, Wilson AJ, Scroop R. Contrast media and the brain: the basis of CT and MR imaging enhancement. *Neuroimaging Clin N Am* 1998;8:695–707
 31. Phan CM, Yoo AJ, Hirsch JA, et al. Differentiation of hemorrhage from iodinated contrast in different intracranial compartments using dual-energy head CT. *AJNR Am J Neuroradiol* 2012;33:1088–94

Intracranial Aneurysmal Pulsatility as a New Individual Criterion for Rupture Risk Evaluation: Biomechanical and Numeric Approach (IRRA Project)

M. Sanchez, O. Ecker, D. Ambard, F. Jourdan, F. Nicoud, S. Mendez, J.-P. Lejeune, L. Thines, H. Dufour, H. Brunel, P. Machi, K. Lobotesis, A. Bonafe, and V. Costalat

ABSTRACT

BACKGROUND AND PURPOSE: The present study follows an experimental work based on the characterization of the biomechanical behavior of the aneurysmal wall and a numerical study where a significant difference in term of volume variation between ruptured and unruptured aneurysm was observed in a specific case. Our study was designed to highlight by means of numeric simulations the correlation between aneurysm sac pulsatility and the risk of rupture through the mechanical properties of the wall.

MATERIALS AND METHODS: In accordance with previous work suggesting a correlation between the risk of rupture and the material properties of cerebral aneurysms, 12 fluid-structure interaction computations were performed on 12 “patient-specific” cases, corresponding to typical shapes and locations of cerebral aneurysms. The variations of the aneurysmal volume during the cardiac cycle (ΔV) are compared by using wall material characteristics of either degraded or nondegraded tissues.

RESULTS: Aneurysms were located on 6 different arteries: middle cerebral artery (4), anterior cerebral artery (3), internal carotid artery (1), vertebral artery (1), ophthalmic artery (1), and basilar artery (1). Aneurysms presented different shapes (uniform or multilobulated) and diastolic volumes (from 18 to 392 mm³). The pulsatility ($\Delta V/V$) was significantly larger for a soft aneurysmal material (average of 26%) than for a stiff material (average of 4%). The difference between ΔV , for each condition, was statistically significant: $P = .005$.

CONCLUSIONS: The difference in aneurysmal pulsatility as highlighted in this work might be a relevant patient-specific predictor of aneurysm risk of rupture.

ABBREVIATION: FSI = fluid-structure interaction

Intracranial aneurysms kill about 15,000 people in Europe each year. Most are young, between 40 and 60 years old. New medical imaging techniques are now able to clearly depict intracranial aneurysm, but no systematic screening of this disease exists at the moment. The main reason is that 2%–6% of the general population lives with an aneurysm,¹ but only 0.5% of these will rupture. Screening for intracranial aneurysm is not justified unless it is capable of detecting vulnerable aneurysms. Subarachnoid hemorrhage is the consequence of aneurysm rupture and approximately 12% of patients with SAH die before receiving medical attention,

40% of patients will die within the first month, and 30% will present with a severe permanent disability. Nevertheless, with brain imaging being more frequently and widely used, a growing number of intracranial aneurysms are being diagnosed, introducing the question of which aneurysms harbor a sufficiently high risk of rupture to merit a prophylactic repair. This question remains unsolved at the moment and the therapeutic decision for an unruptured aneurysm is still a challenging point discussed by the neurosurgeon/neurointerventionist based on sparse epidemiologic clinical data that cannot represent the specific individual risk of the patient.

Recent publications have addressed this issue and have demonstrated that, among other variables affecting the natural history of aneurysms, size and location represent independent predictors of both risk of rupture and surgical/endovascular repair outcomes.^{2,3} Other parameters, such as irregular aneurysm shape and the presence of blebs are recognized as markers of weak wall structure and high risk of rupture. Rapid aneurysm growth is also likely a risk factor for rupture.⁴

From a mechanical point of view, the rupture of an aneurysm occurs when wall tension exceeds the strength of the wall tissue.

Received May 23, 2013; accepted after review November 20.

From Philips Healthcare, Suresnes, France (M.S.); CHU Montpellier Neuroradiology, Montpellier, France (O.E., P.M., A.B., V.C.); CNRS-LMGC Montpellier, Montpellier, France (M.S., F.J., D.A.); CNRS-I3M Montpellier, Montpellier, France (F.N., S.M.); CHU Lille Neurosurgery, Lille, France (J.-P.L., L.T.); CHU Marseille Neurosurgery, Marseille, France (H.D.); CHU Marseille Neuroradiology, Marseille, France (H.B.); and Imperial College Healthcare NHS Trust, London, England (K.L.).

Please address correspondence to Mathieu Sanchez, PhD, LMGC-UMR5508, Université Montpellier 2 CC048 Place Eugène Bataillon, 34095 Montpellier Cedex 5 France; e-mail: mathieu.sanchez@univ-montp.fr

<http://dx.doi.org/10.3174/ajnr.A3949>

Because these quantities cannot be assessed via conventional medical imaging, a natural approach is to compute the wall tension and set a rupture threshold.

Few studies consider the coupled fluid-structure interaction (FSI) problem, where the flow equations for blood are solved together with the structural equations for the tissue.⁵ The problem is the lack of data on mechanical properties of cerebral arteries and aneurysms; most of the studies based on an FSI⁶⁻¹⁰ framework do not use experimental mechanical behavior of the aneurysm wall as input. A few exceptions exist for abdominal aorta aneurysms^{11,12} but not for intracranial aneurysms until recently when, in a study by Costalat et al,¹³ the aneurysm wall properties were characterized and a classification of aneurysm wall behavior was carried out. One of the main conclusions of this work was that the clinical status of the aneurysm (unruptured, pruruptured, and ruptured) was strongly correlated with the mechanical behavior of the aneurysm wall and, hence, a classification was proposed (stiff, intermediate, and soft).

This was followed with FSI computations by Sanchez et al,¹⁴ who demonstrated for 1 specific aneurysm that the different mechanical properties of the aneurysm wall (stiff or soft) are responsible for significantly different variations in aneurysm volume over the cardiac cycle (pulsatility). A parametric study was also achieved in this work and demonstrated that uncertainties did not change the main conclusion.

The further application of these results to the in vivo setting and in particular to cerebral aneurysms arising from the circle of Willis is an additional important step.

Table 1: Material coefficients of the aneurysm walls used in the present study

Aneurysm	C_{10} (MPa)	C_{01} (MPa)	C_{11} (MPa)
Soft	0.024	0.026	0.42
Stiff	0.39	0	22.14

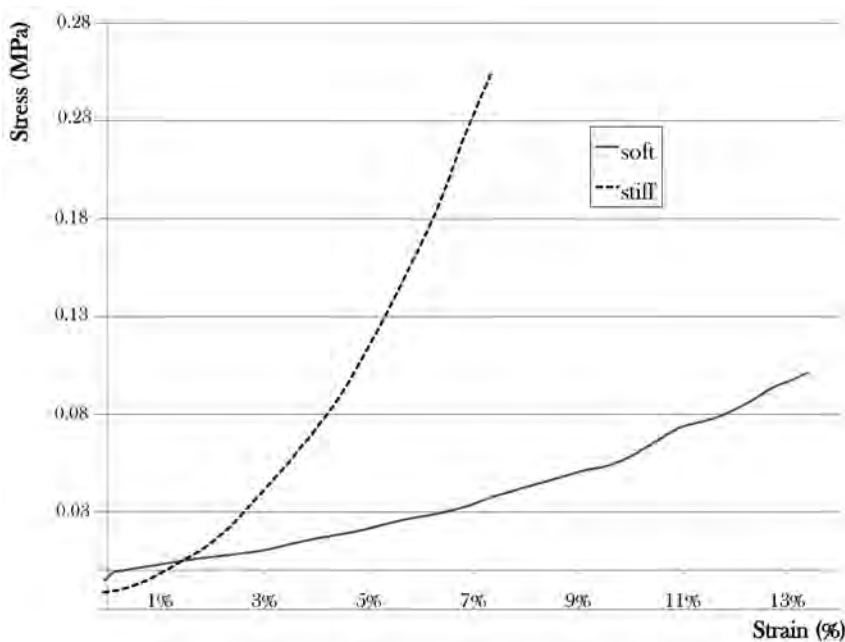


FIG 1. Nominal stress/engineering strain curves representing the average mechanical properties of the soft and the stiff classes.

The aim of this work was to investigate and verify the correlation between wall biomechanical properties (stiff and soft) and aneurysmal volume variation during the cardiac cycle for a variety of Willis.

This study was conceived and carried out as part of the Individual Risk of Rupture Assessment consortium, which is a research project dedicated to the evaluation of patient-specific risk of rupture of cerebral aneurysms. The consortium brings together neurosurgeons, neuroradiologists, and researchers in biomechanical engineering in a common translational research project.

MATERIALS AND METHODS

Identification of Mechanical Behavior of Aneurysm Wall

The details of the study establishing the correlation between the aneurysm status and tissue mechanical properties are given in the work of Costalat et al.¹³ The methodology and main results are briefly given for the sake of completeness. A similar study was conducted by Duprey et al¹⁵ for thoracic aortic aneurysms.

Each sample was studied as appropriate for biomaterials.¹⁶⁻¹⁹ Only the meridional axis of the aneurysm was chosen to preserve maximum length of the aneurysmal tissue in the sample, given the very small size of each specimen and the fragility of the tissue. Using these measurement series, a model of the tissue behavior was proposed for large displacements to represent the evolution of the stress in the materials.²⁰ For this purpose, the assumption that the material is isotropic and noncompressible was made and the hyperelastic model of Mooney-Rivlin with 3 parameters was selected.¹ It reads:

$$1) \quad W = C_{10}(I_1 - 3) + C_{01}(I_2 - 3) + C_{11}(I_1 - 3)(I_2 - 3),$$

where W is the strain energy potential, $I_1 = \text{tr}(C)$ and $I_2 = \frac{1}{2}(\text{tr}^2(C) - \text{tr}(C^2))$ are the first and second strain invariants of the right Cauchy-Green deformation tensor C , and C_{10} , C_{01} , and C_{11} are the material coefficients.

All unruptured aneurysms presented as stiffer tissue than the ruptured aneurysms.

Their mechanical behavior was either stiff or intermediate. Conversely, all ruptured aneurysms correspond to a soft tissue. The corresponding parameters are given in Table 1 while the strain/stress curves are displayed in Fig 1.

Numeric Method

Aneurysmal Geometry. Aneurysm geometry was obtained from 3D rotational angiography. Using dedicated software ScanIP (Simpleware, Exeter, United Kingdom), the aneurysmal geometries were cleaned up by keeping only the aneurysms and the parent vessels to reduce the region of interest. A low-pass filter was applied on the geometries to reduce

noise-to-signal ratio. The results were exported as stereolithography files to proceed to numeric analysis.

Simulation Parameters. The flow boundary conditions imposed were obtained from specific patient examinations by using phase-contrast MR imaging for each aneurysm location (3T Skyra; Siemens, Erlangen, Germany). The velocity profiles were considered as uniform. Outlet pressure was computed by computational fluid dynamics and used as boundary conditions at the outlet of the computational domain. The pressure was obtained by resolving the 1D equations in the arterial network with boundary flow conditions from the imaging measurement.²¹

An intracranial pressure of 20 mm Hg²² was applied on the external surface of the geometries to recreate the in vivo conditions.

Physical Modeling. The blood flow within the computational domain is described by the incompressible Navier-Stokes equations (2) and (3)

$$2) \quad \rho_f \frac{dv_f}{dt} = \text{div } \sigma^f,$$

$$3) \quad \text{div}(v_f) = 0,$$

where v_f is the time dependent flow velocity vector, ρ_f is the attenuation of blood, and σ^f is the stress tensor for the fluid part. The flow is assumed to be laminar, a reasonable assumption given the moderate value of the Reynolds number ($Re \approx 300$). Blood is modeled as a Newtonian fluid,⁴ of attenuation of $\rho_f = 1050 \text{ kg/m}^3$ and dynamic viscosity of $\mu = 0.004 \text{ Pa} \times \text{s}$.^{9,23-25}

$$4) \quad \sigma^f = -pI + 2 \mu D,$$

where p is the pressure, I is the identity tensor, and D is the rate of deformation tensor.

For the parent artery, a linear elastic model was selected to focus the attention on the aneurysmal sac and to reduce the computational time. The structural equation solved for both the artery and aneurysmal sac reads⁵:

$$5) \quad \rho_s \frac{\partial v_s}{\partial t} = \text{div } \sigma^s$$

where σ^s is the Cauchy strain for the structural part and v_s stands for the structural velocity vector.

The aneurysm wall is modeled as an isotropic incompressible hyperelastic material⁶:

$$6) \quad \sigma^s = \rho_s F \frac{\partial W}{\partial E} F^t - pI,$$

where F is the transformation gradient tensor, E is the Green Lagrangian strain tensor, and W is the strain energy potential defined in Eq. (1).

The material used for the parent artery has the following properties: Young modulus $E = 3 \text{ MPa}$, Poisson ratio $\nu = 0.49$, specific mass $\rho_s = 2300 \text{ kg/m}^3$, and thickness $e_{pa} = 0.6 \text{ mm}$.^{24,26} The thickness of the aneurysm wall is $e = 0.38 \text{ mm}$. A linear model was used for the arterial wall because the deformations are small enough in all cases (<5%) to stay in the small deformation theory.

Furthermore, the edge nodes of the arterial extremities are taken away from the displacement in the longitudinal direction.

FSI Computations. Computations were performed by using Workenck version 13 (ANSYS, Canonsburg, Pennsylvania). The fluid motion equations were solved with the software CFX, which uses the finite volume approach and the Newton-Raphson method for solving the subsequent nonlinear system. For the structural part, Mechanical software employed the finite-element method and the Newton-Raphson algorithm. The wall pressure resulting from the fluid was imported as boundary conditions in the structural analysis while wall displacement calculated by the structure solver was imported as a boundary condition for the fluid solver; this procedure was carried out in an iterative manner within each time-step. It was an iterative implicit coupling. At the interface of the 2 physical domains, the element type differs and the nodes of the 2 meshes did not coincide, so surface interpolation was carried out.²⁷ For each FSI computation, a time-step of 0.004 seconds was used. The structural meshes were composed by 2500 to 5000 shell elements and the fluid meshes by 100,000 to 300,000 tetrahedral elements. These meshes were fine enough to ensure the convergence of the computations. The 2 FSI computations of the reference case from Sanchez et al¹⁴ were performed for mesh refinements multiplied by 10 (about 30,000 elements for structural mesh and 1,000,000 elements for fluid mesh). Despite a significant increase of the computation time, the results were similar. For example, in the soft case, the maximal mesh displacement was 0.78 instead of 0.77 mm (variation of 1.3%) and the volume variation was 44.3 mm³ instead of 44 mm³ (variation of 0.7%).

A structural computation was performed before the FSI computation to determine the stress state of the acquired geometry. All the details about the initial stress of the aneurysm geometry are given in Sanchez et al.¹⁴

Wall Motion Analysis. For each aneurysmal geometry, 2 FSI computations were performed by using the 2 different biomechanical properties (stiff and soft) defined in the Identification of Mechanical Behavior of Aneurysm Wall section. Volume variations and wall motions were calculated for each aneurysm. For each case, the systolo-diastolic variation of the volume of the aneurysm (ΔV) was computed from the results. The maximal mesh displacement on the aneurysm sac D_{max} was also calculated. ΔV represents global information about the aneurysmal sac behavior whereas D_{max} provides local information (maximal displacement of a point of the aneurysm boundary).

To compare ΔV and D_{max} between soft and stiff material for different aneurysms, we defined the following ratio:

$$R_v = \Delta V^{soft} / \Delta V^{stiff}$$

$$R_d = D_{max}^{soft} / D_{max}^{stiff}$$

A pulsatility index was also defined as: Pulsatility = $\Delta V/V$, where V is the diastolic volume of the aneurysmal sac.

Statistical Analysis

A statistical analysis was performed to evaluate the influence of ΔV and D_{max} in soft and stiff cases. The comparison was made by using a nonparametric Wilcoxon rank test for continuous variables and a Fisher exact test for categoric ones. Statistical significance threshold was set at 5%. Statistical analyses were performed by using SAS version 9.1 (SAS Institute, Cary, North Carolina).

Table 2: Aneurysm geometry information

Aneurysm	Location	V (mm ³)	Shape	D (mm)	N (mm)	D/N
1	MCA R	61	Simple	4.8	4	1.2
2	MCA L	51	Complex	3.4	3.75	0.91
3	ACA	161	Simple	5.25	5.6	0.94
4	MCA R	188	Complex	5.5	6.5	0.85
5	ICA	392	Complex	9.2	5	1.84
6	VA	45	Simple	4	2.3	1.74
7	MCA L	212	Complex	7.8	6.6	1.18
8	ACA	232	Complex	8	4.5	1.78
9	ACA	79	Complex	6.85	2.9	2.36
10	OA	138	Simple	6.1	4.3	1.41
11	BA	68	Complex	4.4	3.9	1.13
12	BA	18	Simple	3	3	1

Note:—V indicates diastolic volume; D, the dome size; N, the neck size; D/N, the ratio of dome/neck; ACA, anterior cerebral artery; VA, vertebral artery; OA, ophthalmic artery; BA, basilar artery; R, right; L, left.

RESULTS

Aneurysm Population

Twelve aneurysms from 12 different patients were computed with the stiff and the soft materials. These aneurysms were located on 7 different arteries: left and right middle cerebral arteries (4 cases), anterior cerebral artery (3 cases), ICA (1 case), vertebral artery (1 case), ophthalmic artery (1 case), and basilar artery (2 cases). These had a variety of shapes: simple (uniform) or complex (multilobulated). The volume varied from 18 mm³ to 392 mm³. Geometric information is displayed in Table 2.

Wall Motion Results

Figure 2 gives an example of the FSI results for 3 different cases by displaying maximum displacement for the simulations with soft or stiff materials. All results of the patient-specific FSI computations are displayed in Tables 3 and 4. Two aneurysms (5 and 6) show unusual results. For aneurysm 5, the volume variation is 149 mm³. The important initial volume of the aneurysm sac, almost 400 mm³, can explain this important variation. This aneurysm could be considered as a giant aneurysm. Nevertheless, the pulsatility ratio is still in the range of 30% in comparison to an overall mean of 25% for the cases. For aneurysm 6, the pulsatility is much more important than in the other cases. That is the result of a volumetric flow rate more important in this location (vertebral artery) for this specific patient compared with the others (Table 4); this due to the particularity of this cerebral arterial network.

A significant difference was observable between ΔV for a stiff material and for a soft material ($P = .005$). Consequently, the pulsatility index ($\Delta V/V$) was obviously more important for a soft aneurysmal sac (average of 26%) than for a stiff aneurysmal sac (average of 4%), despite the relatively small number of aneurysms considered.

Naturally, we found the same difference for the ratio R_v : R_v varies from 4 (aneurysm 7 and 10) to 16 (aneurysm 2) for an average of 7. R_d also showed differences between stiff and soft materials but to a lesser extent: the minimum was 1.5 (aneurysm 6) and the maximum was 5 (aneurysm 4) and the average was 3 (Table 5). The difference between ΔV and D_{max} for each condition was statistically significant: $P = .005$ for ΔV and $P = .02$ for D_{max} .

DISCUSSION

Our results clearly suggest that the wall displacement provides information about the level of degradation of the aneurysm wall and, thanks to the findings of Costalat et al,¹³ about the rupture risk of the aneurysm sac. Our study shows that whatever the location of the aneurysm on the circle of Willis, the aneurysmal pulsatility was about 7 times higher for soft/ruptured aneurysms in comparison with stiff/unruptured aneurysms (26% versus 4%). That is the result of a volumetric flow rate more important in this location (vertebral artery) compared with the others (Table 4). These observations are consistent with our previous work (the study from Sanchez et al,¹⁴ using FSI computations) where a significant difference between the displacements and volume variations corresponding to the soft (close to the rupture) and stiff (undegraded) tissues was observed in a particular case. This result is generalized to the entirety of the circle of Willis in this paper.

Interestingly, in an observational study on 51 patients, Hayakawa et al,²⁸ using 4D CT angiography, highlighted that the pulsation of the aneurysm sac (or volume variation) between ruptured aneurysms and unruptured aneurysms was significantly different. In their study, 12/51 cerebral aneurysms were ruptured. Among these 12 ruptured cerebral aneurysms, a pulsation was observed in 9 cases (75%). Thirty-nine cerebral aneurysms were unruptured; among these 39 unruptured cerebral aneurysms, a pulsation was observed in 12 cases (30%). Two of these 12 pulsating unruptured cerebral aneurysms were treated by surgery because of the clinical background of the patients. They came to the conclusion that the detection of pulsation in an unruptured aneurysm could therefore be a clue of an important risk factor. Our results confirm this point of view.

Furthermore, the precision needed to identify the aneurysmal wall motion variation between unruptured/ruptured aneurysm would be about 0.1 mm (D_{max}) or 0.5 mm³ (ΔV) according to our study. New imaging techniques may approach this high resolution level in recent literature (for example Ishida et al²⁹ and Zhang et al³⁰).

To date, the most relevant solution has been proposed by Karmonik et al³¹ who used 2D phase contrast MR imaging (1.5T MR imaging) to observe wall displacement over the cardiac cycle on 7 patients (7 aneurysms) and 3 different locations (anterior communicating artery, basilar artery, and ICA). This noninvasive technique was accurate enough to measure wall displacements as small as 0.04 mm, in the range of the expected wall displacement reported in our study. New generation MR imaging at 3T could offer a more accurate depiction of the wall motion in the next future.

As already stated, D_{max} gives local information about the wall displacement and in some cases, this parameter is not accurate enough to clearly demonstrate a difference between degraded/ruptured and nondegraded/unruptured aneurysms. The variation of the maximal mesh displacement measured by the software depends strongly on the displacement of the artery. The deformation of the artery induces an additional displacement of the mesh of the aneurysmal sac. Then, the bulge of the artery is added to the displacement of the sac in relation to the artery to obtain the total maximal mesh displacement.

As shown in Table 4, the value of the ratio R_v is more impor-

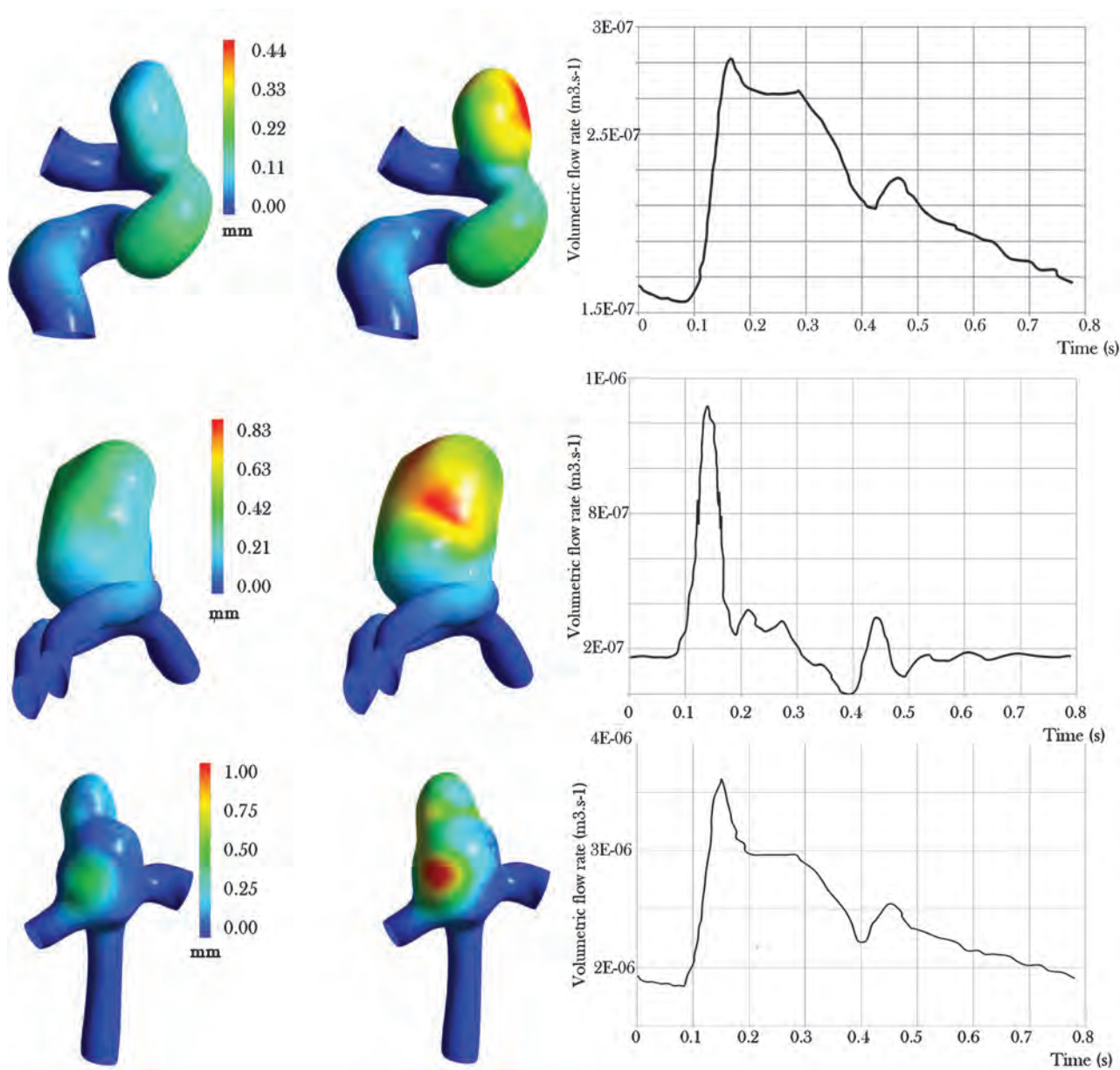


FIG 2. FSI maximal mesh displacement results for the systolic pressure for aneurysms 10 (top), 8 (middle row), and 7 (bottom row) with the volumetric flow rate imposed at the inlet (on the left for the stiff material and on the right for the soft material).

tant than R_d and allows us to better characterize aneurysm status. Furthermore, ΔV is a global indicator and is less sensitive to the uncertainties of the input parameters of the computations.¹⁴ ΔV is thus thought to be a better parameter to evaluate the risk of rupture.

A limitation of this study was the simplification of the aneurysmal environment in the FSI computations, by assuming that the aneurysm lies in a fluid of a given pressure. This environment would probably influence the geometric variations of the aneurysm depending on the location; friction and contact of the wall with other structures (bone, meninges, arachnoid trabeculae, cerebrospinal fluid) will certainly impact the wall motion.^{32,33} The assumptions made regarding the aneurysm wall are another limitation. In the present study, the aneurysm wall was considered as isotropic and homogeneous, but the anisotropy of this kind of biologic material is well known.³⁴ Nevertheless, isotropy and ho-

mogeneity were assumed because they most probably do not change the trends observed when comparing soft and stiff materials in this range of physiologic solicitation. To characterize the behavior of blood, more sophisticated models can be used to account for non-Newtonian effects, especially in the aneurysmal sac (Cebal et al³⁵ and Sforza et al³⁶). However, these effects are expected to be prevalent only when dealing with local quantities like wall shear stress. This is not the case in the present study where the aneurysmal volume, which is primarily influenced by the pressure forces generated by the blood flow, was analyzed.

Numerous parameters are not known precisely when computing the FSI problem for a specific patient: wall thickness, fluid boundary conditions, artery properties, and intracranial pressure.

Despite these last limitations, the parametric study achieved in previous work¹⁴ showed a positive consistency with our results

Table 3: Results of FSI computations for 12 different aneurysms for stiff and soft materials

Aneurysm	Material	V (mm ³)	ΔV (mm ³)	Pulsatility = ΔV/V (%)	D _{max} (mm)
1	Soft	61	10	16	0.35
	Stiff		1	2	0.12
2	Soft	51	8	16	0.32
	Stiff		0.5	1	0.09
3	Soft	161	44	27	0.7
	Stiff		6	4	0.26
4	Soft	188	37	20	0.71
	Stiff		7	4	0.15
5	Soft	392	149	38	1
	Stiff		18	5	0.45
6	Soft	45	33	73	1.8
	Stiff		4	9	1.2
7	Soft	212	60	28	1.05
	Stiff		14	7	0.48
8	Soft	232	54	23	0.84
	Stiff		10	4	0.4
9	Soft	79	15	19	0.48
	Stiff		3	4	0.15
10	Soft	138	26	19	0.47
	Stiff		5	4	0.17
11	Soft	68	11	16	0.42
	Stiff		2.5	4	0.12
12	Soft	18	4	22	0.27
	Stiff		0.5	3	0.14

Table 4: Comparison between volumetric flow rate variation and volume variation of soft aneurysmal sacs

Aneurysm	Systole Flow Rate (m ³ ·s ⁻¹)	Flow Rate Variation (m ³ ·s ⁻¹)	ΔV (mm ³)
1	3.21 × 10 ⁻⁰⁶	1.78 × 10 ⁻⁰⁶	10
2	3.10 × 10 ⁻⁰⁶	1.75 × 10 ⁻⁰⁶	8
3	2.85 × 10 ⁻⁰⁶	1.95 × 10 ⁻⁰⁶	44
4	3.36 × 10 ⁻⁰⁶	1.84 × 10 ⁻⁰⁶	37
5	4.21 × 10 ⁻⁰⁶	2.15 × 10 ⁻⁰⁶	149
6	3.55 × 10 ⁻⁰⁶	4.454 × 10 ⁻⁰⁵	33
7	3.12 × 10 ⁻⁰⁶	1.77 × 10 ⁻⁰⁶	60
8	1.28 × 10 ⁻⁰⁶	1.27 × 10 ⁻⁰⁶	54
9	1.62 × 10 ⁻⁰⁶	7.94 × 10 ⁻⁰⁷	15
10	2.92 × 10 ⁻⁰⁷	1.36 × 10 ⁻⁰⁶	26
11	5.07 × 10 ⁻⁰⁶	3.34 × 10 ⁻⁰⁶	11
12	5.07 × 10 ⁻⁰⁶	3.34 × 10 ⁻⁰⁶	4

Table 5: Results for R_v and R_d for the 12 cases

Aneurysm	Volume (mm ³)	R _v = ΔV ^{soft} / ΔV ^{stiff}	R _d = D _{max} ^{soft} / D _{max} ^{stiff}
1	61	10	2.9
2	51	16	3.5
3	161	7.3	2.7
4	188	5.3	4.7
5	392	8.3	2.2
6	45	8.25	1.5
7	212	4.3	2.2
8	232	5.4	2.1
9	79	5	3.2
10	138	5.2	2.8
11	68	4.4	3.5
12	18	8	1.9

regarding the numerous sources of uncertainty involved in such FSI computations. Therefore, the uncertainties of the input parameters did not change the main conclusion: whatever

the values of the parameters (in a range of physiologic variations), the soft/ruptured aneurysms deform more than the stiff/unruptured ones.

CONCLUSIONS

The difference in aneurysmal pulsatility as highlighted in this work might be a relevant patient-specific predictor of aneurysm rupture. These results are consistent with recent observational data in the literature to date. Development of a new imaging technique in the near future would allow for the accurate measurement of wall motion and therefore characterize the intracranial aneurysm vulnerability for any given patient.

ACKNOWLEDGMENTS

The authors thank Philips Healthcare Inc for the financial support and ANSYS Inc for their technical support. The authors are also grateful to Simpleware Inc. for providing the software Scan IP and for their technical support. The authors also thank the labex NUMEV for the financial support.

Disclosures: Simon Mendez—UNRELATED: Grants/Grants Pending: French National Agency for Research,* OSEO,* Comments: Grants from French institution for Simulation of Flows with Red Blood Cells (unrelated to the present work). Jean-Paul Lejeune—UNRELATED: Travel/Accommodations/Meeting Expenses Unrelated to Activities Listed: B. Braun Company, Comments: Travel and accommodations expenses related to congresses and meetings of neurosurgery in France. Vincent Costalat—UNRELATED: Consultancy: ev3, Codman, Stryker, Balt; Payment for Lectures (including service on speakers bureaus): Stryker, Balt; Payment for Development of Educational Presentations: Covidien; Travel/Accommodations/Meeting Expenses Unrelated to Activities Listed: Stryker, Codman, Balt, MicroVenton. *money paid to institution.

REFERENCES

1. Wardlaw J, White P. The detection and management of unruptured intracranial aneurysms. *Brain* 2000;123:205–21
2. Horikoshi T, Sugita M, Yagishita T, et al. Size of cerebral aneurysms and related factors in patients with subarachnoid hemorrhage. *Surg Neurol* 2002;61:239–45
3. Nahed B, Diluna M, Morgan T, et al. Hypertension, age, and location predict rupture of small intracranial aneurysms. *Neurosurgery* 2005;57:676–83
4. Matsubara S, Hadeishir H, Suzukil A, et al. Incidence and risk factors for the growth of unruptured cerebral aneurysms: observation using serial computerized tomography angiography. *J Neurosurg* 2004;101:908–14
5. Chung S, Vafai K. A coupling model for macromolecule transport in a stenosed arterial wall. *Int J Heat Mass Transfer* 2012;45:371–81
6. Nicoud F, Moreno R, Tayllamin B, et al. Computational hemodynamics in moving geometries without solving the fluid-structure interaction problem. Paper presented at: Conference on Modelling Fluid Flow 2009. The 14th International Conference on Fluid Flow Technologies. Budapest, Hungary. September 9–12, 2009
7. Balocco S, Camara O, Vivas E, et al. Feasibility of estimating regional mechanical properties of cerebral aneurysms in vivo. *Med Phys* 2010;37:1689–706
8. Rissland P, Alemu Y, Einav S, et al. Abdominal aortic aneurysm risk of rupture: patient-specific FSI simulations using anisotropic model. *J Biomech Eng* 2009;131:031001
9. Torii R, Oshima M, Kobayashi T, et al. Fluid structure interaction modeling of a patient-specific cerebral aneurysm: influence of structural modeling. *Comput Mech* 2008;43:151–59
10. Vito R, Hickey J. The mechanical-properties of soft-tissues. 2. The elastic response of arterial segments. *J Biomech* 1980;13:951–57
11. Vande Geest J, Schmidt E, Sacks M, et al. The effects of anisotropy on

- the stress analyses of patient-specific abdominal aortic aneurysms. *Ann Biomed Eng* 2008;36:921–32
12. Vande Geest J, Sacks M, Vorp D. **The effects of aneurysm on the biaxial mechanical behavior of human abdominal aorta.** *J Biomech* 2006;39:1324–34
 13. Costalat V, Sanchez M, Ambard D, et al. **Biomechanical wall properties of human intracranial aneurysms resected following surgical clipping.** *J Biomech* 2011;44:2685–91
 14. Sanchez M, Ambard D, Costalat V, et al. **Biomechanical assessment of the individual risk of rupture of cerebral aneurysms: a proof of concept.** *Ann Biomed Eng* 2013;41:28–40
 15. Duprey A, Khanafer K, Schlicht M. **In vitro characterisation of physiological and maximum elastic modulus of ascending thoracic aortic aneurysms using uniaxial tensile testing.** *Eur J Vasc Endovasc Surg* 2010;39:700–07
 16. Ambard D, Cherblanc F. **Mechanical behavior of annulus fibrosus: a microstructural model of fibers reorientation.** *Ann Biomed Eng* 2009;37:2256–65
 17. Jourdan F, Samida A. **An implicit numerical method for wear modeling applied to hip joint prosthesis problem.** *Comput Methods Appl Mech Eng* 2009;198:2209–17
 18. Malachanne E, Dureisseix D, Jourdan F. **Numerical model of bone remodeling sensitive to loading frequency through a poroelastic behavior and internal fluid movements.** *J Mech Behav Biomed Mater* 2011;4:849–57
 19. Swider P, Pedrono A, Ambard D, et al. **Substructuring and poroelastic modelling of the intervertebral disc.** *J Biomech* 2010;47:1287–91
 20. Hoi Y, Meng H, Woodward S, et al. **Effects of arterial geometry on aneurysm growth: three-dimensional computational fluid dynamics study.** *J Neurosurg* 2004;101:676–81
 21. Van de Vosse FN. **Pulse wave propagation in the arterial tree.** *Ann Rev Fluid Mech* 2011;43:467–99
 22. Steiner L, Andrews J. **Monitoring the injured brain: ICP and CBF.** *Br J Anaesth* 2006;97:26–38
 23. Ai L, Vafai K. **A coupling model for macromolecule transport in a stenosed arterial wall.** *Int J Heat Mass Transfer* 2006;49:1568–91
 24. Watton P, Raberger N, Holzapfel G, et al. **Blood flow dynamics and fluid-structure interaction in patient specific bifurcating cerebral aneurysm.** *J Biomech Eng* 2009;131:1–14
 25. Yang N, Vafai K. **Modeling of low-density lipoprotein (LDL) transport in the artery-effects of hypertension.** *Int J Heat Mass Transfer* 2006;49:850–67
 26. Valencia A, Ledermann D, Rivera R, et al. **Blood flow dynamics and fluid-structure interaction in patient specific bifurcating cerebral aneurysm.** *Int J Numer Methods Fluids* 2009;58:1081–1100
 27. Alnaes M, Isaksen J, Mardal K, et al. **Computation of hemodynamics in the circle of Willis.** *Stroke* 2007;38:2500–05
 28. Hayakawa M, Maeda S, Sadato A, et al. **Detection of pulsation in ruptured and unruptured cerebral aneurysms by electrocardiographically gated 3-dimensional computed tomographic angiography with a 320-row area detector computed tomography and evaluation of its clinical usefulness.** *Neurosurgery* 2011;69:843–51
 29. Ishida F, Ogawa H, Simizu T, et al. **Visualizing the dynamics of cerebral aneurysms with four-dimensional computed tomographic angiography.** *Neurosurgery* 2005;57:460–71
 30. Zhang C, Villa-Urriol M, Craene M, et al. **Morphodynamic analysis of cerebral aneurysm pulsation from time-resolved rotational angiography.** *Med Imag* 2009;28:1105–16
 31. Karmonik C, Diaz O, Grossman R, et al. **In vivo quantification of wall motion in cerebral aneurysm from 2D cine phase contrast magnetic resonance images.** *Rofo* 2010;182:140–51
 32. San Millan Ruiz D, Yilmaz H, Dehdashti A, et al. **The perianeurysmal environment: influence on saccular aneurysm shape and rupture.** *AJNR Am J Neuroradiol* 2006;27:504–12
 33. Seshaiyer P, Humphrey J. **On the potentially protective role of contact constraints on saccular aneurysms.** *J Biomech* 2001;34:607–12
 34. MacDonald D, Finlay H, Canham P. **Directional wall strength in saccular brain aneurysms from polarized light microscopy.** *Ann Biomed Eng* 2000;28:533–42
 35. Cebral J, Castro M, Putman C, et al. **Efficient pipeline for image-based patient-specific analysis of cerebral aneurysm hemodynamics: technique and sensitivity.** *IEEE Trans Med Imag* 2005;24:457–67
 36. Sforza D, Putman C, Cebral J. **Hemodynamics of cerebral aneurysms.** *Ann Rev Fluid Mech* 2008;41:91–107

Effect of Structural Remodeling (Retraction and Recoil) of the Pipeline Embolization Device on Aneurysm Occlusion Rate

L.-D. Jou, B.D. Mitchell, H.M. Shaltoni, and M.E. Mawad



ABSTRACT

BACKGROUND AND PURPOSE: During endovascular treatment of unruptured aneurysms with the Pipeline Embolization Device, an oversized device is often selected to achieve better wall apposition; however, this device oversizing could be related to overelongation and possible delayed enlargement of the stented region. The purpose of this study is to investigate the relationship between oversize and treatment outcome.

MATERIALS AND METHODS: The DynaCT images of 14 aneurysms treated by a single Pipeline Embolization Device were retrospectively analyzed. 3D images of the deployed device were compared with those acquired at the 6-month follow-up for qualitative and quantitative evaluation. The diameter and length of the Pipeline Embolization Device were measured at both time points and compared for determination of the device changes.

RESULTS: Structural changes of the device have been observed, and it was found that the Pipeline Embolization Device influences the vessel curvature in some cases. On average, it increases its diameter by 0.23 mm and decreases its length by 2.88 mm within 6 months of initial deployment. Excessive elongation beyond its nominal length is correlated with a lower aneurysm occlusion rate at the 6-month follow-up.

CONCLUSIONS: Not only does a Pipeline Embolization Device reconstruct the aneurysm and parent artery, but its entire structure goes through a gradual remodeling process. The relative deformation between the device and the artery indicates suboptimal wall apposition. Device oversizing does not have a direct effect on shortening or recoil. The aneurysm occlusion rate, however, is lowered by overelongation of the Pipeline Embolization Device.

ABBREVIATION: PED = Pipeline Embolization Device

Growing enthusiasm for the Pipeline Embolization Device (PED; Covidien, Irvine, California) has prompted a dramatic shift in how unruptured aneurysms are managed since approval of the device.¹ The PED diverts blood away from the aneurysm and reduces rupture risk by stimulating formation of intra-aneurysmal thrombus and lowering hemodynamic forces on the aneurysm dome.

Few aneurysms treated by flow diversion are thrombosed acutely; the aneurysm occlusion rate varies from center to center, but in general, it increases with time, from 68% at the 3-month,² 65%–91% at the 6-month,^{3,4} 90%–93% at the 12-month,⁵ and

84% at the 18-month follow-up.⁶ Nevertheless, it is not uncommon for aneurysms to remain patent >2 years after treatment, and the risk of delayed hemorrhage persists.^{7,8}

Intracranial stents are known to alter vessel curvature⁹; similarly, the parent artery may cause deformation of a flow diverter and influence the device porosity.¹⁰ Vessel tortuosity often renders a nonuniform distribution of the porosity and allows potentially less metal coverage at the aneurysm neck; as a result, prediction of the timing of complete aneurysm occlusion after flow diversion can be a challenge. The PED is a braided self-expanding stent with 12 platinum and 36 cobalt-chromium alloy strands. Radio-opacity of the platinum strands in a PED can be used as a marker and offers an opportunity to visualize the PED in greater detail to reveal suboptimal deployment, which may require further intervention.^{11,12} In this study, we investigated the temporal change of the PED structure in situ after deployment and examined its relationship with the aneurysm occlusion rate.

MATERIALS AND METHODS

This retrospective study was approved by the Human Subject Research Committee at our institution before commencement.

Received October 18, 2012; accepted after revision January 6, 2014.

From the Departments of Radiology (L.-D.J., H.M.S., M.E.M.) and Neurosurgery (B.D.M.), Baylor College of Medicine, Houston, Texas.

Please address correspondence to Liang-Der Jou, PhD, Department of Radiology, Baylor College of Medicine, One Baylor Plaza, Houston, Texas 77030; e-mail: jou@bcm.tmc.edu



Indicates article with supplemental on-line table.



Indicates article with supplemental on-line figure.

<http://dx.doi.org/10.3174/ajnr.A3920>

Nineteen consecutive patients who received only 1 PED device for treatment of internal carotid artery aneurysms between June 2011 and March 2012 were included in the study. Five patients were excluded due to their age or lack of appropriate 3D images. The remaining 14 patients (12 women and 2 men) had a follow-up angiographic examination between 6 and 7 months. Three patients had additional examinations for treatment of other aneurysms before 6 months. Four aneurysms were at the ophthalmic; 4, at the supraclinoid; and 2, at the cavernous segment. The remaining aneurysms were located at the anterior choroidal artery, superior hypophyseal artery, and the petrous or cervical segment of the ICA. Twelve aneurysms were saccular, and 2 were either dissected or dysplastic.

At each treatment, it was determined by the senior neuroradiologist that flow stasis was adequate after the first PED and an additional PED was not required. Patients who were treated by >1 PED during the same session were excluded from the study. After deployment, DynaCT images (Siemens, Erlangen, Germany) with and/or without contrast were acquired.¹³ These DynaCT images were reconstructed at 0.11- to 0.13-mm resolution so that each radio-opaque strand could be visualized and analyzed. The same procedure was repeated at the subsequent follow-up examination.

These patients were divided into 2 groups based on the condition of their aneurysms at the 6-month follow-up: 7 patients with completely occluded aneurysms (group 1) and 7 with incompletely obliterated aneurysms (group 2). The average age of these patients was 61 years (59 years for group 1 and 62 years for group 2), and the mean aneurysm size was 8.1 mm (6.2 mm for group 1 and 9.4 mm for group 2). Neither age nor aneurysm size was statistically different between the 2 groups. Two patients from group 1 and none in group 2 were smokers and hypertensive; these risk factors were not significantly different between the 2 groups.

Qualitative Comparisons

The DynaCT images of the PED acquired at different time points were compared on the Leonardo workstation (Siemens) by intensity thresholding and automatic coregistration. The coregistration was performed with the PED structure as the landmark after removal of all tissues. These comparisons revealed the deformation of each individual strand, and the change of the PED structure and general PED integrity were also scrutinized. The DynaCT images obtained with contrast also permitted evaluation of the relative position between the PED and aneurysm.

Quantitative Measurements

For each case, the proximal and distal circumferences of the PED device were measured on the Leonardo workstation. The circumferences were selected because the cross-section might not be circular, and a direct diameter measurement was prone to errors. The circumference was converted to an equivalent diameter so that a comparison of the size could be made. However, this comparison potentially disregarded any change in the shape of the cross-section.

Six lines consisting of intersection points of metal strands along the PED were constructed, and an example of measuring the PED length by using these lines is demonstrated in Fig 1. The

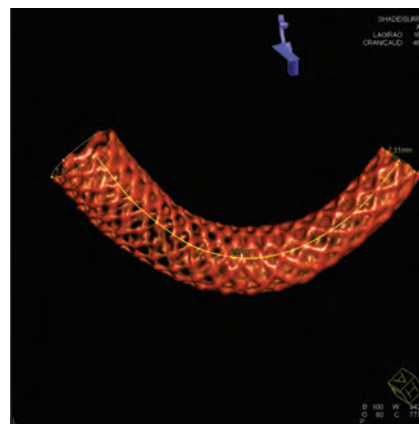


FIG 1. Demonstration of measurement of the PED length. Only 1 of the 6 material lines is shown.

intersection of metal strands yielded the highest signal intensity and could be easily depicted on the DynaCT images. These intersection points were physically present and could be connected by a simple interpolated spline to form a material line aligned in the same direction as the PED. The length measurement of a material line was superior to the measurement of the centerline because the centerline was an imaginary one, while the material line could be easily generated by connecting visible physical points. The process of generating a material line was independent of operators or numeric algorithms. Six material lines along the PED beginning from 6 different strands were generated, and the average length of these lines was regarded as the PED length. Usually, these material lines were of different lengths, with the lines on the outer curve longer.

Each measurement (PED circumference and length) was repeated for assessment of possible errors associated with measurement, and intermeasurement differences were no more than 2%. The measurements were also compared with the nominal dimensions. The radius of the curvature was not measured because most PEDs had >1 curvature and a single curvature could not properly represent the entire device. The Student *t* test was used for testing the statistical significance of these measurements. A *P* value < .05 was deemed statistically significant.

RESULTS

At the 6-month follow-up, many PEDs were observed to retract at either the proximal or distal end (or both), making the PED shorter overall. However, this retraction was not related to any clinical consequences or symptoms; in addition, no migration of the PED was observed.¹⁴ In some cases, aneurysms were seen to decrease in size but remained incompletely thrombosed (group 2). In 1 case (Fig 2), the ophthalmic artery that was originally covered by the PED was later exposed directly to blood flow at 6 months due to device retraction. The demographics of these cases are included in the On-line Table.

The temporal PED changes were observed in group 1 (Fig 3), with retraction at either the proximal or distal end. In these cases, most strands in the device had moved during the retraction, likely altering the metal coverage at the neck of the aneurysm.

Similar results were seen in group 2 as well (Fig 4). By the 6-month follow-up, the arterial curvature distal to the aneurysm was frequently altered by device implantation. In both cases (Fig



FIG 2. A PED covered the ophthalmic artery initially after treatment, but the PED retracted distally and uncovered the ophthalmic artery at 6 months (patient 7 in group 2).

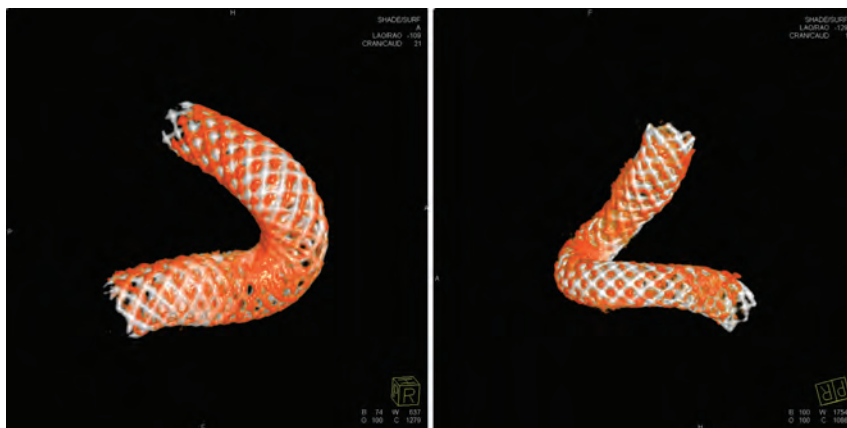


FIG 3. Minor PED retraction is shown in 2 cases in group 1. The PEDs in white are seen immediately after deployment, and the PEDs in red are from the follow-up, (left) case 2 and (right) case 1.

4A, -B), aneurysms were located at the region where the greatest deformation occurred. The deployed length was 12 and 18 mm longer than the nominal length for these 2 cases, respectively, more than 60% longer than their nominal lengths. By 24-month postdeployment, further deformation of the PED could be observed (Fig 4C); however, the deformation was mostly dominated by the curvature change.

Subtle PED deformation was also observed at both the acute and subacute levels. Fig 5 documents both the acute and subacute changes for an 11-mm supraclinoid ICA aneurysm. This patient was first treated for the aneurysm and then imaged 1 month later when another aneurysm at the contralateral ICA was treated. The proximal end of the PED retracted slightly in the first month (acute change), followed by the proximal strands creeping upward later (subacute change). These changes did not involve the aneurysm neck, and the aneurysm was completely obliterated by 7 months. A well-apposed flow diverter should permit no relative movement between the device and artery. The distal part of the PED in this case was well-apposed to the vessel wall; however, the proximal strands gradually moved distally. This strand-creeping indicated a loose wall apposition and a possible gap between the PED and vessel wall. It is hypothesized that because the aneurysm

was located near the distal end of the PED, where the wall apposition had been better, the aneurysm was fully occluded by 7 months.

The Table lists the dimensions of the PEDs immediately after deployment and at the 6-month follow-up. The device oversize is defined as the difference between the nominal diameter and the average of the distal and proximal diameters of a deployed PED, while the PED elongation describes the difference between the deployed PED length and its nominal length. In this study, the PED shortened on average 8.4% and 11.6% after 6 months for groups 1 and 2, respectively. The PED also enlarged 0.23 mm on average for both groups (recoil). The PED remodeling did not appear to be a major factor in determining treatment outcome at 6 months, but the outcome was affected by excessive PED elongation. The difference in elongation (both in magnitude and percentage) between the 2 groups was statistically significant. In cases with considerable PED shortening, the length of the artery remained the same from our image analysis of 3D DSA.

The length of the PEDs at the time of follow-up was closely related to the original deployed length, but the elongation was not affected by the device oversizing, implying multiple mechanisms for device elongation (Fig 6). Furthermore,

device oversizing did not influence the shortening of the PED during the first 6 months after treatment, nor did it affect the PED recoil during the same period (Fig 7). The tapering of the ICA compelled the choice of a larger device. The diameter of the ICA decreased by 0.03 mm for every 1 mm of length (Table), so for the treated section of an artery 30 mm long, one could expect the artery to be almost 1 mm smaller distally, stretching the PED even more and exaggerating the oversizing effects. This level of vessel tapering is not unique to our experience; Fischer et al¹⁵ reported a 0.7-mm difference between the proximal and distal diameters in their study of 101 aneurysms.

DISCUSSION

The advancement of C-arm CT technology permits visualization of radio-opaque strands in the PED at a reasonable resolution, and the entire PED structure can be reconstructed from these images. Our study on the change of PED devices with time challenges the notion that the PED configuration can be predicted by a computer program and that once the PED is implanted, it remains the same permanently.¹⁶ Deformation of the PED and wall apposition are often overlooked on 2D DSA. Our study demonstrates that a deployed PED involves a dynamic remodeling pro-

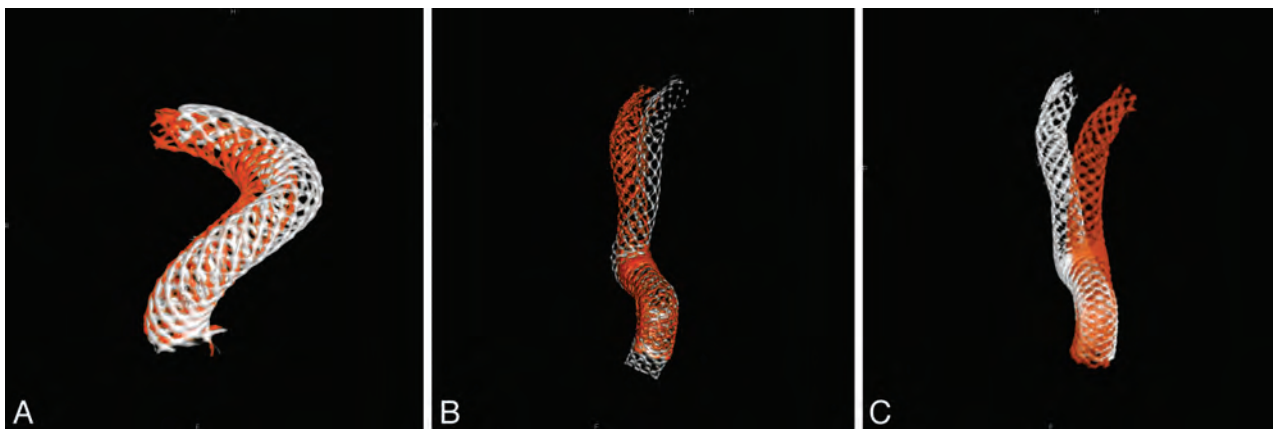


FIG 4. A change of vessel curvature is observed in 2 cases in group 2. A, Case 6 (white is for the posttreatment, and red for 6-month follow-up). B, Case 1 (white indicates posttreatment, and red shows the 6-month follow-up). C, Further PED movement in case 1 is observed between 6 (in white) and 24 (in red) months.

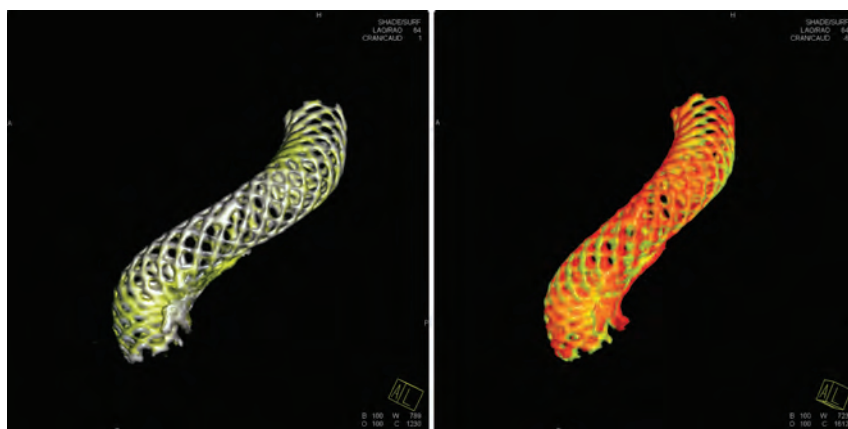


FIG 5. Acute and subacute changes of a 4 × 18 mm PED. The PED in white is immediately after deployment, yellow is the 1-month follow-up, and red is the 7-month follow-up. Left: Acute change in the first month after deployment. Right: Subacute change of the PED between the 1- and 6-month follow-ups.

Dimensions and measurements of the PED^a

	Occlusion (n = 7)	Incomplete (n = 7)	P Value
Nominal PED diameter (mm), D ₀	4.04 (0.45)	4.46 (0.51)	
Nominal PED length (mm), L ₀	17.43 (2.32)	19.43 (4.98)	
Proximal diameter post-Tx (mm), D ₁	3.77 (0.37)	4.13 (0.36)	
Distal diameter post-Tx (mm), D ₂	3.12 (0.45)	3.23 (0.52)	
Deployed length (mm), L ₁	24.27 (5.42)	32.57 (8.89)	
D ₁ at 6 months (mm)	3.93 (0.33)	4.39 (0.28)	
D ₂ at 6 months (mm)	3.32 (0.65)	3.51 (0.55)	
Length at 6 months (mm), L ₂	22.31 (5.73)	28.77 (7.81)	
Oversize post-Tx (mm), D ₀ - (D ₁ + D ₂)/2	0.59 (0.25)	0.78 (0.33)	
Recoil at 6 months (mm), Δ(D ₁ + D ₂)/2	0.18 (0.19)	0.28 (0.18)	
Elongation (mm), L ₁ - L ₀	6.84 (4.28)	13.14 (4.30)	.026
Elongation in %, (L ₁ - L ₀)/L ₀	39.29 (22.42)	66.68 (13.67)	.025
Shortening in 6 months (mm), L ₁ - L ₂	1.96 (1.86)	3.80 (2.14)	

Note:—Tx indicates treatment.

^a SDs are given in parentheses.

cess in which strands may deform individually or together and acutely or with time. As a result, the intra-aneurysmal flow may be evolving. A slight PED retraction demands adjustment of all the strands at least locally (Fig 5); the level of adjustment is greater at the convex side at which the aneurysm is often located than at the concave side where strands are close to each other. Our observation is

different from the previously reported delayed migration that may lead to complications or subarachnoid hemorrhage.¹⁴

Device oversizing is a result of our intention to maintain a proper wall apposition throughout the device, complicated by the tapered ICA. Although in some instances, oversizing has been shown to reduce the therapeutic benefit of flow diversion in hemodynamic simulations,¹⁷ few studies have examined its potential effect on the aneurysm occlusion rate. There was a difference in the oversize between groups 1 and 2 in our study (0.59 versus 0.78 mm), but this difference was not statistically significant. Instead, the oversize was manifested in device elongation. When an oversized PED is selected, the deployed PED tends to be longer than its nominal length because it cannot fully expand. This difference, in turn, will lower the metal coverage over the aneurysm neck, raising the local porosity and causing a potential loss of therapeutic impact of a flow diverter. Thus, while the difference in oversize is rather subtle (~0.19 mm), the deployed PED length is significantly different between the 2 groups (6.84 versus 13.14 mm). A long PED in a highly tapered artery will result in an even longer deployed length, so the selection of the PED length cannot be overlooked.

There are 2 mechanisms by which a PED may remodel, changing its shape and structure in response to the external environment. First, the device could retract at either or both ends. As the retraction progresses, the proximal or distal end enlarges, shortening the device in the meantime and shifting all the strands in between. The PED shortening due to this mechanism is predictable. The second mechanism is the curvature

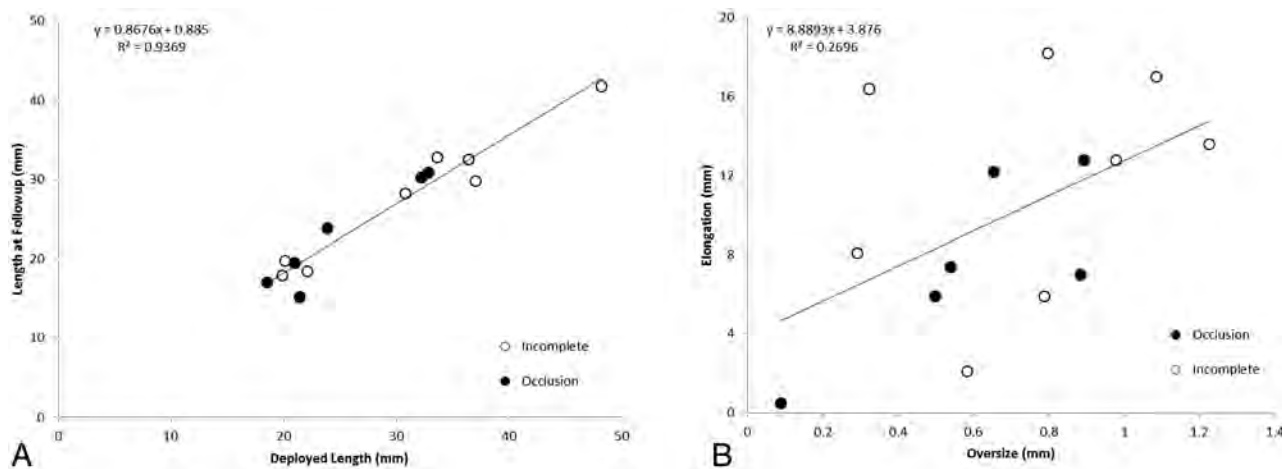


FIG 6. A, A linear relationship between the deployment length and the length at 6-month follow-up. B, The PED elongation is independent of the initial PED oversize.

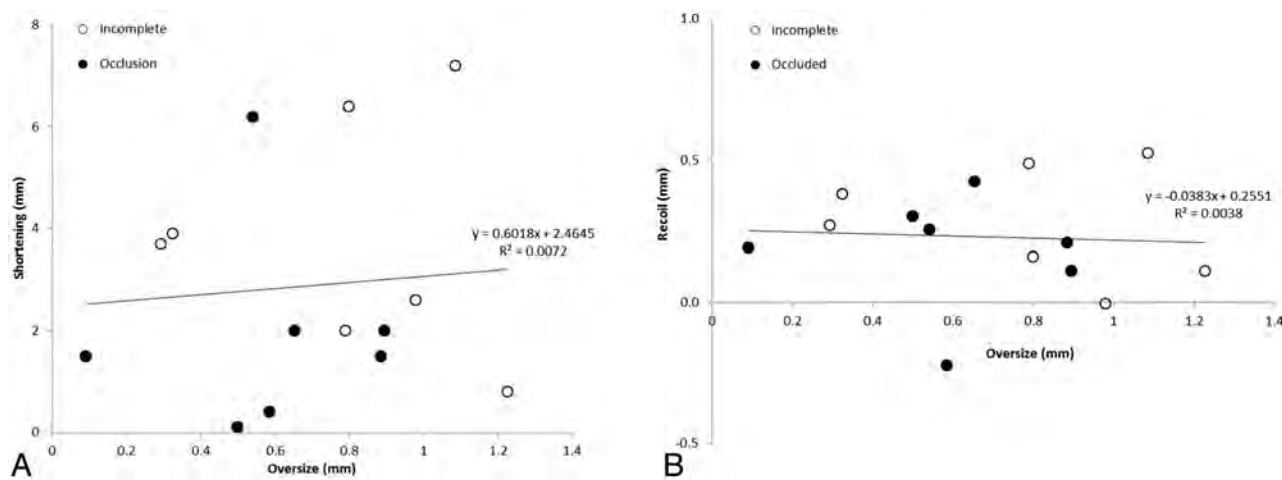


FIG 7. The relationship between device oversize and shortening (A) and recoil (B).

change of the PED with time in response to bending. This phenomenon is commonly seen in cases with other intracranial stents when the artery of interest is tortuous.^{9,12,18} For most cases, the PED remodeling involves both mechanisms, resulting in a complicated relationship between the oversize/elongation (action) and shortening/recoil (reaction). The PED remodeling process becomes even more complicated when 2 PEDs are overlapped or telescoping for treatment of wide-neck or fusiform aneurysms. The first PED device deployed is underneath the others and is highly constrained, and the subsequent PEDs are subject to a different environment. A case of multiple PEDs is included as an example in the On-line Figure in which the proximal PED experienced unexpected and abnormal deformation.

The metal coverage and porosity may evolve with time due to this PED remodeling process. Considering that most PEDs in our studies become shorter and larger with time, the metal coverage will increase at the aneurysm neck, lowering the local porosity. This remodeling brings the device closer to its nominal dimensions, at which the porosity is lower; therefore, the remodeling could be beneficial to aneurysm embolization. Elongation of a PED, however, complicates its deployment. An oversized PED leads to a longer and unpredictable deployed length, challenging

the positioning of a PED relative to the aneurysm and neighboring branches. A sufficient overhang is recommended so the aneurysm neck is well-covered should the PED retract.¹⁵

Braided stents permit a relative motion between the strands,¹⁹ and friction between the strands is not sufficiently great enough to prevent this motion.²⁰ Consequently, individual strands deform, and the PED remodels. Wang and Ravi-Chandar²⁰ have developed a mathematic model that describes the mechanics of braided stents. The radial force for a braided stent increases linearly with device oversizing initially. From their model, we estimate that the contact pressure between the PED and artery increases 5 mm Hg for every 0.5 mm of oversize. This is equivalent to a radial force of 2 mN/mm at the nominal diameter, and 4 and 5 mN/mm for a 0.5- and 1- mm oversize, respectively.^{15,19} Thus, a 0.5-mm oversize doubles the radial force, and any additional oversize produces little or no advantage.

An artery interacts with an implant both biologically and mechanically. The acute elastic recoil, resulting in a smaller lumen, ranges from 9% to 21% after deployment of a balloon-expandable or self-expanding stent.^{21,22} This stent recoil is attributed to the elasticity of plaque/vessel and plastic deformation of the (nitinol or stainless) stent during deployment, independent of the size or

design of stent.²² The stent recoil leads to a suboptimal lumen size and possible restenosis; however, this recoil does subside with time (38% at 8 weeks and 12% at 6 months).^{23,24} The PED remodeling reduces the forces (and strain energy) required to hold all the strands together and seems to diminish with time in our limited number of cases. Bending of a PED, however, constrains the device and limits how the device can remodel. The device is allowed to adjust only at the section that is not subject to bending. If this process fails, then the adjustment of local arterial curvature is required.

We have treated >100 patients with flow diverters since the approval of the PED. However, only a limited number of patients were treated with a single PED, and this contributes to the small sample size in this study. The average number of PEDs used for an aneurysm in the literature is 1.14–2.0,^{2,4–26} and this is very similar to our experience with 1.8 PEDs per case in the first 100 cases. Fifty-three percent of the patients at our institution received 1 PED, compared with 34%–69% at other centers,^{15,25,26} and these aneurysms were, in general, smaller than aneurysms treated by multiple PEDs (6.2 versus 12.2 mm). Additional PEDs may lower the porosity and reduce the intra-aneurysmal flow simultaneously, rendering rapid aneurysm occlusion. However, the decision to implant multiple PEDs is subjective. Overlapped PEDs are less appreciated on DynaCT images, and interaction among PED devices is quite complicated. Because we have very limited knowledge on the long-term behavior of these flow diverters, the current study is only the first step toward an understanding of the flow diverter interacting with the vessel wall.

Our study is limited by the resolution of DynaCT images, which is by no means close to the dimension of the struts in a PED. However, it does not require a ~30- μ m resolution for detection of the PED remodeling,²⁷ and the effect of PED remodeling is well-demonstrated in the study. The shortening of a PED is as large as 6–7 mm, twice the local diameter of the ICA, and the increase in the circumference is 0.65 mm on average. These changes are easily seen even without additional imaging postprocessing.

CONCLUSIONS

Not only does a PED reconstruct the aneurysm and parent artery, but its entire structure goes through a gradual remodeling process. The relative deformation between the PED and the artery indicates suboptimal wall apposition. Device oversizing does not have a direct effect on the shortening or recoil. The aneurysm occlusion rate, however, is lowered by overelongation of the PED.

Disclosures: Liang-Der Jou—UNRELATED: Grants/Grants Pending: Siemens.* Michel E. Mawad—UNRELATED: Board Membership: member of the Scientific Advisory Board at Siemens Medical Solutions,* Consultancy: MicroVention/Terumo, Codman Neurovascular, Payment for Lectures (including service on Speakers Bureaus): MicroVention/Terumo, Stock/Stock Options: Surpass Inc, Other: educational grants to the institution for an educational meeting (Live Interventional Neuroradiology Course Houston) from Siemens Medical Solutions, MicroVention/Terumo, Stryker, Codman Neurovascular, Penumbra.* *Money paid to the institution.

REFERENCES

1. Crobbeddu E, Lanzino G, Kallmes DF, et al. **Marked decrease in coil and stent utilization following introduction of flow diversion technology.** *J Neurointerv Surg* 2013;5:351–53
2. Kan P, Siddiqui AH, Veznedaroglu E, et al. **Early postmarket results after treatment of intracranial aneurysms with the Pipeline embolization device: a U.S. multicenter experience.** *Neurosurgery* 2012;71:1080–87, discussion 1087–88

3. McAuliffe W, Wycoco V, Rice H, et al. **Immediate and midterm results following treatment of unruptured intracranial aneurysms with the Pipeline embolization device.** *AJNR Am J Neuroradiol* 2012;33:164–70
4. Saatci I, Yavuz K, Ozer C, et al. **Treatment of intracranial aneurysms using the Pipeline flow-diverter embolization device: a single-center experience with long-term follow-up results.** *AJNR Am J Neuroradiol* 2012;33:1436–46
5. Nelson PK, Lylyk P, Szikora I, et al. **The Pipeline embolization device for the intracranial treatment of aneurysms trial.** *AJNR Am J Neuroradiol* 2011;32:34–40
6. Yu SC, Kwok CK, Cheng PW, et al. **Intracranial aneurysms: midterm outcome of Pipeline embolization device—a prospective study in 143 patients with 178 aneurysms.** *Radiology* 2012;265:893–901
7. Kulcsár Z, Houdart E, Bonafe A, et al. **Intra-aneurysmal thrombosis as a possible cause of delayed aneurysm rupture after flow-diverter treatment.** *AJNR Am J Neuroradiol* 2011;32:20–25
8. Cruz JP, Chow M, O’Kelly C, et al. **Delayed ipsilateral parenchymal hemorrhage following flow diversion for the treatment of anterior circulation aneurysms.** *AJNR Am J Neuroradiol* 2012;33:603–08
9. King RM, Chueh JY, van der Bom IM, et al. **The effect of intracranial stent implantation on the curvature of the cerebrovasculature.** *AJNR Am J Neuroradiol* 2012;33:1657–62
10. Bing F, Darsaut TE, Salazkin I, et al. **Stents and flow diverters in the treatment of aneurysms: device deformation in vivo may alter porosity and impact efficacy.** *Neuroradiology* 2013;55:85–92
11. Clarençon F, Pötin M, Pistocchi S, et al. **Evaluation of stent visibility by flat panel detector CT in patients treated for intracranial aneurysms.** *Neuroradiology* 2012;54:1121–25
12. Valdivia y Alvarado M, Ebrahimi N, Benndorf G. **Study of conformability of the new Leo plus stent to a curved vascular model using flat-panel detector computed tomography (DynaCT).** *Neurosurgery* 2009;64(3 suppl):ons130–34, discussion ons134
13. Heran NS, Song JK, Namba K, et al. **The utility of DynaCT in neuroendovascular procedures.** *AJNR Am J Neuroradiol* 2006;27:330–32
14. Chalouhi N, Tjoumakaris SI, Gonzalez LF, et al. **Spontaneous delayed migration/shortening of the Pipeline embolization device: report of 5 cases.** *AJNR Am J Neuroradiol* 2013;34:2326–30
15. Fischer S, Vajda Z, Aguilar Perez M, et al. **Pipeline embolization device (PED) for neurovascular reconstruction: initial experience in the treatment of 101 intracranial aneurysms and dissections.** *Neuroradiology* 2012;54:369–82
16. Ma D, Dumont TM, Kosukegawa H, et al. **High fidelity virtual stenting (HiFiVS) for intracranial aneurysm flow diversion: in vitro and in silico.** *Ann Biomed Eng* 2013;41:2143–56
17. Mut F, Cebral JR. **Effects of flow-diverting device oversizing on hemodynamics alteration in cerebral aneurysms.** *AJNR Am J Neuroradiol* 2012;33:2010–16
18. Ebrahimi N, Claus B, Lee CY, et al. **Stent conformity in curved vascular models with simulated aneurysm necks using flat-panel CT: an in vitro study.** *AJNR Am J Neuroradiol* 2007;28:823–29
19. Duda SH, Wiskirchen J, Tepe G, et al. **Physical properties of endovascular stents: an experimental comparison.** *J Vasc Interv Radiol* 2000;11:645–54
20. Wang R, Ravi-Chandar K. **Mechanical response of a metallic aortic stent. Part I. Pressure-diameter relationship.** *J Appl Mech* 2004;71:697–705
21. Aziz S, Morris JL, Perry RA, et al. **Stent expansion: a combination of delivery balloon underexpansion and acute stent recoil reduces predicted stent diameter irrespective of reference vessel size.** *Heart* 2007;93:1562–66
22. Danzi G, Fiocca L, Capuano C, et al. **Acute stent recoil: in vivo evaluation of different stent designs.** *Catheter Cardiovasc Interv* 2001;52:147–53
23. Tanimoto S, Bruining N, van Domburg RT, et al. **Late stent recoil of the**

- bioabsorbable everolimus-eluting coronary stent and its relationship with plaque morphology. *J Am Coll Cardiol* 2008;52:1616–20
24. Berrocal DH, Gonzalez GE, Fernandez A, et al. **Effects of overexpansion on stents' recoil, symmetry/asymmetry, and neointimal hyperplasia in aortas of hypercholesterolemic rabbits.** *Cardiovasc Pathol* 2008;17:289–96
25. Colby GP, Lin LM, Gomez JF, et al. **Immediate procedural outcomes in 35 consecutive Pipeline embolization cases: a single-center, single-user experience.** *J Neurointerv Surg* 2013;5:237–46
26. Lylyk P, Miranda C, Ceratto R, et al. **Curative endovascular reconstruction of cerebral aneurysms with the Pipeline embolization device: the Buenos Aires experience.** *Neurosurgery* 2009;64:632–42, discussion 642–43, quiz N636
27. Ionescu M, Metcalfe RW, Cody D, et al. **Spatial resolution limits of multislice computed tomography (MS-CT), C-arm-CT, and flat panel-CT (FP-CT) compared to MicroCT for visualization of a small metallic stent.** *Acad Radiol* 2011;18:866–75

Enhanced Aneurysmal Flow Diversion Using a Dynamic Push-Pull Technique: An Experimental and Modeling Study

D. Ma, J. Xiang, H. Choi, T.M. Dumont, S.K. Natarajan, A.H. Siddiqui, and H. Meng



ABSTRACT

BACKGROUND AND PURPOSE: Neurovascular flow diverters are flexible, braided stent-meshes for intracranial aneurysm treatment. We applied the dynamic push-pull technique to manipulate the flow-diverter mesh density at the aneurysm orifice to maximize flow diversion. This study investigated the hemodynamic impact of the dynamic push-pull technique on patient-specific aneurysms by using the developed high-fidelity virtual-stenting computational modeling technique combined with computational fluid dynamics.

MATERIALS AND METHODS: We deployed 2 Pipeline Embolization Devices into 2 identical sidewall anterior cerebral artery aneurysm phantoms by using the dynamic push-pull technique with different delivery-wire advancements. We then numerically simulated these deployment processes and validated the simulated mesh geometry. Computational fluid dynamics analysis was performed to evaluate detailed hemodynamic changes by deployed flow diverters in the sidewall aneurysm and a fusiform basilar trunk aneurysm (deployments implemented previously). Images of manipulated flow diverter mesh from sample clinical cases were also evaluated.

RESULTS: The flow diverters deployed *in silico* accurately replicated *in vitro* geometries. Increased delivery wire advancement (21 versus 11 mm) by using a dynamic push-pull technique produced a higher mesh compaction at the aneurysm orifice (50% metal coverage versus 36%), which led to more effective aneurysmal inflow reduction (62% versus 50% in the sidewall aneurysm; 57% versus 36% in the fusiform aneurysm). The dynamic push-pull technique also caused relatively lower metal coverage along the parent vessel due to elongation of the flow diverter. High and low mesh compactions were also achieved for 2 real patients by using the dynamic push-pull technique.

CONCLUSIONS: The described dynamic push-pull technique increases metal coverage of pure braided flow diverters over the aneurysm orifice, thereby enhancing the intended flow diversion, while reducing metal coverage along the parent vessel to prevent flow reduction in nearby perforators.

ABBREVIATIONS: DPPT = dynamic push-pull technique; FD = flow diverter; PED = Pipeline Embolization Device

Used for intracranial aneurysm treatment, a neurovascular flow diverter (FD) is a braided stent-mesh device highly flexible in stretch and compression. A bench top study showed that an FD can form varied mesh densities through longitudinal compression,¹ consistent with our recent findings.² Meanwhile, there are concerns with using FDs in perforator-rich territories due to the likely


occlusion of small vessel ostia. While increased mesh density at the aneurysm orifice may help aneurysmal flow reduction, it would be beneficial for the mesh density to be reducible in perforator-rich regions to preserve the perforators and branch vessels.

We used the dynamic push-pull technique (DPPT) to effectively control the local FD mesh density. The concept of dynamic push-pull was originally introduced to keep the laser-cut stent at vessel centerline during its deployment.³ It was later extensively used in FD deployment to achieve complete opening and good wall apposition at highly curved locations.^{4,5} Here, we further extended the technique, targeting flow control with the following objectives: 1) to adjust for the distal foreshortening of the FD, 2) to optimize the mesh density across the aneurysm neck to increase flow diversion, and 3) to decrease the mesh density to avoid occlusion of perforator ostia and branch vessels. The deployment technique involves individually varying the push and pull of the microcatheter and the delivery wire to control the FD mesh density and the positioning.

Received September 26, 2013; accepted after revision January 30, 2014.

From the Toshiba Stroke and Vascular Research Center (D.M., J.X., A.H.S., H.M.) and Departments of Mechanical and Aerospace Engineering (D.M., J.X., H.M.), Neurosurgery (J.X., S.K.N., A.H.S., H.M.), and Radiology (A.H.S.), University at Buffalo, The State University of New York, Buffalo, New York; Department of Neurosurgery (H.C.), Upstate Medical University, The State University of New York, Syracuse, New York; and Department of Surgery (T.M.D.), The University of Arizona; Tucson, Arizona.

Please address correspondence to Hui Meng, PhD, Toshiba Stroke and Vascular Research Center, University at Buffalo, The State University of New York, 875 Ellicott St, Buffalo, NY 14203; e-mail: huimeng@buffalo.edu

 Indicates article with supplemental on-line figures.

<http://dx.doi.org/10.3174/ajnr.A3933>

To examine the DPPT in detail, we used *in vitro* testing and numerical modeling. Due to the limited resolution of current clinical angiography, it is still difficult to visualize and characterize the real-time FD deployment in patients. However, simulations of FD deployment and aneurysmal hemodynamics allow us to visualize, verify, and better understand the DPPT operation, which represents a significant advancement in intracranial aneurysm intervention.

We have recently developed a finite-element-analysis workflow,⁶ referred to as the high-fidelity virtual stent-placement method. A follow-up study validated it through FD deployment in a fusiform phantom,² where DPPT was used on 2 FDs in 2 identical fusiform (basilar artery) aneurysm phantoms for differential mesh densities. We did not verify the posttreatment hemodynamic changes and did not investigate sidewall aneurysm morphology. In the current study, we further applied DPPT for the sidewall anterior cerebral artery aneurysm both experimentally and numerically. Computational fluid dynamics analyses were then performed in all 4 flow-diversion scenarios, including the sidewall and the previously deployed fusiform morphologies to evaluate the hemodynamic impact of DDPT on intra-aneurysmal flow.

MATERIALS AND METHODS

Aneurysm Models: Numerical and In Vitro

One wide-neck anterior cerebral artery saccular aneurysm (dome \times neck: 15 \times 7 mm) was used as the sidewall aneurysm geometry for our testing. Its maximal parent vessel size was 3 mm. This geometry was chosen because preliminary computational fluid dynamics showed a strong inflow jet impinging on the distal fundus due to vessel curvature; flow diversion could help reduce the impinging flow. The numerical aneurysm model was created from 3D image segmentation. Two polymer phantoms of the aneurysm were created by using the previous method.² The phantom was connected to a flow loop to reduce friction. Microscopic images from the lateral and base (facing the aneurysm neck from the parent vessel) views were obtained during and after FD implantation for mesh analysis. Another model—a fusiform basilar trunk aneurysm—was created previously.²

Flow Diverter

The Pipeline Embolization Device (PED; Covidien, Irvine, California) was used in the current study. It consists of a 48-strand braided FD mounted on a delivery wire (On-line Fig 1). The distal capture coil and the pusher are soldered on the wire at the distal and proximal ends of the FD, respectively. The FD and wire are placed in a microcatheter (inner diameter = 0.027 inch/0.686 mm).

Dynamic Push-Pull Technique

Because the deployed FD geometry mainly depends on the releasing process, our deployment analysis focuses on operations after the delivery system placement over the aneurysm orifice. Dynamic push-pull manipulation is used in 2 phases: pillowing and release/expansion.

Pillowing. The microcatheter is first retracted while the delivery wire is secured without translation (so is the FD attached to the

delivery wire) to allow the FD to be expressed from the distal tip of the microcatheter. Then the microcatheter is pushed with the delivery wire still secured, forcing the FD to radially dilate and conform to the vessel wall. This operation aims to generate sufficient FD-vessel apposition to minimize the distal foreshortening.

Release/Expansion. The pillowed FD is released from the capture coil by rotating the delivery wire clockwise while maintaining the positions of the wire and the microcatheter. Two basic maneuvers may be followed through the rest of the deployment: 1) withdrawing the microcatheter while holding the wire, in effect of unsheathing the FD; and 2) pushing the delivery wire to unsheat and compact the FD. These 2 maneuvers are frequently combined to achieve optimal deployment. The FD is completely released at the end.

Sometimes pushing the delivery wire alone may not be sufficient to overcome the resistance of the FD. The temporary push-back of the microcatheter together with the delivery wire may be necessary for robust compaction.⁵ However, for a controlled study, here we only allowed the microcatheter to be continuously retracted and the delivery wire to be continuously advanced (with varied advancement values), to evaluate the wire advancement alone and to simplify simulations.

Numerical Modeling of FD Deployment

We used our previously described, finite-element-analysis-based high-fidelity virtual-stenting technique^{2,6} to recapitulate the detailed deployment process *in silico* to study FD flow modification by computational fluid dynamics. The high-fidelity virtual stenting workflow incorporated several simplifications: 1) The delivery wire functionality was provided by the distal capture coil (before releasing the distal end of the FD) and the pusher (after the distal release); 2) a pathway was specified to guide the distal capture coil, the microcatheter, and the pusher; and 3) the vascular wall was assumed rigid in FD-vessel interaction. The virtual FD model in the stress-free state was constructed to simulate procedures of crimping, delivery, and expansion.

Analysis of Deployed FD

To quantify the FD mesh geometry after deployment, we used “metal coverage,” defined as the total outer surface area of the FD strands divided by the area of the tubular surface framed by the FD, and “pore density,” defined as the number of pores per unit area of the tubular surface framed by the FD.⁷ Detailed calculation of these parameters was introduced elsewhere.² Following Makoyeva et al,¹ we divided the FD mesh near the aneurysm orifice into 5 segments for mesh analysis: proximal vessel, proximal transition, middle, distal transition, and distal vessel.

Hemodynamic Analysis

Computational fluid dynamics analysis was conducted in 6 scenarios: untreated, low mesh compaction, and high mesh compaction, for both sidewall and fusiform aneurysms. Approximately 1 million and 8 million polyhedral elements were generated respectively for untreated and treated cases by using STAR-CCM+ (CD-adapco; Melville, New York). The flow-governing equations were solved by the second-order finite volume solver of STAR-CCM+ with the assumption of incompressible, steady-state

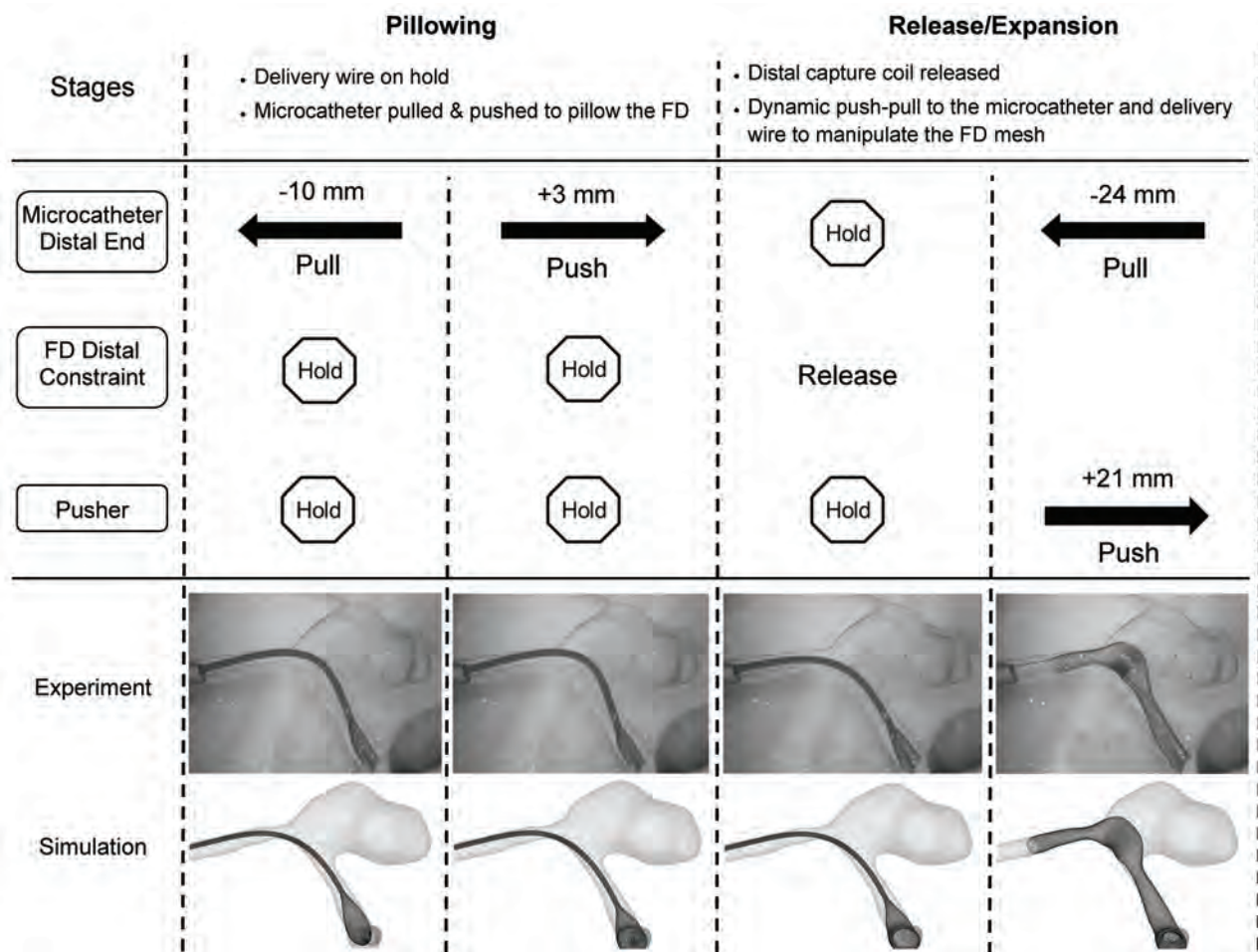


FIG 1. Stepwise deployment of the FD by using DPPT experimentally and numerically (the high-compaction scenario is shown). Displacements of key elements are estimated from the experiment recording and applied to the simulation.

Newtonian flow with rigid-wall conditions. The density and viscosity of blood flow were 1056 kg/m^3 and 3.5 cP , respectively. A typical Reynolds number of 362 was applied to all simulations as the inlet boundary condition. Flow patterns were visualized by streamlines; inflow reduction was calculated as the difference between pre- and posttreatment aneurysmal inflow rates normalized by the pretreatment inflow rate.

Clinical Case Examination

To evaluate the potential effectiveness of DPPT in flow diversion, 2 clinical FD cases, one with high mesh compaction and the other with low mesh compaction, were selected from our hospital. By assuming that the gray-scale intensity of the image is proportional to real mesh density, we analyzed the average metal coverage along the FD by using the method above.

RESULTS

In Vitro and Numerical FD Deployment in the Sidewall Aneurysm

In each of the sidewall phantoms, we deployed a PED by using DPPT. Distal foreshortening of the FD was largely overcome by the pillowing procedure. One PED (labeled $3.5 \times 20 \text{ mm}$) was deployed with greater delivery wire advancement (21 mm) than the other PED (labeled $3 \times 25 \text{ mm}$, wire advanced 11 mm) during

the release/expansion stage, resulting in higher mesh compaction over the aneurysm neck region. These 2 scenarios are referred to as high- and low-compaction, respectively. Numerical simulations recapitulated the in vitro DPPT processes. Figure 1 shows stepwise deployment in vitro and in silico.

Deployed Mesh Geometry: Comparison of In Vitro and Numerical Results

High correlation was achieved between experimental and numerical results of FD deployment. Figure 2 shows mesh geometry and mesh density quantification in the lateral view (the base view is given in On-line Fig 2). Greater delivery wire advancement (21 mm) generated higher compaction at the orifice (50% metal coverage, 40 pores/ mm^2 pore density) compared with that with less wire advancement (11 mm, 36% metal coverage, 38 pores/ mm^2 pore density). Mesh densities at parent vessels and transition zones (30% metal coverage) were similar between high- and low-compaction scenarios and were lower than that in the neck region of the high-compaction case. The nonparametric test confirmed the excellent accuracy of the simulation.

Hemodynamic Evaluation of Flow Diversion

In streamline plots in Fig 3, all 4 FD-treated scenarios showed pronounced reductions of aneurysmal velocity and inflow com-

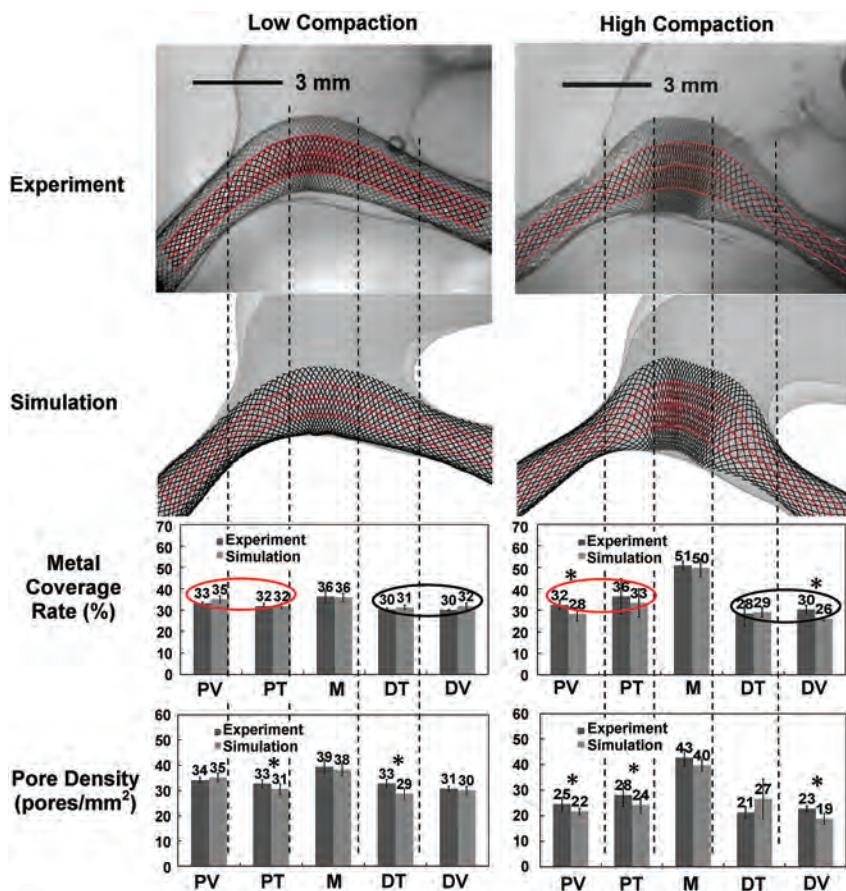


FIG 2. Metal coverage and pore density of the FD mesh (lateral view). Parameter values are calculated from sampling boxes (red) at the central area of the FD mesh. Error bars represent SD. The asterisk indicates a significant difference ($P < .05$) from the nonparametric Wilcoxon rank sum test. Elliptic circles of the same color (red: proximal vessel; black: distal vessel) show that mesh densities at the same parent vessel segments are similar between low- and high-compaction scenarios. PV indicates proximal vessel; PT, proximal transition; M, middle; DT, distal transition; DV, distal vessel.

pared with untreated scenarios. High-compaction mesh diverted more flow than the low-compaction mesh (inflow reduction: 62% versus 50% for sidewall, 57% versus 36% for fusiform). The high-compaction mesh for the sidewall aneurysm attenuated the inertia-driven inflow jet and redirected it to the more proximal region (Fig 3), which potentially alleviates negative impacts of the flow impingement.

Mesh Analysis of Clinical Cases

Figure 4 shows 2 clinical PED cases. The case on top was treated by a PED deployed with high compaction, giving improved FD-vessel apposition. Metal coverage near the orifice (inflow zone) and the distal vessel was estimated as 46% and 18%, respectively. In the second illustrated case, the FD was stretched across the orifice (18%) with normal coverage at the parent vessels (24%–30%).

DISCUSSION

The current study found the following with DPPT: 1) The distal foreshortening of the FD was prevented by the pillowing technique; 2) higher FD metal coverage across the aneurysm orifice could be achieved by greater delivery wire advancement; 3) lower

metal coverage at perforator regions could be achieved by smaller wire advancement and greater withdrawal of the microcatheter; and 4) high-compaction mesh resulted in greater inflow reduction (than low-compaction), which theoretically promotes aneurysm occlusion.

The FD foreshortening has been frequently encountered in practice.^{4,5} Foreshortening occurs once the FD is released from the crimped state. The released FD radially expands and longitudinally foreshortens; this change makes the optimal placement of the FD relatively unpredictable, especially for a poorly sized FD. As a countermeasure, the pillowing technique was effective in preventing distal migration of the FD as it foreshortened.

To actively control the FD mesh, we demonstrated that the additional delivery wire/pusher advancement (approximately 10 mm) was sufficient to generate high-compaction mesh (metal coverage: 50% versus 36%). Similar results were found for the fusiform aneurysm in the previous study (metal coverage: 49% versus 40%, by a 6-mm difference in wire advancements).² In practice, high-compaction mesh can be achieved by pushing the delivery wire, either alone or together with the microcatheter, to radially expand and longitudinally compress the FD. However, when the FD is over important arterial branch ostia (eg, the anterior choroïdal or posterior communicating arteries), we suggest additional pull of the microcatheter while holding the delivery

wire to generate low-compaction mesh for the patency of small vessels.

Our experience shows that the above operations would work better around the orifice than inside parent vessels, because once a given FD fully expands to the vessel, its metal coverage is mainly determined by the vessel size and DPPT becomes less effective. This characteristic was confirmed by our result that mesh densities from the high- and low-compaction scenarios were similar in corresponding parent vessels (Fig 2).

One should also be mindful of potential risks of dense compaction: 1) Denser mesh increases the chance of occluding perforators and side branches, given that these vessels can only tolerate up to 50% ostial coverage as previously suggested⁸; 2) forceful pushing can lead to flattening, torsion, and even intussusceptions of the FD,⁹ compromising the vessel lumen with potentially devastating consequences; 3) controlled, selectively increased metal coverage over the aneurysm neck may take time to master and is more difficult to perform in tortuous vascular anatomies.

Flow simulations showed that high-compaction mesh was more effective (additional 12%–21% reduction) in diverting aneurysmal inflow than low-compaction mesh. Most interesting, the flow reduction by the high-compaction mesh of the

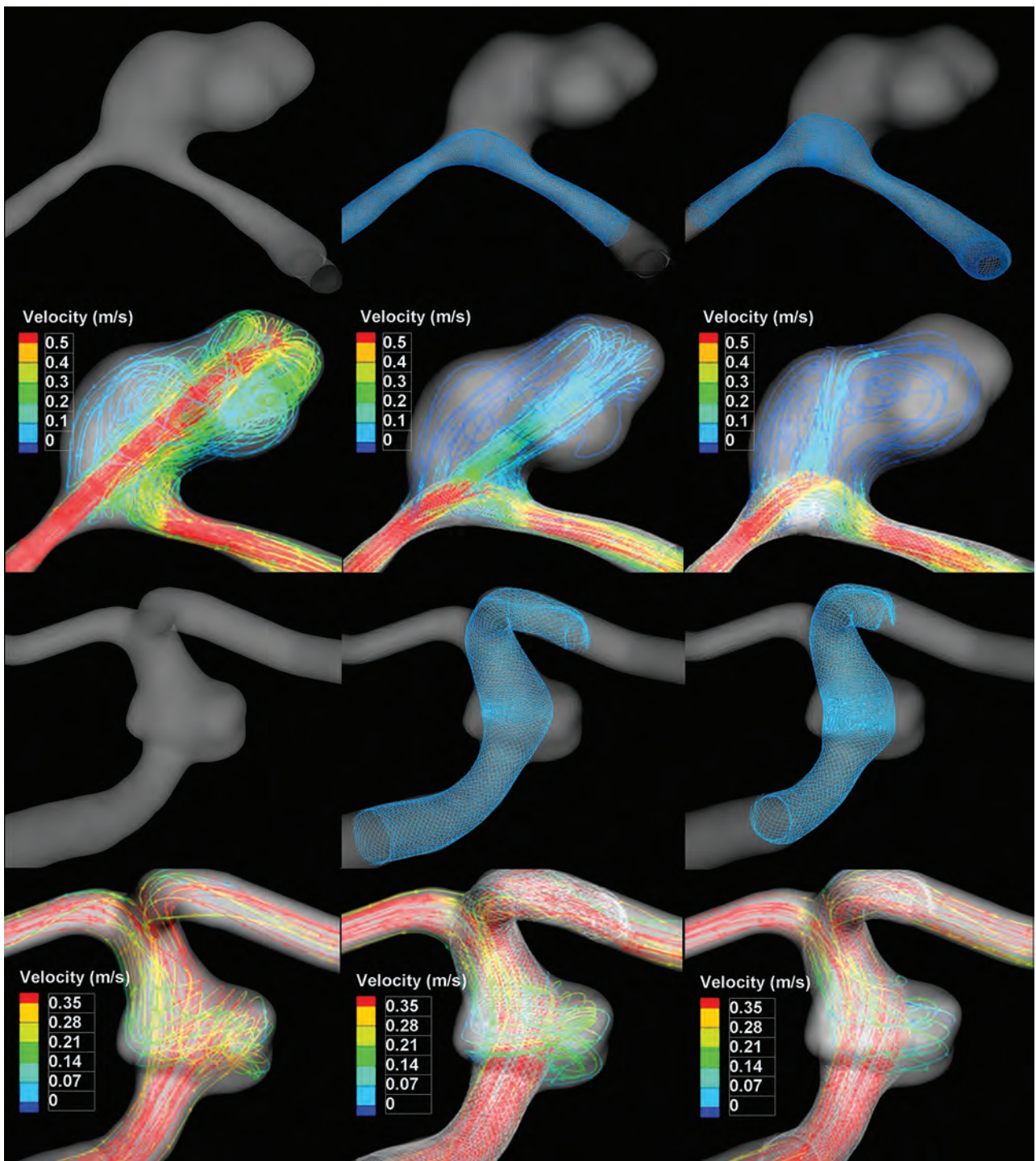


FIG 3. Hemodynamic modification by FD showing streamlines with flow-velocity magnitude (second and fourth rows) in the sidewall and fusiform aneurysms. Left column: untreated. Middle column: low-compaction. Right column: high-compaction.

sidewall aneurysm in the current study (62% inflow reduction) is comparable with the performance of overlapping 2 FDs (69% reduction of mean aneurysmal velocity) reported by Augsburger et al.¹⁰ However, further analysis is needed to verify this observation. With regard to the clinical implications of flow reduction, it is understood that more flow reduction leads to more immediate and complete thrombotic occlusion, therefore avoiding the complications related to aneurysm rupture.^{11,12}

The orifice coverage of the first clinical case matched the current high-compaction mesh of the sidewall aneurysm (46% versus 50%), indicating comparable flow reduction. The low-compaction mesh of the other case was favorable for branch vessel preservation, but with compromised flow reduction. These 2 cases showed high variability of the FD mesh and potentially distinct flow modifications under the DPPT operation.

Limitations of the current study include the following: 1) Only the hemodynamics of 2 aneurysm geometries were analyzed.

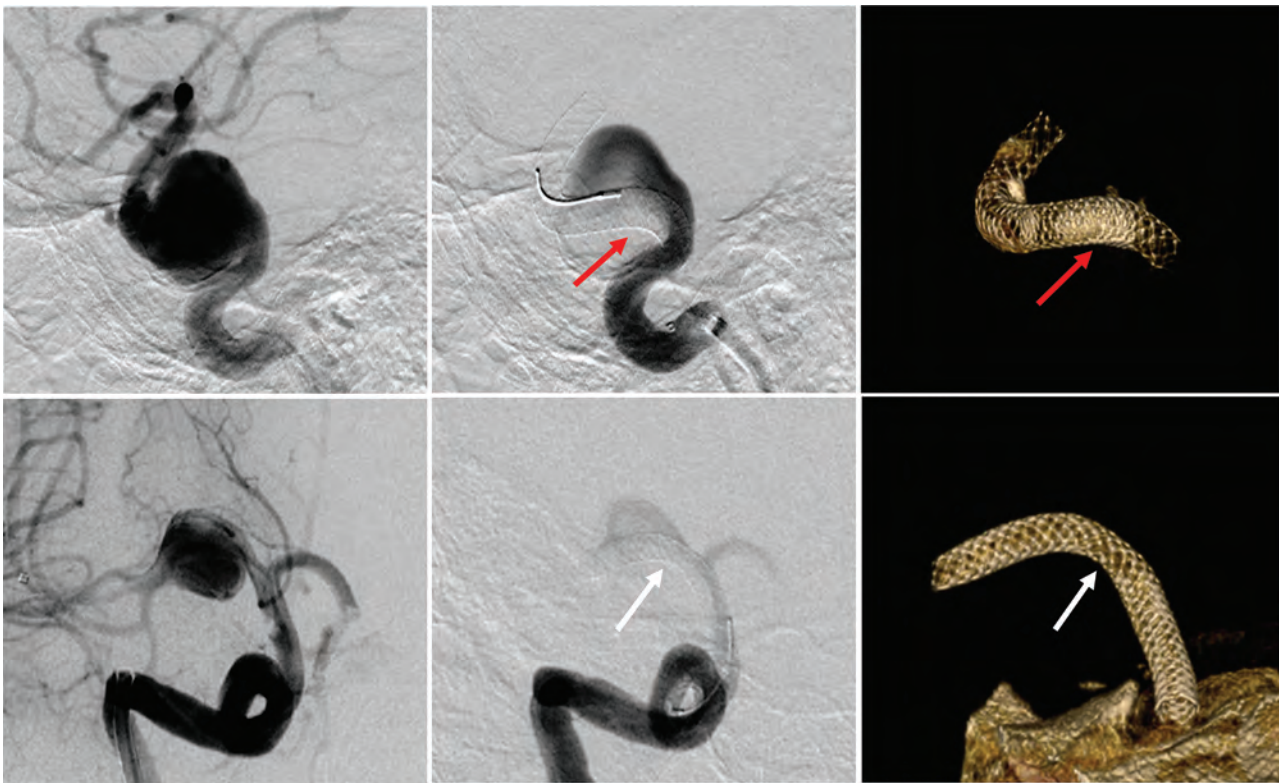


FIG 4. Two clinical PED cases using DPPT. Left and middle: pre- and posttreatment angiography. Right: reconstructed FD images. Top row: wide-neck left cavernous ICA aneurysm (19 × 14 mm) treated by a 4.75 × 25 mm PED with high compaction (46%) over the orifice inflow zone (red arrows). Lower row: right MCA aneurysm (10 × 8 mm) treated by a 3.5 × 30 mm PED with low compaction (18%) near the orifice (white arrows).

However, these 2 were typical cases suitable for flow diversion (wide necks and complex geometries less optimal for coiling or clipping); 2) the 3.5 × 20 mm FD for high-compaction was oversized (3.5 versus 3 mm) due to limited FD sample availability. Oversized FDs were reported to achieve less flow reduction than nonoversized ones,¹³ indicating an underestimation to the flow reduction of the current high-compaction scenario; and 3) rigid wall was assumed through the deployment. Future direction would be to further examine the effects of DPPT on aneurysm occlusion and perforator preservation in clinical cases following flow diversion.

CONCLUSIONS

The current study investigated the variability of the pure braided FD mesh deployed by the DPPT in patient-specific aneurysm models and evaluated the consequent flow-diversion performance. The selective use of DPPT during FD deployment generated enhanced aneurysm flow reduction by creating high mesh compaction over the aneurysm neck. DPPT was also capable of maintaining relatively low compaction over perforators/branch vessels to aid their preservation.

Disclosures: Adnan H. Siddiqui—UNRELATED: Board Membership: Codman & Shurtleff, Covidien Neurovascular, Consultancy: Codman & Shurtleff, Concentric Medical, Covidien Vascular Therapies, Guidepoint Global Consulting, Penumbra, Stryker Neurovascular, Pulsar Vascular, MicroVention. Grants/Grants Pending: National Institutes of Health,* University at Buffalo,* Comments: National Institutes of Health (coinvestigator: National Institute of Neurological Disorders and Stroke, 1R01NS064592-01A1, “Hemodynamic Induction of Pathologic Remodeling Leading to Intracranial Aneurysms”); University at Buffalo (Research Development Award), National Institutes of Health (coinvestigator: National Institutes of Natural Sciences, 5 R01 EB002873-07, “Micro-Radiographic Image for Neurovascular Interventions”),

Payment for Lectures (including service on Speakers Bureaus): Codman & Shurtleff, Stock/Stock Options: Hotspur, Intratech Medical, StimSox, Valor Medical, Blockade Medical, Other: Abbott Vascular, AANS (American Association of Neurological Surgeons) Courses, Penumbra, Comments: honoraria. Hui Meng—UNRELATED: Grants/Grants Pending: National Institutes of Health R01 research grant,* Covidien,* Toshiba,* *Money paid to the institution.

REFERENCES

1. Makoyeva A, Bing F, Darsaut TE, et al. The varying porosity of braided self-expanding stents and flow diverters: an experimental study. *AJNR Am J Neuroradiol* 2013;34:596–602
2. Ma D, Dumont TM, Kosukegawa H, et al. High fidelity virtual stenting (HiFiVS) for intracranial aneurysm flow diversion: in vitro and in silico. *Ann Biomed Eng* 2013;41:2143–56
3. Heller RS, Malek AM. Delivery technique plays an important role in determining vessel wall apposition of the Enterprise self-expanding intracranial stent. *J Neurointerv Surg* 2011;3:340–43
4. Lubicz B, Collignon L, Raphaeli G, et al. Pipeline flow-diverter stent for endovascular treatment of intracranial aneurysms: preliminary experience in 20 patients with 27 aneurysms. *World Neurosurg* 2011;76:114–19
5. Fischer S, Vajda Z, Aguilar Perez M, et al. Pipeline embolization device (PED) for neurovascular reconstruction: initial experience in the treatment of 101 intracranial aneurysms and dissections. *Neuroradiology* 2012;54:369–82
6. Ma D, Dargush GF, Natarajan SK, et al. Computer modeling of deployment and mechanical expansion of neurovascular flow diverter in patient-specific intracranial aneurysms. *J Biomech* 2012;45:2256–63
7. Lieber BB, Sadasivan C. Endoluminal scaffolds for vascular reconstruction and exclusion of aneurysms from the cerebral circulation. *Stroke* 2010;41:S21–25
8. Fiorella D, Lylyk P, Szikora I, et al. Curative cerebrovascular reconstruction with the Pipeline embolization device: the emergence of

- definitive endovascular therapy for intracranial aneurysms. *J Neurointerv Surg* 2009;1:56–65
9. Dumont TM, Mokin M, Snyder KV, et al. **A paradigm-shifting technology for the treatment of cerebral aneurysms: the Pipeline embolization device.** *World Neurosurg* 2013;80:800–03
 10. Augsburg L, Farhat M, Raymond P, et al. **Effect of flow diverter porosity on intraaneurysmal blood flow.** *Clin Neuroradiol* 2009;19:204–14
 11. Kulcsár Z, Houdart E, Bonafe A, et al. **Intra-aneurysmal thrombosis as a possible cause of delayed aneurysm rupture after flow-diversion treatment.** *AJNR Am J Neuroradiol* 2011;32:20–25
 12. D'Urso PI, Lanzino G, Cloft HJ, et al. **Flow diversion for intracranial aneurysms: a review.** *Stroke* 2011;42:2363–68
 13. Mut F, Cebal JR. **Effects of flow-diverting device oversizing on hemodynamics alteration in cerebral aneurysms.** *AJNR Am J Neuroradiol* 2012;33:2010–16

Thromboembolic Complications in Patients with Clopidogrel Resistance after Coil Embolization for Unruptured Intracranial Aneurysms

B. Kim, K. Kim, P. Jeon, S. Kim, H. Kim, H. Byun, J. Cha, S. Hong, and K. Jo

ABSTRACT

BACKGROUND AND PURPOSE: Antiplatelet resistance is known to be associated with symptomatic ischemic complication after endovascular coil embolization. The purpose of our study was to evaluate the relationship between antiplatelet resistance and clinically silent thromboembolic complications using DWI in patients who underwent coil embolization for unruptured intracranial aneurysm.

MATERIALS AND METHODS: Between October 2011 and May 2013, 58 patients with 62 unruptured aneurysms who were measured for antiplatelet response using VerifyNow assay and underwent elective coil embolization for an unruptured aneurysm with posttreatment DWI were enrolled. Diffusion-positive lesions were classified into 3 groups according to the number of lesions ($n = 0$ [grade 0], $n < 6$ [grade I], and $n \geq 6$ [grade II]). The relationship between antiplatelet resistance and diffusion-positive lesions was analyzed.

RESULTS: Sixty-two endovascular coiling procedures were performed on 58 patients. Clopidogrel resistance was revealed in 23 patients (39.7%) and diffusion-positive lesions were demonstrated in 28 patients (48.3%); these consisted of 19 (32.8%) grade I and 9 (15.5%) grade II lesions. Clopidogrel resistance was not relevant to the development of any diffusion-positive lesion (grade I and II, $P = .789$) but was associated with the development of multiple diffusion-positive lesions (grade II, $P = .002$). In the logistic regression prediction model, clopidogrel resistance showed significant correlation with the development of grade II lesions ($P = .001$).

CONCLUSIONS: Multiple diffusion-positive lesions (≥ 6 in number) occurred more frequently in patients with clopidogrel resistance after endovascular coiling for unruptured aneurysms.

ABBREVIATION: PRU = P2Y12 reaction units

Since it was demonstrated that clopidogrel resistance is associated with thromboembolic events after cardiovascular stent placement, many studies in patients undergoing neurovascular stent placement have revealed a similar relationship between antiplatelet drug resistance and thromboembolic complications.^{1,2} Furthermore, recently published reports have documented that clopidogrel resistance had an effect on the occurrence of symptomatic ischemic infarcts in patients undergoing endovascular treatment with or without adjunctive devices for intracranial aneurysms.^{3,4}

The widespread and routine application of DWI after coil em-

bolization has revealed that clinically silent thromboembolic phenomena occur in up to one-third of cases.⁵ Several clinical and procedural factors have been proposed as being associated with those postprocedural diffusion abnormalities.⁶ However, the relationship between the antiplatelet drug reactivity and the thromboembolic complication delineated on DWI has not been well-characterized in patients undergoing coil embolization. The aim of the present study was to evaluate the frequency of posttreatment diffusion-positive lesions associated with coil insertion for treatment of unruptured intracranial aneurysms in patients with antiplatelet drug resistance. In addition, other clinical, aneurysmal, and procedural factors were assessed to reveal the association with the occurrence of posttreatment diffusion-positive lesions.

MATERIALS AND METHODS

Patients

From August 2011 to May 2013, a total of 328 patients with unruptured intracranial aneurysm were treated with elective endovascular coil embolization in our institute. During this period, patients who underwent coil embolization for unruptured aneu-

Received December 22, 2013; accepted after revision March 1, 2014.

From the Departments of Radiology (B.K., K.K., P.J., S.K., H.K., H.B., J.C.) and Neurosurgery (S.H., K.J.), Samsung Medical Center, Sungkyunkwan University School of Medicine, Seoul, Korea.

Please address correspondence to Keonha Kim, MD, PhD, Department of Radiology, Samsung Medical Center, Sungkyunkwan University School of Medicine, 50, Irwon-dong, Gangnam-gu, Seoul, 135-710, Republic of Korea; e-mail: somatom.kim@samsung.com

<http://dx.doi.org/10.3174/ajnr.A3955>

Table 1: Patient characteristics, aneurysmal specifics, technical aspect of the procedure, and antiplatelet drug reactivity associated with any diffusion-positive lesion in patients undergoing endovascular coiling of unruptured intracranial aneurysms

	Category ^a	Grade 0 (n = 30)	Grade I/II (n = 28)	P _{uni}	P _{logistic}
Sex	Male (23, 39.7%)	12	11	.956	
	Female (35, 60.3%)	18	17		
Age (years)	≤60 (35, 60.3%)	21	14	.179	
	>60 (23, 39.7%)	9	14		
HTN	Yes (23, 39.7%)	11	12	.789	
DM	Yes (4, 6.9%)	3	1	.612	
Dyslipidemia	Yes (11, 19.0%)	4	7	.325	
CAD	Yes (3, 5.2%)	1	2	.605	
Stroke	Yes (6, 10.3%)	1	5	.097	.998
Statin	Yes (11, 19.0%)	5	6	.744	
Aspirin	Yes (19, 32.8%)	9	10	.781	
Smoking	Yes (15, 25.9%)	7	8	.767	
Dome size	<7 mm (39, 67.2%)	22	17	.404	
	≥7 mm (19, 32.8%)	8	11		
Neck width	<4 mm (32, 55.2%)	19	13	.291	
	≥4 mm (26, 44.8%)	11	15		
Multiplicity of the procedure ^b	Single (54, 93.1%)	30	24	.048	.072
	Double (4, 6.9%)	0	4		
Procedural methods	Single (16, 27.6%) ^c	10	6	.453	
	Double (18, 41.4%) ^c	10	8		
	Stent (24, 31%)	10	14		
Aspirin resistance	Yes (9, 15.5%)	3	6	.290	.720
Clopidogrel resistance	Yes (23, 39.7%)	11	12	.789	.998

Note:—HTN indicates hypertension; DM, diabetes mellitus; CAD, coronary artery disease.

^a (number, percent).

^b Multiple procedures in a single session.

^c Single or double microcatheter technique, stent-assisted technique.

Table 2: Patient characteristics, aneurysmal specifics, technical aspect of the procedure, and antiplatelet drug reactivity associated with multiple diffusion-positive lesions in patients undergoing endovascular treatment of unruptured intracranial aneurysms

	Category ^a	Grade 0/I (n = 49)	Grade II (n = 9)	P _{uni}	P _{logistic}
Sex	Male (23, 39.7%)	20	3	1.000	
	Female (35, 60.3%)	29	6		
Age (years)	≤60 (35, 60.3%)	30	5	1.000	
	>60 (23, 39.7%)	19	4		
HTN	Yes (23, 39.7%)	20	3	1.000	
DM	Yes (4, 6.9%)	4	0	1.000	
Dyslipidemia	Yes (11, 19.0%)	8	3	.350	
CAD	Yes (3, 5.2%)	2	1	.403	
Stroke	Yes (6, 10.3%)	4	2	.231	
Statin	Yes (11, 19.0%)	8	3	.350	
Aspirin	Yes (19, 32.8%)	16	3	1.000	
Smoking	Yes (15, 25.9%)	13	2	1.000	
Dome size	<7 mm (39, 67.2%)	34	5	.456	
	≥7 mm (19, 32.8%)	15	4		
Neck width	<4 mm (32, 55.2%)	28	4	.717	
	≥4 mm (26, 44.8%)	21	5		
Multiplicity of the procedure ^b	Single (54, 93.1%)	48	6	.010	.051
	Double (4, 6.9%)	1	3		
Procedural methods	Single (16, 27.6%) ^c	15	1	.088	.642
	Double (18, 41.4%) ^c	17	1		
	Stent (24, 31%)	17	7		
Aspirin resistance	Yes (9, 15.5%)	8	1	1.000	.667
Clopidogrel resistance	Yes (23, 39.7%)	15	8	.002	.014

Note:—HTN indicates hypertension; DM, diabetes mellitus; CAD, coronary artery disease.

^a (number, percent).

^b Multiple procedures in a single session.

^c Single or double microcatheter technique, stent-assisted technique.

rysm were prescribed dual antiplatelet therapy 7 days before the procedure and antiplatelet drug reactivity was measured 1 day before the procedure. In addition, posttreatment MR examina-

tion including DWI was done within 48 hours after the procedure. Measurement of antiplatelet drug reactivity and post-treatment MR imaging, however, were performed on the basis of the clinician's individual policy. Therefore, we excluded 51 patients for whom posttreatment diffusion MR images were not available and 119 patients with an incomplete reactivity test for aspirin and clopidogrel. In addition, 100 patients were ruled out because of the lack of both preprocedural reactivity test and posttreatment DWI. Cases of ruptured aneurysm were not included to eliminate the effect of subarachnoid hemorrhage. Finally, we retrospectively reviewed 58 nonconsecutive patients with 62 unruptured intracranial aneurysms who underwent elective coil embolization from our prospective data base collected from August 2011 and May 2013.

The baseline clinical characteristics of the patients were reviewed via their medical charts in our institute and are presented in Tables 1 and 2. The clinical laboratory data of platelet activity and procedural information including specifics of the aneurysm, treatment methods, and devices used in the procedure and intraprocedural complications were recorded in our institute's prospectively maintained data base. The specifics of the aneurysm with which we were concerned were the width of the neck and the dome size of the sac, which were shown to be significantly associated with the rate of thromboembolic complications in the Analysis of Treatment by Endovascular approach of Non ruptured Aneurysms study.⁷ The treatment of 2 aneurysms in a single session was designated as multiple procedures.

Medication Regimen and Platelet Function Testing

Antiplatelet therapy was initiated 7 days before coiling procedure with the standard 100 mg daily aspirin dose and 75 mg daily clopidogrel dose. Because unplanned or unexpected coiling for ruptured aneurysm was already excluded from the present study, the regimen was uniformly adhered to by the enrolled patients. As a daily dose of clopidogrel, 75 mg for 7 days was considered to be enough to reach the therapeutic range of antiplatelet effects, a loading dose of 300 mg clopidogrel, which was the standard dosage for cardiovascular stent-placement procedures, was not adopted for our antiplatelet regimen.^{8,9}

Response to the antiplatelet therapy was routinely checked 1 day before the procedure using a point-of-care antiplatelet function test (VerifyNow; Accumetrics, San Diego, California). The VerifyNow aspirin assay was employed to calculate the aspirin reaction units and the VerifyNow P2Y12 assay was utilized to obtain the P2Y12 reaction units (PRU). Aspirin resistance was defined as aspirin reaction units ≥ 550 following the manufacturer's suggestion and clopidogrel resistance was identified using a PRU > 240 cutoff according to the results of a previous study.^{10,11} Patients were categorized into the resistant group if testing revealed the above defined levels after 7 days of dual antiplatelet therapy.

Procedure and Procedure-Related Complications

Endovascular coil embolization was performed following a standardized protocol in our neuroangiography suite under general anesthesia, as previously described.¹² Systemic anticoagulation was achieved using an intravenous bolus injection of heparin (60 IU per kg, 3000 ~ 5000 IU, range) at the time of the guiding catheter insertion. An additional 1000 IU/h of heparin was administered to keep the activated coagulation time 2~3-fold from the baseline with routine hourly check-ups. In the cases where a stent-assisted coil embolization technique was adopted, 24-hour heparinization was maintained after the procedure based on the

result of a routine check of the activated partial thromboplastin time. A conventional coiling procedure using a single microcatheter and various detachable coils, the double-microcatheter technique, and stent-assisted coil embolization were used according to the geometry of the aneurysm including the width of the neck, dome-to-neck ratio, and presence of an incorporated branch and patient age.

Intraprocedural thromboembolic complication was defined as thrombus formation and/or embolic occlusion in the corresponding parent and distal vessels evident on immediate or delayed postprocedural angiography. In addition, intraprocedural aneurysm perforation was designated as an extravasation of the contrast material after device extrusion from an aneurysm.

Postprocedural thromboembolic complications were divided into 2 categories: 1) symptomatic ischemic complications such as a newly developed transient ischemic attack or permanent ischemic infarctions within 2 days of the procedure; and 2) clinically silent thromboembolic phenomena as represented by diffusion restriction on posttreatment DWI.¹³ MR imaging was performed at 3T (Achieva; Philips Medical Systems, Best, the Netherlands) with an 8-channel sensitivity-encoding head coil.

Posttreatment MR images were reviewed by an independent neuroradiologist for evidence of microembolism, which is defined as a high-signal-intensity lesion ≤ 15 mm in diameter,

according to the imaging features of small artery occlusion of the Trial of Org 10172 in Acute Stroke Treatment classification.¹⁴ Territorial infarction resulting from an occlusion of a branch was individually recorded. Diffusion-positive lesions were further graded into 3 groups according to their number: 1) grade I lesions included diffusion-positive lesions that were < 6 in number (Fig 1); and 2) grade II lesions had more than 6 diffusion-positive lesions (Fig 2). No diffusion restriction was categorized into grade 0. The incidence of and risk factors for any diffusion-positive lesion (both grade I and II lesions), and the association with the antiplatelet resistance were retrospectively analyzed. In addition, risk factors for multiple diffusion-positive lesions (only grade II lesions) and the

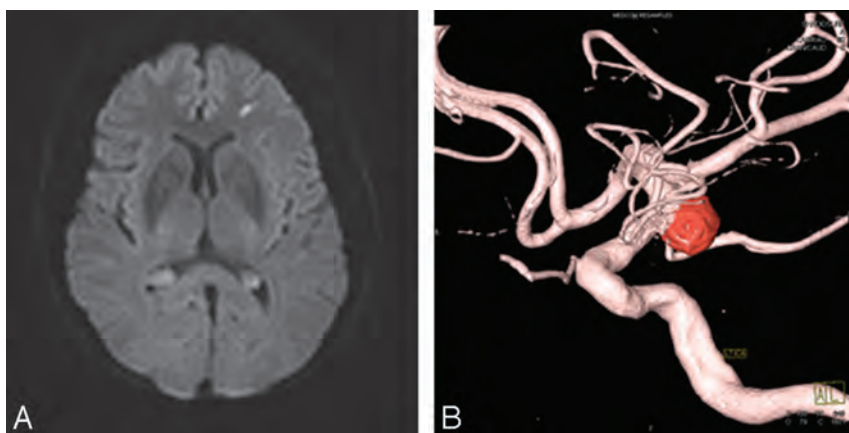


FIG 1. A 74-year-old female patient presented with left posterior communicating artery aneurysm and PRU of 134 (nonresistant group). A, Axial DWI demonstrates typical punctate diffusion restriction after an endovascular procedure. Furthermore, this lesion is related to clinically silent thromboembolic phenomena. B, 3D reconstruction image reveals coil embolized aneurysm arising from the origin of the posterior communicating artery.

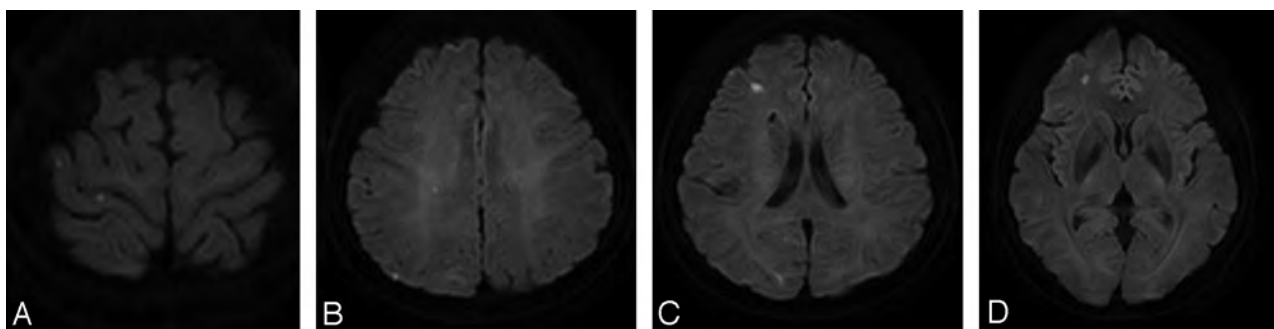


FIG 2. A 59-year-old female patient presented with right posterior communicating artery aneurysm and clopidogrel resistance detected with PRU of 304. A–D, Posttreatment DWI shows multiple scattered microembolic infarcts in right cerebral hemisphere, measured to be more than approximately 10 in number.

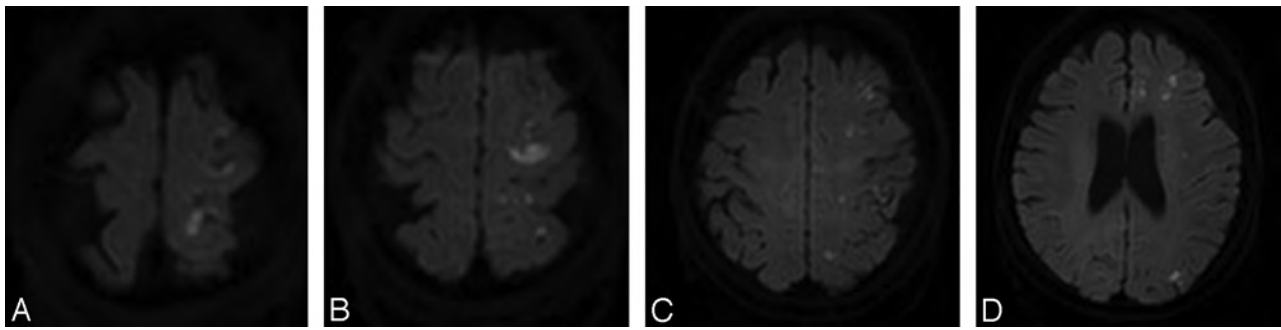


FIG 3. A 75-year-old female patient underwent stent-assisted coil embolization for unruptured left posterior communicating artery aneurysm. The patient complained of dysarthria 22 hours after the procedure. On neurologic examination, abulia, unilateral homonymous hemianopsia, and transcortical sensory aphasia were noted. A–D, Posttreatment DWI shows numerous scattered diffusion-restrictive lesions in left cerebral hemisphere including larger lesion in left frontal cortex. PRU of the patient was 339.

relevance to the antiplatelet responsiveness were evaluated in the same manner.

Statistical Analysis

Statistical analysis was executed using SAS version 9.3 (SAS Institute, Cary, North Carolina). Univariable statistical analysis (χ^2 test or Fisher exact test) was performed to assess the associations between clinical, procedural, and laboratory variables and diffusion-positive lesion as a categorical variable. The variables with P values $< .10$ in univariable analysis were chosen for multivariable models using multiple logistic regression analysis. Aspirin and clopidogrel resistance were included in the variables for multivariable analysis regardless of their P values. The Firth penalized maximum likelihood estimation method was used in cases of rare events of variables. The same process of statistical analysis was conducted to evaluate multiple diffusion-positive lesions as a categorical variable. Statistical significance was defined as $P < .05$ in all analysis. In addition, P values and 95% confidence intervals for odds ratio were corrected by the Bonferroni method because of multiple testing.

RESULTS

During the study period, overall 62 endovascular coiling procedures were performed on 58 patients, and 2 coil embolizations were undertaken in 4 patients in a single session. Among the 58 patients in whom platelet reactivity was measured, 15.5% ($n = 9$) of the patients were aspirin-resistant and 39.7% ($n = 23$) of the patients showed clopidogrel resistance. Five (8.6%) patients were confirmed to be resistant to both aspirin and clopidogrel. In addition, the incidence of antiplatelet resistance in those who were excluded in this study because of the lack of posttreatment MR imaging ($n = 51$) was not appreciably different from that of the enrolled patients (aspirin resistance, 11.8% [$n = 6$]; clopidogrel resistance, 39.2% [$n = 20$]).

Intraprocedural adverse events occurred in 2 (3.2%) of 62 cases, comprising 1/62 (1.6%) intraprocedural thromboembolic events, and 1/62 (1.6%) intraprocedural aneurysmal ruptures. The patient with intraprocedural thrombus formation in the parent artery was treated with an intra-arterial tirofiban infusion and several diffusion-positive lesions—less than 6 in number (grade I lesions)—were delineated on posttreatment DWI. No specific neurologic symptom was reported after the procedure. The pa-

tient with the intraprocedural perforation was managed with further delivery of coils and the extravasation of contrast material was successfully controlled. However, intraprocedural thrombus formation developed during additional coil placement. Therefore, for a patient with aneurysmal leakage-induced thrombus formation, tirofiban was carefully administered after confirmation of the absence of extravasation of contrast material. Although the patient complained of headache after the procedure and multiple diffusion-positive lesions were demonstrated on postprocedural DWI (grade II lesions), neurologic evaluation revealed no neurologic deficit and the NIHSS was scored at 0.

Postprocedural symptomatic ischemic complication without intraprocedural angiographic abnormality was reported in 1 (1.7%) of the 58 patients. A 75-year-old female patient with both aspirin and clopidogrel resistance presented with unruptured left posterior communicating artery aneurysm and endovascular treatment with stent-assisted coil embolization was performed. The patient complained of mild headache and dysarthria 22 hours after the procedure. On neurologic examination, abulia, unilateral homonymous hemianopsia, and transcortical sensory aphasia were detected and the NIHSS was scored at 4 (Fig 3). Multiple diffusion-restricted lesions, more than 6 in number, were delineated on posttreatment MR imaging as well. Prolonged heparinization and antiplatelet agent administration with the addition of ticlopidine (500 mg/d) were applied and the language problem resolved at discharge. No permanent neurologic deficit was reported and there was no procedure-related permanent morbidity or mortality.

Posttreatment MR imaging including DWI and MR angiography was obtained within 48 hours after the procedure in all 58 patients. Among them, 54 patients underwent posttreatment MR imaging as a routine protocol whereas 4 patients had a MR evaluation due to the presence of suspicious neurologic symptoms. Among these 4 patients, only 1 patient showed diffusion abnormalities (grade II lesions) and underwent MR evaluation 10 or 12 hours earlier than was expected because of development of aphasia. No diffusion abnormality was found in postprocedural MR imaging of the remaining 3 patients. The time interval between coil embolization and MR examination ranged from 23 to 46 hours (mean = 34.6 hours). Diffusion-positive lesions on posttreatment DWI were present in 28 (48.3%) of 58 patients, con-

sisting of 19 (32.8%) grade I and 9 (15.5%) grade II lesions. All 28 patients showed diffusion-restricted lesions within the treated vascular territory and incidental diffusion abnormalities that occurred outside the treated vascular territory were found in 2 patients. As shown in Table 1, multiple procedures in a single session were higher in the diffusion-positive group (grade 0 versus I/II lesions, $P_{\text{uni}} = .048$). However, logistic regression analysis proved no significant difference in the occurrence of any diffusion-positive lesion ($P_{\text{logistic}} = .072$). Other variables formerly known as association factors with thromboembolic complications such as age, dyslipidemia, prior thromboembolic event history, and the use of adjunctive devices did not show a statistical difference on the occurrence of any diffusion-positive lesion. In addition, neither aspirin nor clopidogrel resistance was proved to be associated with the occurrence of diffusion abnormality.

The incidence of multiple diffusion-positive lesions, more than 6 in number (grade II lesions), was higher in patients with multiple procedures in a single session and clopidogrel resistance on univariable analysis ($P_{\text{uni}} = .010$ and $P_{\text{uni}} = .002$). However, only clopidogrel resistance showed significant association with the incidence of multiple diffusion-positive lesions in multivariable analysis ($P_{\text{logistic}} = .014$, Table 2). Furthermore, high signal intensities of grade II lesions showed larger size than those of grade I lesions and measured approximately 10–15 mm in diameter. These grade II lesions were grossly distinct from almost all grade I lesions by their larger size as well as irregular configuration (Fig 3).

DISCUSSION

Oral antiplatelet preparation before coiling of an unruptured cerebral aneurysm has been accepted as a standard protocol in many institutes nowadays since the publication of the first proposal by Workman et al.¹⁵ Moreover, there is a growing body of literature that describes the relationship between poor response to clopidogrel and postprocedural thromboembolic complications in patients undergoing endovascular treatment with stent assistance or the Pipeline Embolization Device (Covidien, Irvine, California).^{4,10,16} While the connection between clopidogrel resistance and intraprocedural thromboembolic complications or clinically recognized postprocedural ischemic deficits has been documented in prior studies, an association between antiplatelet resistance and silent ischemia as represented by diffusion-weighted abnormalities has not been reported previously. In the present study, we focused on the frequency and number of diffusion-positive lesions according to the responsiveness to dual antiplatelet therapy with acetylsalicylic acid and clopidogrel. In addition, various clinical, aneurysmal, and technical factors were sought to find any correlation with diffusion-positive lesions.

Clinical implications of diffusion-positive lesions, known for clinically silent thromboembolic phenomena, are still controversial. First, there has been controversy whether silent ischemic lesions on DWI are really silent on clinical grounds. Many authors have raised the possibility of an association between diffusion-positive lesions and neuropsychological deficits with controversial results.^{17–19} It is documented that thorough neuropsychological examination can reveal significant cognitive impairments in

patients with clinically silent diffusion-positive lesions on routine neurologic tests. Given the possible pathophysiological role of diffusion-positive lesions in cognitive decline, not only the frequency and but also the number of diffusion abnormalities were considered to be clinically relevant, even allowing for the contention that diffusion abnormalities do not necessarily translate into a clinically meaningful event.^{20,21} In general, the location of the lesion in an eloquent brain area is known to determine the development of neurologic deficits. However, a recently published report investigated the clinical relevance of the total number of diffusion-positive lesions and documented that the higher rate of diffusion-positive lesions can be a surrogate marker for symptomatic ischemia regardless of their location.²² Furthermore, they suggested the cutoff value of diffusion-positive lesions (≥ 6) for predicting symptomatic ischemia. Therefore, the present study adopted the practice of categorizing patients into subgroups according to the number of diffusion-positive lesions (from grade 0 to III) based on those clinical implications of multiple microembolisms.

Several reports, including a pathologic study, suggested that the explainable embolic sources of diffusion-positive lesions after an endovascular procedure are air embolism, atheroma dislodged during catheterization, thrombus formation from the devices used over the course of the procedure, and hydrophilic coating from the catheters or wires.^{23–26} In this study, multiplicity of the procedure in a single session turned out to be associated with the occurrence of any diffusion-positive lesion. It was considered that multiple procedures in a single session had a tendency to increase the number of catheters used, the total procedure time, and the frequency of vessel probing, which was closely associated with mechanical stress. Therefore our results implied that the occurrence of diffusion-positive lesions was mainly contributed to by the factors that can exacerbate mechanical stress. Contrary to expectations, several factors that were documented to have an association with diffusion abnormalities such as dome diameter ≥ 7 mm, neck width ≥ 4 mm, and patient age 60 years or older in prior studies had only a trend for the occurrence of diffusion-positive lesions and were not independent risk factors on univariate analysis.^{7,22,27}

Although antiplatelet resistance had no relevance to occurrence of any diffusion abnormality, clopidogrel resistance showed significant association with the development of multiple diffusion-positive lesions. Among 9 patients with multiple diffusion-positive lesions (grade II lesions), 8 patients ($n = 8$, 88.9%) showed clopidogrel resistance, which was significantly higher than the risk in patients who did not exhibit clopidogrel resistance ($n = 1$, 11.1%). Moreover, 5 patients with multiple diffusion-positive lesions and clopidogrel resistance displayed numerous (more than 10 in number) tiny diffusion-restricted lesions in the corresponding territory of parent and distal cerebral arteries of the aneurysm. It was therefore speculated that active thrombus formation from endovascular devices by poor platelet inhibition seemed to mainly contribute to the formation of those multiple scattered embolic infarcts. Given the fact that 1 patient with a symptomatic ischemic event was classified as having grade II lesions, clopidogrel resistance seemed to be associated with clini-

cally relevant diffusion-positive lesions in patients undergoing elective coil embolization for unruptured aneurysms.

Use of adjunctive devices for treatment of aneurysms with an unfavorable configuration for conventional coil embolization was proposed as a risk factor that can increase the incidence of thromboembolic complications compared with the single microcatheter technique by some authors, including the author of the prior study from our institute.¹² However, other authors have published studies that show adjunctive device usage does not appear to increase the frequency of embolic or ischemic events.¹³ Alternatively, it was posed that the difference in preoperative antiplatelet medical management in each procedure could be relevant to the occurrence of thromboembolic complications. Our results showed that a difference in procedural devices such as the use of a stent or 2 microcatheters did not influence the development of diffusion-positive lesions under the same premedication strategy. As concluded in the prior study from our institute, appropriate and uniform premedication in a homogeneous patient group and adequate heparinization in all procedures may preclude the difference in the development of thromboembolic complications according to adjunctive devices.

There are several limitations to the present study. The retrospective nature of this study is the first limitation. Second, many patients were excluded for the lack of preprocedural drug reactivity test and postprocedural MR images according to the clinician's individual preference. One attending clinician routinely checked postprocedural MR examination within 1 or 2 postoperative days, whereas the remaining 2 clinicians checked MR imaging in symptomatic cases only. This selection bias might contribute to a higher thromboembolic complication rate. Third, there are no preprocedural MR images for comparison. Given some evidence that aneurysms alone can cause thromboembolic phenomena, this limitation can increase the frequency of diffusion-positive lesions artificially.²⁸ In addition, we excluded patients with ruptured aneurysms for the reason that SAH may also cause diffusion-weighted imaging changes, but an intraprocedural rupture case with subsequent SAH was included. Fourth, a thorough clinical correlation with diffusion-positive lesions was not performed. Although NIHSS was performed on all patients after the procedure, a detailed neuropsychological examination that might help to delineate the clinical implications of diffusion-positive lesions was not performed. Lastly, there was no consideration regarding the degree of atherosclerosis in the aortic arch.

CONCLUSIONS

Antiplatelet drug resistance does not appear to be related with the occurrence of any diffusion-positive lesion after an endovascular coiling procedure for unruptured aneurysm. However, it seems that clopidogrel resistance is associated with the occurrence of multiple diffusion-positive lesions, especially those that are more than 6 in number. The present study suggests that giving premedication consisting of aspirin and clopidogrel and the measurement of antiplatelet activity should be done for patients scheduled to undertake elective coil embolization for unruptured aneurysms. In cases with clopidogrel resistance, adequate modification of the premedication may help to reduce the development of both clinically silent and evident

thromboembolic complications after the procedure, and further study should be performed to seek the proper modification of the premedication.

REFERENCES

1. Gurbel PA, Bliden KP, Hiatt BL, et al. **Clopidogrel for coronary stenting: response variability, drug resistance, and the effect of pre-treatment platelet reactivity.** *Circulation* 2003;107:2908–13
2. Fifi JT, Brockington C, Narang J, et al. **Clopidogrel resistance is associated with thromboembolic complications in patients undergoing neurovascular stenting.** *AJNR Am J Neuroradiol* 2013;34:716–20
3. Kang HS, Kwon BJ, Kim JE, et al. **Preinterventional clopidogrel response variability for coil embolization of intracranial aneurysms: clinical implications.** *AJNR Am J Neuroradiol* 2010;31:1206–10
4. Delgado Almandoz JE, Kadkhodayan Y, Crandall BM, et al. **Variability in initial response to standard clopidogrel therapy, delayed conversion to clopidogrel hyper-response, and associated thromboembolic and hemorrhagic complications in patients undergoing endovascular treatment of unruptured cerebral aneurysms.** *J Neurointerv Surg* 2014 Jan 7. [Epub ahead of print]
5. Cronqvist M, Wirestam R, Ramgren B, et al. **Diffusion and perfusion MRI in patients with ruptured and unruptured intracranial aneurysms treated by endovascular coiling: complications, procedural results, MR findings and clinical outcome.** *Neuroradiology* 2005;47:855–73
6. Altay T, Kang HI, Woo HH, et al. **Thromboembolic events associated with endovascular treatment of cerebral aneurysms.** *J Neurointerv Surg* 2011;3:147–50
7. Pierot L, Spelle L, Vitry F, et al. **Immediate clinical outcome of patients harboring unruptured intracranial aneurysms treated by endovascular approach: results of the ATENA study.** *Stroke* 2008;39:2497–504
8. Lee DH, Arat A, Morsi H, et al. **Dual antiplatelet therapy monitoring for neurointerventional procedures using a point-of-care platelet function test: a single-center experience.** *AJNR Am J Neuroradiol* 2008;29:1389–94
9. Gurbel PA, Tantry US. **Clopidogrel resistance?** *Thromb Res* 2007;120:311–21
10. Delgado Almandoz JE, Crandall BM, Scholz JM, et al. **Pre-procedure P2Y12 reaction units value predicts perioperative thromboembolic and hemorrhagic complications in patients with cerebral aneurysms treated with the Pipeline embolization device.** *J Neurointerv Surg* 2013; 5(suppl 3):iii3–10
11. Maruyama H, Takeda H, Dembo T, et al. **Clopidogrel resistance and the effect of combination cilostazol in patients with ischemic stroke or carotid artery stenting using the VerifyNow P2Y12 assay.** *Intern Med* 2011;50:695–98
12. Jo KI, Yeon JY, Kim KH, et al. **Predictors of thromboembolism during coil embolization in patients with unruptured intracranial aneurysm.** *Acta Neurochir (Wien)* 2013;155:1101–06
13. Brooks NP, Turk AS, Niemann DB, et al. **Frequency of thromboembolic events associated with endovascular aneurysm treatment: retrospective case series.** *J Neurosurg* 2008;108:1095–100
14. Adams HP Jr, Bendixen BH, Kappelle LJ, et al. **Classification of subtype of acute ischemic stroke. Definitions for use in a multicenter clinical trial. TOAST—Trial of Org 10172 in acute stroke treatment.** *Stroke* 1993;24:35–41
15. Workman MJ, Cloft HJ, Tong FC, et al. **Thrombus formation at the neck of cerebral aneurysms during treatment with Guglielmi detachable coils.** *AJNR Am J Neuroradiol* 2002;23:1568–76
16. Delgado Almandoz JE, Crandall BM, Scholz JM, et al. **Last-recorded P2Y12 reaction units value is strongly associated with thromboembolic and hemorrhagic complications occurring up to 6 months after treatment in patients with cerebral aneurysms treated with the Pipeline embolization device.** *AJNR Am J Neuroradiol* 2014;35:128–35
17. Bendszus M, Stoll G. **Silent cerebral ischaemia: hidden fingerprints of invasive medical procedures.** *Lancet Neurol* 2006;5:364–72

18. Knipp SC, Matatko N, Wilhelm H, et al. **Evaluation of brain injury after coronary artery bypass grafting. A prospective study using neuropsychological assessment and diffusion-weighted magnetic resonance imaging.** *Eur J Cardiothorac Surg* 2004;25:791–800
19. Restrepo L, Wityk RJ, Grega MA, et al. **Diffusion- and perfusion-weighted magnetic resonance imaging of the brain before and after coronary artery bypass grafting surgery.** *Stroke* 2002;33:2909–15
20. Rordorf G, Bellon RJ, Budzik RE, Jr., et al. **Silent thromboembolic events associated with the treatment of unruptured cerebral aneurysms by use of Guglielmi detachable coils: prospective study applying diffusion-weighted imaging.** *AJNR Am J Neuroradiol* 2001;22:5–10
21. van Rooij WJ, Sluzewski M, Beute GN, et al. **Procedural complications of coiling of ruptured intracranial aneurysms: incidence and risk factors in a consecutive series of 681 patients.** *AJNR Am J Neuroradiol* 2006;27:1498–501
22. Kang DH, Kim BM, Kim DJ, et al. **MR-DWI-positive lesions and symptomatic ischemic complications after coiling of unruptured intracranial aneurysms.** *Stroke* 2013;44:789–91
23. Hu YC, Deshmukh VR, Albuquerque FC, et al. **Histopathological assessment of fatal ipsilateral intraparenchymal hemorrhages after the treatment of supraclinoid aneurysms with the Pipeline embolization device.** *J Neurosurg* 2014;120:365–74
24. Kim BJ, Lee SW, Park SW, et al. **Insufficient platelet inhibition is related to silent embolic cerebral infarctions after coronary angiography.** *Stroke* 2012;43:727–32
25. Busing KA, Schulte-Sasse C, Fluchter S, et al. **Cerebral infarction: incidence and risk factors after diagnostic and interventional cardiac catheterization—prospective evaluation at diffusion-weighted MR imaging.** *Radiology* 2005;235:177–83
26. Brockmann C, Hofer T, Diepers M, et al. **Abciximab does not prevent ischemic lesions related to cerebral angiography: a randomized placebo-controlled trial.** *Cerebrovasc Dis* 2011;31:353–57
27. Albayram S, Selcuk H, Kara B, et al. **Thromboembolic events associated with balloon-assisted coil embolization: evaluation with diffusion-weighted MR imaging.** *AJNR Am J Neuroradiol* 2004;25:1768–77
28. Qureshi AI, Mohammad Y, Yahia AM, et al. **Ischemic events associated with unruptured intracranial aneurysms: multicenter clinical study and review of the literature.** *Neurosurgery* 2000;46:282–89; discussion 89–90

Transarterial Onyx Embolization of Cranial Dural Arteriovenous Fistulas: Long-Term Follow-Up

R.V. Chandra, T.M. Leslie-Mazwi, B.P. Mehta, A.J. Yoo, J.D. Rabinov, J.C. Pryor, J.A. Hirsch, and R.G. Nogueira

ABSTRACT

BACKGROUND AND PURPOSE: Endovascular therapy with liquid embolic agents is a common treatment strategy for cranial dural arteriovenous fistulas. This study evaluated the long-term effectiveness of transarterial Onyx as the single embolic agent for curative embolization of noncavernous cranial dural arteriovenous fistulas.

MATERIALS AND METHODS: We performed a retrospective review of 40 consecutive patients with 41 cranial dural arteriovenous fistulas treated between March 2006 and June 2012 by using transarterial Onyx embolization with intent to cure. The mean age was 57 years; one-third presented with intracranial hemorrhage. Most (85%) had cortical venous drainage. Once angiographic cure was achieved, long-term treatment effectiveness was assessed with DSA and clinical follow-up.

RESULTS: Forty-nine embolization sessions were performed; 85% of cranial dural arteriovenous fistulas were treated in a single session. The immediate angiographic cure rate was 95%. The permanent neurologic complication rate was 2% (mild facial palsy). Thirty-five of the 38 patients with initial cure underwent short-term follow-up DSA (median, 4 months). The short-term recurrence rate was only 6% (2/35). All patients with occlusion at short-term DSA undergoing long-term DSA (median, 28 months) had durable occlusion. No patient with long-term clinical follow-up (total, 117 patient-years; median, 45 months) experienced hemorrhage.

CONCLUSIONS: Transarterial embolization with Onyx as the single embolic agent results in durable long-term cure of noncavernous cranial dural arteriovenous fistulas. Recurrence rates are low on short-term follow-up, and all patients with angiographic occlusion on short-term DSA follow-up have experienced a durable long-term cure. Thus, angiographic cure should be defined at short-term follow-up angiography instead of at the end of the final embolization session. Finally, long-term DSA follow-up may not be necessary if occlusion is demonstrated on short-term angiographic follow-up.

ABBREVIATIONS: cDAVF = cranial dural arteriovenous fistula; CVD = cortical venous drainage

Endovascular therapy is commonly used for the treatment of noncavernous cranial dural arteriovenous fistulas (cDAVFs). Cyanoacrylates, ethyl alcohol, coils, and particles can be used alone or in combination via transarterial, transvenous, or occasionally direct percutaneous treatment routes. There is no US

Food and Drug Administration–approved liquid embolic agent for the treatment of cDAVFs. The ethylene-vinyl alcohol copolymer liquid embolic system (Onyx; Covidien, Irvine, California) is FDA-approved for the presurgical embolization of brain arteriovenous malformations. Since Onyx has become available, transarterial embolization of cDAVFs by using Onyx as the sole endovascular embolic agent has become our preferred treatment strategy. This endovascular treatment approach represents an “off-label” use of the Onyx liquid embolic system.

The immediate occlusion rate in large cohort studies of patients treated with transarterial Onyx embolization ranges from 62% to 92%, and short-term durable occlusion has been demonstrated.^{1–4} We have previously reported our short-term experience using Onyx in these patients⁵ and have compared the success of this technique with embolization using *n*-butyl cyanoacrylate.⁶ However, there currently remain no published data on the long-term effectiveness for embolization of cDAVFs by using Onyx, to

Received September 17, 2013; accepted after revision December 11.

From the Neuroradiology and Neurovascular Surgery Services, Departments of Diagnostic Imaging and Surgery (R.V.C.), Monash University, Melbourne, Victoria, Australia; Neuroendovascular Service (T.M.L.-M., B.P.M., A.J.Y., J.D.R., J.A.H.), Department of Neurology (T.M.L.-M., B.P.M.), and Department of Radiology (A.J.Y., J.D.R., J.A.H.), Division of Diagnostic Neuroradiology, Massachusetts General Hospital, Harvard Medical School, Boston, Massachusetts; Department of Interventional Neuroradiology (J.C.P.), Boston University, Boston, Massachusetts; and Neuroendovascular and Neurocritical Care Services and Neurology, Neurosurgery, and Radiology (R.G.N.), Marcus Stroke and Neuroscience Center, Grady Memorial Hospital, Emory University School of Medicine, Atlanta, Georgia.

Please address correspondence to Raul Gomes Nogueira, MD, 80 Jesse Hill Dr SE Room 398, Atlanta, GA 30303; e-mail: raul.g.nogueira@emory.edu

<http://dx.doi.org/10.3174/ajnr.A3938>

Table 1: Baseline characteristics of study cohort (n = 40 patients with 41 cDAVFs)

Characteristic	No. of Patients
Age (mean; range)	57 (30–79)
Male (%)	21 (53%)
Presentation	
Tinnitus	14 (35%)
Hemorrhage	13 (33%)
Incidental/nonspecific headache syndrome	10 (25%)
Seizure	2 (5%)
Superficial siderosis	1 (2%)
Cognard grade	
I	5 (12%)
IIA	3 (7%)
IIB	3 (7%)
IIA + B	4 (10%)
III	15 (37%)
IV	11 (27%)
Borden grade	
I	8 (15%)
II	7 (22%)
III	26 (63%)

our knowledge. Here we report our long-term angiographic occlusion rate and clinical follow-up in a cohort of noncavernous cranial DAVFs that were treated by using transarterial Onyx embolization with the intention of complete cure.

MATERIALS AND METHODS

Patient Cohort

Between March 2006 and June 2012, forty consecutive patients with 41 noncavernous cDAVFs treated by using transarterial Onyx embolization as the single embolic agent with the intention of complete cure were retrospectively identified. Baseline characteristics of the study cohort are described in Table 1. This retrospective analysis was approved by the institutional review board of Massachusetts General Hospital.

Embolization Procedure

All procedures were performed with the patient under general anesthesia by using biplane angiographic units (Neurostar, Axion Artis, and Artis zee; Siemens, Erlangen, Germany). Informed consent included the off-label use of Onyx as the primary embolization agent. All procedures were performed via the transfemoral approach by using coaxial techniques with continuous flushing of the catheters with heparinized saline (4000 U of heparin per liter). After initial diagnostic angiography, standard guide catheters were placed into the external carotid artery and dimethyl-sulfoxide-compatible microcatheters were directed into the target arterial pedicle. In most cases, a Marathon microcatheter (Covidien) was placed through a 5F MPC Envoy guide catheter (Codman & Shurtleff, Raynham, Massachusetts) and navigated over an X-Pedion-10 (Covidien) or Mirage 0.008 microwire (Covidien) to reach the distal aspect of the target arterial pedicle. After microcatheter angiography confirmed an optimal position, the microcatheter was flushed with 5 mL of normal saline. The dead space of the microcatheter was subsequently filled with dimethyl-sulfoxide, and Onyx was injected during 90 seconds to fill the microcatheter and replace the dimethyl-sulfoxide in the dead

Table 2: Procedural characteristics of study cohort (n = 41 DAVFs)

Characteristic	No.
No. of feeding pedicles (mean, range)	4 (1–10)
Total No. of embolization procedures	49
No. of embolization procedures per patient (mean; range)	1.2 (1–3)
No. of single-stage embolizations	35 (85%)
Complications (n = 49 embolization procedures)	
Technical events	5 (10%)
All clinical events	7 (14%)
Transient neurologic	1 (2%)
Permanent neurologic	1 (2%)
Death	0

space. Under continuous fluoroscopic guidance, Onyx was slowly infused into the target arterial pedicle by using a “thumb-tapping” technique to form an initial “plug” at the microcatheter tip. Excessive reflux was avoided to minimize challenges related to subsequent microcatheter removal and the risk of nontarget embolization. Once sufficient antegrade flow of Onyx was established, prolonged injections were performed. Intermittent injection pauses of between 30 and 120 seconds were used to avoid Onyx migration into nontarget areas and to facilitate redirection of newly injected Onyx to desired areas. In general, Onyx-34 was used for plug formation with subsequent injection of Onyx-18. Intermittent angiography through the guide catheter was occasionally performed during embolization to assess the extent of residual flow or areas of nontarget embolization. Angiographic cure was defined as formation of an attenuated Onyx cast in the target fistula and the proximal draining venous structures with no residual arteriovenous shunting. In 2 cases, Gelfoam (Phadia, Uppsala, Sweden) was injected into the superficial temporal and occipital arteries to further promote thrombosis of the scalp arteries after Onyx embolization.

Follow-Up

All patients were scheduled for short-term (3-month) follow-up angiography to confirm persistent occlusion of the cDAVF following the endovascular treatment course. If complete occlusion of the shunt was not achieved, further treatment (endovascular or surgical) was planned. No patients underwent radiosurgical treatment. Long-term (>12-month) angiographic follow-up was left to the discretion of the neurointerventionalist; early in the study period, 3-year angiography was scheduled.

RESULTS

Patient Cohort

Mean age was 57 years (range, 30–79 years), and one-third of patients presented with intracranial hemorrhage. Thirty-five (85%) had cortical venous drainage (CVD); the classifications of Cognard et al⁷ and Borden et al⁸ are reported in Table 1.

Embolization Safety Results

Forty-nine embolization sessions were performed for 41 cDAVFs in 40 patients. The procedural characteristics are described in Table 2. Although the cDAVFs had multiple arterial feeding pedicles (mean, 4; range, 1–10), the mean number of embolization ses-

Table 3: Procedural effectiveness at time of treatment, short- and long-term follow-up

Procedural Effectiveness (No. of patients)	Angiographic Cure (No.)
At end of final treatment (40)	35 (95%)
Short-term angiographic follow-up ^a (35)	33 (94%)
Long-term angiographic follow-up ^b (24)	24 (100%)

^a Short-term follow-up occurred at a median of 4.2 months (2–12 months).

^b Long-term angiographic follow-up occurred at a median of 28.2 months (12–63 months).

sions per patient was 1.2 (range, 1–3). Thirty-five (85%) cDAVFs were treated to cure in a single embolization session.

Technical procedural complications without clinical consequence occurred in 5 (10%) of 49 embolization sessions—1 vertebral artery dissection, 1 occipital artery perforation during Onyx embolization that sealed, 1 microcatheter rupture in the middle meningeal artery, 1 instance of nontarget nonocclusive embolization into a superior sagittal sinus leaflet, and a single episode of intraprocedural thrombosis in the external carotid circulation during a treatment session despite heparinization, which raised the suspicion of heparin-induced thrombocytopenia. This particular procedure was aborted, and the cDAVF was cured on the third embolization session.

Adverse clinical events occurred in 7 (14%) of 49 embolization sessions: focal alopecia from radiation injury, transient orbital chemosis of unclear etiology that resolved within 24 hours, 2 cranial nerve palsies (partial facial and maxillary nerve palsies) with near-complete and complete resolution in these 2 patients, transient intraprocedural bradycardia progressing to brief self-resolving asystole without clinical consequence during embolization through the artery of the falx cerebelli for a Cognard III cDAVF at the torcula, and an episode of immediate postextubation respiratory distress leading to secondary asystolic arrest. The patient was resuscitated and recovered without clinical consequences. The final event was pulmonary embolism occurring 4 days after embolization of a ruptured Cognard IV cDAVF in a 71-year-old man. The only permanent neurologic complication was in the patient with partial facial palsy. There were no procedure-related cerebral ischemic or hemorrhagic complications, nor procedural mortality.

Embolization Effectiveness Results

The effectiveness of the embolization procedure at the end of the final treatment, and at short- and long-term angiographic follow up is summarized in Table 3.

Immediate Results. At the end of the final session, angiographic cure was achieved in 38 of 40 (95%) patients. Two patients were not cured after transarterial Onyx injection. A 72-year-old man with an incidental Cognard III cDAVF draining into a single cortical vein had minimal residual arteriovenous shunting at the end of 2 embolization sessions. His second embolization session was complicated by partial left maxillary and facial nerve palsies, and he underwent surgical closure of the shunt. His cranial nerve palsies had recovered by his 6-month clinical follow-up. The second patient, a 54-year-old woman, presented with pulsatile tinnitus from an extensive transverse-sigmoid sinus junction Cognard IIa cDAVF. Although significant reduction in shunting volume was

achieved, her second embolization session was complicated by partial facial nerve palsy. Her pulsatile tinnitus became tolerable; thus, no further treatment was performed. Her facial nerve function recovered to almost normal, with only minimal residual palsy.

Short-Term Follow-Up. Thirty-five (92%) of the 38 patients with immediate angiographic occlusion underwent short-term follow-up DSA at a median of 4.2 months (range, 2–12 months). Two patients (6%) had recurrence of their cDAVF. One patient with recurrence of his Cognard IV cDAVF located at the torcula underwent an additional uncomplicated embolization session to angiographic cure, which was durable at repeat angiography at 10 months posttreatment. The second recurrence occurred in a patient with a Cognard IV cDAVF supplied by the right superficial temporal artery, which was treated with surgical occlusion.

Long-Term Follow-Up. Twenty-four (73%) of the 33 patients with short-term angiographic occlusion underwent long-term (>12-month) DSA at a median of 28.2 months (range, 12–63 months). All patients (100%) had durable occlusion of their cDAVF at 59 patient-years of follow-up. Long-term clinical (>12-month) follow-up was available for 32 patients at a median of 44.8 months (12–80 months). No patient experienced intracranial hemorrhage during 117 patient-years of long-term follow-up.

DISCUSSION

Our results demonstrate the effectiveness of transarterial Onyx embolization as the single embolic agent for achieving long-term durable cure of noncavernous cDAVFs. In addition, in a cohort of patients in which one-third presented with intracranial hemorrhage and 85% demonstrated CVD, clinical outcomes were favorable, with minimal permanent complications and no patient experiencing intracranial hemorrhage during 117 patient-years of long-term follow-up.

Transarterial Onyx embolization has provided a new treatment paradigm for the care of patients with cDAVFs. The characteristics of the compound allow it to penetrate the multiple arterial branches that supply these lesions and occlude vascular passages into the proximal venous component, the ultimate treatment goal. Several large cohort studies by using transarterial Onyx as the primary embolization method have reported high initial cure rates and durable short-term angiographic occlusion. Immediate postembolization or short-term DSA cure rates range from 62% to 92%.^{1–4} Angiographic follow-up varied per series, with a median of 3–6 months. In 2 large cohort series, the short-term DSA occlusion rate was 100%.^{1,2} Therefore, these data provide satisfactory evidence that effective short-term occlusion with Onyx is readily achievable.

However, longer term angiographic and clinical follow-up data have not been published to validate the long-term effectiveness of this treatment strategy. In addition, there have been reports of recurrence of cured cDAVFs after transarterial treatment.⁹ Our data demonstrate that angiographic cure is only definitively confirmed after interval short-term angiography demonstrates cDAVF occlusion. In our cohort, 2 of 35 patients with immediate posttreatment angiographic occlusion had recurrence at short-term (median, 4.2 months) DSA. These recurrences

could be potentially related to intraprocedural vasospasm, which could obscure residual areas of arteriovenous shunting, persistent microfistulas not visible immediately following the initial treatment, or insufficient penetration of Onyx into the proximal draining venous structures. However, once occlusion is demonstrated on short-term DSA, all patients had durable angiographic occlusion at a median of 28.2 months (range, 12–63 months).

The ultimate clinical goal of treatment of cDAVFs is to alter the natural history, particularly with regard to the risk of intracranial hemorrhage. Large population studies reveal that approximately 30% of patients with cDAVF with CVD present with hemorrhage.¹⁰ The risks of early rebleeding can be high—in an earlier cohort of 20 patients with intracranial hemorrhage from cDAVFs, 7 patients (35%) had radiologically confirmed rebleeding within the first 2 weeks after presentation.¹¹ Long-term morbidity and mortality rates are elevated in patients with persistent CVD. In a cohort of 20 patients with persistent long-term CVD followed for a mean of 4.3 years, 7 patients (35%) bled and 9 patients (45%) died.¹² Five of the 20 patients initially presented with intracranial hemorrhage—3 of these 5 patients rebled; 5 of 15 remaining patients developed hemorrhage. The hemorrhages during follow-up occurred at a median of 2.3 years (range, 0.3–5.4) after the initial presentation. Despite treatment, cDAVFs with CVD are associated with excessive long-term mortality,¹³ making long-term clinical follow-up prudent. In our treated cohort, one-third presented with intracranial hemorrhage and 9 of these 13 patients had long-term (>12-month) clinical follow-up (median, 44.5 months; range, 12.3–81.3 months; total, 34 patient-years). All are alive, and none experienced rebleeding.

It has been reported that patients presenting with benign (incidental/pulsatile tinnitus/orbital phenomena) symptoms from cDAVFs with CVD may be at lower annual risk for intracranial hemorrhage (approximately 1.5%) compared with those presenting with aggressive neurologic symptoms.^{14–16} However, these estimates are based on small patient numbers or short follow-up periods. In the series by Strom et al,¹⁵ 1 of 17 patients presenting with benign symptoms from persistent CVD bled 13 years later. In another series by Söderman et al,¹⁴ a complicated “time-at-risk” period was calculated by combining the time between symptom onset/nonangiographic diagnosis, the time between diagnostic angiography and treatment, and clinical follow-up. In the cohort of 53 patients who did not present with intracranial hemorrhage, 1 patient bled during a time-at-risk period of 67.1 patient-years, conferring an annual 1.5% risk for intracranial hemorrhage. Despite the complex methodology and limitations,¹⁷ the per-patient follow-up period of 1.3 years is relatively short. In the most recent publication evaluating this patient cohort, 1 in 24 cDAVFs with benign presentation bled during a total of 23 patient-years of untreated follow-up, leading to an annual hemorrhage rate of 4.3%.¹⁸ Of note, the range of follow-up for the entire cohort of 70 patients was 1 day to 13 years.

Most (24 of 40) of the patients in our cohort had benign presentation—pulsatile tinnitus, nonspecific headache syndrome, or incidental. Eighteen of 24 patients with benign presentation had CVD. In this cohort, the long-term risks of intracranial hemorrhage need to be balanced against the treatment risks. In the entire cohort, only 1 permanent neurologic complication (partial facial

palsy) occurred in 40 patients who underwent 49 embolization sessions. This is within the (0%–7.5%) permanent complication rate in the larger published cohorts treated with transarterial Onyx.^{1,3,4,19} While the natural history of patients with benign symptoms from cDAVFs with CVD remains unclear, we think that the high success rate coupled with a low morbidity rate from transarterial Onyx embolization mandates treatment to angiographic cure once CVD is discovered, for long-term hemorrhage protection.

Our study adds unique and important long-term effectiveness data supporting the use of transarterial Onyx for the embolization of cDAVFs. The strengths of our study include the long-term angiographic and clinical follow-up, the use of DSA to confirm durable occlusion, and the homogeneous and relatively large cohort of noncavernous cDAVFs treated with transarterial Onyx. The limitations are the retrospective study design and the 9 patients with cure on short-term follow-up DSA who did not undergo long-term DSA. This limitation reflected a change in our practice as we gathered experience during the study period. The presence of long-term durable angiographic occlusion in all patients with occlusion on short-term DSA follow-up during the study period led some of our neurointerventionists to perform MR angiography after short-term DSA follow-up.

CONCLUSIONS

Transarterial embolization with Onyx as the sole embolic agent results in durable long-term cure of noncavernous cranial DAVFs. Recurrence rates are low on short-term follow-up, and all patients with angiographic occlusion on short-term DSA follow-up have durable long-term cure. Thus, angiographic cure should be defined at short-term follow-up angiography instead of at the end of the final embolization session. Finally, long-term DSA follow-up may not be necessary if occlusion is demonstrated on short-term angiographic follow-up.

Disclosures: Albert J. Yoo—UNRELATED: Grants/Grants Pending: Penumbra,* Comments: Core Imaging Lab for stroke trials. Johnny C. Pryor—RELATED: Support for Travel to Meetings for the Study or Other Purposes: Travel was paid when Dr Pryor arrived before the meeting to conduct animal research, consult, or teach colloquia prior to meeting; no travel occurred within 36 months of submission, Other: Massachusetts General Hospital was compensated for food and expenses for Onyx Colloquia; Dr Pryor had travel expenses paid directly for research and consultation at ev3 and University of California, Riverside in California; no such activities have occurred within 36 months of submission, UNRELATED: Stock/Stock Options: purchased stock in Chestnut Medical Technologies, which was purchased by ev3. Joshua A. Hirsch—UNRELATED: Consultancy: CareFusion, Aetrium, Comments: Both >12 months but <36 months ago, related to spine, Royalties: CareFusion, Comments: As above, Stock/Stock Options: Intratech, Comments: development-stage stroke company. Raul G. Nogueira—UNRELATED: Consultancy: Stryker Neurovascular (Principal Investigator of Trevo Versus Merci Retrievers for Thrombectomy Revascularisation of Large Vessel Occlusions in Acute Ischaemic Stroke 2 and DWI/PWI and CTP Assessment in the Triage of Wake-Up and Late Presenting Stroke Undergoing Neurointervention Trials), Covidien (Steering Committee for the SWIFT [Solitaire with the Intention for Thrombectomy] and SWIFT Prime Trials, Core Lab for the Solitaire FR Thrombectomy for Acute Revascularization Trial), Penumbra (Executive Committee for the Penumbra 3-D Trial); Rapid Medical (Data and Safety Monitoring Board). *Money paid to the institution.

REFERENCES

1. Abud TG, Nguyen A, Saint-Maurice JP, et al. The use of Onyx in different types of intracranial dural arteriovenous fistula. *AJNR Am J Neuroradiol* 2011;32:2185–91
2. Cognard C, Januel AC, Silva NA Jr, et al. Endovascular treatment of

- intracranial dural arteriovenous fistulas with cortical venous drainage: new management using Onyx. *AJNR Am J Neuroradiol* 2008;29:235–41
3. Hu YC, Newman CB, Dashti SR, et al. **Cranial dural arteriovenous fistula: transarterial Onyx embolization experience and technical nuances.** *J Neurointerv Surg* 2011;3:5–13
 4. Lv X, Jiang C, Zhang J, et al. **Complications related to percutaneous transarterial embolization of intracranial dural arteriovenous fistulas in 40 patients.** *AJNR Am J Neuroradiol* 2009;30:462–68
 5. Nogueira RG, Dabus G, Rabinov JD, et al. **Preliminary experience with Onyx embolization for the treatment of intracranial dural arteriovenous fistulas.** *AJNR Am J Neuroradiol* 2008;29:91–97
 6. Rabinov JD, Yoo AJ, Ogilvy CS, et al. **Onyx versus n-BCA for embolization of cranial dural arteriovenous fistulas.** *J Neurointerv Surg* 2013;5:306–10
 7. Cognard C, Gobin YP, Pierot L, et al. **Cerebral dural arteriovenous fistulas: clinical and angiographic correlation with a revised classification of venous drainage.** *Radiology* 1995;194:671–80
 8. Borden JA, Wu JK, Shucart WA. **A proposed classification for spinal and cranial dural arteriovenous fistulous malformations and implications for treatment.** *J Neurosurg* 1995;82:166–79
 9. Adamczyk P, Amar AP, Mack WJ, et al. **Recurrence of “cured” dural arteriovenous fistulas after Onyx embolization.** *Neurosurg Focus* 2012;32:E12
 10. Piippo A, Niemela M, van Popta J, et al. **Characteristics and long-term outcome of 251 patients with dural arteriovenous fistulas in a defined population.** *J Neurosurg* 2013;118:923–34
 11. Duffau H, Lopes M, Janosevic V, et al. **Early rebleeding from intracranial dural arteriovenous fistulas: report of 20 cases and review of the literature.** *J Neurosurg* 1999;90:78–84
 12. van Dijk JM, terBrugge KG, Willinsky RA, et al. **Clinical course of cranial dural arteriovenous fistulas with long-term persistent cortical venous reflux.** *Stroke* 2002;33:1233–36
 13. Piippo A, Laakso A, Seppa K, et al. **Early and long-term excess mortality in 227 patients with intracranial dural arteriovenous fistulas.** *J Neurosurg* 2013;119:164–71
 14. Söderman M, Pavic L, Edner G, et al. **Natural history of dural arteriovenous shunts.** *Stroke* 2008;39:1735–39
 15. Strom RG, Botros JA, Refai D, et al. **Cranial dural arteriovenous fistulae: asymptomatic cortical venous drainage portends less aggressive clinical course.** *Neurosurgery* 2009;64:241–47, discussion 247–48
 16. Zipfel GJ, Shah MN, Refai D, et al. **Cranial dural arteriovenous fistulas: modification of angiographic classification scales based on new natural history data.** *Neurosurg Focus* 2009;26:E14
 17. van Dijk JM, Terbrugge KG, Willinsky RA, et al. **The natural history of dural arteriovenous shunts: the Toronto experience.** *Stroke* 2009;40:e412, author reply e413–14
 18. Bulter DO, Mathad N, Culliford D, et al. **The natural history of cranial dural arteriovenous fistulae with cortical venous reflux: the significance of venous ectasia.** *Neurosurgery* 2012;70:312–18, discussion 318–19
 19. Stiefel MF, Albuquerque FC, Park MS, et al. **Endovascular treatment of intracranial dural arteriovenous fistulae using Onyx: a case series.** *Neurosurgery* 2009;65(6 suppl):132–39, discussion 139–40

Preoperative Embolization of Intracranial Meningiomas: Efficacy, Technical Considerations, and Complications

D.M.S. Raper, R.M. Starke, F. Henderson Jr, D. Ding, S. Simon, A.J. Evans, J.A. Jane Sr, and K.C. Liu



ABSTRACT

BACKGROUND AND PURPOSE: Preoperative embolization for intracranial meningiomas offers potential advantages for safer and more effective surgery. However, this treatment strategy has not been examined in a large comparative series. The purpose of this study was to review our experience using preoperative embolization to understand the efficacy, technical considerations and complications of this technique.

MATERIALS AND METHODS: We performed a retrospective review of patients undergoing intracranial meningioma resection at our institution (March 2001 to December 2012). Comparisons were made between embolized and nonembolized patients, including patient and tumor characteristics, embolization method, operative blood loss, complications, and extent of resection. Logistic regression analyses were used to identify factors predictive of operative blood loss and extent of resection.

RESULTS: Preoperatively, 224 patients were referred for embolization, of which 177 received embolization. No complications were seen in 97.1%. There were no significant differences in operative duration, extent of resection, or complications. Estimated blood loss was higher in the embolized group (410 versus 315 mL, $P = .0074$), but history of embolization was not a predictor of blood loss in multivariate analysis. Independent predictors of blood loss included decreasing degree of tumor embolization ($P = .037$), skull base location ($P = .005$), and male sex ($P = .034$). Embolization was not an independent predictor of gross total resection.

CONCLUSIONS: Preoperative embolization is a safe option for selected meningiomas. In our series, embolization did not alter the operative duration, complications, or degree of resection, but the degree of embolization was an independent predictor of decreased operative blood loss.

ABBREVIATIONS: ACT = activated clotting time; ECA = external carotid artery; PVA = polyvinyl alcohol

Preoperative embolization has been an option for adjunctive treatment of intracranial meningiomas for almost 4 decades, but it remains used in only a minority of cases.¹ Meningiomas are commonly supplied by the middle meningeal, accessory meningeal, ascending pharyngeal, or occipital branches of the external carotid artery (ECA), which are easily accessible by selective mi-

croatheterization.² Branches of the internal carotid artery and pial feeders supplying the tumor may also be embolized,³⁻⁶ though these vessels are typically more difficult to access and are associated with a higher risk of parenchymal infarct. In an attempt to change the tumor characteristics to increase the likelihood of a gross total resection and minimize operative morbidity, a variety of embolization materials have been used, including polyvinyl alcohol (PVA) particles,^{7,8} large-caliber microspheres,^{8,9} ethylene-vinyl alcohol (Onyx; Covidien, Irvine, California),^{10,11} detachable coils,¹² fibrin glue¹³ and hyperosmolar mannitol.¹⁴ The potential advantages of preoperative embolization include decreased operative duration, reduced operative blood loss, and alteration of tumor consistency, all of which decrease the technical difficulty of surgical resection and increase the likelihood of achieving a more complete resection. Embolization likely causes histopathologic changes within the meningioma, including necrosis, ischemic changes, and microvascular fibrinoid changes.¹⁵ Hypoxia caused by disruption of tumoral blood supply also

Received October 28, 2013; accepted after revision January 14, 2014.

From the Department of Neurosurgery (D.M.S.R., R.M.S., D.D., J.A.J., K.C.L.), Radiology (A.J.E.), and School of Medicine (F.H.), University of Virginia Health System, Charlottesville, Virginia; and Department of Neurosurgery (S.S.), Penn State Hershey, Milton S. Hershey Medical Center, Hershey, Pennsylvania.

Paper previously presented as a Neurosurgical Forum presentation at: Annual Meeting of the Congress of Neurological Surgeons, October 19–23, 2013; San Francisco, California.

Please address correspondence to Daniel Raper, MBBS, University of Virginia, Department of Neurosurgery, Box 800212, Charlottesville, VA 22908; e-mail: raper@virginia.edu

Indicates article with supplemental on-line table.

<http://dx.doi.org/10.3174/ajnr.A3919>

causes changes in protein expression consistent with angiogenesis and promotion of growth,¹⁶ along with cytologic changes, including infiltration of macrophages.¹⁷ The combination of these changes may make histologic examination of embolized meningiomas more difficult because they may histopathologically resemble higher grade tumors.^{15,18-20} Embolization also carries with it the risk of procedural complications, including large-vessel dissection, microcatheter fracture, and unintended arterial or venous occlusion resulting in hemorrhagic or ischemic infarct.^{1,7,21-28}

Series of meningiomas that were preoperatively embolized have been recently published,⁷ but the operative findings and postoperative course for embolized tumors have not been compared with nonembolized tumors in a large modern series. In this study, we sought to review our outcomes following preoperative angiography, embolization when possible, and resection of intracranial meningiomas for the following objectives: 1) to assess the effect of preoperative embolization on operative time, surgical blood loss, and extent of resection; 2) to compare outcomes and complications between resection of embolized and nonembolized meningiomas; and 3) to determine predictors of objective utility of meningioma embolization.

MATERIALS AND METHODS

We performed a retrospective review of all patients treated at the University of Virginia Hospital between March 2001 and December 2012. All patients who underwent craniotomy for resection of meningiomas were included in the study. Five patients were excluded due to incomplete records ($n = 2$), treatment with radiosurgery only ($n = 1$), or final pathology other than meningioma ($n = 2$). Inpatient and outpatient medical charts and imaging were reviewed for patient characteristics, pathologic details, intraoperative and intraoperative findings, complications, and outcomes. Operative notes were reviewed for any comments made by the surgeon as to the ease or difficulty of the resection. The study was approved by the local institutional review board.

Maximal tumor diameter was measured on preoperative imaging studies and taken as the largest measurement in either the coronal, axial, or sagittal plane. Tumors were categorized according to location, and previous treatments were noted. Embolization characteristics, including embolized vessel, method of embolization, estimated percentage of tumor devascularization, and procedure-related complications, were noted. The extent of surgical resection, operative blood loss, and operative time were recorded. In most cases, the extent of tumor resection was recorded in the operative notes, based on the operating surgeon's estimate at the time of surgery. In cases in which no estimate was made, the extent of resection was estimated by the primary author based on review of operative reports and pre- and postoperative imaging. "Gross total" resection was defined as excision without residual tumor and lack of residual tumor on postoperative imaging; "sub-total" resection was defined as either residual tumor at operation $\leq 10\%$ of the total tumor volume or signs of residual tumor on postoperative imaging; "partial" resection included resection of $< 90\%$ of tumor by report or postoperative imaging. Postoperative treatments and perioperative complications were also analyzed by the treatment group.

Patient Selection

Selection of patients for preoperative angiography was made on an individualized patient basis based on the treating neurosurgeon's preference and practice. Embolization was performed after assessment of diagnostic images by the treating interventional radiologist. Selection of patients for preoperative embolization was not formalized as an institutional protocol. Nevertheless, the following principles were generally followed in selection of patients for preoperative embolization: patients with meningiomas located at the sphenoid wing, convexity, or parasagittal locations; or those with meningiomas with imaging characteristics indicative of hypervascularization.

Embolization Procedure

All imaging was performed by using high-resolution biplane digital subtraction angiography, with steroid coverage. Using a 5F micropuncture set, we punctured and cannulated the right common femoral artery and placed a 5F arterial sheath over a guidewire. The sheath was attached to a continuous heparinized saline flush. Intravenous heparin was intermittently administered throughout the procedure, monitored with serial activated clotting time (ACT) measurements, with the ACT maintained at 250–300. The heparin was not reversed following the procedure. Selective catheterization of cerebral arteries, including internal carotids, external carotids, and posterior circulation, was performed. After we selected appropriate vessels for embolization, a microcatheter (most commonly, Echelon 10; Covidien) was advanced to the target vessel and embolization was performed. Embolization materials included PVA, 150- to 250- μm particles; Gelfoam (Pfizer, New York, New York); and/or coil embolization by using a variety of detachable coils. Closure was achieved with Angio-Seal (St. Jude Medical, Minnetonka, Minnesota), when possible, or manual compression. In most cases, an estimate of the percentage devascularization was included in the procedure report from the embolization, as estimated by the treating interventionalist. In cases in which the report did not clearly delineate a percentage devascularization, angiographic images and reports were reviewed and a percentage devascularization was assigned retrospectively by the primary author. In all cases, postprocedure angiographic images were examined and an estimate of the percentage devascularization of the tumor was made.

Statistical Analysis

Data are presented as mean and range for continuous variables and as frequency for categorical variables. Analysis was performed by using an unpaired t test, χ^2 , or Fisher exact test as appropriate. Comparison of means among ≥ 3 groups was performed with analysis of variance with Bonferroni post hoc analysis. Univariate analysis was used to test covariates predictive of the following dependent variables: greater than the median estimated surgical blood loss (250 mL) and gross total resection. Interaction and confounding was assessed through stratification and relevant expansion covariates. Factors predictive in univariate analysis ($P < .20$) were entered into a multivariate logistic regression analysis.²⁹ P values $\leq .05$ were considered statistically significant. Statistical analysis was performed with STATA 10.0 (StataCorp, College Station, Texas).

Table 1: Patient and tumor characteristics

	Total Cohort	Embo	No Embo	P Value
Total patients	470	174	307	—
Total treated meningiomas	504	177	327	—
Mean age (range) (yr)	57 (17–90)	56 (17–82)	58 (18–90)	.2988
Female (%)	336 (71.5)	116 (66.7)	223 (72.6)	.185
Tumor location				<.001 ^a
Olfactory groove (%)	27 (5.5)	5 (2.9)	22 (6.9)	
Planum sphenoidale/tuberculum (%)	42 (8.6)	5 (2.9)	37 (11.6)	
Cavernous sinus (%)	5 (1.0)	0	5 (1.6)	
Sphenoid wing (%)	66 (13.5)	31 (18.0)	35 (11.0)	
Suprasellar (%)	2 (0.4)	0	2 (0.6)	
Convexity (%)	187 (38.2)	65 (37.8)	122 (38.2)	
Parasagittal (%)	88 (18.0)	41 (23.8)	47 (14.7)	
Middle cranial fossa (%)	12 (2.4)	2 (1.2)	10 (3.1)	
Posterior fossa (%)	41 (8.4)	18 (10.5)	24 (7.5)	
Intraosseous (%)	1 (0.2)	1 (0.6)	0	
Intraventricular (%)	9 (1.8)	0	9 (2.8)	
Cerebellopontine angle (%)	10 (2.0)	4 (2.3)	6 (1.9)	
Skull base location (%)	164 (33.4)	47 (27.3)	117 (36.7)	.036 ^a
Max. tumor diameter (mm) (range)	38.7 (5–89)	45.6 (16–89)	34.9 (5–89)	<.001 ^a
Prior resection (%)	59 (11.9)	11 (6.4)	48 (15.0)	.005 ^a
Prior radiosurgery (%)	35 (7.0)	11 (6.3)	24 (7.5)	.626
Prior radiotherapy (%)	12 (2.4)	5 (2.9)	7 (2.2)	.633
WHO grade				.807
I	344 (74.8)	121 (75.2)	223 (74.6)	
II	98 (21.3)	35 (21.7)	63 (21.1)	
III	18 (3.9)	5 (3.1)	13 (4.3)	
Brain invasion	108 (21.4)	42 (23.7)	56 (17.1)	.773

Note:—Embo indicates embolized group; —, not significant; No Embo, non-embolized group; Max., maximum; WHO, World Health Organization.

^aSignificant difference.

RESULTS

Patient and Tumor Characteristics

During the study period, surgical resection of intracranial meningiomas was performed in 470 patients (336 female, 134 male; Table 1). The mean age was 57 years (range, 17–90 years). There were 504 meningiomas treated; 25 patients had multiple operations. Two hundred twenty-four patients were referred for preoperative embolization; in 47 cases, tumor anatomy was not suitable for embolization—either there was no tumor blush or the supply was primarily intradural with concern for en passage blood supply. Patient and tumor details are reported in Table 1. The most common anatomic locations were convexity (38.2%), parasagittal (18.0%), sphenoid wing (13.5%), and planum sphenoidale/tuberculum sella (8.6%). The mean maximal tumor diameter was 38.7 mm (range, 5–89 mm). Prior resection had been performed in 59 cases (11.9%); prior radiosurgery, in 35 cases (7.0%); and prior radiation therapy, in 12 cases (2.4%). There was a significant difference in baseline characteristics between tumors that did and did not receive embolization, including overall location, skull base location, tumor size, and history of resection (Table 1).

Embolization Outcomes

Patients were referred for preoperative embolization in 224 cases. Details of embolization in 177 patients who received preoperative angiography are shown in Table 2. PVA particles were used alone in 67 patients (39%), together with Gelfoam pledgets in 75 patients (43.6%), with coil embolization of the feeding vessel in 26 patients (15.1%), with both Gelfoam and coiling in 1 patient (0.6%), 8 cases of embolization were not recorded. Coiling alone

was used in 3 patients. Among the 177 embolized cases, the middle meningeal artery or branches were used most commonly for access (157 cases), followed by the occipital artery (21 cases), superficial temporal artery (14 cases), and internal maxillary artery (14 cases). Following embolization, $\geq 75\%$ tumor devascularization was achieved in 107 cases, with 50%–74% embolization achieved in 27 cases, 25%–49% in 12 cases, and $< 25\%$ in 10 cases. The mean time from embolization to surgery was 1.6 days (median, 1 day; range, 0–31 days).

Embolization-Related Complications

Embolization-related complications occurred in 6 cases (2.9%): There were 2 cases of dissection (1.1%) and 1 case each of stroke, facial nerve palsy, scalp infarction, and iodine allergy. There were no hemorrhages related to preoperative embolization in our series. Due to the low number of complications from embolization, no statistical analysis of predictors of embolization-related complications was possible.

Determinants of Operative Blood Loss

Preoperative variables predictive of more than median blood loss (estimated blood loss of > 250 mL) in univariate analysis included male sex ($P < .001$), increasing tumor diameter ($P < .001$), skull base location ($P < .001$), increasing number of embolized vessels ($P = .001$), decreasing percentage of tumor embolized ($P = .007$), and history of embolization ($P = .046$). Estimated blood loss at surgery was larger in the embolized group (410 mL) than in the nonembolized group (315 mL, $P = .0074$) but was attributable to differences in baseline patient and tumor characteristics because a history of embolization was not a predictor of operative blood loss in multivariate analysis. Independent preoperative variables predictive in multivariate analysis included male sex (OR = 3.22; 95% CI, 1.09–9.47; $P = .034$), skull base location (OR = 5.37; 95% CI, 1.67–17.28; $P = .005$), and decreasing percentage embolization (OR = 1.02; 95% CI, 1.01–1.04; $P = .037$). These were unchanged when controlling for other variables, including history of embolization, increasing diameter, increasing number of vessels embolized, and World Health Organization grade.

Surgical Outcomes

Operative findings and outcomes are reported in Table 3. The mean operative time was 3 hours 53 minutes in the embolized group and 3 hours 39 minutes in the nonembolized group ($P = .23$). There were no significant differences in operative complications between tumors that did and did not receive embolization and no significant differences in the extent of resection ($P = .249$). There was no significant difference in the proportion of patients

Table 2: Embolization characteristics

	No.
Referred for embolization	224
Successful embolization (%)	177 (79.0)
Method of embolization	
PVA (%)	67 (39.0)
PVA and Gelfoam (%)	75 (43.6)
PVA and coil (%)	26 (15.1)
Coil (%)	3 (1.7)
PVA and Gelfoam and coil (%)	1 (0.6)
Embolized vessel	
Middle meningeal	157 (67.4)
Occipital	21 (9.0)
Internal maxillary	14 (6.0)
Superficial temporal	14 (6.0)
Deep temporal branch	13 (5.6)
Ascending pharyngeal	6 (2.6)
Posterior auricular	1 (0.4)
Sphenopalatine	3 (1.3)
Meningohypophyseal trunk	1 (0.4)
Anterior cerebral artery branch	1 (0.4)
Middle cerebral artery branch	1 (0.4)
Vertebral artery branch	1 (0.4)
Tumor devascularization	
>75%	107 (68.6)
50%–74%	27 (17.3)
25%–49%	12 (7.7)
<25%	10 (6.4)
Mean time from embolization to surgery (days) (range)	1.6 (0–31)
Complications	
Dissection	2 (1.1)
Facial nerve palsy	1 (0.6)
Stroke	1 (0.6)
Scalp infarction	1 (0.6)
Iodine allergy	1 (0.6)

who received postoperative radiation therapy between the groups, but the nonembolized group had a lower rate of postoperative radiosurgery (8.6% versus 14.1%, $P = .042$). Tumor characteristics and operative outcomes were also analyzed by embolization method, the details of which are shown in On-line Tables 1 and 2. There were no significant differences in any parameters between embolization techniques, except for a trend toward a greater percentage of postoperative radiosurgery in the PVA and coil group compared with PVA alone or PVA and Gelfoam groups ($P = .051$).

Predictors of Gross Total Resection

Variables predictive of gross total resection in univariate analysis included smaller diameter ($P < .001$), location other than skull base ($P < .001$), no prior gamma knife radiosurgery ($P < .001$), lower estimated blood loss ($P = .001$), and lower pathologic grade ($P = .001$). Preoperative variables predictive in multivariate analysis included location other than the skull base (OR = 2.50; 95% CI, 1.51–4.17; $P < .005$), no prior gamma knife radiosurgery (OR = 3.33; 95% CI, 1.49–7.14; $P = .003$), and decreasing diameter (OR = 1.03; 95% CI, 1.02–1.04; $P < .005$). These were unchanged when controlling for other variables, including preoperative embolization, percentage embolization, prior resection, and brain invasion.

Table 3: Operative outcomes

	Embolized	Nonembolized	P Value
Operative time (min)	3:53 (0:55–10:39)	3:39 (0:37–13:35)	.2348
Estimated blood loss (mL)	410 (0–2700)	315 (0–2200)	.0074 ^a
Extent of resection			.249
Gross total	116 (69.5)	228 (75.2)	
Subtotal	33 (19.8)	42 (13.8)	
Partial	18 (10.8)	33 (10.9)	
Operative complications			
Subdural hematoma	3 (1.7)	4 (1.2)	.6455
Cerebral infarction	3 (1.7)	3 (0.9)	.4274
ICH/IVH	0	5 (1.5)	.1015
CSF leak	1 (0.6)	3 (0.9)	.7173
Pseudomeningocele	2 (1.1)	1 (0.3)	.2593
Hydrocephalus	1 (0.6)	1 (0.3)	.6129
Seizure	0	6 (1.8)	.0726
Infection	4 (2.2)	6 (1.8)	.7560
Cranial nerve deficit	2 (1.1)	4 (1.2)	.9204
DVT/PE	4 (2.2)	6 (1.8)	.7560
Perioperative mortality	2 (1.1)	2 (0.6)	.5413
Other	1 (0.5)	1 (0.3)	.7242
Total complications	23 (12.9)	43 (13.1)	.960
Postoperative radiotherapy (%)	8 (4.8)	20 (6.3)	.500
Postoperative radiosurgery (%)	23 (14.1)	27 (8.6)	.042 ^a

Note.—ICH/IVH indicates intracerebral hemorrhage/intraventricular hemorrhage; DVT/PE, deep vein thrombosis/pulmonary embolism.

^aSignificant difference.

DISCUSSION

Preoperative embolization is a well-established adjuvant technique in the management of intracranial meningiomas. The theoretic advantages of embolization include devascularization of the tumor with subsequent decreased operative blood loss, increased ease of tumor visualization, improved safety especially when resecting tumors in eloquent areas, and potentially improved ability to gain Simpson grade I or II resection.^{1,2,7,30–34} However, these have not been evaluated in a comparative cohort series. The present report is a large comparative series reporting outcomes of surgery for intracranial meningiomas, evaluating the efficacy and complications of preoperative embolization, and identifying multivariate predictors of operative blood loss and gross total resection. In a cohort of 504 consecutive meningiomas treated at our institution during an 11-year period, preoperative embolization was performed in 44% of cases. Extent of resection and operative time were not significantly different between cases that received preoperative embolization and those that did not. The estimated blood loss was higher in those receiving embolization; this difference was primarily due to variances in patient and tumor characteristics. However, when other important factors were controlled for in multivariate analysis, increasing degree of tumor embolization was associated with decreased operative blood loss. This implies that tumors referred for embolization in our series were more likely to have a greater degree of operative blood loss, and a larger extent of preoperative devascularization resulted in decreased operative blood loss.

Embolization-related complications occurred in 6 cases (2.9%) in our series. There were 2 cases of dissection, 1 of thromboembolic stroke, 1 of facial nerve palsy, 1 of scalp infarction, and 1 of iodine allergy requiring abortion of the procedure. This overall complication rate is comparable with that in other series in the literature.^{1,7,24,35} In a recent systematic review, the overall complication rate of preoperative embolization was 4.6%.¹ Ischemic complications are more likely when the intracranial tumor supply

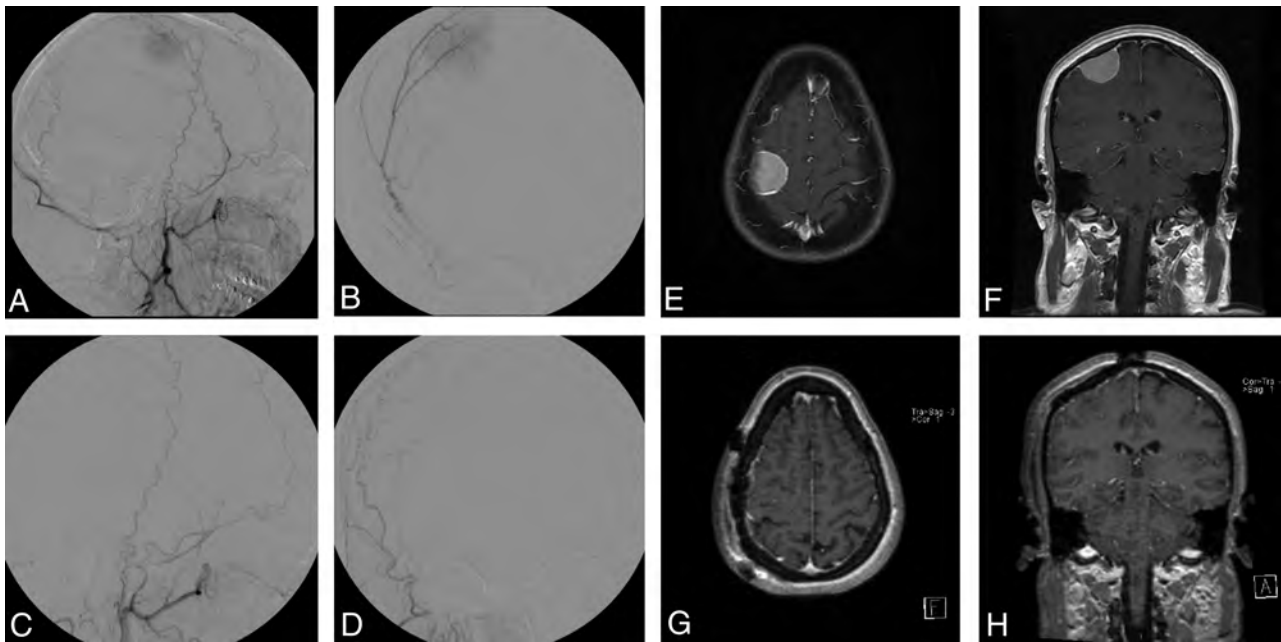


FIG 1. Right frontal meningioma, pre- and postembolization and resection. Pre-embolization right ECA injection demonstrates tumor blush from the middle meningeal artery (A, lateral view; B, frontal view). Embolization was achieved with 150- to 250- μ m PVA particles. Postembolization right ECA injection reveals complete obliteration of tumor blush (C, lateral view; D, frontal view). T1-weighted MR imaging with gadolinium before embolization (E, axial view; F, coronal view). T1-weighted MR imaging with gadolinium postresection (G, axial view; H, coronal view).

is targeted.^{21,23} For this reason, we do not routinely pursue embolization of the pial supply, which is often composed of fine branches from the middle or anterior cerebral arteries. There were no occurrences of hemorrhage in our series, which may be due to a relatively conservative embolization policy in which safety is prioritized over complete tumor devascularization in all cases. Hemorrhage is a potentially devastating complication of preoperative embolization and has been reported in up to 3%–6% of patients in some series.^{21,22,25,26,28} Hemorrhage may be more common after glue than particle embolization,¹ secondary to reflux or distal embolization of liquid embolic material into physiologically important draining veins. Postembolization hemorrhage may also be related to alternation of pressure dynamics in highly vascular tumors or ischemic necrosis within the tumor.²⁸ As a result, an increase in swelling may be observed following embolization, and care must be taken in tumors with significant pre-existing peritumoral edema or brain shift.³⁶ Other important complications of embolization are related to the anatomic location of the target. Monocular blindness may occur as a result of inadvertent occlusion of ECA-to-ophthalmic artery anastomoses during embolization of anterior skull base tumors supplied by ethmoidal branches of the ophthalmic artery.²⁷ Transient neurologic deficit has been reported in up to 12.6% of embolization procedures for skull base meningiomas, with up to 9% of patients experiencing a permanent deficit.²⁷

Despite these limitations, there is evidence that preoperative embolization may be helpful in certain circumstances. Preoperative embolization has been associated with lower intraoperative blood loss and lower transfusion requirements, in previous small single-institution studies.^{32,33} Tumor shrinkage and apparent stabilization of growth has been reported after embolization, even without subsequent surgical resection.^{22,30,31} The technique has

been used for lesions in all intracranial locations, including the skull base (Fig 1).⁵ Although embolization often makes a subjective difference to the presumed difficulty and duration of a case to the operating surgeon, it may be difficult to demonstrate objective differences in surgical outcomes and operative duration.³² For example, embolization that leads to a bloodless field during surgery for a tumor in an eloquent location may provide a subjective difference in tumor removal but may not have a significant overall effect on the surgical complications and outcomes. Additionally, difference may be difficult to quantify because particular cases that are selected for embolization are often larger and more complex lesions. Conventional angiography, with or without embolization, is not an absolute requirement for achieving Simpson grade I or II resections but may be helpful in mapping the intracranial vessels that are involved with or displaced by the tumor, thus assisting in surgical planning. Angiography may also reveal the presence of dural sinus occlusion.² A meticulous surgical technique may allow early identification and devascularization of the meningioma, but tumor vessels on the far side of the lesion that are not immediately apparent can be delineated with angiography.

On the basis of our analysis of 470 patients with meningiomas treated at our institution during the past decade, we recommend consideration for preoperative angiography and embolization in the following situations:

- 1) Tumors >3–4 cm in diameter, with at least 50% of the supply to the tumor originating from accessible branches of the ECA³⁷
- 2) Tumors that appear hypervascular or appear to have a deep-seated vascular supply difficult to surgically access based on noninvasive neuroimaging

- 3) Tumors in eloquent areas
- 4) Tumors without extensive calcification, except in certain circumstances (see below).

Any protocol for preoperative embolization should consider safety more highly than attempting to achieve a complete tumor devascularization. We routinely use the following strategies to minimize complications and ensure the safety of embolization procedures. Each embolization is preceded by selective angiography of the ECA and ICAs bilaterally, as well as the vertebral arteries when appropriate. In particular, careful study of the middle meningeal artery drainage is performed before embolization to exclude meningolacrimal artery connection to the ophthalmic artery.⁵ Particles of <math><150\ \mu\text{m}</math> should be used with great caution, especially in branches of the middle meningeal artery that may contribute supply to the cranial nerves. Although there are no definitive anatomic-location criteria for selecting candidates for embolization, convexity meningiomas that have multidirectional blood supply and appear hypervascular are optimal embolization candidates.¹ Tuberculum or olfactory groove meningiomas are less optimal candidates for embolization because these tumors are often fed by ethmoidal vessels, which are difficult to embolize without jeopardizing the vascular supply of the eye.⁵ Some tumors with extensive calcification are difficult to completely resect due to problems in stemming intraoperative bleeding, and embolization may be helpful in these cases even though calcification can also make successful preoperative exclusion of tumor blood supply more challenging.

The mean time from embolization to surgery was 1.6 days in our series, with most patients being embolized the day before resection. Although this is a common and practical application of preoperative embolization, because patients who have been treated in this manner usually require overnight observation in the hospital, some studies have suggested that delaying surgery for up to 7–9 days after embolization may allow time for maximal tumor softening and minimize blood loss.^{33,34,37,38} Other series have reported no difference in transfusion requirements between patients treated before or after 24 hours from embolization,³⁹ and still others report a trend toward increasing operative transfusion requirements with longer delay between embolization and resection.⁷ The histopathologic findings of necrosis and enlarged nuclei, commonly found in meningiomas that have been embolized, may be confused with more aggressive and higher grade lesions.¹⁸ Most important, these findings increase with increasing time between embolization and surgery and may confound definitive histologic diagnosis in those institutions that routinely delay surgery after embolization for 5 days or longer.

There are some important limitations in our study that should be recognized. There were significant differences between the cohorts in our study. Patients in the embolized group had a higher proportion of sphenoid wing, parasagittal, and posterior fossa meningiomas; had a higher mean maximal tumor diameter; and were less likely to have undergone prior resection. Both skull base location and tumor diameter were found to be multivariate predictors of a more limited extent of resection, and skull base location was found to be a predictor of larger estimated blood loss in multivariate analysis. These differences likely reflect selection bias among the treated population as outlined above. The proportion

of patients in whom embolization was not possible is consistent with other series. Reasons for failure to embolize a meningioma include dangerous intracranial supply with en passage supply to eloquent brain, inaccessible tumoral feeders, and reflux of embolization material from the superselective microcatheter into physiologic branches.²⁴

CONCLUSIONS

Preoperative embolization continues to be a valuable adjunct to surgical resection for selected intracranial meningiomas. In our series, embolization did not alter the operative duration, complications, or degree of resection, but the degree of embolization was an independent predictor of decreased operative blood loss. The benefits of preoperative embolization appear to be similar to previously reported series, despite a shorter interval between embolization and surgery. Embolization should be considered on a case-by-case basis depending on imaging characteristics, anatomic location, and patient-specific factors.

Disclosures: Fraser Henderson Jr.—I have been salaried part-time for several years by the Metropolitan Neurosurgery Group in Bethesda, Maryland, for administrative assistance and office policy research. There is no relationship, financial or otherwise, between that job and my participation in the submitted manuscript, which is through my school in Virginia. Furthermore, that practice does not perform any endovascular work, nor do they treat many intracranial meningiomas. Avery J. Evans—UNRELATED: Consultancy: Stryker, Covidien, Grants/Grants Pending: Stryker,* Payment for Lectures (including service on Speakers Bureaus): Stryker, Royalties: Cook, Payment for Development of Educational Presentations: Stryker. *Money paid to the institution.

REFERENCES

1. Shah AH, Patel N, Raper DM, et al. **The role of preoperative embolization for intracranial meningiomas.** *J Neurosurg* 2013;119:364–72
2. Dowd CF, Halbach VV, Higashida RT. **Meningiomas: the role of preoperative angiography and embolization.** *Neurosurg Focus* 2003;15:E10
3. Hirohata M, Abe T, Morimitsu H, et al. **Preoperative selective internal carotid artery dural branch embolization for petroclival meningiomas.** *Neuroradiology* 2003;45:656–60
4. Kaji T, Hama Y, Iwasaki Y, et al. **Preoperative embolization of meningiomas with pial supply: successful treatment of two cases.** *Surg Neurol* 1999;52:270–73
5. Waldron JS, Sughrue ME, Hetts SW, et al. **Embolization of skull base meningiomas and feeding vessels arising from the internal carotid circulation.** *Neurosurgery* 2011;68:162–69
6. Yoon YS, Ahn JY, Chang JH, et al. **Pre-operative embolization of internal carotid artery branches and pial vessels in hypervascular brain tumors.** *Acta Neurochir (Wien)* 2008;150:447–52, discussion 452
7. Borg A, Ekanayake J, Mair R, et al. **Preoperative particle and glue embolization of meningiomas: indications, results and lessons learned from 117 consecutive patients.** *Neurosurgery* 2013;73(2 Suppl Operative):244–51; discussion 252
8. Sluzewski M, van Rooij WJ, Lohle PN, et al. **Embolization of meningiomas: comparison of safety between calibrated microspheres and polyvinyl-alcohol particles as embolic agents.** *AJNR Am J Neuroradiol* 2013;34:727–29
9. Rodiek SO, Stolzle A, Lumenta CB. **Preoperative embolization of intracranial meningiomas with Embosphere microspheres.** *Minim Invasive Neurosurg* 2004;47:299–305
10. Gore P, Theodore N, Brasiliense L, et al. **The utility of Onyx for preoperative embolization of cranial and spinal tumors.** *Neurosurgery* 2008;62:1204–12, discussion 1211–12
11. Shi ZS, Feng L, Jiang XB, et al. **Therapeutic embolization of menin-**

- giomas with Onyx for delayed surgical resection. *Surg Neurol* 2008; 70:478–81
12. Kusaka N, Tamiya T, Sugiu K, et al. **Combined use of TruFill DCS detachable coil system and Guglielmi detachable coil for embolization of meningioma fed by branches of the cavernous internal carotid artery.** *Neurol Med Chir (Tokyo)* 2007;47:29–31
 13. Probst EN, Grzyska U, Westphal M, et al. **Preoperative embolization of intracranial meningiomas with a fibrin glue preparation.** *AJNR Am J Neuroradiol* 1999;20:1695–702
 14. Feng L, Kienitz BA, Matsumoto C, et al. **Feasibility of using hyperosmolar mannitol as a liquid tumor embolization agent.** *AJNR Am J Neuroradiol* 2005;26:1405–12
 15. Ng HK, Poon WS, Goh K, et al. **Histopathology of post-embolized meningiomas.** *Am J Surg Pathol* 1996;20:1224–30
 16. Jensen RL, Soleau S, Bhayani MK, et al. **Expression of hypoxia inducible factor-1 alpha and correlation with preoperative embolization of meningiomas.** *J Neurosurg* 2002;97:658–67
 17. Jiménez-Heffernan JA, Corbacho C, Canizal JM, et al. **Cytological changes induced by embolization in meningiomas.** *Cytopathology* 2012;23:57–60
 18. Barresi V, Branca G, Granata F, et al. **Embolized meningiomas: risk of overgrading and neo-angiogenesis.** *J Neurooncol* 2013;113:207–19
 19. Matsuda K, Takeuchi H, Yoshikazu A, et al. **Atypical and ischemic features of embolized meningiomas.** *Brain Tumor Pathol* 2012;29: 17–24
 20. Paulus W, Meizensberger J, Hofmann E, et al. **Effect of embolization of meningioma on Ki-67 proliferation index.** *J Clin Pathol* 1993;46: 876–77
 21. Bendszus M, Monoranu CM, Schütz A, et al. **Neurologic complications after particle embolization of intracranial meningiomas.** *AJNR Am J Neuroradiol* 2005;26:1413–19
 22. Carli DF, Sluzewski M, Beute GN, et al. **Complications of particle embolization of meningiomas: frequency, risk factors, and outcome.** *AJNR Am J Neuroradiol* 2010;31:152–54
 23. Celedin S, Rabitsch E, Hausegger KA, et al. **Accidental transtomal microparticle embolization of eloquent brain areas in a case of large temporofrontal meningioma.** *Interv Neuroradiol* 2008;14:339–43
 24. Gruber A, Killer M, Mazal P, et al. **Preoperative embolization of intracranial meningiomas: a 17-years single center experience.** *Minim Invasive Neurosurg* 2000;43:18–29
 25. Hayashi T, Shojima K, Utunomiya H, et al. **Subarachnoid hemorrhage after preoperative embolization of a cystic meningioma.** *Surg Neurol* 1987;27:295–300
 26. Kallmes DF, Evans AJ, Kaptain GJ, et al. **Hemorrhagic complications in embolization of a meningioma: case report and review of the literature.** *Neuroradiology* 1997;39:877–80
 27. Rosen CL, Ammerman JM, Sekhar LN, et al. **Outcome analysis of preoperative embolization in cranial base surgery.** *Acta Neurochir* 2002;144:1157–64
 28. Yu SC, Boet R, Wong GK, et al. **Postembolization hemorrhage of a large and necrotic meningioma.** *AJNR Am J Neuroradiol* 2004;25: 506–08
 29. Altman DG. *Practical Statistics for Medical Research.* Boca Raton, Florida: Chapman & Hall/CRC; 1999
 30. Bendszus M, Martin-Schrade I, Warmuth-Metz M, et al. **MR imaging—and MR spectroscopy—revealed changes in meningiomas for which embolization was performed without subsequent surgery.** *AJNR Am J Neuroradiol* 2000;21:666–69
 31. Bendszus M, Martin-Schrader I, Schlake HP, et al. **Embolization of intracranial meningiomas without subsequent surgery.** *Neuroradiology* 2003;45:451–55
 32. Bendszus M, Rao G, Burger R, et al. **Is there a benefit of preoperative meningioma embolization?** *Neurosurgery* 2000;47:1306–12, discussion 1311–12
 33. Chun JY, McDermott MW, Lamborn KR, et al. **Delayed surgical resection reduces intraoperative blood loss for embolized meningiomas.** *Neurosurgery* 2002;50:1231–37, discussion 1235–57
 34. Nania A, Granata F, Vinci S, et al. **Necrosis score, surgical time, and transfused blood volume in patients treated with preoperative embolization of intracranial meningioma: analysis of a single-centre experience and a review of literature.** *Clin Neuroradiol* 2014;24:29–36
 35. Adler JR, Upton J, Wallman J, et al. **Management and prevention of necrosis of the scalp after embolization and surgery for meningioma.** *Surg Neurol* 1986;25:357–60
 36. Engelhard HH. **Progress in the diagnosis and treatment of patients with meningiomas. Part 1. Diagnostic imaging, preoperative embolization.** *Surg Neurol* 2001;55:89–101
 37. Kai Y, Hamada JI, Morioka M, et al. **Clinical evaluation of cellulose porous beads for the therapeutic embolization of meningiomas.** *AJNR Am J Neuroradiol* 2006;27:1146–50
 38. Kai Y, Hamada JI, Morioka M, et al. **Appropriate interval between embolization and surgery in patients with meningioma.** *AJNR Am J Neuroradiol* 2002;23:139–42
 39. Macpherson P. **The value of pre-operative embolization of meningioma estimated subjectively and objectively.** *Neuroradiology* 1991; 33:334–37

Complex Hemodynamic Insult in Combination with Wall Degeneration at the Apex of an Arterial Bifurcation Contributes to Generation of Nascent Aneurysms in a Canine Model

J. Wang, H.-Q. Tan, Y.-Q. Zhu, M.-H. Li, Z.-Z. Li, L. Yan, and Y.-S. Cheng



ABSTRACT

BACKGROUND AND PURPOSE: The detailed mechanisms of cerebral aneurysm generation remain unclear. Our aim was to investigate whether specific hemodynamic insult in combination with arterial wall degeneration leads to the development of aneurysms in a canine model.

MATERIALS AND METHODS: New branch points in the common carotid artery were created in 18 dogs. Nine animals subsequently received elastase insult at the arterial bifurcation apex (elastase-treated bifurcation group); the control bifurcation group ($n = 9$) received saline, and 3 dogs received an elastase insult to both straight common carotid arteries (elastase-treated straight group). Angiographic and hemodynamic analysis was performed immediately and 12 and 24 weeks' postsurgery; histologic response was evaluated at 12 and 24 weeks.

RESULTS: Angiography revealed nascent aneurysms (mean, 3.2 ± 0.4 mm) at the arterial bifurcation apices in 5/9 models of the elastase-treated bifurcation group (versus 0 in the control bifurcation group and elastase-treated straight group) without any observed aneurysm rupture. Histologic analysis revealed internal elastic lamina discontinuity, elastic fiber disruption, a thinner muscular layer, reduced smooth-muscle cell proliferation, increased inflammatory cell (macrophage) infiltration, and expression of matrix metalloproteinase-2 and matrix metalloproteinase-9 in the media of the elastase-treated bifurcation group compared with that in either the control bifurcation group or the elastase-treated straight group ($P < .001$). Hemodynamic analysis after surgery indicated that the apex experienced extremely low wall shear stress and flow velocity and the highest relative and total pressure in the elastase-treated bifurcation group, while the values returned to normal after arterial wall remodelling.

CONCLUSIONS: In our study, combined hemodynamic insult and arterial wall degeneration at arterial bifurcations are required for the generation of aneurysms in a canine model.

ABBREVIATIONS: CBG = control bifurcation group; CCA = common carotid artery; EBG = elastase-treated bifurcation group; ESG = elastase-treated straight group; MAC387 = antimacrophage antibody; MMP = matrix metalloproteinase; SMC = smooth-muscle cell; WSS = wall shear stress; WSSG = wall shear stress gradient

Bifurcation aneurysms such as cerebral aneurysms have a high prevalence and can cause lethal hemorrhages¹; however, the detailed mechanisms of aneurysm generation, growth, and rupture remain unclear.²

Advances in vascular biology, biomechanics, medical imaging, and computational methods provide an unprecedented opportunity to develop mathematic models to better understand aneurysm generation. Hemodynamic insult and arterial wall deficiency are both thought to play important roles in the generation of cerebral aneurysms because the muscular layer is absent within almost 80% of main cerebral arterial bifurcations,^{3,4} and cellular and molecular changes due to complicated wall shear stress (WSS) or wall shear stress gradient (WSSG) have been demonstrated in the bifurcated arterial wall at the aneurysmal zone.⁵ However, only a few satisfactory specific animal models that simulate the generation or growth of bifurcation aneurysms exist.⁶⁻⁸ We hypothesized that a combination of internal elastic lamina and media elastic fiber disruption and specific hemodynamic flow action may promote the generation and development of aneurysms. Therefore, we designed a canine common carotid artery (CCA) Y-type bifurcation model, with and without internal elastic lamina and media elastic fiber insult, to

Received September 26, 2013; accepted after revision January 6, 2014.

From the Department of Diagnostic and Interventional Radiology (J.W., H.-Q.T., Y.-Q.Z., M.-H.L., L.Y., Y.-S.C.), Shanghai Jiao Tong University Affiliated Sixth People's Hospital, Shanghai, China; and School of Mechanical Engineering (Z.-Z.L.), Shanghai Jiao Tong University, Shanghai, China.

This work was supported by grants from the National Natural Science Foundation of China (No. 81000652, 81370041), Shanghai Venus Program Funds (No. 11QA1405000), and the Med-Technological Crossing Funds (No. YG2011MS22).

We declare there is no conflict of interest in this study.

Please address correspondence to Yue-Qi Zhu, MD, and Ming-Hua Li, MD, No. 600, Yi Shan Rd, Shanghai, 200233, China; e-mail: zhuyueqi@hotmail.com and liminghuaradio@hotmail.com

Indicates open access to non-subscribers at www.ajnr.org

Indicates article with supplemental on-line video.

<http://dx.doi.org/10.3174/ajnr.A3926>

dynamically observe aneurysm growth at the angiographic and histopathologic levels.

MATERIALS AND METHODS

Animals

All protocols used in this study were approved by the Animal Research Committee of our institution and were conducted in accordance with the guidelines of the International Council on Animal Care. Twenty-four 8-month-old beagles of both sexes, weighing 12–20 kg, were used (Agronomic School of Shanghai Jiaotong University, License: SCXK2007–0004).

Animal Surgery Model

Arterial bifurcations with a new branch point were surgically created in the CCA of 18 dogs by using the method described by Meng et al⁷ and then were divided into an elastase-treated bifurcation group (EBG, $n = 9$) and a control bifurcation group (CBG, $n = 9$), with 6 female and 3 male dogs in each group. Elastase (3.0 U/ μ L) was applied for 15 minutes to the apex of the reconstructed arterial bifurcation (approximately 4×4 mm²) in 9 animals in the EBG by dripping it from a curved blunt syringe needle into a trapezoidal plastic tube, to prevent its flowing onto other portions of the arteries; the same volume of saline was applied in 9 animals as controls by using the method identical to that in the elastase model in the CBG. Before elastase or saline was applied, as much of the tunica adventitia at the apex as possible was removed to facilitate the penetration. Meanwhile, 3 dogs with both straight CCAs surgically exposed received elastase insult as an elastase-treated straight group (ESG). The peak velocity of blood flow in the feeding artery at the systolic phase was measured before and after reconstruction surgery by using Doppler ultrasound.

Angiographic Analysis

Angiography was performed immediately and 12 and 24 weeks after surgery. Immediate angiography, including 2D-DSA (anteroposterior and lateral positions) and 3D-DSA reconstructions, was performed to assess morphologic alterations at the apex of the reconstructed arterial bifurcation. If an aneurysm-like bubble was observed, its neck and maximum body width were measured by using the best 3D-DSA projection, and parent artery diameter and the angulation between the parent arteries were determined. We defined an aneurysm formation only if its maximum body width exceeded half of the diameter of the adjacent artery. Ultrasonography was used as a convenient method to monitor the status of the aneurysms at 4 and 8 weeks, check whether aneurysms were generated, determine the size of the aneurysms, and confirm whether the reconstructed arterial bifurcations were patent.

Computational Fluid Dynamics Analysis

Computational fluid dynamics analysis was performed immediately and 12 and 24 weeks after surgery. With in vivo 3D-DSA rotational angiography (syngo Axiom-Artis; Siemens, Erlangen, Germany), the 3D lumen of the bifurcation was reconstructed and, together with the measured flow rates in the vessel branches, served as the boundary conditions for computational fluid dynamics simulations (Mimics 10.0; Materialise, Leuven, Belgium)

to generate an advanced tetrahedral mesh inside the converted 3D surface. The average mesh size was approximately 153,565 U. The 3D computational fluid dynamics solutions were defined under steady-state (average peak Reynolds number = 625), assuming a Newtonian fluid (0.0035 Pa \times s) and incompressible flow by using a rigid-wall model (CFDesign AVL-Fire, Version 2008, AVL List GmbH, Graz, Austria). WSS, velocity field, streamline, surface relative pressure field, and total pressure field were analyzed. The total pressure was defined as the total flow pressure during isentropic stagnation heating, while the relative pressure was defined as the pressure calculated on the basis of the local atmospheric pressure. In this study, the local atmospheric pressure was chosen as 10^5 Pa. The WSSG was calculated. The gradient normal to the streamline was negligible in comparison. Meanwhile, a quantitative analysis on the WSS and WSSG of the bifurcation models in the EBG was also performed.

Histologic Examination

Reconstructed arterial bifurcations were harvested at 12 ($n = 6$) and 24 weeks ($n = 3$) in the EBG and CBG, while straight-vessel samples ($n = 6$) were harvested at 24 weeks after surgery. CCA samples from the pilot study and surgical models were stained with hematoxylin-eosin, Masson trichrome, and elastic fiber stains (Verhoeff van Gieson/Orcein methods). Serial longitudinal sections of the reconstructed arterial bifurcations were obtained to assess tissue changes in relationship to the consistent hemodynamic action. CCA samples were immunostained by using proliferating cell nuclear antigen, smooth-muscle α -actin, CD45, antimacrophage antibody (MAC387), and matrix metalloproteinase-2 (MMP-2) and matrix metalloproteinase-9 (MMP-9) antibodies. Double immunofluorescent staining was performed by using anti-CD45 for pan-leukocytes and anti-MAC387 for macrophages to assess whether macrophages were included in leukocytes. The smooth-muscle cell (SMC) proliferation rate (percentage of proliferating cell nuclear antigen–positive SMCs in the media) and elastic layer and α -actin–positive SMC layer thickness were measured. The inflammatory cell infiltration index was defined as the percentage of CD45–positive cells in the media of the arterial bifurcation apices. The MMP-2 and MMP-9 expression indexes were defined as the percentage of MMP-2/9–positive area in the media of the arterial bifurcation apices.

Statistical analysis of the histopathologic images was performed with Image-Pro Plus, Version 6.0 software (Media Cybernetics, Rockville, Maryland) in at least 20 randomly selected high-power ($\times 400$) tubulointerstitial fields from each section.

Statistical Analysis

GraphPad Prism 5.0 software (GraphPad Software, San Diego, California) was used for statistical analysis. Data were expressed as the mean \pm SD for continuous variables and as counts or proportions (percentage) for categorical variables. The Fisher exact test was used to compare categorical data. Grouped t tests were used to compare the proliferating cell nuclear antigen proliferation index, elastic layer and media α -actin–positive layer thickness, inflammatory cell infiltration index, and MMP-2 and MMP-9 indexes. All tests were 2-tailed, and statistical significance was defined as $P < .05$.

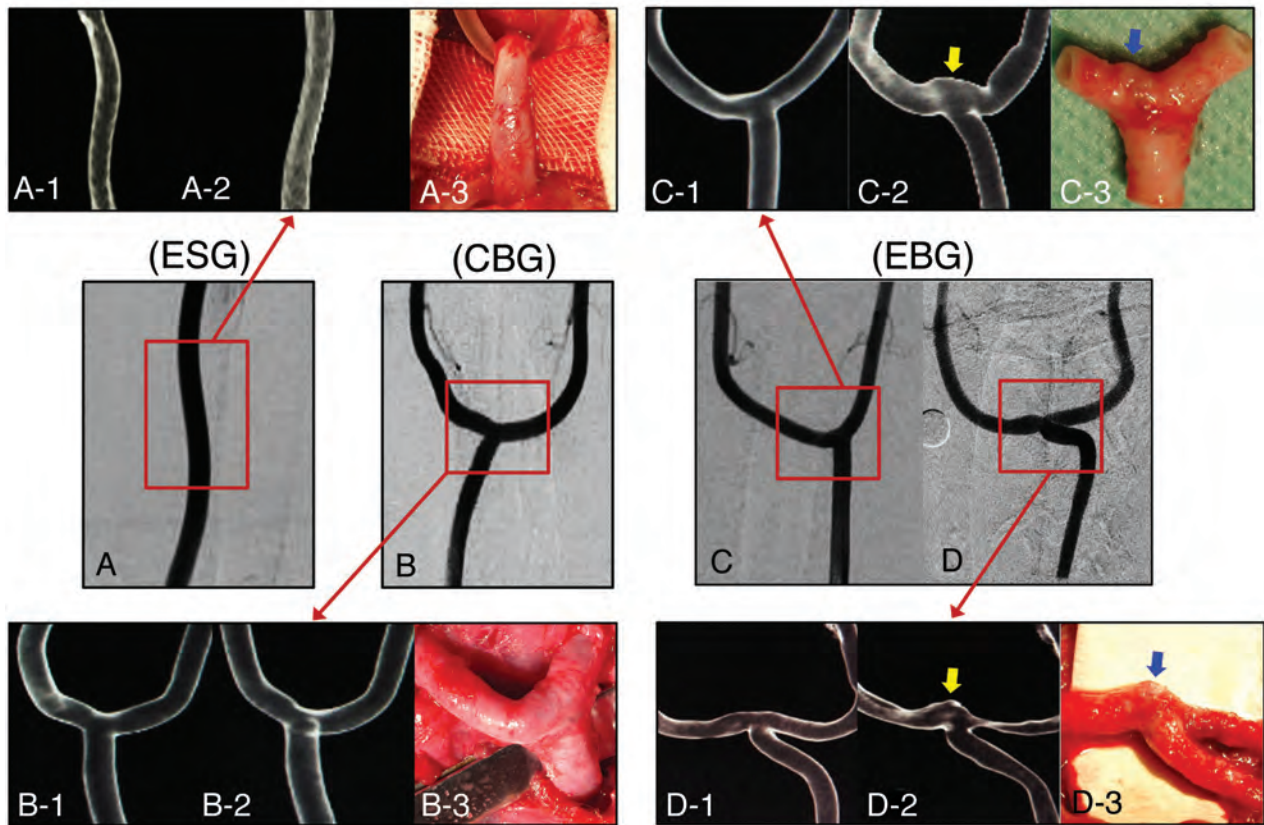


FIG 1. 2D-DSA and 3D-DSA images from immediately after surgery. 3D-DSA follow-up and gross dissection in the ESG (A), CBG (B), and EBG (C and D). Yellow and blue arrows indicate nascent aneurysms.

Summary of the information of dog models in the ESG, CBG, and EBG^a

Group (No.)	Sex (F)	Weight (Kg)	Surgical Results	Blood Flow Velocity (cm/s)		PA Diameter (mm)	PA Angulation (Degrees)	Aneurysm Status		
				Before	After			Sex (No./Female)	Neck (mm)	Body (mm)
ESG (3)	2	14.8 ± 1.4	Success	82.4 ± 6.3	—	4.1 ± 0.2	—	0	—	—
CBG (9)	6	14.7 ± 2.4	Success	84.9 ± 6.5	126.2 ± 12.5 ^b	4.3 ± 0.4	112.9 ± 36.1	0	—	—
EBG (9)	6	14.9 ± 1.7	Success	85.7 ± 8.7	131.4 ± 13.9 ^b	4.3 ± 0.4	120.3 ± 44.2	5/4	6.7 ± 2.3	3.2 ± 0.4

Note:—F indicates female; PA, parent artery.

^a Data are expressed as the mean ± SD for continuous variables and as counts for categorical variables.

^b Statistical significance before and after surgery within each group ($P < .05$).

RESULTS

Animal Surgery Model and Angiographic Findings

The arterial bifurcation model was successfully reconstructed in all animals. Ultrasonography or angiography revealed no stenosis at the anastomoses or arterial occlusion postsurgery or during follow-up in any animal. Angiography indicated that the vessel lumen at the arterial bifurcation apex herniated to form an aneurysm in 5/9 animals, with 4 aneurysms in female dogs (66.7%) and 1 aneurysm in a male dog (33.3%; $P > .05$) from the elastase-treated group, and 2D-DSA and 3D-DSA revealed that bubbles were located at the apices, with a tent shape (mean sac diameter, 3.2 ± 0.4 mm; mean neck diameter, 6.7 ± 2.3 mm; Fig 1). However, the aneurysms were still at their unruptured stage until 24 weeks' follow-up, with only slight saccular enlargement, compared with 12 weeks in the EBG (3.5 ± 0.3 mm versus 3.0 ± 0.2 mm; $P = .076$). Ultrasonography monitoring revealed that all of the aneurysms were detectable at 4 weeks. No animal in the control group displayed any morphologic changes on angiography at

12 weeks. The mean parent artery diameter and angulation were 4.3 ± 0.4 mm and $112.9 \pm 36.1^\circ$ in the CBG and 4.3 ± 0.4 mm and $120.3 \pm 44.2^\circ$ in the EBG, respectively (Table). However, the average parent artery angulation of the 5/9 animals with aneurysms in the EBG was $146.8 \pm 40.84^\circ$ compared with $87.25 \pm 18.87^\circ$ in models with no aneurysms ($P = .032$).

Arterial Wall Remodelling in Histology

In the 5 arterial bifurcation samples with aneurysms on angiography, biopsy confirmed that the entire vessel wall was thinned with a semitransparent appearance and visible blood flow underneath, which enabled herniation and aneurysm formation at the arterial bifurcation apices (On-line Video).

Hematoxylin-eosin and Masson trichrome staining revealed thinning of media at the bifurcation, a reduced numbers of SMCs, and loss of fibronectin in the elastase-treated group. Elastic fiber staining revealed internal elastic lamina discontinuity and elastic fiber disruption/insult in all elastase-treated animals in the ESG

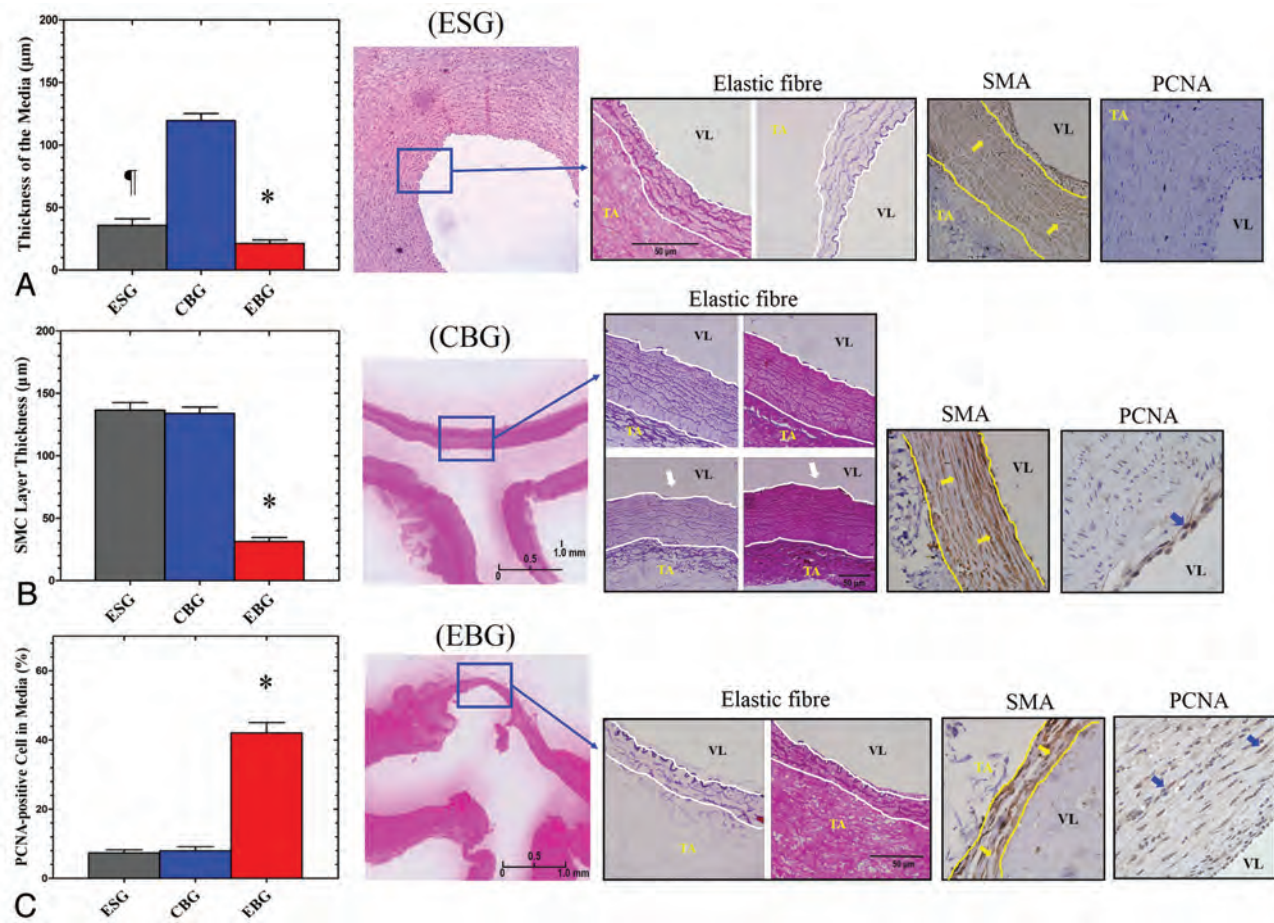


FIG 2. A, Specific elastic fiber staining, which shows the thickness of the media (white lines; $\times 100$), indicated significant thinner of the media in the ESG than in the CBG and EBG. Internal elastic lamina discontinuity is indicated by white arrows. B, Immunostaining of smooth-muscle α -actin (yellow arrows; smooth-muscle actin layer, yellow lines; $\times 100$) and proliferating cell nuclear antigen (C, blue arrows) in the media of the straight artery and arterial bifurcation apices in the ESG, CBG, and EBG ($P < .001$ versus ESG and CBG; $\times 400$). The asterisk indicates $P < .05$ when the ESG, CBG, and EBG were compared. The flag indicates $P < .05$ when the ESG and CBG were compared. VL indicates vessel lumen; TA, tunica adventitia.

and EBG; only 3 animals from the CBG displayed intima layer disruption with mild internal elastic lamina discontinuity at the arterial bifurcation apices. Elastase treatment reduced the media elastic layer thickness in the EBG ($21.2 \pm 15.3 \mu\text{m}$) and ESG ($71.28 \pm 19.47 \mu\text{m}$) compared with that in the CBG ($119.4 \pm 29.9 \mu\text{m}$; $P < .001$; Fig 2).

Immunohistochemical staining revealed increased numbers of proliferating cell nuclear antigen–positive SMCs in the media of elastase-treated arterial bifurcation apices in the EBG ($42.0 \pm 15.7\%$ versus $7.3 \pm 3.8\%$ in ESG and $8.0 \pm 6.3\%$ in the CBG; $P < .001$; Fig 2). The number of smooth-muscle α -actin–positive SMCs also decreased, and the SMC layer was thinner at elastase-treated arterial bifurcation apices in the EBG ($31.3 \pm 16.7 \mu\text{m}$ versus $136.5 \pm 25.5 \mu\text{m}$ in the ESG and $133.9 \pm 26.1 \mu\text{m}$ in the CBG; $P < .001$; Fig 2). The inflammatory cell infiltration index in the media of the aneurysm wall was $38.4 \pm 10.6\%$ in the EBG (versus $5.1 \pm 2.1\%$ in the ESG and $2.9 \pm 2.4\%$ in the CBG; $P < .001$). Macrophage staining showed macrophage infiltration into the aneurysmal wall with a distribution similar to that of leukocytes. Furthermore, double staining with anti-CD45 and anti-MAC387 revealed that some leukocytes in the media of the aneurysm wall in this model were macrophages. The MMP-2 and

MMP-9 expression indexes in the media of the aneurysm wall were $21.0 \pm 8.7\%$ (versus $1.2 \pm 1.4\%$ in the ESG and $0.8 \pm 1.2\%$ in the CBG; $P < .001$) and $13.6 \pm 5.6\%$ (versus $0.9 \pm 0.8\%$ in the ESG and $0.4 \pm 0.6\%$ in the CBG; $P < .001$), respectively (Fig 3).

Computational Fluid Dynamics Analysis

Flow rates in the feeding artery of the de novo bifurcation increased from $85.3 \pm 7.5 \text{ cm/s}$ to $128.8 \pm 13.1 \text{ cm/s}$ (approximately 51%) due to ligation of the contralateral CCA. Computational fluid dynamics analysis immediately after surgery revealed that the feeding artery wall experienced increased WSS in the CBG and EBG, whereas the bifurcation periapical regions were exposed to a more complex hemodynamic environment. The arterial bifurcation apex had extremely low WSS and flow velocity, and from the apex to the bilateral vessel wall, the WSS and flow velocity increased to a maximum and then decreased further downstream to a level similar to that of the feeding artery. This acceleration and deceleration created a WSSG-positive region (before maximum WSS) and -negative region (after maximum WSS). The apex also experienced the highest relative pressure and total pressure, which decreased to normal values toward both branch arms.

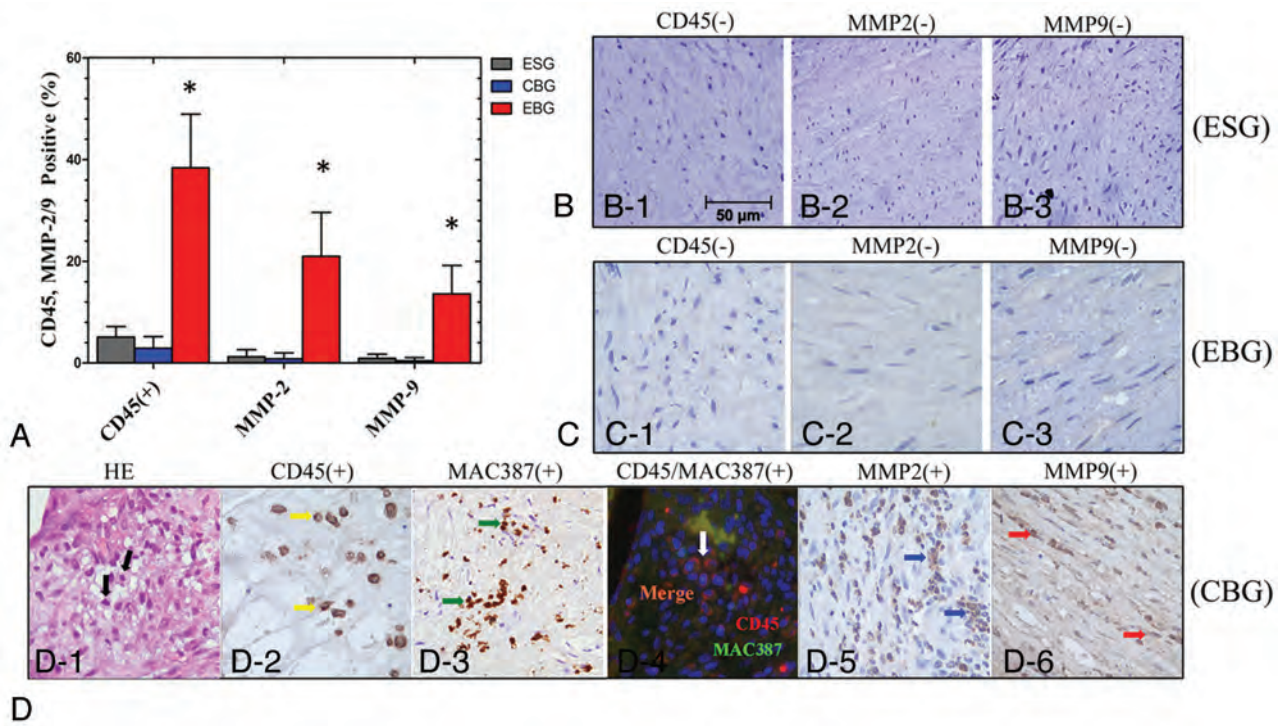


FIG 3. Immunohistochemical staining and quantification analysis (A) of infiltrating inflammatory cells (CD45+/MAC387+) and MMP-2 and -9 expression in the media of straight vessels and at the arterial bifurcation apices ($\times 400$) in the ESG (B), CBG (C), and EBG (D). The asterisk indicates $P < .05$ when the ESG, CBG, and EBG were compared.

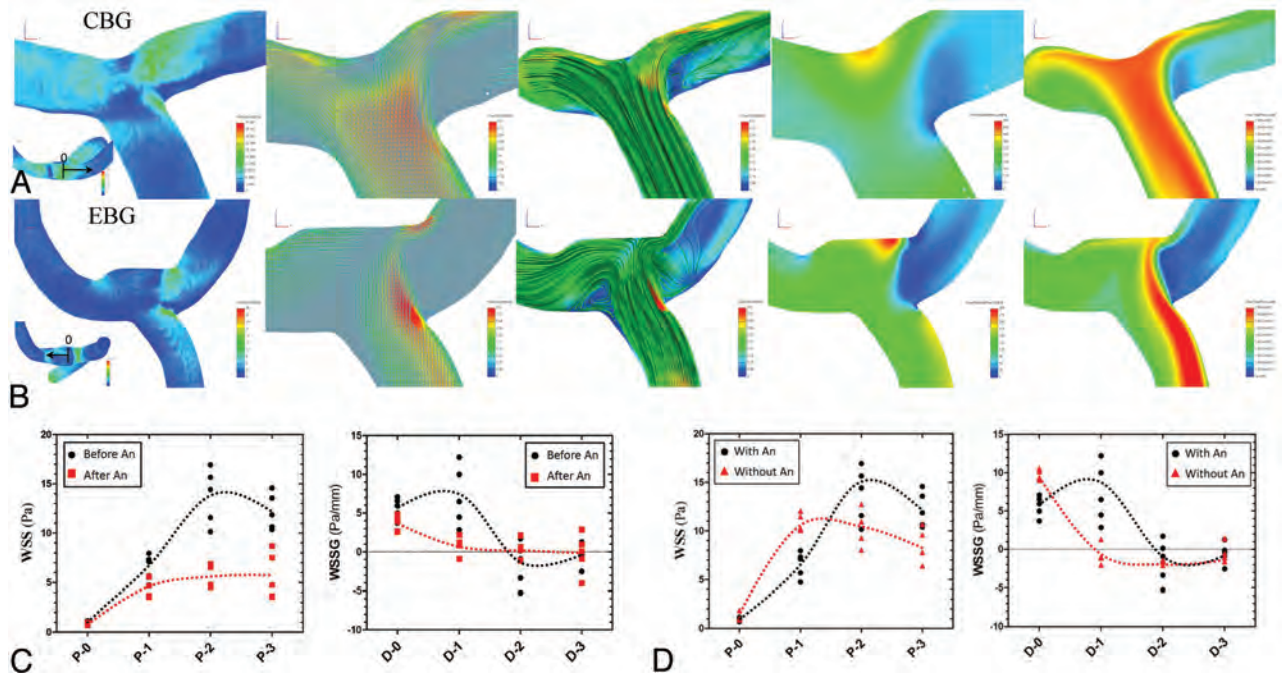


FIG 4. Computational fluid dynamics analysis at 12 weeks of follow-up in the CBG (A) and EBG (B). A comparison of the changes of WSS and WSSG values before and after aneurysm formation in models with an aneurysm in the EBG (C) and the WSS and WSSG values immediately after surgery in models with large and small bifurcation angles in the EBG (D). A dotted line indicates the varying trends of WSS and WSSG in each subgroup.

Hemodynamic parameters including WSS, blood velocity, streamline field, surface relative pressure field, and total pressure field were similar immediately after surgery and 24 weeks after surgery in the ESG, CBG, and the 4/9 animals in the EBG without

morphologic changes, as illustrated in Fig 4A. In the 5/9 elastase-treated animals with aneurysms in the EBG, quantitative analysis of the WSS and WSSG values, including at the apex and equidistant points (1, 2, and 3 mm) on one of the affected sides, indicated

an obvious decrease from immediately after surgery to 24 weeks after surgery (WSS: 13.74 ± 2.82 versus 5.48 ± 1.14 Pa at the 2-mm point, $P < .01$; WSSG: 7.19 ± 3.87 versus 0.85 ± 1.12 Pa/mm at the 1-mm point, $P = .01$), in a manner similar to that in the distal outflow vessel, due to arterial remodeling leading to the formation of an aneurysm sac (Fig 4B, -C). In these animals, the flow velocity, relative pressure, and total pressure at the apex also decreased during follow-up. Further quantitative analysis of the WSS and WSSG values immediately after surgery in the EBG also indicated a higher WSS (often 2 mm besides the apex) and WSSG (often 0–2 mm besides the apex) insult to the arterial wall in models with an aneurysm than in those without one (Fig 4D). The arterial walls subjected to high WSS and WSSG values were confirmed to show remodeling by both angiographic and histologic observations. Considering that models that developed an aneurysm often had larger bifurcation angles, the arterial wall adjacent to the apex would be subjected to higher WSS and WSSG values.

DISCUSSION

Further knowledge of the pathologic mechanisms underlying aneurysm generation or growth may provide the opportunity to develop mathematic models to better understand the progression of vascular diseases. Until recently, animal models have aimed to evaluate the underlying mechanisms of aneurysm formation by simulating possible aneurysm-inducing factors, such as altered hemodynamics, and have compared the morphologic or histopathologic changes with those in humans.^{6–8,9} In 2007, Meng et al⁷ surgically created a new bifurcation site in the canine carotid artery and reported a correlation between high WSS or WSSG and histologic insult; however, arterial wall aneurysms did not develop, and further study is required to confirm whether the observed histologic changes induced aneurysm formation. In 2008, Gao et al⁶ induced nascent cerebral aneurysms by increasing hemodynamic stress via bilateral ligation of rabbit carotid arteries. Increased hemodynamic stress triggered nascent aneurysm formation and correlated with increased blood flow in the basilar artery; however, the histologic changes could not be confirmed by traditional intra-arterial angiograms or other radiologic methods due to the tenuous blood vessel of the rabbit. Subsequent studies have reported that complex hemodynamics at bifurcation sites can induce molecular changes in a manner similar to those in human aneurysmal wall changes, including decreased expression of endothelial nitric oxide synthase, CD68 deficiency, and up-regulation of MMP-2, MMP-9, inducible NO synthase, and interleukin-1 β , which is restricted to the high WSS and high WSSG areas,^{5,10,11} suggesting that altered hemodynamics act at a molecular level to promote aneurysm formation.

Besides constant blood flow action, many studies have supported the suggestion that factors leading to deterioration of the arterial wall structure are the most important step in cerebral aneurysm development.¹² The apex of cerebral vasculature bifurcations differs from that in most large arteries because the median muscular layer is usually absent. In addition, cerebral vessels exhibit a fragile and/or absent external elastic lamina and are surrounded by CSF, thus rendering them susceptible to injury from mechanical forces.^{3,4,12} These observations have led to the hy-

pothesis that structural wall abnormalities and defective collagen and elastin are the major culprits in aneurysm initiation.¹³ In 2009, Nuki et al⁸ reported a novel cerebral aneurysm model by inducing hypertension and the degeneration of elastic lamina in mice and found that cerebral aneurysm generation was closely related to MMP activation⁸; however, the aneurysm site was not controllable.

In this study, we investigated the role of arterial bifurcation hemodynamic simulation combined with arterial wall degeneration and blood flow acceleration in a canine model of aneurysm generation. Specifically, we induced arterial wall degeneration via internal elastic lamina and media elastic fiber insult by using elastase to induce muscular layer degeneration after blood flow action. Using the method of Meng et al,⁷ we reconstructed bilateral CCA bifurcation apices to simulate the hemodynamic conditions and increased blood flow by unilateral CCA ligation. Because inner arterial wall elastase incubation led to a high rate of intra-arterial thrombus occurrence in preliminary experiments, we used an external wall incubation method, which selectively disrupted the internal elastic lamina and elastic fibers to simulate arterial wall degeneration. The removal of as much tunica adventitia as possible to facilitate elastase penetration was key.

Despite the fact that the blood flow pressure and velocity are similar in small animals and humans, the vessel wall structures, especially the arterial muscle layer, are very different. Consequently, aneurysms induced in small animals may not be reproducible in large animals. Here, we used a canine model because canine vessels behave more like human vessels.¹⁴ The long canine CCA (10–12 cm) provides sufficient length to construct an arterial bifurcation model. The caliber of the canine CCA and human ICA are comparable, with a constant diameter of approximately 4 mm. Moreover, the cerebral blood supply in dogs is delivered almost entirely through the vertebrbasilar system, with anastomoses between each network of the ICA,¹⁵ which helps prevent death when the bilateral CCA is temporarily occluded. Additionally, the number of cells, their composition, and the accompanying proteoglycan matrices in the canine CCA are essentially the same as in the human CCA,¹⁶ indicating that canine models may accurately predict the human biologic response to aneurysm-inducing factors.

During 24-weeks' follow-up, aneurysms were successfully induced in 5/9 elastase-treated animals in the EBG and were confirmed by both angiography and histopathology. We hypothesize that arterial wall deterioration, combined with distinct hemodynamics, effectively results in aneurysm initiation. The weakened arterial wall at the apex may adapt or respond to sustained alterations in blood flow, blood pressure, or axial stretch. Aneurysm generation or enlargement is a type of arterial wall remodelling, which may potentially involve increased inflammatory cell infiltration, increased MMP activity, extracellular matrix protein synthesis, and SMC apoptosis, to counteract the mechanical forces induced by altered blood flow.¹⁷ Inflammatory cell infiltration was detected in the media of the aneurysm walls by pan-leukocyte staining by using an anti-CD45 and MAC387 antibody, consistent with observations in animal and human intracranial aneurysms,^{2,18} indicating that macro-

phage infiltration plays a critical role in the formation of the aneurysms observed in this model, especially during the early stages of aneurysmal formation. MMP-2 and MMP-9 were also expressed in the walls of the aneurysms, both of which possess gelatinase and collagenase activity and can degenerate the important extracellular matrix components in the walls of aneurysms, such as elastin and collagen type IV.¹⁹ Taken together, these results indicate that MMP may be released from the infiltrating macrophages and may play an important role in the progression of aneurysms.

The aneurysms had a wide neck, mainly determined by the size of the elastase-incubated area, and a small body; therefore, they can only be termed “nascent aneurysms.” However, these nascent aneurysms had histologic characteristics similar to those in human aneurysms including the following: 1) internal elastic lamina discontinuity with a reduced media elastic layer and SMC layer thickness; 2) degeneration, thinning, or interruption of the media SMC layer; and 3) significantly reduced SMC proliferation. Another feature of this model was that no thrombus formation was revealed in the aneurysm sac at angiography or during the histologic examination. This suggests that the elastase insult to the adventitia of the bifurcation apex kept the endothelial cell layer intact, to prevent thrombosis and platelet aggregation in response to expression of CD39 and secretion of nitric oxide and prostacyclin.²⁰

Blood flow is generally considered an important modulator of normal artery enlargement in response to increased flow to maintain normal shear stress.²¹ In this study, despite all models having simulated elastic fiber insults (arterial wall deterioration), nascent aneurysms were generated in only 5 of 9 models. We hypothesize that the bifurcation angle is an important factor because T-shaped bifurcations ($146.8 \pm 40.84^\circ$) were more likely to induce the generation of aneurysms than Y-shaped bifurcations ($87.25 \pm 18.87^\circ$).²² Small bifurcation angles are associated with high blood flow velocities and dispersed vortex intensities, while increased bifurcation angles result in more concentrated vortex intensities next to the apex and turbulent/disturbed laminar flow, which generates various mechanical stimuli, such as WSS and WSSG.^{23,24} The quantitative analysis of the WSS and WSSG values at the bifurcation sites in our study proved that the arterial wall next to the apex was subjected to higher WSS and WSSG values before the generation of aneurysms in models with large bifurcation angles. Elevated WSS or WSSG levels disrupt the normal function of endothelial cells, stimulate gene transcription, and activate ion channels and the consequent reorganization of the cellular cytoskeleton.^{5,21} The more substantial structural changes, which occur after 6 months, appear to involve the up-regulation of MMP-2 and -9, both of which are implicated in aneurysmal disease.²⁵

However, this model of the carotid artery bifurcation aneurysm still does not completely represent a true cerebral aneurysm model because compared with extracranial arteries, intracranial arteries have their own specific anatomic and biologic characteristics, which could not be simulated in our model: a well-developed internal elastic lamina; a weakened tunica media and tunica adventitia, or even the absence of the tunica adventitia; reduced

elastic fibers; increased proportions of SMCs; and, most important, a CSF environment.

CONCLUSIONS

We established a new canine model to simulate human arterial bifurcation morphology, including hemodynamic action with accelerated blood velocity and arterial wall degeneration at the bifurcation apex. Aneurysms, confirmed by angiography and histology, formed under persistent low WSS/WSSG and high pressure action in elastase-treated animals, but not in control animals. This canine model has the potential for the identification and study of the genes, proteins, or conduction channels responsible for aneurysm generation, development, and rupture.

REFERENCES

- Molyneux A, Kerr R, Stratton, et al. **International Subarachnoid Aneurysm Trial (ISAT) of neurosurgical clipping versus endovascular coiling in 2143 patients with ruptured intracranial aneurysms: a randomised trial.** *Lancet* 2002;360:1267–74
- Hashimoto T, Meng H, Young WL. **Intracranial aneurysms: links among inflammation, hemodynamics and vascular remodeling.** *Neurol Res* 2006;28:372–80
- Canham PB, Finlay HM. **Morphometry of medial gaps of human brain artery branches.** *Stroke* 2004;35:1153–57
- Finlay HM, Whittaker P, Canham PB. **Collagen organization in the branching region of human brain arteries.** *Stroke* 1998;29:1595–601
- Li YS, Haga JH, Chien S. **Molecular basis of the effects of shear stress on vascular endothelial cells.** *J Biomech* 2005;38:1949–71
- Gao L, Hoi Y, Swartz DD, et al. **Nascent aneurysm formation at the basilar terminus induced by hemodynamics.** *Stroke* 2008;39:2085–90
- Meng H, Wang ZJ, Hoi Y, et al. **Complex hemodynamics at the apex of an arterial bifurcation induces vascular remodeling resembling cerebral aneurysm initiation.** *Stroke* 2007;38:1924–31
- Nuki Y, Tsou TL, Kurihara C, et al. **Elastase-induced intracranial aneurysms in hypertensive mice.** *Hypertension* 2009;54:1337–44
- Aoki T, Nishimura M. **The development and the use of experimental animal models to study the underlying mechanisms of CA formation.** *J Biomed Biotechnol* 2011;535921
- Norman PE, Powell JT. **Site specificity of aneurysmal disease.** *Circulation* 2010;121:560–68
- Sadamasa N, Nozaki K, Hashimoto N. **Disruption of gene for inducible nitric oxide synthase reduces progression of cerebral aneurysms.** *Stroke* 2003;34:2980–84
- Kataoka K, Taneda M, Asai T, et al. **Structural fragility and inflammatory response of ruptured cerebral aneurysms: a comparative study between ruptured and unruptured cerebral aneurysms.** *Stroke* 1999;30:1396–401
- Nixon AM, Gunel M, Sumpio BE. **The critical role of hemodynamics in the development of cerebral vascular disease.** *J Neurosurg* 2010;112:1240–53
- Fischell TA, Virmani R. **Intracoronary brachytherapy in the porcine model: a different animal.** *Circulation* 2001;104:2388–90
- Jung F, Beysang R, Guceve L, et al. **Angiography of the cervico-cephalic vessels of the dog: the carotid system [in French].** *J Chir (Paris)* 1975;109:109–18
- Oesterle SN, Whitbourn R, Fitzgerald PJ, et al. **The stent decade: 1987 to 1997.** *Am Heart J* 1998;136(4 pt 1):578–99
- Kassam AB, Horowitz M, Chang YF, et al. **Altered arterial homeostasis and cerebral aneurysms: a molecular epidemiology study.** *Neurosurgery* 2004;54:1450–60, discussion 1460–62
- Tulamo R, Frösen J, Hernesniemi J, et al. **Inflammatory changes in the aneurysm wall: a review.** *J Neurointerv Surg* 2010;2:120–30
- Aoki T, Kataoka H, Morimoto M, et al. **Macrophage-derived matrix**

- metalloproteinase-2 and -9 promote the progression of cerebral aneurysms in rats. *Stroke* 2007;38:162–69
20. Watson SP. Platelet activation by extracellular matrix proteins in haemostasis and thrombosis. *Curr Pharm Des* 2009;15:1358–72
 21. Sharma R, Yellowley CE, Civelek M, et al. Intracellular calcium changes in rat aortic smooth muscle cells in response to fluid flow. *Ann Biomed Eng* 2002;30:371–78
 22. Jagadeesan BD, Kadkhodayan Y, Delgado Almandoz JE, et al. Differences in the basilar artery bifurcation angle among patients who present with a ruptured aneurysm at the top of the basilar artery and patients with perimesencephalic subarachnoid hemorrhage: a retrospective cross-sectional study. *Neurosurgery* 2013;73:2–7
 23. Markl M, Wegent F, Zech T, et al. In vivo wall shear stress distribution in the carotid artery: effect of bifurcation geometry, internal carotid artery stenosis, and recanalization therapy. *Circ Cardiovasc Imaging* 2010;3:647–55
 24. Perktold K, Peter RO, Resch M, et al. Pulsatile non-Newtonian blood flow in three-dimensional carotid bifurcation models: a numerical study of flow phenomena under different bifurcation angles. *J Biomed Eng* 1991;13:507–15
 25. Negishi M, Lu D, Zhang YQ, et al. Upregulatory expression of furin and transforming growth factor-beta by fluid shear stress in vascular endothelial cells. *Arterioscler Thromb Vasc Biol* 2001;21:785–90

Lymphoepithelial Carcinoma of the Salivary Gland: Morphologic Patterns and Imaging Features on CT and MRI

X. Ban, J. Wu, Y. Mo, Q. Yang, X. Liu, C. Xie, and R. Zhang

ABSTRACT

BACKGROUND AND PURPOSE: Lymphoepithelial carcinoma is a rare salivary gland lesion. We retrospectively reviewed CT and MR imaging features of salivary gland lymphoepithelial carcinoma to determine their imaging features and morphologic patterns.

MATERIALS AND METHODS: The clinical data, CT, and MR imaging findings of 28 patients with histologically proved lymphoepithelial carcinoma of the salivary gland were retrospectively reviewed. Morphologic patterns of the lesions were categorized into 3 types on the basis of margin and shape.

RESULTS: There were 17 men and 11 women with a mean age of 39.3 years; 96.4% of patients were positive for Epstein-Barr virus both on histologic staining and Epstein-Barr virus serology. Tumors were parotid in 18 patients, submandibular in 8 patients, sublingual in 1 patient, and palatal in 1 patient. Most tumors (57.1%) manifested as a partially or ill-defined mass with a lobulated or plaque-like shape. Homogeneous enhancement was found in 16 patients, while heterogeneous enhancement was found in 12, including 4 patients with intratumoral necrosis. Invasion into adjacent structures was found in 5 patients; 60.7% of patients exhibited abnormal lymph nodes, with nodal necrosis in 3 patients.

CONCLUSIONS: The characteristic lobulated or plaque-like shape, with a partially or ill-defined margin, of a salivary gland mass associated with ipsilateral lymphadenopathy may suggest a preoperative diagnosis of lymphoepithelial carcinoma.

ABBREVIATIONS: EBV = Epstein-Barr virus-encoded small RNA; LEC = lymphoepithelial carcinoma

Lymphoepithelial carcinoma (LEC) is an uncommon malignant neoplasm characterized by undifferentiated malignant epithelial cells with marked infiltration of lymphoid cells in the stroma.^{1,2} LEC most frequently occurs in the nasopharynx, but it also has been reported arising in various organs such as salivary glands, lungs, thymus, stomach, larynx, soft palate, uterus, bladder, and skin.^{1,3-5} LEC of the salivary gland, first described by Hilderman et al in 1962,⁶ is very rare and accounts for 0.3%~5.9% of malignant tumors of the salivary gland; it also has a striking geographic and ethnic distribution.^{1,7,8} Most LECs of the salivary glands have been reported in Inuit-Yupik and Chinese

populations, with a strong association with the Epstein-Barr virus.⁵ The clinical and pathologic features, treatment, and prognosis of LEC of the salivary gland have been extensively reported.^{1,2,5,9} Limited literature exists, however, describing the imaging features of LEC of the salivary gland.

We retrospectively analyzed CT and MR imaging features in a series of 28 patients with pathologically proved salivary gland LEC to identify any distinct morphologic patterns and imaging features that could be useful for their diagnosis and differential diagnosis.

MATERIALS AND METHODS

Patients

Twenty-eight patients with pathologically confirmed LEC of a major or minor salivary gland were enrolled retrospectively between February 2001 and June 2012. This study was approved by our institutional review board, and patient informed consent was not required in accordance with the requirements of a retrospective study. Clinical data, including age, sex, clinical presentation, laboratory examinations, treatments, and outcomes, were reviewed.

Received December 23, 2013; accepted after revision February 11, 2014.

From the Medical Imaging and Minimally Invasive Interventional Center and State Key Laboratory of Oncology in Southern China, Cancer Center, Sun Yat-sen University, Guangzhou, China.

X. Ban and J. Wu contributed equally to this work.

All authors have no conflict of interest.

Please address correspondence to Rong Zhang, MD, No 651 Dongfeng Rd East, Medical Imaging and Minimally Invasive Interventional Center and State Key Laboratory of Oncology in Southern China, Cancer Center, Sun Yat-Sen University, Guangzhou, 510060, China; e-mail: zhangr@susucc.org.cn

<http://dx.doi.org/10.3174/ajnr.A3940>

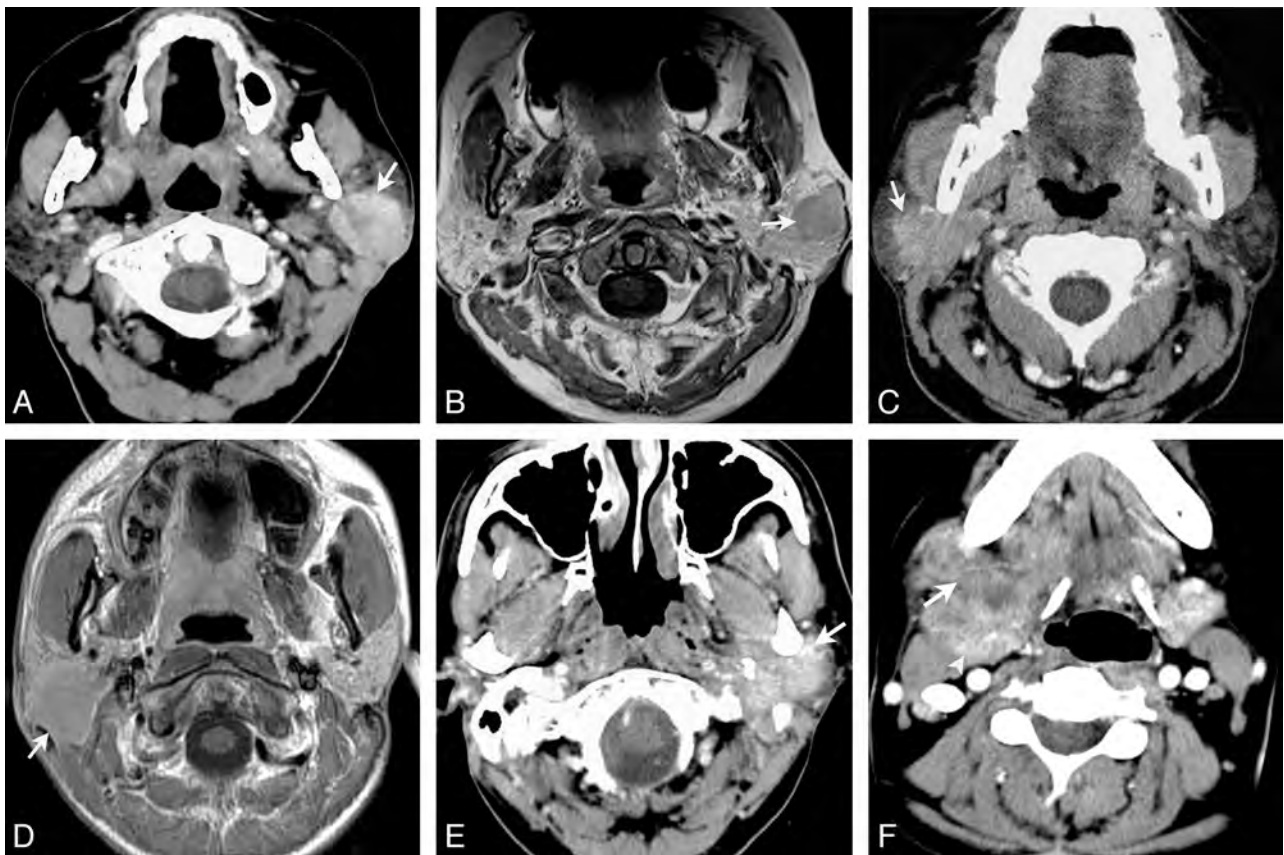


FIG 1. Morphologic patterns of salivary gland LECs. Type 1: Axial contrast-enhanced CT (A) and axial gadolinium-enhanced T1-weighted imaging (B) show round masses with well-defined margins located in the left parotid glands (arrows). Type 2: Axial contrast-enhanced CT (C) and axial gadolinium-enhanced T1-weighted imaging (D) show masses with plaque-like (C) and lobulated (D) shapes and partially defined margins located in the right parotid glands (arrows). Type 3: Axial contrast-enhanced CT shows masses with irregular shapes, ill-defined margins, and diffuse invasive growth (arrow) located in the left parotid (E) and right submandibular (F) glands, respectively. Normal submandibular gland tissue is displaced posteriorly and medially (arrowhead).

Imaging Techniques

All patients had cross-sectional imaging before therapy. Of 28 patients, 22 had CT examinations, 5 had MR imaging, and the remaining patient had both CT and MR imaging. Unenhanced and contrast-enhanced CT and MR imaging were performed in all patients.

CT was performed by using either 16-section CT (Brilliance TM16; Philips Healthcare, Best, the Netherlands) with an axial collimation of 16×0.75 mm and a 1.2 pitch ($n = 17$) or by using dual-section CT (Twin FLASH; Philips Healthcare) with an axial collimation of 2×1 mm and a 1.0 pitch ($n = 6$). Other parameters included the following: section thickness/gap, 3/3 mm ($n = 17$) or 5/5 mm ($n = 6$); current, 250 mA; and voltage, 125 kV. Contrast-enhanced CT was performed after intravenous injection of iopromide at a dosage of 1.5 mL/kg of body weight (Ultravist 300; Schering, Berlin, Germany).

MR imaging was performed on a 1.5T system (Signa Horizon LX, HighSpeed; GE Healthcare, Milwaukee, Wisconsin). The sequences included fast spin-echo T2-weighted images (TR/TE = 2000/120 ms) in the axial plane; and spin-echo T1-weighted images (TR/TE = 450/15 ms) in the axial, coronal, and sagittal planes. Others parameters included a matrix of 256×256 , FOV of 300~380 mm, and a section thickness/gap of 5/0.5 mm for the axial plane and 4/0.4 mm for the coronal

and sagittal planes. Contrast-enhanced sagittal and transverse T1-weighted images and contrast-enhanced coronal T1-weighted images with fat suppression were obtained after intravenous injection of gadopentetate dimeglumine (Magnevist; Schering, Berlin, Germany) at a dosage of 0.2 mmol/kg of body weight. The main parameters were the same as those used preinjection.

Imaging Analysis

All images were reviewed by 2 experienced radiologists (Y.M. and C.X.) by consensus. Tumors were evaluated with regard to the location, size, margin, shape, attenuation or signal intensity (compared with adjacent muscle on CT or T1WI and compared with the contralateral normal salivary gland on T2WI), lesion texture (homogeneous or heterogeneous; with or without calcification, cystic areas, and necrosis), pattern and degree of contrast enhancement, and involvement of adjacent structures. Tumor size was measured in maximal dimensions on the transverse plane. The margin of the lesion was considered well-defined if more than two-thirds of the margin was sharply demarcated from the surrounding tissue and ill-defined if less than one-third of the margin was sharply defined, while intermediate cases were considered partially defined. The shape of

Table 1: Clinical profiles of 28 patients with LEC of the salivary gland

Characteristics	No. of Patients/ Values
Sex	
Female	11 (39.3%)
Male	17 (60.7%)
Age (mean) (yr)	12~60 (39.3)
<20	4 (14.3%)
≥20 ~ <30	4 (14.3%)
≥30 ~ <40	6 (21.4%)
≥40 ~ <50	4 (14.3%)
≥50 ~ <60	8 (28.6%)
≥60	2 (7.1%)
Symptom duration (mean) (mo)	0.~120 (25)
<24	16 (57.1%)
≥24	12 (42.9%)
Epstein-Barr virus	
Positive	27 (96.4%)
Negative	1 (3.6%)
Clinical staging	
I	1 (3.6%)
II	7 (25.0%)
III	8 (28.5%)
IV	12 (42.9%)
Treatment	
Surgery	7 (25%)
Surgery and radiotherapy	18 (64.2%)
Surgery, radiotherapy, and chemotherapy	2 (7.2%)
Radiotherapy and chemotherapy	1 (3.6%)
Local recurrence	3 (10.7%)
Distant metastasis	4 (14.3%)

the lesion was classified as round/oval, lobulated, and/or irregular. Patterns of enhancement were categorized as homogeneous or heterogeneous. Cystic areas were defined as having relatively homogeneous low attenuation (≤ 20 HU) without enhancement and with a relatively clear boundary, while necrotic areas were defined as having heterogeneous low attenuation without enhancement and with an unclear boundary. The degree of enhancement was graded as poor, moderate, and intense, with “poor” defined as attenuation or signal intensity lower than or similar to that of the adjacent muscle, “moderate” as greater than that of the muscle but lower than or similar to that of the contralateral normal submandibular gland, and “intense” as greater than that of the contralateral normal submandibular gland.

The morphologic patterns of tumors were categorized into 3 types according to the margin and shape of the lesions: In type 1, masses were round/ovoid with a well-defined margin (Fig 1A, -B); in type 2, masses showed a lobulated or plaque-like shape with a partially or ill-defined margin (Fig 1C, -D); and in type 3, masses showed an irregular shape with an ill-defined margin and diffuse invasive growth (Fig 1E, -F).

The size, distribution, and attenuation or signal-intensity features of cervical lymphadenopathy were also evaluated. Cervical nodes were subdivided according to the specific anatomic subsites involved, and the assignment of level was predicated on imaging-based delineation of the cervical lymph nodes.¹⁰ The diagnosis of node involvement was defined on the basis of central necrosis and size criteria.¹¹

Table 2: Imaging characteristics of 28 patients with LEC of the salivary gland

Characteristics	No. of Patients/ Values
Tumor location	
Parotid	18 (64.3%)
Submandibular gland	8 (28.5%)
Palate	1 (3.6%)
Sublingual gland	1 (3.6%)
Tumor size (cm)	1.6~7 (3.5)
Tumor margin	
Partially defined	13 (46.4%)
Well-defined	5 (17.9%)
Ill-defined	10 (35.7%)
Morphologic patterns	
Type 1	5 (17.9%)
Type 2	16 (57.1%)
Type 3	7 (25.0%)
Inner nature	
Necrosis	4 (14.3%)
Calcification	0 (0%)
Density on unenhanced CT ($n = 23$)	
Slightly hypodense	19 (82.6%)
Isodensity	4 (17.4%)
Enhancement degree on CT ($n = 23$)	
Poor	6 (26.1%)
Moderate	14 (56.5%)
Intense	3 (17.4%)
Signal intensity on MR imaging ($n = 6$)	
TIWI	
Hyperintense	1 (16.7%)
Isointense	5 (83.3%)
T2WI	
Hypointense	4 (66.7%)
Hyperintense	2 (33.3%)
Enhancement degree on MR imaging ($n = 6$)	
Poor	1 (16.7%)
Moderate	4 (66.6%)
Intense	1 (16.7%)
Inner nature after contrast enhancement	
Homogeneous	16 (57.1%)
Heterogeneous	12 (42.9%)
Adjacent structure invasion	5 (17.9%)
Bone destroyed	2 (7.1%)
Pathologic lymph nodes	17 (60.7%)

RESULTS

Clinical Features

The clinical profiles of 28 patients with LEC of the salivary gland are summarized in Table 1. All patients were southern Chinese, with 17 males and 11 females, 12–60 years of age, with a mean of 39.3 years. Of 28 patients, 20 presented with a slowly growing, palpable mass and 8 experienced a recent, rapidly growing mass. Four patients (3 with rapidly growing tumors and 1 with a slowly growing tumor) had pain or tenderness. One patient with a rapidly growing tumor had progressive facial palsy. The duration of symptoms ranged from 0.2 months to 10 years (mean, 25 months), with 42.9% (12/28) of patients having symptoms for >2 years. Tumors were parotid in 18 patients, submandibular in 8 patients, sublingual in 1 patient, and arising from the upper palate in 1 patient. One patient had a history of non-Hodgkin lymphoma 8 years prior. Twenty-seven cases were positive for Epstein-Barr virus on EBER (Epstein-Barr virus-encoded small RNA) in situ hybridization. The possibility of a metastasis from primary nasopharyngeal carcinoma was excluded in all cases by di-

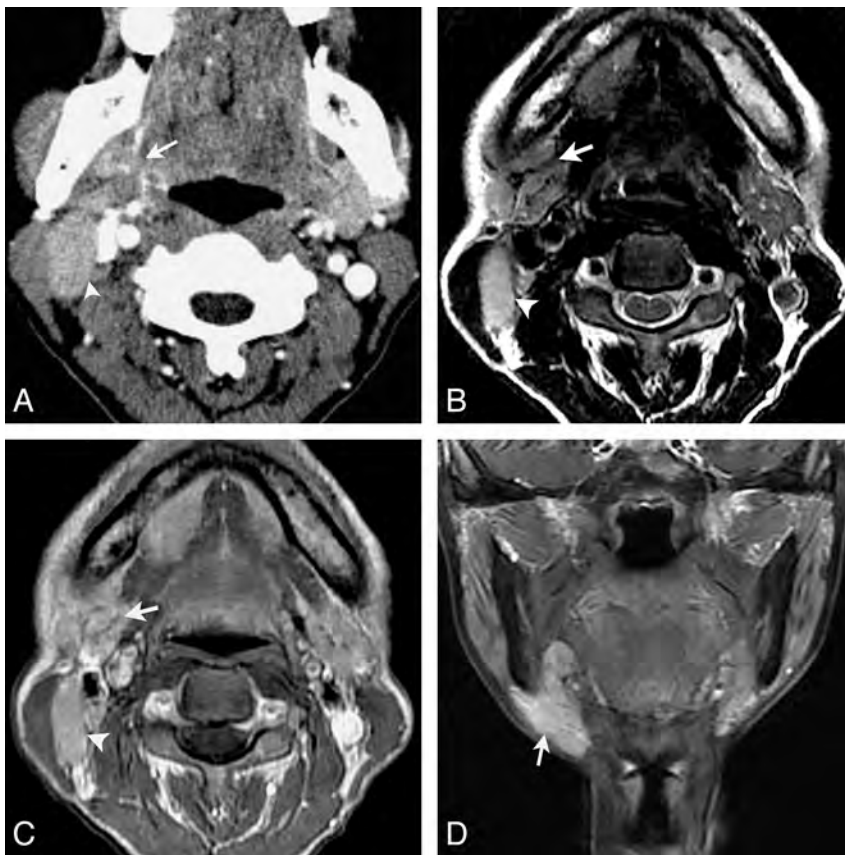


FIG 2. LEC of the right submandibular gland in a 53-year-old woman with a painless mass in the right neck for 1 year. Axial contrast-enhanced CT (A) shows an ill-defined mass in the right submandibular gland with heterogeneous moderate enhancement (arrow). An enlarged lymph node in level IIa is also noted and shows a homogeneous enhancement (arrowhead). Axial T2-weighted image (B) shows a heterogeneous slight hyperintensity mass with curvilinear and linear hypointensity within it (arrow) and an enlarged lymph node in level IIa (arrowhead). Gadolinium-enhanced axial T1-weighted image (C) and coronal T1-weighted image with fat saturation (D) show the mass with a heterogeneous enhancement with hypo-enhanced strands within it. An enlarged region of the lymph node in level IIa is also noted and shows homogeneous enhancement (arrowhead).

rect examination ($n = 28$) and biopsy of the nasopharynx ($n = 8$) by using fiberoptic nasopharyngoscopy. Of our patients, 42.9% were classified as having stage IV, followed by stage III (28.5%), stage II (25.0%), and stage I (3.6%).

Preoperative fine-needle aspiration cytology was performed in 7 patients. Two patients were correctly diagnosed as having LEC, 1 patient was suspicious for having a lymphoepithelial lesion with malignancy, 1 patient was diagnosed as having benign reactive lymphoproliferation, and the other 3 patients were diagnosed as having metastatic poorly differentiated squamous carcinoma. Twenty-seven of 28 patients underwent surgical resection to confirm the definitive diagnosis. After surgery, 18 of 27 patients received postoperative radiation therapy to the gland area and the ipsilateral upper neck with a dose range from 50 to 65 Gy, while 2 patients received postoperative radiation therapy (50 Gy) and chemotherapy. Only 1 patient underwent radiation therapy (50 Gy) and chemotherapy without surgery.

Patient follow-up ranged from 5 to 123 months (mean, 41 months). Local recurrence was found in 3 patients from 12 to 28 months after surgery. Four patients, including 2 patients with local recurrence, developed distant metastases to the brain ($n =$

1), lung ($n = 1$), and liver ($n = 2$) from 7 to 77 months after surgery.

Imaging Findings

The imaging characteristics of 28 patients are summarized in Table 2. Twenty-eight primary tumor masses were found in 28 patients. Lesions were solitary and unilateral in all 28 patients. The parotid gland was the most frequent location (18 of 28 patients, 64.3%) with lesions in the superficial lobe in 11 patients, in the deep lobe in 1 patient, and in the superficial and deep lobes in 6 patients. Other less commonly involved locations were the submandibular gland (28.5%, $n = 8$) (Fig 2), the sublingual gland (3.6%, $n = 1$) (Fig 3), and the palate (3.6%, $n = 1$) (Fig 4). The size of the lesions ranged from 1.6 to 7.0 cm, with a mean of 3.5 cm.

The margin was partially defined in 13 patients (46.4%), ill-defined in 10 patients (35.7%), and well-defined in 5 patients (17.9%). Of the 13 partially defined masses, 7 were lobulated, 3 were plaque-like, and 3 were irregular. Of the 10 ill-defined masses, 5 were lobulated, 1 was plaque-like, and 4 were irregular. All 5 well-defined masses were round/ovoid. Invasion of adjacent soft tissue was found in 5 patients, including 2 patients with bone erosion. According to the shape and margin of the masses, the morphology of tumors could be classified into 3 patterns. The most common pattern was type 2 ($n = 16$, 57.1%), then type 3 ($n = 7$, 25.0%) and type 1 ($n = 5$, 17.9%). Notably,

the shape and size of the lesion in the parotid glands may depend predominantly on the location of the lesion. All masses involving the superficial and deep lobes of the parotid gland were irregular ($n = 5$) or lobulated ($n = 1$). Additionally, almost half of the masses ($n = 5$) located in the superficial lobe of the parotid gland were round-ovoid, and all masses ($n = 11$) in the superficial lobe of the parotid gland were <5 cm.

On CT, 23 masses were detected in 23 patients. Compared with the adjacent muscle, lesions showed slight hypoattenuation in 19 patients and isoattenuation in 4 patients. Necrosis was demonstrated in 14.3% of ($n = 4$) of patients on enhanced CT, and no calcification was found in any patient. After the administration of contrast, lesions showed poor enhancement in 6 patients, moderate enhancement in 13 patients, and intense enhancement in 4 patients. Homogeneous enhancement was found in 14 patients, while heterogeneous enhancement was found in the other 9 patients.

Six patients with 6 masses (parotid glands in 4 patients, submandibular gland in 1, sublingual gland in 1) underwent MR imaging. On T1-weighted imaging, 1 patient had a lesion with a slight hyperintense signal and 5 patients had isointense signal. On

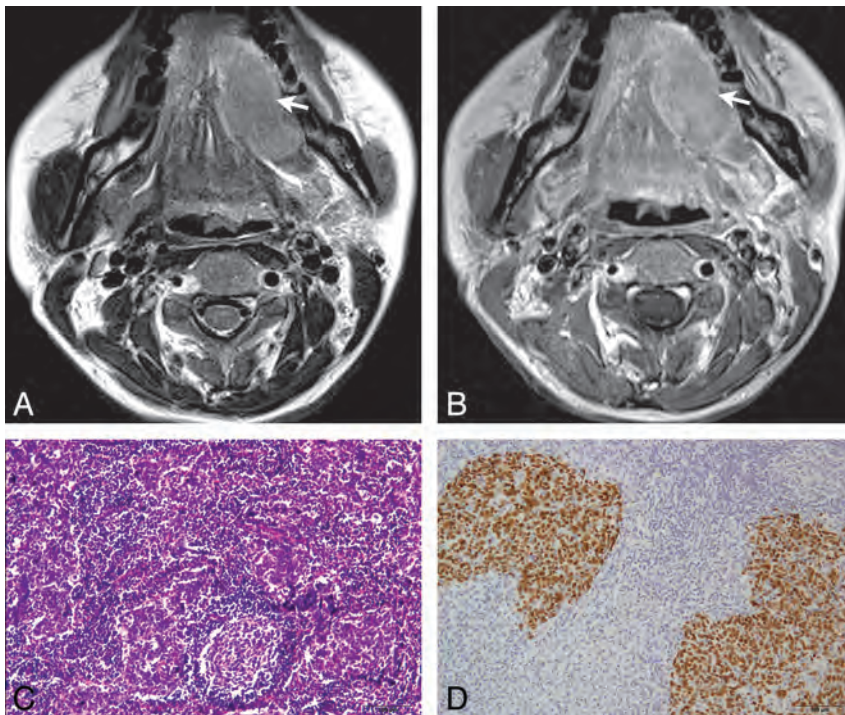


FIG 3. LEC of the left sublingual gland in a 44-year-old woman with a painful mass in the mouth for 8 years. Axial T2-weighted imaging (A) shows a homogeneous slightly hypointensity mass with a partially defined margin in the left sublingual gland (arrow). Axial gadolinium-enhanced T1-weighted image (B) shows the mass with homogeneous moderate enhancement (arrow). Histopathologic examination (C) shows nests of neoplastic epithelial cells separated by abundant lymphoid stroma (hematoxylin-eosin, original magnification $\times 100$). In situ hybridization by using a digoxigenin-labeled EBV probe (D) shows the nuclei of the malignant epithelial cells strongly positive but negative in the surrounding lymphocytes (original magnification $\times 100$).

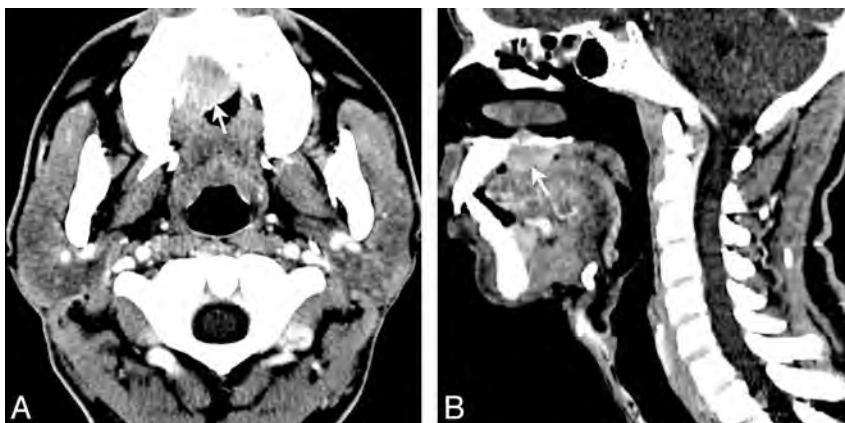


FIG 4. LEC of the right upper palate in a 38-year-old man with a rapidly growing mass in the upper palate for approximately 8 months. Axial contrast-enhanced CT (A) shows the mass with a heterogeneous moderate enhancement (arrow). Sagittal (B) contrast-enhanced CT shows the mass with heterogeneous moderate enhancement (arrow) and bone destruction.

T2-weighted imaging, 4 patients had hypointense signal (Fig 3A) and 2 patients had slightly hyperintense signal. After the administration of contrast, imaging of 1 patient showed poor enhancement, that of 4 patients showed moderate enhancement, and that in 1 patient showed intense enhancement. Homogeneous enhancement was found in 3 patients, and heterogeneous enhancement was found in 3 patients. Cystic/necrotic areas were not found in any of the 6 patients.

Cervical Lymphadenopathy

The incidence of neck node involvement was found in 60.7% (17/28) of patients, including 10 patients (56%, 10/18) with primary lesions in the parotid glands; 6 patients (75%, 6/8), in the submandibular gland; and 1 patient (100%, 1/1), in the palate. Cervical lymphadenopathy was unilateral in all patients. The locations of pathologic lymph nodes were consistent with anatomic drainage without skip metastasis. The intraparotid region and level IIb were involved in 8 patients, respectively; level IIa was involved in 7 patients; level Ib was involved in 3 patients; and level III was involved in 1 patient. Necrosis of the lymph nodes was found in 3 patients (Fig 5B).

Histopathologic Results

The diagnosis of LEC was confirmed histopathologically in all patients by using either surgical resection ($n = 27$) or fine-needle aspiration cytology ($n = 1$). Grossly, all 27 resected tumors were generally grayish or reddish and firm. Calcification was not found in any case, while necrosis was found in 5 cases in these 27 gross specimens. Infiltration into adjacent muscle was found in 3 patients, and bone erosion, in 2 patients. Histopathologic examinations commonly showed infiltrative sheets, nests, and cords of neoplastic epithelial cells separated by lymphoid stroma (Fig 3C). Immunohistochemically, cytokeratin and p63 were positive in 28 and 16 patients, respectively. Twenty-seven tumors showed positive EBV in epithelial neoplastic cells and negative EBV in stromal lymphoid cells and surrounding normal salivary gland tissue (Fig 3D). The remaining tumor showed negative EBV in epithelial neoplastic cells, stromal lymphoid cells, and surrounding normal salivary gland tissue.

DISCUSSION

LEC of the salivary gland, which has been referred to as undifferentiated carcinoma

with lymphoid stroma, malignant lymphoepithelial lesion, malignant lymphoepithelioma, and lymphoepithelial-like carcinoma,^{1,7} is a rare undifferentiated carcinoma with prominent lymphoid stroma and ultrastructural features of squamous cell carcinoma. Increasingly investigators have demonstrated that LEC of the salivary gland is strongly associated with Epstein-Barr virus in endemic areas such as Greenland, Southeast Asia, and Alaska.¹² In our study, all 28 patients were southern Chinese, and

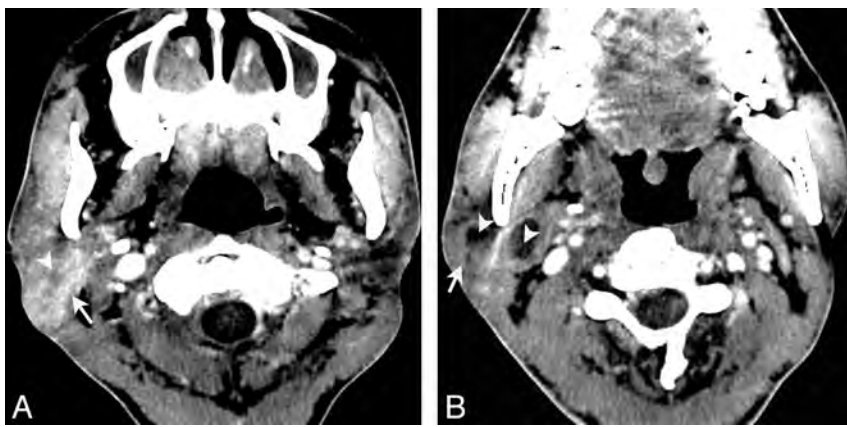


FIG 5. LEC of the right parotid gland in a 38-year-old man with painless masses in the right parotid regions for approximately 3 years. Axial contrast-enhanced CT (A) shows an ill-defined mass located in the right parotid gland (arrow) with heterogeneous enhancement and much intratumoral necrosis (arrowhead). Axial contrast-enhanced CT (B) shows multiple enlarged nodes (arrow) in the intraparotid region and level IIa, with obvious necrosis (arrowhead).

96.4% of tumors were positive for Epstein-Barr virus by using EBER in situ hybridization. Our results support the association of Epstein-Barr virus with salivary gland LEC. In our series, LEC of the salivary gland predominantly occurred in the parotid gland (64.3%), followed by the submandibular gland (28.5%). The mean age was 39.3 years, with a male predominance (1.5:1). A slowly growing, palpable mass was present in 71.4% of patients, and 28.6% presented with a recent, rapidly growing mass. Almost half of our patients (42.9%) experienced a duration of symptoms of >2 years, indicating that LECs of the salivary glands had a relatively long duration of symptoms compared with other malignant tumors in the salivary glands, consistent with prior reports.^{1,2,7}

Treatment for LEC of the salivary gland includes surgical excision, radiation therapy, and chemotherapy. At present, surgical excision followed by postoperative radiation therapy is considered the treatment of choice for LEC of the salivary gland, and the 5-year survival rate is reported to range from 50% to 90%.^{2,7} The prognosis of salivary gland LEC is reported as better than that in other types of undifferentiated carcinoma of the salivary gland.¹³ The incidence of local recurrence and distant metastasis has varied in previous studies. The reported local recurrence rate ranged from 0% to 28.9%.^{5,7} In our cases, 27 patients underwent a surgical excision and 18 patients underwent postoperative radiation therapy. The local recurrence rate in this group was 10.7%. Of our patients, 14.3% developed distant metastasis to the lung, liver, and brain from 7 to 77 months after diagnosis, comparable with a distant metastasis rate of 2.9%~33.3% in previous studies.^{5,7,9}

Fine-needle aspiration cytology is a primary diagnostic tool for salivary gland tumors,^{14,15} but the diagnostic accuracy, sensitivity, and specificity of fine-needle aspiration cytology in the diagnosis of salivary gland lesions are varied owing to diverse morphologic patterns and overlapping features between benign and malignant lesions. In a recent review, the diagnostic accuracy of fine-needle aspiration cytology was 78.6% in 14 patients with LEC of salivary gland.¹⁵ Thus, CT and MR imaging are still valuable tools for the diagnosis, preoperative evaluation, and biopsy guidance for patients with LEC. To our knowledge, however, only

Ahuja et al¹⁶ reported imaging findings of LECs in minor salivary glands in 4 cases in 1999.

LEC of the salivary glands in our series tended to involve the parotid gland with an ill-defined or partially ill-defined margin. Most LECs in the salivary glands showed slight hypoattenuation on CT, isointense signal on T1WI, and hypointense signal on T2-weighted imaging, with moderate enhancement. Unfortunately, these CT and MR imaging characteristics are nonspecific and do not allow a definitive discrimination from other malignant tumors of the salivary glands. However, most of the lesions had homogeneous attenuation/signal intensity on unenhanced CT and MR imaging; no lesions exhibited cystic degeneration or calcification, even in a large mass; and most of our lesions (85.7%) lacked necrotic regions. These features are, in aggregate, different from those in other common primary malignant tumors of the salivary glands, including mucoepidermoid carcinoma and adenoid cystic carcinoma because these more common malignant tumors typically show heterogeneous attenuation or signal intensity with cystic change and necrosis.¹⁷⁻¹⁹ Thus, an ill-defined or partially ill-defined mass without cystic regions or calcification and lacking necrosis is typically seen in salivary gland LEC.

In our cases, salivary gland LECs could be classified into 3 morphologic types on the basis of the margin and shape. Morphologic patterns of salivary gland LECs are useful for the differential diagnosis along with other salivary gland tumors. Types 1 (17.9%) and 3 (25.0%) in our series showed typical morphologic features of benign and malignant tumors in the salivary glands, respectively. Type 2 represented a mass with a lobulated/plaque-like shape and a partially or ill-defined margin. In this study, most tumors belonged to this type. Because most LECs in the salivary glands are less aggressive malignant tumors,⁷ this pattern might be a relatively morphologic characteristic of salivary gland LEC. In addition, previous studies had reported an incidence of lymph node metastases in salivary gland LEC ranging from 10% to 50%.^{2,7,20} In our study, the incidence of lymph node metastases was up to 60.7%, which was higher than that in previous studies.^{2,7,20} Lymphadenopathy in our cases was unilateral, with the intraparotid region and level IIa the most commonly involved regions. Lymph node metastasis was found to spread along with anatomic drainage. No skip metastasis was present. Lymph node necrosis occurred sometimes, as demonstrated in a previous study.¹⁶

There are several limitations to our study. First, as a retrospective study, most of our patients underwent CT and only 6 patients underwent MR imaging with conventional T1 and T2 sequences. Because MR imaging, particularly MR imaging with diffusion-weighted imaging or dynamic contrast-enhanced sequences, is regarded as a better technique for characterizing and delineating salivary gland lesions,²¹ a study using these new techniques may be needed for further determining the imaging features of salivary

gland LEC. Second, our patients had a follow-up from 5 to 123 months. Four patients had follow-up at <12 months, which was less than the time to recurrence or distant metastasis in some other patients. Therefore, it was difficult to conclude the exact long-term recurrence and metastasis rates just on the basis of our data.

CONCLUSIONS

LEC of the salivary gland displays nonspecific attenuation or signal intensity on CT or MR imaging. It is difficult to make a reliable diagnosis of it on the basis of CT and MR images. However, clinically, it predominantly occurs in Inuit-Yupik and southern Chinese with a strong association with Epstein-Barr virus and a relatively long history. Imaging features, including an intraglandular mass with a lobulated/plaque-like shape and ill- or partially ill-defined margins but without calcification and necrosis, accompanied by ipsilateral lymphadenopathy, suggest the diagnosis of salivary gland LEC.

REFERENCES

- Schneider M, Rizzardi C. **Lymphoepithelial carcinoma of the parotid glands and its relationship with benign lymphoepithelial lesions.** *Arch Pathol Lab Med* 2008;132:278–82
- Wang CP, Chang YL, Ko JY, et al. **Lymphoepithelial carcinoma versus large cell undifferentiated carcinoma of the major salivary glands.** *Cancer* 2004;101:2020–27
- Hsiung CY, Huang CC, Wang CJ, et al. **Lymphoepithelioma-like carcinoma of salivary glands: treatment results and failure patterns.** *Br J Radiol* 2006;79:52–55
- Hoxworth JM, Hanks DK, Araoz PA, et al. **Lymphoepithelioma-like carcinoma of the lung: radiologic features of an uncommon primary pulmonary neoplasm.** *AJR Am J Roentgenol* 2006;186:1294–99
- Kuo T, Hsueh C. **Lymphoepithelioma-like salivary gland carcinoma in Taiwan: a clinicopathological study of nine cases demonstrating a strong association with Epstein-Barr virus.** *Histopathology* 1997;31:75–82
- Hilderman WC, Gordon JS, Large HL Jr, et al. **Malignant lymphoepithelial lesion with carcinomatous component apparently arising in parotid gland: a malignant counterpart of benign lymphoepithelial lesion?** *Cancer* 1962;15:606–10
- Ma H, Lin Y, Wang L, et al. **Primary lymphoepithelioma-like carcinoma of salivary gland: 69 cases with long-term follow-up.** *Head Neck* 2013 Aug 22. [Epub ahead of print]
- Nagao T, Ishida Y, Sugano I, et al. **Epstein-Barr virus-associated undifferentiated carcinoma with lymphoid stroma of the salivary gland in Japanese patients: comparison with benign lymphoepithelial lesion.** *Cancer* 1996;78:695–703
- Leung SY, Chung LP, Yuen ST, et al. **Lymphoepithelial carcinoma of the salivary gland: in situ detection of Epstein-Barr virus.** *J Clin Pathol* 1995;48:1022–27
- Gor DM, Langer JE, Loevner LA. **Imaging of cervical lymph nodes in head and neck cancer: the basics.** *Radiol Clin North Am* 2006;44:101–10, viii
- van den Brekel MW, Stel HV, Castelijns JA, et al. **Cervical lymph node metastasis: assessment of radiologic criteria.** *Radiology* 1990;177:379–84
- Tsai CC, Chen CL, Hsu HC. **Expression of Epstein-Barr virus in carcinomas of major salivary glands: a strong association with lymphoepithelioma-like carcinoma.** *Hum Pathol* 1996;27:258–62
- Larbcharoensub N, Tubtong N, Praneetvatakul V, et al. **Epstein-Barr virus associated lymphoepithelial carcinoma of the parotid gland: a clinicopathological report of three cases.** *J Med Assoc Thai* 2006;89:1536–41
- Singh Nanda KD, Mehta A, Nanda J. **Fine-needle aspiration cytology: a reliable tool in the diagnosis of salivary gland lesions.** *J Oral Pathol Med* 2012;41:106–12
- Colella G, Cannavale R, Flamminio F, et al. **Fine-needle aspiration cytology of salivary gland lesions: a systematic review.** *J Oral Maxillofac Surg* 2010;68:2146–53
- Ahuja AT, Teo PM, To KF, et al. **Palatal lymphoepitheliomas and a review of head and neck lymphoepitheliomas.** *Clin Radiol* 1999;54:289–93
- Lee YY, Wong KT, King AD, et al. **Imaging of salivary gland tumours.** *Eur J Radiol* 2008;66:419–36
- Thoeny HC. **Imaging of salivary gland tumours.** *Cancer Imaging* 2007;7:52–62
- Christe A, Waldherr C, Hallett R, et al. **MR imaging of parotid tumors: typical lesion characteristics in MR imaging improve discrimination between benign and malignant disease.** *AJNR Am J Neuroradiol* 2011;32:1202–07
- Bosch JD, Kudryk WH, Johnson GH. **The malignant lymphoepithelial lesion of the salivary glands.** *J Otolaryngol* 1988;17:187–90
- Yabuuchi H, Matsuo Y, Kamitani T, et al. **Parotid gland tumors: can addition of diffusion-weighted MR imaging to dynamic contrast-enhanced MR imaging improve diagnostic accuracy in characterization?** *Radiology* 2008;249:909–16

Use of Non-Echo-Planar Diffusion-Weighted MR Imaging for the Detection of Cholesteatomas in High-Risk Tympanic Retraction Pockets

A. Alvo, C. Garrido, Á. Salas, G. Miranda, C.E. Stott, and P.H. Delano



ABSTRACT

BACKGROUND AND PURPOSE: Non-echo-planar DWI MR imaging (including the HASTE sequence) has been shown to be highly sensitive and specific for large cholesteatomas. The purpose of this study was to determine the diagnostic accuracy of HASTE DWI for the detection of incipient cholesteatoma in high-risk retraction pockets.

MATERIALS AND METHODS: This was a prospective study of 16 patients who underwent MR imaging with HASTE DWI before surgery. Surgeons were not informed of the results, and intraoperative findings were compared against the radiologic diagnosis. Sensitivity, specificity, and positive and negative predictive values were calculated.

RESULTS: Among the 16 retraction pockets, 10 cholesteatomas were diagnosed intraoperatively (62.5%). HASTE showed 90% sensitivity, 100% specificity, 100% positive predictive value, and 85.7% negative predictive value in this group of patients. We found only 1 false-negative finding in an infected cholesteatoma.

CONCLUSIONS: We demonstrate a high correlation between HASTE and surgical findings, suggesting that this technique could be useful for the early detection of primary acquired cholesteatomas arising from retraction pockets and could help to avoid unnecessary surgery.

ABBREVIATION: EP = echo-planar

Middle ear cholesteatomas are benign but locally aggressive nonneoplastic lesions composed of a keratinizing stratified squamous epithelial matrix, an inflammatory perimatrix, and desquamated keratin content.¹ Pathophysiologically, cholesteatomas are divided into congenital (epithelium trapped within the middle ear during fetal development) and acquired. Acquired cholesteatomas are further divided into primary (arising from a tympanic membrane retraction) and secondary (epithelium reaching the middle ear through a tympanic perforation, fracture, or iatrogenic procedure).^{2,3} Cholesteatomas progressively erode the bony structures surrounding the middle ear (ossicles, facial nerve canal, bony labyrinth, and skull base), predisposing to a wide range of complications, including potentially severe infec-

tions such as meningitis and intracranial abscesses.⁴ Surgery is the only known curative treatment and should be performed early because less destruction allows more conservative and hearing-preserving procedures with a reduced risk of complications.

Tympanic retraction pockets are invaginations of the tympanic membrane into the middle ear cleft caused by Eustachian tube dysfunction, which interferes with proper middle ear ventilation.⁵ The diagnosis of a “dangerous” or high-risk retraction pocket is proposed when the bottom of the pocket becomes hidden to the otomicroscope and/or starts retaining skin, because this may lead to primary acquired cholesteatoma.¹ Given that there is a continuum from tympanic retraction pockets to small cholesteatomas, the distinction between retraction pockets that have already developed a cholesteatoma and those that have not remains a problem in otologic surgery because conventional clinical and radiologic methods are often insufficient. In addition, dangerous retraction pockets and small cholesteatomas share similar clinical signs and symptoms, and it is often impossible to differentiate them via otomicroscopy. A substantial number of such patients undergo surgical procedures such as mastoidectomies or atticotomies, but only a subset actually have cholesteatomas.

CT is the most widely used imaging technique for the detection of a middle ear mass and assessing tympanomastoid anatomy

Received December 26, 2013; accepted after revision February 11, 2014.

From the Departments of Otorhinolaryngology (A.A., C.E.S., P.H.D.) and Radiology (C.G., A.S., G.M.), Hospital Clínico Universidad de Chile, Santiago, Chile.

This work was financed with funds from the Sociedad Chilena de Otorrinolaringología-Medicina y Cirugía de Cabeza y Cuello.

Please address correspondence to Andrés Alvo, MD, Servicio de Otorrinolaringología, Hospital Clínico Universidad de Chile, Santos Dumont 999, Independencia, Santiago, Chile, 8380456; e-mail: andresalvo@gmail.com; and Paul H. Delano, MD, Servicio de Otorrinolaringología, Hospital Clínico Universidad de Chile, Instituto de Ciencias Biomédicas, Facultad de Medicina, Universidad de Chile, Santos Dumont 999, Independencia, Santiago, Chile, 8380456; e-mail: phdelano@gmail.com

<http://dx.doi.org/10.3174/ajnr.A3952>

and the extent of bone erosion.⁶ However, it is nonspecific for cholesteatoma and relies on indirect signs for its diagnosis.^{7,8} More recently, MR imaging techniques have been used to differentiate cholesteatoma from other middle ear masses, especially T1-weighted delayed postcontrast imaging and DWI.^{9,10}

DWI techniques are based on the restriction of movement of water molecules, such as that caused by keratin-filled cholesteatomas, producing a hyperintense signal.¹¹ Conventional EPI has been displaced by non-EPI techniques when the temporal bone is the focus, because these sequences have fewer artifacts and thinner sections, allowing the detection of cholesteatomas as small as 2 mm.¹² Several studies of non-echo-planar (EP) DWI have provided excellent sensitivity and specificity for the detection of cholesteatomas. Currently, MR imaging is suggested when the diagnosis of cholesteatoma cannot be established by other means, often in the setting of congenital and residual/recurrent disease.¹⁰

The purpose of this study was to evaluate the sensitivity and specificity of non-EP DWI for the detection of cholesteatomas in skin-retaining and/or otomicroscopically inaccessible tympanic retraction pockets.

MATERIALS AND METHODS

Research Design

A prospective study was conducted at the Department of Otorhinolaryngology in our institution. HASTE non-EP DWI MR imaging was performed within 2 months before surgery, in addition to standard examinations, including audiometry and temporal bone CT. HASTE images were blindly interpreted by an experienced neuroradiologist, and radiologic diagnosis of cholesteatoma was considered when a marked hyperintensity in comparison with brain tissue was noted on DWI. After all patients had been recruited, a second neuroradiologist revised all HASTE images to evaluate the interobserver agreement of the test.

Patients with tympanic membrane retraction pockets in which a cholesteatoma could not be ruled out or confirmed were included. Exclusion criteria included previously operated ears, clinically evident cholesteatomas, contraindications for MR imaging, and refusal by the patient. Staff otologists with at least 5 years of experience in middle ear surgery performed all operations. Surgeons were blind to the results of the MR imaging and independently determined the presence or absence of cholesteatoma in the middle ear. The study was approved by the ethics committee of our hospital (approval No. 68, 2011).

Patients

Sixteen consecutive patients clinically diagnosed with tympanic retraction pockets were recruited and evaluated by an expert otology committee. When a high-risk pocket was scheduled for surgery, the patient was considered a possible candidate and offered an informed consent form. Anonymity was preserved throughout the study.

Imaging Technique

All MRI was performed by using a 1.5T superconducting MR imaging scanner (Magnetom Symphony Maestro Class; Siemens, Erlangen, Germany) with 20-mT/m maximum amplitude gradients. All images were acquired by using a 4-channel circularly

Patient characteristics and MRI and surgical findings

Patient No.	Sex	Age (yr)	Side	HASTE	Size (mm)	Surgery
1	F	27	L	+	3	+
2	M	21	R	-	0	-
3	F	39	R	-	0	-
4	F	35	L	-	0	-
5	M	29	R	+	13	+
6	M	43	R	+	6	+
7	F	39	L	+	5	+
8	F	55	L	+	6	+
9	M	49	R	-	0	+
10	F	42	R	+	5	+
11	F	60	L	+	10	+
12	M	9	L	+	15	+
13	F	58	R	-	0	-
14	F	48	L	+	4	+
15	M	24	L	-	0	-
16	F	43	R	-	0	-

Note:—L indicates left; R, right; +, positive finding; —, negative finding.

polarized head-array coil. To obtain the imaging planes, we performed the following protocol: sagittal T1 turbo inversion recovery magnitude dark fluid sequence (TR, 1710 ms; TE, 12 ms; TI, 860 ms; flip angle, 150°; matrix, 202 × 256; FOV, 219 × 250; section thickness, 5 mm; NEX, 1; twenty sections; acquisition time, 1 minute 44 seconds); axial and coronal T2 TSE imaging with a restore pulse (TR, 5350 ms; TE, 110 ms; flip angle, 180°; matrix, 220 × 384; FOV, 172 × 180; section thickness, 3 mm; NEX, 2; twenty sections; acquisition time, 2 minutes 26 seconds); axial T2 CISS sequence, —64 partitions in 1 slab, 0.8 mm in the axial plane (TR, 10.86 ms; TE, 5.43 ms; flip angle, 70°; matrix, 208 × 256; FOV, 146 × 180; NEX, 1; acquisition time, 4 minutes 16 seconds); and axial and coronal HASTE sequences (TR, 2700 ms; TE, 132 ms; flip angle, 180°; turbo factor, 256; matrix, 256 × 256; FOV, 200 × 200; section thickness, 3 mm; intersection gap, 0 mm; NEX, 4; b factor, 800 s/mm²; 14 sections; acquisition time, 2 minutes 33 seconds). Unless dural involvement secondary to middle fossa bone erosion was suspected, all sequences were performed without intravenous injection of gadolinium-based contrast media.

Statistical Analysis

Patients were dichotomically classified as positive or negative for cholesteatoma. Dubious cases were considered as positive, given that a cholesteatoma could not be ruled out. Data were tabulated in a spreadsheet application (Excel for Mac 2011; Microsoft, Bothell, Washington). Diagnostic tests were evaluated by comparing HASTE results against the intraoperative findings. Statistical measures, including sensitivity, specificity, positive predictive value, and negative predictive value, were calculated. Interobserver agreement was calculated by using the κ coefficient.

RESULTS

Sixteen patients (6 males [37.5%] and 10 females [62.5%]) with ages ranging from 9 to 60 years (mean, 38.8 ± 14.1 years) were included during 2 years (November 2011 to November 2013). There was no difference in the laterality of the disease (8 left- and 8 right-sided).

Intraoperatively, we found cholesteatomas in 10 of 16 retraction pockets (62.5%). Using HASTE resulted in 9 true-positives,

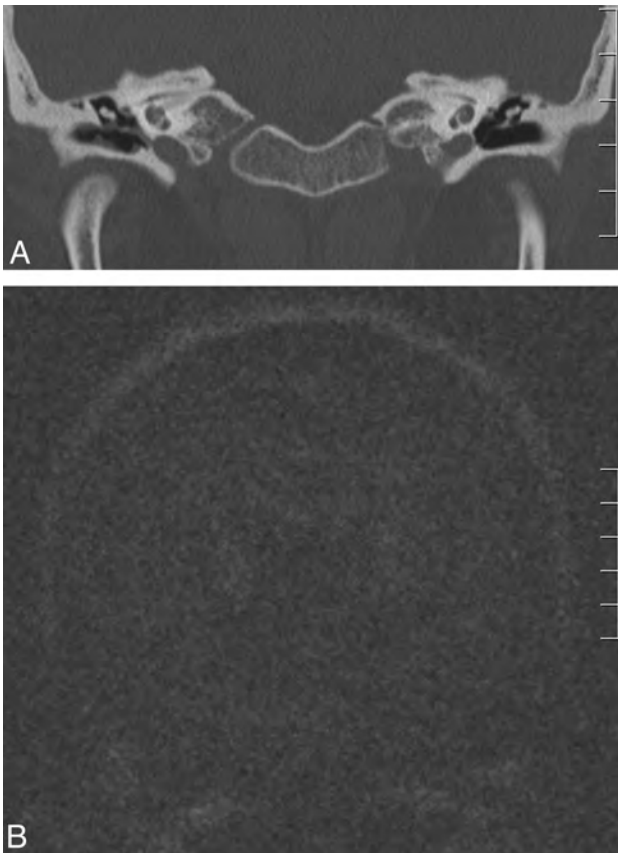


FIG 1. Case 3. A 39-year-old woman with no prior otologic diagnosis. A, Coronal CT scan shows right tympanic membrane thickening with occupation of Prussak space. B, Coronal HASTE shows no hyperintensity. In surgery, a granulomatous mass was identified without evidence of cholesteatoma (not shown).

zero false-positives, 1 false-negative, and 6 true-negatives (Table). Radiologically, the size of the cholesteatomas ranged between 3 and 15 mm (mean, 7.4 mm). Calculated statistical measures for HASTE with their respective 95% confidence intervals were as follows: 90% sensitivity (55.5%–99.8%), 100% specificity (54.1%–100%), 100% positive predictive value (66.4%–100%), and 85.7% negative predictive value (42.1%–99.6%).

Further analysis included a second neuroradiologist to evaluate the interobserver agreement; the calculated κ coefficient was 0.875 (0.640–1.000). There was an additional false-negative in this retrospective analysis, which had been classed as “faintly positive” (a small, weak, hyperintense signal, different from the surrounding tissues) by the first neuroradiologist. Sample images that are representative of different clinical situations are shown in Figs 1–3.

DISCUSSION

Our results show that HASTE can predict the presence of cholesteatomas in cases of retraction pockets that retain skin or cannot be fully evaluated by direct otomicroscopy and in which the diagnosis is uncertain. The presence of keratin in the cholesteatoma leads to a restrictive pattern with characteristic hyperintensity on DWI, and the use of non-EPI enabled the avoidance of susceptibility artifacts at the skull base, which can be mistaken for or hide a cholesteatoma.¹²

Common diagnostic techniques for cholesteatoma, including

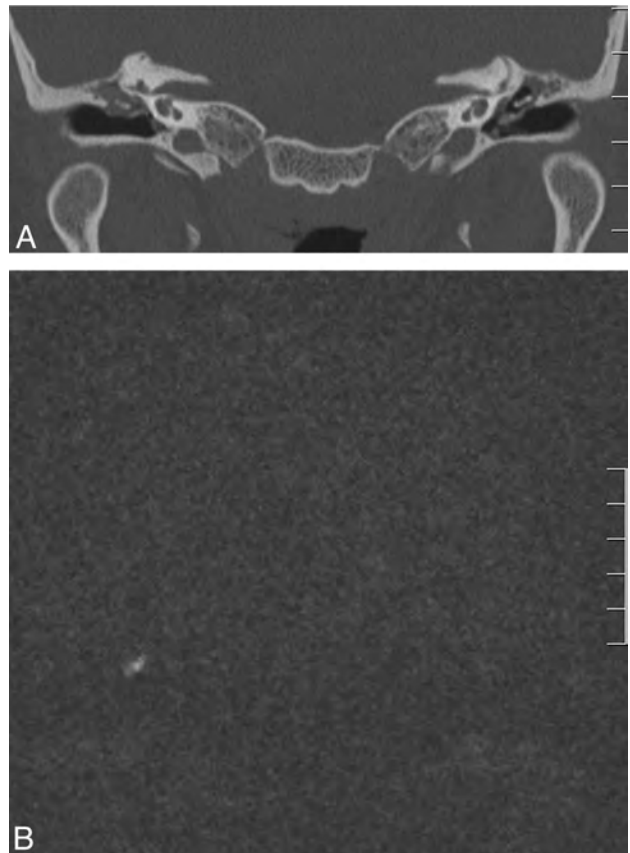


FIG 2. Case 5. A 29-year-old man with a history of chronic bilateral otitis media with effusion with a tympanic ventilation T-tube on the left side. A, Coronal CT scan shows bilateral tympanic thickening and middle ear opacities, with erosion of the scutum; a T-tube can be observed on the left side. B, Coronal HASTE shows a 13-mm right-sided hyperintensity in relation to the epitympanum. The cholesteatoma was found intraoperatively (not shown).

otomicroscopy and CT, are useful but, in many cases, insufficient. Ganaha et al¹³ reported sensitivities, specificities, positive predictive values, and negative predictive values of 77.9%, 92.8%, 97.8%, and 50.0% for otoscopy and 71.1%, 78.5%, 93.3%, and 39.2% for CT, respectively. Although the diagnosis of large cholesteatomas can be adequately accomplished by these methods, detection rates as low as 50%–60% have been described in difficult cases such as residual, recurrent, and congenital cholesteatomas.¹³ In addition, the low negative predictive value for CT and otomicroscopy suggests that in questionable cases, like differentiating a small cholesteatoma and a noncholesteatomatous tympanic retraction pocket, further diagnostic tools are needed to rule out the presence of a middle ear cholesteatoma. For these reasons, MR imaging techniques have been proposed for the evaluation of middle ear disease.

Conventional MR Imaging Sequences for the Diagnosis of Cholesteatoma

Cholesteatomas can be difficult to detect and/or appear as non-specific lesions on standard MR images,^{11,14,15} but keratin shows a restrictive pattern on DWI. Conventional EP DWI, however, has not yielded sufficiently precise results, especially for cholesteatomas smaller than 5 mm. Jindal et al¹¹ reported a sensitivity of 83%

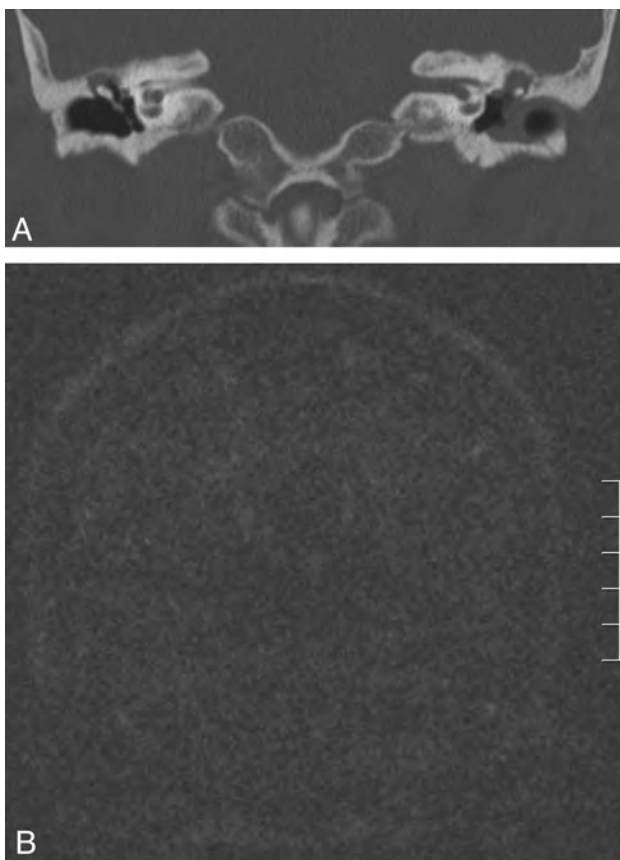


FIG 3. Case 13. A 58-year-old woman with bilateral chronic ear disease (right tympanic retraction pocket and left external ear canal stenosis). A, Coronal CT shows a right-sided tympanic retraction pocket with partial thickening of the tympanic membrane and erosion of the scutum, with an epitympanic middle ear mass. On the left side, there is external ear canal occupation by a soft-tissue attenuation mass, with epitympanic opacity. B, Coronal HASTE image negative for cholesteatoma. Surgery confirmed the presence of a retraction pocket without invasion of skin into the middle ear on the right side (not shown).

and a specificity of 82%, while Vercruyssen et al¹⁶ reported values of 81% and 100% for primary cholesteatomas and 12.5% and 100% for residual/recurrent cholesteatomas. In EP DWI, the relatively thick sections and presence of air-bone susceptibility artifacts account for these problems.¹⁷

The Role of Non-Echo-Planar Diffusion-Weighted MR Imaging in the Diagnosis of Cholesteatomas

Non-EP DWI (including HASTE and PROPELLER sequences) has shown increased sensitivity and specificity, with fewer artifacts and thinner sections, allowing the detection of cholesteatomas measuring 2–3 mm.¹² Several studies have been published since 2006 showing promising results for this technique.^{18–28} Recently, Li et al²⁹ summarized these findings in a meta-analysis including 10 articles (342 patients), reporting an overall sensitivity of 94% and specificity of 94%. False-negatives are rare, often caused by motion artifacts or self-evacuating “mural” cholesteatomas, and false-positives are very infrequent.^{10,12,15,30} Other advantages to DWI are its short acquisition times (2–5 minutes) and avoidance of intravenous contrast.^{22,31}

One of the most studied uses for non-EP DWI in middle ear disease is as an alternative to second-look surgery in canal wall-up

mastoidectomies,³² in which the posterior wall of the external ear canal is preserved. This makes postoperative care easier but impedes direct observation of the mastoidectomy during otomicroscopy, making it impossible to clinically detect residual and recurrent cholesteatomas.³³

Current indications for DWI in cholesteatomas have focused on congenital and residual/recurrent disease,¹⁰ because they can be hidden or difficult to evaluate via otoscopy and postsurgical inflammation may lead to confusion on CT and standard MR imaging. DWI is also helpful in distinguishing differential diagnoses of middle ear masses, especially when combined with delayed postcontrast T1WI.

The usefulness of non-EP DWI for detecting patients with incipient disease has been less well-studied. Although excellent previous reports by Pizzini et al,²³ De Foer et al,²⁶ Profant et al,²⁷ and Ilica et al³⁴ have included primary cholesteatomas among their cases, our research differs in that this was a prospective study that included only retraction pockets with suspicion of cholesteatoma after evaluation by an expert otologic committee. All patients had surgical confirmation, and the data did not include other groups such as recurrent disease. Our aim was to specifically evaluate the diagnostic accuracy of non-EP DWI in difficult cases in which the presence of a middle ear cholesteatoma behind a tympanic retraction pocket was unclear.

The pathogenesis of primary acquired cholesteatomas is complicated and multifactorial, but retraction pockets seem to play an important role³⁵; however, it remains a matter of debate as to whether this pocket can be considered a cholesteatoma. To our knowledge, there are few MR imaging–based articles in the literature assessing the presence of clinically occult cholesteatomas behind tympanic retraction pockets.

Use of Non-EP DW on Tympanic Retraction Pockets

On the basis of our results, we propose that HASTE is a highly sensitive and specific test in the evaluation of high-risk tympanic retraction pockets, where otomicroscopy alone cannot evaluate the extension of skin into the middle ear by direct observation through the external ear canal. CT showing a middle ear mass and/or bone erosion is not specific for cholesteatoma, nor is standard MR imaging. Because DWI gives poor anatomic information, does not evaluate bone erosion, and is not exempt from false-positives and negatives, all of these imaging techniques should be considered as complementary.

In agreement with the literature, we were able to detect cholesteatomas as small as 3 mm. Furthermore, 40% of all HASTE-positive patients in our study had cholesteatomas of ≤ 5 mm, which could have been missed if EP DWI had been used instead.^{12,24}

There was only 1 false-negative in an infected, “wet” cholesteatoma with otorrhea larger than 2–3 mm. We believe that this could be explained by an alteration in the restriction pattern of the suppurated cholesteatoma, but further studies are needed to confirm or refute this hypothesis.

Although the number of subjects is limited because of the specific subset of patients included, this study might broaden the clinical applicability of non-EP DWI, especially in cases in which the diagnosis is uncertain and a more conservative approach is

desirable (dangerous tympanic retraction on the better/only hearing ear, high anesthetic risk). Because most cases of cholesteatoma can be adequately diagnosed with otoscopy and CT, judicious use of HASTE MR imaging is important and should be considered only when clinical benefit is expected.

CONCLUSIONS

We have demonstrated that preoperative HASTE MR imaging is highly accurate with regard to detecting the presence or absence of cholesteatoma in tympanic retraction pockets. Early diagnosis of cholesteatomas arising from tympanic retraction pockets could help to better select patients requiring surgery, thus avoiding unnecessary and aggressive procedures.

Disclosures: Andrés Alvo—RELATED: Grant: Sociedad Chilena de Otorrinolaringología.* Comments: The grant was earned among projects from members of the Chilean Society of Otorhinolaryngology, to finance relevant clinical or basic research. Cristian Garrido—RELATED: Grant: Sociedad Chilena de Otorrinolaringología.* Carlos E. Stott—RELATED: Grant: Sociedad Chilena de Otorrinolaringología.* Paul H. Delano—RELATED: Grant: Sociedad Chilena de Otorrinolaringología.* Comments: Sociedad Chilena de Otorrinolaringología funded MR imaging for patients recruited in this study (research grant). *Money paid to the institution.

REFERENCES

1. Semaan MT, Megerian CA. **The pathophysiology of cholesteatoma.** *Otolaryngol Clin North Am* 2006;39:1143–59
2. Nevoux J, Lenoir M, Roger G, et al. **Childhood cholesteatoma.** *Eur Ann Otorhinolaryngol Head Neck Dis* 2010;127:143–50
3. Chang P, Kim S. **Cholesteatoma: diagnosing the unsafe ear.** *Aust Fam Physician* 2008;37:631–38
4. Wu JF, Jin Z, Yang JM, et al. **Extracranial and intracranial complications of otitis media: 22-year clinical experience and analysis.** *Acta Otolaryngol* 2012;132:261–65
5. Alzahrani M, Saliba I. **Tympanic membrane retraction pocket staging: is it worthwhile?** *Eur Arch Otorhinolaryngol* 2014;271:1361–68
6. Ayache D, Darrouzet V, Dubrulle F, et al. **Imaging of non-operated cholesteatoma: clinical practice guidelines.** *Eur Ann Otorhinolaryngol Head Neck Dis* 2012;129:148–52
7. Tatlipinar A, Tuncel A, Ögredik EA, et al. **The role of computed tomography scanning in chronic otitis media.** *Eur Arch Otorhinolaryngol* 2012;269:33–38
8. Payal G, Pranjali K, Gul M, et al. **Computed tomography in chronic suppurative otitis media: value in surgical planning.** *Indian J Otolaryngol Head Neck Surg* 2012;64:225–29
9. Ayache D, Williams MT, Lejeune D, et al. **Usefulness of delayed post-contrast magnetic resonance imaging in the detection of residual cholesteatoma after canal wall-up tympanoplasty.** *Laryngoscope* 2005;115:607–10
10. Más-Estellés F, Mateos-Fernández M, Carrascosa-Bisquert B, et al. **Contemporary non-echo-planar diffusion-weighted imaging of middle ear cholesteatomas.** *Radiographics* 2012;32:1197–213
11. Jindal M, Doshi J, Srivastav M, et al. **Diffusion-weighted magnetic resonance imaging in the management of cholesteatoma.** *Eur Arch Otorhinolaryngol* 2010;267:181–85
12. De Foer B, Vercruyse JP, Spaepen M, et al. **Diffusion-weighted magnetic resonance imaging of the temporal bone.** *Neuroradiology* 2010;52:785–807
13. Ganaha A, Outa S, Kyuuna A, et al. **Efficacy of diffusion-weighted magnetic resonance imaging in the diagnosis of middle ear cholesteatoma.** *Auris Nasus Larynx* 2011;38:329–34
14. Yoshida T, Ito K, Adachi N, et al. **Cholesteatoma of the petrous bone: the crucial role of diffusion-weighted MRI.** *Eur Arch Otorhinolaryngol* 2005;262:440–41
15. Mateos-Fernández M, Mas-Estellés F, de Paula-Vernetta C, et al. **The role of diffusion-weighted magnetic resonance imaging in cholesteatoma diagnosis and follow-up: study with the diffusion PROPELLER technique** [in English, Spanish]. *Acta Otorrinolaryngol Esp* 2012;63:436–42
16. Vercruyse JP, De Foer B, Pouillon M, et al. **The value of diffusion-weighted MR imaging in the diagnosis of primary acquired and residual cholesteatoma: a surgical verified study of 100 patients.** *Eur Radiol* 2006;16:1461–67
17. Moura M, Taranto D, Garcia M. **Cholesteatoma: utility of non-echo-planar diffusion-weighted imaging.** *Radiol Bras* 2012;45:283–87
18. De Foer B, Vercruyse JP, Pilet B, et al. **Single-shot, turbo spin-echo, diffusion-weighted imaging versus spin-echo-planar, diffusion-weighted imaging in the detection of acquired middle ear cholesteatoma.** *AJNR Am J Neuroradiol* 2006;27:1480–82
19. Dubrulle F, Souillard R, Chechin D, et al. **Diffusion-weighted MR imaging sequence in the detection of postoperative recurrent cholesteatoma.** *Radiology* 2006;238:604–10
20. Dhepnorrrat RC, Wood B, Rajan GP. **Postoperative non-echo-planar diffusion-weighted magnetic resonance imaging changes after cholesteatoma surgery: implications for cholesteatoma screening.** *Otol Neurotol* 2009;30:54–58
21. Lehmann P, Saliou G, Brochart C, et al. **3T MR imaging of postoperative recurrent middle ear cholesteatomas: value of periodically rotated overlapping parallel lines with enhanced reconstruction diffusion-weighted MR imaging.** *AJNR Am J Neuroradiol* 2009;30:423–27
22. Rajan GP, Ambett R, Wun L, et al. **Preliminary outcomes of cholesteatoma screening in children using non-echo-planar diffusion-weighted magnetic resonance imaging.** *Int J Pediatr Otorhinolaryngol* 2010;74:297–301
23. Pizzini FB, Barbieri F, Beltramello A, et al. **HASTE diffusion-weighted 3-Tesla magnetic resonance imaging in the diagnosis of primary and relapsing cholesteatoma.** *Otol Neurotol* 2010;31:596–602
24. Huins CT, Singh A, Lingam RK, et al. **Detecting cholesteatoma with non-echo planar (HASTE) diffusion-weighted magnetic resonance imaging.** *Otolaryngol Head Neck Surg* 2010;143:141–46
25. Plouin-Gaudon I, Bossard D, Fuchsmann C, et al. **Diffusion-weighted MR imaging for evaluation of pediatric recurrent cholesteatomas.** *Int J Pediatr Otorhinolaryngol* 2010;74:22–26
26. De Foer B, Vercruyse JP, Bernaerts A, et al. **Middle ear cholesteatoma: non-echo-planar diffusion-weighted MR imaging versus delayed gadolinium-enhanced T1-weighted MR imaging—value in detection.** *Radiology* 2010;255:866–72
27. Profant M, Sláviková K, Kabátová Z, et al. **Predictive validity of MRI in detecting and following cholesteatoma.** *Eur Arch Otorhinolaryngol* 2012;269:757–65
28. Khemani S, Lingam RK, Kalan A, et al. **The value of non-echo planar HASTE diffusion-weighted MR imaging in the detection, localisation and prediction of extent of postoperative cholesteatoma.** *Clin Otolaryngol* 2011;36:306–12
29. Li PM, Linos E, Gurgel RK, et al. **Evaluating the utility of non-echo-planar diffusion-weighted imaging in the preoperative evaluation of cholesteatoma: a meta-analysis.** *Laryngoscope* 2013;123:1247–50
30. Karandikar A, Goh J, Loke SC, et al. **Mucous retention cyst of temporal bone: a mimic of cholesteatoma on DW-MRI.** *Am J Otolaryngol* 2013;34:753–54
31. Sharifian H, Taheri E, Borghei P, et al. **Diagnostic accuracy of non-echo-planar diffusion-weighted MRI versus other MRI sequences in cholesteatoma.** *J Med Imaging Radiat Oncol* 2012;56:398–408
32. Schwartz KM, Lane JI, Bolster BD Jr, et al. **The utility of diffusion-weighted imaging for cholesteatoma evaluation.** *AJNR Am J Neuroradiol* 2011;32:430–36
33. Nikolopoulos TP, Gerbesiotis P. **Surgical management of cholesteatoma: the two main options and the third way—atticotomy/limited mastoidectomy.** *Int J Pediatr Otorhinolaryngol* 2009;73:1222–27
34. İlca AT, Hıdır Y, Bulakbaşı N, et al. **HASTE diffusion-weighted MRI for the reliable detection of cholesteatoma.** *Diagn Interv Radiol* 2012;18:153–58
35. Louw L. **Acquired cholesteatoma pathogenesis: stepwise explanations.** *J Laryngol Otol* 2010;124:587–93

Clinical Significance of an Increased Cochlear 3D Fluid-Attenuated Inversion Recovery Signal Intensity on an MR Imaging Examination in Patients with Acoustic Neuroma

D.Y. Kim, J.H. Lee, M.J. Goh, Y.S. Sung, Y.J. Choi, R.G. Yoon, S.H. Cho, J.H. Ahn, H.J. Park, and J.H. Baek

ABSTRACT

BACKGROUND AND PURPOSE: The increased cochlear signal on FLAIR images in patients with acoustic neuroma is explained by an increased concentration of protein in the perilymphatic space. However, there is still debate whether there is a correlation between the increased cochlear FLAIR signal and the degree of hearing disturbance in patients with acoustic neuroma. Our aim was to investigate the clinical significance of an increased cochlear 3D FLAIR signal in patients with acoustic neuroma according to acoustic neuroma extent in a large patient cohort.

MATERIALS AND METHODS: This retrospective study enrolled 102 patients with acoustic neuroma, who were divided into 2 groups based on tumor location; 22 tumors were confined to the internal auditory canal and 80 extended to the cerebellopontine angle cistern. Pure tone audiometry results and hearing symptoms were obtained from medical records. The relative signal intensity of the entire cochlea to the corresponding brain stem was calculated by placing regions of interest on 3D FLAIR images. Statistical analysis was performed to compare the cochlear relative signal intensity between the internal auditory canal acoustic neuroma and the cerebellopontine angle acoustic neuroma. The correlation between the cochlear relative signal intensity and the presence of hearing symptoms or the pure tone audiometry results was investigated.

RESULTS: The internal auditory canal acoustic neuroma cochlea had a significantly lower relative signal intensity than the cerebellopontine angle acoustic neuroma cochlea (0.42 ± 0.15 versus 0.60 ± 0.17 , $P < .001$). The relative signal intensity correlated with the audiometric findings in patients with internal auditory canal acoustic neuroma ($r = 0.471$, $P = .027$) but not in patients with cerebellopontine angle acoustic neuroma ($P = .427$). Neither internal auditory canal acoustic neuroma nor cerebellopontine angle acoustic neuroma showed significant relative signal intensity differences, regardless of the presence of hearing symptoms ($P > .5$).

CONCLUSIONS: The cochlear signal on FLAIR images may be an additional parameter to use when monitoring the degree of functional impairment during follow-up of patients with small acoustic neuromas confined to the internal auditory canals.

ABBREVIATIONS: AN = acoustic neuroma; CPA = cerebellopontine angle; IAC = internal auditory canal; PTA = pure tone audiometry; rSI = relative signal intensity

The fluid of the inner ear is normally suppressed on 3D fluid-attenuated inversion recovery MR images. Increased signal intensity of the fluid on FLAIR MR images has been reported in various diseases, including sudden sensorineural hearing loss,

labyrinthine hemorrhage, otosclerosis, Ramsay Hunt syndrome, and acoustic neuromas (ANs).¹⁻⁶ The increased cochlear signal on FLAIR images in patients with ANs is explained by an increased concentration of protein in the perilymphatic space.⁷⁻¹²

FLAIR MR imaging is sensitive to fluids with a high protein content.¹³⁻¹⁷ Furthermore, 3D-FLAIR imaging can minimize the undesired inflow artifacts of CSF flow, has a higher signal-to-noise ratio and spatial resolution, and allows recognition of subtle compositional changes of the inner ear fluid.¹⁸⁻²¹ Therefore, one can assume that the increased protein content in the cochlear perilymph of patients with ANs can be detected on 3D FLAIR imaging with a high sensitivity and good spatial resolution.

Several researchers recently investigated whether there was a correlation between the increased cochlear FLAIR signal in patients with ANs and the degree of their hearing disturbance.^{2,5}

Received December 31, 2013; accepted after revision February 17, 2014.

From the Departments of Radiology and Research Institute of Radiology (D.Y.K., J.H.L., M.J.G., Y.S.S., Y.J.C., R.G.Y., S.H.C., J.H.B.) and Otorhinolaryngology-Head and Neck Surgery (J.H.A., H.J.P.), University of Ulsan College of Medicine, Asan Medical Center, Seoul, Republic of Korea.

Paper previously presented at: Annual Meeting of the Radiological Society of North America, December 1-6, 2013; Chicago, Illinois.

Please address correspondence to Jeong Hyun Lee, MD, PhD, Department of Radiology and Research Institute of Radiology, University of Ulsan College of Medicine, Asan Medical Center, 86 Asanbyeongwon-Gil, Songpa-Gu, Seoul 138-736, Republic of Korea; e-mail: jeonghlee@amc.seoul.kr

<http://dx.doi.org/10.3174/ajnr.A3936>

Table 1: Clinical findings in the study patients

	Total	Tumor Location	
		IAC (AN _{IAC})	IAC and CPA Cistern (AN _{CPA})
No. of patients	102	22	80
Male/female	58:44	10:12	48:32
Mean age (yr)	49.9 ± 12.4 ^a	50.1 ± 12.6 ^a	49.8 ± 12.4 ^a
Time interval between PTA and MRI (days)	25.7 ± 31.2 ^a	23.1 ± 28.1 ^a	26.4 ± 32.0 ^a
No. of patients with hearing disturbance	70 (69%)	11 (50%)	59 (74%)
No. of patients with tinnitus	45 (44%)	9 (41%)	36 (45%)

^aMean ± SD.

However, no such correlation was found, nor was there any difference in the cochlear FLAIR signal according to AN extent.

Accordingly, the purpose of this study was to investigate the clinical significance of an increased cochlear 3D FLAIR signal in a large number patients with ANs by correlating imaging results with audiometric findings and hearing symptoms according to the extent of ANs after dividing the auditory neuromas into 2 groups: those confined to the internal auditory canal (AN_{IAC}) and those extending into the cerebellopontine cistern (AN_{CPA}).

MATERIALS AND METHODS

Study Participants

This retrospective study was approved by the institutional review board of our hospital.

Between 2008 and 2012, one hundred twenty-two patients with AN who had been admitted to our hospital were identified according to the radiology report data base. Twenty patients were excluded for one of the following reasons: 1) no pretreatment 3D FLAIR MR imaging or pure tone audiometry (PTA) data ($n = 13$); 2) any other causes of hearing problems such as chronic otomastoiditis ($n = 6$) based on conventional T1- and T2-weighted images; or 3) intralabyrinthine schwannoma ($n = 1$). Finally, 102 patients were enrolled in the study, including 64 patients with pathologic confirmation of AN after surgery and 38 patients diagnosed according to the typical MR imaging appearance of AN and who underwent gamma knife radiosurgery. ANs were divided into 2 groups: those confined to the internal auditory canal (22 cases) and those involving the cerebellopontine angle cistern and the internal auditory canal (IAC) (80 cases) (Table 1). The results of the preoperative PTA—conducted within 3 months of the pretreatment MR imaging—were obtained (mean intervals: 23.1 ± 28.1 days for AN_{IAC}; 26.4 ± 32.0 days for AN_{CPA}). We also investigated whether patients had hearing symptoms such as a hearing disturbance or tinnitus according to a review of the electronic medical records.

MR Imaging

All MR imaging examinations, including coronal T1- and T2-weighted, turbo spin-echo, and axial 3D T2 and FLAIR imaging, were performed on a 3T MR imaging unit (Achieva; Philips Healthcare, Best, the Netherlands) with an 8-channel head coil. We used a variable refocusing flip angle technique to obtain isotropic 3D T2-weighted and FLAIR MR images. Axial 3D FLAIR MR imaging was performed with the following parameters: TR = 8000 ms; TE_{eff} = 280 ms; inversion time = 2400 ms; fat saturation = spectral adiabatic inversion recovery; flip angle = 90°; number of signal averages = 1; echo-train length = 80; number of encoding steps = 300; FOV = 180 × 180 mm; matrix = 300 ×

300 (reconstruction matrix = 512 × 512); voxel size = 0.6 × 0.6 × 0.6 mm³; slab number = 1; slab thickness = 40 mm; section thickness = 1.2 mm; spacing between sections = 0.6 mm; acquisition time = 8 minutes 48 seconds; and sensitivity encoding factor = 2.

Axial 3D T2-weighted imaging was performed with the following parameters: TR = 2000 ms; TE_{eff} = 250 ms; flip angle = 90°; number of signal averages = 2; echo-train length = 70; number of encoding steps = 300; FOV = 180 × 180 mm; matrix = 300 × 300 (reconstruction matrix = 512 × 512); voxel size = 0.6 × 0.6 × 0.6 mm³; slab number = 1; slab thickness = 40 mm; section thickness = 1.2 mm; spacing between sections = 0.6 mm; acquisition time = 4 minutes 58 seconds; and sensitivity encoding factor = 2.

Image Analysis

Image analysis was performed with ImageJ, a public domain, Java-based image processing program developed at the National Institutes of Health (Bethesda, Maryland; <http://rsbweb.nih.gov/ij/>). Axial 3D FLAIR and conventional T2-weighted images were reviewed to determine the presence of any coexisting abnormalities in the pons, where a reference region-of-interest was to be placed. Our review revealed no patient with a pontine signal-intensity abnormality. After importing the DICOM files of the axial 3D FLAIR and 3D T2-weighted MR images into ImageJ, a neuroradiologist with 5 years of clinical experience placed ROIs on the cochlea on the affected side of the AN and the corresponding brain stem (Fig 1). ROIs were placed directly on the entire cochlea on each section of the 3D FLAIR images by using the Wand tool of ImageJ, which allowed reliable definition of the boundary of the cochlea with increased signal intensity. When the cochlear signal intensity was insufficient to define the boundary, the region-of-interest placements were checked by reference to 3D T2 MR images at the same level. Circular ROIs of the same size (20 pixels, 7.2 mm²) were carefully placed at the center of the brain stem on the same level as every measured cochlea section. We obtained the mean value of the signal intensities within the ROIs of the cochlea and the brain stem, respectively, and calculated the relative signal intensity (rSI) of the entire cochlea to the brain stem. Another neuroradiologist with 4 years of clinical experience independently measured the signal intensities of the cochlea and the brain stem in the same way. These results were compared to determine the interobserver agreement.

Pure Tone Audiometry

Hearing levels were evaluated with an audiometer (Orbiter-922; Madsen, Taastrup, Denmark) in a sound-insulated chamber. The average hearing levels of bone and air conduction were calculated in ANs as the mean of the hearing levels measured at 250, 500, 1000, 2000, and 4000 Hz based on the American Academy of Otolaryngology Head and Neck Surgery guidelines for AN.²²



FIG 1. AN_{CPA} with markedly increased cochlear signal intensity in a 71-year-old man. *A*, On 3D T2-weighted image (TR = 2000 ms, TE = 250 ms, flip angle = 90°), a large acoustic neuroma (*arrowhead*) is visible in the widened internal auditory canal and the cerebellopontine angle cistern that compresses the brain stem. High signal intensity in the cochlea (*arrow*) is also observed. *B*, On 3D FLAIR image (TR = 8000 ms, TE = 280 ms, inversion time = 2400 ms, flip angle = 90°), the signal intensity of the affected cochlea is markedly increased (*arrow*) in contrast to the suppressed CSF signal. *C*, To measure the signal intensity of the cochlea, a region inside the cochlea was selected by using the Wand tool, which resulted in automatic growing of the region of interest by comparing the signal intensities of all unallocated neighboring pixels with that of the selected region with a predetermined threshold (*yellow circle*). A circular region of interest (*red circle*) was placed on the 3D FLAIR image to measure the signal intensity of the pons. These were repeated for each section showing the cochlear turns. The relative signal intensity of the cochlea is 0.690. The PTA result of this patient was a 42-dB hearing level.



FIG 2. AN_{IAC} with a slightly increased cochlear signal intensity in a 39-year-old woman. *A*, On 3D T2-weighted image (TR = 2000 ms, TE = 250 ms, flip angle = 90°), there is a small acoustic neuroma (*arrowhead*) that is confined to the internal auditory canal. High signal intensity of the cochlear fluid (*arrow*) is also observed. *B*, On 3D FLAIR image (TR = 8000 ms, TE = 280 ms, inversion time = 2400 ms, flip angle = 90°), the signal intensity of the affected cochlea is slightly increased (*arrow*). *C*, Two ROIs are placed on the 3D FLAIR image to measure the signal intensities of the cochlea (*yellow circle*) and the pons (*red circle*) in the same way as described in Fig 1. The relative signal intensity of the cochlea is calculated as 0.294 from the region-of-interest measurement. The PTA result of this patient was an 11-dB hearing level.

Statistical Analysis

Independent *t* tests were performed to compare the rSIs of the cochlea and the PTA results between the AN_{IAC} and AN_{CPA} groups. Pearson correlation tests for AN_{ALL}, AN_{CPA}, and AN_{IAC} were used to investigate the correlation between the PTA and rSI results. Independent *t* tests for AN_{CPA} and Mann-Whitney *U* tests for AN_{IAC} were used to compare the rSIs according to the existence of hearing symptoms. All statistical analyses were performed with the Statistical Package for the Social Sciences (Version 18 for Windows; IBM, Armonk, New York). Interobserver agreement for the rSI of the entire cochlea to the brain stem between 2 observers was investigated by using an intraclass correlation coefficient.

RESULTS

Table 1 summarizes the clinical findings, including the demographic data and the frequency of hearing disturbance or tinnitus, obtained

in this study. Statistical analysis revealed no significant differences in the age, sex, or time interval from PTA to MR imaging examination between those patients with AN_{IAC} and those with AN_{CPA}. Figures 1 and 2 show representative AN_{CPA} and AN_{IAC} cases.

The PTA results and the mean values of the cochlear rSIs in the 3D FLAIR MR images are summarized in Table 2. The PTA results demonstrated that hearing ability was significantly more impaired in patients with AN_{CPA} than in those with AN_{IAC} (46.2 ± 21.4 dB versus 30.3 ± 17.3 dB; *P* < .001). The mean rSI was also significantly higher in patients with AN_{CPA} than in those with AN_{IAC} (0.60 ± 0.17 versus 0.42 ± 0.15; *P* < .001). The correlation test revealed that the hearing impairment measured by PTA and the rSI of the cochlea on 3D FLAIR MR images was moderately correlated in patients with AN_{IAC} (*r* = 0.471; *P* = .027) and weakly correlated in all patients (*r* = 0.277; *P* = .005). There was no significant correlation between the hearing impairment measured by PTA and the cochlear rSI on 3D

Table 2: Pure tone audiometry and rSI results of the cochlea on 3D FLAIR MR images according to tumor location

	Tumor Location			P ^a
	Total	IAC (AN _{IAC})	IAC and CPA Cistern (AN _{CPA})	
Measured cochlear volume (mm ³)	181.98 ± 26.5	177.5 ± 26.0	183.1 ± 25.8	.637
PTA (dB) ^b	43.4 ± 21.5	30.3 ± 17.3	46.2 ± 21.4	<.001
rSI of the cochlea on 3D FLAIR ^b	0.57 ± 0.18	0.42 ± 0.15	0.60 ± 0.17	<.001
Correlation coefficient ^c	<i>r</i> = 0.277	<i>r</i> = 0.471	<i>r</i> = 0.090	
P ^c	.005	.027	.427	

Note:—rSI indicates relative signal intensity divided by the mean of the signal intensities of the corresponding brain stem.

^a P between the results of AN_{IAC} and AN_{CPA}.

^b The results are expressed as the mean ± SD.

^c Correlation coefficient and P between the results of PTA and the rSI of the cochlea on 3D FLAIR images.

Table 3: Cochlear rSI results as determined by the presence of symptoms in patients with AN_{IAC} and AN_{CPA}

Symptoms	Cochlear rSIs	
	AN _{IAC}	AN _{CPA}
Hearing disturbance		
No ^a	0.418 ± 0.150	0.609 ± 0.164
Yes ^a	0.419 ± 0.127	0.615 ± 0.185
P ^b	.870	.600
Tinnitus		
No ^a	0.388 ± 0.139	0.590 ± 0.139
Yes ^a	0.464 ± 0.124	0.628 ± 0.189
P ^b	.443	.506

^a The results are expressed as mean ± SD.

^b P according to the presence of symptoms in patients with AN_{IAC} and AN_{CPA}.

FLAIR MR images in patients with AN_{CPA} (*r* = 0.090; *P* = .427). There was no significant difference in the rSI of the cochlea on 3D FLAIR images according to the presence of subjective hearing symptoms, such as hearing disturbance or tinnitus, in patients with AN_{IAC} and AN_{CPA} (Table 3).

Interobserver agreement for the rSI of the entire cochlea to the pons between 2 observers was excellent, with an intraclass correlation coefficient score of 0.928 (*P* < .001).

DISCUSSION

Our study results can be summarized as follows: 1) The increased cochlear signal of intracanalicular ANs on 3D FLAIR images correlated with the degree of hearing impairment measured by PTA; and 2) the degree of correlation was stronger with tumors confined to the IAC compared with the result of all patients, though there was no correlation with tumors extending to the CPA cistern. In addition, the cochlear signal intensity on 3D FLAIR images was significantly higher in patients with AN_{CPA} than in those with AN_{IAC}.

Previous studies have reported results that contrast with those of our present study. They found no correlation between the audiometric results and the degree of the signal increase of the cochlea^{2,5} or no difference in the rSI of the cochlea on FLAIR images according to tumor extent.^{1,2,5}

Our study has several advantages over previous studies. First, we measured the average signal intensity of the entire cochlea, including all 3 turns on each section of the MR images. In our analyses, the mean rSI of the affected cochlea on 3D FLAIR images was 0.57 ± 0.18 in all patients. A literature review revealed 3 articles that reported increased rSIs of the cochlea on FLAIR images in patients with ANs, ranging from 0.59 to 0.99.^{1,2,5} The wide range in the reported values

may be due to the methods used to measure the cochlear signal. Two of these previous studies used small ROIs at the basal/middle turn (ROIs ranging from 2 to 3 mm²) or at the most hyperintense area (ROIs ranging from 1.2 to 1.5 mm²) of the cochlea,^{1,2} thus resulting in higher mean values such as 0.89 ± 0.18 and 0.99 ± 0.29, respectively. In the study of Yamazaki et al,⁵ the authors drew a region of interest encompassing the 3 turns of each cochlea at the level of the modiolus on a single image, and the result was 0.59 ± 0.18, which is similar to ours. In contrast to these previous studies, we measured the average signal intensity of the entire cochlea in our current study, including all 3 turns on each section of the MR images, to obtain the most representative value of the cochlear signal change.

The reliability of our method is also supported by the almost perfect interobserver agreement for the rSI of the entire cochlea to the brain stem. This interobserver reliability probably results from the objectivity of the analytic method, which used the seeded region-growing method with a constant threshold for the ROIs to determine the boundary between the small cochlea and the adjacent petrous bone. Another advantage of our study is that it contains the largest series of any of the studies to date investigating the correlation between increased cochlear FLAIR signal and the audiometric results in patients with ANs. We, therefore, determined that the degree of signal increase of the cochlea on 3D FLAIR MR images is significantly correlated not only with the tumor extent but also with hearing impairment, contrary to the conclusions of previous reports.

Although an increase in perilymph protein in the affected cochlea is well-established in patients with ANs, the exact pathophysiologic mechanism remains unknown.^{7,10-12} The most plausible mechanisms include blockage of the neuroaxonal transport of proteins caused by compression of the vestibulocochlear nerve, cochlear membrane damage caused by arterial stasis and a consequent increased permeability, and a cell-mediated immune reaction to the inner ear caused by the antigenic properties of AN.^{7-12,23} Among the 3 hypotheses, protein blockage from compression of the corresponding nerve is considered to be the dominant mechanism, with the others being minor in their contribution. Given that the cochlear signal reflecting the protein concentration correlates well with the degree of hearing loss represented by PTA in AN_{IAC} but not in AN_{CPA}, we could hypothesize that the degree of nerve compression is a major contribution to increasing the protein concentration while the tumor is confined to the internal auditory canal. However, the compression effect on nerve bundles would not be proportional to tumor growth when the tumor begins to grow into or originate within the CPA cistern because the CPA cistern is a relatively open space as opposed to the internal auditory canal. This problem should be investigated further with future studies.

The results of our study could be important when following patients before definitive treatment. Many patients are followed with MR imaging examinations before surgery or radiation therapy to see if the tumor is growing. The cochlear signal on FLAIR images may be an additional parameter to use when monitoring

the degree of functional impairment during the follow-up of patients with small ANs confined to the internal auditory canals.

Finally, we selected the brain stem as a reference when calculating the rSI of the cochlea instead of the contralateral cochlea because we believed that the baseline audiometric finding of the contralateral cochlea could vary from individual to individual; this difference might affect the cochlear signal on the 3D FLAIR images and, thus, the fidelity of the method. In contrast, it is easy to rule out any abnormality of the brain stem with both MR imaging and clinical history, and no patient had a brain stem abnormality in our current series. Therefore, we selected the brain stem to calculate the rSI of the cochlea instead of the contralateral cochlea.

Our study has several limitations. Because of its retrospective nature, there may be potential biases related to the heterogeneous participants and the various time intervals between the PTA and MR imaging examinations. However, we strictly applied exclusion criteria and enrolled a large number of patients within a relatively short time interval to minimize any possible influence related to this limitation. Second, to measure cochlear signal intensity, we imported image data to ImageJ and used the Wand tool, which uses a threshold to determine the boundary of the small cochlea showing signal alteration. Although this is a reproducible and reliable method compared with the placement of a hand-drawn region of interest on the small cochlea, it may inaccurately define the cochlear boundaries when the cochlea shows a subtle or no signal increase. To overcome this limitation, we created 3D T2-weighted MR images with the same section thickness as a reference and copied and pasted the ROIs drawn on the 3D T2-weighted MR images onto the same 3D FLAIR images. The interobserver agreement, which was almost perfect, also validated the reliability of our analytic method. Finally, we did not attempt to correlate tumor volume with the cochlear signal intensities on 3D FLAIR images or the results of PTA, especially in patients with tumors confined to the IAC. We believe that further studies could clarify the relationship between them with a larger number of patients with AN_{IAC} in the near future.

CONCLUSIONS

The increased cochlear signal on 3D FLAIR images was proved to correlate with the degree of hearing impairment measured by PTA for small tumors confined to the internal auditory canal. The cochlear signal on FLAIR images may be an additional parameter to use when monitoring the degree of functional impairment during the follow-up of patients with small ANs confined to the internal auditory canals.

ACKNOWLEDGMENTS

The authors gratefully acknowledge the technical support received from Biomedical Imaging Infrastructure, Department of Radiology, Asan Medical Center.

REFERENCES

1. Bhadelia RA, Tedesco KL, Hwang S, et al. **Increased cochlear fluid-attenuated inversion recovery signal in patients with vestibular schwannoma.** *AJNR Am J Neuroradiol* 2008;29:720–23
2. Lee IH, Kim HJ, Chung WH, et al. **Signal intensity change of the labyrinth in patients with surgically confirmed or radiologically diagnosed vestibular schwannoma on isotropic 3D fluid-attenuated inversion recovery MR imaging at 3 T.** *Eur Radiol* 2010;20:949–57
3. Sugiura M, Naganawa S, Nakata S, et al. **3D-FLAIR MRI findings in a patient with Ramsay Hunt syndrome.** *Acta Otolaryngol* 2007;127:547–49
4. Sugiura M, Naganawa S, Sone M, et al. **Three-dimensional fluid-attenuated inversion recovery magnetic resonance imaging findings in a patient with cochlear otosclerosis.** *Auris Nasus Larynx* 2008;35:269–72
5. Yamazaki M, Naganawa S, Kawai H, et al. **Increased signal intensity of the cochlea on pre- and post-contrast enhanced 3D-FLAIR in patients with vestibular schwannoma.** *Neuroradiology* 2009;51:855–63
6. Yoshida T, Sugiura M, Naganawa S, et al. **Three-dimensional fluid-attenuated inversion recovery magnetic resonance imaging findings and prognosis in sudden sensorineural hearing loss.** *Laryngoscope* 2008;118:1433–37
7. O'Connor AF, France MW, Morrison AW. **Perilymph total protein levels associated with cerebellopontine angle lesions.** *Am J Otol* 1981;2:193–95
8. Palva T, Raunio V. **Cerebrospinal fluid and acoustic neuroma specific proteins in perilymph.** *Acta Otolaryngol* 1982;93:201–03
9. Rasmussen N, Bendtzen K, Thomsen J, Tos M. **Antigenicity and protein content of perilymph in acoustic neuroma patients.** *Acta Otolaryngol* 1984;97:502–08
10. Silverstein H. **Labyrinthine tap as a diagnostic test for acoustic neuroma.** *Otolaryngol Clin North Am* 1973;6:229–44
11. Silverstein H, Schuknecht HF. **Biochemical studies of inner ear fluid in man: changes in otosclerosis, Meniere's disease, and acoustic neuroma.** *Arch Otolaryngol* 1966;84:395–402
12. Thomsen J, Saxtrup O, Tos M. **Quantitated determination of proteins in perilymph in patients with acoustic neuromas.** *ORL J Otorhinolaryngol Relat Spec* 1982;44:61–65
13. Busse RF, Hariharan H, Vu A, et al. **Fast spin echo sequences with very long echo trains: design of variable refocusing flip angle schedules and generation of clinical T2 contrast.** *Magn Reson Med* 2006;55:1030–37
14. Chagla GH, Busse RF, Sydnor R, et al. **Three-dimensional fluid attenuated inversion recovery imaging with isotropic resolution and nonselective adiabatic inversion provides improved three-dimensional visualization and cerebrospinal fluid suppression compared to two-dimensional flair at 3 Tesla.** *Invest Radiol* 2008;43:547–51
15. Kallmes DF, Hui FK, Mugler JP. **Suppression of cerebrospinal fluid and blood flow artifacts in FLAIR MR imaging with a single-slab three-dimensional pulse sequence: initial experience.** *Radiology* 2001;221:251–55
16. Melhem ER, Jara H, Eustace S. **Fluid-attenuated inversion recovery MR imaging: identification of protein concentration thresholds for CSF hyperintensity.** *AJR Am J Roentgenol* 1997;169:859–62
17. Mugler JP, Bao S, Mulkern RV, et al. **Optimized single-slab three-dimensional spin-echo MR imaging of the brain.** *Radiology* 2000;216:891–99
18. Naganawa S, Koshikawa T, Nakamura T, et al. **Comparison of flow artifacts between 2D-FLAIR and 3D-FLAIR sequences at 3 T.** *Eur Radiol* 2004;14:1901–08
19. Otake H, Sugiura M, Naganawa S, et al. **3D-FLAIR magnetic resonance imaging in the evaluation of mumps deafness.** *Int J Pediatr Otorhinolaryngol* 2006;70:2115–17
20. Sugiura M, Naganawa S, Sato E, et al. **Visualization of a high protein concentration in the cochlea of a patient with a large endolymphatic duct and sac, using three-dimensional fluid-attenuated inversion recovery magnetic resonance imaging.** *J Laryngol Otol* 2006;120:1084–86
21. Sugiura M, Naganawa S, Teranishi M, et al. **Inner ear hemorrhage in systemic lupus erythematosus.** *Laryngoscope* 2006;116:826–28
22. **Committee on Hearing and Equilibrium guidelines for the evaluation of hearing preservation in acoustic neuroma (vestibular schwannoma): American Academy of Otolaryngology-Head and Neck Surgery Foundation, INC.** *Otolaryngol Head Neck Surg* 1995;113:179–80
23. O'Connor AF, Luxon LM, Shortman RC, et al. **Electrophoretic separation and identification of perilymph proteins in cases of acoustic neuroma.** *Acta Otolaryngol* 1982;93:195–200

Imaging Appearance of the Lateral Rectus–Superior Rectus Band in 100 Consecutive Patients without Strabismus

S.H. Patel, M.E. Cunnane, A.F. Juliano, M.G. Vangel, M.A. Kazlas, and G. Moonis

ABSTRACT

BACKGROUND AND PURPOSE: The lateral rectus–superior rectus band is an orbital connective tissue structure that has been implicated in a form of strabismus termed sagging eye syndrome. Our purpose was to define the normal MR imaging and CT appearance of this band in patients without strabismus.

MATERIALS AND METHODS: Orbital MR imaging and CT examinations in 100 consecutive patients without strabismus were evaluated. Readers graded the visibility of the lateral rectus–superior rectus band on coronal T1WI, coronal STIR, and coronal CT images. Readers determined whether the band demonstrated superotemporal bowing or any discontinuities and whether a distinct lateral levator aponeurosis was seen. Reader agreement was assessed by κ coefficients. Association between imaging metrics and patient age/sex was calculated by using the Fisher exact test.

RESULTS: The lateral rectus–superior rectus band was visible in 95% of coronal T1WI, 68% of coronal STIR sequences, and 70% of coronal CT scans. Ninety-five percent of these bands were seen as a continuous, arc-like structure extending from the superior rectus/levator palpebrae muscle complex to the lateral rectus muscle; 24% demonstrated superotemporal bowing; and in 82% of orbits, a distinct lateral levator aponeurosis was visible. Increasing patient age was negatively associated with lateral rectus–superior rectus band visibility ($P = .03$), positively associated with lateral rectus–superior rectus band superotemporal bowing ($P = .03$), and positively associated with lateral levator aponeurosis visibility ($P = .01$).

CONCLUSIONS: The lateral rectus–superior rectus band is visible in most patients without strabismus on coronal T1WI. The age effect with respect to its visibility and superotemporal bowing could represent age-related connective tissue degeneration.

ABBREVIATIONS: LR-SR band = lateral rectus–superior rectus band

The presence of stereotypic connective tissue structures within the orbit has been recognized on histologic studies for decades.^{1,2} More recent investigations have refined the anatomy and revealed the role these structures play in normal eye motility.³⁻⁷ Critical among these structures are the rectus muscle pulleys.^{8,9} The pulleys are collagenous rings within the Tenon fascia that encircle the rectus muscles near the globe equator. They inflect

rectus muscle paths in a manner analogous to the trochlea with respect to the tendon of the superior oblique muscle.

The rectus muscle pulleys are themselves interconnected by suspensory connective tissue bands that extend between each adjacent rectus muscle pulley. These connective tissue bands variably comprise collagen, elastin, smooth muscle, and fat.⁴

One connective tissue band that has garnered recent clinical interest is the lateral rectus–superior rectus band (LR-SR band). The LR-SR band is an arc-like collagenous band that connects the lateral rectus muscle to the superior muscle complex at the level of their respective pulleys (schematically represented in Fig 1). Degeneration of this band has been implicated in the development of 2 related forms of strabismus: heavy eye syndrome and sagging eye syndrome.^{10,11} Heavy eye syndrome affects elderly patients with high axial myopia. Patients present with esotropia (inward eye deviation) and hypotropia (downward eye deviation) due, in part, to inferior displacement of the lateral rectus muscle and nasal displacement of the superior rectus muscle. The staphylo-

Received September 29, 2013; accepted after revision February 19, 2014.

From the Departments of Radiology (S.H.P., M.E.C., A.F.J., G.M.) and Ophthalmology (M.A.K.), Massachusetts Eye and Ear Infirmary, Boston, Massachusetts; Biostatistics Center (M.G.V.), Massachusetts General Hospital, Boston, Massachusetts; and Department of Ophthalmology (M.A.K.), Boston Children's Hospital, Boston, Massachusetts.

Paper previously presented at: Annual Meeting of the American Society of Neuro-radiology, May 18–23, 2013; San Diego, California.

Please address correspondence to Sohil H. Patel, MD, Department of Radiology, Massachusetts Eye and Ear Infirmary, 243 Charles St, Boston, Massachusetts, 02114; e-mail: spatel57@partners.org

<http://dx.doi.org/10.3174/ajnr.A3943>

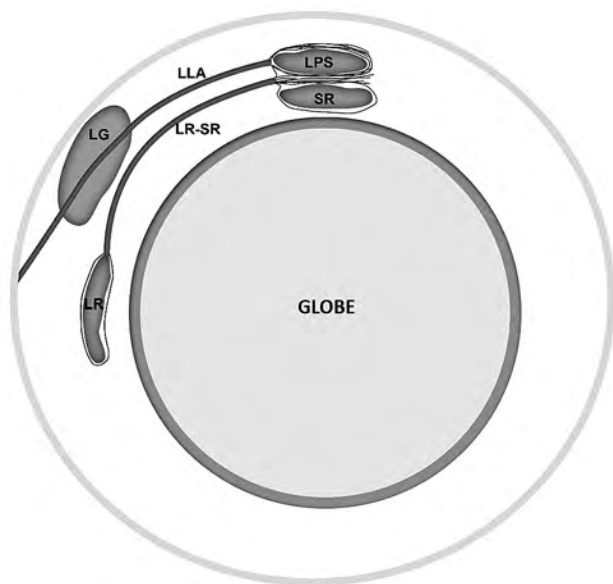


FIG 1. Schematic representation of orbital connective tissues within the superotemporal orbit. LG indicates lacrimal gland; LLA, lateral levator aponeurosis; LPS, levator palpebrae superioris; LR, lateral rectus muscle; SR, superior rectus muscle.

matous globes seen in these patients appear to produce this characteristic extraocular muscle displacement by mass effect.¹² On the other hand, patients with sagging eye syndrome do not have high axial myopia (or staphylomas), yet they have a strabismus pattern similar to that of patients with heavy eye syndrome. In sagging eye syndrome, it is speculated that degeneration of the LR-SR band allows inferior displacement of the lateral rectus muscle and pulley. Evidence for this theory comes from 2 recent reports demonstrating LR-SR band degeneration in elderly patients with strabismus, using an experimental MR imaging technique in which a quasicoronal imaging plane was used and gaze direction was controlled.^{10,11}

No prior studies have focused on defining the normal MR imaging appearance of the LR-SR band in a large cohort of patients without strabismus, to our knowledge. Moreover, no reports exist on the 3T MR imaging or CT appearance of the LR-SR band in clinical orbital imaging examinations. The purpose of this study was to define the normal appearance of the LR-SR band in patients without strabismus on clinical 3T MR imaging scans of the orbits. When available, the CT appearance of the band is also characterized.

MATERIALS AND METHODS

Patient Selection

Institutional review board approval for this Health Insurance Portability and Accountability Act–compliant retrospective review of patient data was obtained.

Patients who underwent orbital MR imaging examinations at our institution from June 2012 to October 2012 were candidates for inclusion in this study. The medical records and imaging examinations of these patients were reviewed. Patients were excluded from the study for any of the following: 1) strabismus, 2) high axial myopia (worse than -4.5 diopters), 3) staphyloma, 4) pathology affecting the location of the LR-SR band, and 5) lack of

coronal nonfat suppressed T1 and/or coronal STIR images of the orbits. One hundred patients who underwent orbital MR imaging examinations from June 2012 to October 2012 met the study criteria and were included in this study. There were 60 women and 40 men. Patient ages ranged between 9 and 81 years (mean, 50 ± 16 years). Patients underwent orbital imaging examinations for the following indications: mass/tumor ($n = 27$), unexplained vision loss or optic neuropathy ($n = 25$), suspected optic neuritis ($n = 13$), orbital infection/inflammation ($n = 10$), suspected ischemic optic neuropathy ($n = 5$), elevated intraocular pressure ($n = 5$), elevated intracranial pressure ($n = 4$), cranial nerve palsy ($n = 3$), and other ($n = 8$).

Imaging Technique

MR imaging examinations were performed on a 3T Achieva (Philips Healthcare, Best, the Netherlands) MR imaging scanner using an 8-channel phased array coil. Coronal T1-weighted imaging of the orbits was performed with the following parameters: TR/TE = 659/11 ms, FOV = 165 cm², section thickness = 3 mm, gap = 0.3 mm, matrix = 472 × 469, NEX = 2. Coronal STIR imaging of the orbits was performed with the following parameters: TR/TE = 3800/30 ms, FOV = 160 cm², section thickness = 3 mm, gap = 0.6 mm, matrix = 268 × 259, NEX = 2.

CT examinations were performed on a Somatom Sensation (Siemens, Erlangen, Germany) multidetector row CT scanner, at 120 kV(peak) and 200 mA, by using a pitch of 0.8 mm, collimation of 0.6 mm, reconstructed with 2-mm coronal section thickness.

Image Analysis

The MR imaging examinations were evaluated by 2 independent reviewers: a fifth-year neuroradiology attending and a first-year neuroradiology fellow. The reviewers characterized the appearance of the LR-SR band on coronal non-fat-suppressed T1-weighted images and coronal STIR sequences (the LR-SR band was not clearly visible in the axial and sagittal imaging planes). Each reader independently determined the following metrics (yes or no): 1) Is the LR-SR band visible on coronal non-fat-suppressed T1-weighted images? 2) Is the LR-SR band visible on coronal STIR images? 3) When visible, is the LR-SR band seen as a continuous, uninterrupted structure from the superior muscle complex to the lateral rectus? 4) When visible, does the LR-SR band demonstrate superotemporal bowing (indicated by extension of any component of the LR-SR band lateral to the lateral rectus muscle and/or superior to the superior muscle complex)? 5) Is a distinct lateral levator aponeurosis visible? If a CT scan through the orbits was available in any patient, LR-SR band visibility on CT was determined on the basis of coronal reformations. After independent collection of the data, the readers reviewed, in consensus, any case over which they disagreed on the T1WI visibility of the band and identified potential factors that led to discrepancies. To familiarize themselves with the appearance of the LR-SR band, the readers reviewed the available literature depicting the LR-SR band on imaging studies and consulted with an experienced strabismus surgeon (M.A.K.) to ensure correct identification of the band.

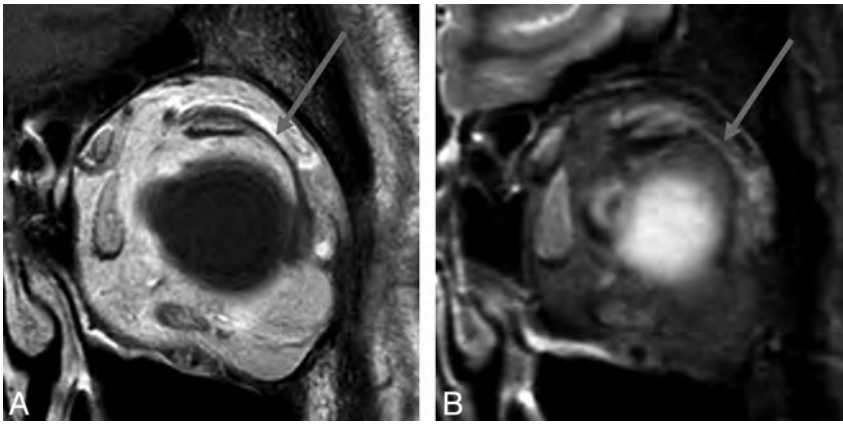


FIG 2. MR imaging appearance of the LR-SR band in a 44-year-old woman. Coronal T1-weighted image (A) and coronal STIR image (B) of the left orbit demonstrate the LR-SR band (arrows) as a curvilinear structure extending from the superior margin of the lateral rectus muscle to the lateral margin of the superior rectus/levator palpebrae superioris muscle complex.

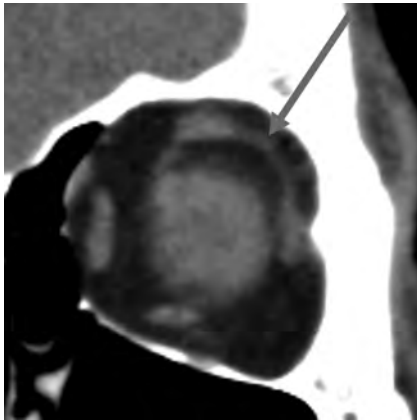


FIG 3. CT appearance of the LR-SR band in a 54-year-old woman. Coronal image of the left orbit demonstrates the LR-SR band (arrow).

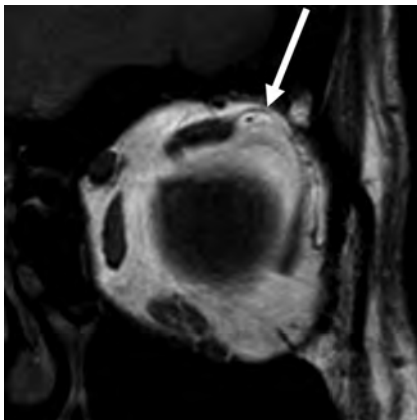


FIG 4. LR-SR band bowing in a 54-year-old woman. Coronal T1-weighted image of the left orbit shows superior bowing of the LR-SR band (arrow), higher than the upper margin of the superior muscle complex.

Statistical Analysis

The imaging metrics determined by each reader were tabulated. Reader agreement was assessed by κ coefficients. The Fisher exact test was used to determine correlation between age and sex with each of the imaging metrics. P value $< .05$ was considered statistically signifi-

cant. Statistical analysis was performed with R software (<http://www.r-project.org/>).¹³

RESULTS

The LR-SR band was visible in 95% of orbits on coronal non-fat-suppressed T1-weighted sequences and 68% of orbits on coronal STIR sequences (Fig 2). A CT scan through the orbits was available in 23 patients. The LR-SR band was visible in 70% of orbits on coronal CT reformations (Fig 3). For both readers, in every case in which the LR-SR band was visible on the STIR sequence or CT, it was also visible on the T1-weighted sequence.

In 95% of cases, the LR-SR band was seen as an uninterrupted structure extending from the lateral margin of the superior rectus/levator palpebrae muscle complex to the superior margin of the lateral rectus muscle (no discontinuities within the band). Twenty-four percent of visible LR-SR bands demonstrated superotemporal bowing (Fig 4). In most cases of superotemporal bowing, it was the posterior segment of the LR-SR band that was bowed. In 82% of orbits, a distinct lateral levator aponeurosis was visible (Fig 5).

Data per reader are displayed in Table 1. The calculated κ coefficients between readers were 0.38 for T1 visibility, 0.26 for STIR visibility, 0.60 for CT visibility, 0.22 for continuous/discontinuous scores, 0.33 for superotemporal bowing scores, and 0.59 for lateral levator aponeurosis visibility scores. With respect to T1 visibility, of 200 cases, there were 12 disagreements between the readers; in all 12 cases, reader 1 detected the LR-SR band and reader 2 did not. With respect to STIR visibility, there were 74 disagreements between the readers; in 73 of these cases, reader 1 detected the LR-SR band and reader 2 did not. In 184 of 200 cases (92%), the readers independently agreed that the LR-SR band was visible on T1WI. In 173 of the 200 cases (87%), the readers independently agreed that the LR-SR band was both visible on T1WI and continuous.

After independent collection of the data, the readers reviewed, in consensus, the 12 cases over which they disagreed on T1WI visibility of the band. In consensus, the readers deemed the LR-SR band visible in 9 of the 12 cases and not visible in 3 of the 12 cases. The readers identified potential factors that led to discrepancies in these 12 cases. These included the following: close apposition of the LR-SR band to globe surface (5 cases); inhomogeneous orbital fat (4 cases); patient motion (2 cases); and a very thin band (1 case).

Data were further analyzed by using the Fisher exact test. A negative association was demonstrated between increasing quartiles of age and T1 visibility of the LR-SR band ($P = .03$). A positive association was demonstrated between increasing quartiles of age and superotemporal bowing of the LR-SR band ($P = .03$). A positive association was demonstrated between increasing quartiles of age and visibility of a distinct lateral levator aponeurosis ($P = .01$). No significant correlation was demonstrated between age and the remaining imaging metrics. Table 2 displays imaging



FIG 5. MR imaging appearance of the LR-SR band and the lateral levator aponeurosis in a 50-year-old man. Consecutive coronal T1-weighted images of the right orbit, from posterior (A) to anterior (C), show that the lateral levator aponeurosis (white arrows) lies superior and temporal to the LR-SR band (gray arrows) and traverses the lacrimal gland.

Table 1: Data per reader

	LR-SR Visible on TIWI ^a	LR-SR Visible on STIR ^a	LR-SR Visible on CT ^a	LR-SR Continuous ^b	LR-SR Bowing ^c	LLA Visible ^d
Reader 1	98%	86%	63%	97%	22%	79%
Reader 2	92%	50%	76%	93%	26%	85%

Note:—LLA indicates lateral levator aponeurosis.

^a The percentage of cases in which the LR-SR band was visible on the given imaging modality/sequence.

^b When visible, the percentage of cases in which the LR-SR band formed a continuous structure extending from the superior muscle complex to the lateral rectus muscle (ie, no gaps or discontinuities).

^c When visible, the percentage of cases in which the LR-SR band demonstrated superotemporal bowing.

^d The percentage of cases in which the lateral levator aponeurosis was visible, distinct from the LR-SR band.

Table 2: Imaging metrics per patient age quartile^a

	Quartile 1	Quartile 2	Quartile 3	Quartile 4	P Value
LR-SR visible on TIWI ^b	96%	99%	95%	90%	.03
LR-SR continuous ^c	95%	96%	95%	91%	.40
LR-SR bowing ^d	19%	17%	28%	34%	.03
LLA visible ^e	73%	77%	89%	87%	.01

Note:—LLA indicates lateral levator aponeurosis.

^a Quartile 1: 9–39 years of age; quartile 2: 40–49 years of age; quartile 3: 50–61 years of age; quartile 4: 62–81 years of age.

^b The percentage of cases in which the LR-SR band was visible on TIWI.

^c The percentage of cases in which the LR-SR band was visible as a continuous structure extending from the superior muscle complex to the lateral rectus muscle (ie, no gaps or discontinuities).

^d The percentage of cases in which the LR-SR band demonstrated superotemporal bowing.

^e The percentage of cases in which the lateral levator aponeurosis was visible, distinct from the LR-SR band.

metrics per age quartile. There was no sex correlation with any of the imaging metrics.

DISCUSSION

We describe the normal appearance of the LR-SR band on clinical imaging examinations in a large cohort of patients without strabismus, both on 3T MR imaging and CT. Our results indicate that the LR-SR band is a readily visible structure on coronal T1-weighted images obtained without fat suppression. Visibility of the band is much less reliable with coronal STIR sequences and coronal CT. When visible on MR imaging, the band appears as a hypointense, arc-like structure extending from the superior margin of the lateral rectus muscle to the lateral margin of the superior rectus/levator palpebrae muscle complex. On CT, the band appears as a soft-tissue attenuation structure conforming to its shape on the corresponding MR imaging. Of note, it has previously been stated that the LR-SR band is not visible on CT¹¹; our

results indicate that CT does, in fact, display the band in a substantial majority of orbits.

Both LR-SR band discontinuity (or “rupture”) and superotemporal displacement have been reported as features of band degeneration in patients with strabismus.^{10,11} In our cohort of patients without strabismus, we report the appearance of a noncontinuous LR-SR band in 5% of cases and superotemporal bowing of the LR-SR band in 24% of cases. These results indicate that band discontinuity may represent a more specific sign of pathologic band degeneration than superotemporal bowing. LR-SR band “thinning” has also been described as a feature of band degeneration.^{10,11} We found no reliable criteria with which to distinguish “thick” and “thin” LR-SR bands, so we did not assess LR-SR bands for this feature.

Our results demonstrate a negative age effect with respect to LR-SR band visibility

and a positive age effect with respect to superotemporal bowing of the LR-SR band. These findings may represent normal age-related connective tissue degeneration and laxity of the LR-SR band. Supportive evidence for this phenomenon comes from histologic investigations by Rutar and Demer,¹¹ demonstrating progressive attenuation and superotemporal displacement of the LR-SR band in specimens of progressively older individuals.

The lateral levator aponeurosis is a slip of connective tissue extending from the lateral aspect of the levator palpebrae superioris, through the lacrimal gland, to the orbital wall near the lateral canthus.⁴ This structure is normally located superior and temporal to the LR-SR band. The study by Rutar and Demer¹¹ reported the finding that the LR-SR band was indistinguishable from the overlying lateral levator aponeurosis in the specimen of the oldest patient examined histologically but it was distinct from the lateral levator aponeurosis in the other specimens. Thus, we expected the

lateral levator aponeurosis to be more difficult to visualize in older patients than in younger patients. Our findings showed the opposite result: The lateral levator aponeurosis is easier to see in older individuals. We hypothesize that this is due to increased fat content within the lacrimal gland. On non-fat-suppressed T1-weighted images, this provides higher contrast between the hypointense aponeurosis and the surrounding hyperintense lacrimal gland.

Our reported κ values are mixed, with some imaging metrics showing low levels of interreader agreement. This finding is not unexpected in the evaluation of a structure not previously characterized in the radiology literature. Moreover, we evaluated a group of nominally healthy (ie, without strabismus) patients. Therefore, abnormalities of the LR-SR band (nonvisibility, bowing, discontinuity) are de-emphasized by design. When present in our patient cohort, these abnormalities are expected to be more subtle and infrequent than those seen in patients with strabismus, also predicting that κ values might be negatively affected. However, despite the relatively low κ values, the readers independently showed agreement in identifying a continuous LR-SR band in most orbits on T1WI.

In the course of their consensus review, the readers identified several factors that potentially led to the discrepancies

(and which, in general, may complicate the confident identification of the LR-SR band). These factors included the following: the close apposition of the LR-SR band to the globe surface, inhomogeneous orbital fat, patient motion, and very thin bands.

There are limitations to our study. No histologic correlate was provided for the structures determined to represent the LR-SR band and the lateral levator aponeurosis. Thus, in cases in which the LR-SR band was not visible, it is unclear whether the band was not present or whether the lack of visibility represented a limitation in the sensitivity of our imaging technique. It is also possible that orbital connective tissues are better imaged with MR imaging sequences other than those evaluated in this study. For instance, in our limited experience, we have found that steady-state high-resolution T2-weighted sequences (eg, CISS or FIESTA) can provide excellent delineation of the LR-SR band and the lateral levator aponeurosis, with thin-section reconstructions and no intersection gap (Fig 6). Finally, CT scans were available in only a minority of our patients. Nonetheless, it seems clear from our experience that CT is far less reliable in imaging orbital connective tissues than MR imaging, mainly due to worse contrast resolution.

The role of imaging the LR-SR band in clinical practice remains unclear. While heavy eye syndrome and sagging eye syndrome are diagnosed mainly on clinical grounds, early reports indicate that orbital MR imaging may add diagnostic specificity in the work-up of these disorders. In particular, it can readily clinch the diagnosis of heavy eye syndrome (Fig 7). Imaging is also useful in excluding other causes of strabismus (mass lesions, infarcts, and so forth). It is conceivable that imaging findings might help stratify patients with strabismus in whom the outcomes of surgical therapies differ. Further studies will be required to answer such questions and confirm the clinical use of imaging in the management of heavy eye and sagging eye syndromes.

Other questions of potential clinical import relate to the significance of the LR-SR band beyond its physiologic role as a suspensory ligament. For instance, it is possible that the LR-SR band constrains the spread of orbital pathology in a manner analogous to the orbital septum.^{14,15} Anecdotally, we have observed several

cases of extraconal orbital tumors that seem to displace, but not clearly transgress, the LR-SR band (Fig 8). Perhaps some pathologies more frequently displace and/or transgress the LR-SR band than others. If so, these distinctions might improve diagnostic specificity when evaluating orbital lesions on imaging studies and affect surgical approaches to orbital lesions.

CONCLUSIONS

The LR-SR band is readily visible in clinical orbital imaging studies of patients without strabismus. The LR-SR band is seen in 95% of orbits on coronal T1-weighted images obtained without fat

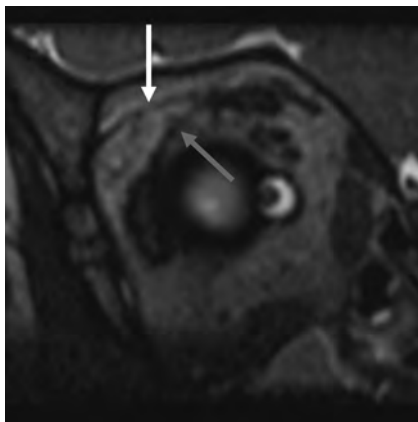


FIG 6. Coronal image of the right orbit from a CISS sequence in a 5-year-old boy displays the LR-SR band (gray arrow) and the lateral levator aponeurosis (white arrow).

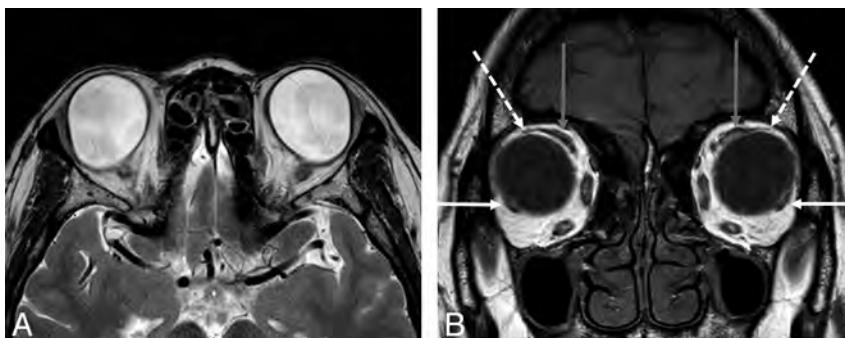


FIG 7. A 65-year-old woman with heavy eye syndrome who presented with high myopia and extreme esotropia (inward eye deviation), resulting in poor peripheral vision. Axial T2WI (A) shows large bilateral staphylomas and esotropia. Coronal T1WI (B) shows thinned/incomplete LR-SR bands (white dashed arrows) stretched over the enlarged globes and nasal displacement of the superior muscle complexes (gray arrows) and inferior displacement of the lateral rectus muscles (white solid arrows).

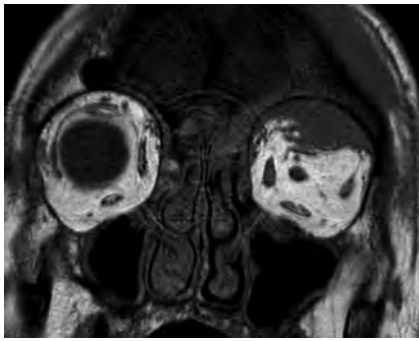


FIG 8. A 74-year-old man with B-cell lymphoma. Coronal precontrast T1-weighted image demonstrates lymphoma involving the superotemporal left orbit. Tumor appears to cause inferior bowing/displacement of the LR-SR band but does not definitely transgress it. Note the normal LR-SR band in the right orbit.

suppression. It nearly always appears as an uninterrupted, arc-like structure extending from the lateral rectus to the superior rectus/levator palpebrae muscle complex. There is an age effect with respect to visibility and superotemporal bowing of the LR-SR band, possibly representing normal age-related connective tissue degeneration of the band. The lateral levator aponeurosis is more easily visible with increasing age, possibly due to increased fat content within the lacrimal glands of older individuals.

Disclosures: Melanie A. Kazlas—UNRELATED: Employment: I am a pediatric ophthalmologist employed by Boston Children's Ophthalmology Foundation, Grants/Grants Pending: Children's Hospital Boston Ophthalmology Foundation In-House Grant of \$25,000 to study effect of light deprivation in amblyopia, Payment for Lectures (including service on Speakers Bureaus): invited lecturer, Ophthalmic Anesthesia Society (September 11, 2013). Gul Moonis—UNRELATED: Other: Grand Rounds Beth Israel, New York (honorarium).

REFERENCES

1. Koornneef L. New insights in the human orbital connective tissue: result of a new anatomical approach. *Arch Ophthalmol* 1977;95:1269–73
2. Koornneef L. Details of the orbital connective tissue system in the adult. *Acta Morphol Neerl Scand* 1977;15:1–34
3. Demer JL. Pivotal role of orbital connective tissues in binocular alignment and strabismus: the Friedenwald lecture. *Invest Ophthalmol Vis Sci* 2004;45:729–38
4. Kono R, Poukens V, Demer JL. Quantitative analysis of the structure of the human extraocular muscle pulley system. *Invest Ophthalmol Vis Sci* 2002;43:2923–32
5. Miller JM. Understanding and misunderstanding extraocular muscle pulleys. *J Vis* 2007;7:11–15
6. Miller JM, Demer JL, Poukens V, et al. Extraocular connective tissue architecture. *J Vis* 2003;3:240–51
7. Miller JM. Functional anatomy of normal human rectus muscles. *Vision Res* 1989;29:223–40
8. Clark RA, Miller JM, Demer JL. Three-dimensional location of human rectus pulleys by path inflections in secondary gaze positions. *Invest Ophthalmol Vis Sci* 2000;41:3787–97
9. Demer JL. The orbital pulley system: a revolution in concepts of orbital anatomy. *Ann N Y Acad Sci* 2002;956:17–32
10. Chaudhuri Z, Demer JL. Sagging eye syndrome: connective tissue involution as a cause of horizontal and vertical strabismus in older patients. *JAMA Ophthalmol* 2013;131:619–25
11. Rutar T, Demer JL. “Heavy eye” syndrome in the absence of high myopia: a connective tissue degeneration in elderly strabismic patients. *J AAPOS* 2009;13:36–44
12. Kowal L, Troski M, Gilford E. MRI in the heavy eye phenomenon. *Aust N Z J Ophthalmol* 1994;22:125–26
13. R Core Team. **R: A language and environment for statistical computing.** *R Foundation for Statistical Computing* 2013. www.R-project.org
14. Botting AM, McIntosh D, Mahadevan M. Paediatric pre- and post-septal peri-orbital infections are different diseases: a retrospective review of 262 cases. *Int J Pediatr Otorhinolaryngol* 2008;72:377–83
15. Wald ER. Periorbital and orbital infections. *Pediatr Rev* 2004;25:312–20

Screening CT Angiography for Pediatric Blunt Cerebrovascular Injury with Emphasis on the Cervical “Seatbelt Sign”

N.K. Desai, J. Kang, and F.H. Chokshi



ABSTRACT

BACKGROUND AND PURPOSE: There are no standard screening guidelines to evaluate blunt cerebrovascular injury in children. The purpose of this retrospective study was to understand the clinical and radiologic risk factors associated with pediatric blunt cerebrovascular injury on CTA of the neck with primary attention to the cervical “seatbelt sign.”

MATERIALS AND METHODS: Radiology reports from 2002 to 2012 were queried for the examination “CTA neck.” The electronic medical record was reviewed for mechanism of injury, Glasgow Coma Scale score, and physical examination findings. Radiology reports from adjunct radiographic studies were reviewed. CTA neck examinations with reported blunt cerebrovascular injury were reviewed to confirm imaging findings. Patients with penetrating injury or those without a history of trauma were excluded.

RESULTS: Four hundred sixty-three patients underwent CTA of the neck; 137 had blunt trauma. Forty-two of 85 patients involved in a motor vehicle collision had a cervical seatbelt sign; none had blunt cerebrovascular injury. Nine vessels (4 vertebral arteries, 4 ICAs, 1 common carotid artery) in 8 patients ultimately were diagnosed with various grades (I–IV) of blunt cerebrovascular injury, representing 5.8% (8/137) of the population screened for blunt neck trauma. The mean Glasgow Coma Scale score was significantly lower ($P = .02$) in the blunt cerebrovascular injury group versus the non-blunt cerebrovascular injury group. Although not statistically significant, patients with blunt cerebrovascular injury had a higher tendency to have additional traumatic injuries, primarily basilar skull fractures ($P = .05$) and intracranial hemorrhage ($P = .13$).

CONCLUSIONS: A common indication for neck CTA, the cervical seatbelt sign, was not associated with blunt cerebrovascular injury. With the exception of Glasgow Coma Scale score, no single risk factor was statistically significant in predicting vascular injury in this series.

ABBREVIATIONS: BCVI = blunt cerebrovascular injury; EAST = Eastern Association for the Surgery of Trauma; GCS = Glasgow Coma Scale; MVC = motor vehicle collision; NPTR = National Pediatric Trauma Registry

The incidence of blunt cerebrovascular injury (BCVI) in adult-predominant series is estimated at approximately 1% and as high as 2.7% in patients with polytrauma.^{1,2} Despite its fairly low incidence, BCVI has potentially catastrophic neurologic sequelae, including serious morbidity with dense neurologic deficits necessitating costly long-term medical care and even death.³ Most cur-

rent literature supports fairly liberal screening of adult patients based on these studies, especially with the advent of noninvasive CTA having replaced conventional catheter-based angiography.^{4,5} Although screening criteria for adults seem to be well-established,^{6,7} there are currently no standard screening guidelines to evaluate BCVI in children. Moreover, the current recommendations of the Eastern Association for the Surgery of Trauma (EAST), the organization that has published screening guidelines based on the most extensive review of the available literature on this topic, including 68 references from the National Library of Medicine/National Institutes of Health MEDLINE data base, state that pediatric patients should be evaluated by using the same criteria as those used in the adult population.⁸ This recommendation is based on limited case series data, however, for which prospective scientific evidence is lacking.⁸

Two recent retrospective studies have evaluated the applicability of adult criteria set forth by EAST to the pediatric population.^{9,10} While one study supported the notion that risk factors for

Received November 17, 2013; accepted after revision February 1, 2014.

From the Division of Neuroradiology (N.K.D.), Department of Radiology and Imaging Sciences, Emory University School of Medicine, Children’s Healthcare of Atlanta, Atlanta, Georgia; Department of Biostatistics and Bioinformatics (J.K.), Department of Radiology and Imaging Sciences, Emory University School of Medicine and Rollins School of Public Health, Atlanta, Georgia; and Division of Neuroradiology (F.H.C.), Department of Radiology and Imaging Sciences, Emory University School of Medicine, Atlanta, Georgia.

Please address correspondence to Nilesh K. Desai, MD, Department of Radiology and Imaging Sciences, Division of Neuroradiology, Emory University School of Medicine, Children’s Healthcare of Atlanta, 1364 Clifton Rd. NE, EUH B115, Atlanta, GA 30322; e-mail: nilesh.k.desai@emory.edu



Indicates article with supplemental on-line table.

<http://dx.doi.org/10.3174/ajnr.A3916>



FIG 1. Cervical seatbelt sign. Dermal bruising at the base of the neck, just cephalad to the clavicle indicating injury by a seatbelt. Courtesy of Matthew Clifton, MD, Children's Healthcare of Atlanta, Atlanta, Georgia.

BCVI in children parallel those of adults, the other, in contradistinction, demonstrated that as many as two-thirds of patients experiencing stroke from BCVI did not meet screening criteria according to those used for adults.^{9,10}

At our institution, adult criteria seem to be generally followed by our trauma team colleagues. One criterion contained within the criteria proposed for the general population by authors such as Biffi et al⁶ is that of seatbelt abrasion or seatbelt injury to the anterior neck, the so-called cervical "seatbelt sign" (Fig 1).⁸ While the EAST recommends that the seatbelt sign not be used as an independent criterion without additional risk factors and physical examination findings to stratify patients for screening,⁸ it remains a physical sign that even in isolation, often prompts clinicians to pursue CTA of the neck at our institution and perhaps at many others.

The purpose of this retrospective study was to further understand the risk factors associated with BCVI in children by examining various clinical and radiologic findings on CTA of the neck and adjunct imaging studies, with a primary regard for the predictive value of the cervical seatbelt sign for BCVI.

MATERIALS AND METHODS

This retrospective study was approved by our local institutional review board and is in compliance with the Health Insurance Portability and Accountability Act. From the PACS at 2 pediatric trauma centers within our institution (a level I and a level II), CTA neck radiology reports between March 2002 and November 2012 were retrieved. The electronic medical record was reviewed for the following: 1) pertinent clinical history; 2) mechanism of injury; 3) Glasgow Coma Scale (GCS) score; and 4) physical examination findings, including the designation by the clinician of cervical seatbelt sign. To consider it a seatbelt injury, the attending pediatric surgeon or pediatric emergency medicine physician must have used terminology explicitly mentioning the presence of seatbelt injury either independently or in cosignature with a trainee note. "Soft-tissue injury of the neck," if so stated, for example, would therefore not qualify as a cervical seatbelt sign for the purpose of this study, even if, in reality, the findings were consistent with a seatbelt injury. Reports from adjunct radiographic, CT, and MR imaging studies performed during the initial trauma encounter were reviewed specifically for internal carotid, common carotid, and vertebral artery injury; intracranial hemorrhage; and

fractures of the cervical spine, skull base, maxillofacial region, ribs, and clavicle. Imaging findings of arterial injury were confirmed by independent review of the CTA by 1 of 2 neuroradiologists with Certificates of Added Qualification, (N.K.D. or F.H.C.) for patients with reported BCVIs. In addition, vascular injury severity was graded according to the injury scale proposed by Biffi et al¹¹: grade I injury indicating intimal irregularity with <25% narrowing, grade II injury indicating dissection or intramural hematoma with >25% narrowing, grade III indicating pseudoaneurysm, grade IV indicating vessel occlusion, and grade V indicating transection with extravasation. All other findings were recorded on the basis of the radiology report alone. Neuroradiologic studies at our institution are interpreted by Certificate of Added Qualification neuroradiologists. Patients with penetrating injury or without history of trauma were excluded.

Neck CTA was performed on 1 of 2 CT scanners: between March 2002 and May 2006, each CTA was performed on a 16-slice unit (Lightspeed VCT; GE Healthcare, Milwaukee, Wisconsin); this was subsequently replaced with a 64-slice unit (Lightspeed VCT; GE Healthcare) in June 2006. Standard helical CTA neck-scanning protocol was used from the aortic arch to the cranial margin of the sella turcica with the technique tailored to each patient with 120 kV(peak) for all patients and a variable manual technique based on weight with predesignated milliampere-second ranging from 200 to 500 and adaptive statistical iterative reconstruction at 10%. Table speed ranged from 19.37 to 39.37 mm/s with a rotation time of 0.4 seconds and a pitch at 0.984. Images were acquired at 0.625-mm section thickness in soft-tissue algorithm. Injection rates and technique, either via central or peripheral intravenous lines, would have varied with age and the caliber of the venous line, with the youngest of children below 15 kg requiring manual injection and all others requiring power injection at 3–4 mL/s (Medrad, Pittsburgh, Pennsylvania). Our policy for CTA is that the patient either already has or that all reasonable attempts are made to establish a 20-ga or larger intravenous line, especially for older children. Power injection is only performed in patients with at least a 22-ga intravenous line. For children under 20 kg, we typically perform a timing delay based on data we have collected at our institution. This includes an 8- to 9-second delay for patients up to 14 kg and a 9- to 10-second delay for patients 15–19 kg. In children \geq 20 kg, a monitoring scan was used, with a small test bolus to calculate the delay time for the actual examination. Optiray 320 (ioversol; Mallinckrodt, St. Louis, Missouri) was administered at a dosage of 2.0 mL/kg with a maximum dosage of 150 mL for all patients.

Statistical Analysis

Contingency tables were created for the presence of BCVI by the CTA and each of the other examinations (CT of the cervical spine, which was performed by default in all patients as a result of the CTA neck coverage, cervical spine radiographs, noncontrast head CT, maxillofacial CT, chest radiographs, and chest CT). Sensitivity, specificity, positive predictive value, and negative predictive value were calculated for the outcome of the CTA and the presence of cervical spine, basilar skull, maxillofacial, rib, and clavicle fractures and intracranial hemorrhage. Descriptive statistics (mean, SD, and frequency) were summarized for GCS score and

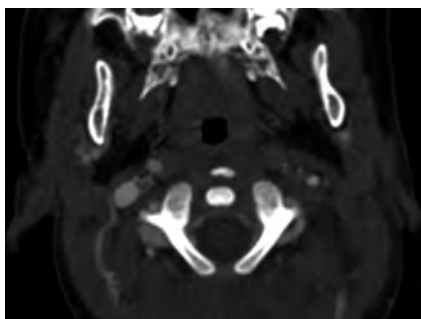


FIG 2. Internal carotid artery injury in patient 6. CTA of the neck demonstrating occlusion of the left internal carotid artery (grade IV injury) at the level of C1 vertebral body in a 1.17-year-old boy who presented neurologically intact after experiencing a witnessed low-speed motor-pedestrian collision.

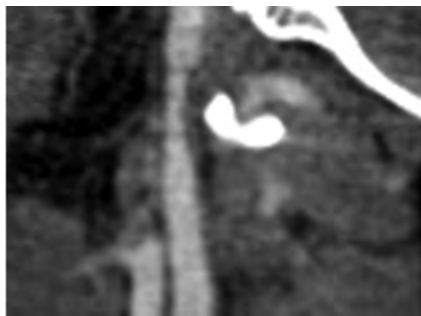


FIG 3. Internal carotid artery injury in patient 3. Sagittal reformat of a neck CTA image showing >25% ICA narrowing related to grade II injury in a 9.92-year-old girl, status post MVC with ejection, who was found unconscious in the field with fixed and dilated pupils.

demographic variables. Also, a Fisher exact test was used to check the independence between the CTA and each of the other examinations. A Wilcoxon test was used to compare GCS scores between BCVI and non-BCVI groups. A logistic regression model by using age to predict BCVI or lack of BCVI was performed.

RESULTS

During the nearly 10-year period, 463 patients underwent CTA of the neck for various indications, of whom, 152 had blunt neck trauma. Fifteen patients were excluded due to incomplete medical charts and documentation of mechanism of injury or because a physical examination could not be obtained. Incomplete medical charts were, in all cases, physician notes that had failed to become available during the transition from paper to electronic medical records, primarily between 2002 and 2004. The average age of patients was 9.60 ± 4.32 years, including 74 male and 63 female patients ranging between 0.67 and 17 years of age, with 18 patients younger than 5 years. The average age of patients involved in a motor vehicle collision (MVC) ($n = 85$) was 9.5 ± 4.39 years, ranging from 1.33 to 17 years of age.

Nine vessels (4 vertebral arteries, 4 ICAs, 1 common carotid artery) in 8 patients ultimately were diagnosed with various grades (I–IV) of BCVI, representing 5.8% (8/137) of the blunt neck trauma population (On-line Table and Figs 2 and 3). The mean age of patients with BCVI was 8.19 ± 6.14 years, ranging from 1.17 to 16 years of age, whereas those without BCVI had a mean age of 9.65 ± 4.20 years, ranging from 0.67 to 17 years of age.

Five patients with vascular injury were not involved in an MVC (On-line Table).

All patients with BCVI had at least 1 nonvascular injury such as cervical spine fracture (Table 1). Nearly statistically significant, patients with BCVI had a higher tendency to have additional traumatic injuries, primarily basilar skull fractures ($P = .05$) and intracranial hemorrhage ($P = .13$) (Table 2). Of the 4 patients with vertebral artery injury, 2/4 had cervical spine fracture, whereas both cervical spine fractures and vertebral artery injuries were found in 2 additional patients. Additionally, 6 of 8 patients with BCVI and 107 of 129 without BCVI had documented GCS scores. In patients with BCVI, the mean GCS score was 8.67 ± 6.22 versus 12.92 ± 3.90 in patients without BCVI. This difference was statistically significant ($P = .02$). Age was not a statistically significant predictive factor for BCVI or a lack of BCVI (logistic regression coefficient = $-.04$, $P = .64$).

Of the patients with BCVI, 3 had neurologic sequelae. One patient, patient 3, an unrestrained ejected motor vehicle passenger, developed cerebral infarction (total MCA distribution) with eventual death secondary to severe closed-head injury with malignant cerebral edema and multicompartimental hemorrhage resulting in transtentorial herniation. Large MCA distribution infarct may have been contributory but not primary to this patient's death (On-line Table). Patient 4 presented with right hemiparesis with MR imaging–confirmed foci of an embolic-type infarction in the left frontal and temporal lobes after an MVC. Another patient, patient 8, presented with head and neck pain, tingling in the hands, facial paresthesias, and subjective oral motor difficulty several days after a dirt bike accident (On-line Table).

Of eighty-five patients involved in an MVC, 42 had a documented cervical seatbelt sign with an average age of 8.5 ± 3.84 years, none of whom had BCVI (positive predictive value = 0). None of the 3 patients with BCVI involved in an MVC had a documented cervical seatbelt sign. Twenty-two additional patients in an MVC had some form of soft-tissue injury to the neck that was not specifically listed as a seatbelt sign. Of these 22 patients, patient 7 demonstrated BCVI with a grade IV right cervical vertebral artery injury. This patient, who later died from severe cerebral edema and hemorrhage with probable upper cervical cord transection, met multiple criteria (EAST criteria) for screening, including a GCS score of 3 and a C4–C5 fracture dislocation injury.

DISCUSSION

The Eastern Association for the Surgery of Trauma has put forth recommendations for screening criteria for BCVI in the adult population based on the most extensive review of references on this topic.⁸ The EAST recommends screening for BCVI in adult patients with any neurologic abnormality that is not explained by a diagnosed traumatic injury and in trauma patients with epistaxis from a suspected arterial source. For asymptomatic, adult blunt trauma patients with the following risk factors screening is also recommended: Glasgow Coma Scale (GCS) score ≤ 8 ; petrous temporal bone fracture, diffuse axonal injury (DAI), cervical spine fracture especially those from C1 to C3, fracture through the foramen transversarium, and those with a rotational component or subluxation and Le Fort II or III facial fractures. While the

Table 1: Associated injuries in patients with and without blunt cerebrovascular injury

	Cervical Spine Fracture		Basilar Skull Fracture		Intracranial Hemorrhage		Maxillofacial Fracture		Rib Fracture		Clavicle Fracture	
	No	Yes	No	Yes	No	Yes	No	Yes	No	Yes	No	Yes
BCVI												
No	108	21	79	24	55	27	9	20	84	11	89	6
Yes	6	2	4	4	3	5	1	2	6	1	6	1
Percentage												
No	83.7	16.2	76.7	23.3	67.1	32.9	31.0	69.0	88.4	11.6	88.4	11.6
Yes	75.0	25.0	50.0	50.0	37.5	62.5	33.3	66.7	85.7	14.3	85.7	14.3

Table 2: Risk factor analysis for blunt cerebrovascular injury based on associated injuries

	PPV	NPV	Sensitivity	Specificity	P Value
Cervical spine fracture	0.09	0.95	0.25	0.84	.62
Basilar skull fracture	0.14	0.96	0.50	0.81	.05
Intracranial hemorrhage	0.16	0.95	0.63	0.67	.13
Maxillofacial fracture	0.09	0.9	0.67	0.31	1
Rib fracture	0.08	0.93	0.14	0.88	1
Clavicle fracture	0.14	0.94	0.14	0.94	.4

Note:—PPV indicates positive predictive value; NPV, negative predictive value.

EAST practice guidelines offer a level III recommendation that pediatric patients be screened by using these same adult criteria, prospective trials evaluating risk factors and therefore screening criteria for children are lacking in the current literature.⁸

Furthermore, the EAST recommends that an isolated cervical seatbelt sign should not be used as a screening reason without other risk factors in the presence of normal physical examination findings; however, the cervical seatbelt sign has been endorsed in retrospective series, including Biffl et al,⁶ as a single criterion for screening for BCVI.⁸ One retrospective review by Rozycki et al¹² addressed the possible clinical relevance of the cervical seatbelt sign. In 131 patients with seatbelt sign, 4 patients (3% of the screened population) were found to have carotid artery injuries using CTA or conventional angiography with the presence of BCVI strongly associated with a GCS score of <14, Injury Severity Score > 16, and clavicle and/or first rib fracture in a statistically significant manner.¹² While the authors in this study concluded that the cervicothoracic seatbelt sign and abnormal neurovascular physical examination findings are an effective combination in screening for BCVI for both adult and pediatric patients,¹² we believe that there is insufficient evidence based on the small number of pediatric patients ($n = 16$) and the relatively mild or even absent additional injuries to definitively recommend such criteria in children.¹² Most interesting, on the basis of the available information in the series by Rozycki et al, the EAST guidelines would not have called for screening in 3 of 4 patients with seatbelt signs and BCVI. Therefore, the recommendation by the EAST regarding the cervical seatbelt sign warrants further investigation in both adults and children.

Our study was performed to address the unresolved issues regarding BCVI screening related to cervical seatbelt injury in children; this criterion is still used at our 2 children's hospitals. Of the 85 children in an MVC, 42 demonstrated a cervical seatbelt injury, but none had BCVI. While there was a higher tendency for patients with BCVI to have polytrauma including basilar skull fracture and intracranial hemorrhage, no single risk factor for BCVI met statistical significance in our series with the exception of GCS score (Table 2). Although GCS score ≤ 8 is used as part of the adult criteria for BCVI screening, our study may offer some

initial information about the importance of the GCS score as a screening marker in the pediatric population.

The incidence of BCVI in children is rare. We found that despite nearly 150 patients undergoing CTA screening for blunt injury, the incidence of BCVI was unsurprisingly small, though we did not calculate an incidence due to the unavailability of the number of admissions for blunt trauma to the emergency department. In a recent retrospective case series of nearly 15,000 patients from the general population by Jones et al⁹ during a 15-year period, only 45 patients were diagnosed by either CTA or conventional angiography with BCVI, representing 0.3% of the admitted population.¹³ Another similar recent pediatric retrospective study by Kopelman et al¹⁰ demonstrated an incidence of 0.9%. Last, in a review of the National Pediatric Trauma Registry (NPTR) in a more remote study between December 1987 and July 1997, only 15 of 57,659 registered patients with blunt trauma were diagnosed with BCVI, representing an incidence of 0.03%.¹³ Admittedly, the relative increase in the incidence found in more recent reviews compared with the NPTR is likely due to increasing physician awareness and use of noninvasive CTA screening.

While it was not our primary goal to directly investigate or propose complete screening criteria for the pediatric population, it is clear that most patients with BCVI in our series met screening criteria as suggested by the EAST recommendations, with the exception of patients 5, 6, and 8, representing a not insignificant 37.5% of the BCVI population. Patient 6 experienced a motor-pedestrian collision with skull base fractures, including temporal bone fractures but without involvement of the petrous portion. Two patients did have evidence of high-force thoracic injuries not only by history (all-terrain vehicle and dirt bike crash) but also by coincident injury as evidenced by first-rib fracture in patient 5 and T4 compression fracture in patient 8, which the EAST recommendations do recognize, along with severe head injury, as pediatric risk factors for BCVI, given the findings from the NPTR.^{8,13} Our results are, thus, generally in agreement with that of Jones et al,⁹ in that adult criteria may not direct clinicians to screen for BCVI in all cases. The inclusion of mechanism, specifically those involving high forces, and significant thoracic injuries may improve such criteria for children. For those patients without BCVI, 89 patients did not meet the EAST screening criteria, whereas 40 did.

There are inherent limitations to our study, many of which originate from the retrospective nature of our series. The primary objective being evaluated, the cervical seatbelt sign, was deemed present on the basis of the clinician specifically recording the exact term in the medical chart. Therefore, while a patient may have had a true cervical seatbelt sign, if the physician only recorded "neck abrasion" or "bruising of the neck," such a patient would not be

deemed to have the sign by our criteria. While we admit that there may have been a subset of patients missed, we considered it important also to ensure that those who were included as having such a clinical sign were with certainty truly positive. Patient 7, in fact, did have recorded "anterior neck swelling" without a recorded seatbelt injury. However, this child was noted to have a GCS score of 3 and severe cervical spine injury, including fracture dislocation at C4–C5 with severe distraction, findings that would warrant screening for BCVI. Another uncorrectable issue is the lack of standardization and agreed-upon clinical findings that qualify as a seatbelt injury. It is conceivable that a light abrasion on the low neck may be entirely dismissed by one clinician, but yet another may have recorded the finding as a cervical seatbelt sign. Further, it is possible that recording such a finding may have been forgotten altogether or not properly assessed due to a variety of factors.

In this series, we chose to include patients by searching a radiology data base of all CTA neck examinations performed since early 2002 followed by an electronic medical chart search for all other information. It is, therefore, possible and certainly likely that a child with a cervical seatbelt injury may have not received a screening CTA, depending on physician judgment and lack or presence of coexisting injuries. While we would assume that this patient population would ultimately not be diagnosed with BCVI, this study did not attempt to evaluate all children presenting to the emergency department with a cervical seatbelt sign but rather investigated a CTA-screened population. Finally, we purposely chose to evaluate children with CTA because this remains the standard for noninvasive screening of adults and children at our institution. For >10 years, since the presence of our 16-slice and now 64-slice CT scanners, CTA has entirely replaced conventional angiography for BCVI screening. We believe it is possible, however, that a small number of patients very early in our retrospective series may have undergone digital subtraction angiography for possible BCVI.

And finally, our series did not include analysis of the presence or type of restraint because such data were often not recorded in the medical records. Car seats and booster seats generally prevent cervical seatbelt injuries by improving the position of the shoulder strap from over the neck to over the shoulder. The seatbelt sign, therefore, should occur less frequently in young patients who are properly restrained in such devices. In fact, car seats with 5-point harnesses seldom cause seatbelt injury because the straps do not cross over the cervicothoracic region. We believe that restraint history and protective effects should be considered in future prospective trials assessing pediatric risk factors for BCVI.

CONCLUSIONS

BCVI is an uncommon occurrence in the pediatric trauma population. A common indication for neck CTA, the cervical seatbelt

sign, was not associated with BCVI. These findings suggest that especially when found in isolation, the seatbelt sign in children may not be an appropriate reason to perform neck CTA, consistent with EAST recommendations. With the exception of GCS score, no single risk factor was statistically significant in predicting vascular injury in this series, though there was a tendency for those with vascular injury to have multiple risk factors, especially basilar skull fractures and intracranial hemorrhage. Larger, multicenter prospective trials evaluating BCVI in children should be undertaken.

Disclosures: Niles K. Desai—UNRELATED: Grants/Grants Pending: Siemens USA,* Comments: DTI metrics using DTI Resolve in patients with cervical myelopathy secondary to spondylosis. Role of coinvestigator with 1% salary support. *Money paid to the institution.

REFERENCES

1. Biffl WL, Moore EE, Ryu RK, et al. **The unrecognized epidemic of blunt carotid arterial injuries: early diagnosis improves neurologic outcome.** *Ann Surg* 1998;228:462–70
2. Mutze S, Rademacher G, Matthes G, et al. **Blunt cerebrovascular injury in patients with blunt multiple trauma: diagnostic accuracy of duplex Doppler US and early CT angiography.** *Radiology* 2005;237:884–92
3. Cothren CC, Moore EE, Ray CE Jr, et al. **Screening for blunt cerebrovascular injuries is cost-effective.** *Am J Surg* 2005;190:845–49
4. Chokshi FH, Munera F, Rivas LA, et al. **64-MDCT angiography of blunt vascular injuries of the neck.** *AJR Am J Roentgenol* 2011;196:W309–15
5. Munera F, Foley M, Chokshi FH. **Multi-detector row CT angiography of the neck in blunt trauma.** *Radiol Clin North Am* 2012;50:59–72
6. Biffl WL, Moore EE, Offner PJ, et al. **Optimizing screening for blunt cerebrovascular injuries.** *Am J Surg* 1999;178:517–22
7. Cothren CC, Moore EE, Biffl WL, et al. **Anticoagulation is the gold standard therapy for blunt carotid injuries to reduce stroke rate.** *Arch Surg* 2004;139:540–45, discussion 545–46
8. Bromberg WJ, Collier BC, Diebel LN, et al. **Blunt cerebrovascular injury practice management guidelines: the Eastern Association for the Surgery of Trauma.** *J Trauma* 2010;68:471–77
9. Jones TS, Berlew CC, Kornblith LC, et al. **Blunt cerebrovascular injuries in the child.** *Am J Surg* 2012;204:7–10
10. Kopelman TR, Berardoni NE, O'Neill PJ, et al. **Risk factors for blunt cerebrovascular injury in children: do they mimic those seen in adults?** *J Trauma* 2011;71:559–64, discussion 564
11. Biffl WL, Moore EE, Offner PJ, et al. **Blunt carotid arterial injuries: implications of a new grading scale.** *J Trauma* 1999;47:845–53
12. Rozycki GS, Tremblay L, Feliciano DV, et al. **A prospective study for the detection of vascular injury in adult and pediatric patients with cervicothoracic seat belt signs.** *J Trauma* 2002;52:618–23, discussion 623–24
13. Lew SM, Frumiento C, Wald SL. **Pediatric blunt carotid injury: a review of the National Pediatric Trauma Registry.** *Pediatr Neurosurg* 1999;30:239–44

Large-Volume Blood Patch to Multiple Sites in the Epidural Space through a Single-Catheter Access Site for Treatment of Spontaneous Intracranial Hypotension

J. Griauzde, J.J. Gemmete, N. Chaudhary, T.J. Wilson, and A.S. Pandey

ABSTRACT

BACKGROUND AND PURPOSE: Spontaneous intracranial hypotension can be a therapeutic challenge to the treating physician. In this study, we present our experience with the administration of a large-volume blood patch to multiple sites in the epidural space through a single-catheter access site.

MATERIALS AND METHODS: A retrospective review was conducted of patients with spontaneous intracranial hypotension who underwent a large-volume blood patch to multiple sites in the epidural space through a single-catheter access site from 2010 to 2012. Patient demographic data, clinical charts, indications for treatment, radiographic images, procedure notes, and postprocedure hospital course were reviewed.

RESULTS: Overall, 9 patients were identified who underwent 20 blood patch procedures. Patients were selected to undergo the large-volume procedure either because they had a failed site-directed epidural blood patch or if imaging demonstrated multiple possible leak sites. There were 6 women and 3 men, with an average age of 33.5 years. The mean volume of blood injected per procedure was 54.1 mL (median = 55 mL; range = 38–70 mL). All patients had an orthostatic headache as one of their presenting symptoms; 22% also presented with neurocognitive decline and behavioral changes; 89% of patients had improvement or resolution of their symptoms; and 80% of patients who had a previously failed site-directed epidural blood or fibrin glue patch improved with a large volume catheter-directed blood patch.

CONCLUSIONS: Our experience supports the use of a large-volume blood patch to multiple sites in the epidural space through a single-catheter access site for the treatment of spontaneous intracranial hypotension. Additionally, our results indicate a role for this procedure in refractory cases of spontaneous intracranial hypotension.

ABBREVIATION: SIH = spontaneous intracranial hypotension

Spontaneous intracranial hypotension (SIH) is a well-recognized entity associated with a CSF leak. The characteristic clinical presentation is a positional headache, which is often severe. CSF leak can occur spontaneously or can be the result of trauma or an iatrogenic cause. Epidural blood patch has long been considered the procedure of choice for treatment of a CSF leak. In cases of SIH or idiopathic intracranial hypotension, the CSF leak site may not be identified or multiple areas of leak may be present. Additionally in iatrogenic cases, the leakage may be refractory to

small-volume single-site injection of epidural blood. Treatment in these cases presents a unique challenge. Administration of a large-volume blood patch at multiple sites in the epidural space is a recently reported novel technique for the treatment of SIH.¹ Direct injection of blood to multiple sites allows directed therapy at suspected leak sites and treatment of occult sites. Additionally, this treatment avoids puncture of the epidural space in the thoracic and cervical spine, making it theoretically less challenging for the operator. We present our experience with the use of a large-volume blood patch to multiple sites in the epidural space through a single-catheter access site for the treatment of SIH.

MATERIALS AND METHODS

This study was approved by the institutional review board at the University of Michigan. We retrospectively reviewed cases of spontaneous or refractory intracranial hypotension that were

Received January 2, 2014; accepted after revision February 18.

From the Departments of Radiology (J.G., J.J.G., N.C.), Neurosurgery (J.J.G., N.C., T.J.W., A.S.P.), and Otolaryngology (J.J.G.), University of Michigan Hospitals, Ann Arbor, Michigan.

Please address correspondence to Joseph J. Gemmete, MD, FACR, FSIR, Departments of Radiology, Neurosurgery, and Otolaryngology, University of Michigan Hospitals, UH BID 328, 1500 E Medical Center Dr, Ann Arbor, MI 48109; e-mail: gemmete@med.umich.edu

<http://dx.doi.org/10.3174/ajnr.A3945>

Table 1: Case characteristics

Patient	Age (yr)	Sex	Possible Imaging Leak Site ^a	Possible Causes	Symptoms
1 ^b	39	F	Lower thoracic spine; L4–5	Lumbar fixation removed; Chiari s/p craniotomy; dural patch repair	Orthostatic HA
2 ^b	59	F	Mid- or lower thoracic; no definite site	Chiari s/p craniotomy, prior traumatic pelvic fracture	Orthostatic HA, cochleovestibular manifestations, personality changes, frontotemporal dementia-like picture
3	21	M	Arachnoid cyst L1–L5; L2–3	None	Orthostatic HA
4	30	M	C6–T2	None	Orthostatic HA
5 ^b	32	F	L2–3	None	Orthostatic HA
6 ^b	37	F	Cervical, thoracic, upper lumbar	Dural tear during pregnancy	Orthostatic HA
7 ^b	53	M	Multilevel cervical spine; T6–L1	Remote frontal head injury with LOC	Orthostatic HA, cochleovestibular manifestations, personality changes, memory decline, change in level of consciousness
8	22	F	Midthoracic; T12–L1	None	Orthostatic HA
9	9	F	Thoracic, lumbar, sacral	Chiari s/p craniotomy; Marfan syndrome	Orthostatic HA, nausea with emesis

Note:—s/p indicates status post; LOC, loss of consciousness; HA, headache.

^a Determined by the attending diagnostic neuroradiologist or the treating neurointerventionalist using CT or MR myelography.

^b Denotes a patient who had failed prior therapy.

Table 2: Multisite epidural blood patch procedures and outcomes^a

Patient	No. of Procedures	Access Site	Levels Injected	Volume Injected (Autologous Blood/DuraSeal) (mL/mL)	Follow-Up (mo)	Outcome ^b
1	3	L3; L3; L4	C5–L3; C5–L3; C5–L3	60/2; 55/3; 60	1	2b
2	2	L3; L3	C4–L3; C5–L3	60; 45/2	2	2c
3	1	L3	C4–L3	70	2	1
4	2	L3; L3	C3–L3; C5–L3	50; 65	1	2b
5	2	T12, L4; L4	C6–T12, L4; C3–L4	18, 20; 65	7	2a
6	5	T12, L3; L3; L2; L2; L4	C7–T12, L3; C3–L3; C3–L2; C6–L2; C6–L4	20, 18; 55; 45/0.5; 65/3; 70/3	1	3
7	2	T12, L4; L3	C7–T12, L2; C4–L3	18, 20; 60/1.5	4	2c
8	2	T12, L4; L1, L3	C5–T12, L4; C3–L1, L3	25, 20; 28, 20	2.5	2a
9	1	L4	C5–L4	50	0.25	1

^a Data from separate procedures are noted by a semicolon.

^b Outcomes: 1 = resolution without recurrence; 2a = improvement, recurrence, followed by resolution with subsequent treatment; 2b = stepwise improvement to resolution; 2c = improvement but not to resolution; 3 = transient improvement with worsening back to baseline; 4 = no improvement; 5 = worsening.

treated with a large-volume epidural blood patch to multiple sites in the epidural space through a single-catheter access site at our institution from 2010 to 2012 for the treatment of SIH. Pertinent medical records including operative notes, laboratory values, and clinical notes were reviewed and correlated with imaging (Table 1). Radiologic imaging, including CT, MR imaging, myelography, CT myelography, and MRI myelography, was reviewed. Preprocedural imaging was reviewed by attending neuroradiologists and by the procedural operators to assess possible sites of leakage before the procedure. Patient outcomes were graded on the basis of symptom response to therapy and symptom recurrence. Our grading system is further defined in Table 2.

Procedure

Patients were brought to the angiography suite and placed prone. The access site was prepped and draped in a sterile fashion. Local anesthesia was achieved by using a 2% lidocaine injection. Under fluoroscopic guidance, a 19-ga Tuohy needle was advanced into the epidural space at a spinal level (L3 was most commonly used) (Fig 1). Contrast was injected into the epidural space to confirm the position. An angled 0.035 Glidewire (Terumo, Tokyo, Japan) was advanced through the 19-gauge needle into the epidural space and extended superiorly into the midthoracic region and looped

in the epidural space (Fig 2A, -B). The needle was removed. A 4F sheath (Terumo) was then placed over the wire into the epidural space, and a 4F vertebral catheter (Cordis Sheath Terumo, Miami Lakes, Florida) was advanced over the Glidewire (Terumo). The wire and catheter were advanced superiorly to the desired level within the midcervical spine (Fig 2C). The goal was to advance the catheter in the dorsal epidural space. The wire was removed, and contrast was injected through the catheter to confirm the position in the epidural space. DynaCT (Siemens, Erlangen, Germany) was performed to confirm the catheter position when the catheter was not definitely determined to be in the epidural space (Fig 2D), given that we were injecting a large volume of blood. At this time, an aliquot of autologous blood was obtained from a previously placed intravenous access site. DuraSeal (Covidien, Irvine, California) was mixed with autologous blood in cases that had recurrent symptoms following a prior large-volume blood patch procedure. The autologous blood was injected into the epidural space while we slowly withdrew the catheter to the access site (approximately 1–2.5 mL per vertebral body level). The 4F catheter and the sheath were removed, and hemostasis was achieved with manual pressure.

An additional access site in the epidural space of the lower



FIG 1. Spot fluoroscopic image shows a 19-ga Tuohy needle at the L3 vertebral body with contrast opacifying the epidural space.

lumbar spine by using a 19-gauge spinal needle was obtained if either epidural scarring from a prior patch procedure prevented catheter advancement or if a blood patch was needed to target the lower lumbar and/or sacral regions. In these cases, a single-catheter access site was still obtained above the level of scarring to allow large-volume administration cranial to the scarring site.

RESULTS

Nine patients were identified. Twenty large-volume blood patches to multiple sites in the epidural space through a single-catheter access site were performed for the treatment of SIH. The average patient age at the time of the first procedure was 33.5 years. There were 6 women and 3 men. All patients had an orthostatic headache as one of their presenting symptoms. Twenty-two percent (2/9) of patients presented with neurocognitive decline; 56% (5/9) had undergone prior blood patch procedures with a single-site-directed injection; and all of these had either pro-

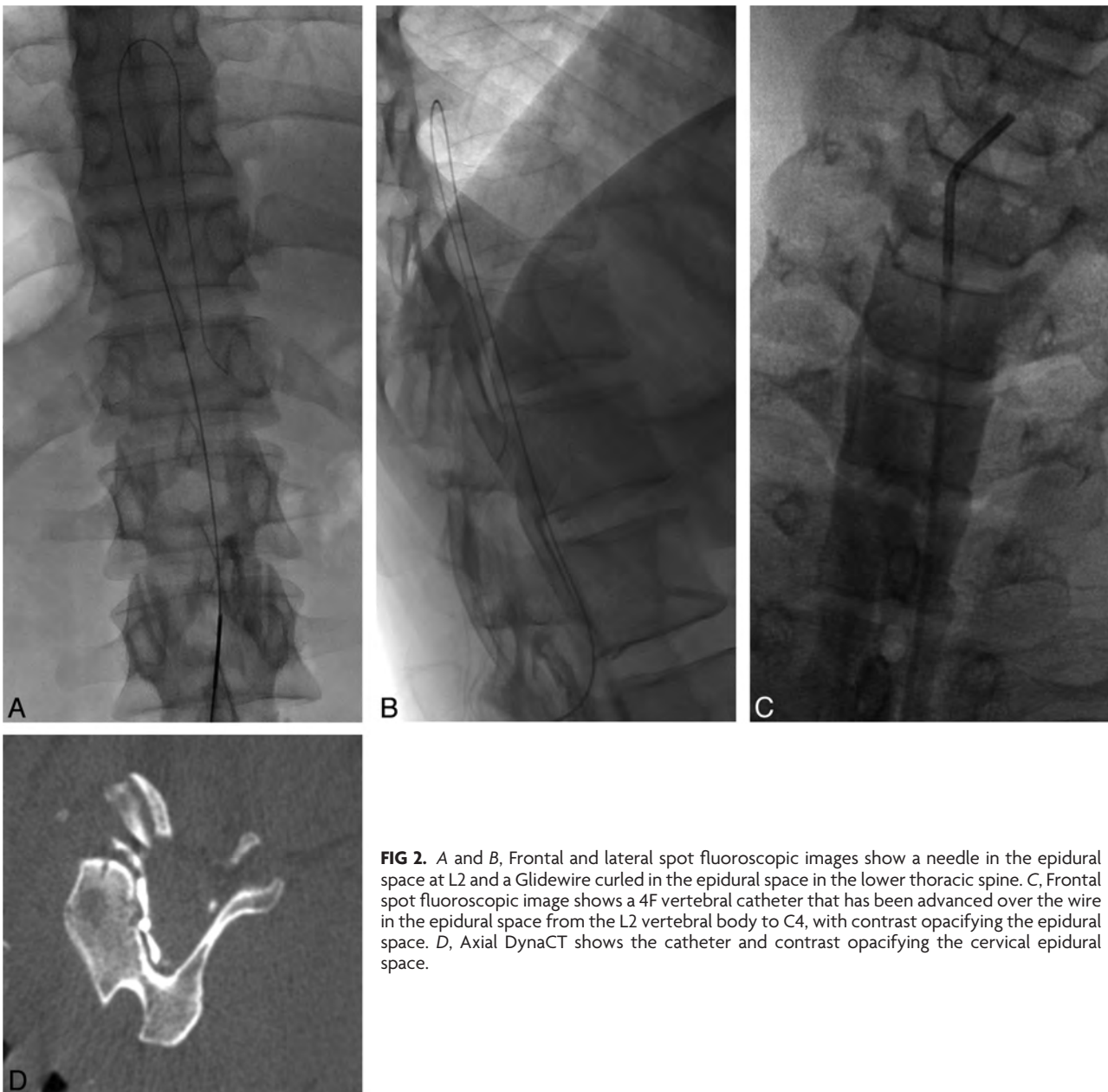


FIG 2. A and B, Frontal and lateral spot fluoroscopic images show a needle in the epidural space at L2 and a Glidewire curled in the epidural space in the lower thoracic spine. C, Frontal spot fluoroscopic image shows a 4F vertebral catheter that has been advanced over the wire in the epidural space from the L2 vertebral body to C4, with contrast opacifying the epidural space. D, Axial DynaCT shows the catheter and contrast opacifying the cervical epidural space.

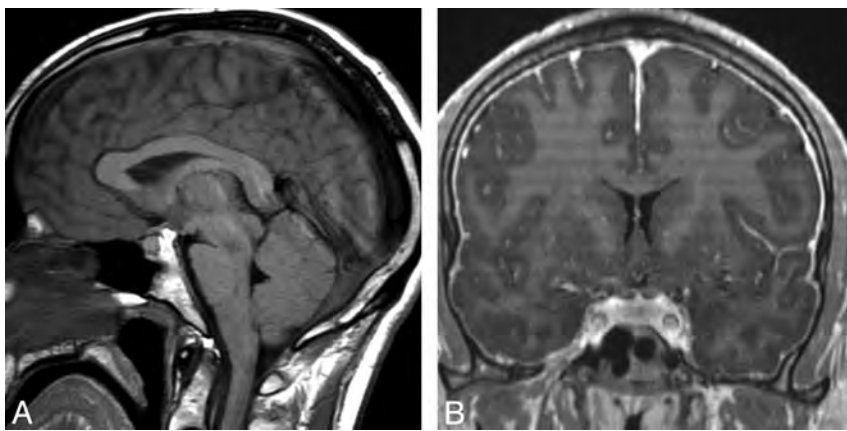


FIG 3. A, Sagittal T1-weighted MR image shows descent (“sagging” or “sinking”) of brain, enlargement of the pituitary gland, and obliteration of the cisterns. B, Coronal postcontrast T1-weighted MR image of the same patient shows diffuse pachymeningeal enhancement.

gressed back to baseline or had not improved at all. These patients were referred for our procedure because of their persistent symptoms and their desire for further management. Forty-four percent (4/9) of patients had not undergone prior traditional therapeutic measures and were referred because of an ambiguous leak site or suspicion of multiple leak sites; 78% (7/9) of patients did not have an identifiable event that caused their intracranial hypotension and symptoms. Preprocedural data for all patients are presented in Table 1.

The average number of large-volume multisite blood patch procedures per patient was 2.2 (range = 1–5). Average follow-up time after the final procedure was 2.3 months (median = 2 months; range = 0.25–7 months). The mean amount of total autologous blood injected per procedure was 54.1 mL (median = 55 mL; range = 38–70 mL). DuraSeal was used in 35% of cases (8/20). There were no significant procedural complications. Eighty-nine percent (8/9) of patients had improvement of their symptoms. One patient improved transiently but then worsened back to her baseline headache. No patients had worsening of their symptoms after the immediate postprocedural period. Eighty percent (4/5) of patients who initially did not respond to a conventional blood patch procedure improved with the multisite epidural blood patch technique. One hundred percent of patients who had failed conventional therapy required >1 multisite epidural blood patch procedure (5/5). Patient 7 had improved mental status after 2 procedures but had persistent encephalopathy and elected to undergo experimental therapy at another institution. Procedural and outcome data for all patients are presented in Table 2.

Illustrative Case

A 22-year-old woman (patient 8 from Tables 1 and 2) with a long-standing history of migraines presented with new onset of disabling orthostatic headaches for 1 month. These headaches were described as a pressure sensation of severe intensity (10/10) and located over the entire cranium. The patient also noted nausea and neck stiffness. She denied any trauma or chiropractic manipulation. She was started on caffeine and theophylline, which did not alleviate her headaches. She was later prescribed ketorolac

(Toradol) and corticosteroids, which still did not provide headache relief.

Findings of initial CT of the head were unremarkable. MR imaging of the head showed findings consistent with intracranial hypotension (Fig 3A, -B). MR imaging myelography showed multiple areas of possible CSF leak throughout the thoracic spine. The patient underwent a blood patch procedure with 20 mL of autologous blood injected into the epidural space at L4. A 4F vertebral catheter was advanced over a Glidewire from T12 to C5, and 25 mL of autologous blood was injected through the catheter via a pullback technique from C5–T12. The patient’s headaches decreased to 2/10 postprocedure but began to worsen again after

2 weeks. The patient underwent a second blood patch procedure with injection of 20 mL of autologous blood at L3 (Fig 1), a 4F vertebral catheter advanced over a Glidewire from L2 to C3, and 28 mL of autologous blood injected through the catheter by using a pullback method from C3–L2 (Fig 2A–D). In both procedures, a separate lumbar access site was used to allow increased blood patch coverage in the more caudal epidural space.

Her headaches completely resolved postprocedure and have not recurred at 3-month follow-up. MR imaging of the brain showed complete resolution of the diffuse pachymeningeal enhancement, descent (“sagging” or “sinking”) of the brain, enlargement of the pituitary gland, and engorgement of the cerebral venous sinuses (Fig 4A, -B).

DISCUSSION

In this study, we evaluated our experience with administration of a large-volume blood patch to multiple sites in the epidural space by using a single-catheter access site for the treatment of spontaneous intracranial hypotension. SIH is a multifactorial process associated with CSF leak. The hallmark symptom of SIH is an orthostatic headache, which was present in all of our patients.² Additional possible symptoms include nausea, vomiting, dizziness, tinnitus, neck pain, or radiculopathies.^{2,3} Two patients in our series presented with neurocognitive decline and behavioral changes. This presentation is rarer but has also been reported.^{4,5}

Clinical suspicion for SIH can be confirmed by demonstrating low opening pressure on lumbar puncture or with imaging.⁶ Brain MR imaging findings include diffuse pachymeningeal enhancement, descent (“sagging” or “sinking”) of the brain, subdural fluid collections, enlargement of the pituitary gland, engorged cerebral venous sinuses, and a decrease in size of the ventricles.^{6–8} Spinal imaging with CT or MR imaging can show extra-arachnoid fluid collections, extradural extravasation of fluid, meningeal diverticula, spinal dural enhancement, and engorgement of the spinal epidural venous plexus.^{6–8} In some cases, however, no definite leak site or other abnormality is identified.

Cases in which a definite leak site is not identified or those in which multiple sites are found present a therapeutic challenge.

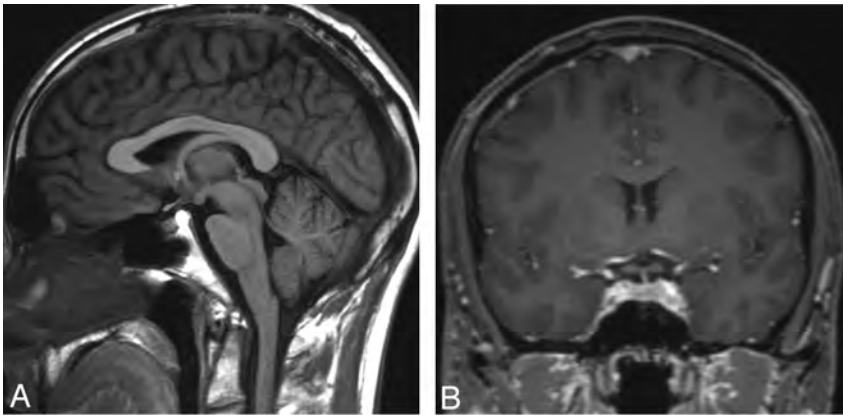


FIG 4. A, Sagittal T1-weighted MR image 6 weeks after treatment shows an image of the brain with normal findings. B, Coronal postcontrast T1-weighted MR image after treatment shows resolution of the diffuse pachymeningeal enhancement.

Most interesting, it is believed that spontaneous CSF leaks occur most often at the cervicothoracic junction or in the thoracic spine.⁹ Prior authors have reported symptomatic improvement rates ranging from 50% to 100% with site-directed epidural blood/fibrin patch procedures by using CT or fluoroscopic guidance.¹⁰⁻¹⁵ These treatment options, however, often require epidural punctures in the upper thoracic and cervical spine. Epidural puncture in these regions is technically more challenging due the anatomy and the epidural space becoming smaller as you ascend from the lumbar to the cervical region. Also, in cases with multiple leak sites, multiple punctures in the thoracic and cervical spine may be required. To address this shortcoming, Ohtonari et al¹ recently reported their experience with multiple-site epidural blood patch through a single-catheter access site in 5 patients. All their patients improved, with an average injection of 45 mL of autologous blood at multiple levels in the epidural space.

In our series, we injected an average of 54 mL of autologous blood at multiple sites in the epidural space and had an outcome similar to that of Ohtonari et al.¹ Eighty-nine percent of patients in our series had improvement or resolution of their symptoms. Furthermore, 80% (4/5) of patients in our series who had previously failed therapy with a site-directed blood and/or fibrin glue patch improved with our large-blood-volume catheter-based procedure, without recurrence to their baseline symptoms. This outcome suggests a role for this procedure in challenging or refractory cases of SIH. In 35% of our cases, we used DuraSeal in addition to the blood patch for possible added sealant properties. DuraSeal was used at the discretion of the operator, mostly in those cases that had recurred or had severe residual symptoms after large-volume blood patch. Additionally, it was used in those deemed to have an extensive CSF leak. In patients improving with large-volume blood patch and less severe residual symptoms, DuraSeal was considered unnecessary.

Because our procedure is relatively novel, the risk profile is unknown. We did not experience any significant complications in our patient population. Hypothetic complications include persistent epidural hematoma and epidural abscess with or without neurologic sequela. The authors suspect that the occurrence of these complications would be low, as evidenced in patients instrumented with epidural pain catheters. In these cases, epidu-

ral hematoma is rare, being reported in approximately 1:150,000.¹⁶ Clinically symptomatic hematoma rates are expected to be even lower.¹⁶ Similarly, epidural abscesses are rare with epidural pain catheters, reported in 1:1930 cases.¹⁷ Additionally, epidural abscesses are noted only in patients in whom the catheter remains for >3 days.¹⁷ To further decrease the rates of these complications, we recommend proper sterile technique, minimizing procedural length, and avoidance of anticoagulants in the perioperative period. Also, looping the wire and catheter in the epidural space (as displayed in the figures) before advancing them cranially should limit epidural vessel injury by avoiding

a relatively sharp leading edge. Similarly, by only placing the catheter in the dorsal epidural space, more lateral nerve root sleeves and ventral vascular structures such as the artery of Adamkiewicz and the epidural venous plexus can be avoided. An additional risk consideration is damage to suspensory ligaments of the dural sac. These play a role in supporting the spinal cord in the canal. Damage to the dorsal suspensory ligaments could cause dural leaks and has been shown to cause flexion myelopathy in animal models.¹⁸ Care should be taken to gently advance the catheter and wire and to cautiously redirect them if there is any evidence of difficulty advancing the wire or catheter in the epidural space.

Our results suggest that multisite epidural blood patch through a single catheter access site is a safe alternative to traditional site-directed epidural blood patch in patients with multiple suspected CSF leak sites or in those in whom no definite leak site is identified. In addition, our procedure may improve outcomes in patients who are refractory to traditional techniques. Our procedure provides the treating physician with an additional technique for this challenging pathology and may be technically less challenging with practice than is site-directed epidural blood patch in the thoracic and cervical spine.

Our experience is limited by the small cohort size and retrospective nature. In addition, our average follow-up was relatively short at 2.3 months. Future studies should include larger patient cohorts and longer follow-up periods.

CONCLUSIONS

Our experience supports the use of a large-volume blood patch to multiple sites in the epidural space through a single-catheter access site for the treatment of SIH, where no definite or multiple CSF leak sites are identified. Additionally, our results indicate a role for this procedure in SIH, which is refractory to traditional directed epidural patch procedures. Future studies should evaluate outcomes in larger patient populations with a particular focus on outcomes in patients who have failed prior lumbar epidural puncture procedures or leak-site-directed procedures.

Disclosures: Aditya S. Pandey—UNRELATED: Grants/Grants Pending: Covidien,* MicroVention,* Comments: industry grant support for research unrelated to the current manuscript. *Money paid to the institution.

REFERENCES

1. Ohtonari T, Ota S, Nishihara N, et al. **A novel technique of multiple-site epidural blood patch administration for the treatment of cerebrospinal fluid hypovolemia.** *J Neurosurg* 2012;116:1049–53
2. Paldino M, Mogilner AY, Tenner MS. **Intracranial hypotension syndrome: a comprehensive review.** *Neurosurg Focus* 2003;15:ECP2
3. Chung SJ, Kim JS, Lee MC. **Syndrome of cerebral spinal fluid hypovolemia: clinical and imaging features and outcome.** *Neurology* 2000;55:1321–27
4. Beck CE, Rizk NW, Kiger LT, et al. **Intracranial hypotension presenting with severe encephalopathy: case report.** *J Neurosurg* 1998;89:470–73
5. Peng PW. **Intracranial hypotension with severe neurological symptoms resolved by epidural blood patch.** *Can J Neurol Sci* 2004;31:569–71
6. Schievink WI, Maya MM, Louy C, et al. **Diagnostic criteria for spontaneous spinal CSF leaks and intracranial hypotension.** *AJNR Am J Neuroradiol* 2008;29:853–56
7. Christoforidis GA, Mehta BA, Landi JL, et al. **Spontaneous intracranial hypotension: report of four cases and review of the literature.** *Neuroradiology* 1998;40:636–43
8. Chiapparini L, Ciceri E, Nappini S, et al. **Headache and intracranial hypotension: neuroradiological findings.** *Neurol Sci* 2004;25(suppl 3):S138–41
9. Schievink WI, Meyer FB, Atkinson JL, Mokri B. **Spontaneous spinal cerebrospinal fluid leaks and intracranial hypotension.** *J Neurosurg* 1996;84:598–605
10. Berroir S, Loisel B, Ducros A, et al. **Early epidural blood patch in spontaneous intracranial hypotension.** *Neurology* 2004;63:1950–51
11. Patel MR, Caruso PA, Yousuf N, et al. **T-guided percutaneous fibrin glue therapy of cerebrospinal fluid leaks in the spine after surgery.** *AJR Am J Roentgenol* 2000;175:443–46
12. Watanabe K, Hashizume K, Kawaguchi M, et al. **Fluoroscopically guided epidural blood patch with subsequent spinal CT scans in the treatment of spontaneous cerebrospinal fluid hypovolemia.** *J Neurosurg* 2011;114:1731–35
13. Hayek SM, Fattouh M, Dews T, et al. **Successful treatment of spontaneous cerebrospinal fluid leak headache with fluoroscopically guided epidural blood patch: a report of four cases.** *Pain Med* 2003;4:373–78
14. Kranz PG, Gray L, Taylor JN. **CT-guided epidural blood patching of directly observed or potential leak sites for the targeted treatment of spontaneous intracranial hypotension.** *AJNR Am J Neuroradiol* 2011;32:832–38
15. Schievink WI, Maya MM, Moser FM. **Treatment of spontaneous intracranial hypotension with percutaneous placement of a fibrin sealant: report of four cases.** *J Neurosurg* 2004;100:1098–100
16. Horlocker TT, Wedel DJ. **Neurologic complications of spinal and epidural anesthesia.** *Reg Anesth Pain Med* 2000;25:83–98
17. Wang LP, Hauerberg J, Schmidt JF. **Incidence of spinal epidural abscess after epidural analgesia: a national 1-year survey.** *Anesthesiology* 1999;91:1928–36
18. Kimmel KT, Dayoub H, Shakir H, et al. **Spinal dural attachments to the vertebral column: an anatomic report and review of the literature.** *Surg Neurol Int* 2011;2:97–100

Target® Detachable Coil

See package insert for complete indications, contraindications, warnings and instructions for use.

INTENDED USE / INDICATIONS FOR USE

Target Detachable Coils are intended to endovascularly obstruct or occlude blood flow in vascular abnormalities of the neurovascular and peripheral vessels.

Target Detachable Coils are indicated for endovascular embolization of:

- Intracranial aneurysms
- Other neurovascular abnormalities such as arteriovenous malformations and arteriovenous fistulae
- Arterial and venous embolizations in the peripheral vasculature

CONTRAINDICATIONS

None known.

POTENTIAL ADVERSE EVENTS

Potential complications include, but are not limited to: allergic reaction, aneurysm perforation and rupture, arrhythmia, death, edema, embolus, headache, hemorrhage, infection, ischemia, neurological/intracranial sequelae, post-embolization syndrome (fever, increased white blood cell count, discomfort), TIA/stroke, vasospasm, vessel occlusion or closure, vessel perforation, dissection, trauma or damage, vessel rupture, vessel thrombosis. Other procedural complications including but not limited to: anesthetic and contrast media risks, hypotension, hypertension, access site complications.

WARNINGS

- Contents supplied STERILE using an ethylene oxide (EO) process. Do not use if sterile barrier is damaged. If damage is found, call your Stryker Neurovascular representative.
- For single use only. Do not reuse, reprocess or resterilize. Reuse, reprocessing or resterilization may compromise the structural integrity of the device and/or lead to device failure which, in turn, may result in patient injury, illness or death. Reuse, reprocessing or resterilization may also create a risk of contamination of the device and/or cause patient infection or cross-infection, including, but not limited to, the transmission of infectious disease(s) from one patient to another. Contamination of the device may lead to injury, illness or death of the patient.
- After use, dispose of product and packaging in accordance with hospital, administrative and/or local government policy.
- **This device should only be used by physicians who have received appropriate training in interventional neuroradiology or interventional radiology and preclinical training on the use of this device as established by Stryker Neurovascular.**
- Patients with hypersensitivity to 316LVM stainless steel may suffer an allergic reaction to this implant.
- MR temperature testing was not conducted in peripheral vasculature, arteriovenous malformations or fistulae models.
- The safety and performance characteristics of the Target Detachable Coil System (Target Detachable Coils, InZone Detachment Systems,

delivery systems and accessories) have not been demonstrated with other manufacturer's devices (whether coils, coil delivery devices, coil detachment systems, catheters, guidewires, and/or other accessories). Due to the potential incompatibility of non Stryker Neurovascular devices with the Target Detachable Coil System, the use of other manufacturer's device(s) with the Target Detachable Coil System is not recommended.

- To reduce risk of coil migration, the diameter of the first and second coil should never be less than the width of the ostium.
- In order to achieve optimal performance of the Target Detachable Coil System and to reduce the risk of thromboembolic complications, it is critical that a continuous infusion of appropriate flush solution be maintained between a) the femoral sheath and guiding catheter, b) the 2-tip microcatheter and guiding catheters, and c) the 2-tip microcatheter and Stryker Neurovascular guidewire and delivery wire. Continuous flush also reduces the potential for thrombus formation on, and crystallization of infusate around, the detachment zone of the Target Detachable Coil.
- Do not use the product after the "Use By" date specified on the package.
- Reuse of the flush port/dispenser coil or use with any coil other than the original coil may result in contamination of, or damage to, the coil.
- Utilization of damaged coils may affect coil delivery to, and stability inside, the vessel or aneurysm, possibly resulting in coil migration and/or stretching.
- The fluoro-saver marker is designed for use with a Rotating Hemostatic Valve (RHV). If used without an RHV, the distal end of the coil may be beyond the alignment marker when the fluoro-saver marker reaches the microcatheter hub.
- If the fluoro-saver marker is not visible, do not advance the coil without fluoroscopy.
- Do not rotate delivery wire during or after delivery of the coil. Rotating the Target Detachable Coil delivery wire may result in a stretched coil or premature detachment of the coil from the delivery wire, which could result in coil migration.
- Verify there is no coil loop protrusion into the parent vessel after coil placement and prior to coil detachment. Coil loop protrusion after coil placement may result in thromboembolic events if the coil is detached.
- Verify there is no movement of the coil after coil placement and prior to coil detachment. Movement of the coil after coil placement may indicate that the coil could migrate once it is detached.
- Failure to properly close the RHV compression fitting over the delivery wire before attaching the InZone® Detachment System could result in coil movement, aneurysm rupture or vessel perforation.
- Verify repeatedly that the distal shaft of the catheter is not under stress before detaching the Target Detachable Coil. Axial compression or tension forces could be stored in the 2-tip microcatheter causing the tip to move during coil delivery. Microcatheter tip movement could cause the aneurysm or vessel to rupture.
- Advancing the delivery wire beyond the microcatheter tip once the coil has been detached involves risk of aneurysm or vessel perforation.
- The long term effect of this product on extravascular tissues has not been established so care should be taken to retain this device in the intravascular space.

Damaged delivery wires may cause detachment failures, vessel injury or unpredictable distal tip response during coil deployment. If a delivery wire is damaged at any point during the procedure, do not attempt to straighten or otherwise repair it. Do not proceed with deployment or detachment. Remove the entire coil and replace with undamaged product.

- After use, dispose of product and packaging in accordance with hospital, administrative and/or local government policy.

CAUTIONS / PRECAUTIONS

- Federal Law (USA) restricts this device to sale by or on the order of a physician.
- Besides the number of InZone Detachment System units needed to complete the case, there must be an extra InZone Detachment System unit as back up.
- Removing the delivery wire without grasping the introducer sheath and delivery wire together may result in the detachable coil sliding out of the introducer sheath.
- Failure to remove the introducer sheath after inserting the delivery wire into the RHV of the microcatheter will interrupt normal infusion of flush solution and allow back flow of blood into the microcatheter.
- Some low level overhead light near or adjacent to the patient is required to visualize the fluoro-saver marker; monitor light alone will not allow sufficient visualization of the fluoro-saver marker.
- Advance and retract the Target Detachable Coil carefully and smoothly without excessive force. If unusual friction is noticed, slowly withdraw the Target Detachable Coil and examine for damage. If damage is present, remove and use a new Target Detachable Coil. If friction or resistance is still noted, carefully remove the Target Detachable Coil and microcatheter and examine the microcatheter for damage.
- If it is necessary to reposition the Target Detachable Coil, verify under fluoroscopy that the coil moves with a one-to-one motion. If the coil does not move with a one-to-one motion or movement is difficult, the coil may have stretched and could possibly migrate or break. Gently remove both the coil and microcatheter and replace with new devices.
- Increased detachment times may occur when:
 - Other embolic agents are present.
 - Delivery wire and microcatheter markers are not properly aligned.
 - Thrombus is present on the coil detachment zone.
- Do not use detachment systems other than the InZone Detachment System.
- Increased detachment times may occur when delivery wire and microcatheter markers are not properly aligned.
- Do not use detachment systems other than the InZone Detachment System.

Copyright © 2014 Stryker
NV00009006.AA

Trevo® XP ProVue Retrievers

See package insert for complete indications, complications, warnings, and instructions for use.

INDICATIONS FOR USE

The Trevo Retriever is intended to restore blood flow in the neurovasculature by removing thrombus in patients experiencing ischemic stroke within 8 hours of symptom onset. Patients who are ineligible for intravenous tissue plasminogen activator (IV t-PA) or who fail IV t-PA therapy are candidates for treatment.

COMPLICATIONS

Procedures requiring percutaneous catheter introduction should not be attempted by physicians unfamiliar with possible complications which may occur during or after the procedure. Possible complications include, but are not limited to, the following: air embolism; hematoma or hemorrhage at puncture site; infection; distal embolization; pain/headache; vessel spasm; thrombosis; dissection; or perforation; emboli; acute occlusion; ischemia; intracranial hemorrhage; false aneurysm formation; neurological deficits including stroke; and death.

COMPATIBILITY

3x20 mm retrievers are compatible with Trevo® Pro 14 Microcatheters (REF 90231) and Trevo® Pro 18 Microcatheters (REF 90238). 4x20 mm retrievers are compatible with Trevo® Pro 18 Microcatheters (REF 90238). Compatibility of the Retriever with other microcatheters has not been established. Performance of the Retriever device may be impacted if a different microcatheter is used. The Merci® Balloon Guide Catheters are recommended for use during thrombus removal procedures. Retrievers are compatible with the Abbott Vascular DOC® Guide Wire Extension (REF 22260).

WARNINGS

- Contents supplied STERILE, using an ethylene oxide (EO) process. Nonpyrogenic.
- To reduce risk of vessel damage, adhere to the following recommendations:
 - Take care to appropriately size Retriever to vessel diameter at

intended site of deployment.

- Do not perform more than six (6) retrieval attempts in same vessel using Retriever devices.
- Maintain Retriever position in vessel when removing or exchanging Microcatheter.
- To reduce risk of kinking/fracture, adhere to the following recommendations:
 - Immediately after unsheathing Retriever, position Microcatheter tip marker just proximal to shaped section. Maintain Microcatheter tip marker just proximal to shaped section of Retriever during manipulation and withdrawal.
 - Do not rotate or torque Retriever.
 - Use caution when passing Retriever through stented arteries.
- Do not resterilize and reuse. Structural integrity and/or function may be impaired by reuse or cleaning.
- The Retriever is a delicate instrument and should be handled carefully. Before use and when possible during procedure, inspect device carefully for damage. Do not use a device that shows signs of damage. Damage may prevent device from functioning and may cause complications.
- Do not advance or withdraw Retriever against resistance or significant vasospasm. Moving or torquing device against resistance or significant vasospasm may result in damage to vessel or device. Assess cause of resistance using fluoroscopy and if needed resheath the device to withdraw.
- If Retriever is difficult to withdraw from the vessel, do not torque Retriever. Advance Microcatheter distally, gently pull Retriever back into Microcatheter, and remove Retriever and Microcatheter as a unit. If undue resistance is met when withdrawing the Retriever into the Microcatheter, consider extending the Retriever using the Abbott Vascular DOC guidewire extension (REF 22260) so that the Microcatheter can be exchanged for a larger diameter catheter such as a DAC® catheter. Gently withdraw the Retriever into the larger diameter catheter.
- Administer anti-coagulation and anti-platelet medications per standard institutional guidelines.

PRECAUTIONS

- Prescription only – device restricted to use by or on order of a physician.
- Store in cool, dry, dark place.
- Do not use open or damaged packages.
- Use by "Use By" date.
- Exposure to temperatures above 54°C (130°F) may damage device and accessories. Do not autoclave.
- Do not expose Retriever to solvents.
- Use Retriever in conjunction with fluoroscopic visualization and proper anti-coagulation agents.
- To prevent thrombus formation and contrast media crystal formation, maintain a constant infusion of appropriate flush solution between guide catheter and Microcatheter and between Microcatheter and Retriever or guidewire.
- Do not attach a torque device to the shaped proximal end of DOC® Compatible Retriever. Damage may occur, preventing ability to attach DOC® Guide Wire Extension.



Concentric Medical
301 East Evelyn
Mountain View, CA 94041



EMERGO Europe
Molenstraat 15
2513 BH, The Hague
The Netherlands



Stryker Neurovascular
47900 Bayside Parkway
Fremont, CA 94538-6515

stryker.com/neurovascular

Date of Release: JUN/2014

EX_EN_US

Stryker Neurovascular
47900 Bayside Parkway
Fremont, CA 94538-6515

stryker.com/neurovascular
stryker.com/emea/neurovascular

Date of Release: JUN/2014

EX_EN_GL

Copyright © 2014 Stryker
NV00009028.AA



Target[®] Nano[™] DETACHABLE COILS

Beyond Soft

The softest coil technology* available, combined with Target Coil's consistently smooth deployment and exceptional microcatheter stability, results in an experience that is beyond soft. Designed to treat small spaces, the Target Nano Coil's incredible softness delivers increased conformability and shape adjustment.

Target Nano Coils—**Smooth and Stable** has never been so soft.

For more information, please visit www.strykerneurovascular.com/Target

stryker[®]
Neurovascular

*Testing performed by Stryker Neurovascular. n=3. Data are on file at Stryker Neurovascular and will be made available upon request. Bench test results may not necessarily be indicative of clinical performance.

Copyright © 2014 Stryker
NV00009006.AA

Stroke: Our Only Focus. Our Ongoing Promise.